

SALTS OF ELECTROPHILIC CATIONS AND LEWIS ACID-BASE ADDUCTS WITH WEAKLY COORDINATING ANIONS: SYNTHESIS, CHARACTERIZATION AND QUANTUM CHEMICAL CALCULATIONS

THÈSE N° 3809 (2007)

PRÉSENTÉE LE 11 JUIN 2007

À LA FACULTÉ DES SCIENCES DE BASE
INSTITUT DES SCIENCES ET INGÉNIERIE CHIMIQUES
PROGRAMME DOCTORAL EN CHIMIE ET GÉNIE CHIMIQUE

ÉCOLE POLYTECHNIQUE FÉDÉRALE DE LAUSANNE

POUR L'OBTENTION DU GRADE DE DOCTEUR ÈS SCIENCES

PAR

Ines RAABE

Diplom-Chemikerin, Universität Karlsruhe, Allemagne
et de nationalité allemande

acceptée sur proposition du jury:

Prof. P. Vogel, président du jury
Prof. I. Krossing, directeur de thèse
Prof. L. Helm, rapporteur
Prof. D. Naumann, rapporteur
Prof. M. Scheer, rapporteur



ÉCOLE POLYTECHNIQUE
FÉDÉRALE DE LAUSANNE

Suisse
2007

Die vorliegende Arbeit entstand in der Zeit von Februar 2003 bis März 2007 am Institut für Anorganische und Analytische Chemie der Universität Karlsruhe (TH), am Institut des Sciences et Ingénierie Chimiques der Ecole Polytechnique Fédérale de Lausanne und am Institut für Anorganische und Analytische Chemie der Albert-Ludwigs-Universität Freiburg i. Br. unter der Anleitung von Prof. Dr. Ingo Krossing. An Teilen der Arbeit haben Esther Birtalan und Sonja Müller im Rahmen ihrer Fortgeschrittenen- bzw. Vertiefungspraktika mitgewirkt.

Nichts ist so schlecht, als daß es nicht auch etwas Gutes hätte.

An dieser Stelle möchte ich all jenen herzlich danken, die zum Gelingen dieser Arbeit beigetragen haben:

- meinem Doktorvater Prof. Dr. Ingo Krossing für die interessante Aufgabenstellung, seine Unterstützung und Betreuung sowie seinen grenzenlosen Optimismus
- den Mitgliedern der Prüfungskommission Prof. Dr. Lothar Helm, Prof. Dr. Dieter Naumann, Prof. Dr. Manfred Scheer sowie Prof. Dr. Pierre Vogel
- meinen aktuellen und ehemaligen AK-Kollegen Dr. Andreas Reisinger, Boumahdi Benkmil, Dr. Carsten Knapp, Dr. Daniel Himmel, Fadime Bitgül, Dr. Gunther Steinfeld, Dr. Gustavo Santiso, Jelliarko Palgunadi, Dr. John Slattery, Katrin Wagner, Kristin Guttsche, Lucia Alvarez, Lutz Müller, Dr. Marcin Gonsior, Nadja Tröndle, Nils Trapp, Petra Klose, Philipp Eiden, Şafak Bulut, Tobias Köchner, Ulrich Preiss und Dr. Werner Deck für die angenehme Arbeitsatmosphäre
- Benjamin Gaertner, Gregor Stößer und Nils Trapp für die Lösung zahlreicher Computerprobleme
- Tobias Köchner und Dr. Carsten Vock für das sorgfältige Korrekturlesen der vorliegenden Arbeit
- Vera Brucksch, Monika Kayas, Gerda Probst, Sylvia Soldner und Christina Zamanos Epremian für ihren erfolgreichen Kampf gegen Verwaltung und Bürokratie
- den Gruppen von Prof. Dr. Reinhart Ahlrichs und PD Dr. Andreas Unterreiner für gewährtes „Asyl“ in Karlsruhe
- Prof. Dr. Matthias Olzmann für Rechenzeit auf seinem Cluster
- Melanie Schroeder für den „Karlsruher Geist“ in Freiburg
- Prof. Dr. Martin Kaupp für die Berechnung von relativistischen NMR-Verschiebungen
- Petra Hauser, Prof. Dr. Caroline Röhr und Dr. Rosario Scopelliti für die Hilfe bei der Durchführung und Auswertung von Röntgenstrukturanalysen

- Dr. Alain Razaname und Dr. Carsten Vock für die Aufnahme von Massenspektren
- Helga Berberich, Dr. Manfred Keller, Dr. Eberhart Matern und Sibylle Schneider für die Aufnahme von zahlreichen NMR-Spektren, Prof. Dr. Lothar Helm für seine unendliche Geduld, wenn das NMR-Gerät mal wieder nicht das tat, was es tun sollte, sowie Dr. Saša Antonijevic für die Aufnahme der Festkörper-NMR-Spektren und seinen unerschöpflichen Vorrat an Fisherman's Friend
- Dr. Gunther Steinfeld für die Durchführung der Cyclovoltammetrie-Messungen
- der Firma Iolitec für die Bereitstellung ihres Konduktometers
- Sonja Müller für ihre Arbeiten rund um CH_2I_2 und CHI_3 im Rahmen ihres Vertiefungspraktikums
- Esther Birtalan und Tobias Köchner für die gute Zusammenarbeit auf der Suche nach dem NO_2^+ -Kation
- Kalam Keilhauer, Peter Neuenschwander und Tim Oelsner für die Anfertigung und Reparatur von Glasgeräten
- den Mitarbeitern der Chemikalien- und Materialausgaben Jacques Gremaud, Gabi Kuhne, Gladys Pache und Giovanni Petrucci
- Patrick Favre und Donald Zbinden für die gelungene Wiederbelebung meines Rechners
- den Mitarbeitern der feinmechanischen Werkstätten, insbesondere Renato Bregonzi und Roger Ith für den Umbau der Handschuhbox
- den Mitgliedern der Gruppen von Prof. Dr. Hansgeorg Schnöckel und Prof. Dr. André Merbach für die angenehme Atmosphäre im 4. bzw. 3. Stock, insbesondere Petra Hauser (nicht nur für Melonen-Vernichtungsaktionen), sowie Dr. Edina Balogh und Gabriella Bodizs für ihre aufmunternden Kommentare

Meiner Familie und Helge danke ich für ihre großartige Unterstützung und dafür, daß sie immer an mich geglaubt haben.

List of Abbreviations

abbreviation	meaning
[al-f-al] ⁻	fluorine bridged aluminate [(RO) ₃ Al-F-Al(OR) ₃] ⁻ , R = OC(CF ₃) ₃
Ar ^F	fluorinated aryl group, -C ₆ H ₃ (CF ₃) ₂
BHC	Born-Haber cycle
b.p.	boiling point
br	broad
Bu	n-butyl, -C ₄ H ₉
cp	cyclopentadienyl, -C ₅ H ₅
cp*	pentamethylcyclopentadienyl, -C ₅ Me ₅
CuD	copper decomposition
d	doublet
δ	chemical shift; partial charge
DSC	difference scanning calorimetry
ε	dielectric constant
EN	electronegativity (χ)
Et	ethyl, -C ₂ H ₅
FIA	fluoride ion affinity
G	Gibbs energy, free energy
H	enthalpy
[hfip] ⁻	hexafluoroisopropoxyoxyaluminate, [Al(OC(H)CF ₃) ₂) ₄] ⁻
[hftb] ⁻	hexafluorotertbutoxyaluminate, [Al(OC(CH ₃)CF ₃) ₂) ₄] ⁻
HA	hydride affinity
IL	ionic liquid
IR	infrared
IHD	inverse halogen dependence
ⁱ Pr	isopropyl, -C(H)(CH ₃) ₂
J	coupling constant
L	ligand
LA	ligand affinity
Ln	lanthanide
m	multiplet; medium
μ	bridging ligand; absorption coefficient

abbreviation	meaning
M	Metal or metalloidal atom; central atom of a complex compound
<i>mBE</i>	mean bond enthalpy
Me	methyl, -CH ₃
m.p.	melting point
<i>MSE</i>	methyl stabilization energy
<i>PD</i>	proton decomposition
[pftb] ⁻	perfluorotertbutoxyaluminate, [Al(OC(CF ₃) ₃) ₄] ⁻
PES	potential energy surface
Ph	phenyl, -C ₆ H ₅
R ^F	fluorinated alkyl group
^t Bu	tert-butyl, -C(CH ₃) ₃
s	singlett; strong
<i>S</i>	entropy
sh	shoulder
t	triplett
<i>U</i>	energy
UV/VIS	ultra-violet / visible
<i>V_{therm} V_{ion}</i>	thermochemical volume (ion volume)
VBT	volume-based thermodynamics
w	weak
WCA	weakly coordinating anion
<i>WCE</i>	water complexation energy
<i>ZPE</i>	zero point energy

TABLE OF CONTENTS

1	Abstract / Zusammenfassung	1
2	Introduction	3
2.1	What Are Weakly Coordinating Anions (WCAs)? – A Definition	3
2.2	Different Types of WCAs	4
2.2.1	Borate-Based and Related Anions.....	4
2.2.2	Carborane-Based Anions.....	5
2.2.3	Alkoxy- and Aryloxymetallates	6
2.2.4	Teflate-Based Anions.....	8
2.2.5	AsF ₆ ⁻ , SbF ₆ ⁻ and Related Anions.....	9
2.2.6	Triflimides and Triflides	10
2.3	Applications of WCAs.....	10
2.3.1	Stabilization of Weak Lewis Acid-Base Adducts and of Highly Electrophilic Cations.....	10
2.3.2	Catalysis	11
2.3.3	Ionic Liquids (ILs)	12
2.3.4	Electrochemistry.....	12
2.3.5	Lithium Ion Batteries	12
2.3.6	Extraction of Ln(III) Ions.....	13
2.4	Available Starting Materials	13
2.5	Theoretical Considerations on the Special Properties of WCAs	15
2.5.1	Lattice Enthalpies of WCAs.....	15
2.5.2	Solubility and Solvation Enthalpies	16
2.6	Limits of WCAs: Coordination and Decomposition	19
3	Relative Stability of WCAs – A Computational Study	23
3.1	Different Anchor Points for the Evaluation of Anion Stabilities.....	24
3.1.1	Anchor Point I: Direct Calculation of the <i>FIA</i> of Al ₂ F ₆ with G2 and CBS-Q	25
3.1.2	Anchor Point II: Direct Calculation of the <i>LA</i> of [F ₃ Al-L] ⁻ with MP2/TZVPP and other Methods.....	26

3.1.3	Concepts to Analyze the Stability and Coordinating Ability of a WCA on Computational Grounds	27
3.1.4	Reactions with SiMe_3^+ and cp_2ZrMe^+	31
3.1.4.1	Reactions with SiMe_3^+	31
3.1.4.2	Reactions with Cp_2ZrMe^+	33
3.2	The Stability and Coordinating Ability of the WCAs Based on <i>LA</i>, <i>FIA</i>, <i>PD</i>, <i>CuD</i>, HOMO-Level, HOMO-LUMO-Gap and Partial Charges.	34
3.2.1	Investigations in the Gas Phase.....	34
3.2.2	Inclusion of Solvation Enthalpies	37
3.2.2.1	Gas Phase Values vs. (calculated) Solution Values: Are Solvation Energies Necessary to Evaluate the WCAs?.....	37
3.2.2.2	Relative Stabilization by Solvation	38
3.2.3	Prediction of Reactions	40
3.2.3.1	Application of the <i>LA</i> : Assessment of the WCA-Stability in the Presence of a Target Cation	40
3.2.3.2	Estimating the Success of a Fluoride Ion Abstraction Reaction: The Synthesis of $\text{FCO}^+[\text{X}]^-$ as a Target Salt.....	41
3.3	Concluding Remarks about the Stability Calculations of WCAs:.....	43
4	Depolymerization Energy and Fluoride Ion Affinity of Sb_nF_{5n} ($n = 2-4$) – A Computational Study	45
4.1	Selection of the Model: Basis Sets and Correlation Effects.....	46
4.2	Molecular Structures of Sb_nF_{5n} and $[\text{Sb}_n\text{F}_{5n+1}]^-$ ($n = 2-4$)	48
4.3	Depolymerization and Interconversion of Sb_nF_{5n} ($n = 2-4$).....	51
4.4	<i>FIAs</i> of n SbF_5 and Sb_nF_{5n} ($n = 1-4$) in the Gas Phase	53
4.5	<i>FIA</i> of n $\text{SbF}_{5(0)}$ ($n = 1-4$)	55
4.6	Standard Enthalpies of Formation $\Delta_f H^\circ$ of Sb_nF_{5n} and $[\text{Sb}_n\text{F}_{5n+1}]^-$ ($n = 1-4$).....	57
4.7	Concluding Remarks.....	57
5	Tetraalkylammonium Salts of Weakly Coordinating Aluminates.....	59
5.1	Results and Discussion	60
5.1.1	Syntheses	60
5.1.2	Solid-State Structures	62
5.1.3	Vibrational Spectra of the Aluminates	69

5.1.4	Conductivity Measurements.....	79
5.1.5	Cyclovoltammetry.....	82
5.1.6	Mass Spectrometry.....	84
5.2	Concluding Remarks.....	84
6	Weakly Bound Cationic Ag(P₄S₃) Complexes	87
6.1	Likely Bonding Sites of P ₄ S ₃ in the [Ag(P ₄ S ₃) _n] ⁺ (n = 1-3) and [Ag ₂ (P ₄ S ₃)] ²⁺ Cations from DFT Calculations	88
6.2	Syntheses and Solution NMR Characterization.....	92
6.3	Solid-State ³¹ P NMR Spectra	95
6.4	Solid-State Structures	102
6.5	On the Existence of the Ag ₂ (P ₄ S ₃) ₆ ²⁺ Dication in all Phases: a Born-Haber Cycle Investigation	109
6.6	IR and Raman Spectra	110
6.7	Concluding Remarks.....	113
7	Chemistry of Halocarbenium Ions – Theoretical and Experimental Studies.....	117
7.1	Stable Cl ₃ ⁺ Salts and Attempts to Prepare CHI ₂ ⁺ and CH ₂ I ⁺	117
7.1.1	Synthesis and NMR Characterization	117
7.1.2	Solid-State Structures	124
7.1.3	IR and Raman Spectroscopy	128
7.1.4	UV-Vis Spectroscopy of the Cl ₃ ⁺ salts.....	130
7.1.5	Fluoride Ion Affinities (FIAs) of EX ₃ ⁺⁰ and EH _n X _{3-n} ⁺⁰	132
7.1.6	Bonding in Cl ₃ ⁺ and BI ₃	133
7.1.7	Properties of CH _n X _{3-n} ⁺ (X = F-I; n = 0, 1, 2)	136
7.1.8	Stability of [pftb] ⁻ and [al-f-al] ⁻ Anions against Electrophilic Attack of CX ₃ ⁺ (X = F-I) and CH _n X _{3-n} ⁺ (n = 1, 2) Cations.....	139
7.2	Enthalpies of Formation Δ _f H° and Mean Bond Enthalpies (<i>mBEs</i>) of H _{4-n} EX _n ⁻⁰ and H _{3-n} EX _n ^{0/+} (E = C, B; X = F-I; n = 1-3) - A Computational Study	140
7.2.1	Methodology and Results.....	141
7.2.1.1	Overview and Strategy	141

7.2.1.2	Choice of the Quantum Chemical Method	143
7.2.1.3	Anchor Points	144
7.2.1.4	$\Delta_f H^\circ$ of $H_{4-n}EX_n^{0/-}$ and $H_{3-n}EX_n^{+/0}$ (E = C, B; X = F-I)	148
7.2.2	Discussion	151
7.2.2.1	Heats of Formation $\Delta_f H^\circ$:	151
7.2.2.2	Mean E-X Bond Energies (E = B, C):	154
7.2.2.3	Relative E-X Bond Strengths in the Isoelectronic $H_{3-n}CX_n^+ / H_{3-n}BX_n$ and $H_{4-n}CX_n / H_{4-n}BX_n^-$ (n = 1-3) Pairs:	156
7.3	Water Adducts of BX_3 and CX_3^+: Implications for Structure, Bonding and Reactivity.....	159
7.3.1	Structures of Free $EX_3^{0/+1}$	160
7.3.1.1	Structures of Isomers of the Water Adducts $H_2O \rightarrow EX_3^{0/+1}$	161
7.3.1.2	Structures of Related Compounds	164
7.3.2	Discussion	165
7.3.2.1	H-Bonding as a Component of the Minimum Geometries of $H_2O \cdot BX_3$	166
7.3.2.2	π -Bonding as a Structure-Determining Component of the Minimum Geometries of $H_2O \cdots CX_3^+$	168
7.3.2.3	Positive Charge as an Efficient Driving Force for π -Bond Formation	170
7.4	Exploring the Chemistry of Free Cl_3^+: Reactions with the Weak Lewis Bases PX_3 (X = Cl-I), AsI_3 and Et_2O	175
7.4.1	Syntheses and NMR Characterization.....	175
7.4.2	Solid-State Structures	178
7.4.3	Vibrational Spectra of $[X_3P-Cl_3]^+[pftb]^-$ 19, 20 and 21	181
7.4.4	Bonding in $I_3C-PX_3^+$	185
7.4.5	Further Reactivity of $I_3C-PI_3^+$: Evidence for a Non-Classical $I_2C-I \cdots PI_3^+$ Intermediate.....	190
7.5	Concluding Remarks.....	193
8	Synthesis, Characterization and Reactivity of $[NO_2]^+[pftb]^-$ 25	199
8.1	Synthesis and NMR characterization.....	199
8.2	Solid-State Structures	203
8.3	The $[NO_2]^+$ Cation as an Oxidizing Agent: The Reaction of NO_2^+ with P_4.....	207
8.3.1	Preliminary Reactions of 25 with P_4 :	208
8.3.2	Reaction of 26 with P_4 :.....	211
8.3.3	Reaction of 26 with $[Ag(P_4)_2]^+[pftb]^-$:.....	211

9	Summary and Outlook.....	213
10	Experimental Section	219
10.1	General Experimental Techniques	219
10.1.1	General Procedures and Starting Materials	219
10.1.2	NMR Spectroscopy	221
10.1.3	Vibrational Spectroscopy	222
10.1.4	Melting Point Determination.....	222
10.1.5	Mass Spectroscopy	222
10.1.6	X-Ray Diffraction and Crystal Structure Determination	222
10.1.7	Conductivity and Cyclovoltammetric Measurements.....	223
10.2	Syntheses and Characterization of the Prepared Compounds	224
10.2.1	Syntheses and Characterization of the Compounds Addressed in Chapter 5	224
10.2.1.1	Synthesis of [NBu ₄][pftb] 1	224
10.2.1.2	Synthesis of [NEt ₄][pftb] 2	225
10.2.1.3	Synthesis of [NMe ₄][pftb] 3	226
10.2.1.4	Synthesis of [NBu ₄][hftp] 4	227
10.2.1.5	Synthesis of [NEt ₄][hftp] 5	228
10.2.1.6	Synthesis of [NMe ₄][hftp] 6	229
10.2.1.7	Synthesis of [NBu ₄][hftb] 7	230
10.2.1.8	Synthesis of [NEt ₄][hftb] 8	231
10.2.1.9	Synthesis of [NMe ₄][hftb] 9	232
10.2.1.10	Synthesis of [NBu ₄][al-f-al] 10.....	233
10.2.2	Syntheses and Characterization of the Compounds Addressed in Chapter 6	234
10.2.2.1	Synthesis and Characterization of [(P ₄ S ₃)Ag[hftb]] 13.....	234
10.2.2.2	Synthesis and Characterization of [Ag ₂ (P ₄ S ₃) ₆] ²⁺ [al-f-al] ₂ ⁻ 14.....	235
10.2.3	Syntheses and Characterization of the Compounds Addressed in Chapter 7	236
10.2.3.1	Synthesis and Characterization of [Cl ₃] ⁺ [pftb] ⁻ 15	236
10.2.3.2	Synthesis and Characterization of [Cl ₃] ⁺ [al-f-al] ⁻ 16	237
10.2.3.3	Synthesis and Characterization of [Ag(CH ₂ I ₂) ₃] ⁺ [pftb] ⁻ 17	238
10.2.3.4	Synthesis and Characterization of [Ag(CH ₂ Cl ₂)(CH ₂ I ₂)] ⁺ [pftb] ⁻ 18	238
10.2.3.5	Reaction of CHI ₃ with Ag[pftb].....	239
10.2.3.6	Reaction of [Cl ₃] ⁺ [pftb] ⁻ with Et ₂ O.....	240
10.2.3.7	Synthesis and Characterization of [I ₃ C-PI ₃] ⁺ [pftb] ⁻ 19.....	241
10.2.3.8	Synthesis and Characterization of [I ₃ C-PBr ₃] ⁺ [pftb] ⁻ 20.....	242
10.2.3.9	Synthesis and Characterization of [I ₃ C-PI ₃] ⁺ [pftb] ⁻ 21	243
10.2.3.10	Synthesis and Characterization of [I ₃ C-PI ₃] ⁺ [al-f-al] ⁻ 23 and [PI ₄] ⁺ [pftb] ⁻ 24	244
10.2.3.11	Synthesis and Characterization of [I ₃ As-Cl ₃] ⁺ [pftb] ⁻ 23	244

10.2.4	Syntheses and Characterization of the Compounds Addressed in Chapter 8	245
10.2.4.1	Synthesis of $[\text{NO}_2]^+[\text{pftb}]^-$ 25.....	245
10.2.4.2	Alternative attempt to synthesize $[\text{NO}_2]^+[\text{pftb}]^-$ 25 from $\text{Li}[\text{pftb}]$ and $[\text{NO}_2]^+[\text{BF}_4]^-$ 26 in 1,2- $\text{C}_6\text{F}_2\text{H}_4$	245
10.2.4.3	Alternative attempt to synthesize $[\text{NO}_2]^+[\text{pftb}]^-$ 25 from Cl_2 , NO_2 and $\text{Ag}[\text{pftb}]$	246
10.2.4.4	Attempt to synthesize $[\text{NO}_2]^+[\text{f-alor}_3]^-$	246
10.2.4.5	Attempts to synthesize $[\text{NO}_2]^+[\text{al-f-al}]^-$	247
10.2.4.6	Reaction of $[\text{NO}_2]^+[\text{pftb}]^-$ 25 with 1.25 P_4	248
10.2.4.7	Reaction of $[\text{NO}_2]^+[\text{pftb}]^-$ 25 with 2.25 P_4	248
10.2.4.8	Reaction of $[\text{NO}_2]^+[\text{BF}_4]^-$ 26 with $[\text{Ag}(\text{P}_4)_2][\text{pftb}]^-$ and $\text{Ag}[\text{pftb}]$	249
10.2.4.9	Attempt to synthesize $[\text{P}_4\text{-NO}_2]^+[\text{BF}_4]^-$	249
10.3	Quantum Chemical Calculations.....	250
11	References	252
12	Appendix	273
12.1	List of Named Compounds	273
12.2	Appendix to Chapter 3.....	274
12.3	Appendix to Chapter 5.....	276
12.4	Appendix to Chapter 6.....	279
12.5	Appendix to Chapter 7.....	281
12.6	Crystal Structure Tables	287
12.7	Publications and Conference Contributions.....	293
12.8	Curriculum Vitae	297

1 Abstract / Zusammenfassung

Abstract:

During the last decades, weakly coordinating anions (WCAs) have become a field of great interest both in basic and applied chemistry, as – if compared to “normal” classical anions like Cl^- or SO_4^{2-} – they have a lot of unique and unusual properties, such as high solubility in low dielectric media (like CH_2Cl_2 or toluene), “pseudo gas phase conditions” in condensed phases and the stabilization of strong electrophilic cations as well as of weakly bound and low charged complexes.

Within the present thesis, several contributions to the chemistry of WCAs were made: Based on quantum chemical calculations, the stability of the most widely used WCAs have been investigated, using parameters such as the fluoride ion affinity (*FIA*), partial charges or frontier orbital energies.

One class of the WCAs, the poly- and perfluorinated alkoxyaluminates of the type $[\text{Al}(\text{OR}^{\text{F}})_4]^-$ and $[(\text{R}^{\text{F}}\text{O})_3\text{Al-F-Al}(\text{OR}^{\text{F}})_3]^-$, has been used to investigate weakly bound $\text{Ag}(\text{P}_4\text{S}_3)$ Lewis acid-base adducts and electrophilic cations: When the silver salts of fluorinated alkoxyaluminates are reacted with P_4S_3 , different structure types are found for the adducts, depending on the anion used. The dynamics of these complexes has been explored by different spectroscopic methods (IR, Raman, MAS-NMR, NMR in solution) and X-ray diffraction.

The first structurally characterized trihalocarbenium ions Cl_3^+ as salts of different aluminates have been prepared and fully characterized using various spectroscopic techniques, e.g. NMR and vibrational spectroscopy, as well as single-crystal diffraction. The Lewis acidities of the halocarbenium ions have been investigated both on experimental and theoretical grounds and they have been compared to those of the isoelectronic haloboranes.

The NO_2^+ salt of the $[\text{Al}(\text{OC}(\text{CF}_3)_3)_4]^-$ anion has been synthesized by a metathesis reaction. It has been reacted with P_4 in order to obtain naked phosphorus cations P_x^+ .

Another project was the synthesis and characterization of the tetraalkylammonium salts of the $[\text{Al}(\text{OR}^{\text{F}})_4]^-$ anions, a promising class of substances for the use in electrochemical applications in non-polar solvents.

All subjects treated experimentally within this thesis have been accompanied by quantum-chemical calculations.

Keywords: weakly coordinating anions, halocarbenium ions, Lewis acid-base adducts, quantum chemical calculations

Zusammenfassung:

Im Laufe der letzten Jahrzehnte hat sich die Chemie der schwach koordinierenden Anionen (WCAs, von engl: weakly coordinating anions) zu einem Gebiet entwickelt, das sowohl in der Grundlagenforschung als auch in der angewandten Chemie von großem Interesse ist, da diese Anionen – im Gegensatz zu den „normalen“ klassischen Anionen wie Cl^- oder SO_4^{2-} – einige einzigartige und ungewöhnliche Eigenschaften aufweisen. So sind sie beispielsweise gut in unpolaren Lösungsmitteln wie CH_2Cl_2 oder Toluol löslich, sie erzeugen „Pseudo-Gasphasen-Bedingungen“ in kondensierter Phase und sind daher in der Lage, stark elektrophile Kationen sowie schwach gebundene, niedrig geladene Komplexe zu stabilisieren.

Die vorliegende Doktorarbeit enthält einige Beiträge zur Chemie mit WCAs: Ausgehend von quantenchemischen Rechnungen wurde die Stabilität der am häufigsten verwendeten WCAs untersucht, wobei als Kenngrößen beispielsweise die Fluoridionen-Affinität (*FIA*), Partialladungen und die Energien der Grenzorbitale verwendet wurden.

Eine Klasse der WCAs, die poly- und perfluorierten Alkoxyaluminate des Typs $[\text{Al}(\text{OR}^{\text{F}})_4]^-$ und $[(\text{R}^{\text{F}}\text{O})_3\text{Al}-\text{F}-\text{Al}(\text{OR}^{\text{F}})_3]^-$ wurde dazu verwendet, um schwach gebundene $\text{Ag}(\text{P}_4\text{S}_3)$ Lewis-Säure-Base-Addukte zu untersuchen: Lässt man Silbersalze der fluorierten Alkoxyaluminate mit P_4S_3 reagieren, erhält man je nach verwendetem Anion verschiedene Strukturtypen. Zur Aufklärung der Dynamik in diesen Komplexen wurden verschiedene spektroskopische Methoden (IR, Raman, MAS-NMR, NMR in Lösung) und Röntgenbeugung eingesetzt.

Die ersten strukturell charakterisierten Trihalogencarbeniumionen Cl_3^+ wurden in Form von Salzen verschiedener Aluminate dargestellt und vollständig sowohl mit Hilfe spektroskopischer Verfahren (z. B. NMR und Schwingungsspektroskopie) als auch durch Einkristall-Diffraktometrie charakterisiert. Die Lewis-Aciditäten der Halocarbenium-Ionen wurden experimentell und theoretisch untersucht und mit denen der isoelektronischen Haloborane verglichen.

Das NO_2^+ -Salz des $[\text{Al}(\text{OC}(\text{CF}_3)_3)_4]^-$ -Anions wurde über eine Metathesereaktion dargestellt. Es wurde anschließend mit P_4 umgesetzt, um nackte Phosphorkationen (P_x^+) zu erhalten.

Ein letztes Projekt bestand in der Synthese und Charakterisierung der Tetraalkylammoniumsalze der $[\text{Al}(\text{OR}^{\text{F}})_4]^-$ -Anionen, einer vielversprechenden Substanzklasse für den Einsatz bei elektrochemischen Anwendungen in unpolaren Lösungsmitteln.

Alle experimentellen Ergebnisse, die im Rahmen dieser Doktorarbeit erhalten wurden, wurden von quantenchemischen Rechnungen begleitet.

Schlagnworte: Schwach koordinierende Anionen, Halocarbeniumionen, Lewis-Säure-Base-Addukte, Quantenchemische Berechnungen

2 Introduction

2.1 What Are Weakly Coordinating Anions (WCAs)? – A Definition

Until the late 70's, the term “non-coordinating anion” was used when a small anion like a halide was replaced by a bigger complex anion such as BF_4^- , CF_3SO_3^- , ClO_4^- , AlX_4^- or MF_6^- ($\text{X} = \text{F-I}$, $\text{M} = \text{P, As, Sb, etc.}$). But with the advances in structure determination – mainly when single-crystal X-ray diffraction became a routine method – it became obvious that also these complex anions can easily be coordinated if only partnered with a suitable counterion^[1], and therefore, the term “non-coordinating” became evidently inadequate for these anions. In the early 90's, the expression “weakly coordinating anion” (WCA) was created, which more accurately describes the interaction between those anions and their counterions, but already includes the potential of such complexes to serve as a precursor of the “non-coordinated” cation, i.e. in catalytic processes, and during the last decade, many efforts were undertaken to finally reach the ultimate goal of a truly “non-coordinating anion”. However, non-coordination is physically impossible, but due to the importance of such WCAs both in fundamental^[2-4] and applied^[5] chemistry, plenty of new, also called “superweak anions”^[6] have been developed. $[\text{B}(\text{C}_6\text{F}_5)_4]^-$ ^[7], $[\text{Sb}(\text{OTeF}_5)_6]^-$ ^[8, 9], $[\text{CB}_{11}\text{Me}_6\text{X}_6]^-$ ^[2, 10] or $[\text{Al}(\text{OC}(\text{CF}_3)_3)_4]^-$ ^[11, 12] are some of the most common examples of a new generation of rather large and chemically robust WCAs.

When can an anion be considered to be a WCA? One criterion a WCA has to meet is certainly its low coordinating ability, determined by the existence (and / or accessibility) of the remaining most basic sites of the anion. In addition the total surface charge density of those anions should be minimized with respect to the attraction of electron deficient species. Thus, it follows that the ideal WCA should have at best a univalent negative charge, and should be substituted by many electron withdrawing groups, over which the charge is dispersed. In most cases this is achieved by using F-containing substituents that build a hardly polarizable periphery. If a basic site, like the O atoms in the $[\text{Al}(\text{OR}^{\text{F}})_4]^-$ anions (R^{F} = fluorinated alkyl group), is hidden within the anion, its accessibility can be considerably reduced by using bulky groups, which provide a very important additional kinetic stabilization. Since WCAs are frequently used to stabilize very reactive electrophiles, they should only be constructed from chemically inert moieties, as a very weakly coordinating anion is of only little use, if it is unable to survive the attack of its reactive counteranion. Apparently, this goal can be achieved with various chemically robust ligands; however, the perfluorinated alkyl groups

with strong covalent C–F bonds used throughout this work gave excellent results for this type of chemistry.

2.2 Different Types of WCAs

Many different types of WCAs exist today, but all of them have in common that their negative charge is delocalized over a large area of non-nucleophilic and chemically robust moieties. The most popular WCAs are presented in this section. They are used in different applications (see below), since important factors such as coordination ability, chemical robustness, cost of synthesis and preparative accessibility vary with each application.

2.2.1 Borate-Based and Related Anions

Exchanging the fluorine atoms in the $[\text{BF}_4]^-$ anion against Ph groups leads to the well-known $[\text{BPh}_4]^-$ anion (its sodium salt is known as “Kalignost”), but this anion is still relatively strong coordinating, and its Ph groups can easily be hydrolyzed^[13]. Therefore, it is better to attach fluorinated groups like $-\text{C}_6\text{F}_5$ or $-\text{C}_6\text{H}_3-3,5-(\text{CF}_3)_2$ to the boron center, which results in the anions $[\text{B}(\text{C}_6\text{F}_5)_4]^-$ ^[7] and $[\text{B}(\text{Ar}^{\text{F}})_4]^-$ (with $\text{Ar}^{\text{F}} = \text{C}_6\text{H}_3-3,5-(\text{CF}_3)_2$)^[14, 15], which are frequently used in homogenous catalysis^[5] as well as in other applications; salts of them are also commercially available. To make these type of anions less coordinating and more soluble in non-polar solvents, the ligands were then modified, which resulted in modified $[\text{B}(\text{Ar}^{\text{F}})_4]^-$ anions like $[\text{B}((\text{C}_6\text{H}_3)-3,5-(\text{R}^{\text{F}})_2)_4]^-$ (with $\text{R}^{\text{F}} =$ perfluorinated alkyl group, e.g. $2-\text{C}_3\text{F}_7$, $n-\text{C}_6\text{F}_{13}$, $n-\text{C}_4\text{F}_9$)^[16], $[\text{B}(\text{C}_6\text{F}_4(\text{CF}_3))_4]^-$ ^[17], $[\text{B}(\text{C}_6\text{F}_4(\text{Si}(\text{Pr})_3))_4]^-$ ^[18, 19], $[\text{B}(\text{C}_6\text{F}_4(\text{SiMe}_2\text{tBu}))_4]^-$ ^[18, 19], or $[\text{B}(\text{C}_6\text{F}_4(\text{C}(\text{F})(\text{C}_6\text{F}_5)_2))_4]^-$ ^[20].

Another modification was the exchange of the Lewis acidic boron atom for aluminium or gallium, but unfortunately both compounds are prone to hydrolysis and the aluminium anion tends to be explosive^[21].

A further modification was more successful: the reaction of two equivalents of $\text{B}(\text{C}_6\text{F}_5)_3$ with a strong and hard nucleophile X^- (like CN^- ^[22, 23], NH_2^- ^[24]) resulted in dimeric, bridged $[(\text{F}_5\text{C}_6)_3\text{B}(\mu\text{-X})\text{B}(\text{C}_6\text{F}_5)_3]^-$, which are easy to prepare and surprisingly stable: The $[\text{H}(\text{OEt}_2)_2]^+[(\text{F}_5\text{C}_6)_3\text{B}(\mu\text{-NH}_2)\text{B}(\text{C}_6\text{F}_5)_3]^-$ can be stored at ambient temperature without the formation of NH_3 ^[24].

The smallest anions in the series of fluorinated borates are $[\text{B}(\text{CF}_3)_3]^-$ ^[25] and $[\text{B}(\text{CF}_3)_4]^-$ ^[26-28]. The latter one is very robust (stable against Na in liquid NH_3 and against F_2 in anhydrous HF), and very weakly coordinating: under CO pressure its silver salt coordinates this weak Lewis base to give a $[\text{Ag}(\text{CO})_4]^+$ complex^[26]. In Figure 1, structures of some of the borate-based anions addressed in this section are shown.

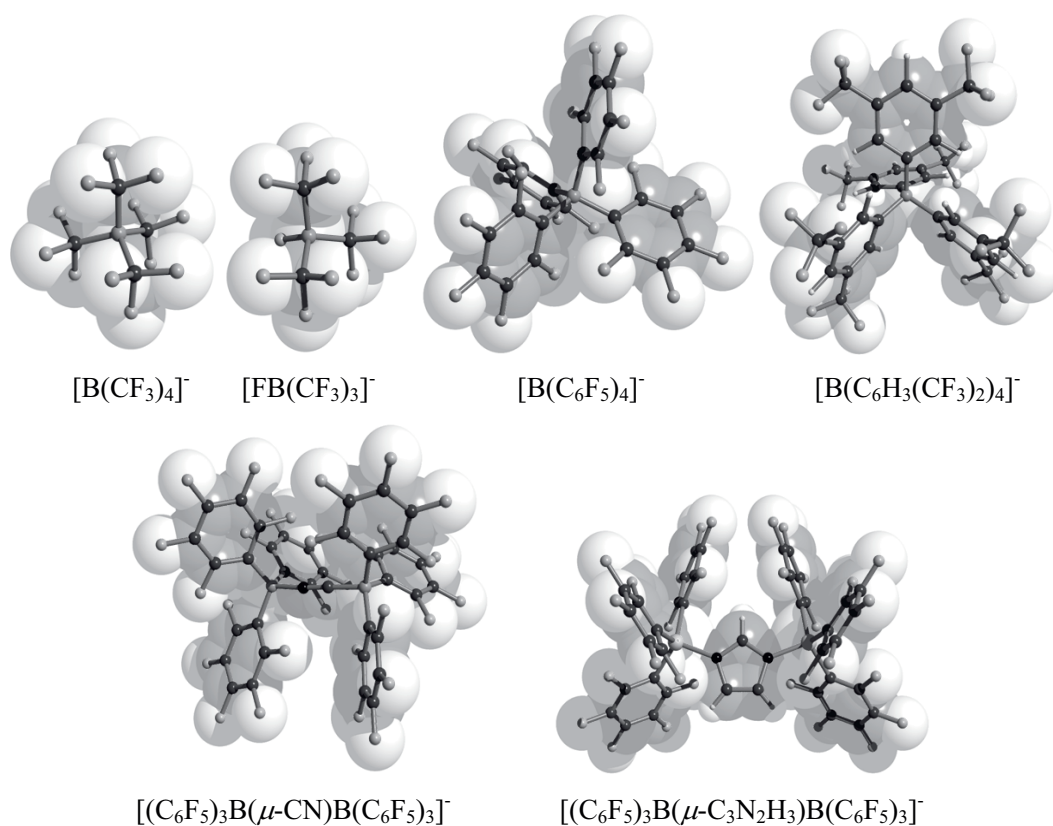


Figure 1: Structures of selected borate-based WCAs.

2.2.2 Carborane-Based Anions

These anions are derived from *closo*-boranes by exchanging one boron with a carbon atom to give $[\text{CB}_{11}\text{H}_{12}]^-$ ^[29] or $[\text{CB}_9\text{H}_{10}]^-$. Their negative charge is highly delocalized over the stable, univalent polyhedral central moiety, and their exohedral B-H bonds are very stable; however, both anions are prone to oxidation. It was shown that partial halogenation and methylation leads to a reduced stability and also to lower coordination ability. These $[\text{CB}_{11}\text{H}_6\text{X}_6]^-$ or $[1\text{-H-CB}_{11}\text{Me}_5\text{X}_6]^-$ anions ($\text{X} = \text{Cl}, \text{Br}$) developed by Stibr^[30] and Reed^[2, 10] emerged as one of the most robust type of WCAs known today, e.g. it is possible to stabilize their free Brønsted acid^[31], the H_5O_2^+ salt^[32], a free silylium ion^[33], the two fullerene cations C_{60}^+ and HC_{60}^+ ^[34],

^{35]}, an approximation of the aluminium cation AlEt_2^{+} ^[36] as well as protonated benzene^[37] and toluene^[38].

Other groups synthesized almost completely halogenated or partially methylated or ethylated^[39] carboranates, e.g. $[\text{1-H-CB}_{11}\text{X}_5\text{Y}_6]^-$ (X,Y = Cl, Br, I), $[\text{1-Me-CB}_{11}\text{H}_5\text{X}_6]^-$ (X = Cl, Br, I) or $[\text{CB}_{11}\text{Me}_{12}]^-$. Also the explosive pertrifluoromethylated $[\text{CB}_{11}(\text{CF}_3)_{12}]^-$ and the highly fluorinated $[\text{1-R-CB}_{11}\text{F}_{11}]^-$ (R = Me, Et) anions were prepared. The latter one is – according to the ²⁹Si NMR shift of its $[\text{Si}^i\text{Pr}_3]^\delta+$ derivate – the least coordinating carborane-based anion. In Figure 2, the structures of some anions of this family are shown.

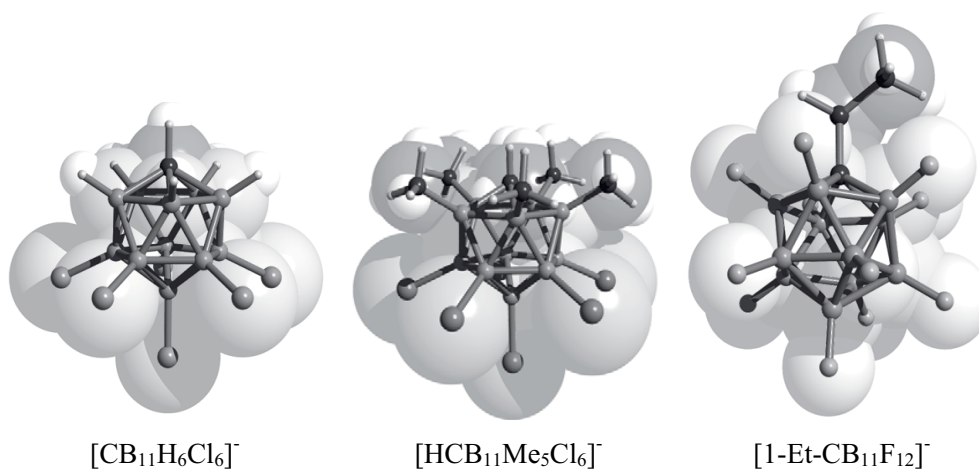


Figure 2: Structures of selected carborane-based WCAs.

Despite their chemical robustness, the carboranate anions are limited in applications, because their synthesis is very expensive and time-consuming.

2.2.3 Alkoxy- and Aryloxymetallates

These metallate anions of the general formula $[\text{M}(\text{OR}^{\text{F}})_n]^-$ and $[\text{M}(\text{OAr}^{\text{F}})_n]^-$ (R^{F} = fluorinated alkyl group, Ar^{F} = fluorinated aryl group $\text{M} = \text{Al}^{\text{III}}$, Nb^{V} , Ta^{V} , Y^{III} or La^{III}) are structural alternatives to the fluorinated tetraalkyl- and tetraarylborates described in Section 2.2.1 (Figure 3).

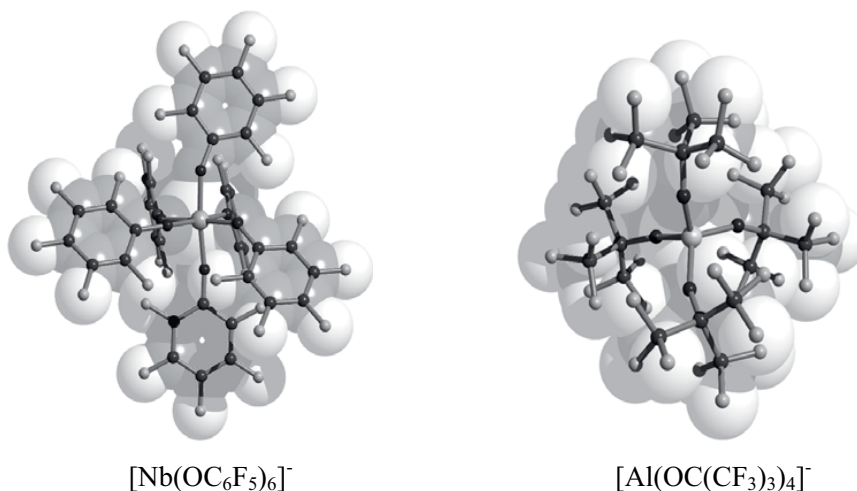


Figure 3: Structures of selected fluorinated alkoxy- and aryloxy-metallate-based WCAs.

Compared to $[\text{B}(\text{C}_6\text{F}_5)_4]^-$ and related borates, their salts are easily and safely accessible, even in larger scales. With the $[\text{M}(\text{OC}_6\text{F}_5)_n]^-$ anions, highly active catalysts for cationic polymerization reactions can be generated^[17, 40]. However, with Nb or Ta as a central atom, these anions are prone to decomposition due to OC_6F_5 abstraction by cationic zirconocene catalysts like $[\text{cp}_2\text{ZrMe}]^{+40}$.

The substitution of OAr^{F} for sterically demanding OR^{F} moieties like $\text{OC}(\text{CF}_3)_3$, $\text{OC}(\text{CH}_3)(\text{CF}_3)_2$ or $\text{OC}(\text{H})(\text{CF}_3)_2$ leads to the very stable and very weakly coordinating anions $[\text{Al}(\text{OC}(\text{CF}_3)_3)_4]^-$ (= [pftb]⁻), $[\text{Al}(\text{OC}(\text{CH}_3)(\text{CF}_3)_2)_4]^-$ (= [hftb]⁻) and $[\text{Al}(\text{OC}(\text{H})(\text{CF}_3)_2)_4]^-$ (= [hfip]⁻)^[11, 12]. Their donor-free naked Li^+ salts can be easily prepared in 200 g scale within two days in 97% yield from commercially available starting materials. In contrast to the easily hydrolyzed alkoyaluminates, the [pftb]⁻ anion is stable in nitric acid^[11], and also its Brønsted acid $[\text{H}(\text{OEt}_2)_2]^+[\text{pftb}]^-$ can be prepared in high yields^[41]. This stability against hydrolysis was attributed both to steric shielding of the oxygen atoms by the bulky $\text{C}(\text{CF}_3)_3$ moieties and to the electronic stabilization resulting from perfluorination. The following relation between the Lewis basicity of the $[\text{Al}(\text{OR}^{\text{F}})_4]^-$ anions and the pK_a value of their parent acids HOR^{F} is found: the pK_a values of $\text{HOC}(\text{H})(\text{CF}_3)_2$ (9.5) and $\text{HOC}(\text{CF}_3)_3$ (5.5) are much lower than that of the non-fluorinated $\text{HO}(\text{CH}_3)_3$ (19.3), thus, the aluminate $[\text{Al}(\text{OC}(\text{CH}_3)_3)_4]^-$ is a much stronger Lewis base than the fluorinated ones, which means that it is stronger coordinating^[12].

A systematic analysis of the solid-state contacts of several silver salts of WCAs including $[\text{B}(\text{OTeF}_5)_4]^-$ and $[\text{CB}_{11}\text{H}_6\text{Cl}_6]^-$ showed the $[\text{pftb}]^-$ anion^[11] to be at least as weakly coordinating as the $[\text{CB}_{11}\text{H}_6\text{Cl}_6]^-$ anion, which claimed the title “least coordinating anion”^[2]. Also the adducts of several weak Lewis bases to the silver salts of $[\text{pftb}]^-$, $[\text{hftb}]^-$ and $[\text{hfip}]^-$ have been prepared, such as of P_4 ^[42, 43], P_4S_3 ^[44], S_8 ^[45] or C_2H_4 ^[46], which revealed that with the least basic anion of these three – the $[\text{pftb}]^-$ – the cationic complexes do not coordinate to the anion.

The $[\text{pftb}]^-$ anion is not only very weakly coordinating, but also very robust: it is possible to prepare for example its $\text{Cl}_3^+[\text{47}]$, PX_4^+ , P_2X_5^+ , P_5X_2^+ ($\text{X} = \text{Br}, \text{I}$)^[48, 49] and $\text{AsBr}_4^+[\text{50}]$ salts. But the only disadvantage of this anions the fact that its most basic sites – the oxygen atoms – are still accessible by small, highly electrophilic cations like PX_2^+ ($\text{X} = \text{Cl}, \text{Br}, \text{I}$)^[49, 51] or SiX_3^+ ($\text{X} = \text{Cl}, \text{Br}$)^[52], which then leads to the decomposition of the $[\text{pftb}]^-$ anion and the formation of the fluorine-bridged $[\text{((CF}_3)_3\text{CO)}_3\text{Al-F-Al(OC(CF}_3)_3)]^-$ anion (= $[\text{al-f-al}]^-$).

2.2.4 Teflate-Based Anions

If the fluorine atoms in $[\text{BF}_4]^-$ or $[\text{MF}_6]^-$ are not replaced by fluorinated alkyl or aryl moieties (to give the borate-based anions described in section 2.2.1) or by fluorinated alkoxy or aryloxy groups (to obtain the alkoxy- and aryloxymetallates in section 2.2.3), but by the large, univalent OTeF_5 ligand, the teflate anions $[\text{B}(\text{OTeF}_5)_4]^-[\text{53}]$ and $[\text{M}(\text{OTeF}_5)_6]^-$ ($\text{M} = \text{As}[\text{54}]$, $\text{Sb}[\text{8, 9}]$, $\text{Bi}[\text{54}]$, $\text{Nb}[\text{8}]$) shown in Figure 4 are obtained. In these robust WCAs, the negative charge is delocalized over 20 or 30 fluorine atoms, respectively. The borate $[\text{B}(\text{OTeF}_5)_4]^-$ seems to be less stable than the other teflates; it is prone to the loss of one OTeF_5 ligand in the presence of SiR_3^+ or even $\text{Ag}^+[\text{53}]$.

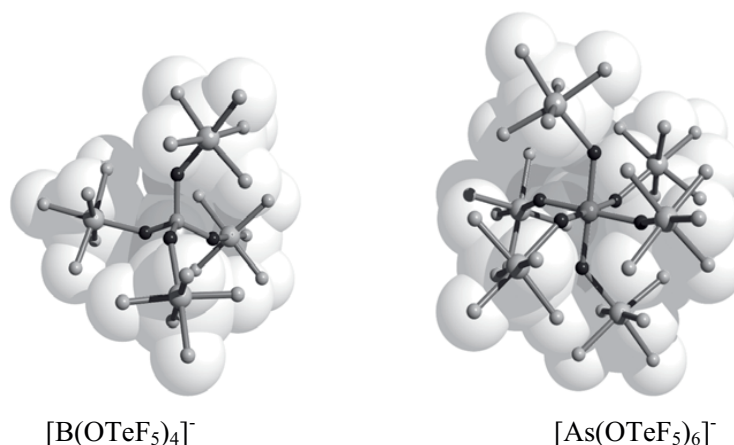


Figure 4: Structures of selected teflate-based WCAs.

All teflate-based WCAs require the strict exclusion of moisture. Nevertheless, the borate, arsenate and antimonate were used to stabilize complexes of weak Lewis bases like $[\text{Ag}(\text{CO})_2]^{+[\text{55}]}$ as well as electrophilic cations such as $\text{AsX}_4^{+[\text{56}]}$, $\text{SbX}_4^{+[\text{57}]}$ and CX_3^+ ($\text{X} = \text{Cl}, \text{Br}$)^[58].

2.2.5 AsF_6^- , SbF_6^- and Related Anions

These anions can be introduced to a system by metathesis with a $\text{M}^{\text{I}}[\text{M}^{\text{V}}\text{F}_6]$ salt. However, when working in very weakly basic media such as anhydrous HF, SO_2 , SO_2ClF or liquid SbF_5 , it is often more convenient to use the strong Lewis acid MF_5 itself to form $[\text{MF}_6]^-$ anions by F^- abstraction. With excess of MF_5 , also di-, tri- and tetrameric anions of the general formula $[\text{M}_n\text{F}_{5n+1}]^-$ are formed (selected structures are shown in Figure 5. Of those, the $[\text{As}_2\text{F}_{11}]^-$ anion has been known for a long time^[59], but was only recently structurally verified^[60, 61].

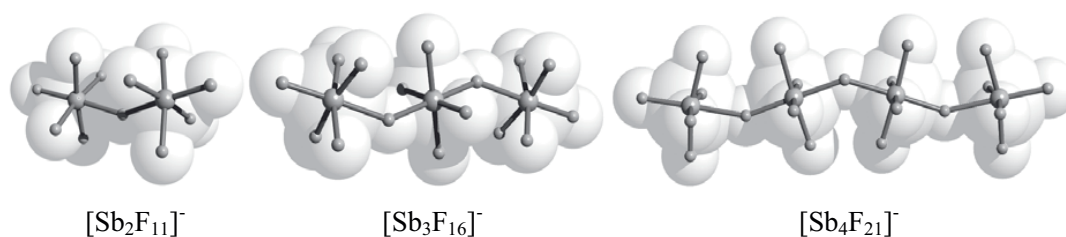


Figure 5: Structures of selected multinuclear fluoroantimonate-based WCAs of decreasing coordination power.

With the fluoroantimonate-based anions, it was possible to stabilize highly reactive cations such as $\text{Br}_2^{+ [62]}$ and $\text{Xe}_2^{+ [63]}$ as well as weakly bound adducts like $[\text{Au}(\text{Xe})_n]^+$ ($n = 1, 2^{[64]}, 4^{[65]}$). There are two problems associated with all fluorometallates, i.e. their extreme sensitivity towards moisture and the tendency to form mixtures of different $[\text{M}_n\text{F}_{5n+1}]^-$ with n from 1-4, leading to severe difficulties in crystallizing their salts.

2.2.6 Triflimides and Triflides

Two other important classes of WCAs are the triflimides $[\text{N}(\text{SO}_2\text{F})_2]^-$ and $[\text{N}(\text{SO}_2\text{CF}_3)_2]^-$ (Figure 6) – derived from bis(fluorosulfonyl) amine^[66, 67] and bis(trifluoromethylsulfonyl) amine^[66] – and the analogous triflides $[\text{C}(\text{SO}_2\text{F})_3]^-$ and $[\text{C}(\text{SO}_2\text{CF}_3)_3]^-$, which are based on the corresponding methanes^[68].

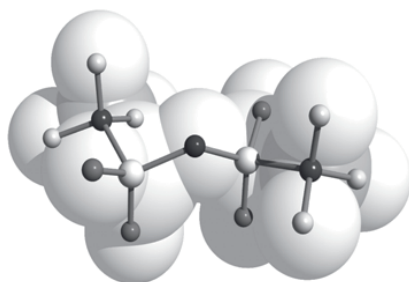


Figure 6: Structure of the $[\text{N}(\text{SO}_2\text{CF}_3)_2]^-$ anion.

These very robust anions are stable in water^[69] and generate highly active catalysts for various reactions, e. g. Diels-Alder reactions^[14, 70], Friedel-Crafts acylations^[71], and others^[72]. But the most successful fields of application of these WCAs are electrochemistry (e.g. in Li-ion batteries^[73] or as electrolytes^[74-76]) and ionic liquids^[75, 77] (see chapters 2.3.2 to 2.3.5).

2.3 Applications of WCAs

2.3.1 Stabilization of Weak Lewis Acid-Base Adducts and of Highly Electrophilic Cations

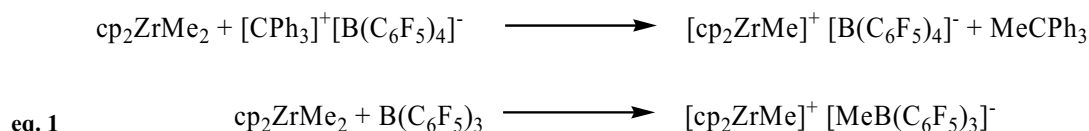
WCA allow stabilizing highly electrophilic cations and weakly bound Lewis acid-base adducts in condensed phase, so that it becomes possible to structurally characterize these highly reactive species. Some of which were before only observed in the mass spectrometer (MS) or as short-living intermediates in chemical reactions. A good example for such a

cationic complex is the $[\text{AgP}_8]^+$ cation, which was studied in the MS already in 1995^[78], but the structure of which was not known. Initial quantum chemical calculations suggested a $[\text{Ag}(\eta^1\text{-P}_4)_2]^+$ geometry to be the global minimum^[78], but only with the WCAs $[\text{pftb}]^-$ and $[\text{al-f-al}]^-$ it was possible to obtain crystals, which revealed that the two P_4 moieties coordinate over an edge to the silver^[42, 43, 52].

Other reactive cationic species stabilized by WCAs in the condensed phase were for example the complexes $[\text{Ag}(\text{C}_2\text{H}_4)_3]^+$ ^[79] or $[\text{AuXe}_4]^{2+}$ ^[64], and electrophiles like CX_3^+ ($\text{X} = \text{Cl}, \text{Br}, \text{I}$)^[47, 58], PX_4^+ , ($\text{X} = \text{F}, \text{Cl}, \text{Br}, \text{I}$)^[48, 51, 80, 81], $[\text{cp}^*\text{Si}]^+$ ^[82] or $[(\text{cp}^*)_2\text{P}]^+$ ^[83].

2.3.2 Catalysis

WCA salts can be successfully used in homogenous catalysis such as olefin polymerization processes or hydrogenation reactions^[5, 84]. Group-14-metallocene cations $[\text{cp}_2\text{M}(\text{Me})]^+$ ($\text{M} = \text{Zr}, \text{Ti}$) that are active catalysts for the Ziegler-Natta polymerization require a stable and weakly coordination counterion. Generally, the strong Lewis acid and anion generator methylalumoxane (MAO) is used, however trityl or tertiary ammonium salts of WCAs or their parent Lewis acids generate very reactive and well defined catalysts when being reacted with the metallocene^[5, 85] (see eq. 1 for exemplarily shown reactions).



It has been found that the activity of the catalyst is higher the less coordinating the anion is: $[\text{MeB}(\text{Ar}^{\text{F}})_3]^- \ll [\text{B}(\text{Ar}^{\text{F}})_4]^- < [(\text{Ar}^{\text{F}})_3\text{B-X-B}(\text{Ar}^{\text{F}})_3]^- < [(\text{Ar}^{\text{F}})_3\text{Al-X-Al}(\text{Ar}^{\text{F}})_3]^-$ ($\text{X} = \text{CN}^-$ or 1, 3-imidazoly1)^[23, 86, 87].

Li^+ catalyzed reactions like Diels-Alder- or 1,4-conjugate addition reactions or pericyclic rearrangements are traditionally performed in concentrated $\text{Li}[\text{ClO}_4]$ solutions^[88, 89]. “Naked” Li salts of WCAs can replace this potentially explosive reagent and also allow running the reactions in non-polar solvents like hexane or toluene. Some Diels-Alder reactions also use a silver ion catalyst^[89]. In a recent investigation it was shown that the air- and moisture stable $[\text{Ag}(\text{PPh}_3)]^+[\text{CB}_{11}\text{H}_6\text{Br}_6]^-$ is the best catalyst for such reaction and is also very active when only used in small amounts like 0.1 mol%^[90].

2.3.3 Ionic Liquids (ILs)

Ionic liquids (ILs) are salts with melting points below 100°C. Usually they consist of organic cations (e.g. unsymmetrically substituted imidazolium, pyridinium, ammonium or phosphonium cations, but also a few ILs with inorganic cations are known) and mostly (complex) inorganic anions like AlCl_4^- , but also WCAs^[91]. As these ILs are non-volatile, polar, non-flammable and thermally stable, they are considered as “green solvents”, and they are able to replace classical organic solvents in industrial processes such as Friedel-Crafts reactions or Diels-Alder cycloadditions. In hydrovinylation reactions, the influence of the anion in the IL was studied, and ILs with WCAs (for example $[\text{Al}(\text{OC}(\text{Ph})(\text{CF}_3)_2)_4]^-$ or $[\text{B}(\text{C}_6\text{H}_3(\text{CF}_3)_2)_4]^-$) were found to be most effective in enhancing the conversion^[92]. Also some $[\text{Al}(\text{OR}^{\text{F}})_4]^-$ ^[12, 93] and carboranate^[94] melts are known.

Recently, a method to easily determine the properties of ILs (like viscosity or conductivity) based only on the volume of the consisting anions and cations was established^[95, 96]. So it becomes possible to “design” the IL which perfectly fits the requirements of a given process.

2.3.4 Electrochemistry

In electrochemical processes like cyclovoltamperometry (CVA) or cyclovoltammetry (CV), which are usually carried out in non-aqueous media, $[\text{NR}_4]^+[\text{A}]^-$ salts ($\text{R} = \text{Me, Et, Pr, Bu}$; $\text{X} = \text{BF}_4^-, \text{PF}_6^-, \text{ClO}_4^-, \text{CF}_3\text{SO}_3^-$) are commonly used as supporting electrolytes^[97]. However, the generated oxidized species often react with the anions. Thus, new salts with a large “electrochemical window” are required, i.e. salts which are stable against oxidation and reduction. Besides, the ideal salts should be soluble in non-polar solvents like CH_2Cl_2 . Both requirements are fulfilled by quarternary ammonium salts of robust WCAs. $[\text{NBu}_4]^+[\text{B}(\text{C}_6\text{F}_5)_4]^-$ and $[\text{NBu}_4]^+[\text{B}(\text{C}_6\text{H}_3(\text{CF}_3)_2)_4]^-$ have been reported both to be very stable and to effectively solubilize the positively charged species formed in anodic processes^[98, 99]. Also the $[\text{F}_3\text{P}(\text{C}_2\text{F}_5)_3]^-$ anion is now commercially available^[100] and its salts provide higher solubility than the parent $[\text{PF}_6]^-$ salts.

2.3.5 Lithium Ion Batteries

Lithium Ion Batteries commonly use $\text{Li}[\text{PF}_6]$ as conducting salt in ethylene carbonate or propylene carbonate. However, to further increase the possible battery current, more stable

anions A^- that still generate highly conducting $Li^+[A]^-$ solutions are needed. To increase the conductivity of the Li electrolyte, both size and coordinating ability appear to be important. Therefore the ultimate $Li^+[A]^-$ electrolyte should contain a very small but very weakly coordinating WCA $[A]^-$. Additionally it should be non toxic, hydrolytically stable and easily be prepared from cheap starting materials. Likely candidates are mainly communicated in the patent literature and some of the recent small but robust candidates are $[F_{4-n}B(CF_3)_n]^-$ ($n = 2, 3, 4$)^[27], $[F_{6-n}P(CF_3)_n]^-$ ($n = 3, 4, 5$)^[101], $[F_3P(C_2F_5)_3]^-$ ^[100], and $[B(O-C(CF_3)_2-C(CF_3)_2-O)_2]^-$ ^[102].

2.3.6 Extraction of Ln(III) Ions

Lanthanide ions Ln^{III} can be extracted from HNO_3 solutions into an organic phase when partnered with a suitable extractant. It has recently been found that the distribution between the organic and the aqueous phase can be enhanced by orders of magnitude when the extractant is added as its $[B(C_6H_3(CF_3)_2)_4]^-$ salt^[103]. This anion can also be used for a selective separation of Am^{III} from Ln^{III} ions^[104].

2.4 Available Starting Materials

In Table 1, an overview of all known starting materials of the most common WCAs is given, i.e. their Li^+ , Ag^+ , M^+ , $CPh_3^+ H^+$, $[H(OEt_2)_2]^+$, $[HL_n]^+$ ($L = \text{ligand}$) and ammonium salts. If a field is marked with “-“, no simple preparation of this salt is known.

Table 1: Overview of the available starting materials for the preparation of WCA salts. R^F = fluorinated alkyl, Ar^F = fluorinated aryl.

WCA	Li^+	Ag^+	Tl^+	M^+	$[CPH_3]^+$	H^+	$[H(OEt)_2]^+$	$[H(L)_n]^+$	$[NR^1R^2R^3R^4]^{+(b)}$
$[Al(OR^F)_4]^-$	[11, 12, 105-107]	[11]	[106, 108]	$CS^+ [109]$	[109]	-	[41]	$THF^{(41)}, Me_2O^{(110)}$	[12]
$[Al(OAr^F)_4]^-$	[107]	-	-	-	[40]	-	-	-	-
$[M(OR^F)_4]^-$	$Nb^{[107, 111]}$	-	-	-	[111]	-	-	-	-
$[M(OAr^F)_4]^-$	$Nb, Ta, Y, La^{[40, 107]}$	-	-	-	$Nb, Ta, Y, La^{[40]}$	$Y, La^{[40]}$	-	-	$B^{[112]}$
$[M(OTeF_5)_n]^-$	-	$Sb, Nb, B^{[53]}$	$B^{[53]}$	$Sb:CS^+ [9], Nb, Ta:CS^+ [113]$	$Sb, Nb, B^{[53]}$	-	-	-	$As, Sb, Bi, Nb, Ta, B^{[53]}$
$[B(C_6H_3(CF_3)_2)_4]^-$	[114]	-	-	$Na^+ [114-116]$	-	-	[115, 117]	-	[118]
$[B(C_6F_5)_4]^-$	[7]	-	[119]	-	[120]	-	[121]	$L = C_6Me_5H^{[38]}$	[115, 122]
$[B(C_6F_4R)_3]^-$	$4-CF_3^{[17]}, Si^iPr, SiMe_2/Bu^{[19]}$	-	-	-	$4-CF_3^{[17]}, Si^iPr, SiMe_2/Bu^{[18, 19]}$	-	-	-	$B^{(b)}, 4-CF_3^{[17]}$
$[(F_5C_6)_3B-(\mu-X)-B(C_6F_5)_3]^{n-(c)}$	$C_6F_4^{[123]}, C_3H_3N_2^{[124](f)}$	-	-	$Na^+, NH_2^{[24]}$	$NH_2^{[24]}, CN^- [22, 23]$	-	$NH_2^{[24]}, C_3H_3N_2^{[124](f)}$	-	-
other borates	$[B(CF_3)_4]^{[26]}$	$[B(CF_3)_4]^- [26]$	-	$K^+, Cs^+, [B(CF_3)_4]^{[26]}$	$A^{[87, 125](g)}$	-	$A^{[126](g)}$	-	-
$[1-H-CB_{11}R_5X_6]^{-(a)}$	-	[127-129]	-	$Na^+ : C^{(i)}, CS^+ [30, 129]$	[128, 129]	[10, 34, 37, 38]	[130]	$C_6H_6^{[10, 34, 37, 38]}, Ph_2CO, PhNO_2^{[130]}$	[94]
$[CB_{11}R_nX_{12-n}]^{-(c)}$	[131]	[132-134]	[131]	$CS^+ [134-136], K^+, Rb^+, Cs^+ [131]$	[134]	[137]	[137]	[32, 137]	[132, 133]
$[CB_9R_nX_{10-n}]^{-(c)}$	-	[132]	-	$CS^+ [132]$	[132]	[137]	[137]	[137]	[132]
$[CB_{11}R_nF_{12-n}]^{-(d)}$	-	[138]	-	$CS^+ [138]$	[138, 139]	-	-	-	[138]

^(a) $R = H, Me; X = Cl, Br, I$. ^(b) $R^1-R^4 = H, Me, Et, Ph$, etc., also imidazolium salts for ionic liquids. ^(c) $R = H, Me, CF_3$. ^(d) $R = H, Me, Et$. ^(e) $\mu-X$ = bridging ionic ligand, such as CN^- , imidazolyl, NH_2 , C_6F_4 , etc. $n = 1, 2$. ^(f) Also $X = 4,5$ -dimethylimidazole and benzimidazole. ^(g) $A = [C_6F_4-1,2-(B(C_6F_5)_2)(\mu-X)]^-$ with $X = F, OMe, OC_6F_5$. ^(h) $B = [B[(C_6F_4-4-C(C_6F_5)_2F)_4]]^-$. ⁽ⁱ⁾ $C = [B(C_6H_3-3-5(C_6F_5)_2)_4]^-$.

2.5 Theoretical Considerations on the Special Properties of WCAs

Why is it possible to stabilize highly reactive cationic species that have only been observed in the gas phase, using a WCA as a counterion? In this section, the special properties of WCAs will be explained using thermodynamic approaches like Born-Haber cycles (BHC) and volume-based thermodynamics (VBT): that is to understand how the WCAs “work” and which kind of cation-anion interactions occur in the solid state and in solution.

2.5.1 Lattice Enthalpies of WCAs

The most important value that influences the properties of any given salt (like its melting point, solubility, etc.), is the value of its lattice enthalpy $\Delta_{\text{latt}}H$. By definition, $\Delta_{\text{latt}}H$ is the enthalpy that is needed to separate one mole of the ions of a solid salt into its constituting ions and to bring them to infinite separation. Since according to the empirically found Kapustinskii equation (eq. 2)^[140] the lattice energies $\Delta_{\text{latt}}U$ are inversely proportional to the sum of the ionic radii (or volumes if the modified Jenkins equation (eq. 3)^[141] is used), the lattice enthalpies of WCA salts are very low. In Table 2, the lattice energies U_{latt} of salts with different thermochemical volumes V_{therm} are listed.

eq. 2

$$\Delta_{\text{latt}}U = -\frac{12000 \cdot n \cdot z^+ \cdot z^-}{r^+ + r^-} \cdot \left(1 - \frac{34.5}{r^+ + r^-}\right) \text{ in kJ/mol}^{[140]}$$

eq. 3

$$\Delta_{\text{latt}}U = z^+ \cdot z^- \cdot n \cdot \left(\frac{\alpha}{V_{\text{therm}}^3} + \beta\right) \text{ in kJ/mol}^{[141]}$$

In eq. 2 and eq. 3, r^+ and r^- are the ionic radii of the ions, n is the number of ions in the formula unit, z^+ and z^- are the charge of the ions, α and β are empirically found constants.

Table 2: Thermochemical volumes (V_{therm} in \AA^3) and lattice potential enthalpies ($\Delta_{\text{latt}}U$ in kJ/mol) of several M^+A^- salts.

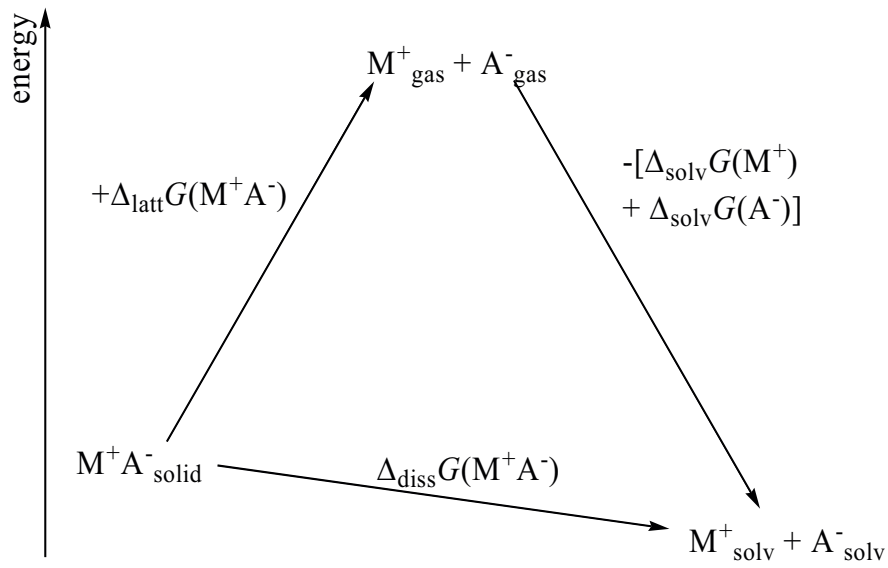
	$V_{\text{therm}} [\text{\AA}^3]$	$\Delta_{\text{latt}}U [\text{kJ/mol}]$
Li^+F^-	27	1036 ^(a)
Cs^+F^-	43	740 ^(a)
$\text{Cs}^+[\text{AsF}_6]^-$	128	568 ^(b)
$\text{Cs}^+[\text{pftb}]^{-(c)}$	776	362 ^(b)
$[\text{Ag}(\text{S}_8)_2]^+[\text{pftb}]^{-(c)}$	1169	326 ^(b)

^(a) experimental value^[142]. ^(b) calculated from the V_{therm} .^[141] ^(c) $[\text{pftb}]^- = [\text{Al}(\text{OC}(\text{CF}_3)_3)_4]^-$.

Compared to classical salts like LiF or CsF, in which a strong electrostatic field is created, in the $[\text{pftb}]^-$ salts the environment of the ions closer resembles the situation in the gas phase (or to that of a molecular solid like C_{60}). Therefore, the electrostatic interactions between cations and anions are minimized up to a point where they approximate gas-phase conditions or, more precisely, where they resemble the interactions between the neutral species in a molecular solid. This fact allows the stabilization of highly reactive gas-phase cations with WCAs owing to the “pseudo gas-phase conditions” in the solid state.

2.5.2 Solubility and Solvation Enthalpies

Also in solution, the “pseudo gas-phase conditions” are present, since the solvation free energy $\Delta_{\text{solv}}G$ in solution plays a similar role to $\Delta_{\text{latt}}G$ in the solid state. A salt is soluble if $\Delta_{\text{solv}}G$ is larger than $\Delta_{\text{latt}}G$ (see Born-Haber cycle in Scheme 1), so $\Delta_{\text{diss}}G$ becomes negative. If the anion is very large, $\Delta_{\text{latt}}G$ is small; that’s the reason why WCA salts are generally soluble even in rather non-polar solvents like CH_2Cl_2 ($\epsilon = 8.93$) or toluene ($\epsilon = 2.2$).



Scheme 1: Born-Haber cycle for a soluble M^+A^- salt.

$\Delta_{\text{solv}}G$, which is depending on the dielectric constant ε of the solvent, can be calculated from the Born equation (eq. 4):

eq. 4

$$\Delta_{\text{solv}}G = \frac{1}{2} \left(\frac{z^2 \cdot e \cdot N_A}{4 \cdot \pi \cdot \varepsilon_0 \cdot r} \right) \left(1 - \frac{1}{\varepsilon} \right)$$

In this equation, z is the charge of the ion, e is the charge of an electron, N_A is the Avogadro constant, ε_0 is the dielectric constant of the vacuum and r is the ionic radius. From Figure 7, it can be seen that the effect of decreasing the dielectric constant of the solvent on $\Delta_{\text{solv}}G$ is stronger for non-polar solvents.

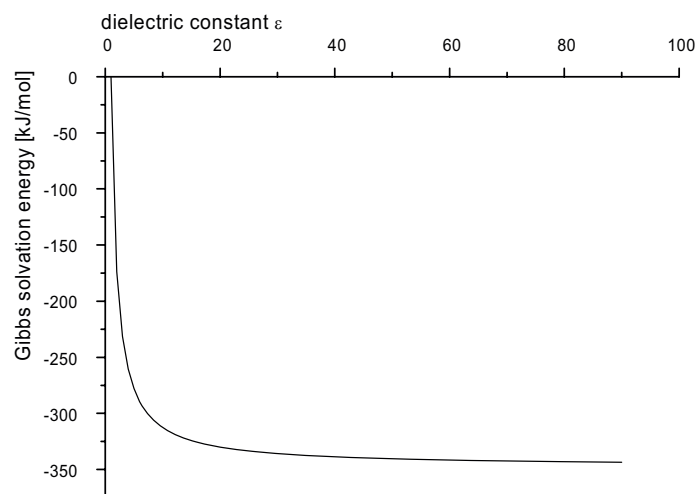


Figure 7: Plot of the free solvation energy $\Delta_{\text{solv}}G$ calculated with the Born equation for a univalent ion with a radius of 200 pm versus the dielectric constant of the solvent.

In Figure 8, these considerations are summarized: It can be seen that the solvation and lattice energies decrease rapidly with increasing size of the ions. The shapes of solvation and lattice energy curves differ: With increasing size of the anion the solvation energies relatively soon reach a plateau region and remain almost constant while the lattice energy decreases more steadily with increasing anion size. The less polar the solvent, the later the intersection of the solvation energy with the lattice energy curve, which marks the change from insoluble to soluble, is observed. This indicates that only very large anions X^- with a volume of larger than approximately 890 \AA^3 induce a sufficiently low lattice energy to dissolve salts A^+X^- in toluene (dashed vertical line in Figure 8). In more polar solvents such as CHCl_3 or CH_2Cl_2 the rough minimum size of the anion has to be less, that is 120 \AA^3 or 60 \AA^3 (dashed vertical lines in Figure 8). In agreement with this $\text{K}[\text{Al}(\text{OR})_4]$ ($V_{\text{therm}} = 762 \text{ \AA}^3$) is slightly soluble in toluene but $\text{K}[\text{BF}_4]$ ($V_{\text{therm}} = 77 \text{ \AA}^3$) only in CH_2Cl_2 . Of course these values should not be taken absolute and suffer from an exact evaluation of solvation effects, dispersion energies, temperature effects etc.; however, the general trend holds: large WCAs lead to salts soluble in low dielectric solvents that often are also soluble at very low temperatures.

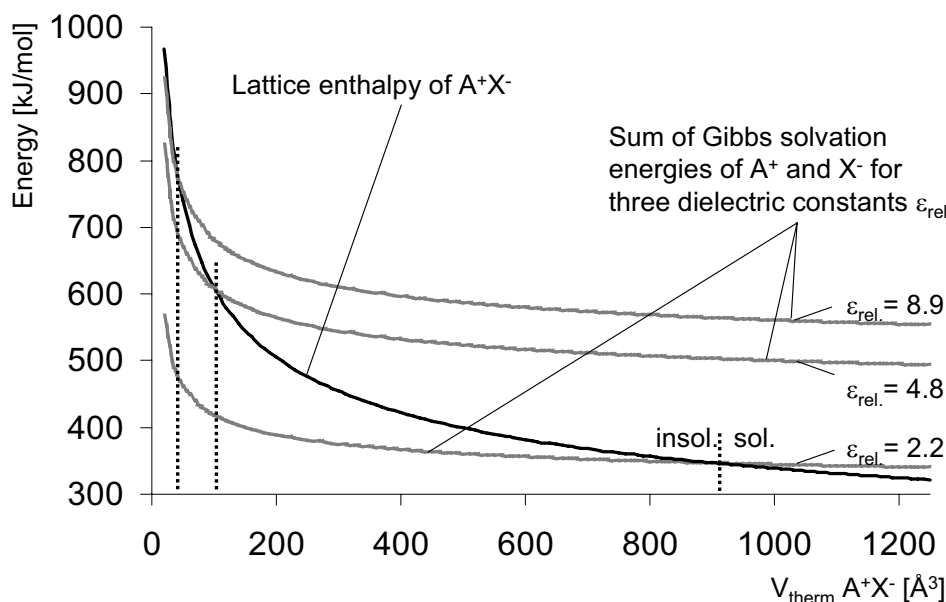


Figure 8: Plot of $\Delta_{\text{latt}}U$ and $\Delta_{\text{sol}}G$ (in different solvents with $\epsilon = 2.2$ (toluene), 4.8 (CHCl_3) and 8.9 (CH_2Cl_2)) of a M^+A^- salt versus its thermochemical Volume V_{therm} . The ionic radius of the cation M^+ was kept constant at roughly that of a K^+ cation (2.0 Å), and the ionic radius of the anion was changed from very small (halide) to very large (large WCA).

2.6 Limits of WCAs: Coordination and Decomposition

WCAs can be used for many different types of applications, but there are also two major limits: coordination and decomposition. Given the right cation, all WCAs can coordinate with its most basic site, like a chain breaking at its weakest link. Two prominent examples of such a coordination are $[\text{SiR}_3]^+$ and $[\text{AlR}_2]^+$ cations ($\text{R} = \text{Me}, \text{Et}, i\text{Pr}$), which decompose almost every WCA. The exception are the halogenated carboranates and the heteroleptic aluminate $[\text{F-Al}(\text{O}(\text{C}(\text{CF}_3)_3)]^{[143]}$, with which they form coordination complexes $\text{R}_3\text{Si}^{\delta+}\text{-WCA}^{\delta- [33, 128, 144]}$ and $\text{R}_2\text{Al}^{\delta+}\text{-WCA}^{\delta- [36]}$ (Figure 9). These species are called “ion-like”, because although they are molecules, the Si-WCA resp. the Al-WCA distance in the solid state is rather long, and in solution, there is some evidence that the properties of the cations are partially retained.

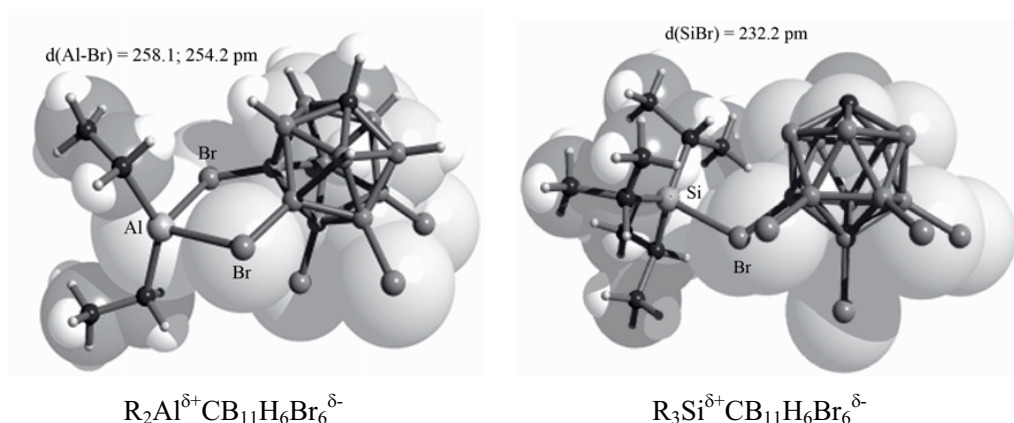


Figure 9: Molecular, „ion-like“ coordination compounds.

Also other WCAs, like the widely used $[B(C_6H_3(CF_3)_2)_4]^-$ anion, are prone to η^3 , η^4 or even η^6 coordination of the aromatic ligands, if the countercations are highly electrophilic and small enough to fit between the rings, like Rh^I or Ag^I .

The $[Sb_2F_{11}]^-$ anion can also be coordinated by a suitable electrophilic cation like Au^{2+} . Thus, upon evacuation of $[AuXe_4]^{2+}[Sb_2F_{11}]_2$, partial loss of Xe is observed, and the molecular compound $[AuXe_2(Sb_2F_{11})_2]$ containing coordinated $[Sb_2F_{11}]^-$ ions forms (Figure 10).

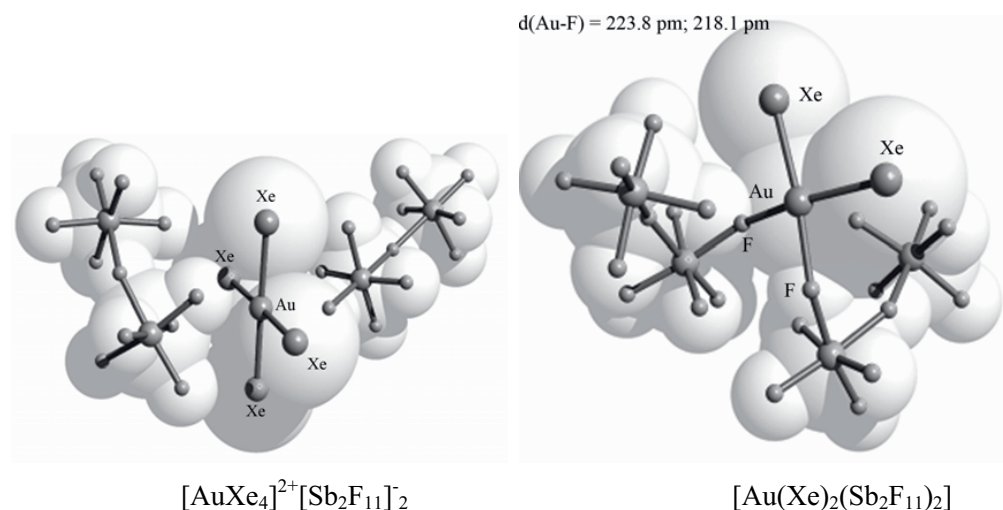
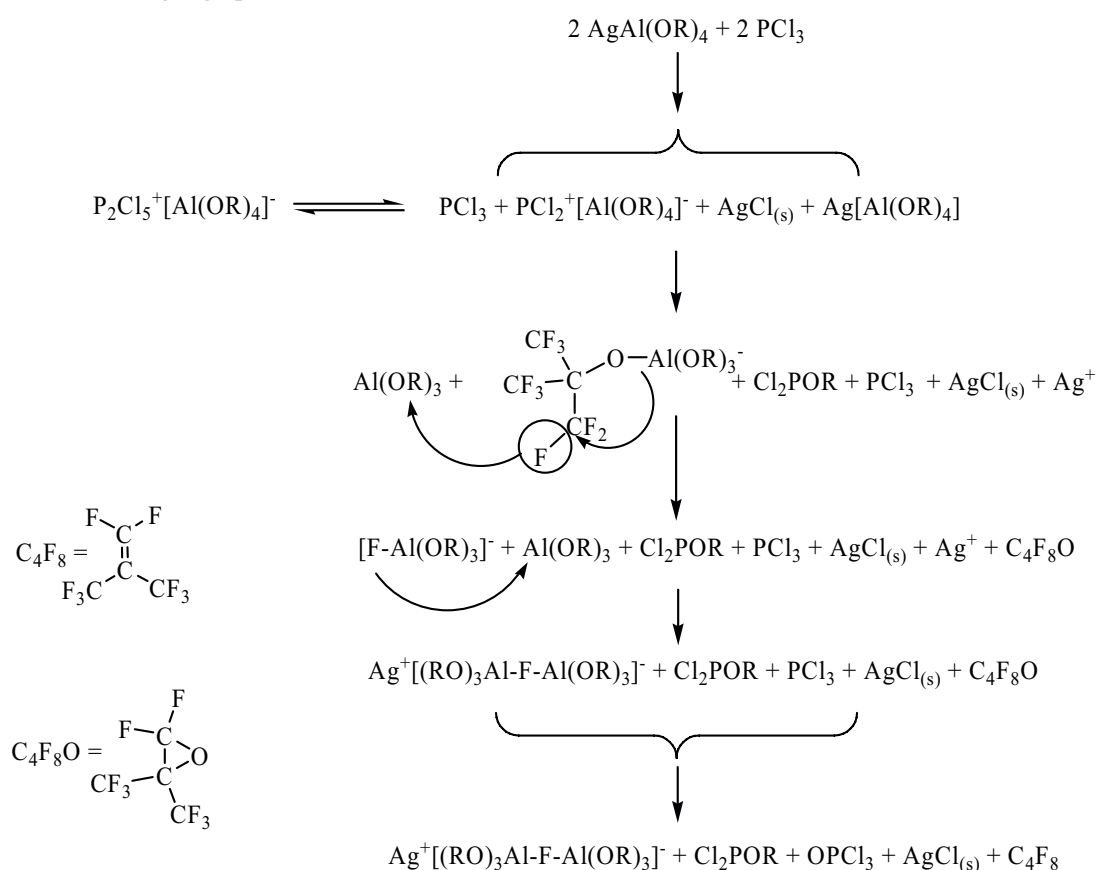


Figure 10: Comparison of salt formation in $[AuXe_4]^{2+}[Sb_2F_{11}]_2^-$ and ion coordination in $[Au(Xe)_2(Sb_2F_{11})_2]$.

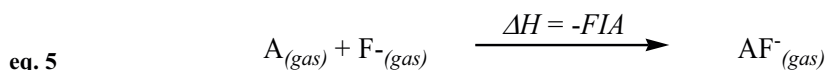
Anion coordination can be the starting point for the degradation of the WCA provided that the (may be only transient) counteranion is reactive enough to induce the decomposition. Often decomposition can be slowed down or even hindered by working at low temperatures. In general the following rule can be applied: solid compounds are less sensitive towards decomposition than WCA-salts in solution. But such decomposition reactions are not necessarily a disadvantage, like the formation of the salt $[(C_6F_5)Xe]^+[F_2B(C_6F_5)_2]^-$ starting from XeF_2 and $B(C_6F_5)_3$ ^[145]. Sometimes anion decomposition also opens the door to a new, very promising anion. This has been the case for the [al-f-al]⁻ anion, which was discovered when reacting $Ag^+[pftb]^-$ with SiX_4 or PX_3 ($X = Cl, Br$)^[52] (Scheme 2).



Scheme 2: Hypothetical mechanism for the formation of the [al-f-al]⁻ anion^[52] ($R = C(CF_3)_3$).

3 Relative Stability of WCAs – A Computational Study

One question that is still open to discussion is a reliable ordering of the relative stabilities and coordinating abilities of all types of WCAs known today. Earlier attempts used the ^{29}Si -NMR shift of the $\text{Si}(\text{iPr})_3^{\delta+}\text{X}^{\delta-}$ silylium ion pair ($\text{X} = \text{WCA}$) as a measure with shifts at lower field indicating a higher cationic character of the $\text{Si}(\text{iPr})_3^{\delta+}$ part which is an indication for a less coordinating anion $\text{X}^{-[10]}$. However, inertness and coordinating ability of WCAs do not always come hand in hand and, therefore, the reactive nature of the $\text{Si}(\text{iPr})_3^{\delta+}$ part precludes the investigation of many anions that else proved to be very weakly coordinating due to anion decomposition (for example all fluorometallates and teflate based anions). A very recent publication by C. A. Reed *et al.*^[146] evaluates the N-H stretching vibration of a series of $(n\text{-oct})_3\text{N-H}^+[\text{X}]^-$ ammonium salts in CCl_4 solution ($\text{X} = \text{WCA}$) on the basis of the following assumption: The higher the frequency of the stretching vibration, the less the anion interacts with the cation and the more weakly coordinating is $[\text{X}]^{-[146]}$. This scale gives an ordering of the relative coordinating ability of the WCA towards the $(n\text{-oct})_3\text{N-H}^+$ cation in CCl_4 solution. To investigate the stabilities of fluorometallate anions such as BF_4^- , MF_6^- ($\text{M} = \text{P}, \text{As}, \text{Sb}, \dots$), the fluoride ion affinities (*FIAs*) of their parent Lewis acids A , that are BF_3 , MF_5 etc., were estimated on thermodynamic grounds (eq. 5)^[141, 147].



The higher the *FIA* of the parent Lewis acid A of a given WCA, the more stable it is against decomposition on thermodynamic grounds. K.O. Christe and D. Dixon chose a computational approach to obtain a larger relative Lewis acidity scale based on the calculation of the *FIA* in an isodesmic^[i] reaction with $[\text{OCF}_3]^-$ and the experimental *FIA* of OCF_2 of 209 kJ/mol^[148]. Others used the same methodology^[11, 108, 149-152]. Hitherto, this approach was limited to relatively small systems.

In this study, an entirely computational approach has been chosen, in order to allow for a comparison of the properties of very different types of WCAs, such as the fluoroantimonates with the perfluoroarylborates. The structures of WCAs of type $[\text{M}(\text{L})_n]^-$ ($\text{L} = \text{monoanionic ligand}$), their parent Lewis acids $\text{A} = \text{M}(\text{L})_{n-1}$ as well as the $\text{A-F}^- = [\text{F-M}(\text{L})_{n-1}]^-$ anions were optimized with DFT methods at the (RI-)BP86/SV(P) level. With these calculated data and

^[i] isodesmic reaction: number and type of bonds are not changed.

auxiliary (RI-)MP2/TZVPP, G2 and CBS-Q calculations, the thermodynamic stability and coordinating ability of the WCAs was established based on the ligand affinity LA of the parent Lewis Acid $A = M(L)_n$, the FIA of the parent Lewis acid A as calculated with Christe's and Dixon's methodology^[148], the decomposition of a given anion in the presence of a hard (H^+ , proton decomposition PD) and a soft electrophile (Cu^+ , copper decomposition CuD), the position of the HOMO as well as the HOMO-LUMO gap and population analyses of the anions providing partial charges for all atoms. All these calculations were done in the gas phase. To include media effects the decomposition reactions of a subset of 14 WCAs with the most simple silylium ion, $SiMe_3^+$, and the prototype of a metallocene catalyst for olefin polymerization, Cp_2ZrMe^+ , were also calculated in the typically employed solvents Ph-Cl and 1,2- $F_2C_6H_4$ (COSMO solvation model). Figure 11 gives an overview of all larger WCAs investigated in this study.

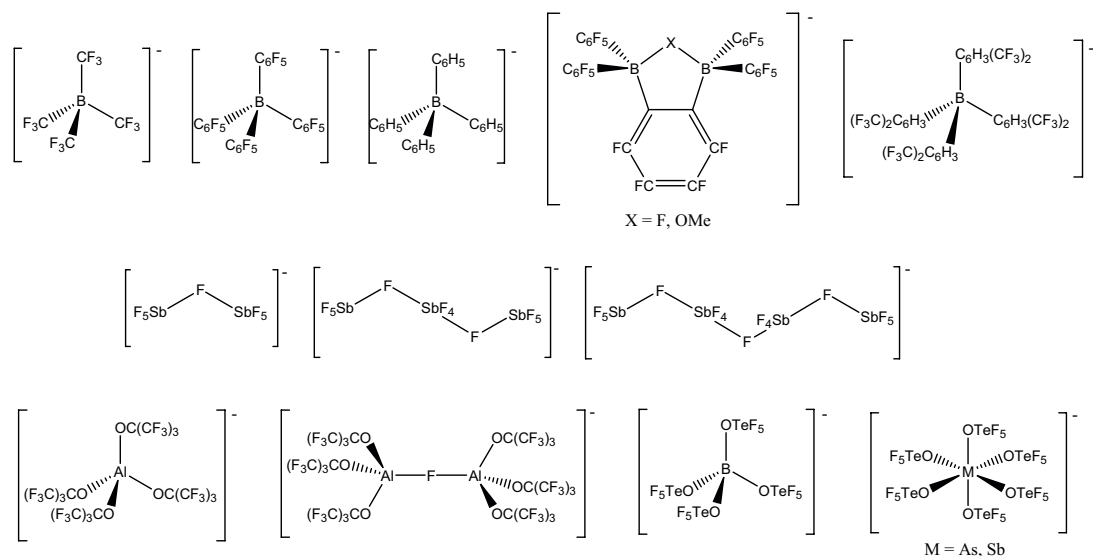


Figure 11: Overview of the larger WCAs investigated in this study.

3.1 Different Anchor Points for the Evaluation of Anion Stabilities

The size of the necessary computations with anions containing up to 87 heavy atoms (excluding H) only allowed the use of DFT theory to establish the properties of these species. To obtain data that is more reliable, the assessed quantities were calculated through isodesmic reactions. If some parts of the calculations could not be done isodesmic, higher levels such as MP2/TZVPP, G2 or CBS-Q were selected to obtain reliable values for these reactions.

3.1.1 Anchor Point I: Direct Calculation of the *FIA* of Al_2F_6 with G2 and CBS-Q

To obtain a reliable anchor point for the calculation of the *FIA* of compounds with fluoride bridges, the structures and total energies of AlF_3 (D_{3h}), AlF_4^- (T_d), Al_2F_6 (D_{2d}), OCF_2 (C_{2v}) and OCF_3^- (C_{3v}) were calculated at the G2 and CBS-Q compound levels (Table 1; total energies, structural parameters and comment in the appendix 12.2). For comparison, also the MP2/TZVPP results are included. With these results, the standard enthalpies of reaction for the formation of AlF_4^- and Al_2F_7^- from AlF_3 , 2 AlF_3 and Al_2F_6 were calculated. For comparison with experimental data^[153], also the standard enthalpies for the reaction of the formation of Al_2F_7^- from AlF_3 and AlF_4^- as well as the dissociation of Al_2F_6 giving 2 AlF_3 were assessed (Table 3).

Table 3: Standard enthalpies of reaction ΔH° and reaction energies $\Delta U(0K)$ for the formation Al_2F_7^- and related species in kJ/mol. Experimental enthalpies of reaction ΔH° for entries a) and b)^[153]. Fluoride ion affinities of AlF_3 , 2 AlF_3 and Al_2F_6 in kJ/mol.

Reaction	Experimental values ^[153]	$\Delta U(0K)$ (MP2/TZVPP)	ΔH° (G2)	ΔH° (CBS-Q)
(a) $\text{Al}_2\text{F}_6 \rightarrow 2 \text{AlF}_3$	215	205.8	210.4	201.5
(b) $\text{AlF}_4^- + \text{AlF}_3 \rightarrow \text{Al}_2\text{F}_7^-$	-208 ^(a)	-224.3	-228.0	-226.1
(c) $\text{Al}_2\text{F}_6 + \text{OCF}_3^- \rightarrow \text{Al}_2\text{F}_7^- + \text{OCF}_2$	-	-291.8	-286.7	-294.1
(d) $2\text{AlF}_3 + \text{OCF}_3^- \rightarrow \text{Al}_2\text{F}_7^- + \text{OCF}_2$	-	-497.6	-497.1	-495.6
(f) $\text{AlF}_3 + \text{OCF}_3^- \rightarrow \text{AlF}_4^- + \text{OCF}_2$	-	-273.3	-269.1	-269.5
(g) $ \Delta H(\text{Eq. c}) + 209^{(b)} = FIA(\text{Al}_2\text{F}_6)$	-	500.8	495.7	503.1
(h) $ \Delta H(\text{Eq. d}) + 209^{(b)} = FIA(2 \text{AlF}_3)$	-	706.6	706.1	704.6
(i) $ \Delta H(\text{Eq. f}) + 209^{(b)} = FIA(\text{AlF}_3)$	-	482.3	478.1	478.5

^(a) This value is not very reliable because the error bars for the experimental standard enthalpies of formation of AlF_4^- and Al_2F_7^- are quite large (± 100 and ± 15 kJ/mol). ^(b) The *FIA* of OCF_2 is 209 kJ/mol.

The calculated reaction enthalpies/energies with all three methods are very similar and differ by a maximum of 9 kJ/mol (entry (a) in Table 3), and the correlation with the available experimental data is good. By addition of the *FIA* of OCF_2 of 209 kJ/mol^[148] to the enthalpies/energies of entries (c)-(e) in Table 1, the *FIAs* of AlF_3 , 2 AlF_3 and Al_2F_6 were obtained (entries (g)-(i) in Table 3). The *FIA* of AlF_3 of 478 to 482 kJ/mol is in very good agreement with that obtained by the simpler BP86/SV(P) level (467 kJ/mol) which was used for the assessment of the *FIAs* of the parent Lewis acids of the larger WCAs above.

The average of the *FIAs* of 2 AlF_3 (705 kJ/mol) and Al_2F_6 (500 kJ/mol) calculated by the most reliable G2 and CBS-Q levels will be used for the evaluation of the *FIA* of compounds with fluoride bridges as described below.

3.1.2 Anchor Point II: Direct Calculation of the *LA* of $[\text{F}_3\text{Al-L}]^-$ with MP2/TZVPP and other Methods

For the reliable evaluation of the ligand affinity *LA* of a WCA $[\text{M}(\text{L})_n]^-$, the structures of the free ligand $[\text{L}]^-$ and its AlF_3 -complex $[\text{F}_3\text{Al-L}]^-$ were calculated at the BP86/SV(P), B3LYP/TZVPP and at the MP2/TZVPP level. As seen in the preceeding section, the MP2/TZVPP, G2 and CBS-Q calculations for the aluminium fluoride species agree within 5 kJ/mol. Since the size of the compounds calculated in this section is prohibitive for the application of compound methods such as G2 and CBS-Q, the MP2/TZVPP method as the best applicable level that gives reliable results has been chosen. To check the quality of the calculations, also the BP86/SV(P) and selected B3LYP/TZVPP results are included in Table 4. Next the energies $\Delta U(0\text{K})$ of the reaction in eq. 6 were calculated at these three levels.

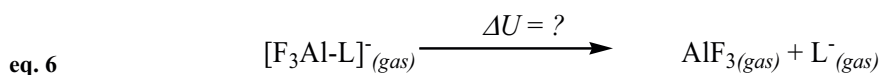


Table 4: The reaction energies $\Delta U(0\text{ K})$ of the dissociation of $[\text{F}_3\text{Al-L}]^-$ to give $[\text{L}]^-$ and AlF_3 (eq. 6) at the BP86/SV(P), B3LYP/TZVPP and the MP2/TZVPP level (L = OTeF_5 , C_6H_5 , C_6F_5 , $\text{C}_6\text{H}_3(\text{CF}_3)_2$, CF_3 , OCH_3 , $\text{OC}(\text{CF}_3)_3$). Values are given in kJ/mol.

L =	BP86/ SV(P)	B3LYP/TZVPP	MP2/TZVPP
$[\text{C}_6\text{H}_5]^-$	433	-	425
$[\text{C}_6\text{F}_5]^-$	321	298	315
$[\text{C}_6\text{H}_3(\text{CF}_3)_2]^-$	395	-	380
$[\text{CF}_3]^-$	406	355	344
$[\text{OC}(\text{CF}_3)_3]^-$	331	298	321
$[\text{OCH}_3]^-$	472	-	475
$[\text{OTeF}_5]^-$	248	251	273

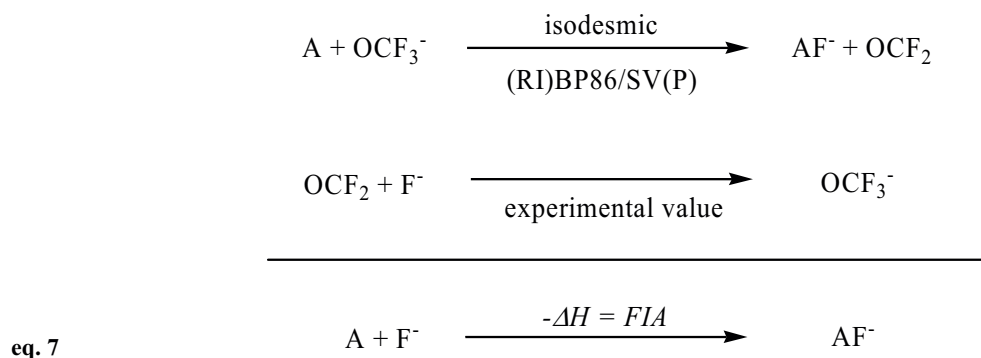
Generally, the agreement between the BP86/SV(P) reaction energies and the MP2/TZVPP values in Table 4 is good and within less than 25 kJ/mol. The same holds for the B3LYP vs.

the MP2 values. The only exception from this notion includes the $[\text{CF}_3]^-$ anion. For the correct energetic description of this species, with the highest relative fluorine content of all $[\text{L}]^-$ in Table 4, the delocalization of the negative charge is presumably very important. This requires more flexible basis sets than SV(P) as used for the BP86 calculation and, consistently, the B3LYP and MP2 values with the larger TZVPP basis agree within 11 kJ/mol. Therefore, if the reaction energy with $[\text{L}]^- = [\text{CF}_3]^-$ was calculated at the BP86/TZVPP level, it decreases from 406 kJ/mol (SV(P)) to 349 kJ/mol well within the range of the MP2 (344 kJ/mol) and B3LYP (355 kJ/mol) values. Thus it follows that reaction energies for non-isodesmic reactions with the flexible TZVPP basis are more reliable. Since, to our experience and as shown in the preceding section, the MP2/TZVPP level gives better geometries and energies than the B3LYP/TZVPP level^[4, 51], the MP2/TZVPP values in Table 4 were chosen as the anchor point for the calculation of the ligand affinity LA below.

3.1.3 Concepts to Analyze the Stability and Coordinating Ability of a WCA on Computational Grounds

With the following reasonable suggestions the relative stability and coordinating ability of the WCAs were compared:

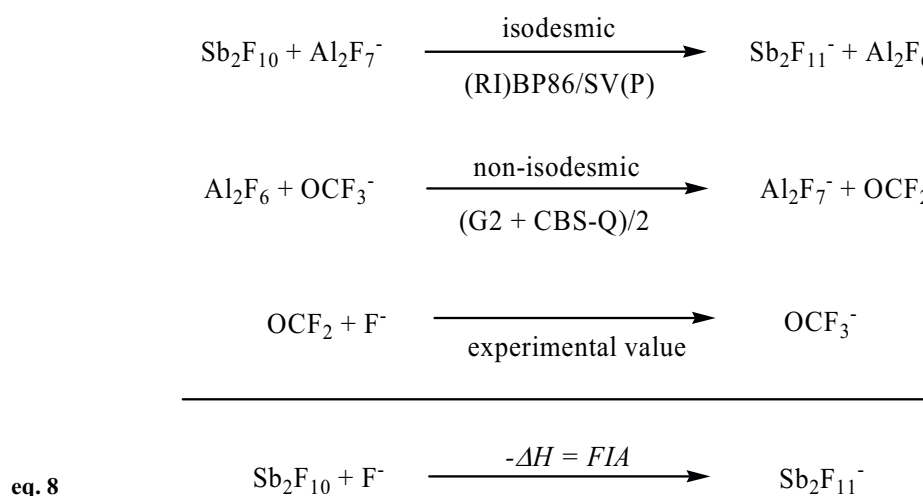
1) All anions that are based on a Lewis acidic central atom are prone to ligand abstraction as a decomposition reaction^[4]. A measure for the intrinsic stability of a given WCA is the Lewis acidity of the parent Lewis acid A, that is, the $\text{B}(\text{C}_6\text{F}_5)_3$ acid for the $[\text{B}(\text{C}_6\text{F}_5)_4]^-$ anion. A firmly established measure for Lewis acidity is the fluoride ion affinity FIA calculated through an isodesmic reaction (eq. 7):^[148]



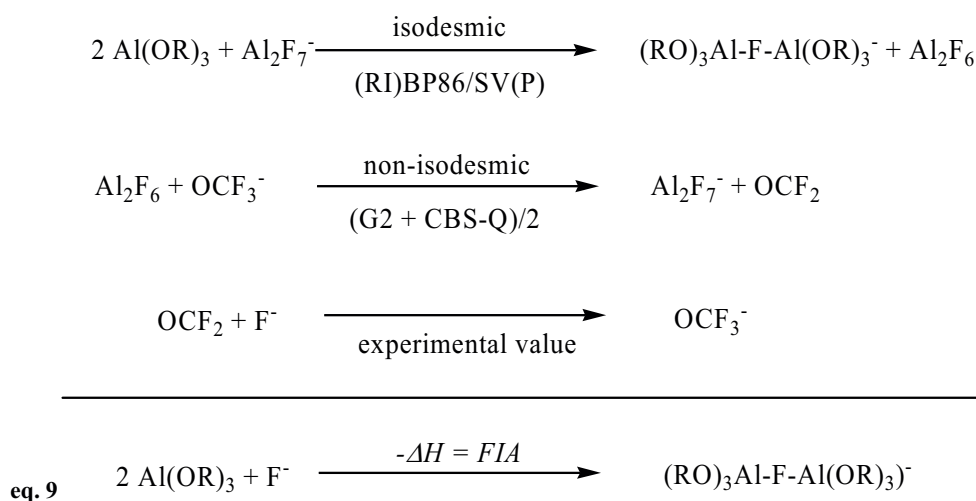
The calculation of the *FIAs* was done according to this known^[148] scheme and all *FIA* values of the parent Lewis acids A of the WCAs examined are included in Table 7. The previously established^[148] anchor point for this scale is the experimental *FIA* of OCF₂ of 209 kJ/mol. The higher the *FIA*-value of A, the more stable is the respective WCA against ligand abstraction. For comparison, the *FIAs* calculated^[148] by Christe and Dixon are included in Table 7 below.

The approach as in eq. 7 works very well as long as the WCAs do *not* include fluoride bridges. In this case the reactions are non-isodesmic and, therefore, additional calculations had to be performed to allow for a reliable evaluation of the *FIA* of the parent Lewis acids of these WCAs. To evaluate the *FIA* of Sb_nF_{5n} (n = 2, 3, 4) giving the fluoride bridged anions [Sb_nF_{5n+1}]⁻ (n = 2, 3, 4) the *FIA* was calculated by two separate calculations:

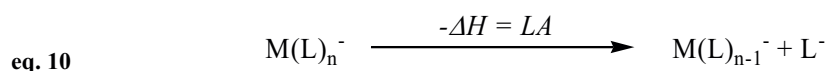
- The *FIA* of the doubly fluoride bridged Al₂F₆ (D_{2h}), giving the singly fluoride bridged Al₂F₇⁻ anion, was calculated based on the average of G2 and CBS-Q calculations as 500 kJ/mol. This step is non-isodesmic, but the G2 and CBS-Q levels are reported^[154] to reproduce experimental values with a uncertainty of less than 8 kJ/mol lending credibility to these values.
- *FIAs* of Sb_nF_{5n} (n = 2, 3, 4) were then calculated in an isodesmic reaction of Al₂F₇⁻ and Sb_nF_{5n} giving Sb_nF_{5n+1}⁻ and Al₂F₆ by adding the reaction enthalpy of the latter reaction to the *FIA* of Al₂F₆ of 500 kJ/mol, i.e. for Sb₂F₁₁⁻ (eq. 8):



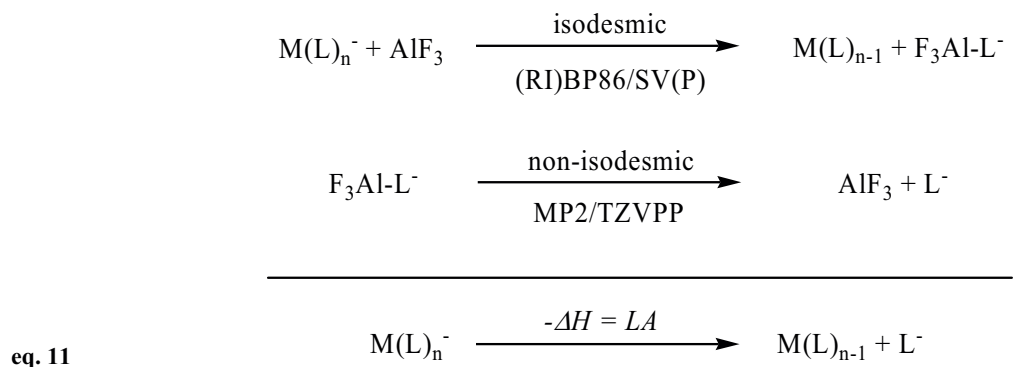
Similarly the *FIAs* of $[(\text{RO})_3\text{Al-F-Al}(\text{OR})_3]^-$ and $[(\text{F}_4\text{C}_6(1,2-(\text{B}(\text{C}_6\text{F}_5)_2)_2\text{F})^-]$ were assessed in isodesmic reactions of Al_2F_7^- and the Lewis acids $2 \text{Al}(\text{OR})_3$ and $\text{F}_4\text{C}_6(1,2-(\text{B}(\text{C}_6\text{F}_5)_2)_2$ giving 2AlF_3 and the fluoride bridged anion. From this reaction energy and the *FIA* of two AlF_3 - calculated based on the average of G2 and CBS-Q calculations of -705 kJ/mol – the *FIA* of $2 \text{Al}(\text{OR})_3$ and $\text{F}_4\text{C}_6\{1,2-(\text{B}(\text{C}_6\text{F}_5)_2)_2\}_2$ followed, i.e. for $[(\text{RO})_3\text{Al-F-Al}(\text{OR})_3]^-$ (eq. 9):



2) Additionally, the ligand affinity *LA* of all types of WCAs was also directly assessed. The *LA* is the enthalpy of reaction necessary to remove the anionic ligand $[\text{L}]^-$ from the anion $[\text{M}(\text{L})_n]^-$ (eq. 10):

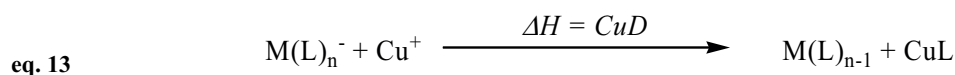
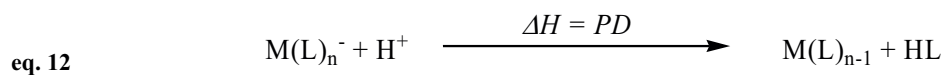


The *LA* was partitioned in two parts: the first was an isodesmic reaction that also allowed calculating reliably very large systems with the DFT level BP86/SV(P). The second reaction contains much smaller species, however, is non-isodesmic. Therefore, the computationally much more expensive but also more reliable MP2/TZVPP level was selected to assess the second part. The *LA* was then obtained by a simple addition of the two equations (eq. 11).



The LA is always endothermic and the higher the positive LA -value in Table 7, the more stable is the WCA versus a ligand abstraction. However, a word of caution is needed here: The LA also reflects the stability of the generated $[\text{L}]^-$ anion. Thus, if $[\text{L}]^-$ is stable such as $[\text{L}]^- = [\text{OC}(\text{CF}_3)_3]^-$ or $[\text{OTeF}_5]^-$, the LA is relatively low compared to less stable anionic ligands such as $[\text{L}]^- = [\text{C}_6\text{H}_5]^-$ or $[\text{C}_6\text{H}_3(\text{CF}_3)_2]^-$.

3) To assess the stability of a WCA towards an attack of a hard or soft electrophile and to eliminate the contribution of the intrinsic stability of $[\text{L}]^-$ in **2**, the isodesmic decomposition reactions of $[\text{M(L)}_n]^-$ with H^+ (hard, eq. 12) and Cu^+ (soft, eq. 13) were calculated:



PD stands for proton-decomposition (eq. 12) and CuD for copper-decomposition (eq. 13). PD and CuD allow drawing conclusions on the stability of a given WCA of type $[\text{M(L)}_n]^-$ upon reaction with a hard (H^+ , PD) or soft (Cu^+ , CuD) electrophile. Since a gaseous anion and a gaseous cation react in eq. 12 and eq. 13 giving two neutral species, PD and CuD are both exothermic. The less negative PD - and CuD -values in Table 7 are, the more stable the WCA is against electrophilic attack. For gas phase acidities of neutral Brønsted acids including $\text{H}[\text{CB}_{11}\text{F}_{12}]$ see reference 155.

4) The energy of the HOMO of a WCA relates to its resistance towards oxidation. The lower the HOMO energy, the more difficult it is to remove an electron and thus oxidize to the WCA.

5) The HOMO-LUMO gap in Table 7 can be associated with the resistance of an anion towards reduction, and the larger the gap, the more stable the anion is with respect to reduction. Very small gaps such as those for $[\text{Sb}_4\text{F}_{21}]^-$ or $[\text{As}(\text{OTeF}_5)_6]^-$ are an indication of the potentially oxidizing character of these anions that may interfere with counteranions sensitive towards oxidation.

6) As a measure for the coordinating ability of an anion the partial charges of the most negatively charged atom ($q_{\text{neg.}}$) as well as the most negatively charged surface atom ($q_{\text{surf.}}$) are collected in Table 7. It is clear that low charges are an indication for low coordination ability. However, steric effects may also be of importance and the most basic atoms may be hidden in the center of a large WCA and are, therefore, *not* available for coordination. In this case the charge of the most basic accessible surface atoms $q_{\text{surf.}}$ appears to be a better measure.

3.1.4 Reactions with SiMe_3^+ and Cp_2ZrMe^+

To illustrate the meaning of the abstract figures such as *FIA*, *LA*, *PD* and *CuD*, the reactions of the examined anions with two very common reactive counter cations have explicitly been calculated: SiMe_3^+ as the most simple organometallic silylium ion and Cp_2ZrMe^+ as the prototype for all zirconocene-based olefin polymerization catalysts. To account for effects of the reaction medium, the respective solvation enthalpies with the COSMO model at the BP86/SV(P) level was also calculated. The total energies and COSMO solvation energies for SiMe_3^+ , Cp_2ZrMe^+ , L-SiMe_3 and $\text{Cp}_2\text{Zr}(\text{Me})\text{L}$ in Ph-Cl , $\epsilon = 5.69$, and $1,2\text{-F}_2\text{C}_6\text{H}_4$, $\epsilon = 13.38$ as solvents are included in the appendix (12.2). Since two ions react with formation of two neutral molecules, solvation effects are crucial for the sign of the decomposition enthalpy.

3.1.4.1 Reactions with SiMe_3^+

The free SiMe_3^+ cation is unknown in condensed phases, however, its arene adduct is accessible. Free simple SiR_3^+ ($\text{R} = \text{Me}, \text{Et}, \dots$) silylium ions either coordinate or decompose the counterions. The only structurally characterized example of a free and truly tricoordinate silylium ion is the bulkier substituted $\text{Si}(\text{Mes})_3^+$ cation ($\text{Mes} = 2,4,6\text{-Me}_3\text{C}_6\text{H}_2$) partnered with

the $[\text{CB}_{11}\text{Cl}_6\text{Me}_5\text{H}]^-$ anion^[33]. However, it is known that this cation is also moderately stable with the $[\text{B}(\text{C}_6\text{F}_5)_4]^-$ anion. For an overview on the literature before 1998 see references 2 and 156. With this background, it is instructive to analyze Table 5 in which all reaction energies in the gas phase and in solution according to eq. 14 are collected.

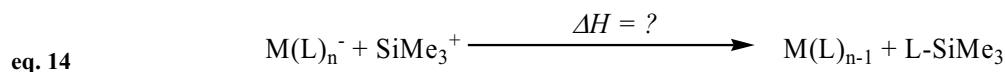


Table 5: Reaction energies in the gas phase and in solution in PhCl, ($\varepsilon = 5.69$) and 1,2- $\text{F}_2\text{C}_6\text{H}_4$, ($\varepsilon = 13.38$) according to eq. 14.

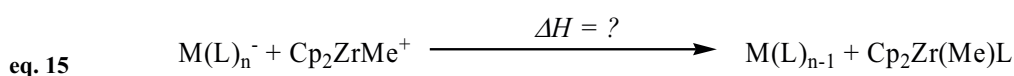
Anion	$\Delta_r U_{\text{gas}}$	$\Delta_r U_{\text{Ph-Cl}}$	$\Delta_r U_{1,2-\text{F}_2\text{C}_6\text{H}_4}$
$[\text{BF}_4]^-$	-622	-272	-210
$[\text{PF}_6]^-$	-566	-228	-168
$[\text{AsF}_6]^-$	-534	-203	-145
$[\text{SbF}_6]^-$	-471	-164	-109
$[\text{Sb}_2\text{F}_{11}]^-$	-437	-149	-98
$[\text{Sb}_3\text{F}_{16}]^-$	-404	-140	-93
$[\text{Sb}_4\text{F}_{21}]^-$	-402	-145	-100
$[\text{B}(\text{OTeF}_5)_4]^-$	-404	-157	-114
$[\text{As}(\text{OTeF}_5)_6]^-$	-388	-144	-102
$[\text{Sb}(\text{OTeF}_5)_6]^-$	-337	-94	-52
$[\text{Al}(\text{OR})_4]^-$ ^(a)	-400	-142	-96
$[(\text{RO})_3\text{Al-F-Al}(\text{OR})_3]^-$ ^(a)	-301 (-379) ^(b)	-65	-23
$[\text{B}(\text{C}_6\text{F}_5)_4]^-$	-488	-232	-187
$[\text{B}(\text{CF}_3)_4]^-$	-348	-49	+5

^(a) $\text{R} = \text{C}(\text{CF}_3)_3$, ^(b) kinetic (thermodynamic) value, i.e. Isomer I (Isomer II) of $\text{Al}_2(\text{OR})_5\text{F}$ (see appendix section 12.2).

Since the number of particles on each side of eq. 14 is the same, entropy is not expected to change the reaction energies. All anions except for the smaller $[\text{B}(\text{CF}_3)_4]^-$ in the most polar solvent 1,2- $\text{F}_2\text{C}_6\text{H}_4$ are incompatible with the reactive SiMe_3^+ cation. However, for $[\text{B}(\text{CF}_3)_4]^-$ other decomposition pathways were described and it is now known that this WCA is not compatible with silylium ions^[157].

3.1.4.2 Reactions with Cp_2ZrMe^+

To achieve living polymerization and a high catalytic activity, the zirconocenium catalyst should be long lived, and thus many efforts were made to keep the anion out of the active site of the cationic catalyst^[4, 5]. The reactive Cp_2ZrMe^+ cation certainly is the prototype of these kind of catalysts^[4, 5], and therefore it is important to understand whether the stability of the mainly used $[\text{B}(\text{C}_6\text{F}_5)_4]^-$ and related WCAs is thermodynamic or kinetic and how other types of WCAs compare to the $[\text{B}(\text{C}_6\text{F}_5)_4]^-$ anion. Therefore, the decomposition as in eq. 15 was analyzed in Table 6.



Similar to eq. 14 the number of particles on both sides of eq. 15 is the same and, therefore, entropy is not expected to change the reaction energies.

Table 6: Reaction energies in the gas phase and in solution in PhCl, ($\varepsilon = 5.69$) and 1,2- $\text{F}_2\text{C}_6\text{H}_4$, ($\varepsilon = 13.38$) according to eq. 15.

Anion	$\Delta_r U_{\text{gas}}$	$\Delta_r U_{\text{Ph-Cl}}$	$\Delta_r U_{1,2-\text{F}_2\text{C}_6\text{H}_4}$
$[\text{BF}_4]^-$	-542	-215	-155
$[\text{PF}_6]^-$	-486	-170	-113
$[\text{AsF}_6]^-$	-454	-146	-90
$[\text{SbF}_6]^-$	-391	-106	-55
$[\text{Sb}_2\text{F}_{11}]^-$	-356	-92	-44
$[\text{Sb}_3\text{F}_{16}]^-$	-324	-83	-39
$[\text{Sb}_4\text{F}_{21}]^-$	-322	-88	-45
$[\text{B}(\text{OTeF}_5)_4]^-$	-346	-117	-76
$[\text{As}(\text{OTeF}_5)_6]^-$	-330	-104	-64
$[\text{Sb}(\text{OTeF}_5)_6]^-$	-279	-55	-14
$[\text{Al}(\text{OR})_4]^-$ ^(a)	-347	-107	-63
$[(\text{RO})_3\text{Al-F-Al}(\text{OR})_3]^-$ ^(a)	-249 (-171) ^(b)	-30	+10
$[\text{B}(\text{C}_6\text{F}_5)_4]^-$	-353	-118	-75
$[\text{B}(\text{CF}_3)_4]^-$	-214	+64	+115

^(a) $\text{R} = \text{C}(\text{CF}_3)_3$, ^(b) kinetic (thermodynamic) value, i.e. Isomer I (Isomer II) of $\text{Al}_2(\text{OR})_5\text{F}$ (see appendix section 12.2).

From Table 6 one notes that Cp_2ZrMe^+ is less electrophilic than SiMe_3^+ . However, the majority of the solution decomposition reactions are still exothermic thus showing that the stability of catalyst for example with the WCA $[\text{B}(\text{C}_6\text{F}_5)_4]^-$ is kinetic. The formation of a Zr-C bond appears to be less favorable than that of a Si-C bond and thus WCAs in which a Zr-C bond is formed during the decomposition (i.e. $[\text{B}(\text{C}_6\text{F}_5)_4]^-$, $[\text{B}(\text{CF}_3)_4]^-$) perform much better than in the reaction with SiMe_3^+ . Still there are other easily accessible WCAs such as $[\text{Al}(\text{OR})_4]^-$ which have the same stability as those most frequently employed (i.e. $[\text{B}(\text{C}_6\text{F}_5)_4]^-$).

3.2 The Stability and Coordinating Ability of the WCAs Based on *LA*, *FIA*, *PD*, *CuD*, HOMO-Level, HOMO-LUMO-Gap and Partial Charges.

3.2.1 Investigations in the Gas Phase

Ligand abstraction^[21, 53, 158, 159] and hydrolysis are frequently observed decomposition pathways for WCA's and, therefore, the computational approach to calculate *LA*, *PD* and *CuD* mimics experimental observations. Examples for ligand abstraction include reactions of SiPh_3^+ with $[\text{B}(\text{OTeF}_5)_4]^-$ ^[53] and the dissolved $[\text{Me}(\text{Ph}_3\text{P})_2\text{Pt-OEt}_2]^+[\text{B}(\text{Ar}^{\text{F}})_4]^-$ salt ($\text{Ar}^{\text{F}} = \text{C}_6\text{H}_3(\text{CF}_3)_2$)^[158]; also the $\text{B}(\text{C}_6\text{F}_5)_4^-$ anion rapidly degrades in the presence of AlR_2^+ ^[21], RZn^+ ^[159] and H^+ ions ($\text{R} = \text{Me}, \text{Et}$) if no donor solvent is present (i.e. OEt_2). However, by calculations only the underlying thermodynamics can be assessed, kinetic barriers against decomposition may additionally stabilize a given WCA (see $\text{Al}_2(\text{OR})_5\text{F}$ structure below). Also other decomposition pathways than ligand abstraction may occur; this was recently shown for example for the $[\text{B}(\text{CF}_3)_4]^-$ anion^[4, 151]. The data included in Table 7 may not be taken absolute; however, since the same methods were used for all computations, relative trends will definitely be correct. For the carborane-based anions, the *FIA*, *LA*, *PD*, and *CuD* cannot directly be assessed and, therefore, these WCAs were excluded from this approach. All calculated values are collected in Table 7:

Table 7: Calculated properties of WCAs: FIA of the parent Lewis acid (in kJ/mol), LA , PD and CuD of the WCA (all in kJ/mol), position of the HOMO of the WCA in eV, HOMO-LUMO gap of the WCA in eV, partial charge of the most negatively charged atom q_{neg} , and partial charge of the most negatively charged surface atom q_{surf} .

anion	Sy.	FIA	$FIA^{[148]}$	LA	PD	CuD	HOMO	gap	q_{neg}	q_{surf}
$[BF_4]^-$	T_d	338	348 ^[148]	a)	-1212	-521	-1.799	10.820	-0.25 F	-0.25 F
$[PF_6]^-$	D_{4h}	394	397 ^[148]	a)	-1156	-465	-2.672	8.802	-0.44 F	-0.44 F
$[AsF_6]^-$	D_{4h}	426	443 ^[148]	a)	-1124	-433	-3.149	6.284	-0.44 F	-0.44 F
$[SbF_6]^-$	D_{4h}	489	503 ^[148]	a)	-1061	-371	-3.911	5.135	-0.44 F	-0.44 F
$[Sb_2F_{11}]^-$ vs. Sb_2F_{10}	C_1	549	-	a)	-1026	-336	-5.540	4.336	-0.40 F	-0.40 F
$[Sb_3F_{16}]^-$ vs. Sb_3F_{15}	C_i	582	-	a)	-994	-303	-6.342	3.886	-0.38 F	-0.38 F
$[Sb_4F_{21}]^-$ vs. Sb_4F_{20}	C_{2v}	584	-	a)	-991	-301	-6.579	3.256	-0.39 F	-0.39 F
$[B(OTeF_5)_4]^-$	C_1	550	-	274	-1040	-420	-5.811	2.593	-0.40 F	-0.40 F
$[As(OTeF_5)_6]^-$	C_3	593	-	290	-1023	-403	-6.335	2.204	-0.62 O	-0.40 F
$[Sb(OTeF_5)_6]^-$	C_3	633	-	341	-973	-353	-6.610	2.326	-0.61 O	-0.39 F
$[Al(OR)_4]^-$ ($R = C(CF_3)_3$)	S_4	537	-	342	-1081	-395	-4.100	6.747	-0.24 O	-0.20 F
$[(RO)_3AlF-Al(OR)_3]^-$ ($R = C(CF_3)_3$) ^{(b), (c)}	C_i	685 ^(b)	-	441 (363)	-983 (-1061 ^(c))	-297 (-375 ^(c))	-4.987	6.500	-0.23 O	-0.20 F
$[B(C_6H_5)_4]^-$	S_4	342	-	324	-1402	-649	-2.150	4.087	-0.45 B	-0.05 H
$[B(C_6H_3(CF_3)_2)_4]^-$	S_4	471	-	382	-1251	-506	-3.789	3.816	-0.44 B	-0.22 F
$[B(C_6F_5)_4]^-$	S_4	444	-	296	-1256	-538	-3.130	4.196	-0.21 F	-0.21 F
$[B(CF_3)_4]^-$	T	552	-	490	-1136	-379	-3.530	9.158	-0.58 B	-0.21 F
$[(F_4C_6\{1,2-(B(C_6F_5)_2)_2F\}]^-$ ^(c)	C_1	510	-	328 ^(c)	-1224 ^(c)	-506 ^(c)	-3.274	3.861	-0.54 B	-0.22 F
$[(F_4C_6\{1,2-(B(C_6F_5)_2)_2OMe\}]^-$ ^(d)	C_1	510	-	586 ^(d)	-1061 ^(d)	-332 ^(d)	-3.101	3.754	-0.68 B	-0.22 C
$[(F_4C_6\{1,2-(B(C_6F_5)_2)_2OMe\}]^-$ ^(c)	C_1	-	-	305 ^(c)	-1247 ^(c)	-529 ^(c)	-	-	-	-

^{a)} LA and FIA are identical; ^{b)} FIA vs. 2 $Al(OR)_3$; ^(c) against $-C_6F_5^-$ (LA) or EC_6F_5 abstraction ($E = H: PD, E = Cu: CuD$); ^(d) against OMe^- (LA) or $EOMe$ abstraction ($E = H: PD, E = Cu: CuD$); ^(e) values in parenthesis correspond to the formation of the $Al_2(OR)_5F$ isomer I (see appendix 12.2).

Table 7 reveals the outstanding capability of the WCAs $[\text{Sb}_3\text{F}_{16}]^-$, $[\text{Sb}_4\text{F}_{21}]^-$ and $[\text{Sb}(\text{OTeF}_5)_6]^-$ to stabilize highly oxidizing cations even in anhydrous HF (see *FIA*, *PD*, HOMO-level). This stability versus oxidation has to be traded in for sensitiveness against reduction (see gap in Table 7). Moreover, the fluoroantimonates and teflate anions are extremely moisture sensitive and decompose in the presence of traces of water in glassware with autocatalytic formation of HF that reacts with SiO_2 to form SiF_4 and H_2O , which re-enters the cycle. This sensitivity towards moisture allows the use of these WCAs only in a few laboratories worldwide. In terms of coordinating ability, those WCAs are more coordinating than others (compare q_{bas} and q_{surf}).

For the borate based-anions it becomes obvious from Table 7 that fluorination greatly increases the thermodynamic stability of all fluorinated borates compared to the non-fluorinated $[\text{B}(\text{C}_6\text{H}_5)_4]^-$ anion (see *FIA*, *LA*, *PD*, *CuD*, HOMO-level, gap). The differences between the commercially available $[\text{B}(\text{C}_6\text{F}_5)_4]^-$ and $[\text{B}(\text{C}_6\text{H}_3(\text{CF}_3)_2)_4]^-$ WCAs are small, but, bridged borane-based anions such as $[(\text{F}_4\text{C}_6\{1,2\text{-(B}(\text{C}_6\text{F}_5)_2\}_2\text{X})]^-$ ($\text{X} = \text{F, OMe}$) are even more stable WCAs. Of all borates, the novel $[\text{B}(\text{CF}_3)_4]^-$ anion is the most stable with respect to the examined decomposition pathways. However, an experimental investigation of other decomposition pathways has already been described^[151].

The stability of the perfluoroalkoxyaluminate $[\text{Al}(\text{OR})_4]^-$ ($\text{R} = \text{C}(\text{CF}_3)_3$) with respect to *FIA*, *PD*, *CuD*, HOMO-level and gap in Table 7 is remarkable and higher than that of all borates except the $[\text{B}(\text{CF}_3)_4]^-$ anion which has comparable values. The $[\text{Al}(\text{OR})_4]^-$ anion comes even close to the oxidation resistance and low *PD*s of the fluoroantimonates and is in part even better than the teflate-based anions. In contrast to the latter two types of anions, the synthesis of the perfluoroalkoxyaluminate $[\text{Al}(\text{OR})_4]^-$ is straightforward and may be performed in conventional inorganic laboratories all over the world. This shows the great prospect of this special type of anion for chemistry. An even better choice would be the fluoride bridged $[(\text{RO})_3\text{Al-F-Al}(\text{OR})_3]^-$ anion, which is among the best WCAs according to each entry in Table 7, but this WCA was long known only as a decomposition product^[49, 51]. However, a direct synthesis of a silver salt of this WCA has recently been established^[52] (for other new, fluorine-bridged aluminates, see reference 160).

3.2.2 Inclusion of Solvation Enthalpies

Silylium and zirconocenium ion chemistry are two prominent examples for the application of WCAs to stabilize reactive cations. To compare the relative stabilities of the examined WCAs like $[M(L)_n]^+$, their decomposition reactions with SiMe_3^+ and Cp_2ZrMe^+ as reactive counterion in the gas phase and in solution (PhCl and 1,2- $\text{F}_2\text{C}_6\text{H}_4$, see eq. 14 and eq. 15 above) were also investigated.

3.2.2.1 Gas Phase Values vs. (calculated) Solution Values: Are Solvation Energies Necessary to Evaluate the WCAs?

In this section, it is investigated how far the gas phase data in Table 7 can be transferred to reactions taking place in solution. To illuminate this point the solvation reaction energies $\Delta_r U$ of eq. 14 and eq. 15 in PhCl and 1,2- $\text{F}_2\text{C}_6\text{H}_4$ were plotted against the *FIA* of the respective WCA in the gas phase (Figure 12).

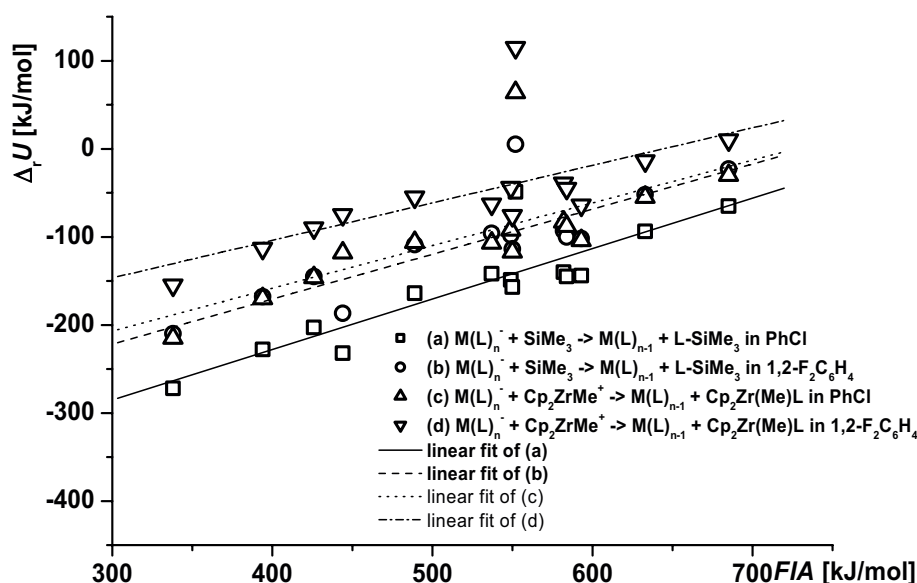


Figure 12: Reaction energies $\Delta_r U$ of eq. 14 and eq. 15 in Ph-Cl and 1,2- $\text{F}_2\text{C}_6\text{H}_4$ against the *FIA* of the respective WCA in the gas phase. The lines represent the best linear fit for each set of data.

Figure 12 shows that roughly a linear relationship exists between the *FIA* in the gas phase and the reaction energies $\Delta_r U$ in solution. This is taken as clear evidence that the results obtained from gas phase calculations (i.e. those in Table 7) may be used to extract meaningful answers for reactions actually occurring in solution. The only exception from this notion is found for the relatively small $[\text{B}(\text{CF}_3)_4]^-$ anion (see below for reasons).

3.2.2.2 Relative Stabilization by Solvation

The extent to which a reaction is stabilized by solvation enthalpies is analyzed in Figure 3. Here the stabilization $\Delta(\Delta_r U)$ of the gas phase reaction by solvation enthalpies in the most polar solvent 1,2-F₂C₆H₄ (i.e. $\Delta(\Delta_r U) = \Delta_r U_{\text{gas}} - \Delta_r U_{1,2\text{-F}_2\text{C}_6\text{H}_4}$) was plotted against the number of the atoms of the anion. The number of the atoms of an anion is taken as a measure of its size and thus also for the absolute value of the solvation enthalpies which are roughly inversely proportional to the ionic radius (i.e. see the simple Born equation). Thus, reactions with smaller anions are expected to be relatively more stabilized by solvation enthalpies than those with larger anions (Figure 13).

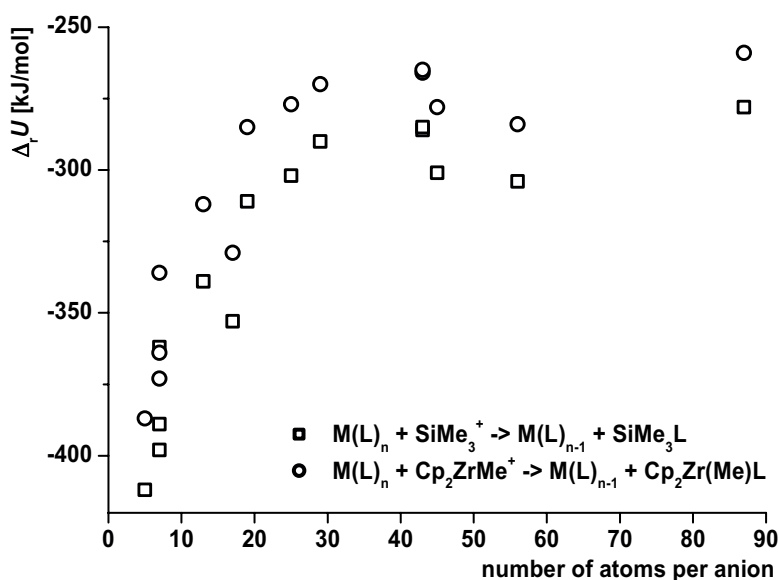


Figure 13: The stabilization $\Delta(\Delta_r U) = \Delta_r U_{\text{gas}} - \Delta_r U_{1,2\text{-F}_2\text{C}_6\text{H}_4}$ of the gas phase reaction by solvation enthalpies in the most polar solvent 1,2-F₂C₆H₄ plotted against the number of the atoms of the anion.

For small anions such as [BF₄][−] or [PF₆][−] the stabilization $\Delta(\Delta_r U)$ is large and may approach 400 kJ/mol; with increasing anion size, the relative stabilization decreases quickly to about 250 to 300 kJ/mol. Remarkably, starting from an anion size of about 25 atoms, the stabilization by solvation remains almost constant and only adds a constant value to the gas phase reaction energy. This may also be seen from Figure 14 and Figure 15, in which the gas phase and solution reaction energies of eq. 14 and eq. 15 are plotted for all WCAs.

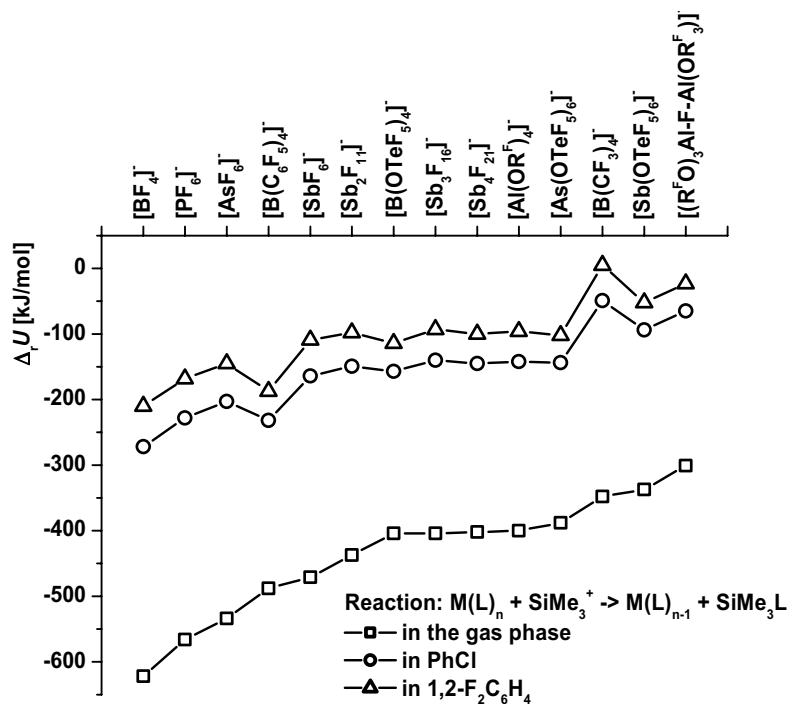


Figure 14: Plot of the gas phase and solution reaction energies $\Delta_r U$ [kJ/mol] of eq. 14 against the WCA. $R^F = C(CF_3)_3$.

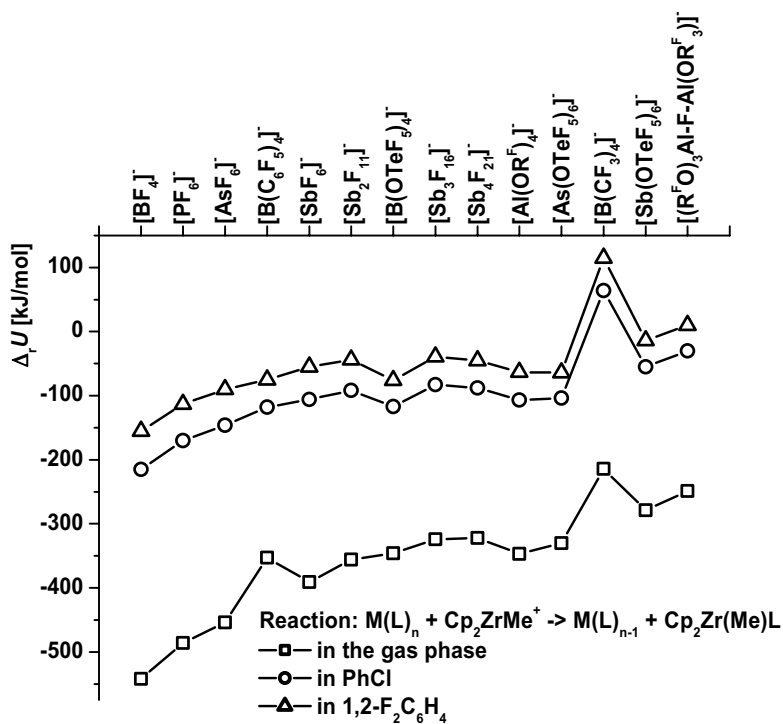


Figure 15: Plot of the gas phase and solution reaction energies $\Delta_r U$ [kJ/mol] of eq. 15 against the WCA. $R^F = C(CF_3)_3$.

From the preceding, the following conclusions can be drawn:

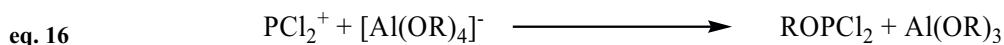
- 1) For larger WCAs exceeding about 25 atoms, the most important input for the stabilization of a reactive cation in a given solvent is its stability against ligand abstraction. To assess the anion stability also gas phase values such as *FIA*, *PD* or *CuD* may be used.
- 2) The best resolution for stabilizing a given reactive cation would be a very small WCA that is very stable against ligand abstraction and very weakly coordinating to exclude the competition with anion coordination. Probably one of the best compromises in this respect is the $[\text{B}(\text{CF}_3)_4]^-$ anion; however, recently^[151] other decomposition reactions of the latter anion were found, leading to the conclusion that this anion is not as ideal to stabilize reactive cation as may be anticipated from the data in Table 7.

3.2.3 Prediction of Reactions

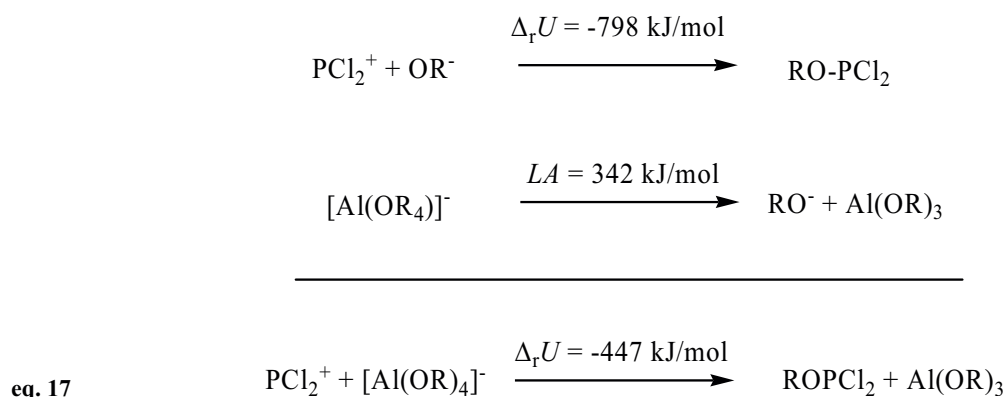
Especially the *FIA* and *LA* in Table 7 are valuable tools for the prediction of the outcome of hitherto unknown reactions.

3.2.3.1 Application of the *LA*: Assessment of the WCA-Stability in the Presence of a Target Cation

With some small extra calculations or estimations, the *LA* in Table 7 may also be taken to assess the stability of a WCA in the presence of a reactive target cation. Let us consider the carbene analogous PCl_2^+ cation as an example for any desired reactive target cation and the $[\text{Al}(\text{OR})_4]^-$ WCA as the counterion (i.e. the decomposition as in eq. 16).



The first step is to calculate the target cation and the neutral resulting from the reaction of the cation and the anion, i.e. PCl_2^+ and RO-PCl_2 . If the (affordable) BP86/SV(P) level is chosen, one may use eq. 16 and the total energies of $[\text{Al}(\text{OR})_4]^-$ and $\text{Al}(\text{OR})_3$ given in this study to directly calculate the (isodesmic) gas phase reaction energy of eq. 16 (which is -447 kJ/mol). However, if other, for example higher correlated methods shall be used, the next step is to separate eq. 16 in two parts (eq. 17 and *LA*):

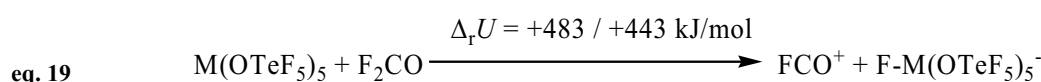
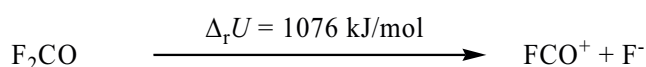
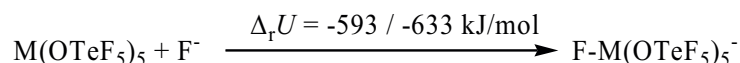
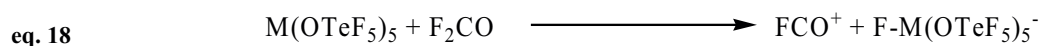


The first part of eq. 17 may be calculated directly, however, more accurate is an isodesmic route. Adding up the first reaction in eq. 17 and the *LA* gives the desired gas phase reaction energy of eq. 16 as -447 kJ/mol. Thus, with two relatively small calculations and the data from this study, the stability of the 18 WCAs collected here with a desired target cation in the gas phase can be checked. eq. 16 contains two particles on both sides, so that entropy may be neglected. However, since two ions react forming two neutrals solvation should be taken into account. Thus, to examine if the salt $\text{PCl}_2^+[\text{Al}(\text{OR})_4]^-$ is stable in PhCl or 1,2- $\text{F}_2\text{C}_6\text{H}_4$ solution, the COSMO solvation enthalpies of PCl_2^+ and RO- PCl_2 have to be calculated at the BP86/SV(P) level. Together with the COSMO solvation enthalpies of $[\text{Al}(\text{OR})_4]^-$ and $\text{Al}(\text{OR})_3$ included with this study the solution stability of eq. 16 was assessed in a next step. As expected, solvation greatly stabilizes eq. 16 in Ph-Cl by 291 kJ/mol and in 1,2- $\text{F}_2\text{C}_6\text{H}_4$ by 343 kJ/mol; however, in both solvents the decomposition is still considerably favorable (by -157 and -104 kJ/mol). This correlates well with recent experiments showing that the PCl_2^+ cation, generated from $\text{Ag}^+[\text{Al}(\text{OR})_4]^-$ and PCl_3 , completely decomposed the $[\text{Al}(\text{OR})_4]^-$ anion^[52]. However, the analysis for the fluoride bridged $[(\text{RO})_3\text{Al-F-Al}(\text{OR})_3]^-$ as WCA in eq. 17 shows that the gas phase reaction is only unfavorable by -348 kJ/mol and taking solvation into account by -31 kJ/mol in the most polar solvent thus suggesting that the PCl_2^+ cation may be marginally stable in a low temperature solution with this WCA.

3.2.3.2 Estimating the Success of a Fluoride Ion Abstraction Reaction: The Synthesis of $\text{FCO}^+[\text{X}]^-$ as a Target Salt

With the *FIAs* collected in Table 7, fluoride ion abstraction reactions may be planned. One likely candidate for such a reaction is the formation of a OCF^+ salt from OCF_2 and a Lewis acid. As example in eq. 19, the $\text{M}(\text{OTeF}_5)_5$ Lewis acids ($\text{M} = \text{As}, \text{Sb}$) were selected, which - although the antimony representative is very unstable and by no means a compound in the

bottle - are the strongest monomeric Lewis acids known (cf. Table 7). Also eq. 18 contains two particles on each side of the equation and, therefore, entropy is not important.



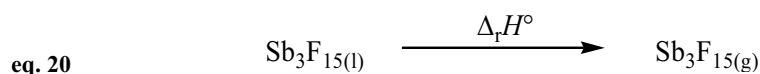
The reaction energy of the second reaction in eq. 19 is most accurately obtained by an isodesmic reaction and with the small effort of calculating OCF^+ , OCF_2 and OCF_3^- as well as taking the *FIA* of $\text{M}(\text{OTeF}_5)_5$ included in Table 7 one can estimate that eq. 18 is unfavorable in the gas phase by 483 (As) or 443 (Sb) kJ/mol. To account for the important solvation effects, the COSMO solvation enthalpies of F_2CO , FCO^+ , $\text{M}(\text{OTeF}_5)_5$ and $[\text{F-M}(\text{OTeF}_5)_5]^-$ were calculated; next the reaction energy of eq. 18 in the most polar solvent ($\epsilon = 13.38$) followed as +98 (As) and +58 (Sb) kJ/mol. This estimate suggests that the salt $\text{OCF}^+[\text{F-M}(\text{OTeF}_5)_5]^-$ is not a promising target for synthesis in solvents of this polarity. Possibly, 1,2- $\text{F}_2\text{C}_6\text{H}_4$ is not a suitable solvent for this reaction, but liquid SO_2 , which has a very similar polarity of $\epsilon = 14$ at 20°C, might be. A weakly basic and more polar solvent with $\epsilon > 14$ may promote the formation of dissolved $\text{OCF}^+[\text{F-Sb}(\text{OTeF}_5)_5]^-$ due to the higher solvation enthalpies for the ions. With respect to these considerations it appears unlikely to prepare a FCO^+ salt in solution with the Lewis acids in Table 7. This conclusion is in agreement with previous unsuccessful attempts to prepare FCO^+ salts by reaction with F_2CO with even an large excess of MF_5 ($\text{M} = \text{As}, \text{Sb}$)^[161]. However, it was found that the less reactive ClCO^+ may be obtained from FClCO and Sb_3F_{15} ^[161, 162]. Similar to the procedure for FCO^+ described above the reaction energy of a reaction of Sb_3F_{15} with ClFCO giving $\text{ClCO}^+[\text{Sb}_3\text{F}_{16}]^-$ was estimated as favorable in solution by -15 kJ/mol and thus in good agreement with the experiment and lending confidence to the predictive power of the data collected in this study.

3.3 Concluding Remarks about the Stability Calculations of WCAs:

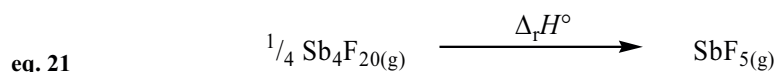
The calculation of *FIA*, *LA*, *PD*, *CuD*, HOMO-level, HOMO-LUMO-gap and partial charges of a large group of representative good WCAs was performed (Table 7). An analysis of the calculated data showed that there is no simple “best anion” and that a decision for a particular anion has to be based on several criteria. Some anions are more stable towards soft electrophiles (see *CuD*) and others towards hard electrophiles (see *PD*). In terms of coordinating abilities, the fluorinated organoborates and alkoxyaluminates are clearly less coordinating than all fluorometallates or teflate-based anions (see $q_{bas.}$ and $q_{surf.}$). Media effects, that is solvation enthalpies, are important. However, starting from an anion size of about 25 atoms, solvation only adds a constant factor to the gas phase reaction energy. The calculated energies for decomposition reactions with SiMe_3^+ and Cp_2ZrMe^+ in PhCl and 1,2- $\text{F}_2\text{C}_6\text{H}_4$ as solvents showed that the frequently used $[\text{B}(\text{C}_6\text{F}_5)_4]^-$ counterion is thermodynamically unstable with these cations and that the observed (small) solution stability of substituted silylium and zirconocenium salts should be kinetically. However, other available WCAs perform better than $[\text{B}(\text{C}_6\text{F}_5)_4]^-$ and should therefore be used in future in silylium and zirconocenium ion chemistry. It has been shown that the *FIA* and the *LA* in combination with COSMO solvation calculations are valuable tools for estimating the outcome known reactions, i.e. the solution stability of PCl_2^+ and OCX^+ salts ($\text{X} = \text{F}, \text{Cl}$). The calculated thermodynamics of these reactions correlated very well with the experiment and, by extrapolation to unknown reactions, this approach should be valuable for predictions of completely unknown transformations. The calculated data collected in Table 7 permit to assess relative thermodynamic stabilities of the respective anions in the presence of a desired target cation and help to find a particular anion in preparative chemistry based on several calculated thermodynamic criteria, not only on chemical intuition.

4 Depolymerization Energy and Fluoride Ion Affinity of Sb_nF_{5n} ($n = 2-4$) – A Computational Study

Antimony pentafluoride is a reagent frequently used to generate salts containing highly reactive counteranions (cf. section 2.2.5)^[149, 163] Under ambient conditions SbF_5 is a highly viscous liquid which contains polymeric macromolecules of the formula $(\text{SbF}_5)_x$ (x is very large) in which the octahedrally coordinated antimony atoms are connected via cis-bridging fluorine atoms. The X-ray structure showed that solid SbF_5 is a tetramer^[164]. $\text{SbF}_5(l)$ acts as an oxidizing agent as well as a very strong Lewis acid and generates anions of the general formula $[\text{Sb}_n\text{F}_{5n+1}]^-$; salts with $n = 1-4$ were hitherto characterized in the solid state by X-ray diffraction. It was shown by electron diffraction^[165] and vapor density measurements^[166, 167] that a mixture of mostly $\text{Sb}_3\text{F}_{15(g)}$ with little $\text{Sb}_4\text{F}_{20(g)}$ evaporates from $\text{SbF}_5(l)$ and the standard enthalpy $\Delta_{\text{vap}}H^\circ$ for the process in eq. 20



was 43.4 or 45.2 kJ/mol^[168] The depolymerization of gaseous Sb_4F_{20} to monomeric SbF_5 given in eq. 21



was estimated to be $\Delta_{\text{depoly}}H^\circ = +18.5$ kJ/mol^[167]. Both values are important in order to assess the fluoride ion affinity (*FIA*) of liquid SbF_5 , which is, in turn, often used to predict the outcome of hitherto unknown reactions.

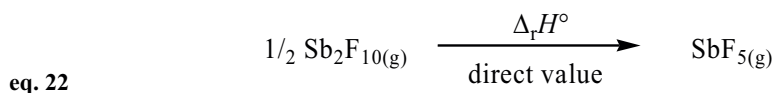
The present computations suggest that the enthalpy of depolymerization $\Delta_{\text{depoly}}H^\circ$ of +18.5 kJ/mol for $\frac{1}{4} \text{Sb}_4\text{F}_{20}$ as in eq. 21 is by about 50 kJ/mol in error, based on a series of quantum chemical calculations at various levels and with increasingly larger basis sets. The structures of the gaseous $[\text{Sb}_n\text{F}_{5n+1}]^-$ anions were also calculated at various levels and include the most accurate calculation of the *FIA*s of n $\text{SbF}_{5(g)}$ and $\text{Sb}_n\text{F}_{5n(g)}$ currently available. The revised $\Delta_{\text{depoly}}H^\circ$ of gaseous Sb_nF_{5n} was then included to extract the *FIA*s of n SbF_5 in the liquid state

and to establish standard enthalpies of formation $\Delta_f H^\circ$ of Sb_nF_{5n} as well as for $[\text{Sb}_n\text{F}_{5n+1}]^-$ ($n = 1-4$).

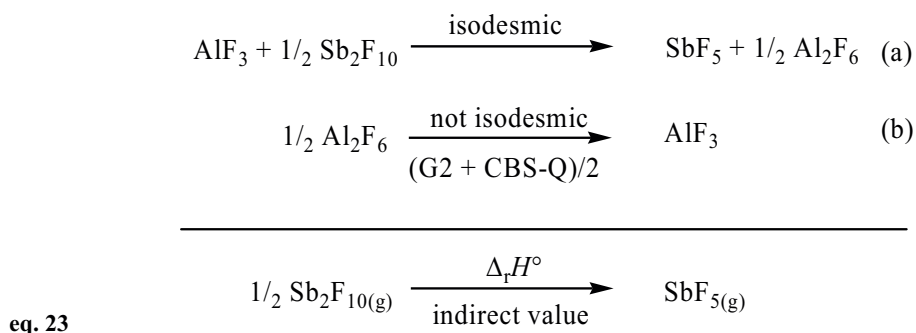
The strategy adopted in this study is to address some accuracy considerations and then select a suitable model for the calculations giving a brief description of the global minimum geometries. Using the selected model, the thermodynamics of the system are then analyzed with regard to the depolymerization and interconversion of Sb_nF_{5n} as well as the fluoride ion affinities (*FIAs*) of various antimony fluorides. The standard enthalpies of formation ($\Delta_f H^\circ$) of Sb_nF_{5n} , as well as those for the anions $[\text{Sb}_n\text{F}_{5n+1}]^-$ are also assessed based on these quantum chemical calculations and compared to available literature data.

4.1 Selection of the Model: Basis Sets and Correlation Effects

Modeling fluorine-containing molecules is known to represent a difficult computational challenge. Thus, first it has been considered how satisfactory the different levels and basis sets available are able to describe a simple test reaction in eq. 22:



This provides a convenient and relatively computationally fast test reaction, due to the high local symmetry of both, Sb_2F_{10} (D_{2h}) and SbF_5 (D_{3h}). Since the *direct* calculation of $\Delta_{\text{depoly}} H^\circ$ from eq. 22 is not isodesmic, an additional approach was required in order to independently assess this quantity indirectly. Here an isodesmic reaction was used in conjunction with a highly accurate compound method (G2 and CBS-Q were selected) and eq. 23 was chosen for the indirect calculation:



eq. 23(a) represents an isodesmic process and its computation is likely to be accurate and any errors are likely to cancel. The second reaction eq. 23 (b) is a non isodesmic process which utilizes the average of the values calculated by the G2 and CBS-Q compound methods, which are reported^[154] to reproduce experimental quantities with an accuracy of better than ± 8 kJ/mol. The latter computation was taken from reference 108, in which G2 gave $\Delta_{\text{depoly}}H^\circ$ of Al_2F_6 to be 204.4 kJ/mol while CBS-Q gave the value 195.2 kJ/mol. The average: $(\text{G2} + \text{CBS-Q})/2 = 199.8$ kJ/mol was used to indirectly establish $\Delta_{\text{depoly}}H^\circ$ of eq. 23.

Table 8 summarizes values of $\Delta_{\text{depoly}}H^\circ$ and $\Delta_{\text{depoly}}G^\circ$ based on the direct and indirect computational routes above and obtained using pure DFT (BP86), hybrid HF-DFT (B3-LYP) and *ab initio* (MP2) calculations and with increasing the basis set size from SVP (double zeta quality, one d polarization function) through TZVPP (triple ζ quality, two d and one f polarization functions) to cc-pVQZ (quadruple ζ quality, three d, two f and one g polarization functions). A TZVPP basis is reported to be already close to the basis set limit of the DFT and HF-DFT calculations while the quadruple zeta basis cc-pVQZ is close to the basis set limit of MP2.

Table 8: $\Delta_{\text{depoly}}H^\circ$ (eq. 22 / eq. 23) and $\Delta_{\text{depoly}}G^\circ$ (eq. 22 / eq. 23) values in kJ/mol obtained with pure DFT (BP86), hybrid HF-DFT (B3-LYP) and *ab initio* (MP2) calculations with increasing basis set sizes from SVP to TZVPP and cc-pVQZ. Values in bold are considered being the most accurate ones.

	$\Delta_{\text{depoly}}H^\circ$ (eq. 22 / eq. 23)			$\Delta_{\text{depoly}}G^\circ$ (eq. 22 / eq. 23)		
method	SVP	TZVPP	cc-pVQZ	SVP	TZVPP	cc-pVQZ
BP86	62 / 45	41 / 51	31 / 43	37 / 23	15 / 29	7 / 20
B3-LYP	66 / 43	42 / 47	33 / 41	40 / 21	16 / 25	9 / 17
MP2	73 / 46	57 / 54	44 / 46	48 / 25	31 / 32	21 / 21

The values collected in Table 8 show consistent trends throughout and both the free energy and the enthalpy of depolymerization differ by a maximum of 42 kJ/mol. Analyzing firstly the non isodesmic *direct* values: Increasing the basis set size from SVP through TZVPP to cc-pVQZ lowers the direct values (of both $\Delta_{\text{depoly}}H^\circ$ and $\Delta_{\text{depoly}}G^\circ$) by up to 31 kJ/mol. The *direct* values obtained using the TZVPP and the cc-pVQZ basis sets agree more closely than those generated using SVP and are within 7 to 13 kJ/mol. BP86 and B3-LYP give almost identical values in all cases. From this it is inferred that the low $\Delta_{\text{depoly}}H^\circ$ (eq. 22) and $\Delta_{\text{depoly}}G^\circ$ (eq. 22)

values obtained with the BP86 and B3-LYP levels with the largest basis set are at the basis set limit of the respective methods and therefore represent the “best” direct DFT values of approximately 31 ($\Delta_{\text{depoly}}H(\text{eq. 22})$) and 7 kJ/mol ($\Delta_{\text{depoly}}G^\circ(\text{eq. 22})$). In contrast, the MP2 method at the basis set limit gives values about 10 to 15 kJ/mol higher for $\Delta_{\text{depoly}}H^\circ(\text{eq. 22})$ and $\Delta_{\text{depoly}}G^\circ(\text{eq. 22})$. Thus, there is only moderate agreement between DFT and MP2 calculations when using the *direct* values. Turning now to the *indirect* values calculated according to the procedure in eq. 23: As expected, direct and indirect values differ more (up to 27 kJ/mol) with the smaller SVP basis. With the larger basis sets, the maximum deviation between direct and indirect values is much reduced, 12 kJ/mol being typical. Regardless the basis set, all indirect values ($\Delta_{\text{depoly}}H^\circ(\text{eq. 23})$) lie in the narrow range of 41 to 54 kJ/mol and of 17 to 21 kJ/mol ($\Delta_{\text{depoly}}G^\circ(\text{eq. 23})$). The "best" *indirect* values with the largest cc-pVQZ basis are marked in bold in Table 8 and agree to within 3 to 5 kJ/mol both for $\Delta_{\text{depoly}}H^\circ(\text{eq. 23})$ and $\Delta_{\text{depoly}}G^\circ(\text{eq. 23})$, due to error cancellation. The more accurate depolymerization values are thus the *indirect* ones. Since the difference between the indirect values calculated with a TZVPP and a cc-pVQZ basis is at most 8 kJ/mol, the computationally much more economic TZVPP basis and the indirect procedure as in eq. 23 were used for all further computations. BP86 and B3-LYP give almost identical values and, therefore, the less demanding BP86 method was used for further work.

4.2 Molecular Structures of Sb_nF_{5n} and $[\text{Sb}_n\text{F}_{5n+1}]^-$ ($n = 2-4$)

The molecular structures of the optimized compounds are shown in Figure 16 (neutrals) and Figure 17 (anions), the calculated structural parameters are collected in Table 2 and are compared to available experimental data. The calculated and available experimental data displayed in Table 9 are in good qualitative agreement. The MP2 derived geometries are particularly close to experiment. However, many of the experimental structures are hampered by the lack of librational correction of the bond lengths and bond angles and, therefore, consistently give too short bond distances and bond angles that are too wide. Therefore, it is reasonable to assume that the correct structural parameters of these antimony fluorine compounds are likely to be intermediate between the MP2 values and the experimental values collected in Table 9.

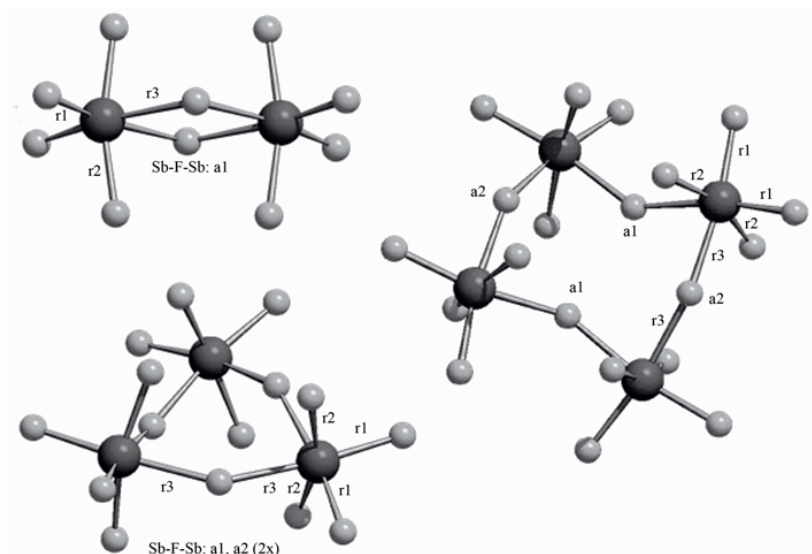


Figure 16: Molecular structures of Sb_nF_{5n} with $n = 2-4$. The structural parameters at the BP86/TZVPP and MP2/TZVPP levels are collected in Table 9.

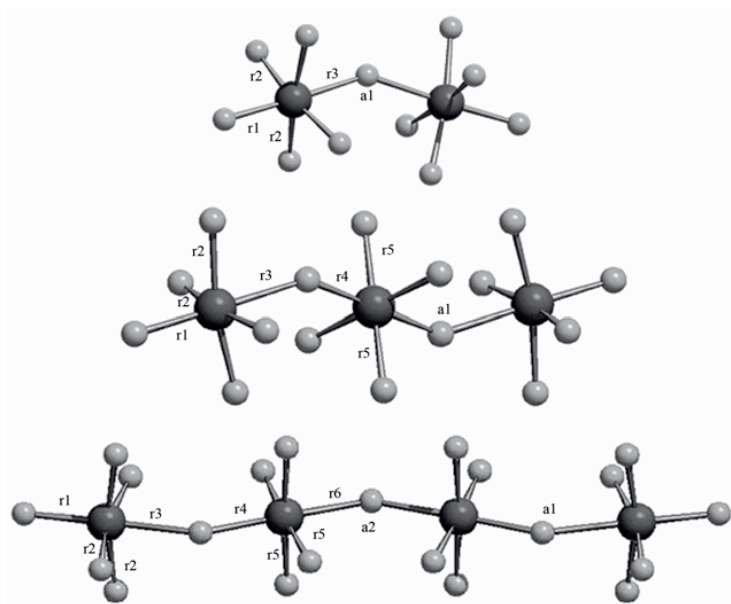


Figure 17: Molecular structures of $[\text{Sb}_n\text{F}_{5n+1}]^-$ with $n = 2-4$. The structural parameters at the BP86/TZVPP and MP2/TZVPP levels are collected in Table 9.

Table 9: The structural parameters of Sb_nF_{5n} as well as $[\text{Sb}_n\text{F}_{5n+1}]^-$ ($n = 2-4$) at the BP86/TZVPP and MP2/TZVPP levels. Distances are given in pm, angles in $^\circ$. Labeling according to Figure 16 and Figure 17.

Parameter	Exp.	Sb_2F_{10}			Sb_3F_{15}			Sb_4F_{20}		
		BP86	MP2	Exp.	BP86	MP2	Exp.	BP86	MP2	Exp.
$r1$ [pm]	-	187	185	181	187-188	184-185	182	187-188	184-185	184-185
$r2$ [pm]	-	188	185	181	187-188	184-185	182	187-188	184-185	184-185
$r3$ [pm]	-	210	206	204	208-209	204-205	203	208	204	204
$a1$ [$^\circ$]	-	108	109	150	153	154	141	154-155	151	151
$a2$ [$^\circ$]	-	-	-	150	152	153	170	148-149	150	150
$[\text{Sb}_2\text{F}_{11}]^-$										
Parameter	Exp.	BP86	MP2	Exp.	$[\text{Sb}_3\text{F}_{16}]^-$			$[\text{Sb}_4\text{F}_{21}]^-$		
$r1$ [pm]	185	191	187	181-184	190	187	184-185	189	186	186
$r2$ [pm]	185	190	187	181-184	190	187	184-185	189-190	186-187	186-187
$r3$ [pm]	202	210	204	210	216	210	210	220	214	214
$r4$ [pm]	-	-	-	197	203	198	198	200	196	196
$r5$ [pm]	-	-	-	181-184	189	186	184-185	188-189	185-186	185-186
$r6$ [pm]	-	-	-	-	-	-	201	208	203	203
$a1$ [$^\circ$]	flexible	147	160	146	150	150	-	149	149	149
$a2$ [$^\circ$]	-	-	-	-	-	-	-	150	150	150

4.3 Depolymerization and Interconversion of Sb_nF_{5n} ($n = 2-4$)

Let's now turn to the question, as to whether the literature value of the experimentally derived^[6] enthalpy of depolymerization $\Delta_{\text{depoly}}H^\circ(\text{eq. 21})$ of +18.5 kJ/mol is correct or in error. Our starting point for this discussion shall be the assessment of $\Delta_{\text{depoly}}G^\circ(\text{eq. 21})$ based on the experimental standard depolymerization enthalpy $\Delta_{\text{depoly}}H^\circ(\text{eq. 21})$ of +18.5 kJ/mol: $\Delta_{\text{depoly}}G^\circ(\text{eq. 21})$ was obtained as -15.1 kJ/mol based on the estimation of the reaction entropies and associated thermal contributions to the enthalpy at 298 K, as calculated with the help of the BP86/SVP derived vibrational frequencies for SbF_5 and Sb_4F_{20} . Since $\text{Sb}_3\text{F}_{15}(\text{g})$ and $\text{Sb}_4\text{F}_{20}(\text{g})$ were shown to be in equilibrium in the gas phase it is assumed that they are thus close in energy. Further the depolymerizations of $\frac{1}{3} \text{Sb}_3\text{F}_{15}$ and of $\frac{1}{4} \text{Sb}_4\text{F}_{20}$ to give monomeric SbF_5 are expected to be almost equal in energy and therefore a similar value of $\Delta_{\text{depoly}}G^\circ(\frac{1}{3} \text{Sb}_3\text{F}_{15})$ of approximately -15 kJ/mol can be anticipated. If these values of $\Delta_{\text{depoly}}G^\circ$ are correct, then one would expect $\text{SbF}_5(\text{l})$ to evaporate exclusively to give monomeric $\text{SbF}_5(\text{g})$. However, this is clearly not the case and indicates that the published $\Delta_{\text{depoly}}H^\circ(\text{eq. 21})$ of +18.5 kJ/mol is wrong. This conclusion and the BP86/SVP calculated thermal and entropic corrections to the free energy at 298 K (which sum to -33.6 kJ/mol) then allow us to estimate that the experimental $\Delta_{\text{depoly}}H^\circ(\text{eq. 21})$ should at least amount to 60 ± 15 kJ/mol and thus that $\Delta_{\text{depoly}}G^\circ(\text{eq. 21})$ should be about 26 ± 15 kJ/mol in order to allow for the exclusive presence of Sb_3F_{15} and Sb_4F_{20} in the gas phase at the temperatures corresponding to those of the electron diffraction studies^[165] (423 K). With these values in mind, the standard enthalpy and free energy changes on depolymerization of $1/n \text{Sb}_n\text{F}_{5n}(\text{g})$ to give $\text{SbF}_5(\text{g})$, (eq. 24 to eq. 29) were further studied, the values which are cited in Table 10.

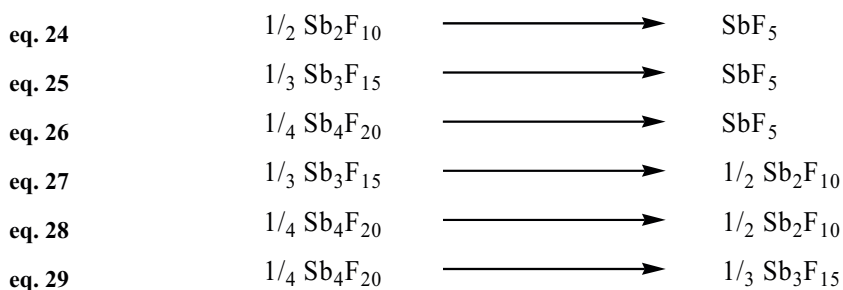


Table 10: Standard enthalpies and free energies for the depolymerization of $1/n \text{ Sb}_n\text{F}_{5n(g)}$ to give $\text{SbF}_{5(g)}$ and for the interconversion of Sb_nF_{5n} with differing n . Only the (more reliable) indirect values are included [in kJ/mol] (using a TZVPP basis).

	$\Delta_r H^\circ$		$\Delta_r G^\circ$		$\Delta_r G^{423\text{K}}$		$\Delta_r G^{498\text{K}}$	
	BP86	MP2	BP86	MP2	BP86	MP2	BP86	MP2
eq. 24	50	53	29	32	20	22	14	17
eq. 25	54	65	25	36	12	23	4.7	15
eq. 26	54	68	20	34	5	19	-3.4	11
eq. 27	4.2	12	-3.9	3.8	-7	0.5	-9	-1.5
eq. 28	2.6	14	-9	2.3	-14	-2.9	-17	-6
eq. 29	-0.4	3.2	-5.1	-1.5	-7	-3.5	-8	-4.6

To enable a direct comparison with the conditions of the electron diffraction^[165] and vapor density measurement^[166, 167] studies also the $\Delta_{\text{depoly}}G^{423\text{K}}$ and $\Delta_{\text{depoly}}G^{498\text{K}}$ values were calculated and these are included in Table 10. At 423 K the vapor above liquid SbF_5 consists of mostly Sb_3F_{15} with little Sb_4F_{20} while at 498 K the major component is Sb_2F_{10} . Only the more reliable *indirect* values obtained by procedures related to eq. 23 are given. The enthalpies and free energies for the interconversion ($\Delta_{\text{conv}}H$ and $\Delta_{\text{conv}}G$) of Sb_nF_{5n} in eq. 27 to eq. 29 reflect the gas phase behavior of the Sb_nF_{5n} molecules as well as the degree of association in the gas phase that was determined experimentally^[166, 167]. Therefore, $\Delta_{\text{conv}}H$ and $\Delta_{\text{conv}}G$ were also studied. The latter reactions are isodesmic and thus the computations made should be accurate.

The depolymerization enthalpies $\Delta_{\text{depoly}}H^\circ$ in eq. 24 to eq. 26 lie in the range of 59 ± 9 kJ/mol and are thus close to the value predicted above based on experimental considerations (60 ± 15 kJ/mol). On inspection of eq. 27 to eq. 29 one realizes that only the MP2/TZVPP calculations describe the experimental electron diffraction and vapor density measurement results adequately (much Sb_3F_{15} and little Sb_4F_{20} at 423 K and much Sb_2F_{10} at 498 K in the gas phase). Thus, in agreement with the experiment, the interconversion of the slightly less favorable Sb_4F_{20} into the slightly more favorable Sb_3F_{15} in eq. 29 is at 298 and 423 K slightly exergonic by 1.5 kJ/mol and 3.5 kJ/mol. By contrast, the BP86/TZVPP values would suggest that in the gas phase at 423 K only Sb_2F_{10} is (exclusively) formed (i.e. eq. 27 and eq. 28 are already exergonic at 298 K by 3.9 or 9 kJ/mol and at 423 K by 7 and 14 kJ/mol). This does

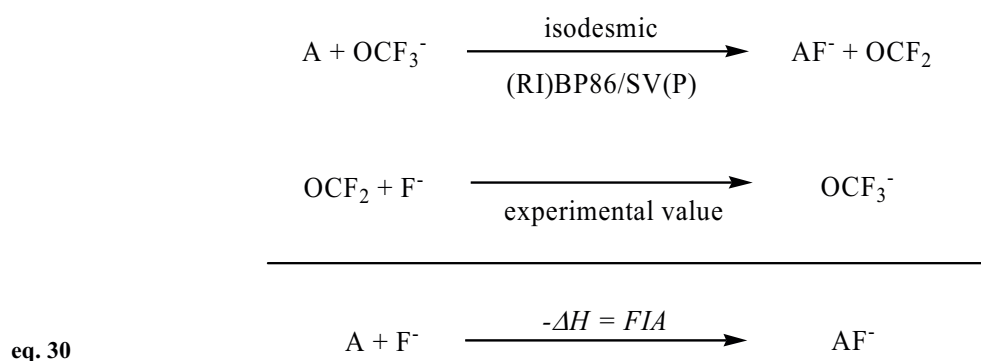
not correspond to the situation found in the experiment. However, in agreement with the experiment, at 498 K also the MP2/TZVPP predicted $\Delta_{\text{conv}}G^{498\text{K}}$ suggests that the most favored species in the gas phase is Sb_2F_{10} (eq. 27 is now exergonic by -1.5 kJ/mol). Since the MP2 results appear to predict the experimental outcome best, the BP86/TZVPP values were excluded from further discussion and exclusively the MP2/TZVPP values were used in order to establish the *FIAs* and other properties.

Assignment of error bars:

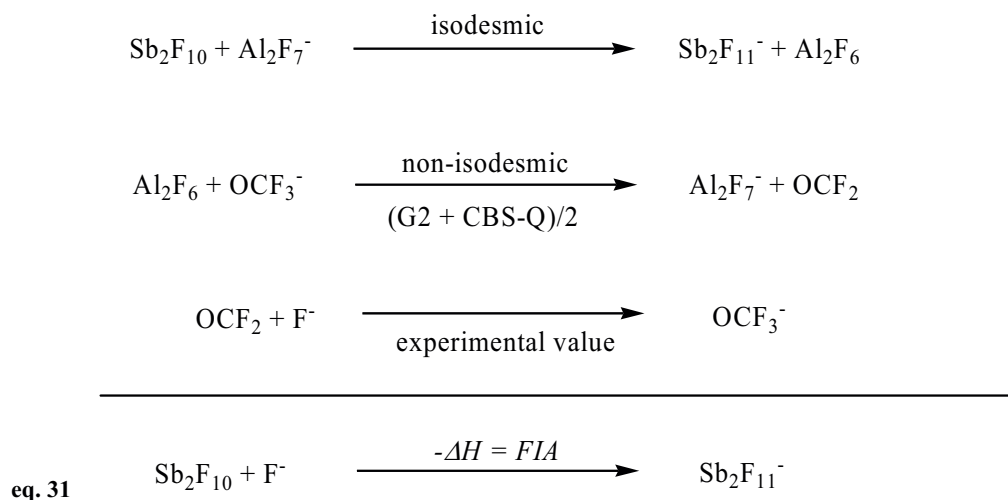
Due to the excellent agreement of the MP2/TZVPP values with available experimental data, error bars are judged to be at most ± 10 kJ/mol for the calculations (enthalpies, free energies and *FIAs*) are estimated. For the assignment of the enthalpies of formation below, the experimental $\Delta_f H(\text{SbF}_5(\text{g}))$ with an uncertainty of ± 15 kJ/mol has to be used. For the assessed enthalpies of formation, the error bars, therefore, add up to $(10^2 + 15^2)^{1/2} = \pm 18$ kJ/mol (enthalpies of formation below).

4.4 *FIAs* of $n \text{ SbF}_5$ and Sb_nF_{5n} ($n = 1-4$) in the Gas Phase

The *FIAs* of $n \text{ SbF}_5$ and Sb_nF_{5n} ($n = 1-4$) in the gas phase are assessed in this section. The case for $n = 1$ is simple and the same isodesmic reaction as was initially introduced by Christe and Dixon^[148] may be used, i.e. eq. 30:



However, when fluoride bridged Sb_nF_{5n} or $[\text{Sb}_n\text{F}_{5n+1}]^-$ species are involved, the situation is more complicated and eq. 30 becomes non isodesmic and thus less reliable. Accordingly, an alternative scheme is introduced in order to assess the *FIAs* of fluoride bridged species reliably that is shown exemplarily for Sb_2F_{10} in eq. 31 and for $n \text{ SbF}_5$ in eq. 32.



All non isodesmic reactions were calculated by the very accurate compound methods G2 and CBS-Q and, therefore, the addition of the isodesmic reaction with the average of the enthalpies calculated by G2 and CBS-Q as eq. 31 gives very reliable values of the *FIAs* of Sb_nF_{5n} . To further obtain the *FIAs* of n monomeric SbF_5 molecules one simply has to add the best indirect $\Delta_{\text{depoly}}H^\circ$ values in Table 10 to the *FIAs* of Sb_nF_{5n} , i.e. eq. 32:

$$\text{eq. 32} \quad FIA(n \text{ SbF}_{5(\text{g})}) = FIA(\text{Sb}_n\text{F}_{5n(\text{g})}) + \Delta_{\text{depoly}}H^\circ$$

All *FIA* values are included in Table 11 and compared to available literature data.

Table 11: *FIAs* of $n \text{ SbF}_5$ and Sb_nF_{5n} ($n = 1-4$) in the gas phase (at the MP2/TZVPP level) and comparison to available literature data. All values are given in kJ/mol.

	<i>FIA</i> (Dixon)	<i>FIA</i> (Jenkins)	$-\Delta_r H^\circ = FIA$ (this study)	$-\Delta_r G^\circ$ (this study)
$\text{SbF}_{5(\text{g})}$	503	506 ± 63	514	512
$\text{Sb}_2\text{F}_{10(\text{g})}$	556	-	559	521
$\text{Sb}_3\text{F}_{15(\text{g})}$	570	-	572	543
$\text{Sb}_4\text{F}_{20(\text{g})}$	-	-	580	561
$2 \text{ SbF}_{5(\text{g})}$	-	671 ± 63	667	585
$3 \text{ SbF}_{5(\text{g})}$	-	728 ± 39	767	651
$4 \text{ SbF}_{5(\text{g})}$	-	-	855	697

The data included in Table 11 is in good agreement with existing literature data, however, it becomes possible to estimate a more complete set of *FIA* values and the first values for Sb_4F_{20} and 4 SbF_5 . One realizes that the Lewis acidity of Sb_nF_{5n} increases with increasing n more slowly and that the Lewis acidity of Sb_4F_{20} is only little higher than that of Sb_3F_{15} . This accords with experimental experience^[149].

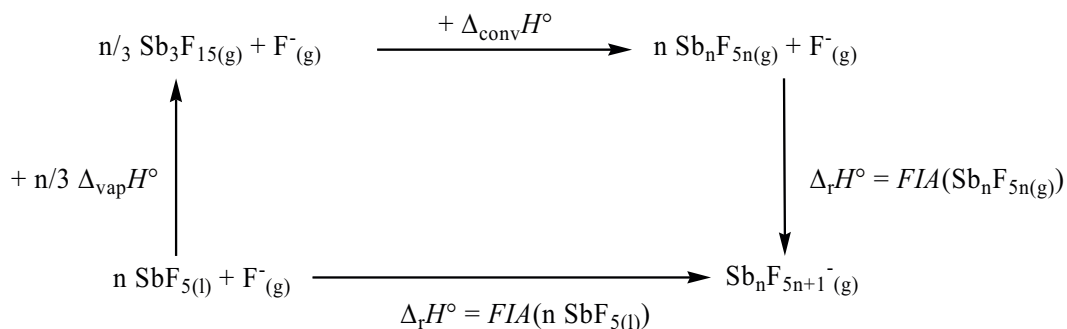
4.5 *FIA* of $n \text{ SbF}_{5(l)}$ ($n = 1-4$)

Having established the *FIAs* of gaseous antimony fluorides let's now turn to the *FIA* of n liquid SbF_5 molecules, since liquid SbF_5 itself is frequently used as a reaction medium. Comparison of melting point (m.p.), boiling point (b.p.) and $\Delta_{\text{vap}}H^\circ$ of SbF_5 with those of several related binary halides having a similar liquid state temperature range as SbF_5 (Table 12) leads us to the conclusion that the experimental standard enthalpy of vaporization $\Delta_{\text{vap}}H^\circ$ (averaging to 44 kJ/mol as in eq. 20) appears to be reasonably consistent with $\Delta_{\text{vap}}H^\circ$ values for all other related halides and, therefore, is considered to be accurate.

Table 12: Comparison of the melting point (m.p. in °C), boiling point (b.p. in °C) and $\Delta_{\text{vap}}H^\circ$ (in kJ/mol) of SbF_5 with those of several binary halides with a similar liquid state range as SbF_5 .

binary halide	m.p. [°C]	b.p.[°C]	$\Delta_{\text{vap}}H^\circ$ [kJ/mol]
SbF_5	8.3	141	43.4 / 45.2
AsCl_3	-16	130	43.5
TiCl_4	-25	136	41.0
SiBr_4	5.2	154	41.8
PBr_3	-40	173	45.2

Therefore, for the determination of the *FIA* of liquid SbF_5 the average value $\Delta_{\text{vap}}H^\circ \approx 44$ kJ/mol was employed and a thermochemical cycle was developed, from which this quantity may be assessed; a suitable cycle is shown in Scheme 3:



Scheme 3: Born-Haber cycle for the determination of the *FIA* of $n \text{ SbF}_5(\text{l})$ ($n = 1-4$).

All quantities in the peripheral cycle are known and therefore the *FIAs* of $n \text{ SbF}_5(\text{l})$ can be established (Table 13) based on the MP2/TZVPP values in Table 10 and Table 11 and the experimental $\Delta_{\text{vap}}H^\circ$ verified above. The values in Table 13 are compared to available literature data.

Table 13: *FIAs* of $n \text{ SbF}_5$ as a liquid according to Scheme 3 ($n = 1-4$) [in kJ/mol]. Comparison to available literature data. The literature values in parentheses were corrected for the wrong enthalpy of depolymerization (see text).

	$FIA(n \text{ SbF}_5(\text{l}))$ (Jenkins) ^[169]	$-\Delta_rH^\circ(\text{Scheme 3}) = FIA(n \text{ SbF}_5(\text{l}))$ (this study)
1 $\text{SbF}_5(\text{l})$	475±63 (425±63)	434±18
2 $\text{SbF}_5(\text{l})$	609±63 (510±63)	506±18
3 $\text{SbF}_5(\text{l})$	635±39 (487±39)	528±18
4 $\text{SbF}_5(\text{l})$	-	534±18

Naturally, the calculated *FIAs* of n liquid SbF_5 molecules are much lower than those of the gaseous compounds. Again the same trend as for gaseous antimony fluorides is evident: The higher n , the higher is the *FIA*, however, the increase in *FIA* is slowing down for increasing n . The large difference to the published values arises from adoption of too low a value for the enthalpy of depolymerization of Sb_4F_{20} giving $1/4 \text{ SbF}_5$ (+18.5 kJ/mol instead of 68 kJ/mol in Table 10). When the published values are corrected for this error, i.e. lowered by 49.5 kJ/mol per SbF_5 , then present and corrected literature values are in good qualitative agreement.

4.6 Standard Enthalpies of Formation $\Delta_f H^\circ$ of Sb_nF_{5n} and $[\text{Sb}_n\text{F}_{5n+1}]^-$ ($n = 1-4$)

The standard enthalpies of formation $\Delta_f H^\circ$ of $\text{SbF}_5(\text{g})$ (-1301 ± 15 kJ/mol), and F^- (-249 kJ/mol) are known and thus $\Delta_f H^\circ$ of $\text{Sb}_n\text{F}_{5n}(\text{g})$ and $[\text{Sb}_n\text{F}_{5n+1}]^-(\text{g})$ can be calculated from $\Delta_{\text{depoly}} H^\circ$ (Table 10) and the *FIAs* of $\text{Sb}_n\text{F}_{5n}(\text{g})$ (Table 11). Thus:

$$\text{eq. 33} \quad \Delta_f H^\circ (\text{Sb}_n\text{F}_{5n(\text{g})}) = n \cdot \Delta_f H^\circ (\text{SbF}_5(\text{g})) - \Delta_{\text{depoly}} H^\circ (\text{Sb}_n\text{F}_{5n(\text{g})})$$

and

$$\text{eq. 34} \quad \Delta_f H^\circ ([\text{Sb}_n\text{F}_{5n+1}]^-(\text{g})) = n \cdot \Delta_f H^\circ (\text{Sb}_n\text{F}_{5n(\text{g})}) + \Delta_f H^\circ (\text{F}^-) - \text{FIA}(\text{Sb}_n\text{F}_{5n})$$

All $\Delta_f H^\circ$ values calculated by this approach are collected in Table 14 and compared to available literature data.

Table 14: $\Delta_f H^\circ$ values of $\text{Sb}_n\text{F}_{5n}(\text{g})$ and $[\text{Sb}_n\text{F}_{5n+1}]^-(\text{g})$ calculated according to eq. 33 and eq. 34 [in kJ/mol]. Comparison to available literature data.

$n =$	$\Delta_f H^\circ (\text{Sb}_n\text{F}_{5n}(\text{g}))$ (this study)	$\Delta_f H^\circ ([\text{Sb}_n\text{F}_{5n+1}]^-(\text{g}))$ (this study)	$\Delta_f H^\circ ([\text{Sb}_n\text{F}_{5n+1}]^-(\text{g}))$ (Jenkins) ^[169]
1	$-1301 \pm 15^{[10]}$	-2064 ± 18	-2075 ± 52
2	-2708 ± 21	-3516 ± 25	-3520 ± 63
3	-4098 ± 26	-4919 ± 31	-4874 ± 39
4	-5476 ± 30	-6305 ± 36	-

The standard enthalpies for the formation of $\text{Sb}_n\text{F}_{5n}(\text{g})$ and $[\text{Sb}_n\text{F}_{5n+1}]^-(\text{g})$ increase with increasing n and are in good agreement with available literature data. They may be used to assess the thermodynamics of known and unknown reactions. See reference ^[149] for examples.

4.7 Concluding Remarks

In this study it has been shown that the literature value for the enthalpy of depolymerization of $\text{Sb}_4\text{F}_{20}(\text{g})$ to give $\text{SbF}_5(\text{g})$ was by about 50 kJ/mol in error. This error contributes n times to

the previously established *FIAs* of $n \text{ SbF}_5(l)$ such that the reported literature values^[169] were by up to 148.5 kJ/mol ($n = 3$) in error. The present enthalpies of depolymerization of $1/n \text{ Sb}_n\text{F}_{5n(g)} \rightarrow \text{SbF}_{5(g)}$ are the most accurate values currently available and are in agreement with the experimental results obtained by electron diffraction^[165] and vapor density measurements^[166, 167]. All subsequently derived quantities such as *FIAs* of $\text{Sb}_n\text{F}_{5n(g)}$, $n \text{ SbF}_5(g)$, $n \text{ SbF}_5(l)$ and the standard enthalpies of formation of $\text{Sb}_n\text{F}_{5n(g)}$ and $[\text{Sb}_n\text{F}_{5n+1}]^-(g)$ are considered to be equally accurate and thus will be very useful to assess the thermodynamics of known as well as hitherto unknown reactions (see reference^[149]).

5 Tetraalkylammonium Salts of Weakly Coordinating Aluminates

Tetraalkylammonium salts of complex anions play an important role especially in electrochemistry, where they are widely used as supporting electrolytes for applications like cyclic voltammetry in non-aqueous media ^[75, 76, 97, 114, 170]. However, the generated oxidized species often react with the anions and therefore, new salts with a large “electrochemical window” are required, i.e. salts which are stable against oxidation and reduction under the experimental conditions, especially in low polarity solvents like CH₂Cl₂, CHCl₃ or toluene. Both requirements are fulfilled by quaternary ammonium salts of robust WCAs^[4]. [NBu₄]⁺[B(C₆F₅)₄]⁻ and [NBu₄][B(C₆H₃(CF₃)₂)₄]⁻ have been reported both to be very stable and to effectively solubilize the positively charged species formed in anodic processes^[98, 99]. However, electrochemical investigations in very non polar solvents like toluene or benzene are limited to only very few anions, e.g. the [CB₁₁Me₁₂]⁻^[135, 171]. Unfortunately the synthesis of this anion is very complicated, which makes it impossible to be widely used as a WCA for electrochemical applications.

Quantum chemical calculations^[172] as well as electrochemical measurements^[173-175] of the lithium salts predicted the fluoroalkoxyaluminates [pftb]⁻, [hftb]⁻ and [hfip]⁻ to be very redox stable^[ii],^[4, 172, 175] their salts are usually soluble in media with low dielectric constants. Moreover it has been shown that even very reactive cations like simple carbenium ions (Cl₃⁺^[47, 176], see chapter 7) or binary P-X (X = halogen) cations like PX₄⁺^[48, 177], AsBr₄⁺^[50], P₂X₅⁺^[48], P₅X₂⁺^[48], P₅S₂X₂⁺^[178] or P₇S₆I₂⁺^[179] are compatible with these aluminates. Especially the P-X cations are incompatible with all other anion types. This also holds for a series of silver complexes with very weakly basic ligands, e.g. P₄^[42, 43], P₄S₃^[44, 180] (see chapter 6), S₈^[45], P₃N₃Cl₆^[181] or C₂H₄^[46, 182]. Since the starting materials to prepare compounds of the fluorinated aluminates are commercially available (best at P&M Invest Russia; <http://www.fluorine.ru>) and the synthesis of the lithiumaluminate salts^[11, 41, 109] is a simple high yield procedure that can be performed in scales up to 250 g per batch^[179], it only appeared logical to extend the available substance classes to NR₄⁺ salts. Therefore their synthesis and full characterization as possible new materials for electrochemical applications was undertaken.

^[ii] stability against Li/Li⁺ in DME: >5.0 V for [hfip]⁻ and 5.5 V for [pftb]⁻.

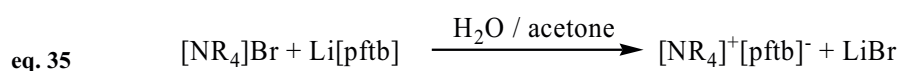
Moreover, the $[\text{NR}_4]^+$ salts were used for the assignment of the ion volumes^[96, 141, 183] and of the vibrational bands of the anions, as these compounds serve as model compounds for an undisturbed anion environment with all cation bands well known. The anion bands are assigned to the different vibrations by comparison to quantum chemical DFT calculations of the vibrational modes. The influence of coordination on the position and splitting of the anion vibrations may help to understand the kind and the strength of cation - anion interactions in cases where the crystal structure of a given compound is not available.

The tetraalkylammonium salts were also chosen to investigate the anion decomposition pathways in the mass spectrometer by ESI techniques.

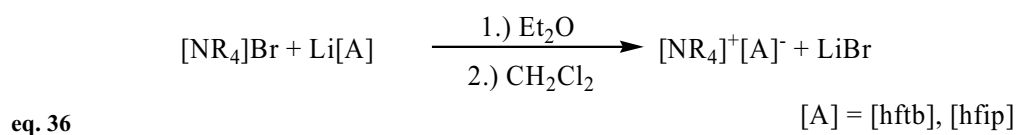
5.1 Results and Discussion

5.1.1 Syntheses

Two different strategies were used to prepare the tetraalkylammonium salts of the fluoroalkoxyaluminates: The $[\text{NR}_4]^+[\text{pftb}]^-$ (R = Me **1**, Et **2**, Bu **3**) were obtained by the reaction of $[\text{NR}_4]\text{Br}$ with $\text{Li}[\text{pftb}]$ in a water / acetone mixture (85 Vol.% : 15 Vol.%) according to the following equation:



The formed $[\text{NR}_4]^+[\text{pftb}]^-$ is insoluble and crystallizes upon evaporation of the co-solvent acetone over night in quantitative yield. After some washings with water and testing for bromide with Ag^+ , the compound is analytically pure (spectra, elemental analyses). This method is only possible for the $[\text{pftb}]^-$ anion; as the other anions $[\text{hftb}]^-$ and $[\text{hfip}]^-$ are slightly sensitive towards moisture. Therefore, all of the other tetraalkylammonium compounds were synthesized in $\text{Et}_2\text{O} / \text{CH}_2\text{Cl}_2$ using the appropriate lithium salts (eq. 36).



The metathesis is done in ether; however, to get rid of traces of dissolved LiBr-ether complexes, the ether solvent is removed in vacuum and replaced by CH₂Cl₂, in which all the NR₄⁺ aluminates are easily soluble. After filtration the pure compounds (spectra, elemental analyses) crystallize easily upon cooling the CH₂Cl₂ filtrate to 2°C.

As seen from DSC measurements, the melting points of all [hfip][−] and [hftb][−] salts are rather low (between 40°C and 110°C), which qualifies some of them as ionic liquids (ILs), however decomposition may start already below 200°C, e.g. [NBu₄]⁺[hfip][−] **4** decomposes at approx. 190°C. By contrast, the salts of the [pftb][−] anion are all thermally stable and they have much higher melting and decomposition points (for **2** and **3** > 300°C).

Table 15: Melting points (*T_m*) and decomposition temperatures (*T_d*) of the NR₄⁺ salts investigated in this study.

	<i>T_m</i> [°C]	<i>T_d</i> [°C]
[NBu ₄] ⁺ [pftb] [−] 1	198	> 250 ^(a)
[NEt ₄] ⁺ [pftb] [−] 2	> 300	> 300 ^(a)
[NMe ₄] ⁺ [pftb] [−] 3	> 300	> 300 ^(a)
[NBu ₄] ⁺ [hfip] [−] 4	40	190
[NEt ₄] ⁺ [hfip] [−] 5	56	> 100 ^(a)
[NMe ₄] ⁺ [hfip] [−] 6	43	> 70 ^(a)
[NBu ₄] ⁺ [hftb] [−] 7	106	> 150 ^(a)
[NEt ₄] ⁺ [hftb] [−] 8	110	> 150 ^(a)
[NMe ₄] ⁺ [hftb] [−] 9	94	> 150 ^(a)

^(a) only tested up to this temperature. No decomposition observed.

Additionally, [NBu₄]⁺[al-f-al][−] **10** has been prepared from [NBu₄]Br and the silver salt of the fluorine-bridged aluminate. But as its electrochemical properties have not been tested, it will not be discussed in the main text of this thesis. For further information concerning this compound see appendix 12.3 and experimental section.

5.1.2 Solid-State Structures

For some of the $[\text{NR}_4]^+$ salts (**2**, **5**, **6**, **7**, and **9**), crystals suitable for X-ray diffraction could be obtained. The diffraction measurements were carried out at low temperatures (between 100 and 150K) in order to minimize rotation of the CF_3 groups. In all of the solid-state structures, isolated cations and anions with only weak $\text{H}\cdots\text{F}$ contacts are found (Figure 22 to Figure 25) (for bond lengths see appendix 12.3, where pictures of cation-anion interactions are shown). The crystal structure of $[\text{NEt}_4]^+[\text{pftb}]^-$ **2** shows no special or unexpected parameters and, therefore, it will not be discussed in here. A picture of **2** is shown in appendix 12.3. For the $[\text{hfip}]^-$ and the $[\text{hftp}]^-$ anions, the tetraalkylammonium salts are the first examples of really ionic solid-state structures with isolated anions and cations, while all the other species containing these anions, contain molecular structures with coordinated anions, e.g. $[(\text{P}_4\text{S}_3)\text{AgA}]^{[44, 180]}$, $[(\text{P}_4)\text{AgA}]^{[43]}$, $[(\text{L})_2\text{AgA}]^{[182, 184]}$ or $[(\text{L})\text{AgA}]^{[182, 184]}$ ($[\text{A}] = [\text{hfip}]$, $[\text{hftb}]$, $\text{L} = \text{C}_2\text{H}_2$, C_2H_4). Therefore, the tetraalkylammonium salts of these anions serve as model compounds for undisturbed anions. Sections of their solid-state structures are shown in Figure 18 to Figure 21.

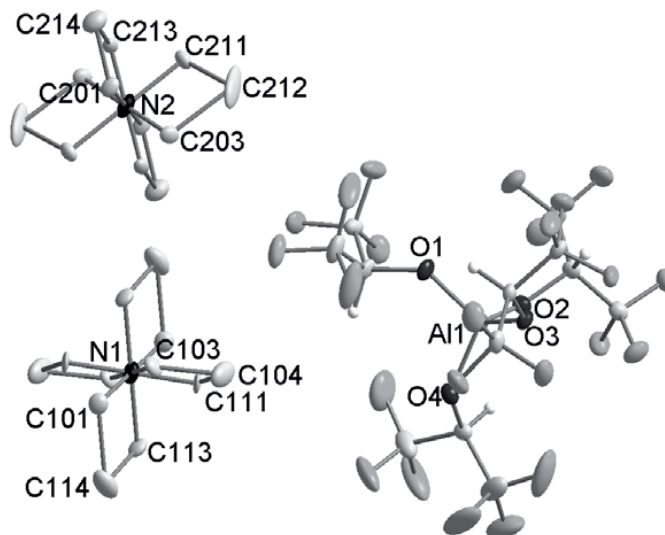


Figure 18: Section of the solid-state structure of $[\text{NEt}_4]^+[\text{hfip}]^-$ **5** at 100K. Thermal ellipsoids are drawn at the 25% probability level. In the asymmetric unit, there are two half disordered cations, the other atoms have been symmetry-generated. H atoms at the ethyl groups have been omitted for clarity. Selected distances and bond angles: $d(\text{Al1}-\text{O1}) = 173.9(2)$ pm, $d(\text{Al1}-\text{O2}) = 173.7(2)$ pm, $d(\text{Al1}-\text{O3}) = 175.0(3)$ pm, $d(\text{Al1}-\text{O4}) = 174.2(3)$ pm, $\angle(\text{O4}-\text{Al1}-\text{O1}) = 109.88(13)^\circ$, $\angle(\text{O4}-\text{Al1}-\text{O3}) = 116.25(12)^\circ$, $\angle(\text{O1}-\text{Al1}-\text{O3}) = 102.92(12)^\circ$, $\angle(\text{O4}-\text{Al1}-\text{O2}) = 104.02(12)^\circ$, $\angle(\text{O1}-\text{Al1}-\text{O2}) = 115.42(12)^\circ$, $\angle(\text{O3}-\text{Al1}-\text{O2}) = 108.80(12)^\circ$.

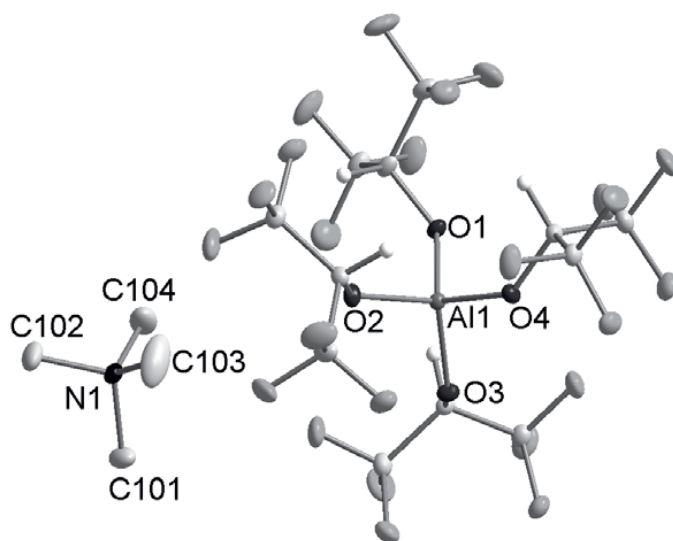


Figure 19: Section of the solid-state structure of $[\text{NMe}_4]^+[\text{hfp}]^-$ **6** at 100K. Thermal ellipsoids are drawn at the 25% probability level. In the asymmetric unit, there are two half cations, the other atoms have been symmetry-generated. H atoms at the methyl groups have been omitted for clarity. Selected distances and bond angles: $d(\text{Al1-O1}) = 174.32(9)$ pm, $d(\text{Al1-O2}) = 174.44(10)$ pm, $d(\text{Al1-O3}) = 174.35(9)$ pm, $d(\text{Al1-O4}) = 173.67(19)$ pm, $\angle(\text{O4-Al1-O1}) = 115.05(5)^\circ$, $\angle(\text{O4-Al1-O3}) = 106.50(5)^\circ$, $\angle(\text{O1-Al1-O3}) = 106.10(5)^\circ$, $\angle(\text{O4-Al1-O2}) = 109.96(5)^\circ$, $\angle(\text{O1-Al1-O2}) = 107.52(5)^\circ$, $\angle(\text{O3-Al1-O2}) = 111.71(5)^\circ$.

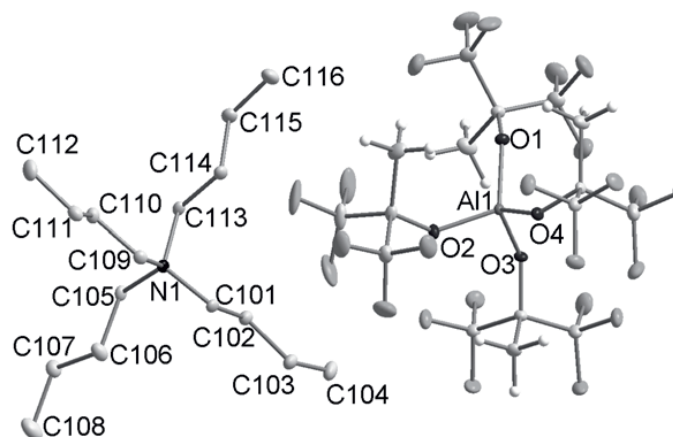


Figure 20: Section of the solid-state structure of $[\text{NBu}_4]^+[\text{hftb}]^-$ **7** at 100K. Thermal ellipsoids are drawn at the 25% probability level. In the asymmetric unit, there is one entire cation and one entire anion. H atoms at the butyl groups have been omitted for clarity. Selected distances and bond angles: $d(\text{Al1-O1}) = 174.02(13)$ pm, $d(\text{Al1-O2}) = 174.03(12)$ pm, $d(\text{Al1-O3}) = 174.24(12)$ pm, $d(\text{Al1-O4}) = 173.50(11)$ pm, $\angle(\text{O4-Al1-O1}) = 109.29(6)^\circ$, $\angle(\text{O4-Al1-O3}) = 113.19(6)^\circ$, $\angle(\text{O1-Al1-O3}) = 108.14(6)^\circ$, $\angle(\text{O4-Al1-O2}) = 105.90(6)^\circ$, $\angle(\text{O1-Al1-O2}) = 114.03(6)^\circ$, $\angle(\text{O3-Al1-O2}) = 106.38(6)^\circ$.

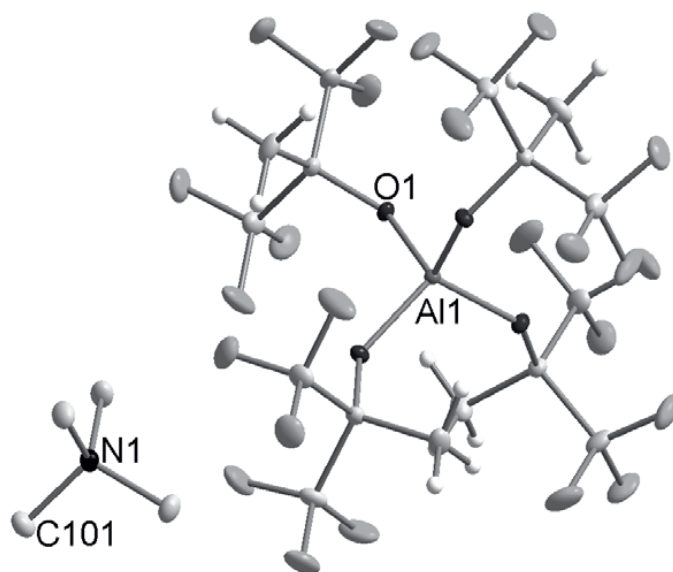


Figure 21: Section of the solid-state structure of $[\text{NMe}_4]^+[\text{hftb}]^- \mathbf{2}$ at 100K. Thermal ellipsoids are drawn at the 25% probability level. In the asymmetric unit, there is one quarter cation and one quarter anion, the other atoms have been symmetry-generated. H atoms at the methyl groups have been omitted for clarity. Selected distances and bond angles: $d(\text{Al1}-\text{O1}) = 174.23(6)$ pm, $\angle(\text{O1}-\text{Al1}-\text{O1}) = 109.5^\circ$.

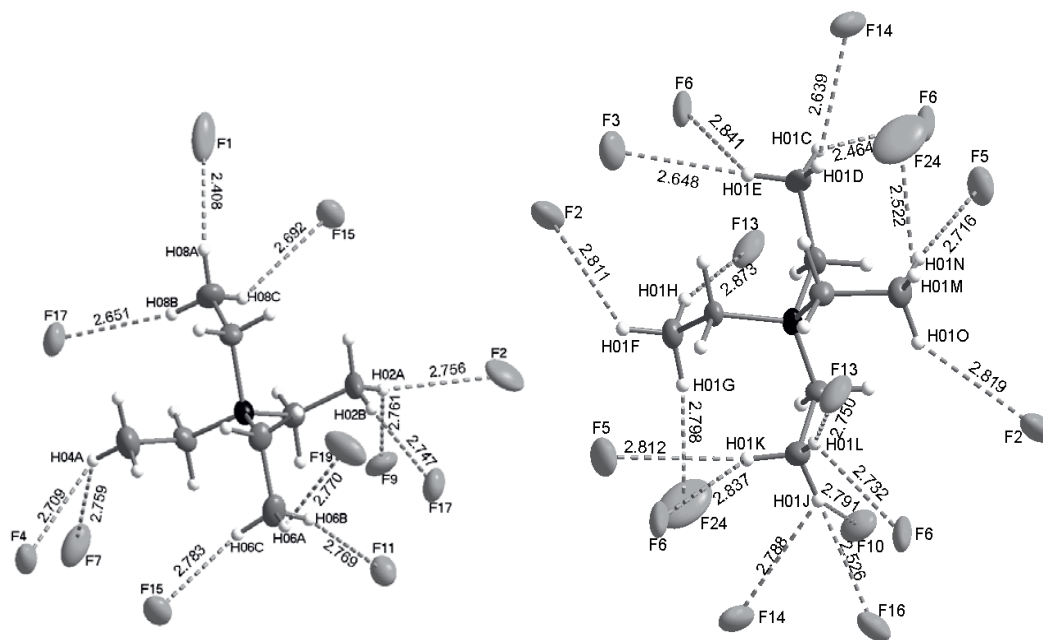


Figure 22: Cation-anion contacts in $[\text{NEt}_4]^+[\text{hfip}]^- \mathbf{5}$ at 140K.

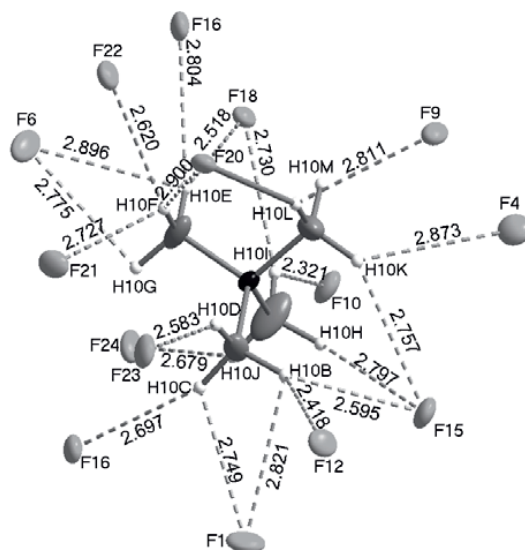


Figure 23: Cation-anion contacts in $[\text{NMe}_4]^+[\text{hfp}]^-$ **6** at 100K.

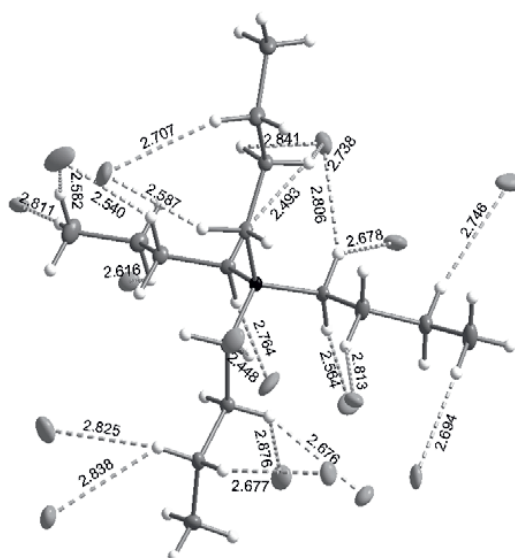


Figure 24: Cation-anion contacts in $[\text{NBu}_4]^+[\text{hfb}]^-$ **7** at 100K.

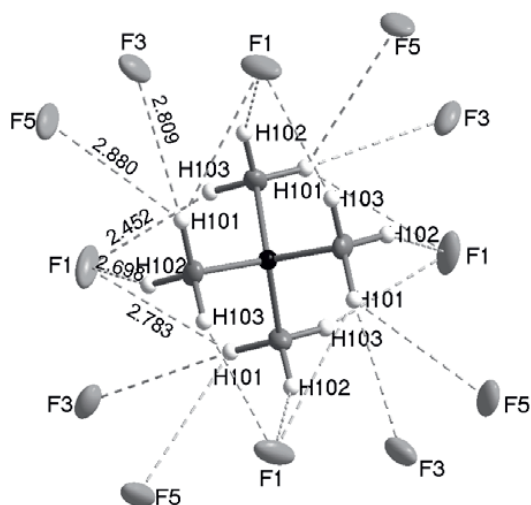


Figure 25: Cation-anion contacts in $[\text{NMe}_4]^+[\text{hftb}]^-$ **2** at 100K.

In Table 16, the most characteristic parameters, i.e. the Al-O distance and the O-Al-O and Al-O-C bond angles, are listed. The Al-O distances of the $[\text{hfip}]^-$ and the $[\text{hftb}]^-$ anions are similar within the standard deviation, while those in the $[\text{pftb}]^-$ salt are slightly shorter. The most significant difference between the perfluorinated and the other two anions are the Al-O-C bond angles. In the $[\text{pftb}]^-$ anion, the alkoxy moieties are larger and due to this sterical hindrance, the Al-O-C angle is greater.

Table 16: Characteristic structural information of the $[\text{Al}(\text{OR}^{\text{F}})_4]^-$ anions in their tetraalkylammonium salts at 100K. Distances are given in pm, bond angles are given in $^\circ$.

	$[\text{NEt}_4]^+[\text{pftb}]^-$	$[\text{NEt}_4]^+[\text{hfip}]^-$	$[\text{NMe}_4]^+[\text{hfip}]^-$	$[\text{NBu}_4]^+[\text{hftb}]^-$	$[\text{NMe}_4]^+[\text{hftb}]^-$
	2	5	6	7	9
$d(\text{Al-O})$	172.3(4)–174.2(4)	173.7(2)–175.0(3)	173.7(2)–174.4(1)	173.1(1)–174.2(1)	174.2(1)
[pm]	av. 173.4	av. 174.2	av. 174.2	av. 174.0	
$\angle(\text{O-Al-O})$	107.2(1)–112.7(2)	102.9(1)–116.3(1)	106.5(1)–115.1(1)	105.9(1)–114.0(1)	109.5
[$^\circ$]	av. 109.5	av. 109.5	av. 109.5	av. 109.5	
$\angle(\text{Al-O-C})$	144.9(4)–147.9(4)	124.5–133.7(2)	126.6(1)–136.3(1)	135.0(1)–141.6(1)	135.2(1)
[$^\circ$]	av. 146.8	av. 129.5	av. 129.6	av. 138.2	

From the data in Table 16 it may be concluded that the Al-O bond in the $[\text{pftb}]^-$ salts is slightly more stable; similar experiences have been made in experiments aiming at the

synthesis of reactive cation salts with the [hfip][−] and [hftb][−] anions being less suitable to reach the extremes than [pftb][−].

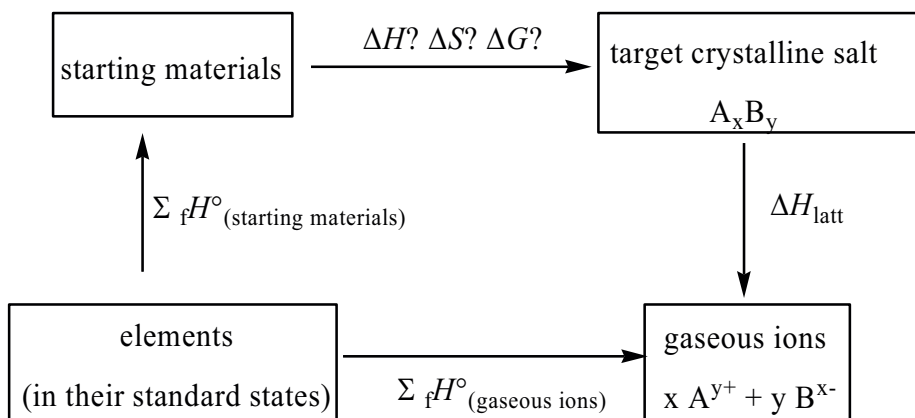
In all these 1:1 salts, different packing types are found in the solid state. A short description of these packing patterns is given in Table 17. Since the anions are larger than the cations, their packing description will be based on the anion lattice.

Table 17: Description of the solid-state packing in the [NR₄]⁺ salts.

	anion packing	cation environment
[NEt ₄] ⁺ [pftb] [−] 2	B-centered lattice	distorted cubic
[NEt ₄] ⁺ [hfip] [−] 5	C-centered lattice	distorted octahedral
[NMe ₄] ⁺ [hfip] [−] 6	C-centered lattice	strongly distorted octahedral
[NBu ₄] ⁺ [hftb] [−] 7	distorted cubic P lattice	distorted cubic
[NMe ₄] ⁺ [hftb] [−] 9	I-centered lattice	distorted octahedral

Establishment of the ion volumes of the [Al(OR^F)₄][−] anions:

Lattice energies derived from thermochemical volumina of the ions in a salt (V_{ion}) are the fundamental anchor point in the concept of Volume-Based Thermodynamics (VBT) established first by N. Bartlett^[147] and later in more detail by Glasser and Jenkins^[141, 185]. This concept allows thermodynamic predictions for condensed phases principally via formula unit volumes (cf. Scheme 4): This method, being independent of detailed knowledge of crystal structures, is applicable to liquids and amorphous materials as well as to crystalline solids. In the case of Ionic Liquids, the knowledge of V_{ion} also allows to predict physical properties like melting points or dielectric constants^[95].



Scheme 4: Born–Haber–Fajans thermochemical cycle, which provides an indirect route for the estimation of ΔH for the preparation of a crystalline salt $A_x B_y$ [185].

For these reasons, it is indispensable to have very accurate values of V_{ion} in order to get reliable values for the VBT calculations. The $[\text{NR}_4]^+$ salts of the $[\text{Al}(\text{OR}^{\text{F}})_4]^-$ anions were chosen to establish precise V_{ion} of these anions, since in these salts, the anions have a nearly undisturbed environment and therefore, they are ideal candidates for such purpose. In Table 18, the values obtained from the solid-state structures of their $[\text{NR}_4]^+$ salts are compiled.

Table 18: Ion volumes V_{ion} of the $[\text{Al}(\text{OR}^{\text{F}})_4]^-$ anions, based on the solid-state structures of their $[\text{NR}_4]^+$ salts at 100K. All values are given in nm^3 .

	$[\text{hfip}]^-$	$[\text{hftb}]^-$	$[\text{pftb}]^-$
$[\text{NBu}_4]^+ [\text{Al}(\text{OR}^{\text{F}})_4]^-$	-	$0.6491 \pm 0.009^{(c)}$	-
$[\text{NEt}_4]^+ [\text{Al}(\text{OR}^{\text{F}})_4]^-$	0.5727 ± 0.006	-	$0.7361 \pm 0.016^{(a)}$
$[\text{NMe}_4]^+ [\text{Al}(\text{OR}^{\text{F}})_4]^-$	$0.5826 \pm 0.015^{(b)}$	$0.6664 \pm 0.015^{(b)}$	-
average	0.577	0.658	0.736

^(a) $V_{\text{ion}}(\text{NEt}_4^+)$ from Ref. [141] ^(b) $V_{\text{ion}}(\text{NMe}_4^+)$ from Ref. [141] ^(c) $V_{\text{ion}}(\text{NBu}_4^+)$ from $[\text{NBu}_4]^+ [\text{IO}_4]^-$ [186] and $V_{\text{ion}} \text{IO}_4^-$ from Ref. [141].

5.1.3 Vibrational Spectra of the Aluminates

The solid-state structures of the $[\text{NR}_4]^+$ salts ($\text{R} = \text{Me}, \text{Et}, \text{Bu}$) contain undisturbed anions with only very weak H--F contacts (see section 5.1.2). If the cation is more electrophilic (e.g. $\text{Ag}(\text{CH}_2\text{Cl}_2)^+$, Ag^+ or Li^+), the symmetry of the anion is lowered which leads to the splitting of some anion vibrational bands. In this section, the different IR spectra are discussed – together with simulations from DFT-calculations ((RI)BP86/SV(P) level, which usually slightly underestimate the vibrational frequencies). An explanation of the influence of the cations is given.

IR Spectra of the [pftb]⁻ Salts:

In Table 19 the vibrational frequencies of the $[\text{pftb}]^-$ anion in different compounds, i.e its $[\text{NR}_4]^+$, $[\text{Ag}(\text{CH}_2\text{Cl}_2)]$, Ag and Li salts, are listed, together with the simulated IR spectrum of the isolated anion.

Table 19: Calculated (RI-BP86/SV(P)) and experimental vibrational (IR and Raman) frequencies (in cm^{-1}) of the $[\text{pftb}]^-$ anion in $[\text{NBu}_4]^+[\text{pftb}]^-$ **1**, $[\text{NEt}_4]^+[\text{pftb}]^-$ **2**, $[\text{NMe}_4]^+[\text{pftb}]^-$ **3**, $[\text{Ag}(\text{CH}_2\text{Cl}_2)[\text{pftb}]$, $\text{Ag}[\text{pftb}]$ and $\text{Li}[\text{pftb}]$.

$[\text{pftb}]^-$	$[\text{NBu}_4]^+[\text{pftb}]^-$ 1		$[\text{NEt}_4]^+[\text{pftb}]^-$ 2		$[\text{NMe}_4]^+[\text{pftb}]^-$ 3		$[\text{Ag}(\text{CH}_2\text{Cl}_2)[\text{pftb}]$		$\text{Li}[\text{pftb}]$		assignment
Calc.	IR exp.	Raman exp.	IR exp.	Raman exp.	IR exp.	Raman exp.	IR exp.	Raman exp.	IR exp.	Raman exp.	
189 (w)	227 (w)	233 (w)	228 (w)	234 (w)	-	235 (w)	-	-	-	234 (mw)	-
274 (w)	303 (w)	291 (w)	285 (mw)	289 (w)	289 (w)	289 (w)	288 (w)	290 (w)	289 (w)	297 (w)	C-C
301 (w)	315 (m)	322 (ms)	316 (m)	323 (ms)	316 (w)	322 (s)	316 (m)	319 (m)	-	326 (w)	C-C, Al-O
319 (w)	-	-	331 (w)	-	-	-	332 (w)	332 (w)	326 (w)	327 (m)	C-C, C-F, Al-O
352 (w)	367 (w)	369 (w)	367 (mw)	368 (w)	-	368 (m)	367 (w)	-	369 (w)	363 (w)	C-C, C-F, Al-O
364 (w)	382 (w)	-	377 (mw)	-	-	-	387 (mw)	391 (mw)	-	390 (w)	C-C, C-O
421+436 (mw)	448 (ms)	-	446 (ms)	-	449 (m)	453 (ms)	443 (m)	435 (m)	-	-	C-C, C-O
-	-	-	-	-	-	-	468 (mw)	468 (m)	464 (m)	-	-
520 (mw)	536 (m)	538 (mw)	537 (m)	538 (w)	536 (m)	538 (mw)	537 (mw)	538 (ms)	539 (m)	539 (mw)	C-C, C-O
-	-	-	-	-	-	-	-	553 (mw)	546 (mw)	-	-
547 (mw)	559 (mw)	561 (w)	562 (mw)	563 (w)	560 (mw)	562 (mw)	561 (mw)	567 (mw)	562 (mw)	-	Al-O, C-C
556 (w)	573 (w)	572 (w)	571 (w)	-	571 (w)	572 (mw)	572 (mw)	575 (mw)	572 + 582 (m)	573 (mw)	Al-O, C-C
-	-	-	-	-	-	-	-	694 (w)	-	-	-
708 (m)	726 (ms)	-	727 (s)	-	725 (ms)	-	727 (ms)	727 (s)	726 (s)	730 (s)	C-C, C-O
-	-	744 (ms)	-	747 (ms)	-	747 (s)	-	743 (m)	740 (ms)	745 (s)	-
735 (w)	755 (w)	-	756 (mw)	-	756 (mw)	-	754 (w)	759 (w)	756 + 760 (m)	-	C-C, C-O
-	-	799 (ms)	-	798 (s)	-	794 (s)	796 (w)	796 (mw)	798 (m)	801 (w)	-
816 (w)	830 (m)	-	833 (m)	834 (w)	831 (m)	832 (w)	833 (mw)	827 (w)	844 (ms)	843 (w)	Al-O, C-C
825 (w)	-	-	-	-	-	-	-	862 (mw)	863 (ms)	-	Al-O, C-C
-	-	-	-	-	947 (sh)	-	-	-	936 (ms)	-	-
-	-	-	-	-	967 (sh)	-	964 (s)	-	964 (vs)	-	-

Table 19 continued: Calculated (RI-BP86/SV(P)) and experimental vibrational (IR and Raman) frequencies (in cm^{-1}) of the $[\text{pftb}]^-$ anion in $[\text{NBu}_4]^+[\text{pftb}]^-$ **1**, $[\text{NEt}_4]^+[\text{pftb}]^-$ **2**, $[\text{NMe}_4]^+[\text{pftb}]^-$ **3**, $[\text{Ag}(\text{CH}_2\text{Cl}_2)][\text{pftb}]$, $\text{Ag}[\text{pftb}]$ and $\text{Li}[\text{pftb}]$.

Calc.	$[\text{NBu}_4]^+[\text{pftb}]^-$ 1		$[\text{NEt}_4]^+[\text{pftb}]^-$ 2		$[\text{NMe}_4]^+[\text{pftb}]^-$ 3		$[\text{Ag}(\text{CH}_2\text{Cl}_2)][\text{pftb}]$		$\text{Ag}[\text{pftb}]$		$\text{Li}[\text{pftb}]$		assignment
	IR exp.	Raman exp.	IR exp.	Raman exp.	IR exp.	Raman exp.	IR exp.		IR exp.		IR exp.	Raman exp.	
960 (s)	975 (vs)	975 (mw)	973 (s)	978 (mw)	976 (s)	976 (mw)	974 (ms)		974 (vs)		976 (vs)	978 (w)	C-C, C-F
1110 (w)	-	1133 (mw)	-	1139 (mw)		1135 (mw)	-		-		-	1113 (w)	C-C, C-F
1134 (w)	1176 (ms)	1173 (mw)	-	1173 (mw)	1163 (s)	-	1182 (m)		1182 (m)		1184 (ms)	1171 (w)	C-C, C-F
1218 (vs)	1223 (vs)	-	1217 (vs)	-		-	1224 (vs)		1218 (vs)		1225 (vs)	1214 (mw)	C-C, C-F
1230 (vs)	1236 (vs)	1237 (mw)	1240 (s)	1235 (mw)	1237 (vs)	1239 (mw)	1245 (vs)		1245 (vs)		1243 (s)	1250 (mw)	C-C, C-F
1260 (vs)	-	-	1254 (s)	-	-	-	1256 (s)		1259 (vs)		-	-	C-C, C-F
-	1274 (s)	1276 (mw)	1274 (vs)	1274 (mw)	1271 (vs)	1272 (mw)	-		-		1270 (s)	1281 (mw)	C-C, C-F
-	1299 (s)	-	1298 (s)	1300 (m)	1296 (s)	1307 (w)	1299 (ms)		1301 (s)		1297 (s)	-	C-C, C-F
1344 (vs)	1349 (ms)	1353 (w)	1353 (ms)	-	1351 (ms)	1352 (w)	1355 (mw)		1354 (m)		1353 (ms)	1337 (mw)	C-C, C-F

Vibrational bands of the [pftb]⁻ anion are found both in the MIR and the FIR region, the most characteristic absorptions are observed at 727 cm⁻¹ (C–C, C–O) and 974 cm⁻¹ (C–C, C–F) as well as many strong bands in the range from 1100 cm⁻¹ to 1400 cm⁻¹ (C–C, C–F). The comparison of the simulated spectra (Table 19) with those of [NR₄]⁺[pftb]⁻ shows that the anion has nearly S₄ symmetry in these compounds, because only the expected absorption maxima are observed. This is also in good agreement with the solid-state structure of [NEt₄]⁺[pftb]⁻ **2** determined by X-ray (see above).

In the case of the [Ag(CH₂Cl₂)]⁺ salt, splitting occurs for the bands at 974 cm⁻¹ (→ 964 and 974 cm⁻¹) and at 447 cm⁻¹ (→ 443 and 468 cm⁻¹). If [Ag(CH₂Cl₂)] [pftb] is dried in high vacuum (about 10⁻³ mbar) for a two to four days, the coordinated CH₂Cl₂ molecule can be removed. As shown in Table 19, the IR spectra split further: Without the CH₂Cl₂ ligand, some new bands appear (at 553, 694, 743 and 862 cm⁻¹). In both silver salts the silver atom is supposed to be coordinated to the [pftb]⁻ anion. Therefore, the symmetry is reduced, which leads to band splitting in the vibrational spectrum. Although the solid state structure of Ag(CH₂Cl₂)[pftb] is yet unknown, it is very likely that – in analogy to the corresponding silver salts of [hfip]⁻ and [hftb]⁻ as well as in [Ag(C₆H₄(CF₃)₂)] [pftb]^[11], – the oxygen atoms are involved in this coordination. According to quantum mechanical calculations, the oxygen atoms are also the most basic parts of the [pftb]⁻ anion (partial charge: -0.24)^[4, 172], and their polarizability is higher (0.802 instead of 0.557 for F)^[187]. In Ag[pftb], the symmetry is even more lowered due to stronger coordination. This causes the increased splitting of more anion bands. The same holds for the Li salt, but in this case, the splitting is even more distinct: between 539 and 582 cm⁻¹ five signals are observed, next to the band at 760 cm⁻¹, a second one arises at 756 cm⁻¹, and the band at 964/976 cm⁻¹ shows a broad shoulder. This is in line with the small size and the high charge density of the Li cation, which allows a strong interaction with the lone pairs of the oxygen atoms of the anion.

In all salts of the [pftb]⁻ anion investigated in this study, the broader bands of the CF₃ groups (between 1100 and 1400 cm⁻¹) remain nearly unchanged upon anion coordination.

IR Spectra of the [hfip]⁻ and [hftb]⁻ Salts:

Also for the anions [hfip]⁻ and [hftb]⁻, characteristic vibrational excitations are observed (Table 20 and Table 21), which can also be used to distinguish between the different anions: in the case of the [hftb]⁻ anion, the intense C–C / C–O and the C–C / C–F modes are found at 736 cm⁻¹ and 995 cm⁻¹, while for [hfip]⁻ salts, they are found at around 730 cm⁻¹ and 1012 cm⁻¹ (cf. 727 and 974 cm⁻¹ for the [pftb]⁻). In both hydrogen-containing anions, C–H vibrations were found: at 1375, 2715 (only in the Raman spectra) and 2950 cm⁻¹ for [hftb]⁻ and at around 1455 and 2960 cm⁻¹ for [hfip]⁻. For the [hftb]⁻ anion, also two weak bands above 3000 cm⁻¹ were predicted by quantum chemical calculations, but in the case of the alkylammonium salts, these absorptions are covered by the bands of the cations, and in the Ag⁺ and Li⁺ salt, they are most probably too weak to be seen.

The influence of the anion-cation interactions on the vibrational spectra can also be seen for the [hftb]⁻ and the [hfip]⁻ anions: In the case of the [hfip]⁻, the most affected bands are those between 700 and 900 cm⁻¹ (C–C, Al–O and C–O vibrations): while for the NR₄⁺ salts, only three bands are found in the IR and Raman spectra – as expected from the simulated spectrum of the anion – one observes splitting in the Ag⁺ and Li⁺ salt due to lowered symmetry, which leads to up to six bands (see arrows in Figure 26). The vibrations of the CF₃ moieties remain, like those in the [pftb]⁻ salts, unchanged upon coordination.

Similar observations are also made for the [hftb]⁻ anion: The Al–O, C–C and C–O vibrations are strongly dependent on the coordination ability of the countercation: the strong coordination to the Li⁺ and Ag⁺ in these salts also lowers the anion symmetry, and again, this can be seen from the vibrational spectra: The NR₄⁺ salts have four absorptions between 730 and 1000 cm⁻¹, whereas in the case of Li⁺, six different bands appear. Also for this anion, the bands of the CF₃ groups are not affected by coordination.

All these findings are also in very good agreement with the solid-state structures, in which nearly ideal symmetric anion environments have been found for their NR₄⁺ salts.

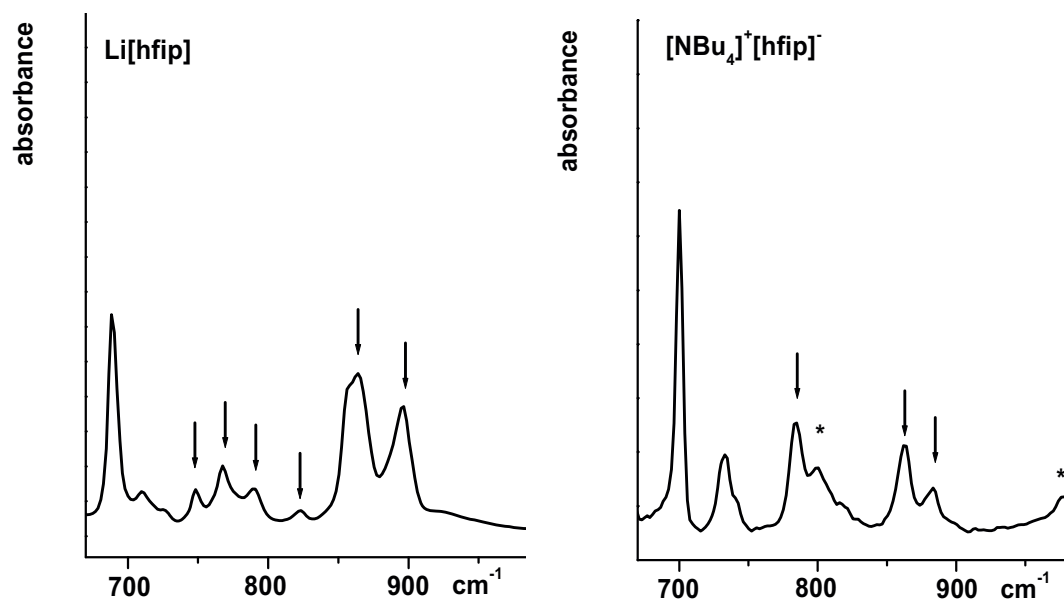


Figure 26: Comparison of sections of the IR spectra of Li[hfip] and [NBu₄]⁺[hfip]⁻ **4**. Bands marked with asterisks are assigned to the cation.

Table 20: Calculated (RI-BP86/SV(P)) and experimental vibrational (IR and Raman) frequencies (in cm^{-1}) of the [hfp]⁻ anion in its Ag⁺, Li⁺, [NBu₄]⁺, [NEt₄]⁺ and [NMe₄]⁺ salts.

[hfp] ⁻ calc.	[NBu ₄] ⁺ [hfp] ⁻ 4		[NEt ₄] ⁺ [hfp] ⁻ 5		[NMe ₄] ⁺ [hfp] ⁻ 6		Ag[hfp]		Li[hfp]		assignment
	IR exp.	Raman exp.	IR exp.	Raman exp.	IR exp.	Raman exp.	IR exp.		IR exp.	Raman exp.	
289 (w)	-	298 (w)	302 (w)	299 (w)	-	298 (w)	-	-	-	301 (w)	C-C, Al-O
-	-	-	-	-	-	-	-	-	320 (mw)	-	-
-	328 (w)	333 (mw)	330 (w)	331 (mw)	-	331 (mw)	332 (w)	-	-	333 (mw)	-
370 (mw)	377 (w)	369 (w)	367 (w)	357 (w)	-	-	-	-	379 (mw)	364 (mw)	C-C, C-F, Al-O
448 (w)	445 (mw)	-	438 (mw)	417 (mw)	444 (w)	-	421 (mw)	427 (mw)	450 (w)	450 (w)	C-C, C-O
487 (w)	-	-	-	-	-	-	463 (w)	470 (w)	485 (mw)	485 (mw)	C-C, C-O
514 (w)	524 (mw)	526 (w)	521 (w)	524 (w)	522 (w)	525 (w)	523 (mw)	521 (mw)	527 (w)	527 (w)	C-C, C-O
-	536 (w)	537 (w)	-	536 (w)	-	537 (w)	537 (w)	537 (w)	539 (w)	539 (w)	-
547 (w)	567 (w)	569 (w)	570 (w)	566 (w)	570 (w)	571 (w)	563 (w)	563 (w)	556 (w)	556 (w)	C-C, Al-O
-	-	-	-	-	-	-	578 (w)	577 (w)	576 (w)	576 (w)	-
607 (mw)	597 (w)	600 (w)	-	-	-	-	-	-	-	-	C-C, Al-O
-	-	-	-	-	-	-	669 (w)	-	-	-	-
679 (m)	685 (m)	-	684 (m)	-	685 (m)	-	688 (m)	689 (ms)	-	-	C-C, Al-O
-	-	697 (w)	-	696(w)	-	698 (m)	-	-	-	692 (w)	-
-	-	-	-	-	-	-	-	-	-	708 (w)	-
721 (m)	-	729 (w)	727 (mw)	-	-	729 (w)	727 (w)	-	-	733 (w)	C-C, C-O
754 (m)	-	-	-	-	-	-	-	748 (w)	752 (mw)	752 (mw)	C-C, C-O
-	-	763 (mw)	-	762 (mw)	777 (w)	765 (m)	760 (mw)	767 (w)	769 (m)	769 (m)	-
-	-	-	-	-	-	-	780 (mw)	-	-	-	-
-	791 (w)	-	783 (w)	-	-	-	793 (w)	790 (w)	829 (w)	829 (w)	-
-	-	-	-	-	-	-	-	828 (w)	-	-	-
874 (m)	855 (w)	860 (m)	854 (w)	857 (m)	858 (m)	853 (m)	859 (m)	864 (m)	858 (ms)	-	C-C, Al-O

Table 20 continued: Calculated (RI-BP86/SV(P)) and experimental vibrational (IR and Raman) frequencies (in cm^{-1}) of the [hfp]⁻ anion in its Ag⁺, Li⁺, [NBu₄]⁺, [NEt₄]⁺ and [NMe₄]⁺ salts.

[hfp] ⁻ calc.	[NBu ₄] ⁺ [hfp] ⁻ 4		[NEt ₄] ⁺ [hfp] ⁻ 5		[NMe ₄] ⁺ [hfp] ⁻ 6		Li[hfp]		assignment
	IR exp.	Raman exp.	IR exp.	Raman exp.	IR exp.	Raman exp.	IR exp.	Raman exp.	
-	888 (mw)	884 (w)	890 (mw)	891 (w)	891 (m)	893 (w)	896 (m)	898 (w)	-
-	-	910 (w)	-	905 (w)	-	-	-	-	-
-	-	930 (w)	-	-	-	933 (w)	-	-	-
1012 (ms)	-	1053 (w)	-	-	-	-	-	-	C-C, C-F
-	-	1068 (w)	-	1069 (w)	-	-	-	-	-
1033 (s)	1100 (m)	-	1096 (m)	-	1096 (m)	-	1102 (s)	1098 (mw)	C-C, C-F
-	-	1112 (mw)	-	1117 (mw)	-	1117 (mw)	-	-	-
1126 (vs)	-	1133 (mw)	-	-	-	-	1136 (vs)	1133 (mw)	C-C, C-F
1147 (s)	-	1155 (mw)	-	-	1152 (m)	-	-	-	C-C, C-F
1174 (s)	1180 (vs)	1179 (w)	1169 (vs)	1187 (w)	1179 (vs)	1190 (w)	1188 (vs)	-	C-C, C-F
1195 (vs)	-	-	1207 (s)	1209 (w)	-	-	-	1204 (mw)	C-C, C-F
1225 (s)	1252 (vs)	-	-	-	-	-	1237 (vs)	1242 (mw)	C-C, C-F
-	-	-	-	-	-	1266 (w)	-	1266 (w)	-
1294 (ms)	1288 (s)	1295 (mw)	1288 (s)	1300 (mw)	1294 (s)	1298 (w)	1293 (s)	1297 (w)	C-C, C-F
1330 (s)	-	1324 (w)	-	-	-	-	-	-	C-C, C-F, C-H
-	1375 (ms)	1383 (w)	1377 (ms)	1379 (w)	1376 (ms)	1379 (ms)	1379 (ms)	1381 (w)	-
-	-	-	-	-	-	-	-	1390 (w)	-
-	-	2716 (w)	-	2715 (w)	-	2722 (w)	-	2732 (w)	-
-	-	2757 (w)	-	2759 (w)	-	-	-	2759 (w)	-
2923 (m)	2975 (mw)	2944 (mw)	2951 (w)	2952 (mw)	-	2953 (m)	-	2958 (mw)	C-H

Table 21 continued: Calculated (RI-BP86/SV(P)) and experimental vibrational (IR and Raman) frequencies (in cm^{-1}) of the $[\text{hfb}]^-$ anion in its Ag^+ , Li^+ , $[\text{NBu}_4]^+$, $[\text{NEt}_4]^+$ and $[\text{NMe}_4]^+$ salts.

$[\text{hfb}]^-$ calc.	$[\text{NBu}_4]^+[\text{hfb}]^- \mathbf{7}$		$[\text{NEt}_4]^+[\text{hfb}]^- \mathbf{8}$		$[\text{NMe}_4]^+[\text{hfb}]^- \mathbf{9}$		$\text{Li}[\text{hfb}]$		assignment
	IR exp.	Raman exp.	IR exp.	Raman exp.	IR exp.	Raman exp.	IR exp.	Raman exp.	
1105 (s)	1112 (s)	-	1112 (s)	1117 (mw)	1115 (s)	1118 (w)	1118 (s)	1121 (w)	C-C, C-F
1156 (s)	1177 (s)	1187 (w)	1178 (s)	1174 (w)	-	1167 (w)	1185 (s)	-	C-C, C-F
1177 (vs)									
1198 (s)	-	-	-	-	1183 (vs)	1202 (w)	1210 (vs)	1213 (w)	C-C, C-F
1243 (s)									
1255 (vs)	1233 (s)	1237 (mw)	1235 (s)	1242 (w)	1232 (s)	1235 (w)	1229 (vs)	1250 (w)	C-C, C-F
1306 (vs))	1307 (s)		1308 (s)	1300 (w)	1307 (ms)	-	1311 (s)	-	C-C, C-F
-	-	1323 (w)	-	-	-	1319 (w)	-	1317 (w)	-
1351 (m)	1384 (mw)	1387 (w)	1386 (s)	1395 (w)	1389 (w)	1390 (w)	-	1392 (mw)	C-C, C-F
1432 (w)	1457 (w)	1453 (ms)	1462 (s)	1464 (ms)	1460 (w)	1456 (m)	1460 (mw)	1464 (m)	C-H
2975 (w)	2968 (mw)	-	-	2958 (m)	2963 (w)	2958 (m)	-	2901 (m)	C-H
3071 (w)	^(a)	^(a)	^(a)	^(a)	^(a)	^(a)	2962 (ms)	2965 (s)	C-H
3080 (w)	^(a)	^(a)	^(a)	^(a)	^(a)	^(a)	3012 (mw)	3017 (ms)	C-H

^(a) hidden under the bands of the NR_4^+ cations.

5.1.4 Conductivity Measurements

Tetraalkylammonium salts are often applied in electrochemical measurements, where they serve as supporting electrolytes in organic solvents like CH₃CN. The problem with the commonly used [NR₄]⁺[PF₆]⁻ and [NR₄]⁺[BF₄]⁻ electrolytes is, that when the experiments are carried out in solvents with very low polarity (e.g. in CH₂Cl₂ or even HCCl₃), these salts are not very well suited to solubilize the electrochemically produced (multiply) charged cations and therefore, tend to form insoluble layers on the electrode preventing the measurement. Moreover many higher charged cations that are generated *in situ* in the electrochemical cell are too reactive for those counterions and decompose the [PF₆]⁻ anion. Since the [Al(OR^F)₄]⁻ anions are chemically rather robust and large, their electrochemical performance both with respect to electrochemical stability as well as conductivity in non polar solvents has been tested. In Table 22, the molar conductivities of the [NBu₄]⁺ salts in CH₂Cl₂ are listed, together with the values for [NBu₄]⁺[PF₆]⁻ examined in our laboratories.

Table 22: Molar conductivities of $[\text{NBu}_4]^+[\text{pftb}]^-$ **1**, $[\text{NBu}_4]^+[\text{hfp}]^-$ **4**, $[\text{NBu}_4]^+[\text{hfb}]^-$ **2** and $[\text{NBu}_4]^+[\text{PF}_6]^-$ in CH_2Cl_2 at 25°C.

$[\text{NBu}_4]^+[\text{pftb}]^-$ 1		$[\text{NBu}_4]^+[\text{hfp}]^-$ 4		$[\text{NBu}_4]^+[\text{hfb}]^-$ 2		$[\text{NBu}_4]^+[\text{PF}_6]^-$	
c	Λ_m	c	Λ_m	c	Λ_m	c	Λ_m
[mmol L ⁻¹]	[S cm ² mol ⁻¹]	[mmol L ⁻¹]	[S cm ² mol ⁻¹]	[mmol L ⁻¹]	[S cm ² mol ⁻¹]	[mmol L ⁻¹]	[S cm ² mol ⁻¹]
10.7	31.2	80.7	20.4	328.1	10.5	178.1	10.6
13.3	29.9	89.7	20.2	364.5	9.9	197.9	10.2
16.4	29.2	100.9	19.9	410.1	9.0	222.6	10.2
19.1	28.8	115.3	18.7	468.7	8.2	254.4	10.3
24.6	28.8	134.6	17.7	546.8	7.4	296.8	10.1
30.0	27.7	161.5	16.5	656.1	6.4	356.2	9.9
35.7	28.6	201.9	14.9	820.2	5.3	445.2	9.5
41.2	26.6	269.1	13.1	1093.6	3.9	593.7	8.6

Analogous conductivity measurements have been performed in CHCl_3 and toluene. To obtain the limiting molar conductivity (i.e. the molar conductivity at infinite dilution) Λ_∞ , all data have been fitted using the Kohlrausch law (eq. 37). The Λ_∞ values of the NBu_4 salts in the different solvents are listed in Table 23, plots of some fitting curves are shown in appendix 12.2.

eq. 37
$$\Lambda_m(c) = \Lambda_\infty - k \cdot \sqrt{c}$$

Table 23: Solubility and limiting molar conductivity Λ_∞ (in $\text{S cm}^2 \text{ mol}^{-1}$) at 25°C of $[\text{NBu}_4]^+[\text{pftb}]^-$ **1**, $[\text{NBu}_4]^+[\text{hfip}]^-$ **4**, $[\text{NBu}_4]^+[\text{hftb}]^-$ **7** and $[\text{NBu}_4]^+[\text{PF}_6]^-$. n.d. = not determined.

salt	solvent	solubility [mol L^{-1}]	Λ_∞ [$\text{S cm}^2 \text{ mol}^{-1}$]
$[\text{NBu}_4]^+[\text{pftb}]^-$ 1	CH_2Cl_2	0.04	38.75
	CHCl_3	<0.01	n.d.
	toluene	almost insoluble	-
$[\text{NBu}_4]^+[\text{hfip}]^-$ 4	CH_2Cl_2	0.27	29.90
	toluene	0.03	$4.8 \cdot 10^{-3}$
$[\text{NBu}_4]^+[\text{hftb}]^-$ 7	CH_2Cl_2	1.09	18.01
	CHCl_3	0.03	1.81
	toluene	0.05	$1.8 \cdot 10^{-3}$
$[\text{NBu}_4]^+[\text{PF}_6]^-$	CH_2Cl_2	0.59	12.64
	CHCl_3	1.12	2.80
	toluene	0.02	— ^(a)

^(a) identical to the conductivity of the pure solvent

If compared to the widely used $[\text{NBu}_4]^+[\text{PF}_6]^-$, only the $[\text{NBu}_4]^+[\text{hftb}]^-$ **7** shows a higher molar solubility in CH_2Cl_2 , however all tested aluminates have much higher limiting molar conductivities Λ_∞ in this solvent, indicating less ion pairing and higher mobility of the ions. The limiting molar conductivities Λ_∞ are in accord with the coordinating ability of the anions which decrease according to: $[\text{PF}_6]^- > [\text{hftb}]^- > [\text{hfip}]^- > [\text{pftb}]^-$ ^[4, 179]. Thus, less coordinating anions have higher limiting molar conductivities. In CHCl_3 , the Λ_∞ values are in the same order of magnitude. In toluene, which was the least polar solvent used in this study, the

solubilities and Λ_{∞} are very small (in the range of $\text{mS cm}^2 \text{ mol}^{-1}$), and in the case of $[\text{NBu}_4]^+[\text{PF}_6]^-$, no conductivity at all was measured in toluene. Overall, the aluminate salts are good alternatives as supporting electrolytes in non-polar media.

The higher solubility ($> 1 \text{ mol L}^{-1}$ in CH_2Cl_2) of $[\text{NBu}_4]^+[\text{hftb}]^-$ **7** can be explained by the influence of the CH_3 moieties, which make this anion more lipophilic than the perfluorinated $[\text{pftb}]^-$. The lipophilicity of the $[\text{hfip}]^-$ anion lies in between that of $[\text{pftb}]^-$ and $[\text{hftb}]^-$, which is also in good agreement with the solubility of its NBu_4 salt.

5.1.5 Cyclovoltammetry

The electrochemical stability of the NBu_4^+ salts has been tested by cyclovoltammetry (CV) in CH_2Cl_2 , 1,2- $\text{F}_2\text{C}_6\text{H}_4$ and CH_3CN . All salts were stable in the electrochemical windows of the used solvents (no currents larger than $0.5 \mu\text{A}$ measured), but **7** tends to precipitate at the electrode during the oxidation process. This phenomenon has also been previously observed for the $\text{Li}[\text{hfip}]$ salt^[iii], therefore the values obtained for this salt will not be used for a detailed discussion. In a second test series, the CV measurements were be done with the addition of ferrocene. The obtained results are listed in Table 24, and as an example, one CV plot is shown in Figure 27.

^[iii] However, $\text{Li}[\text{hfip}]$ is very stable, it does not undergo oxidation at potentials less than or equal 5 V vs. $\text{Li}^{+/0}$ in dimethylcarbonate[175] S. Tsujioka, B. G. Nolan, H. Takase, B. P. Fauber, S. H. Strauss, *Journal of the Electrochemical Society* **2004**, *151*, A1418..

Table 24: Electrochemical stability of the NBu_4^+ salts **1**, **4**, **7** and $[\text{NBu}_4][\text{PF}_6]$. U_{max} and U_{min} are given relative to the internal ferrocenium / ferrocene redox couple.

salt	solvent	U_{max} [V]	U_{min} [V]
$[\text{NBu}_4]^+[\text{pftb}]^-$ 1	CH_2Cl_2	1.4	-2.3
	1,2- $\text{F}_2\text{C}_6\text{H}_4$	1.4	-0.8
	CH_3CN	1.5	-1.3
$[\text{NBu}_4]^+[\text{hftb}]^-$ 7	CH_2Cl_2	1.1	-2.2
	1,2- $\text{F}_2\text{C}_6\text{H}_4$	1.1	-0.9
	CH_3CN	1.1	-1.1
$[\text{NBu}_4]^+[\text{PF}_6]^-$	CH_2Cl_2	0.9	-1.8
	1,2- $\text{F}_2\text{C}_6\text{H}_4$	0.7	-2.1
	CH_3CN	1.1	-0.4

It was found that especially the $[\text{pftb}]^-$ salt **1** is very stable against anodic oxidation (+1.5 V in acetonitrile), while the $[\text{PF}_6]^-$ anion already gets oxidized at +1.1V relative to ferrocene. This is in very good agreement with earlier results found for the Li^+ salts^[173, 175].

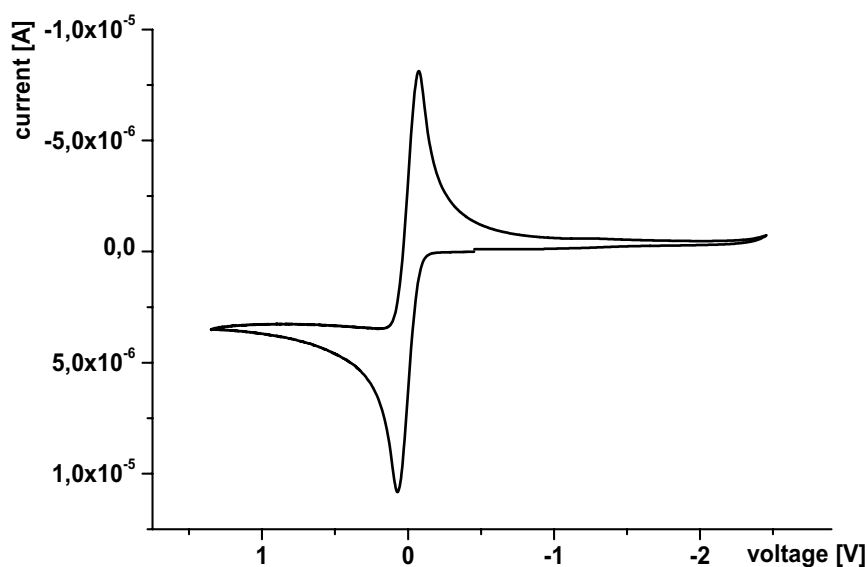
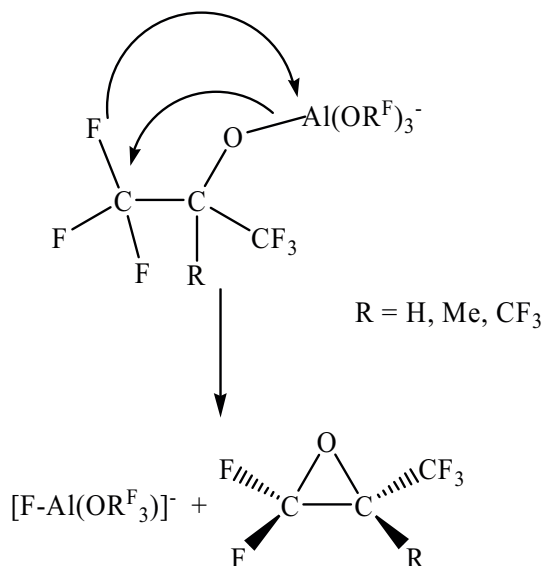


Figure 27: Cyclic voltammogram of 0.1 M CH_2Cl_2 solution of $[\text{NBu}_4]^+[\text{pftb}]^-$ **1**, showing the reversible ferrocenium / ferrocene reduction.

5.1.6 Mass Spectrometry

From some of the $[\text{NR}_4]^+$ salts of the $[\text{pftb}]^-$, $[\text{hfip}]^-$ and $[\text{hftb}]^-$ anions, ESI mass spectra in CH_3CN have been recorded in order to investigate anion decomposition pathways and correlate them to observed decomposition pathways with extremely electrophilic cations. Under the relatively mild conditions of the electrospray ionization, all three anions remain intact ($m/z = 967$ for $[\text{pftb}]^-$, 695 for $[\text{hfip}]^-$ and 751 for the $[\text{hftb}]^-$ anion), but upon collision experiments, in all three cases, the major decomposition product is the $[\text{F-Al}(\text{OR}^{\text{F}})_3]^-$ anion. The mechanism of this degradation is sketched in Scheme 5. For the $[\text{pftb}]^-$ anion, this decomposition route has also been observed in the condensed phase, i.e. during the formation of the $[\text{al-f-al}]^-$ anion^[52].



Scheme 5: Decomposition of the $[\text{Al}(\text{OR}^{\text{F}})_4]^-$ anions in the mass spectrometer.

5.2 Concluding Remarks

The tetraalkylammonium salts of the fluorinated alkoxyaluminates are easily accessible in large scale with good yields by simple metathesis reactions of their lithium salts with $[\text{NR}_4]\text{Br}$ ($\text{R} = \text{Me}, \text{Et}, \text{Bu}$) in water or $\text{Et}_2\text{O} / \text{CH}_2\text{Cl}_2$. The $[\text{NR}_4]^+[\text{A}]^-$ salts provide nearly undisturbed anion environments, which allows to determine reliable values for the thermochemical volumes of the anions. This property – to serve as model compounds with ideal anion geometries – also made it possible to investigate their vibrational spectra in comparison to

those of their Li^+ and Ag^+ salts, in which some of the bands are split because the anions are strongly coordinated by the cations.

The high solubility of $[\text{NR}_4]^+[\text{A}]^-$ salts in non-polar solvents like CH_2Cl_2 or CHCl_3 (up to 1.09 M for $[\text{NBu}_4]^+[\text{hftb}]^-$ **7** in CH_2Cl_2 and 0.41 M for $[\text{NBu}_4]^+[\text{hfip}]^-$ **4** in CHCl_3) makes them ideal candidates as supporting electrolytes in electrochemical processes, such as cyclic voltammetry. $[\text{NBu}_4]^+[\text{hftb}]^-$ **7** may even be suitable for toluene solution. Besides, they are also very stable against redox processes, i.e. their electrochemical window is larger than those of all tested solvents, and especially the $[\text{pftb}]^-$ salt **1** performs much better than the commonly used $[\text{NBu}_4]^+[\text{PF}_6]^-$. The $[\text{hfip}]^-$ anion tends to precipitate at the anode. Overall one can say that in their electrochemical properties, they resemble the $[\text{NR}_4]^+$ salts of the $[\text{B}(\text{C}_6\text{F}_5)_4]^-$ anion^[99], but the synthesis of this fluorinated borate is much more complicated and also more expensive. They provide also a good alternative to the widely used $[\text{PF}_6]^-$ salts, as in non-polar media, they exhibit less ion pairing which leads to higher limiting molar conductivities. In contrast to $[\text{NBu}_4]^+[\text{PF}_6]^-$, they even show a small conductivity in toluene ($\epsilon_r = 2.2$), a solvent in which the most tetraalkylammonium salts are insoluble or only dissolve as ion-pairs.

6 Weakly Bound Cationic Ag(P₄S₃) Complexes

Lewis acid-base adducts of small inorganic cluster molecules such as P₄, S₈, P₃N₃Cl₆ or P₄S₃ are of fundamental interest for coordination chemistry, although not many examples of such complexes are currently known^[45, 181, 188, 189]. The first P₄S₃ complex, Mo(CO)₅(P₄S₃), was reported by Cordes *et al.* in 1974^[190]. In this compound, as well as in the rare later examples such as [(np₃)Ni(P₄S₃)]^[188] or (P₄S₃)(BX₃) (X = Br, I)^[191] the P₄S₃ cage is bound via the apical P atom. When P₄S₃ acted as a bridging ligand, oxidative addition and bond cleavage of P-P and P-S bonds was observed^[192]. Generally, the P₄S₃ molecule is prone to degradation when reacted with transition metal compounds. This fragmentation is supposed to proceed both through the S and / or P atoms, as indicated by the respective reaction products^[193, 194].

For studying models for the primary steps of such degradation reactions in more detail, complexes with a d¹⁰ metal cation such as silver appeared ideal, since it seemed unlikely that the d¹⁰ electron configuration will be given up upon coordination; however, Ag⁺ is a soft transition metal and as such will seek the same reactive sites in P₄S₃ than other more reactive transition metal fragments that usually induce degradation. Yet, these silver-P₄S₃ complexes are only weakly bound and not accessible with normal counterions. One method to obtain such weak transition metal complexes uses solid-state reaction conditions and CuI as matrix, e.g. (CuI)₃P₄S₄^[195]. Another approach is the use of weakly coordinating anions (WCAs), which are ideal counterions to stabilize weak cationic Lewis acid-base adducts like [Ag(P₄)₂]^{+[42, 43]}, [Ag(S₈)₂]^{+[45]}, [Au(Xe)₄]^{+[196]}, [Ag(P₃N₃Cl₆)_n]^{+[181]}, {[Ag(cp*Fe(P₅))₂]^{+[189]}, [Ag(C₂H₄)_n]^{+[46, 197]} or [Ag(C₂H₂)_n]^{+[198]}. With the silver salts of the WCAs [pftb]⁻ (= [Al(OC(CF₃)₃)₄]⁻) and [hfip]⁻ (= [Al(OC(H)(CF₃)₂)₄]⁻) it was possible to obtain the Ag(P₄S₃) adducts (P₄S₃)Ag[hfip] **11** and (Ag(P₄S₃)₂)[pftb] **12**^[44]. Although both anions are rather similar, the structures of the adducts are very different. In fact, they are both polymeric, but while for [(P₄S₃)Ag[hfip]] **11** molecular chains are formed, [Ag(P₄S₃)₂][pftb] **12** has an ionic structure with homoleptic polymeric cations and isolated anions. In these species, an unprecedented η^1 -P_{basal} and η^1 -S coordination was observed. In the same year of this initial publication, Peruzzini *et al.* also reported structures of P₄S₃ adducts with η^1 -P_{basal} coordination^[199, 200].

To further investigate the influence of the counterions on the structure and coordination behavior of the P_4S_3 cage towards a Ag^+ ion, the reactions with the WCAs $[hftb]^-$ ($= [Al(OC(CH_3)(CF_3)_2)_4]^-$), and $[al-f-al]^-$ ($= [((CF_3)_3CO)_3Al-F-Al(OC(CF_3)_3)_3]^-$) were studied.

Since the ^{31}P solution NMR spectra of **11** and **12** displayed two resonances similar to those of free P_4S_3 even at $-90^\circ C$ as well as no coupling to $^{107}Ag/^{109}Ag$ - indicating weakly bound complexes with dynamic structures - solid-state ^{31}P MAS NMR was used in this study to provide more insight into the nature of the Ag-P and Ag-S bonds, dynamics of the system and (perhaps cluster-like) bonding within the P_4S_3 cages. Quantum chemical calculations on model compounds have also been performed to investigate energetics and thermodynamics as well as spectroscopic properties of the species.

6.1 Likely Bonding Sites of P_4S_3 in the $[Ag(P_4S_3)_n]^+$ ($n = 1-3$) and $[Ag_2(P_4S_3)]^{2+}$ Cations from DFT Calculations

In order to investigate principal bonding sites of P_4S_3 , quantum chemical calculations at the (RI)-BP86/SV(P) level of theory were performed. For each $[Ag(P_4S_3)_n]^+$ cation ($n = 1-3$) different coordination geometries and their relative energies were calculated. By using frequency calculations, it could be determined if these complexes were local minima or transition states on the PES (potential energy surface). In Figure 28 to Figure 30 the structures and relative energies of the different adducts are compared.

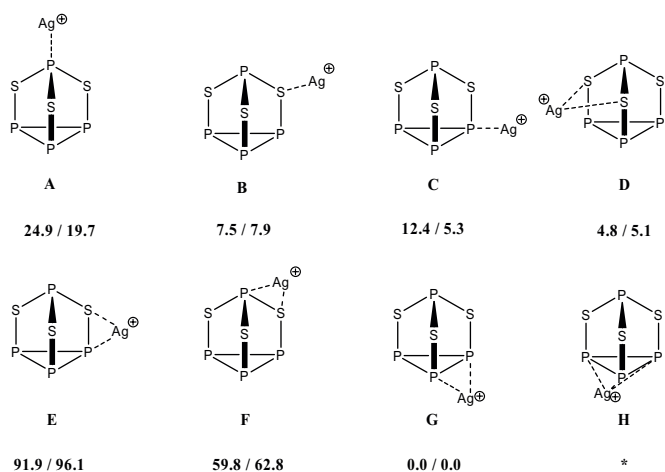


Figure 28: Assessed isomers of $Ag(P_4S_3)^+$ **1** and their relative energies (ΔG in the gas phase / ΔG in CH_2Cl_2 [kJ/mol]) at the (RI)-BP86/SV(P) level. The * indicates that this isomer is not a local minimum on the PES.

For compound **I** (AgP_4S_3^+) the isomer **IG** is lowest in energy in the gas phase and in CH_2Cl_2 ; however, other geometries shown in Figure 28 have similar free energies and are, with the exception of the η^3 coordinated **IH**, all local minima on the PES.

The next figure collects the assessed isomers of the 1:2 complexes $\text{Ag}(\text{P}_4\text{S}_3)_2^+$ **II**.

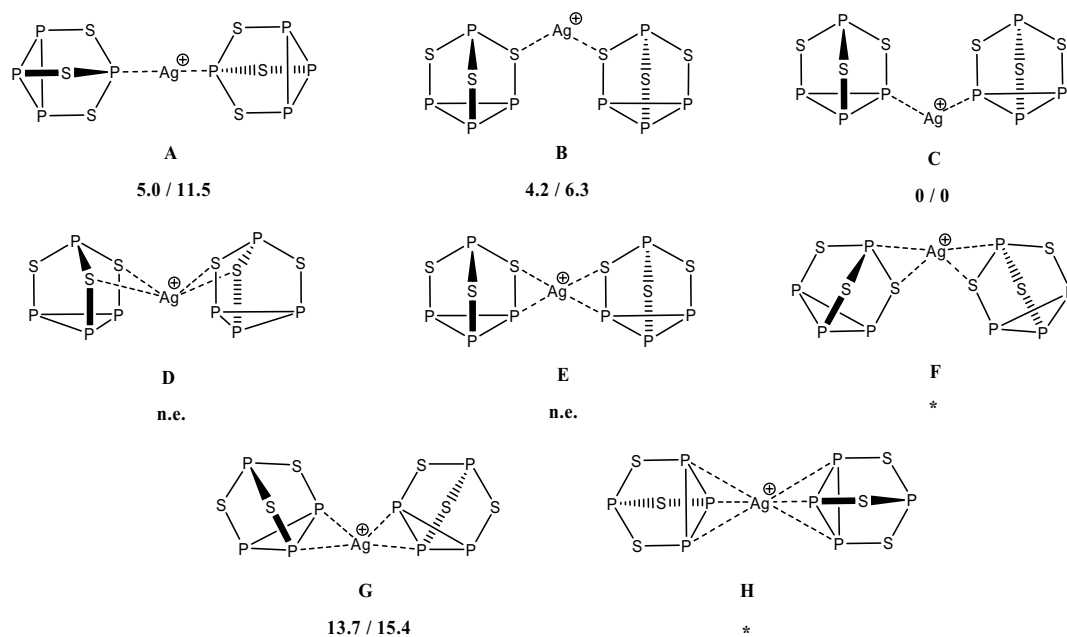


Figure 29: Assessed isomers of $\text{Ag}(\text{P}_4\text{S}_3)_2^+$ **II** and their relative energies (ΔG in the gas phase / ΔG in CH_2Cl_2 [kJ/mol]) at the (RI)-BP86/SV(P) level. * indicates that the species are no local minima on the PES. n.e. = such an isomer does not exist at this level of calculations; i.e. a compound with such a starting geometry collapses to another isomer shown in the figure.

Also for these model compounds, the relative energies between the different isomers differ only slightly. It is interesting to note that for **II** ($\text{Ag}(\text{P}_4\text{S}_3)_2^+$) no η^3 coordinated species is a local minimum on the PES. This is also in agreement with the fact that **no** such P_4S_3 adduct has been observed so far. Moreover, it is clear from Figure 29 that the most stable isomers of **4** are η^1 -bound. Therefore, mainly η^1 coordinated isomers were used as starting geometries for the larger and computationally more demanding $[\text{Ag}(\text{P}_4\text{S}_3)_3]^+$ **III** cations and omitted some less likely candidates. The results for the optimizations of **III** are shown in Figure 30.

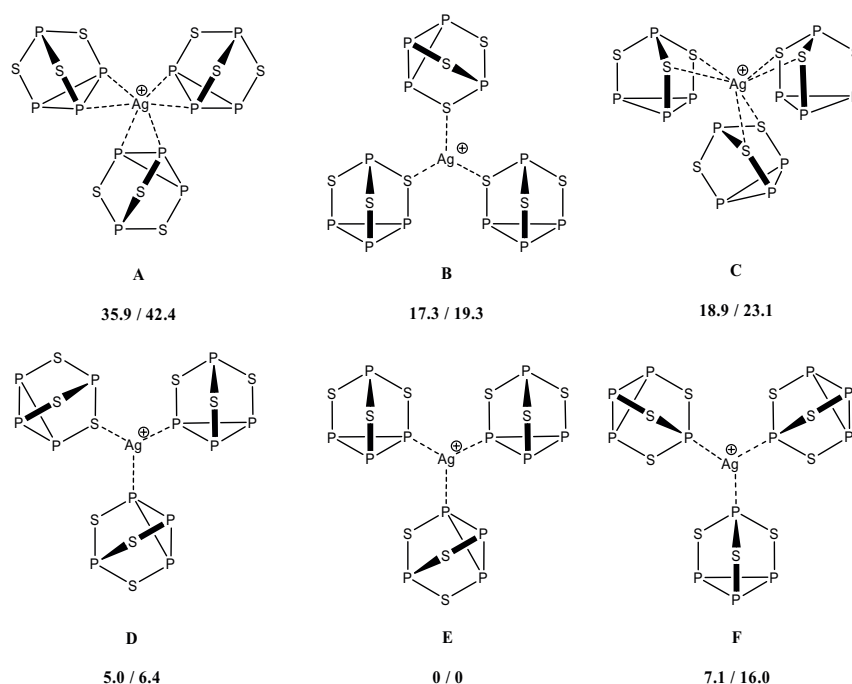


Figure 30: Assessed isomers of $\text{Ag}(\text{P}_4\text{S}_3)_3^+$ **III** and their relative energies (ΔG in the gas phase / ΔG in CH_2Cl_2 [kJ/mol]) at the (RI)-BP86/SV(P) level.

Here, the energetically most favored isomer **III** has three Ag-P_b coordinations, but again all other structures are not much higher in energy. It should also be noted that the relative energies of those isomers in which the silver atom has a six-fold coordination (i.e. **IIIA** and **IIIC**) are thermodynamically less favorable.

As further model compounds, different isomers of the $[\text{Ag}_2(\text{P}_4\text{S}_3)]^{2+}$ **IV** dications were also assessed (Figure 31). Since no η^3 coordinated species appeared to be favorable for the other calculated compounds, such isomers were omitted for this dication.

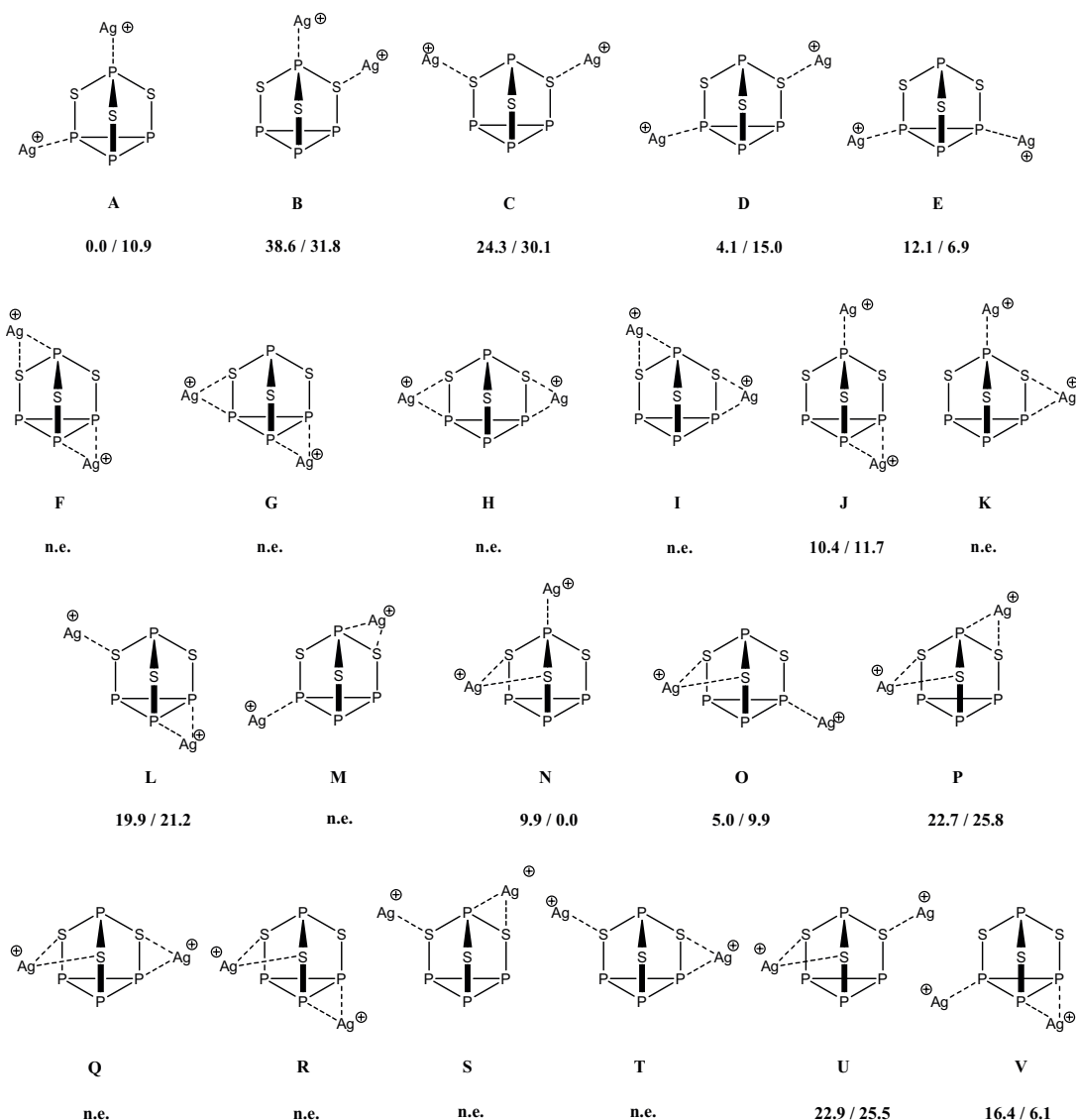


Figure 31: Assessed isomers of $\text{Ag}_2(\text{P}_4\text{S}_3)^{2+}$ **IV** and their relative energies (ΔG in the gas phase / ΔG in CH_2Cl_2 [kJ/mol]). Isomer **IVD** is related to the main form of $[(\text{P}_4\text{S}_3)\text{Ag}[\text{hfp}]]$ and isomer **A** to the side form of $[(\text{P}_4\text{S}_3)\text{Ag}[\text{hfp}]]$ as well as **1**. Calculations at the (RI)-BP86/SV(P) level of theory. n.e. = such an isomer does not exist at this level of calculations.

As for the previous calculations, the relative energies of all calculated isomers of the model compounds **IV** ($\text{Ag}_2\text{P}_4\text{S}_3^{2+}$) are all very similar (within 34.9 kJ/mol in the gas phase or 32.0 kJ/mol in CH_2Cl_2).

From the preceding figures it is clear that the PES of the $\text{Ag}_x(\text{P}_4\text{S}_3)_y^{n+}$ cations is rather flat. This indicates that several different coordination modes in the $\text{Ag}(\text{P}_4\text{S}_3)$ complexes should be accessible in solution, which is in agreement with the dynamic solution behavior reported. For

comparison, all global minima of the model compounds calculated in this study are summarized in Figure 32 along with important structural details.

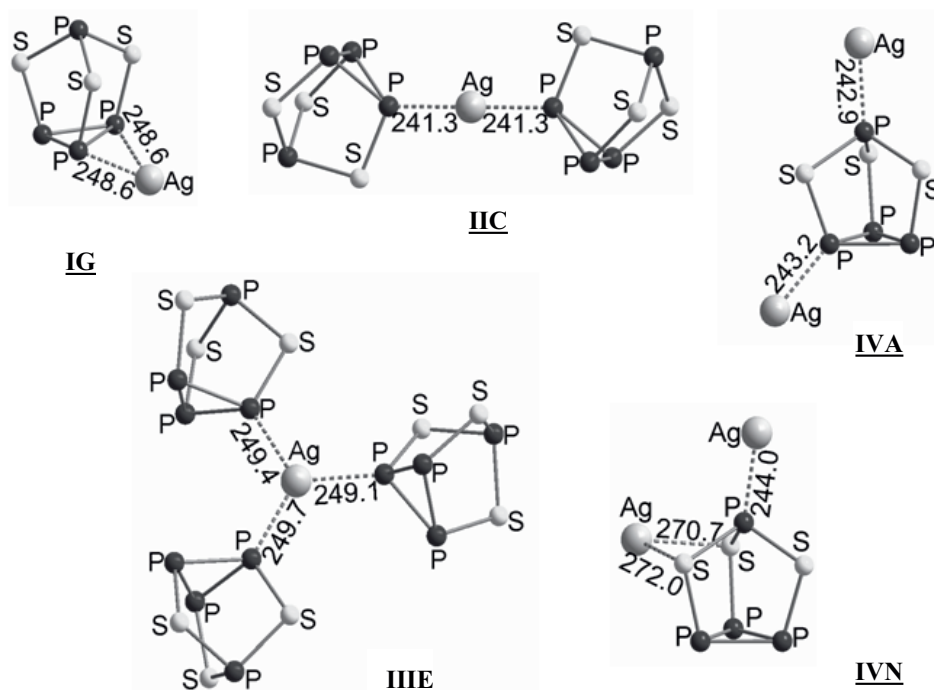


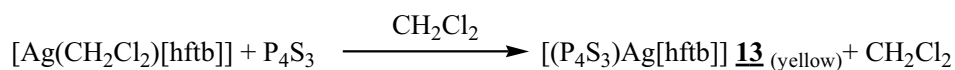
Figure 32: Geometries of the global minima (ΔG in the gas phase / ΔG in CH_2Cl_2) of $\text{Ag}(\text{P}_4\text{S}_3)^+$ **I**, $\text{Ag}(\text{P}_4\text{S}_3)_2^+$ **II**, $\text{Ag}(\text{P}_4\text{S}_3)_3^+$ **III** and $\text{Ag}_2(\text{P}_4\text{S}_3)^{2+}$ **IV** at the (RI)-BP86-SV(P) level of theory. **IIA** is the minimum in the gas phase and **IVN** the minimum with inclusion of solvation (COSMO).

In most of the global minimum energy structures in Figure 32 η' coordination is favored, except for those in which the silver cations do not have access to other ligands which could saturate the positive charge, i.e. in **IG**. These findings are in good agreement with the experimentally determined structures of the P_4S_3 adducts **11** and **12**, as well as those presented below, where only η' coordination has been observed.

6.2 Syntheses and Solution NMR Characterization

Reacting P_4S_3 with $\text{Ag}(\text{CH}_2\text{Cl}_2)[\text{hftb}]$ or $\text{Ag}(\text{CH}_2\text{Cl}_2)_3[\text{al-f-al}]$ in CH_2Cl_2 or $\text{CH}_2\text{Cl}_2/\text{CS}_2$ mixtures at r.t. leads to the very air and moisture sensitive adducts $[(\text{P}_4\text{S}_3)\text{Ag}[\text{hftb}]]_\infty$ **13** (eq. 38) and $[\text{Ag}_2(\text{P}_4\text{S}_3)_6]^{2+}[\text{al-f-al}]_2^-$ **14** (eq. 39). They are both highly soluble in CH_2Cl_2 and $\text{CH}_2\text{Cl}_2/\text{CS}_2$ mixtures.

eq. 38



eq. 39



Initial *in situ* reactions in sealed NMR tubes with CD_2Cl_2 as a solvent, showed the same very simple ^{31}P signals as those found for $[(\text{P}_4\text{S}_3)\text{Ag}[\text{hfip}]]$ **11** and $[(\text{Ag}(\text{P}_4\text{S}_3)_2[\text{pftb}]]$ **12**: one quartett and one dublett with shifts similar to free P_4S_3 in the same solvent ($\delta^{31}\text{P}(\text{P}_4\text{S}_3) = 73.1$ (q), -117.4 (d) ppm); in **13** and **14** the quartet of P_{apical} shifted by -6.9 and $+0.4$ ppm, the doublet of P_{basal} shifted by -10.8 and -0.7 ppm. This indicates that the bonding towards the Ag is only weak and that – in solution – exchange reactions take place. Even at temperatures as low as -90°C , where pure P_4S_3 is insoluble in CH_2Cl_2 , the spectra remained simple and unchanged. In none of the ^{31}P spectra, could coupling to $^{107/109}\text{Ag}$ be observed. In a static system the multiplicity of these signals should change as the three P_{basal} would not be chemically equivalent. Such changes were observed in more tightly bound complexes with other metals^[200]. The ^{13}C , ^1H and ^{27}Al NMR spectra showed that the anions remained intact during the reaction, however, the formation of adducts with small cation-anion interactions and thus shifted anion resonances may be concluded for **13** (see Table 25)

Table 25: Comparison of some NMR shifts of **13** and **14** with those of the silver salts of [hfb]⁻ and [al-f-al]⁻, free P₄S₃ and the calculated shifts of P₄S₃, **IV A**, **IV N**, **III E** and [Ag₂(P₄S₃)₆]²⁺. All spectra were recorded at r.t. in CD₂Cl₂. Calculations at the (RI)BP86 level of theory (basis sets: SVPallS2 for Ag, SV(P) for P and S). All values are given in ppm.

	13	14	Ag[hfb]	Ag[al-f-al] ^[52]	P ₄ S ₃	Δδ	Δδ	for	Δδ	P ₄ S ₃ calc.	Δδ _{calc}	for	Δδ _{calc}	for	Δδ _{calc}	for	Δδ _{calc}
						13 ^(a)	14 ^(a)		IV A ^(b)	IV N ^(b)	III E ^(b)		IV A ^(b)	IV N ^(b)	III E ^(b)		[Ag ₂ (P ₄ S ₃) ₆] ^{2+(b)}
δ ¹ H	1.63 (s)	-	1.57 (s)	-	-	+0.05	-	-	-	-	-	-	-	-	-	-	-
δ ¹³ C	124.0 (q)	121.0 (q)	124.1 (q)	121.0	-	-0.1	0.0	-	-	-	-	-	-	-	-	-	-
	76.3 (m)	78.4 (m)	76.2 (m)	78.7	-	-0.1	-0.3	-	-	-	-	-	-	-	-	-	-
	18.0 (s)		17.9 (s)	-	-	+0.1	-	-	-	-	-	-	-	-	-	-	-
δ ³¹ P	-128.2 (d)	-116.7 (d)	-	-	-117.4 (d)	-10.8	0.7	-129.5	37.0	20.8	-15.7	-25.1	-35.5	-50.8	1.5	-40.0	-
	66.2 (q)	73.5 (q)	-	-	73.1 (q)	-6.9	0.4	87.6	-	-	-	-	-	-	-	-	-
δ ²⁷ Al	47.2 (s)	37.5 (s)	47.1 (s)	33.5 (s)	-	+0.1	4.0	-	-	-	-	-	-	-	-	-	-
	(ω _{1/2} = 299 Hz)	(ω _{1/2} = 3100 Hz)	(ω _{1/2} = 184 Hz)	(ω _{1/2} = 2200 Hz)													

^(a) Δδ = δ(adduct) – δ(silver salt or P₄S₃). ^(b) Δδ_{calc} = δ_{calc}(model compound) – δ_{calc}(P₄S₃). For all P_{basal} and all P_{apical}, the average value of the calculated tensors has been use

For the model compounds **IVA** and **IVN** the calculated $\Delta\delta$ values do not fit very well to the signals observed in the ^{31}P NMR in solution. This can be explained by the lack of other coordinating molecules that exist in solutions of **13** (i.e. the coordinated $[\text{hftb}]^-$ counterion or the solvent). For the $[\text{Ag}(\text{P}_4\text{S}_3)_3]^+$ cation, the calculated $\Delta\delta$ values are very close to the observed shifts of **14** – even closer than those calculated for the $[\text{Ag}_2(\text{P}_4\text{S}_3)_6]^{2+}$ dication that was found in the solid state. This could be an indication that in solution the dication is not present. To ascertain this hypothesis for **14**, an ESI-MS in CH_2Cl_2 has been recorded. In the cationic mode, signal groups for $[\text{Ag}(\text{P}_4\text{S}_3)_2]^+$ and $[\text{Ag}(\text{P}_4\text{S}_3)_3]^+$ are detected and, according to the mass distribution, no $[\text{Ag}_2(\text{P}_4\text{S}_3)_6]^{2+}$ is present in the solution. The reasons for this observation are discussed in a later section. In the negative mode, the $[\text{al-f-al}]^-$ anion ($m/z = 1483$, 22%) as well as its following decomposition products $[\text{F-Al}(\text{OC}(\text{CF}_3)_3)_3]^-$ ($m/z = 752$, 100%), $[\text{Al}(\text{OC}(\text{CF}_3)_3)_4]^-$ ($m/z = 968$, 94%), $[\text{((CF}_3)_3\text{CO)}_3\text{-Al-F-Al}(\text{O}(\text{C}(\text{CF}_3)_2)_2)]^-$ ($m/z = 1247$, 7%) and $[\text{((CF}_3)_3\text{CO)-Al-F}_2\text{-Al}(\text{OC}(\text{CF}_3)_3)_3]^-$ ($m/z = 1501$, 18%) are observed.

6.3 Solid-State ^{31}P NMR Spectra

In the weakly bound cationic complexes in **12**, **13** and **14**, silver acts as a bridging atom between P_4S_3 cages, where the electrons of the molecular orbitals formed over the P-Ag-P bridge mediate dipole-dipole interactions between the phosphorus atoms, also known as J-coupling. In solution, these two-bond $^2J_{\text{P-Ag-P}}$ -couplings remain unobserved in NMR spectra of the $[\text{Ag}(\text{P}_4\text{S}_3)_n]^+$ complexes due to fast exchange between the P_4S_3 cages. In solids, such an exchange is unlikely. So if the $^2J_{\text{P-Ag-P}}$ couplings are observed they could provide more insight into a structure of these materials. In order to characterize solid Ag-complexes the ^{31}P magic angle spinning (MAS) experiment^[201] was utilized, along with two-dimensional ^{31}P J-resolved^[202], and incredible natural abundance double-quantum transfer experiments (INADEQUATE)^[203], were used. These two-dimensional methods have first been proposed to study molecules in liquids and with some adaptations they have been successfully applied to characterize solids.

The INADEQUATE experiment was designed to study through-bond connectivities of molecules in solution by correlating resonances of the same nuclei between which J-coupling exists. Few variants of this experiment have been proposed to study solids under MAS^[204, 205]. The complexes analyzed in this work show a degree of structural disorder, so the double-

quantum (DQ) refocused INADEQUATE MAS sequence has been utilized as it offers an increased sensitivity^[205]. An important question with this method is if the observed correlation peaks are the result of excitation of the double-quantum transition exclusively through a J-coupling mechanism, which provides information on through-bond connectivities, or if they appear due to the through-space dipole-dipole interactions. This issue was elaborated in recent paper of Fyon *et al.* in which it was demonstrated that the INADEQUATE MAS experiment is indeed a suitable probe of through-bond connectivities, although the interpretation of the obtained spectra should be taken with special care^[206]. The two-dimensional J-resolved MAS experiment was used to measure homonuclear ^{31}P J-couplings^[207].

P_4S_3 :

The different modifications of P_4S_3 (α , β and γ) have previously been studied in great detail by neutron diffraction and X-ray crystallography^[208, 209], thermodynamic methods^[208, 210], infrared and Raman spectroscopy^[211, 212] and solid-state NMR spectroscopy^[213-216]. It is found that the nearly spherical P_4S_3 molecules have a rigid structure^[208, 209], while the entire molecules undergo reorientational jumps around the uniaxial three-fold axis^[213, 216]. The rate of this motion at room temperature is estimated to be $k < 10^7 \text{ s}^{-1}$ ^[214]. Chemical shift anisotropy (CSA) tensor parameters of the ^{31}P sites have been determined from the single crystal and MAS NMR spectra^[213, 216]. Due to fast reorientational motion each P_4S_3 molecule gives only one ^{31}P resonance for all P_{basal} sites at an averaged chemical shift and one resonance for P_{apical} . The two P_{apical} atoms of the asymmetric unit cell experience the non-averaged chemical shift anisotropy δ_{CSA} of 156 and 164 ppm, while the averaged δ_{CSA} for all P_{basal} atoms is $\approx 277 \text{ ppm}$ ^[216]. The through-space dipole-dipole coupling constant between pairs of $^{31}\text{P}_{\text{basal}}-^{31}\text{P}_{\text{basal}}$ in the absence of motion in a single P_4S_3 unit is $\approx 1.7 \text{ kHz}$, taking into account the average distance of 224 pm. The plastic phase $\beta\text{-P}_4\text{S}_3$ is formed at 314 K through a first-order crystal-to-plastic phase transition. As the phase transition is approached the increase in librational amplitudes of P_4S_3 cages around the uniaxial three-fold axis is predominant. Once the plastic phase is formed, the P_4S_3 cages undergo a fast pseudo-isotropic motion in which the centers of gravity of P_4S_3 are well defined. The plastic β -form remains stable on cooling until 259 K when it is transformed back into crystalline α -form.

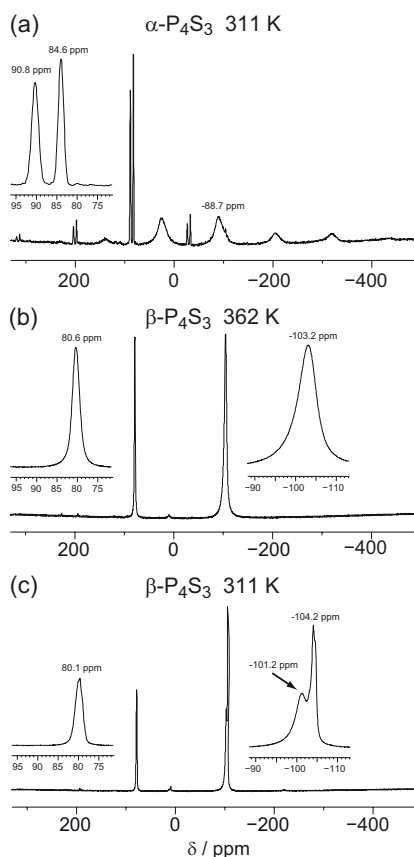


Figure 33: ^{31}P MAS NMR spectra of (a) $\alpha\text{-P}_4\text{S}_3$ and (b, c) $\beta\text{-P}_4\text{S}_3$ solids recorded at (a, c) 311 K and (b) 362 K. The center bands are shown on an enlarged scale. Spectra are the result of averaging 8 transients with a recycle interval of 60 s.

Figure 33 the ^{31}P MAS NMR spectra of $\alpha\text{-P}_4\text{S}_3$ (a) and $\beta\text{-P}_4\text{S}_3$ (b, c), while the ^{31}P isotropic chemical shifts (δ_{iso}) and the spin-lattice relaxation time-constants (T_1) are listed in Table 26 and Table 27 respectively. From the rotor-synchronized MAS spectra (not shown) the intensity ratios of $^{31}\text{P}_{\text{apical}}:^{31}\text{P}_{\text{basal}}$ resonances are estimated to be 1:3. The ^{31}P MAS spectrum of $\alpha\text{-P}_4\text{S}_3$ exhibits an envelope of spinning side-bands covering ca. 100 kHz of spectral width. They are to be expected due to large CSA interaction^[216]. The line-width (full-width at half-height) of $^{31}\text{P}_{\text{apical}}(\text{I})$ is 200 Hz and $^{31}\text{P}_{\text{apical}}(\text{II})$ is 250 Hz while that of $^{31}\text{P}_{\text{basal}}(\text{I, II})$ are ≈ 2.4 kHz. Distinctively larger line-widths of $^{31}\text{P}_{\text{basal}}$ arise from the motional broadening that is the result of a combine effect of CSA interaction, MAS and molecular motion^[217]. Molecular reorientation of P_4S_3 around the uniaxial three-fold axis only brings time averaging of the CSA interaction to $^{31}\text{P}_{\text{basal}}$ resonances, so the $^{31}\text{P}_{\text{apical}}$ resonances remain free from any motional broadening. This broadening is typically observed for the reorientational rates of $10^3 \text{ s}^{-1} < k < 10^8 \text{ s}^{-1}$. Barely any spinning sidebands are observed in ^{31}P MAS NMR spectra

(Figure 33 b, c) of β -P₄S₃, which is not surprising since the P₄S₃ cages in the plastic phase undergo a fast pseudo-isotropic motion that completely averages the CSA interaction. Despite this random motion the P₄S₃ cages do have an averaged preferred orientation as evidenced by two nicely resolved $^{31}\text{P}_{\text{basal}}$ resonances in the spectrum recorded at 311 K (Figure 33). The possible existence of two inequivalent P₄S₃ units in β -P₄S₃ has been proposed in an earlier work of Schnering and co-workers^[208, 209], however, it is NMR spectroscopy that provides unambiguous evidence. It has been found that spin-lattice relaxation in both α - and β -P₄S₃ is dominated by the chemical shift anisotropy mechanism, while dipole-dipole interactions contributes to a lesser extent^[214]. The much shorter relaxation times of ^{31}P in β -P₄S₃ in comparison to those of α -P₄S₃ are due to fast pseudo-isotropic motion of P₄S₃ cages which is estimated to be $k > 10^8 \text{ s}^{-1}$ ^[214].

Table 26: Chemical shifts of ^{31}P resonances (δ_{iso} in ppm) in α -P₄S₃, β -P₄S₃ and the complexes **13**, **12** and **14** measured at 311 K.

	α -P ₄ S ₃	β -P ₄ S ₃	13	12	14
$^{31}\text{P}_{\text{apical}}(\text{I})$	90.8	80.1	67.5	86.3	87.3
$^{31}\text{P}_{\text{apical}}(\text{II})$	84.6	80.1	63.8	81.0	73.3
$^{31}\text{P}_{\text{apical}}(\text{III})$	-	-	-	79.9	72.3
$^{31}\text{P}_{\text{apical}}(\text{IV})$	-	-	-	75.3	-
$^{31}\text{P}_{\text{basal}}(\text{I})$	-88.7	-101.2	-134.1	-102.2	-106.6
$^{31}\text{P}_{\text{basal}}(\text{II})$	-88.7	-104.2	-134.1	-105.8	-112.4
$^{31}\text{P}_{\text{basal}}(\text{III})$	-	-	-	-107.7	-115.9
$^{31}\text{P}_{\text{basal}}(\text{IV})$	-	-	-	-112.0	-

Table 27: Spin-lattice relaxation time constants T_1 (in s) of ^{31}P resonances in $\alpha\text{-P}_4\text{S}_3$, $\beta\text{-P}_4\text{S}_3$ and the complexes **13**, **12** and **14**. They were measured at 311 K using an inversion recovery experiment with a single π pulse used to invert the magnetization.

	$\alpha\text{-P}_4\text{S}_3$	$\beta\text{-P}_4\text{S}_3$	13	12	14
$^{31}\text{P}_{\text{apical}}(\text{I})$	67	2.6	2.5	0.91	1.7
$^{31}\text{P}_{\text{apical}}(\text{II})$	67	2.6	2.7	1.0	1.1
$^{31}\text{P}_{\text{apical}}(\text{III})$	-	-	-	1.7	1.1
$^{31}\text{P}_{\text{apical}}(\text{IV})$	-	-	-	2.0	-
$^{31}\text{P}_{\text{basal}}(\text{I})$	67	2.2	1.1	0.15	0.26
$^{31}\text{P}_{\text{basal}}(\text{II})$	67	2.2	1.1	0.29	0.19
$^{31}\text{P}_{\text{basal}}(\text{III})$	-	-	-	0.22	0.19
$^{31}\text{P}_{\text{basal}}(\text{IV})$	-	-	-	0.39	-

[Ag(P₄S₃)₂]/[pftb] **12**, [(P₄S₃)Ag(hftb)] **13** and [Ag₂(P₄S₃)₆]²⁺[al-f-al]²⁻ **14**:

Figure 34 shows ^{31}P MAS NMR spectra of (a) **13**, (b) **12**, and (c) **14**, complexes recorded at 311 K. They all show an envelope of spinning sidebands spread over ca. 100 kHz indicating that the amplitudes of the ^{31}P CSA interactions are of the same order as those measured for $\alpha\text{-P}_4\text{S}_3$. The line-widths of the spinning sidebands are remarkably narrow, typically about 200-300 Hz. In addition, the ^{31}P spin-lattice relaxation time constants (Table 27) are of the order of seconds or shorter. These observations indicate that the P_4S_3 cages undergo reorientational motions around the uniaxial three-fold axis with a rate of $k > 10^8 \text{ s}^{-1}$. Spectra obtained with slower spinning rates (5 kHz) also exhibit narrow ^{31}P resonances suggesting that homonuclear dipole-dipole ^{31}P interactions, particularly those of the P_{basal} atoms, are significantly averaged by a fast molecular motion. However, scalar J-couplings (either homonuclear or heteronuclear) remain unresolved except for a few of the $^{31}\text{P}_{\text{apical}}$ resonances of **12** and **14**, where ill-resolved $^2\text{J}_{\text{P-S-P}}$ -couplings are evident. The asymmetric unit cell of **13** contains two P_4S_3 units resulting in two nicely resolved $^{31}\text{P}_{\text{apical}}$ resonances (Figure 34 a), while $^{31}\text{P}_{\text{basal}}$ resonances of the two units are having very similar averaged isotropic chemical shifts, so only a single resonance is observed. From the rotor-synchronized MAS spectra (Figure 35a, b) the relative intensity ratios of $^{31}\text{P}_{\text{apical}}\text{:}^{31}\text{P}_{\text{basal}}$ in all complexes studied here are estimated to be 1:3. Eight ^{31}P resonances in Figure 34b and six in Figure 34c correspond to the four and three different P_4S_3 cages of the asymmetric unit in **12** and **14**, respectively. In the temperature

range between 249 and 338 K, the ^{31}P MAS NMR spectra of **12** reveal a slight chemical shift change (up to a few ppm) for all resonances, while only the $^{31}\text{P}_{\text{basal(IV)}}$ resonance displays a dramatic increase in broadening on lower temperatures, suggesting slower reorientational motion for this $\text{P}_4\text{S}_3(\text{IV})$ cage, where $k < 10^7 \text{ s}^{-1}$. It is found that the complexes **13** and **12** remain stable over a long period of time in a sealed container at room temperature while the spectrum of complex **14** recorded after few days storage in the MAS container shows additional resonances with the same chemical shift and the same relaxation times of the ^{31}P resonances as $\alpha\text{-P}_4\text{S}_3$. This is in agreement with DFT calculations, which showed that in the model system $\text{Ag}(\text{P}_4\text{S}_3)_3^+$ the third ligand is only very weakly bound. Similar energetics should also apply for the dication. After a few weeks the ^{31}P MAS spectrum of **14** is identical to the one of $\alpha\text{-P}_4\text{S}_3$. This observation confirms that complex **14** is metastable and one of its decomposition products is most likely to be the $\alpha\text{-P}_4\text{S}_3$ phase.

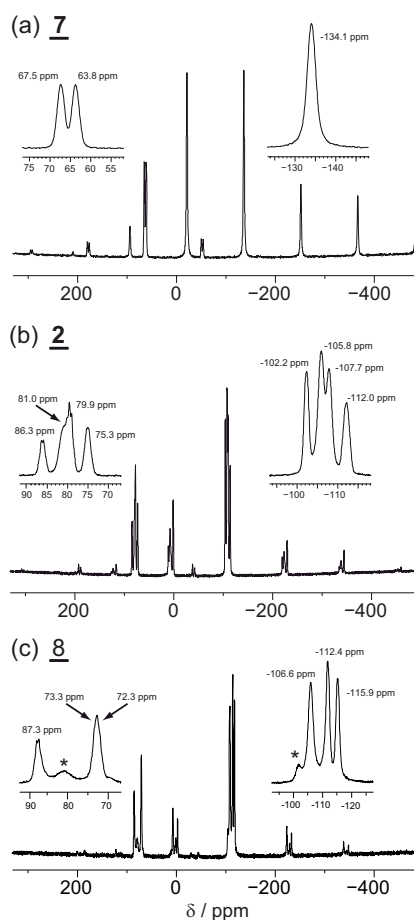


Figure 34: ^{31}P MAS NMR spectra of (a) **13**, (b) **12** and (c) **14** recorded at 311 K. The center bands are shown on an enlarged scale. Spectra are the result of averaging 64 transients with a recycle interval of 10 s.

The rotor-synchronized ^{31}P MAS, J-resolved MAS and INADEQUATE MAS NMR spectra of **12** and **14** are shown in Figure 35. Due to rotor synchronization the $^{31}\text{P}_a$ resonances are aliased in the direct dimension (δ_2) and the ppm scale is not reflecting their real chemical shifts. Similarly, in the indirect dimension (δ_1) of the INADEQUATE spectra all ^{31}P resonances are aliased and the scale is adjusted to reflect genuine shifts. For resonances where this was not possible the isotropic chemical shifts are annotated on the spectrum. The projections of the ^{31}P resonances in the J-resolved spectra (Figure 35 c, d) on to the δ_2 dimension reflect the homonuclear J-couplings multiples. Due to fast molecular motion the refocused line-widths of $^{31}\text{P}_{\text{apical}}$ are remarkably narrow (except for complex **13**, spectra not shown) and consequently the $^{31}\text{P}_{\text{apical}}$ quartets arising from $^2\text{J}_{\text{P-S-P}}$ are nicely resolved. For complex **12** the following values are found: $^2\text{J}_{\text{P-S-P}}(\text{I}) = 74 \text{ Hz}$, $^2\text{J}_{\text{P-S-P}}(\text{II}) = 71 \text{ Hz}$, $^2\text{J}_{\text{P-S-P}}(\text{III}) = 69 \text{ Hz}$ and $^2\text{J}_{\text{P-S-P}}(\text{IV}) = 79 \text{ Hz}$, and for **14**: $^2\text{J}_{\text{P-S-P}}(\text{I}) = 70 \text{ Hz}$, $^2\text{J}_{\text{P-S-P}}(\text{II}) = 72 \text{ Hz}$ and $^2\text{J}_{\text{P-S-P}}(\text{III}) = 72 \text{ Hz}$. Similar values for $^2\text{J}_{\text{P-S-P}}$ couplings are measured in solutions. Somewhat larger refocused line-widths of $^{31}\text{P}_b$ limit the resolution of these resonances. If $^2\text{J}_{\text{P-Ag-P}}$ couplings exist then these complex multiples are hidden behind what appears to be a broad $^{31}\text{P}_{\text{basal}}$ doublet structure. The two-dimensional ^{31}P DQ INADEQUATE MAS NMR spectra in Figure 35 e, f show correlation peaks for pairs of ^{31}P resonances between which J-coupling exists. In the δ_1 dimension they are found at the sum of their chemical shifts. The INADEQUATE spectra allow one to assign $^{31}\text{P}_{\text{apical}}$ and $^{31}\text{P}_{\text{basal}}$ resonances of the same cage (peaks at $-50 \text{ ppm} < \delta_1 < -20 \text{ ppm}$) as given in Table 26 and Table 27, and to resolve peaks that are overlapped in the ^{31}P MAS spectra, e.g., $\text{P}_{\text{apical}}(\text{II})$ and $\text{P}_{\text{apical}}(\text{III})$ of complexes **12** and **14**. More importantly, correlation peaks are also observed between phosphorus atoms of different P_4S_3 cages, providing a direct evidence for the existence of $^2\text{J}_{\text{P-Ag-P}}$ couplings mediated via bridging Ag^+ cations. For the complex **14** the correlation peaks at $\delta_1 = -222.5 \text{ ppm}$ (Figure 35 f) are the consequence of a chemical bond between $\text{P}_{\text{basal}}(\text{I})$ - $\text{P}_{\text{basal}}(\text{III})$ formed via the Ag^+ bridging cation. These are the only peaks expected to be seen since the other cages are linked via S atoms. Correlation peaks connected with dashed-lines are assigned to a small amount of unknown impurities or possible degradation products, even though spectra were recorded immediately after the sample preparation. Only two sets of correlation peaks at δ_1 of -209.9 and -208.0 ppm are observed for complex **12** suggesting a correlation between $\text{P}_{\text{basal}}(\text{I})$ - $\text{P}_{\text{basal}}(\text{II})$ and $\text{P}_{\text{basal}}(\text{I})$ - $\text{P}_{\text{basal}}(\text{III})$. This is surprising since the cluster arrangement in this compound should result in a total of six pairs of peaks. As the refocused line-widths are of the same order for all $^{31}\text{P}_{\text{basal}}$ resonances, the most likely explanation for the missing peaks is that all other $^2\text{J}_{\text{P-Ag-P}}$ couplings are considerable smaller.

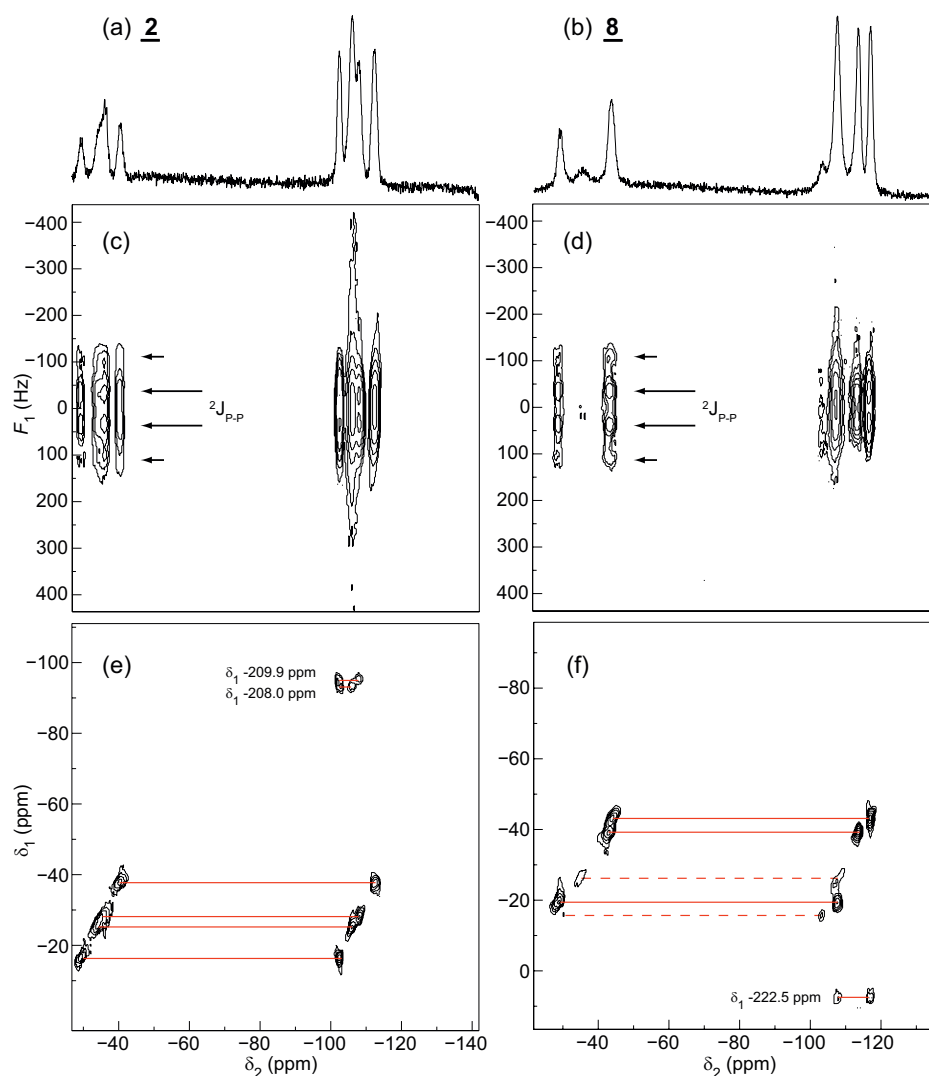


Figure 35: (a, b) Rotor-synchronized ^{31}P MAS, (c, d) ^{31}P J-resolved MAS and (e, f) ^{31}P INADEQUATE MAS spectra of (a, c and e) **12** and (b, d and f) **14**. The spectra (a, b) are the result of averaging 8 transients with a recycle interval of 5 s. The two-dimensional spectra are the result of averaging 32 transients for each of (c, d) 64 and (e, f) 156 t_1 increments of (c, d) 1.142 ms and (e, f) 71.4 μs , with a relaxation interval of 5s. The excitation and reconversion intervals were 2.57 ms.

6.4 Solid-State Structures

Re-determination of the structures of α - and γ - P_4S_3 :

The structures of α - and γ - P_4S_3 were re-determined at 140 K (see appendix 12.4) in order to compare the solid-state structure of the adducts with that of the free ligand under similar conditions; both data sets also have a better quality ($R1 = 1.73\%$ for γ - P_4S_3 and 2.77% for α - P_4S_3) than those reported before^[194, 209, 218]. These new data are used to compare bond lengths and angles with those of the $\text{Ag}(\text{P}_4\text{S}_3)$ adducts.

[Ag(P₄S₃)₂]/[pftb] 12:

³¹P solid-state NMR measurements on this compound during this study clearly showed that the previously published space group P2₁/n^[44] was not correct. Therefore, the crystal structure was re-determined in P2₁, in which the number of the symmetrically independent P₄S₃ moieties is doubled if compared to P2₁/n. Since the bond lengths and angles did not change significantly, the structural parameters are not discussed in the main text of this thesis (a detailed figure of the re-determined solid-state structure of 12 is shown in the appendix 12.4).

[(P₄S₃)Ag[hftb]] 13:

13 crystallizes in the triclinic space group P1 with Z = 2. A section of the solid-state structure is shown in Figure 36. Although it is also possible to solve the structure as monoclinic with space group P2₁, solid-state ³¹P NMR clearly reveals that there are two independent P₄S₃ moieties in the asymmetric unit. As it can be seen from Figure 36 and Table 28, where the characteristic bond lengths of 13 are listed, the two parts of the asymmetric units differ only very slightly, but these small changes are enough to give rise to different peaks in the solid-state NMR. This adduct forms one-dimensional, polymeric chains. In these chains, the Ag⁺ cation is coordinated by one apical and one basal P atom of the P₄S₃ cages. Additionally, two oxygen atoms of the anion are also coordinated to the silver atom, which leads to a molecular species with the same structural pattern as in the side form of the [(P₄S₃)Ag[hfip]]^[44]. The structural parameters of the anion are normal^[11]. The Ag-P distances are at 245.67(8) / 246.09(7) pm (P_{apical}) and at 254.76(8) / 254.64(8) pm (P_{basal}); the Ag-O bonds are at 241.85(11) / 241.72(12) pm and at 239.36(11) / 239.19(11) pm. These values differ from those of the (disordered) side form of [(P₄S₃)Ag[hfip]] by up to 17.5 pm (*d*(Ag-P_{apical}) = 228.5(3) pm, *d*(Ag-P_{basal}) = 249.7(7) pm^[44]). However, these differences should be attributed to the inherent disorder in [(P₄S₃)Ag[hfip]] and the structure of 13 should be used as a reference for the structural parameters of such a structural motif.

X-ray diffraction at 283 K shows essentially the same structure with larger thermal displacement parameters (tdp's) for the CF₃ groups of the anion; the tdp's for the Ag and the P₄S₃ moieties remain very small and almost spherical (see figure in appendix 12.4). This implies that on the time-scale of X-ray scattering the structure is static and any dynamics, except rotation about the CF₃ groups, has to be short lived with no long-living resting-state that may add to the diffraction pattern as a second orientation. A similar conclusion was drawn from an analysis of the Raman and IR spectrum of 13 (see below).

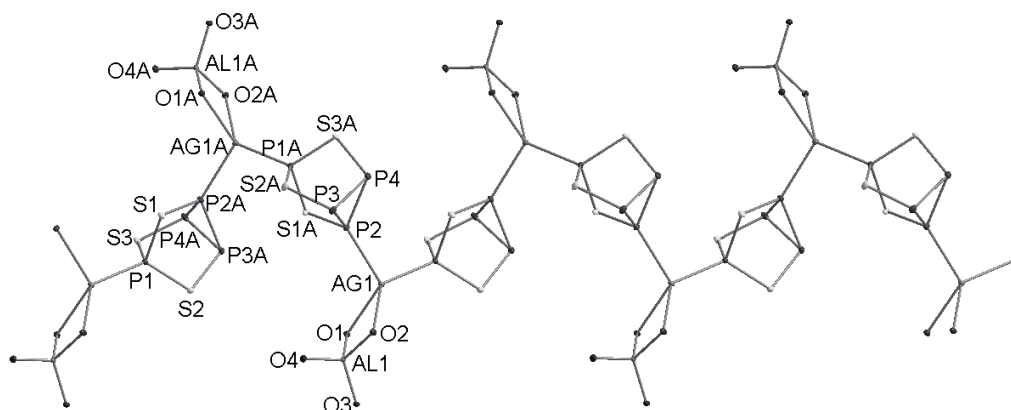


Figure 36: Section of the polymeric chain of $[(P_4S_3)Ag[hftb]]$ **13** in the solid state at 100 K. The $C(CH_3)(CF_3)_2$ groups have been omitted for clarity. Selected bond lengths (in pm): Ag1-O1 / Ag1a-O1a: 241.85(11) / 241.72(12); Ag1-O2 / Ag1a-O2a: 239.36(11) / 239.19(11); Ag1-P2 / Ag1a-P2a: 254.76(8) / 254.64(8); Ag1-P1a / Ag1a-P1: 245.67(8) / 246.09(7); P2-P3 / P2a-P3a: 222.80(9) / 223.73(8); P3-P4 / P3a-P4a: 225.22(7) / 225.22(9); P2-P4 / P2a-P4a: 223.52(8) / 222.93(9); P2-S1a / P2a-S1: 209.42(8) / 209.02(8); P3-S2a / P3a-S2: 210.44(8) / 210.48(8); P4-S3a / P4a-S3: 210.85(8) / 210.17(8); P1-S1 / P1a-S1a: 209.15(8) / 209.86(7); P1-S2 / P1a-S2a: 209.59(5) / 209.68(5); P1-S3 / P1a-S3a: 208.65(7) / 208.95(8).

$[Ag_2(P_4S_3)_6]^{2+} [al-f-al]_2$ **14:**

14 crystallizes in the monoclinic space group $P2_1$ with $Z = 2$. The solid-state structure of the cation at 130 K is shown in Figure 37.

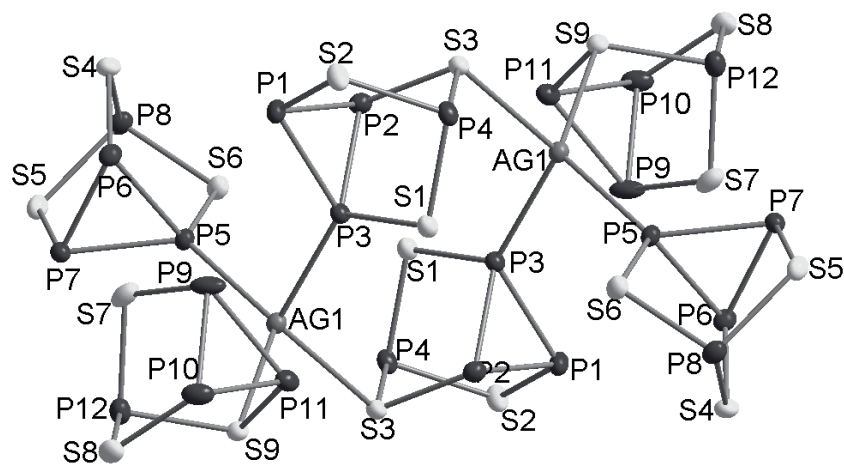


Figure 37: Solid-state structure of the $[Ag_2(P_4S_3)_6]^{2+}$ dication in **14** at 130 K, thermal displacement ellipsoids showing 25 % probability. Selected bond lengths (in pm): Ag1-P5: 248.30(15), Ag1-P3: 258.84(15), Ag1-S3: 262.52(16), Ag1-S9: 263.39(15), P1-S2: 209.2(3), P1-P3: 222.4(2), P1-P2: 224.8(2), P2-S3: 211.2(2), P2-P3: 222.55(19), P3-S1: 208.0(2), P4-S2: 209.3(2), P4-S1: 210.1(2), P4-S3: 213.5(2), P5-S6: 206.9(2), P5-P7: 221.3(2), P5-P6: 223.7(2), P6-S4: 208.4(2), P6-P7: 224.1(2), P7-S5: 207.3(2), P8-S5: 210.0(2), P8-S4: 210.8(2), P8-S6: 211.0(2), P9-S7: 209.9(3), P9-P10: 222.3(2), P9-P11: 223.3(2), P10-S8: 209.0(3), P10-P11: 222.8(3), P11-S9: 211.3(2), P12-S7: 209.0(2), P12-S8: 209.1(2), P12-S9: 212.8(2).

14 is an ordered AB₂ salt with isolated C_i symmetric [Ag₂(P₄S₃)₆]²⁺ dications A and [al-f-al]⁻ anions B. In the centrosymmetric dications, only η¹ coordination of the P₄S₃ cages towards the silver atoms is observed. The two bridging ligands coordinate with one basal P atom and one S atom; the terminal ligands coordinate only with one P_{basal} or one S atom to Ag. The structural parameters of the anion are normal^[52]. However, in contrast to other salts, the Al-F-Al bridge in **14** is not linear, but has an angle of 172.4(2)°. This is probably due to packing effects in the crystals.

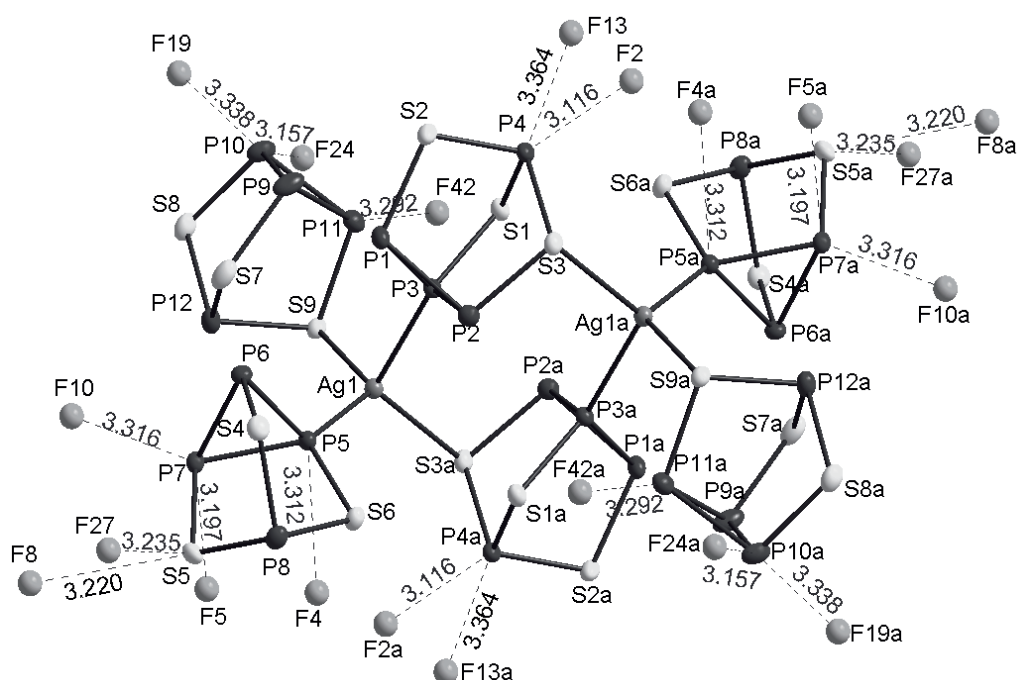


Figure 38: Cation-anion interactions in **14** below the sum of the van der Waals radii.

As it can be seen from Figure 38, the cation anion interactions are very weak (4 Ag-S and 14 Ag-P contacts between 311.6 (P)/ 320.0 (S) and 336.4 (P)/ 323.5 (S) pm, average value: 327.0 (P)/322.8 (S) pm). No Ag-F contacts below the sum of the van der Waals radii of 320 pm could be observed. Since only S5/S5a show weak contacts towards the fluorine atoms, but 10 P atoms have contacts to the F atoms it appears reasonable to argue that the phosphorus atoms are more positively charged than the sulfur atoms. In the solid state, these dications form stacked structures (Figure 39).

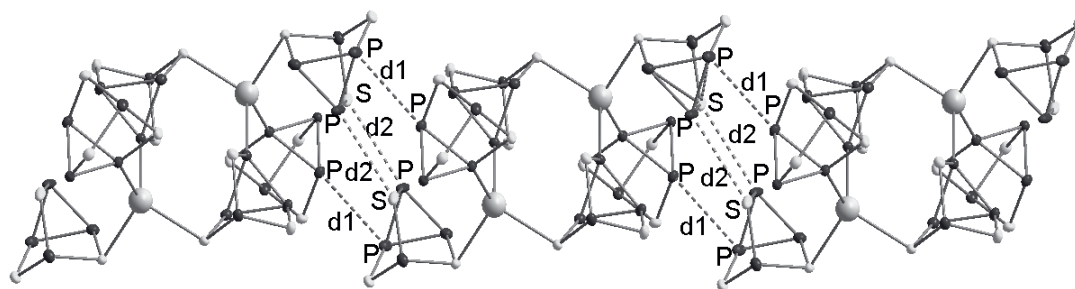


Figure 39: Stacked structure of the $[\text{Ag}_2(\text{P}_4\text{S}_3)_6]^{2+}$ dications of **14** in the solid state at 130 K. $d1(\text{P-P}) = 373.9$ pm, $d2(\text{P-S}) = 353.0$ pm.

The stacks are connected by very weak P-P (at 373.9 pm) and slightly stronger P-S contacts (at 353.0 pm; cf. sum of the Van-der-Waals radii: 380 (P-P) and 370 (P-S) pm). These stacked structures are probably formed by electrostatic interactions between the more electronegative partially negatively charged S atoms and the more electropositive partially positively charged P atoms. The even weaker P-P contacts should then result from packing effects.

Table 28: Comparison of selected bond lengths of **12** at 150K, **13** at 100 K, **14** at 130K and P₄S₃ (α and γ modification) at 140 K.

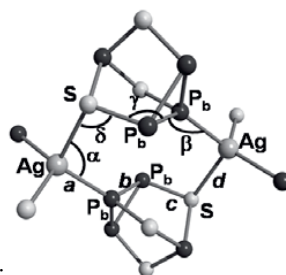
	12 (150K)	13 (100K)	14 (130K)	γ -P ₄ S ₃ (140K)	α -P ₄ S ₃ (140K)
$d(\text{Ag-O})$ [pm]	-	239.19(11) – 241.85(11) av. 240.5	-	-	-
$d(\text{Ag-P}_{\text{basal}})$ [pm]	250.9(3) – 254.9(3) 253.2	254.64(8) – 254.76(8) av. 254.7	258.84(15) (bridging) 248.30(15) (terminal)	-	-
$d(\text{Ag-P}_{\text{apical}})$ [pm]	-	245.67(8) – 246.09(7) av. 245.9	-	-	-
$d(\text{Ag-S})$ [pm]	265.5(3) – 265.6(3) av. 265.6	-	262.52(16) (bridging) 263.39(15) (terminal)	-	-
$d(\text{P}_{\text{basal}}\text{-P}_{\text{basal}})$ [pm]	222.1(4) – 226.2(5) 224.1	222.93(9) – 225.22(9) 223.9	221.3(2) – 224.8(2) av. 223.0	223.57(7) – 224.49(9) av. 224.2	223.74(6) – 224.83(8) av. 224.1
$d(\text{P}_{\text{basal}}\text{-S})$ [pm]	206.6(4) – 210.2(5) 208.0	209.02(8) – 210.85(8) 209.9	206.9(2) – 211.3(2) av. 209.0	209.60(7) – 210.65(10) av. 209.9	210.57(7) – 210.93(5) av. 210.7
$d(\text{P}_{\text{apical}}\text{-S})$ [pm]	210.1(5) – 213.8(4) 211.2	208.47(7) – 209.68(7) 209.1	209.0(2) – 213.5(2) av. 210.6	210.36(10) – 211.36(6) av. 211.0	210.55(7)

In the complexes **12**, **13** and **14**, the bond lengths of the P_4S_3 moieties do not change very much when compared to those of free P_4S_3 – again, indicative of weak coordination. The Ag- P_{basal} distance in **13** is the longest of all (excluding that of the bridging ligand in **14**), which may be explained with its two additional Ag-O bonds towards the $[\text{hftb}]^-$ anion, which is the most basic anion of this series.

If compared to the P_4S_3 adduct of $\text{Ag}[\text{pftb}]^{[44]}$, **14** shows some similar structural properties. The 8-membered folded ring in the dication is also found in the structure of $[\text{Ag}(\text{P}_4\text{S}_3)_2][\text{pftb}]^{[44]}$ (Figure 40). In Table 29, bond lengths and angles of both compounds, as well as the computed values for a C_i symmetric $[\text{Ag}_2(\text{P}_4\text{S}_3)_6]^{2+}$ dication, are compared.

Table 29: Comparison of the geometries of the 8-membered rings in **14** and in **12** with the calculated structure of a C_i symmetric $[\text{Ag}_2(\text{P}_4\text{S}_3)_6]^{2+}$ dication.

		12 exp.	14 exp.	$[\text{Ag}_2(\text{P}_4\text{S}_3)_6]^{2+}$ calc. ^(a)
$d(\text{Ag}-P_b)$ [pm]	A	253.8(3), 250.9(3)	258.8(2)	254.8
$d(P_b-P_b)$ [pm]	B	223.4(4), 223.2(4)	222.6(2)	228.7
$d(S-P_b)$ [pm]	C	211.1(4), 211.2(4)	211.2(2)	214.5
$d(\text{Ag}-S)$ [pm]	D	265.5(3), 265.6(3)	262.5(2)	279.1
$\angle (S-\text{Ag}-P_b)$ [°]	α	110.8(1), 110.6(1)	111.7(1)	104.9
$\angle (Ag-P_b-P_b)$ [°]	β	123.9(1), 124.1(1)	119.6(1)	128.7
$\angle (P_b-P_b-S)$ [°]	γ	101.3(19), 100.7(1)	101.1(1)	101.5
$\angle (P_b-S-\text{Ag})$ [°]	δ	103.5(1), 103.5(1)	98.9(1)	107.0



^(a)at the (RI)-BP86/SV(P) level; labeling according to:

This comparison clearly shows that the rings in the two adducts are very similar and also are in good agreement with the calculation. The calculated bond lengths are all longer than those measured, which is a usual effect for this level of computation^[iv]. Not only the cationic structures show similarities, but also the packing diagrams of both compounds are related. The packing of both substances is determined by the cations, which are aligned along the crystallographic *b* axis. The anions are placed in the space between the polymeric chains (for $(\text{Ag}(\text{P}_4\text{S}_3)_2)[\text{pftb}]$ **12**) or the stacked dication (in the case of **14**). As the $[\text{al-f-al}]^-$ anions are much larger than $[\text{pftb}]^-$ they “break” the cationic chain, and the resulting free coordination sites are filled by additional P_4S_3 molecules. Overall, this effect may lead to the formation of the dication (Figure 40).

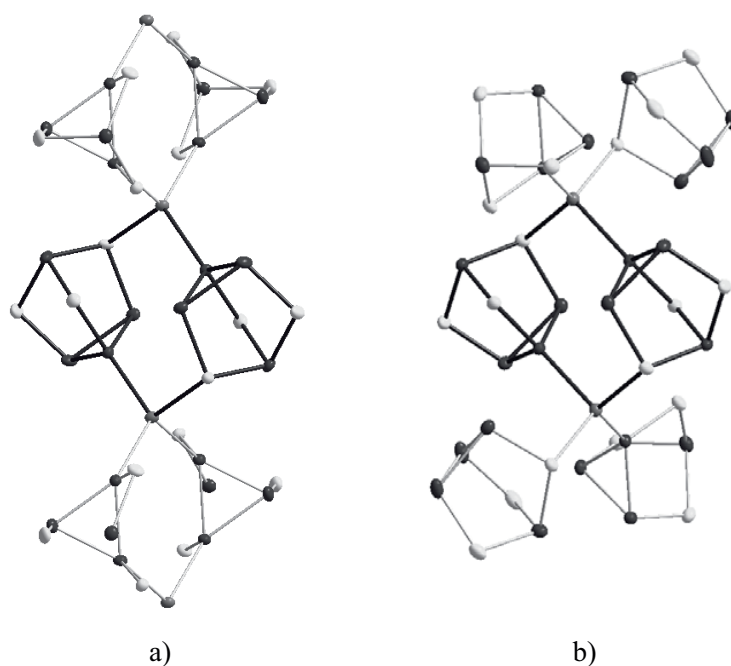


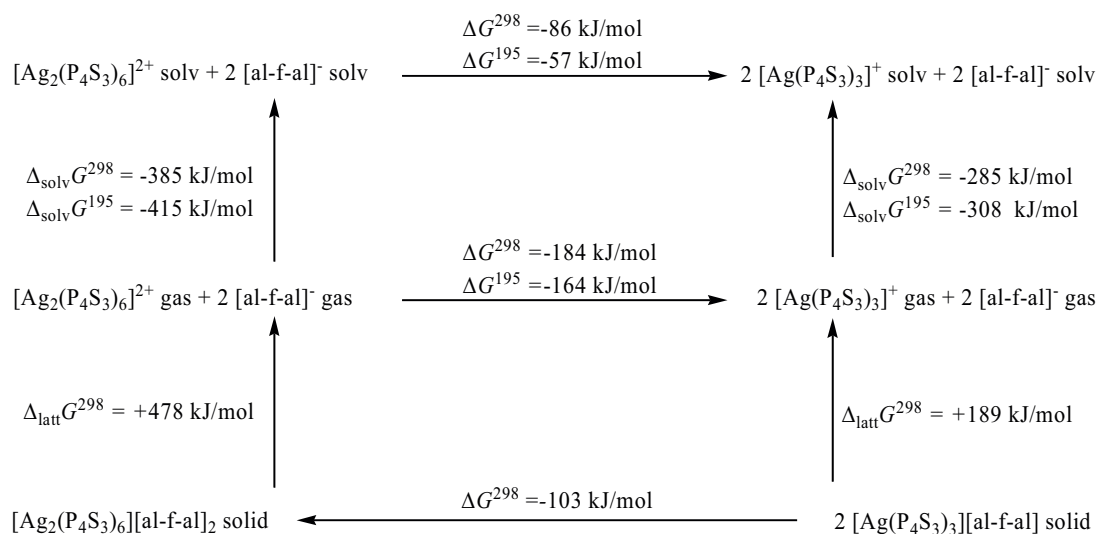
Figure 40: Relation between the cationic structures of the polymeric cation in $[(\text{Ag}(\text{P}_4\text{S}_3)_2)[\text{pftb}]]$ **12**^[44] (a, left) and the isolated dication in **14** (b, right).

6.5 On the Existence of the $\text{Ag}_2(\text{P}_4\text{S}_3)_6^{2+}$ Dication in all Phases: a Born-Haber Cycle Investigation

To answer the question of why the $[\text{Ag}_2(\text{P}_4\text{S}_3)_6]^{2+}$ dication was found in the solid state but $[\text{Ag}(\text{P}_4\text{S}_3)_3]^+$ monocations were found in solution (as suggested by ESI mass spectrometry and

^[iv] Only the calculated Ag-S distance deviates by +16 pm from the experiment, however, this is attributed to the weak bonds that reside in shallow potential energy wells where small changes in energy may lead to larger distortions in distance.

NMR shift calculations) a suitable Born-Haber cycle has been established. The lattice enthalpies of both salts were calculated using Volume Based Thermodynamics (VBT)^[150, 185] methods based on the ionic volumes (3.30 nm³ for **14** and 1.65 nm³ for [Ag(P₄S₃)₃]⁺[al-f-al]⁻) (Scheme 6). Gas phase and solution free energies stem from BP86/SV(P) calculations including the COSMO solvation model (CH₂Cl₂ as solvent) as well as thermal and entropic contributions to the Gibbs energy at 195 and 298 K.



Scheme 6: Born-Haber cycle for the lattice stabilization in **14**. Values at the (RI)-BP86/SV(P) level of theory. The lattice free energies were calculated using VBT^[150, 185].

The formation of two [Ag(P₄S₃)₃]⁺ monocations is thermodynamically favored in the gas phase and in solution (Coulomb explosion), whereas in the solid state, the higher lattice enthalpy of the 2:1 salt **14** leads to a stabilization of the dicationic form. Analogous coulomb explosions have been observed for the cation pair S₄²⁺ / 2 S₂⁺; S₃N₂²⁺ / SN⁺ and S₂N⁺ and others.

6.6 IR and Raman Spectra

In the Raman and the IR spectra of **13** the bands of the Ag(P₄S₃) moieties can be observed between 117 and 495 cm⁻¹. These frequencies fit very well with those assigned to the side isomer of [(P₄S₃)Ag[hfip]]^[44] and with those obtained by simulating the vibrational spectrum of the [Ag₂(P₄S₃)₆]²⁺ dication and isomer **IVA** in Figure 31. Compared to other P₄S₃ complexes (e.g. (P₄S₃)(BX₃) (X = Br, I)^[191]) the energy of the highest bands (e symmetry, at 488/9 cm⁻¹) remain nearly unchanged if compared to free P₄S₃. In case of a stronger

coordination of the ligand, the energy of this vibrational band should be lowered. In our complexes, due to the very weak coordination, the interaction between the Ag^+ and the P_4S_3 cages in which only leads to a disturbed symmetry, while the bonding in the ligands remains unchanged. The same observation has been made in the $[\text{Ag}(\text{P}_4)_2]^{+42}$ cation. In Table 30, the vibrational frequencies of **13** and **14** are compared with those in **11**, free P_4S_3 as well as with the calculated frequencies of the model compounds $[\text{Ag}_2(\text{P}_4\text{S}_3)]^{2+}$ (**IVA**) and the $[\text{Ag}_2(\text{P}_4\text{S}_3)_6]^{2+}$ dication.

Table 30: Comparison of the vibrational frequencies of **13** and **14** (bands of the anions have been omitted for clarity) with free P_4S_3 , the calculated frequencies for the isomer **IVA** of the $[Ag_2(P_4S_3)_6]^{2+}$ fragments and for the $[Ag_2(P_4S_3)_6]^{2+}$ dication. Values are given in cm^{-1} . Calculations at the (RI)-BP86/SV(P) level of theory. Raman intensities are given in %; IR intensities are given as follows: w = weak, mw = medium weak, m = medium, ms = medium strong, s = strong, vs = very strong.

P_4S_3 exp. Raman	P_4S_3 exp. IR ^[211]	P_4S_3 calc. IR (Sym.) ^[44]	$[P_4S_3)Ag[hfb]]$ 13 exp. Raman	$[(P_4S_3)Ag[hfb]]$ 13 exp. IR	isomer IVA calc. IR	$[Ag_2(P_4S_3)_6]^{2+}[al-f-al]^-$ 14 exp. Raman	$[Ag_2(P_4S_3)_6]^{2+}[al-f-al]^-$ 14 exp. IR	$[Ag_2(P_4S_3)_6]^{2+}$ calc. IR
489	488(m)	463 E	498(15%)	495(mw))	492	493(38%)	491(w)	484, 469
-	-		470(100%)	485(mw)	478	468(50%)	-	-
-	-	447 A ₁	-	-	457	447(100%)	-	457, 442
443	438(vs)	428 A ₁	444(18%)	-	437	432(38%)	430(ms)	427
-	-	-	-	-	410 (2x)	415(24%)	409(m)	418
422	414(s)	387 A ₁	-	394(ms)	400	-	-	400
-	-	389 E	-	-	-	-	377(ms)	382, 367
-	-	-	364(25%)	363(w)	-	-	-	-
-	-	-	352(49%)	351(w)	357	-	-	355
-	-	-	-	-	-	-	-	-
343	339(w)	323 E	-	338(mw)	334	346(86%)	347(w)	343
-	-	-	-	-	-	325(26%)	318(mw)	316
286	286(m)	287 E	299(30%), 289(37%)	298(ms)	285, 267	289(64%)	288(m)	289
-	-	-	-	-	-	246(24%)	-	247
221	218(s)	219 E	224(39%)	-	214, 209	222(40%)	-	226
187	184(s)	190 A ₂	198(3%)	-	177	193(8%)	-	214
-	-	-	117(8%)	-	127	-	-	112

6.7 Concluding Remarks

Although the fluorinated silver alkoxy aluminates used in this study are very similar, their P_4S_3 adducts are not. In Table 31 some properties of these compounds are summarized. For the smaller and more basic anions $[hfip]^-$ and $[hftb]^-$, polymeric molecular structures are obtained, in which Ag is coordinated by P_4S_3 and by two alkoxy groups from the anion. In the case of the less basic $[pftb]^-$, the anion does not coordinate the silver cation and polymeric $[Ag(P_4S_3)_2]_\infty$ cations are formed. For the largest and least basic $[al-f-al]^-$ anion, the adduct is dicationic with well separated dications and monoanions. However, even the large $[al-f-al]^-$ anion is too small to allow preparation of a simple isolated $Ag(P_4S_3)_n^+$ monocation, instead dimerization in the solid state with formation of the lattice stabilized dimeric $[Ag_2(P_4S_3)_6]^{2+}$ dication is seen. This $[Ag_2(P_4S_3)_6]^{2+}[al-f-al]_2^-$ salt **14** is the first 2:1 salt of a fluorinated aluminate anion. As shown by ESI-MS, DFT and Born-Haber cycle calculations, this dication is unstable in the gas phase and in solution (“Coulomb explosion”) (Figure 41).

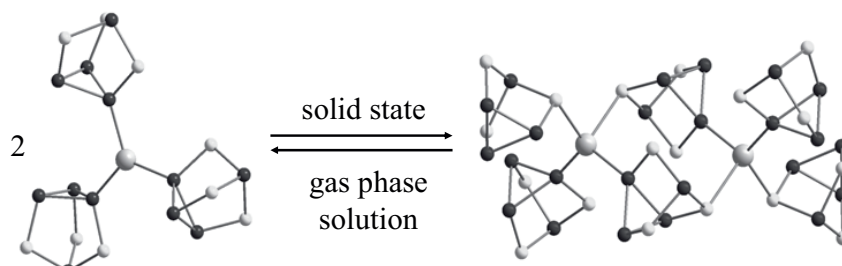


Figure 41: Likely equilibrium between 2 $[Ag(P_4S_3)_3]^+$ (**III**) and $[Ag_2(P_4S_3)_6]^{2+}$ in **14**.

Table 31: Comparison of the Ag(P₄S₃) adducts of the [hfip][−], [hftb][−], [pftb][−] and [al-f-al][−] anion.

	[hfip] [−] 11 ^[44]	[hftb] [−] 13	[pftb] [−] 12 ^[44]	[al-f-al] [−] 14
basicity of the anion	highest		low	lowest
thermochemical volume of the anion [nm ³]	0.599 ^[109]	0.663 ^(a)	0.758 ^[109]	1.113 ^(b)
P ₄ S ₃ per Ag	1	1	2	3
coordination towards Ag	1 P _{apical} , 1 P _{basal} , 2 O ^(c)	1 P _{basal} , 1 S, 2 O	3 P _{basal} , 1 S	2 P _{basal} , 2 S
δ ³¹ P in CD ₂ Cl ₂ [ppm]	+67 (q) -126 (d)	+67 (q) -128 (d)	+72 (q) -118 (d)	+73 (q) -117 (d)
av. d(P-S) [pm]	216 _{apical} , 207 _{basal}	209 _{apical} , 208 _{basal}	211 _{apical} , 208 _{basal}	211 _{apical} , 209 _{basal}
av d(P-P) [pm]	226	223	224	223
cation structure	polymeric	polymeric	polymeric	dimeric
structure of the adduct	molecular	molecular	ionic	ionic

^(a) determined by using the thermochemical volume of the [hfip][−] anion^[109] and the crystal structures of [(P₄S₃)Ag[hfip]] **11** and **13**. ^(b) determined by using the thermochemical volume of the [pftb][−] anion^[109] and the crystal structures of [Cl₃][pftb]^[47] and [Cl₃][al-f-al] (see chapter 7) ^(c) main form; side form: 1 P_{basal}, 1 S, 2 O.

According to the BHC in Scheme 6, one would need a weakly coordinating anion [A][−] of approximately 3.8 nm³ to stabilize a monomeric [Ag(P₄S₃)₃]⁺[A][−] salt. This should be contrasted with the volume of [al-f-al][−] of 1.113 nm³. Currently no well defined WCA with a volume as large as 3.8 nm³ is known. From one can also see that with larger and less basic anions more P₄S₃ cages can be coordinated. In all of these adducts, only η¹ coordination is

observed, which is in agreement with the calculation of the model compounds, which only predict an η^2 coordinated global minimum for $[\text{Ag}(\text{P}_4\text{S}_3)]^+ \mathbf{I}$. In this case the η^2 coordination is probably due to the fact that there are no other molecules which could coordinate to the silver cation. In all other assessed cases η^1 -coordination is preferred.

In solution, the NMR shifts of all adducts remain nearly unchanged if compared to the free ligand, which indicates dynamics and fast exchange processes. However, for **14** the ESI-MS and also the calculated $\Delta\delta$ ^{31}P NMR values indicate the solution presence of the $[\text{Ag}(\text{P}_4\text{S}_3)_3]^+$ cation, while in the solid state the dication $[\text{Ag}_2(\text{P}_4\text{S}_3)_6]^{2+}$ is favored (Scheme 6). Thus, the dynamics is likely to be due to exchanging $\text{Ag}(\text{P}_4\text{S}_3)_x^+$ structures and not due to exchange with the solvent CH_2Cl_2 . The same conclusion can be drawn from the solid-state ^{31}P NMR spectra, which clearly reveal that these systems are very dynamic – even at low temperature –, although the X-ray diffraction measurements of the $\text{Ag}(\text{P}_4\text{S}_3)$ complexes investigated in this study suggest rigid structures. Since X-ray crystallography is an average method, this notion implies that the resting states for the dynamics observed by MAS-NMR are long lived. Those conformations which are intermediates for the dynamic exchange are very short lived and do not contribute, as “disorder”, to the intensity data of the crystal structure determination. These conclusions are also in agreement with the flat calculated PES’s of the various $\text{Ag}(\text{P}_4\text{S}_3)_x^+$ isomers with $x = 1-3$. These flat PES’s – and the fact that both S and P coordination is observed in the solid-state structures – also indicates that degradation can occur both via sulfidic and phosphidic pathways.

7 Chemistry of Halocarbenium Ions – Theoretical and Experimental Studies

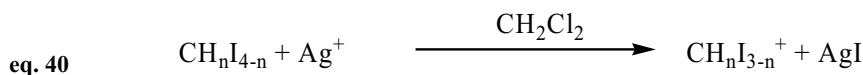
Small carbon-containing cations^[219, 220] like CX_3^+ ^[220-223] and XCO^+ ^[161, 162, 224] (X = halogen) are of continuing interest in organic, inorganic and theoretical chemistry as they are postulated to be intermediate species in organic reactions and are often observed as fragmentation products of gaseous ions in the mass spectrometer^[225, 226]. Not much is known about the properties and reactivity of these carbocations in condensed phases. However, over the last few years, some of them became accessible in the solid state^[223], e.g. Me_2CF^+ ^[60], $(H_3CO)C(H)X^+$ ($X = F, Cl$)^[227], $ClCO^+$ ^[162], $CS_2Br_3^+$ ^[228], $C(OH)_3^+$ ^[229], $CBr_n(OTeF_5)_{3-n}^+$ ($n = 0-3$)^[58], $C(ER)_3^+$ ($E = S, Se, Te, R = 2,4,6-iPrC_6H_2$)^[230], $(C_6H_4Cl)C(Cl)(C_6H_5)^+$ ^[231], $C(CH_3)_3^+$ ^[232], $FC(p-C_6H_4F)_2^+$ ^[233], $FC(Me)(p-C_6H_4F)^+$ ^[233] and CX_3^+ ($X = Cl, Br$)^[58], I ^[47].

Within this thesis, the halocarbenium cations of the type $H_{3-n}CX_n^+$ ($n = 1-3$) have been investigated. In order to get insight into their structural and spectroscopic properties as well as to gain information about their bonding, reactivity and thermodynamic stability, they have been investigated with experimental and quantum chemical methods. The obtained results have then been used for a comparison of the halocarbenium cations with the isoelectronic haloboranes.

7.1 Stable Cl_3^+ Salts and Attempts to Prepare CHI_2^+ and CH_2I^+

7.1.1 Synthesis and NMR Characterization

The route chosen to prepare the halomethyl cations $CH_nI_{3-n}^+$ ($n = 1-3$) was to react the parent halomethanes CH_nI_{4-n} ($n = 1-4$) with an Ag^+ salt (eq. 40).



Initial quantum chemical calculations showed that all these reactions should be exergonic both in the gas phase and in CH_2Cl_2 solution when assuming the formation of solid AgI during the course of the reaction (see Table 32); and red-brown $[Cl_3]^+[pftb]^-$ **15** was prepared

quantitatively from Ag[pftb] and Cl₄ with the strict exclusion of light.^[47] Analogously, [Cl₃]⁺[al-f-al]⁻ **16** was synthesized.

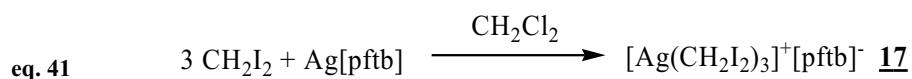
Table 32: $\Delta_r G^\circ$ in the gas phase and in CH₂Cl₂ for the formation of Cl₃⁺, CHI₂⁺ and CH₂I⁺ from Ag⁺ and CHI₃ resp. CH₂I₂ and CH₃I at the MP2/TZVPP level. The formation of solid AgI, i.e. the experimental $\Delta_{\text{subl},G}$ of AgI = 197.9 kJ/mol, has been considered. The values in parenthesis are without AgI precipitation (in kJ/mol).

Reaction	$\Delta_r G^\circ$ in the gas phase	$\Delta_r G^\circ$ in CH ₂ Cl ₂ ^(a)
Cl ₄ + Ag ⁺ → [Cl ₃] ⁺ + AgI	-287.0 (-89.1)	-150.3 (+47.6)
CHI ₃ + Ag ⁺ → [CHI ₂] ⁺ + AgI	-227.5 (-29.6)	-109.1 (+88.8)
CH ₂ I ₂ + Ag ⁺ → [CH ₂ I] ⁺ + AgI	-144.8 (+53.1)	-54.3 (+143.6)

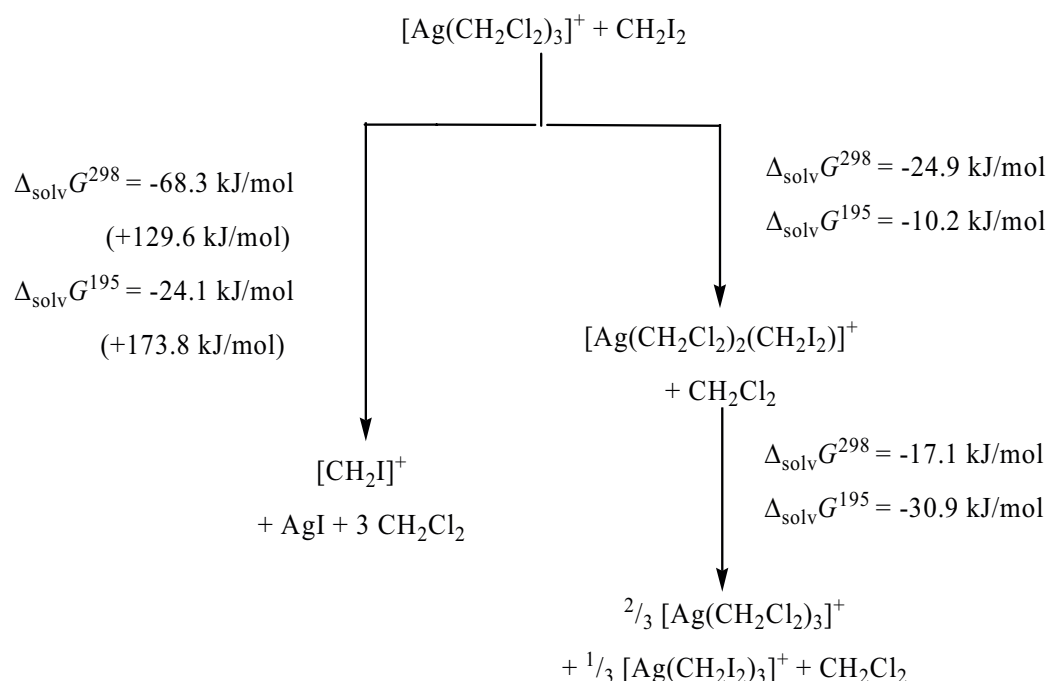
^(a)For the calculations in solution, [Ag(CH₂Cl₂)₃]⁺ has been used instead of Ag⁺. The formation of 3 eq. CH₂Cl₂ molecules has been considered.

The NMR spectra of **15** and **16** recorded in CD₂Cl₂ only showed the peaks of the Cl₃⁺ cation ($\delta^{13}\text{C} = 97.0$) and the anion (for **15**: $\delta^{13}\text{C} = 121.5$ and 78.8 , $\delta^{27}\text{Al} = 38.0$ with $\omega_{1/2} = 7$ Hz; $\delta^{19}\text{F} = -75.5$; for **16**: $\delta^{13}\text{C} = 121.0$ and 78.8 , $\delta^{27}\text{Al} = 33.0$ with $\omega_{1/2} = 2244$ Hz). The experimentally observed ¹³C NMR shift of the Cl₃⁺ cation is in very good agreement with that of G. Olah *et al.* observed in the pioneering study in SO₂ClF solution at 95 ppm^[234] and the value of 106 ppm predicted by spin-orbit corrected quantum chemical calculations^[235].

Since **15** and **16** are stable at ambient temperature for more than half a year in the solid state, it was attempted to stabilize the analogous CHI₂⁺ and CH₂I⁺ salts. Since these cations were predicted to be more reactive, these reactions were started at low temperatures to avoid decomposition. When reacting CH₂I₂ with Ag[pftb] at -78°C, even after a couple of days no precipitation of AgI was observed, so the mixture was stirred at room temperature for a few days, but again no AgI was formed. From the NMR spectra it could be seen that the anion remained intact. But in the ¹³C NMR the peak of CH₂I₂ was shifted 8 ppm to lower field if compared to a reference spectrum of free CH₂I₂ recorded under the same conditions. In the ¹H NMR, $\Delta\delta$ is +0.3 ppm. This indicated that CH₂I₂ remained coordinated to silver. To prove that in this reaction the [Ag(CH₂I₂)₃]⁺ adduct was formed (eq. 41)



another reaction with a 3:1 stoichiometry has been performed. After the solution has been concentrated, colorless crystals of $[\text{Ag}(\text{CH}_2\text{I}_2)_3]^+[\text{pftb}]^-$ **17** formed in nearly quantitative yield. In yet another reaction, $[\text{Ag}(\text{CH}_2\text{Cl}_2)][\text{pftb}]$ and CH_2I_2 were mixed in a 1:1 stoichiometry without the addition of solvent. The mixture was ground for a couple of hours at ambient temperature. Also in this case, the formation of the expected CH_2I^+ cation was not observed, but the adduct $[\text{Ag}(\text{CH}_2\text{Cl}_2)(\text{CH}_2\text{I}_2)][\text{pftb}]$ was formed, which followed from the NMR and IR spectra of the reaction mixture. It appears that complexation of CH_2I_2 is kinetically favored over AgI elimination leading to the thermodynamic CH_2I^+ cation; this finding is also supported by quantum chemical calculations (Scheme 7).



Scheme 7: Gibbs free energies $\Delta_r G$ (in kJ/mol) of ligand exchange vs. CH_2I^+ formation reactions of CH_2I_2 with $[\text{Ag}(\text{CH}_2\text{Cl}_2)_3]^+[\text{pftb}]^-$ in CH_2Cl_2 solution. Calculations were done at the MP2/TZVPP level. Values in parenthesis: without consideration of the sublimation enthalpy of AgI (197.9 kJ/mol).

According to the quantum chemical predictions, the CHI_2^+ cation is more stable than CH_2I^+ and its formation in CH_2Cl_2 should be exergonic by -109.1 kJ/mol (with inclusion of the precipitation of solid AgI ; Table 32). Thus, it was anticipated it would be possible to prepare $[\text{CHI}_2]^+[\text{pftb}]^-$ according to eq. 40. Both solid starting materials were weighed together in a 1:1 stoichiometry, CH_2Cl_2 was condensed onto this mixture at 77 K which was then slowly warmed to ambient temperature. The mixture turned red-brown and AgI precipitated. In the

^{13}C NMR of the reaction mixture, the two signals of the $[\text{pftb}]^-$ anion (a quartet at $\delta = 121.5$ and a multiplet at $\delta = 78$) and two singlets at $\delta = 96.2$ and $\delta = -57.0$ were observed. The first is assigned to the Cl_3^+ cation^[47], the second originates from CH_2I_2 coordinated to silver (see above). Thus, the intermediately prepared CHI_2^+ cation disproportionates immediately to give Cl_3^+ and CH_2I_2 .

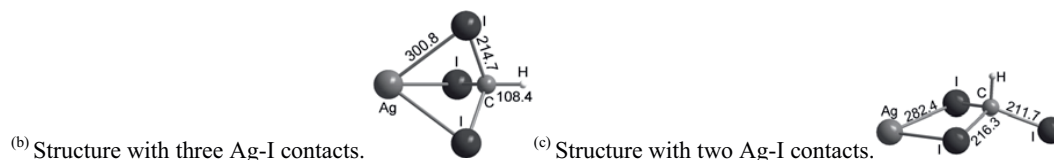
Prior to investigate the system further with low temperature NMR studies and to search the signals of the CHI_2^+ intermediate experimentally, one should be aware of potential complications: Since all of the species addressed in this study contain the heavy elements iodine and / or silver, their NMR shifts are strongly affected by relativistic effects^[236, 237]. In particular, atoms directly bonded to iodine substituents may exhibit very large spin-orbit (SO) effects. For a clear assignment of the species observed in solution, calculations have to be carried out including SO contributions.

Table 33 provides nonrelativistic, as well as SO corrected values computed for various species. As has been shown previously for similar systems (with main group elements in their highest oxidation state)^[236, 237], spin-orbit corrections to the ^{13}C shifts due to directly bonded iodine substituents are strongly shielding, and the shielding effect increases more than linearly with the number of iodine substituents present. This can be seen, e.g., when comparing CH_2I_2 with CHI_3 . SO effects on ^1H shifts are moderately shielding for CH_2I_2 and its complex and somewhat more shielding for CHI_3 . Surprisingly, for the hypothetical cations CHI_2^+ and CH_2I^+ , the ^1H SO effects are dramatically deshielding, by about 6 ppm. As even the nonrelativistic values are already strongly deshielded, the computations predict extremely large shifts around +20-21 ppm. This is at the absolute low-field (high-frequency) end of the ^1H shift scale for diamagnetic compounds, only comparable to some low-barrier hydrogen bonds^[238] (and even slightly more deshielded than organomercury hydrides^[239, 240]). Closer analysis of MO contributions to the SO shifts, and of the nonrelativistic shieldings, indicates the planar structure and the resulting character of the frontier orbitals to be responsible for the large shifts: The SO shieldings are dominated by an SO-induced coupling between an occupied $\sigma\text{-C-H}$ bonding MO, having appreciable $\sigma\text{-C-I}$ antibonding character, to the LUMO which contains an antibonding iodine p_z admixture. The fact that the frontier MOs are of σ -character and mix strongly C-H bonding and C-I antibonding character accounts for the unusually large SO effects on the proton shieldings^[236, 240]. Similar orbital couplings account for the large paramagnetic contributions to the nonrelativistic part of the shieldings.

Table 33: Calculated ^1H and ^{13}C NMR shifts (GIAO-BP86/IGLO-II level with SO corrections^(a)). All shifts are given in ppm relative to SiMe_4 . NR = non-relativistic; SO = spin-orbit contributions; n.o. = not observed.

Compound	$\delta\ ^1\text{H}$ (NR)	$\delta\ ^1\text{H}$ (NR + SO)	$\delta\ ^1\text{H}$ (exp.)	$\delta\ ^{13}\text{C}$ (NR)	$\delta\ ^{13}\text{C}$ (NR + SO)	$\delta\ ^{13}\text{C}$ (exp.)
Cl_3^+	-	-	-	338.6	123.8	97.0
CHI_2^+	13.86	19.80	n.o.	333.7	229.8	n.o.
CH_2I^+	14.96	21.08	n.o.	358.9	287.1	n.o.
CHI_3	7.76	6.03	4.96	67.7	-116.7	-160
$[\text{Ag}(\text{CHI}_3)]^+ (\text{Ag} \cdots \text{I}_3)^{(b)}$	6.17	4.96	5.03	67.2	-169.0	-140.3
$[\text{Ag}(\text{CHI}_3)]^+ (\text{Ag} \cdots \text{I}_2)^{(c)}$	8.40	6.17	5.03	81.0	-140.8	-140.3
CH_2I_2	4.62	4.24	3.90	29.1	-50.7	-62.7
$[\text{Ag}(\text{CH}_2\text{I}_2)(\text{CH}_2\text{Cl}_2)_2]^+$	4.49	4.20	4.21	32.1	-41.8	-52.4

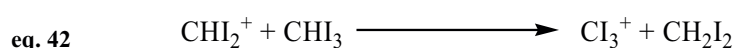
^(a)Uncoupled DFT-GIAO calculations, DZVP basis on Ag, IGLO-II basis on all other atoms. The full one- and two-electron spin-orbit contributions at Breit-Pauli level have been obtained from a third-order perturbation approach (cf. Ref. 241 and Computational Details).



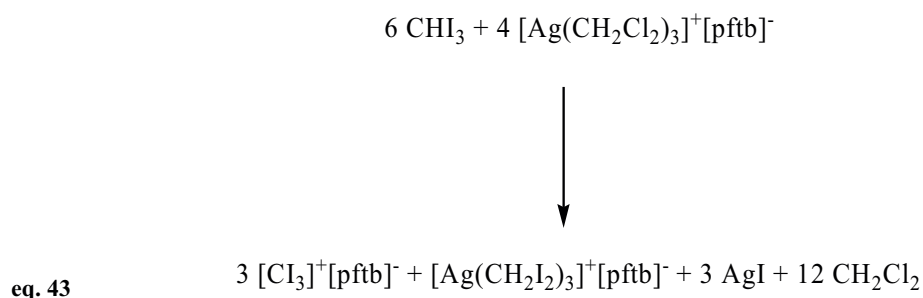
Experimentally, the coordination of CH_2I_2 or CHI_3 to a silver cation moves both ^{13}C and ^1H shifts to somewhat less shielded values. This is reproduced computationally only for the ^{13}C shift of CH_2I_2 vs. $[\text{Ag}(\text{CH}_2\text{I}_2)(\text{CH}_2\text{Cl}_2)_2]^+$, whereas the other computed values exhibit the opposite trend (the more stable doubly-bridged structure of $[\text{Ag}(\text{CHI}_3)]^+$ gives the correct direction of the coordinated ^1H shift). Currently no full explanation for this can be given. Variations in basis sets and in the Fermi-contact finite perturbation parameter λ did not change the qualitative trends. MO analyses provided no clearcut explanation for the different ^{13}C coordination shifts of the complexes with CHI_3 vs. CH_2I_2 ligands.

With these additional informations let's now turn back to the experiments: From a second *in situ* reaction in a flame-sealed NMR tube, which was kept at -78°C and measured at -80°C (CD_2Cl_2 as solvent), it is noticed that the formation of Cl_3^+ and CH_2I_2 immediately occurs at

low temperatures. In the ^1H NMR, the signals of the following species were observed: free CH_2I_2 (s, $\delta = 3.90$, very small), coordinated CH_2I_2 (s, $\delta = 4.21$) and coordinated CHI_3 (s, $\delta = 5.03$). In the ^{13}C NMR – apart from the anion peaks at $\delta = 121.5$ (q) and 78.8 (m) – signals of coordinated CHI_3 (s, $\delta = -140.3$), coordinated CH_2I_2 (s, $\delta = -52.4$) and CI_3^+ (s, $\delta \approx 96$, very small) are found. It is assumed that the CHI_2^+ cation is so reactive that it only exists as an intermediate and even at -78°C immediately reacts with CHI_3 to form CI_3^+ and CH_2I_2 according to the following equation (eq. 42):



Quantum chemical calculations suggest that this reaction is exergonic by 32.2 kJ/mol in CH_2Cl_2 at 298K and by 30.4 kJ/mol at 195K (calculations at the MP2/TZVPP level). Caused by these considerations, a 2:1 reaction was performed aimed at the preparation of the CI_3^+ salt **15** but from a starting material which is not light sensitive. The volatile side product CH_2I_2 should then be pumped off. However, the $^{13}\text{C}\{^1\text{H}\}$ NMR spectrum, recorded after exposure to high vacuum (10^{-3} mbar) for a few days, not only contained the CI_3^+ peak, but also that of the $[\text{Ag}(\text{CH}_2\text{I}_2)_3]^+$ cation. Thus, the CH_2I_2 is bound very strongly to the silver and prevents the complexed $[\text{Ag}(\text{CH}_2\text{I}_2)_3]^+$ from further participation in iodide abstraction from CHI_3 . This is also indicated by the strong low field shift if compared to free CH_2I_2 ($\Delta\delta = +8$). Both $[\text{CI}_3]^+[\text{pftb}]^-$ and $[\text{Ag}(\text{CH}_2\text{I}_2)_3]^+[\text{pftb}]^-$ **17** crystallize from this reaction (unit cell determinations), but this reaction can not be used as a selective synthesis of the CI_3^+ salt **15** due to the very similar solubilities of both substances. Since CH_2I_2 formed in this process coordinates to the silver to give the $[\text{Ag}(\text{CH}_2\text{I}_2)_3]^+$ complex, the equilibrium of eq. 42 is additionally shifted towards CI_3^+ formation. The overall eq. 43 describes this process:



This reaction is exergonic by 479 kJ/mol at 298K and by 381.1 kJ/mol at 195K in CH_2Cl_2 (MP2/TZVPP).

If the reaction is carried out without any solvent (by mixing the two starting materials in a mortar) a highly reactive green powder forms when a 1:1 stoichiometry is used. After the addition of more CHI_3 , the powder turns red-brown and $[\text{Cl}_3]^+[\text{pftb}]^-$ **15** is formed. The green substance could not be characterized further due to its reactivity (it turns brown after a few minutes at ambient temperature and immediately when CH_2Cl_2 is added). Quantum chemical calculations of the structure (MP2/TZVPP) and UV-Vis spectrum (TD-DFT) of HCl_2^+ and $\text{Ag}(\text{HCl}_3)^+$ (Figure 42) suggest that the green species is more likely a $\text{Ag}(\text{HCl}_3)^+$ complex, which is only metastable at low temperatures in the solid state.

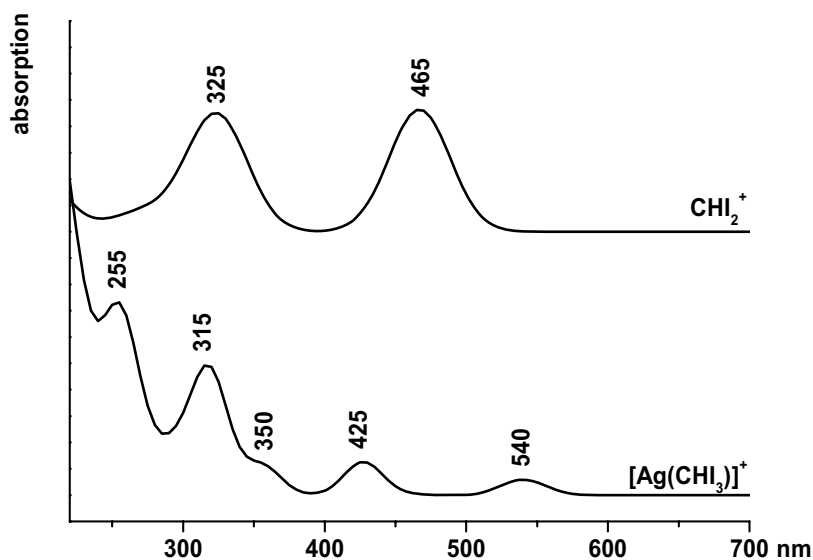


Figure 42: Simulation of the UV-Vis spectra of $[\text{Ag}(\text{CHI}_3)]^+$ and $[\text{CHI}_2]^+$ (TD-DFT at the (RI-)BP86/SV(P) level).

7.1.2 Solid-State Structures

*Solid-State Structures of $[Cl_3]^+[pftb]^-$ **15** and $[Cl_3]^+[al-f-al]^-$ **16***

Orange-yellow crystals of **15** have been used for determining its solid state structure, which is displayed in Figure 43.

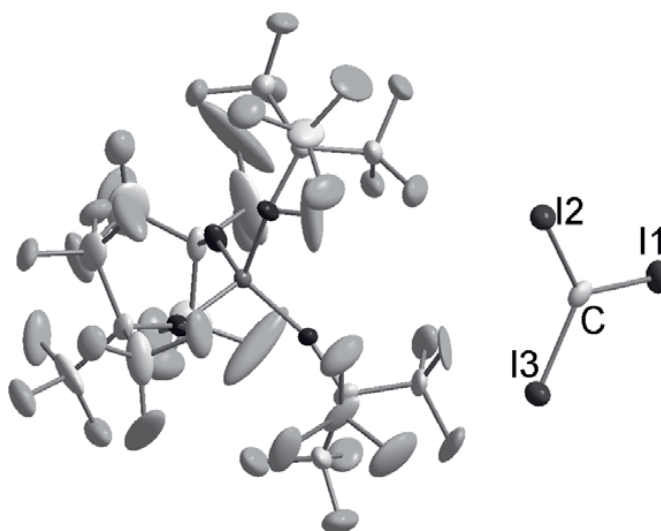


Figure 43: Section of the solid state structure of **15** at 150K, thermal displacement ellipsoids showing 25% probability. For clarity the disorder of some CF_3 groups it not shown. Selected bond lengths (in pm) and angles (in $^\circ$): $d(C-I1) = 200.7(9)$, $d(C-I2) = 199.3(8)$, $d(C-I3) = 203.9(10)$, $\angle(I1-C-I2) = 122.1(5)$, $\angle(I1-C-I3) = 119.1(4)$, $\angle(I2-C-I3) = 118.8(4)$.

15 crystallizes in the orthorhombic space group $Pna2_1$ with $Z = 4$. The structure contains isolated cations and anions, which are only connected via 13 very weak I-F contacts. The Cl_3^+ cation in **15** is planar (sum of the I-C-I bond angles = 360.0°). The average C-I distance is 201.3 pm, which is significantly shorter than that in Cl_4 (215.9 pm)^[242] or the B-I bonds in the isoelectronic BI_3 molecule (212.5 pm)^[243]. Single crystals of **16**, which were suitable for X-ray diffraction measurements, were grown from a concentrated solution of **16** in CH_2Cl_2 at $-78^\circ C$. **16** crystallizes in the monoclinic space group $P2_1/c$ with $Z = 4$. In the asymmetric unit, there is one cation and two half anions with the bridging fluorine atoms residing on centers of inversion. In Figure 44 a section of the solid state structure of **16** is shown.

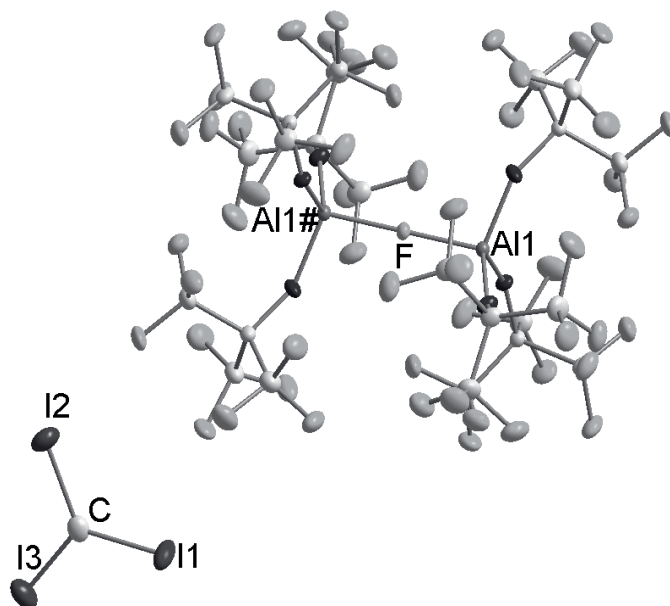


Figure 44: Section of the solid-state structure of **16** at 150K, thermal displacement ellipsoids showing 25% probability. The second (half) anion has been omitted for clarity. Selected bond lengths (in pm) and angles (in °): $d(\text{C-I1}) = 199.8(8)$, $d(\text{C-I2}) = 200.2(8)$, $d(\text{C-I3}) = 201.9(8)$, $\angle(\text{I1-C-I2}) = 121.0(4)$, $\angle(\text{I1-C-I3}) = 119.3(4)$, $\angle(\text{I2-C-I3}) = 119.8(4)$.

Cation-anion contacts of **15** and **16** are shown in Figure 45.

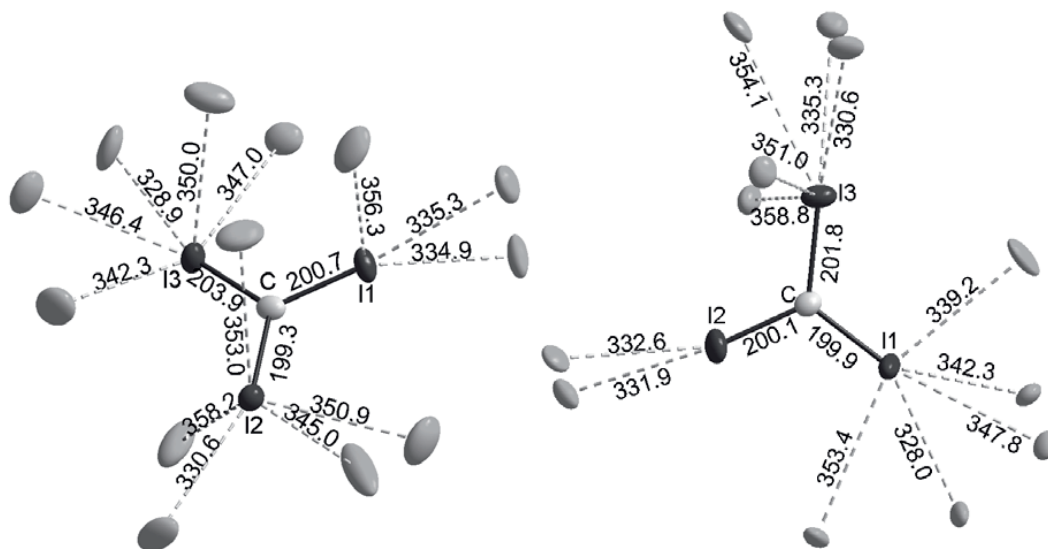


Figure 45: Cation-anion contacts in $[\text{Cl}_3]^+[\text{pftb}]^-$ **15** (left) and **16** (right).

As it can be seen from Figure 46, the cations and anions are aligned in alternating layers parallel to the crystallographic *bc* plane.

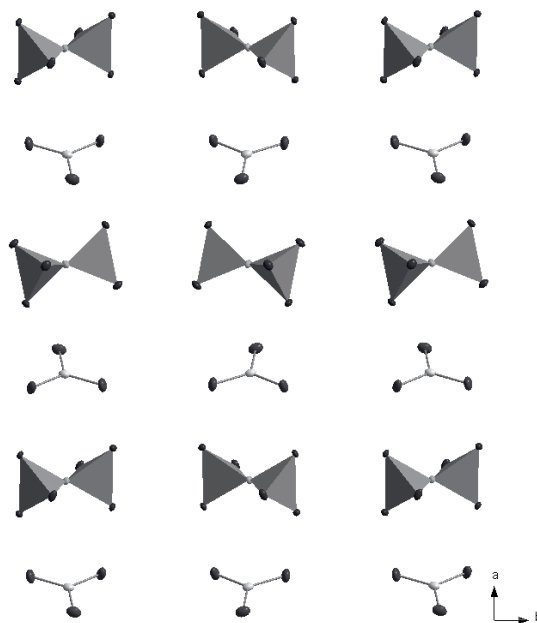


Figure 46: Packing diagram of **16**. View along the crystallographic *c* axis. All C and F atoms (except the bridging F's) have been omitted for clarity. The [al-f-al]⁻ anions are drawn as Al₂O₆F polyhedra.

Like in the solid state structure of [Cl₃]⁺[pftb]⁻ **15**, the Cl₃⁺ cation is planar (sum of I-C-I angles = 360.1(12)°) and the C-I bonds ($d_{av}(\text{C-I}) = 200.6 \text{ pm}$) have about the same lengths. In **15** and **16**, 13 resp. 12 weak I-F contacts are found (see appendix appendix 12.5), but there is no C-F contact below the sum of the van der Waals radii, indicating that the positive charge in the Cl₃⁺ cation resides on the I atoms and not on the carbon.

Solid-State Structure of [Ag(CH₂I₂)₃]⁺[pftb]⁻ **17**:

Colorless crystals of [Ag(CH₂I₂)₃]⁺[pftb]⁻ **17** were obtained from a concentrated solution of the 3:1 reaction in CH₂Cl₂. **17** crystallizes in the monoclinic space group P2₁/c with *Z* = 4. In Figure 47 a section of the solid state structure of **17** is shown.

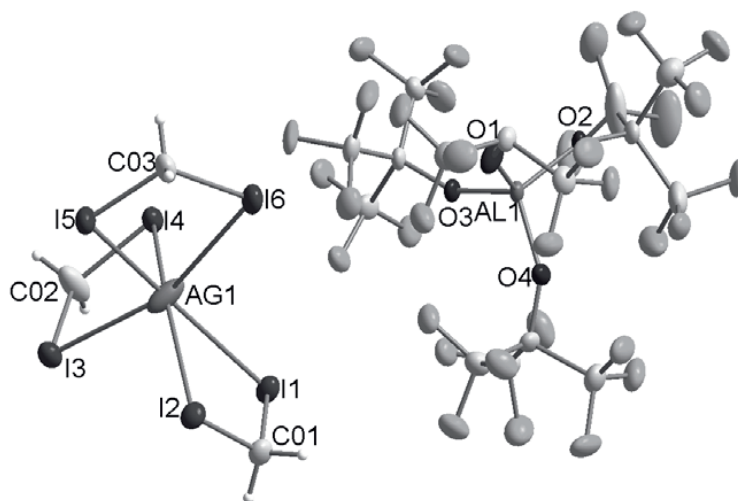


Figure 47: Section of the solid-state structure of **17** at 140K, thermal displacement ellipsoids showing 25% probability. Selected bond lengths (in pm) and angles (in °): $d(\text{Ag1-I1}) = 308.53(13)$, $d(\text{Ag1-I2}) = 302.57(15)$, $d(\text{Ag1-I3}) = 310.37(16)$, $d(\text{Ag1-I4}) = 299.84(14)$, $d(\text{Ag1-I5}) = 294.41(13)$, $d(\text{Ag1-I6}) = 314.42(16)$, $d(\text{C01-I1}) = 212.50(4)$, $d(\text{C01-I2}) = 211.01(4)$, $d(\text{C02-I3}) = 211.38(5)$, $d(\text{C02-I4}) = 212.19(4)$, $d(\text{C03-I5}) = 209.28(4)$, $d(\text{C03-I6}) = 211.47(4)$, $d(\text{Al1-O1}) = 170.7(6)$, $d(\text{Al1-O2}) = 170.5(6)$, $d(\text{Al1-O3}) = 172.5(6)$, $d(\text{Al1-O4}) = 170.9(6)$, $\angle(\text{C01-I1-Ag1}) = 87.2(3)$, $\angle(\text{C01-I2-Ag1}) = 89.0(3)$, $\angle(\text{C02-I3-Ag1}) = 86.5(4)$, $\angle(\text{C02-I4-Ag1}) = 89.1(4)$, $\angle(\text{C03-I5-Ag1}) = 91.4(3)$, $\angle(\text{C03-I6-Ag1}) = 85.6(3)$, $\angle(\text{I1-C01-I2}) = 113.2(5)$, $\angle(\text{I3-C02-I4}) = 113.4(6)$, $\angle(\text{I5-C03-I6}) = 112.8(5)$.

17 is the first example of a homoleptic $\text{Ag-CH}_2\text{I}_2$ complex. In the isolated $[\text{Ag}(\text{CH}_2\text{I}_2)_3]^+$ moieties, the silver atom is coordinated by six iodine atoms in a distorted octahedral fashion. The average Ag-I distance in **17** is 305.0 pm and ranges from 294.41(13) to 314.42(16) pm. The C-I bond lengths lie between 209.3(11) and 212.2(13) pm ($d_{\text{av}}(\text{C-I}) = 211.3$ pm). The C-I-Ag angles average to 88.1° ($85.6(3)$ to $91.4(3)^\circ$).

Although silver complexes with CH_2I_2 as a ligand are already known since 1906^[244], their structure only was revealed in the 1990's, when Powell *et al.* reported the solid state structures of the silver-iodoalkane complexes, $[(\text{I}-(\text{CH}_2)_3)\text{-I})_2\text{Ag}]^+[\text{PF}_6]^-$ ^[245], $\text{AgNO}_3 \cdot \text{CH}_2\text{I}_2$ ^[245], $[\text{Ag}(\text{CH}_2\text{I}_2)_2][\text{PF}_6]$ ^[245, 246], $[(\text{I}-(\text{CH}_2)_3)\text{-I})_2\text{Ag}]^+[\text{PF}_6]^-$ ^[245] and $[\{\text{Ag}_2(\text{O}_2\text{CCF}_3)_2(\text{CH}_2\text{I}_2)_2\}_n]$ ^[247], in which diiodomethane acts as a bridging ligand. In the latter compound, the relatively basic $[(\text{CF}_3)\text{COO}]^-$ anion coordinates to the silver atom. This strong coordination of the two electron rich oxygen atoms ($d_{\text{av}}(\text{Ag-O}) = 224.3$ pm) leads to a partial saturation of the positive charge, so that only one iodine atom of the two CH_2I_2 ligands coordinates to the silver ($d_{\text{av}}(\text{Ag-I}) = 207.5$ pm), and if compared to **17**, the Ag-I bonds are weaker. The same holds for $\text{AgNO}_3 \cdot \text{CH}_2\text{I}_2$ ($d_{\text{av}}(\text{Ag-I}) = 284.6$ pm). If $[\text{PF}_6]^-$ is used as a

counterion, the resulting species is not longer molecular, but it consists of cationic chains, in which the CH_2I_2 molecules act as bridging ligands between two silver centers ($d_{\text{av}}(\text{Ag-I}) = 285.9 \text{ pm}$). In this case the Ag-I bonds are shorter than in **17**, but this is due to the fact that silver is only fourfold coordinated. With the least coordinating anion $[\text{pftb}]^-$, three diiodomethane molecules coordinate to each silver and a salt structure with isolated cations and anions is formed. This tendency, i.e. the less coordinating the anion, the more ligands are coordinated and the more ionic is the resulting adduct, was also noticed found for many other ligands like P_4S_3 ^[44, 248] (see also chapter 6), P_4 ^[43], C_2H_4 ^[110, 182] or C_2H_2 ^[110, 198]. If compared to free CH_2I_2 ($d(\text{C-I}) = 213.4 \text{ pm}$)^[249], the ligands in **17** remain nearly unchanged, which is an indication for a weakly bound Lewis acid base complex.

7.1.3 IR and Raman Spectroscopy

*Vibrational Spectroscopy of $[\text{Cl}_3]^+[\text{pftb}]^-$ **15** and $[\text{Cl}_3]^+[\text{al-f-al}]^-$ **16**:*

IR spectra in Nujol have been recorded of both Cl_3^+ salts **15** and **16**. The characteristic anion vibrations were identified and are included with a table in appendix 12.5. Let's now turn to the IR spectra of the Cl_3^+ cations, for which four bands at 792 (e' , strong), 378 (a_2'' , weak), 236 (a_1' , inactive) and 127 (e' , inactive) cm^{-1} are expected according to a MP2/TZVPP frequency calculation. Two of the four bands can be assigned from the experiment: In a Nujol mull of **15** the weak a_2'' band is observed at 329 cm^{-1} , while the C-I stretch at about 739 cm^{-1} (e') is a shoulder of the anion vibration at 727 cm^{-1} . At 1068 cm^{-1} , a combination mode of the e' (739 cm^{-1}) and the a_2'' (329 cm^{-1}) of the Cl_3^+ cation is observed. When recording the IR spectrum on a diamond ATR unit, the 739 cm^{-1} C-I stretch is clearly resolved from the anion vibration at 727 cm^{-1} (Figure 48). However, the combination mode was not observed and the weak a_2'' band is a bit broadened and its maximum shifts slightly (to 337 cm^{-1}), which may be caused to recording the spectrum under pressure in an ATR unit.

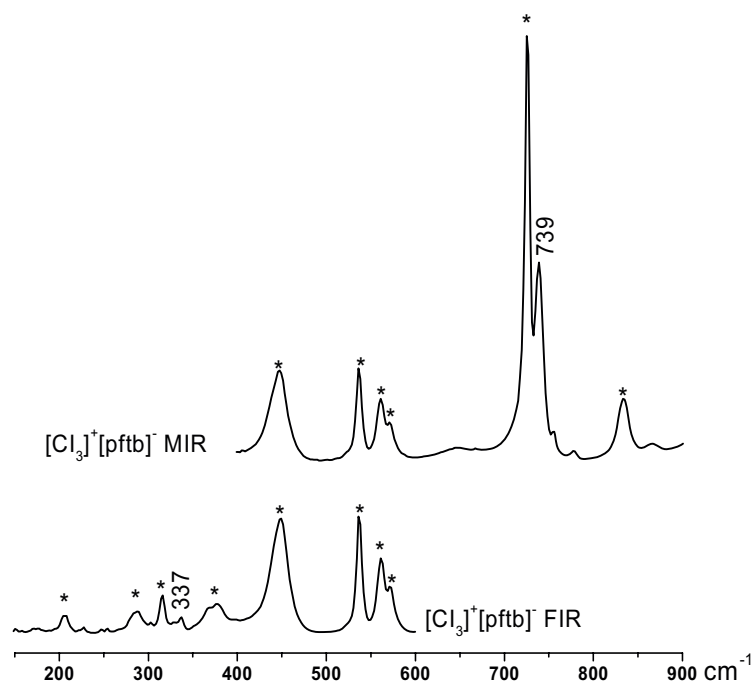


Figure 48: IR spectrum of $[\text{Cl}_3]^+[\text{pftb}]^-$ **15** (diamond ATR unit). Bands marked with * are assigned to the anion.

If $[\text{al-f-al}]^-$ is used as a counterion, the weak a_2'' band (332 cm^{-1}) and e' band (shoulder at $\approx 740\text{ cm}^{-1}$) were observed in Nujol mull.

Attempts to record Raman spectra of **15** and **16** remained unsuccessful, as – even with very low laser intensities, wide focus and at low temperature (100 K) – only strong fluorescence and rapid I_2 formation was observed upon irradiation with the 1064 nm Laser of the FT-Raman spectrometer.

Reaction of CHI_3 with $\text{Ag}[\text{pftb}]$:

The IR spectrum of the 2:1 reaction of CHI_3 with $\text{Ag}[\text{pftb}]$ showed peaks at 329 cm^{-1} , 737 cm^{-1} and 1066 cm^{-1} that are assigned to the Cl_3^+ cation^[47], the bands at 496 cm^{-1} and 1108 cm^{-1} can be assigned to $[\text{Ag}(\text{CH}_2\text{I}_2)_3]^+$, all other bands are caused by the anion. The two small bands observed at 640 cm^{-1} and 864 cm^{-1} are typical for the $[\text{al-f-al}]^-$ anion, thus, a small amount of degradation of the $[\text{pftb}]^-$ anion can be assumed.

7.1.4 UV-Vis Spectroscopy of the Cl_3^+ salts

The single-crystals of the Cl_3^+ salts **15** and **16** have – in contrast to the isoelectronic colorless BI_3 – a yellow-orange color. UV-Vis spectra of both compounds were recorded and compared with the calculated electronic transitions and those of BI_3 . First attempts to record the spectra in CH_2Cl_2 did not meet with success, because in highly diluted solutions both compounds rapidly decomposed to give I_2 (broad peak at $\lambda \approx 500$ nm). Therefore, the measurements were performed on solid samples as Nujol mulls between quartz plates. The electronic transitions of the Cl_3^+ cations were observed at $\lambda = 274, 307$ and 349 nm (Figure 49), which is in very good agreement with the simulated UV-Vis spectrum (TD-DFT at the (RI)BP86/SV(P) level).

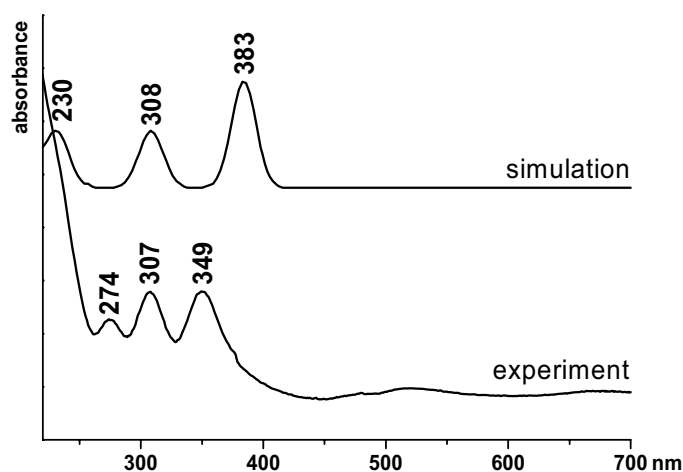


Figure 49: UV-Vis spectrum of $[\text{Cl}_3]^+[\text{pftb}]^-$ **15** in Nujol between quartz plates and comparison with the calculated spectrum of the Cl_3^+ cation (TD-DFT at the (RI)BP86/SV(P) level).

In Figure 50, the part of the MO diagram CX_3^+ , to which the p orbitals of the carbon and halogens contribute, is shown. The four p_z orbitals of the C and X atoms form a binding π MO (a_2''), two non-bonding MOs (e'') and an anti-bonding, empty π^* MO (a_2''). The binding combination (π bonding) is delocalized over the entire molecule. In contrast to the Cl_3^+ cation, which has its first absorption maximum at 349 nm, the first transition ($n \rightarrow \pi^*$) in the isoelectronic BI_3 molecule is found at 313 nm, i.e. in near UV^[250, 251]. In the Cl_3^+ cation, the $n \rightarrow \pi^*$ (i.e. $e'' \rightarrow a_2''$) transitions are shifted towards lower energies and therefore in the visible region. From Table 34, where the HOMO and LUMO energies as well as the energies of the first electronic transition is given for all CX_3^+ and BX_3 particles as well as from Figure 51, it can be seen that for all pairs of isoelectronic species, the same trend is found, i.e. the

first absorption is always redshifted in CX_3^+ with respect to BX_3 and the transition energies decrease from fluorine to iodine.

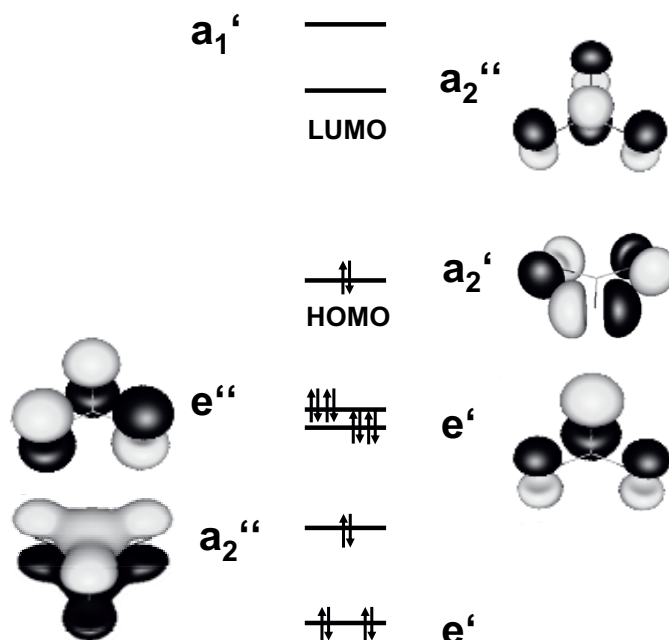


Figure 50: Qualitative MO diagram of CX_3^+ . An analogous diagram can be drawn for BX_3 .

Table 34: Energies of the orbitals of CX_3^+ and BX_3 contributing to the first $n \rightarrow \pi^*$ UV-Vis absorption (BP86/SV(P)). Experimental values for ΔE are given in parenthesis.

	CX_3^+			BX_3		
X =	$E(e'')$ [eV]	$E(a_2'')$ [eV]	ΔE [nm]	$E(e'')$ [eV]	$E(a_2'')$ [eV]	ΔE [nm]
F	-20.83	-11.82	115	-10.72	-0.18	118 ^(a) (108 ^[252])
Cl	-15.21	-10.93	224	-8.35	-2.28	180 (172 ^[252])
Br	-13.73	-10.43	284	-7.71	-2.82	221 (206 ^[252])
I	-12.24	-9.81	367 (349)	-7.10	-3.34	286 (313 ^[251])

^(a)The first irrep e' excitation for BF_3 has also a 31% contribution of the transition $e' - a_1'$ (105 nm), resulting in an average excitation energy of 107 nm.

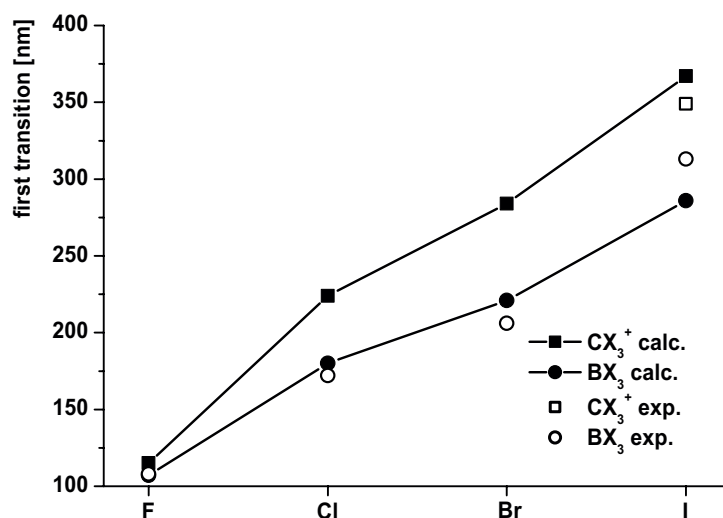


Figure 51: Comparison of the first electronic transitions in CX_3^+ and BX_3 (experimental and BP/SV(P)).

7.1.5 Fluoride Ion Affinities (*FIAs*) of $EX_3^{+/0}$ and $EH_nX_{3-n}^{+/0}$

Both the halocarbenium ions and the haloboranes are electron deficient species and therefore, strong Lewis acids. A common scale for the Lewis acidity of a given species is its fluoride ion affinity (*FIA*). The *FIA* values of CX_3^+ and $CH_nI_{3-n}^+$ cations and for the isoelectronic haloboranes are listed in Table 35.

Table 35: *FIA* of $EX_3^{+/0}$ and $EH_nX_{3-n}^{+/0}$ (E = C, B; X = F-I) in the gas phase and in CH_2Cl_2 (ΔH° at the MP2/TZVPP level). All values are given in kJ/mol.

X =	CX ₃ ⁺ / BX ₃		HCX ₂ ⁺ / HBX ₂		H ₂ CX ⁺ / H ₂ BX	
	<i>FIA</i> (gas)	<i>FIA</i> (CH ₂ Cl ₂)	<i>FIA</i> (gas)	<i>FIA</i> (CH ₂ Cl ₂)	<i>FIA</i> (gas)	<i>FIA</i> (CH ₂ Cl ₂)
F	1096 / 350	497 / 216	1054 / 309	453 / 184	1057 / 293	454 / 175
Cl	901 / 402	360 / 254	939 / 375	383 / 237	992 / 339	417 / 210
Br	867 / 429	345 / 273	915 / 404	376 / 258	977 / 361	414 / 226
I	809 / 444	299 / 275	865 / 427	340 / 268	944 / 384	392 / 239

In each of these series of carbocations, the *FIA* values both in CH₂Cl₂ and in the gas phase decrease from F to I, and they increase if – for a given halogen – the cation contains more hydrogen atoms. For the isoelectronic haloboranes, these trends are inverted (Figure 52).

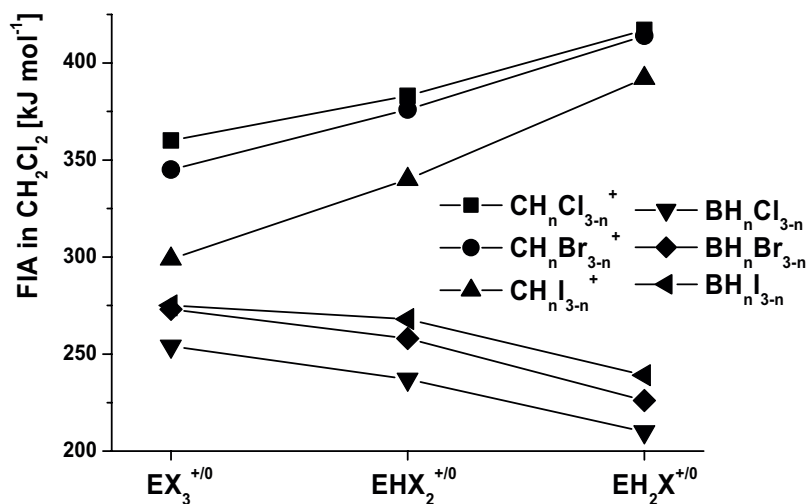


Figure 52: *FIA*s (in CH₂Cl₂) of EX₃⁺⁰ and EHX_{3-n}⁺⁰ (E = C, B; X = Cl-I) at the MP2/TZVPP level.

7.1.6 Bonding in Cl₃⁺ and BI₃

Significant differences are found when comparing the isoelectronic species Cl₃⁺ and BI₃, which are likely caused by the positive charge of the carbocation. The most important physical observables for a solid comparison are listed in Table 36 and Table 65.

Table 36: Comparison of experimental and calculated data of Cl₃⁺ and BI₃. Structures have been calculated at the ccsd(t)/aug-cc-pVTZ level, vibrational spectra have been calculated at the (RI)BP86/SV(P) level, n.o. = not observed in the IR spectra.

	Cl ₃ ⁺ in 15	Cl ₃ ⁺ in 16	Cl ₃ ⁺ calc.	BI ₃ exp.	BI ₃ calc.
<i>d</i> (E-I) [pm]	201.3	200.6	204.0	212.50 ^[253]	212.77
$\tilde{\nu}_1$ (e') [cm ⁻¹ / (km mol ⁻¹)]	739 (s)	740 (s)	715 (174) ^[47]	693(¹¹ B) ^[254]	693 (256) ^[47]
$\tilde{\nu}_2$ (a ₂ '') [cm ⁻¹ / (km mol ⁻¹)]	329 (w)	332 (w)	340 (10) ^[47]	305(¹¹ B) ^[254]	309 (1) ^[47]
$\tilde{\nu}_3$ (a ₁ ') [cm ⁻¹ / (km mol ⁻¹)]	n.o.	n.o.	209 (0) ^[47]	189(¹¹ B) ^[254]	187 (0) ^[47]
$\tilde{\nu}_4$ (e') [cm ⁻¹ / (km mol ⁻¹)]	n.o.	n.o.	116 (0) ^[47]	101(¹¹ B) ^[254]	99 (0) ^[47]

The high energy of the C-I stretching vibrations (739 cm^{-1} for ClI_3^+ , compared to 693 cm^{-1} for BI_3 ^[254]) is at the first glance in contradiction to what would be expected from the atom weights (^{12}C vs. ^{11}B) and indicates a strong C-I bond. Another experimental proof for the strengths of this bond is found in the geometries of the two species: The C-I distance is about 11 pm (5.5%) shorter than the B-I distance in BI_3 . From the MO diagram (Figure 50) it may be deduced that in ClI_3^+ – like in the other heavier halocarbenium ions – the positive charge is delocalized over the three iodine atoms, which act as σ and π donors. So from these experimental data, it becomes evident that a carbenium-like resonance structure **I** of ClI_3^+ (shown on the left in Figure 53) with the positive charge remaining on the carbon is not important and that only the three resonance structures **II** to **IV** with $\text{C}=\text{I}^+$ double bonds describe the bonding in this cation.

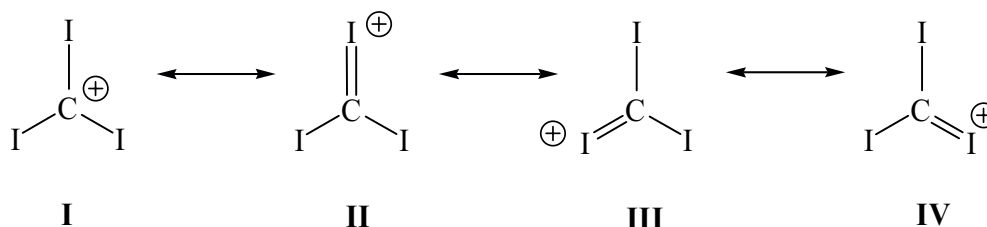


Figure 53: Possible mesomeric formula of the ClI_3^+ cation. The structure **I** doesn't describe the real distribution of the positive charge and therefore can be neglected.

The positive partial charge residing on the halogen atoms is also the reason why, in contrast to the isoelectronic BX_3 molecules, the Lewis acidities of the CX_3^+ cations decrease from F to I: The heavier the halogen is, the better the positive charge can be delocalized due to the higher σ and π donor ability of Br and I. In the haloboranes this positive charge is missing, and therefore, π bonding is not important in BX_3 . This can also be seen from the energetics of the bonding π MO (HOMO-5, a_2'' symmetry in Figure 50) of the p orbitals of the halogens with the central atom. The energy difference between this π -MO and the LUMO is always larger in CX_3^+ than in BX_3 ($\Delta\Delta E = 1.04 - 1.68\text{ eV}$), indicating an energetic favoring of this orbital in the carbenium ions and therefore more important π bonding contributions. Overall one may conclude that the heavier CX_3^+ cations with more important π bonds are less willing to accept an incoming Lewis base, since upon formation of an adduct they have to give up the delocalized π -bond. For the boranes this seems to be reversed and thus the Lewis acidities are also reversed.

The reversed trends of the Lewis acidities may also be explained using the energies of the LUMOs: In the series of the BX_3 molecules, the LUMO energy is – independent of the quantum chemical method – highest in BF_3 ^[255], while in the CX_3^+ cations, the LUMO energy increases from CF_3^+ to Cl_3^+ (see Figure 54).

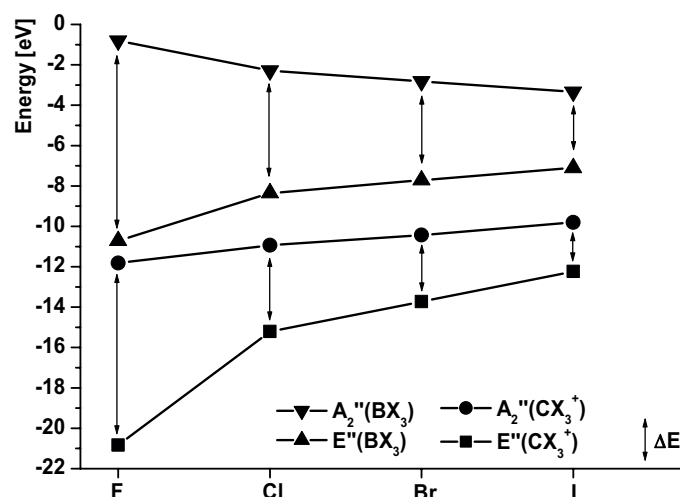


Figure 54: Energies of the orbitals of CX_3^+ and BX_3 contributing to the first UV-Vis absorption (BP86/SV(P)). A_2'' = LUMO, E'' = HOMO -1.

According to the frontier orbital model of chemical reactivity^[256], a lower LUMO energy indicates stronger covalent interactions with an occupied orbital of a donor species (= Lewis base) and therefore a higher Lewis acidity. Thus, among the boranes, BI_3 with the lowest lying LUMO is a more potent Lewis acid than BF_3 , which has the LUMO highest in energy, while this trend is reversed for the isoelectronic CX_3^+ cations.

Why are the Bulk Phase and the Solutions of the Cl_3^+ Salts 15 and 16 Red-Brown?

While the single crystals of **15** and **16** are orange-yellow, the colors of the bulk phase of the Cl_3^+ salts as well as their solutions in CH_2Cl_2 are red-brown. This is assigned to small impurities of I_2 which are – even when the reaction is carried out with the total exclusion of light – probably caused by a partial decomposition of very light sensitive Cl_4 . These small amounts of I_2 may then form a weak adduct $\text{Cl}_3 \cdots \text{I}_2^+$. According to quantum chemical calculations, this complex formation is exergonic by 10 kJ/mol in the gas phase (MP2/TZVPP). The simulation of the UV-Vis spectrum of this complex by TD-DFT shows absorption maxima up to 611 nm and may be of the reason for the very intense red-brown color.

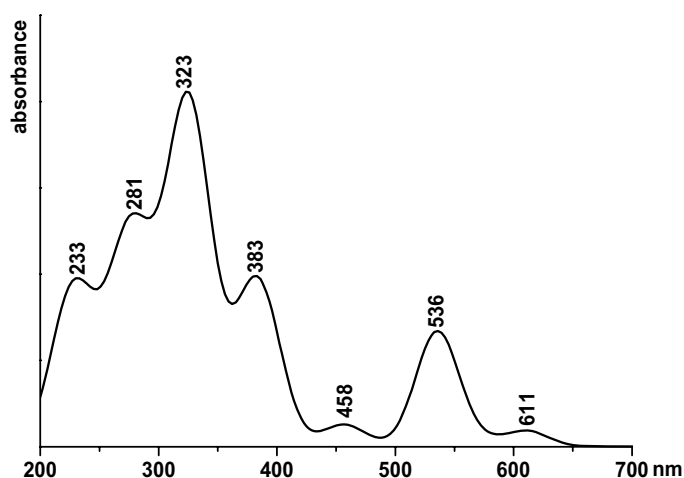


Figure 55: Simulated UV-Vis spectrum of the $[\text{Cl}_3 \cdots \text{I}_2]^+$ adduct (TD-DFT at the (RI)BP86/SV(P) level).

The minimum geometry (at the MP2/TZVPP level) of that complex is shown in Figure 56. This C_s symmetric structure is obtained even when the optimizations were run from very different starting geometries. In this adduct, the C-I bond lengths and the I-C-I bond angles do not change significantly. This indicates – like the structure of the water adduct of the Cl_3^+ cation^[257] – that the π bonding in Cl_3^+ is very strong and remains undisturbed upon complexation with I_2 .

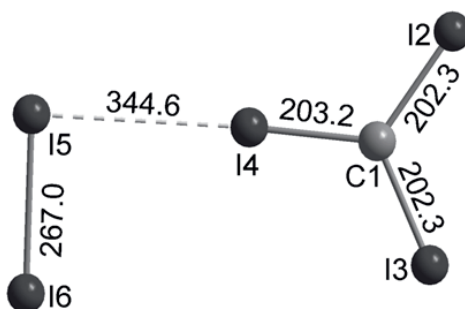


Figure 56: Calculated geometry of the $[\text{Cl}_3 \cdots \text{I}_2]^+$ adduct (MP2/TZVPP). Distances are given in pm. $\angle(\text{I-C-I}) = 119.6 - 120.3^\circ$ (Σ : 360.0°).

7.1.7 Properties of $\text{CH}_n\text{X}_{3-n}^+$ ($\text{X} = \text{F-I}$; $n = 0, 1, 2$)

In this subsection, an overview of calculated and experimentally known properties of all halocarbenium cations of the types CX_3^+ and $\text{CH}_n\text{X}_{3-n}$ ($\text{X} = \text{F-I}$; $n = 1, 2$) is given (Table 65). Except $\text{CCl}_3^{+[58]}$, $\text{CBr}_3^{+[58]}$ and $\text{Cl}_3^{+[47]}$, all these cations have only been observed in the gas

phase (mass spectrometer) and some of them have been characterized in matrix experiments, where they have been generated *in situ*, e.g. as photolysis products of CHCl_3 or CH_2F_2 [258-260]. Their heats of formation H_f° are also included in this table.^[v] The values collected in the table may aid experimental identification of these elusive species.

From the values collected in Table 65 it can be seen that for the heavier $\text{CH}_n\text{X}_{3-n}^+$ cations, the C-X bond lengths shrink with decreasing halogen content (e.g. 204.0 pm in Cl_3^+ , 200.0 pm in CHI_2^+ and 195.6 pm in CH_2I^+). This indicates higher partial double bond character for the cations with lower halogen content. By contrast, in the fluorine containing species, the C-F distance remains unchanged. This observation is in good agreement with little impact of π bonding to the C-F bond. Overall, the conclusions drawn from the CX_3^+ cations hold: the heavier the halogen is, the more π bonding and charge delocalization is favored. In CHX_2^+ and CH_2X^+ , the total positive charge of the cation has to be transferred to only two resp. one halogen atom, what gives a formal bond order of 1.5 for CHX_2^+ and even 2.0 for CH_2X^+ , resulting in considerably shorter C-X bonds. The stronger C-X bonds can also be observed in the (calculated) IR spectra: for the heavier halogens, the C-X stretches considerably shift to higher energy when more hydrogen atoms are present, while for the fluorine containing cations, the C-F frequency is even a bit lowered.

^[v] The $\Delta_f H^\circ$ values of all $\text{EX}_n\text{H}_{3-n}^{0/+}$ (E = B, C; X = F-I; n = 0-2) have been established based on high-level quantum chemical calculations (isodesmic reactions at the CCSD(T)/aug-cc-pVTZ level) cross-checked with very accurate experimental values (see chapter 7.2).

Table 37: Characteristics of CX_3^+ and $CH_nX_{3-n}^+$ ($X = F-I$; $n = 1, 2$).

known exp. ^(a)	$d(E-X)$ [pm]		$\delta^{13}C$ [ppm]		ν (IR) [cm^{-1}]		λ_{max} [nm] ^(e)		$\Delta_f H^\circ$ [kJ/mol]	
	exp.	calc. ^(b)	exp.	calc.	exp. ^(d)	calc. ^(f)	exp.	calc. ^(h)	exp.	establ. ^(k)
CF_3^+	g	–	123.4	–	798, 1622, 1662	573(11), 766(56), 1019(0), 1640(424)	–	115	449 ^{[261](i)}	416
CCl_3^+	g, sol, s	162.1 ^[58]	165.1	237.1 ^[58]	226.6 ^[235]	1037 ^[238]	–	230	862 ^{[261, 262] (i)}	850
CBr_3^+	g, sol, s	180.7 ^[58]	181.6	209.7 ^[58]	212.2 ^[235]	874	–	151(sh), 220, 295	1004 ^[261, 263]	992
CI_3^+	g, sol, s	201.3 (in 15) 200.6 (in 16)	204.0	97.0	123.8	329, 739	274, 307, 349	121, 148(sh), 202, 230, 308, 383	approx. 1047 ⁽ⁱ⁾	1116
CHF_2^+	g	–	123.3	–	1608 ^[260]	652(31), 1027(0), 1270(53), 1624(326), 3088(32)	–	118(sh), 178	599 ^{[261](i)}	602
$CHCl_2^+$	g	–	162.8	–	845, 860, 1044, 1291, 3033 ^[258, 259, 264-267]	350(2), 826(20), 851(19), 1044(253), 1282(36), 3074(37)	250 ^{[259](d)}	151(sh), 226	884 ^{[261](i)}	888
$CHBr_2^+$	g	–	178.5	–	897, 1229 ^[260, 264, 268]	213(0), 658(8), 778(34), 900(224), 1225(30), 3084(43)	–	145(sh), 190, 274	976 ^{[261, 263] (i)}	984
CHI_2^+	g	–	200.0	–	229.8 ^(c)	43(0), 526(2), 686(45), 776(197), 1198(38), 3088(41)	–	130, 181, 262, 349	1087 ^{[269](i)}	1059
CH_2F^+	g	–	123.4	–	1530 \pm 30 ^{(e)[267]}	1210(15), 1224(4), 1402(102), 1575(68), 2986(6), 3145(48)	–	–	838 ^{[261](i)}	824
CH_2Cl^+	g	–	159.7	–	1040 \pm 30 ^[266, 267]	1015(0), 1027(81), 1087(28), 1418(0), 3011(22), 3147(60)	–	172	955 ^{[261](i)}	956
CH_2Br^+	g	–	174.9	–	860 \pm 30 ^[266, 267]	854(62), 946(2), 1032(39), 1390(0), 3023(31), 3160(63)	–	199	988 ^[261, 263]	1004
CH_2I^+	g	–	195.6	–	287.1 ^(c)	726(42), 860(5), 962(47), 1359(0), 3034(39), 3173(59)	–	241	1029 ^[261, 270]	1030

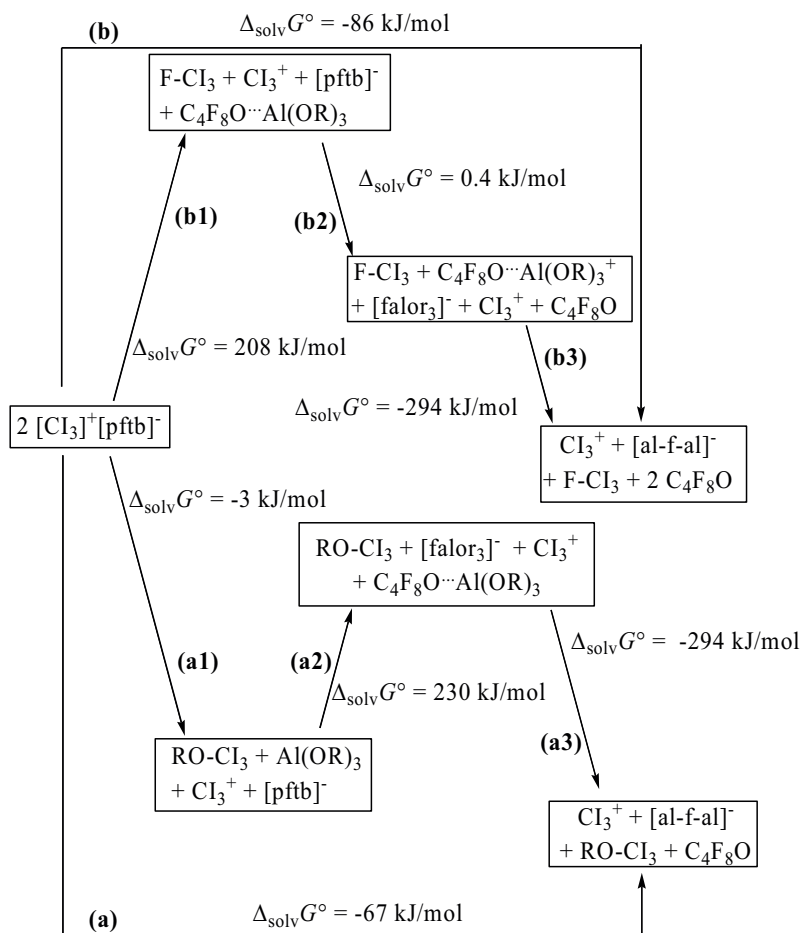
^(a) g = gas phase, sol = solution, s = solid state. ^(b) optimized at the ccscd(t)/aug-cc-pVTZ level. ^(c) δ^1H_{calc} [ppm] = 19.80 (CHI_2^+), 21.08 (CH_2I^+). ^(d) measured in the matrix. ^(e) CD_2F^+ ^(f) calculated at the (R)BP86/SV(P) level. Values in parenthesis: IR intensities in $km\ mol^{-1}$. ^(g) only excitations from 100 – 800 nm have been considered. ^(h) TD-DFT at the (R)BP86/SV(P) level. ⁽ⁱ⁾ H_f° (cation) = from AP and H_f° (fragments). ^(j) H_f° (cation) = H_f° (neutral radical) + I E(neutral radical). ^(k) values established through isodesmic reactions. ^[271] ^(l) J. L.M. Abboud, personal communication. The value of 531 kJ/mol given in Ref. 225 is wrong.

7.1.8 Stability of [pftb]⁻ and [al-f-al]⁻ Anions against Electrophilic Attack of CX₃⁺ (X = F-I) and CH_nX_{3-n}⁺ (n = 1, 2) Cations

Since it is possible to synthesize Cl₃⁺ salts using [pftb]⁻ and [al-f-al]⁻ as counterions, the question arises, if also the other halomethyl cations CX₃⁺ (X = F-I) and CH_nX_{3-n}⁺ (n = 1, 2) can be stabilized using these WCAs.

Although both the [pftb]⁻ and the [al-f-al]⁻ anions are very robust, they are also decomposed in the presence of very strong electrophilic cations. Generally two different possibilities of decomposition exist, depending on the nature of the electrophilic species: the anions can be attacked at their oxygen atoms (which are the most basic sites of the anions) or at one of their peripheral fluorine atoms. For the [pftb]⁻ anion these two pathways are shown in Scheme 8. A table where the ΔG° values for reaction (a) and (b) for all CX₃⁺ and CH_nX_{3-n}⁺ cations is given in the appendix 12.5.

Calculations of ΔG° both in the gas phase and in solution suggest that the [pftb]⁻ anion is thermodynamically unstable against all CX₃⁺ and CH_nX_{3-n}⁺ cations. For CF₃⁺, H CX₂⁺ and H₂CX⁺, the [pftb]⁻ anion is cleaved by OR abstraction (in the case of H CBr₂⁺ and H Cl₂⁺, both reaction enthalpies are similar), while for CCl₃⁺ – Cl₃⁺, the decomposition reactions are predicted to proceed through the F⁻ abstraction pathway due to steric reasons. But as the first step for that reaction (b1) is endergonic for these CX₃⁺ cations (X = Cl-I) in CH₂Cl₂, their salts should be stable in solution. In Scheme 8, as one example, the detailed ΔG° values for the different decomposition steps are listed.



Scheme 8: Decomposition pathways of the $[\text{pftb}]^-$ anion by Cl_3^+ : F^- vs. OR^- abstraction ($\text{R} = \text{C}(\text{CF}_3)_3$). Calculations at the BP86/SV(P) level. Analogous decomposition pathways can be obtained for the other CX_3^+ and $\text{CH}_n\text{X}_{3-n}^+$ cations.

7.2 Enthalpies of Formation $\Delta_f H^\circ$ and Mean Bond Enthalpies ($mBEs$) of $\text{H}_{4-n}\text{EX}_n^{-/0}$ and $\text{H}_{3-n}\text{EX}_n^{0/+}$ ($\text{E} = \text{C}, \text{B}$; $\text{X} = \text{F-I}$; $n = 1-3$) - A Computational Study

From the data presented in section 7.1 as well as from other studies^[47, 222, 272], it becomes clear that the bonding in halocarbenium ions and the isoelectronic haloboranes differs considerably: In the halomethyl cations, the positive charge is delocalized over the halogen atoms, leading to partial π bonding contributions. However, the amount of π bonding present in haloboranes is under debate. In order to find out more about the bonding in these species, an important input would be systematically derived mean Bond Enthalpies ($mBEs$) of the E-X bonds ($\text{E} = \text{B}, \text{C}$) in compounds that formally have and have not the possibility to π backbond. A direct

access to the *mBEs* is the use of the heats of formations $\Delta_f H^\circ$ of the species in question. Therefore, one sub-project within this thesis was the establishment of accurate $\Delta_f H^\circ$ values and mean E-X bond energies (*mBE*) of the species collected in Figure 57.

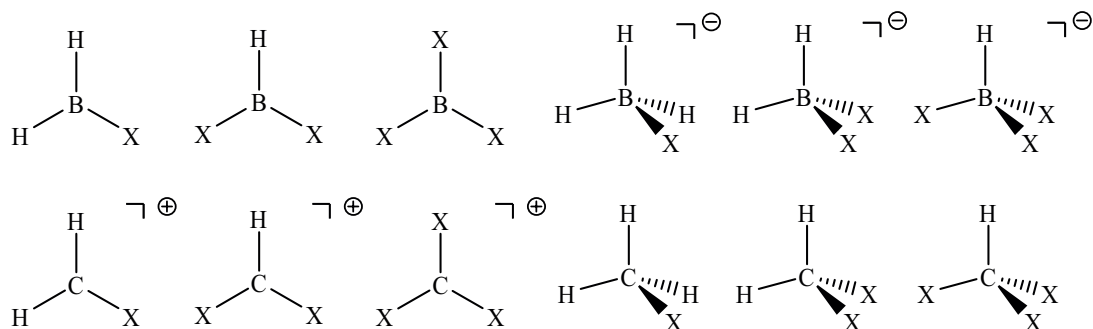


Figure 57: Overview of the species investigated in this study (X = F-I).

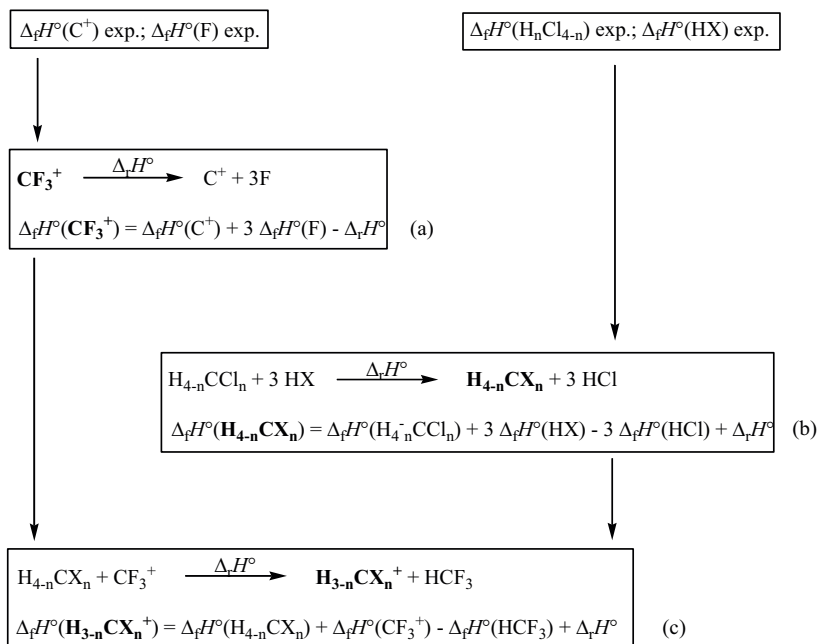
However, only for the minority of compounds shown in Figure 57 - as well as the further small particles needed to assign *mBEs* - reliable experimental $\Delta_f H^\circ$ values are known. Especially for some small and reactive species formed upon the E-X bond cleavage reactions, but also for some of the halocalocarbenium ions or halomethanes (e.g. CF_3^+ , H_2CBr_2 , HCX_3 with X = Br, I), no accurate data are available. The same holds for the haloboranes and the haloborate anions. For the bromine- and iodine-containing halomethanes, calculated $\Delta_f H^\circ$ values (at the QCISD(T)/6-311+G(3df,2p) level have been published two years ago^[273]. It has been decided to also re-determine these values to have a cross-check for our method and because the same methodology should be used for all particles as only this approach allows for maximum error cancellation and internal consistency.

7.2.1 Methodology and Results

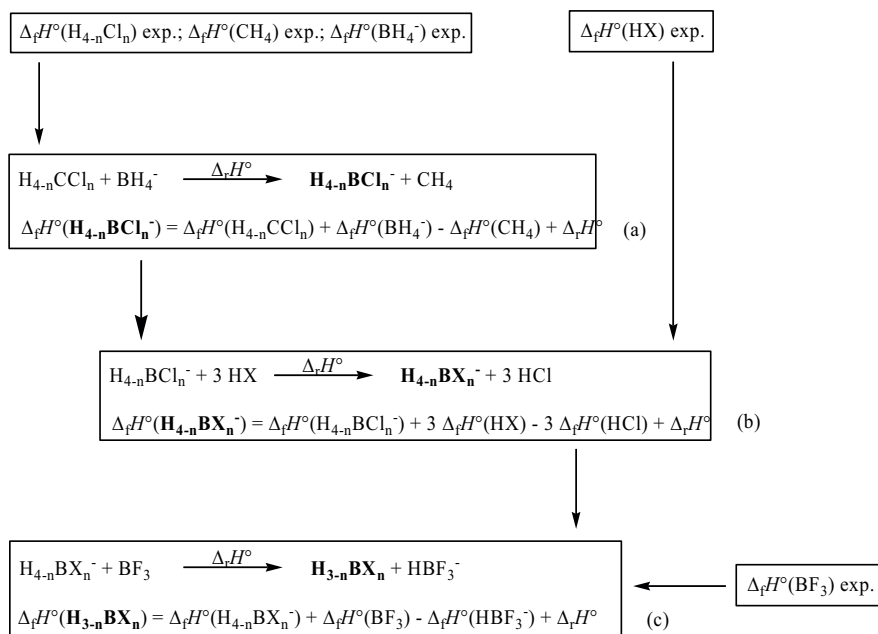
7.2.1.1 Overview and Strategy

Flow-charts to establish the desired $\Delta_f H^\circ$ values are delineated in Scheme 9 and Scheme 10. Based on these equations, the $\Delta_f H^\circ$ values were assessed with either G3 and/or coupled-cluster methods up to the complete basis set extrapolation (ccsd(t)/CBS) (in the case of CF_3^+), or in isodesmic reactions using either G3 (for F and Cl containing species) or ccsd(t)/aug-cc-pVTZ (for Br and I containing species). As a control, also MP2/TZVPP was used for the isodesmic reactions. ZPEs and thermal contributions to the enthalpies were included at the unscaled (RI)BP86/SV(P) level, which usually gives scaling factors close to unity.

Experimental data were taken from the NIST database and are referenced with their original publications. All $\Delta_f H^\circ$ values given in this study are gas phase values at 298.15 K.

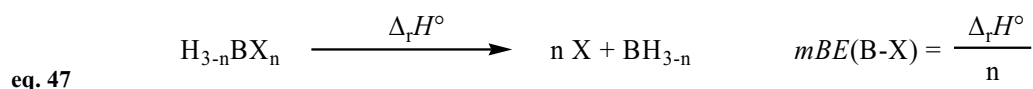
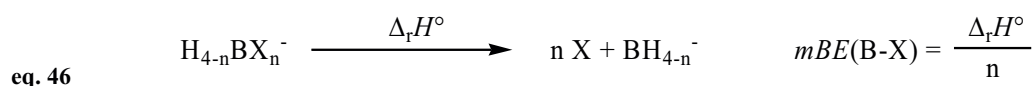
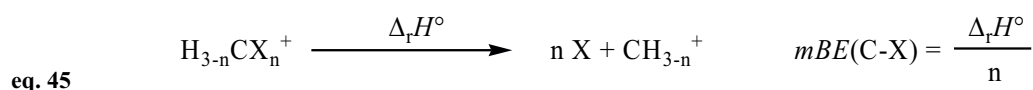
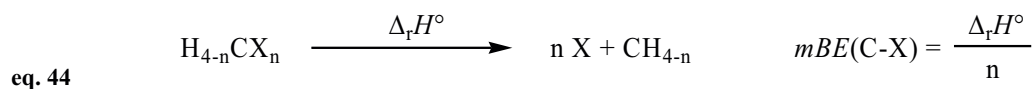


Scheme 9: Strategy to obtain $\Delta_f H^\circ$ of halomethanes and halomethyl cations.



Scheme 10: Strategy to obtain $\Delta_f H^\circ$ of haloboranes and haloborate anions.

Once the $\Delta_f H^\circ$ values are established properly, they are used to calculate the mean E-X (E = B, C) bond energies mBE in these species through the following homolytic bond cleavage reactions (eq. 44 to eq. 47):



For all equations n ranges from 1 to 3. Thus, the $\Delta_f H^\circ$ values of the small particles X, CH_{4-n} , CH_{3-n}^+ , BH_{4-n}^- and BH_{3-n} are needed. They were either taken from very reliable experimental data or calculated using the G3 method.

7.2.1.2 Choice of the Quantum Chemical Method

Before starting the calculations of $\Delta_f H^\circ$ values, one has to choose the most appropriate quantum chemical method for each system, and also the “best” reaction equation. In the ideal case, these reactions are isodesmic, which means that the number and the type of bonds both of starting materials and products are equal, so that error cancellation is maximal. In cases where no isodesmic reaction was possible, highly accurate methods have to be used.

To find out which method and basis set is the best compromise between accuracy and computing time, the electronically demanding homolytic cleavage of the F_2 molecule and the dissociation of the CF_3^+ cation in C^+ and three F atoms have been chosen as test reactions for the method and basis set dependence. In Table 38, the enthalpies for these two reactions obtained with different methods and basis sets are collected.

Table 38: Basis-set dependence of the homolytic dissociation energies ΔH° of the F_2 molecule (according to Scheme 9(a)) and the CF_3^+ cation at the ccscd(t) level and comparison with the G3 and the experimental values. All energies are given in kJ/mol.

Reaction	ccscd(t) / aug-cc-pVDZ	ccscd(t) / aug-cc-pVTZ	ccscd(t)/ aug-cc-pVQZ	ccscd(t) / CBS ^[274]	G3	exp. value
$F_2 \rightarrow 2 F^\bullet$	111	143	151	152	155	159 ^[261]
						365 ^[261] (a);
$CF_3^+ \rightarrow C^+ + 3 F^\bullet$	537	440	422	419	412	449 ^[261] (b);
						359 ^[261, 275] (c)

(a) from AP and $\Delta_f H(CF_4)$. (b) from $\Delta_f H(HCF_3)$ and $\Delta_f H(H)$. (c) from $\Delta_f H(CF_3)$ and $IE(CF_3)$.

For both reactions, the ccscd(t)/aug-cc-pVDZ value lies far away from the data obtained by larger basis sets or by the G3 method. The average value from ccscd(t)/CBS and G3 (153 kJ/mol) differs only by 6 kJ/mol from the experimental value (159 kJ/mol^[261]), indicating that the quantum chemical methods used in this study are even suitable to describe such electronically delicate and problematic reactions.

For CF_3^+ , the available experimental data range from 359 to 449 kJ/mol, depending on the method used to determine the $\Delta_f H^{[261, 275]}$. This underlines the difficulties coming along with the experimental measurements. The value obtained by the G3 and CBS extrapolation calculations lies in between the experimentally measured data and can therefore be considered to be reasonable and reliable.

Since it appeared that G3 is slightly better than ccscd(t)/CBS, all quantities derived for species that do not contain Br or I were calculated using the G3 method. For species containing heavier atoms, G3 is not applicable and therefore, the ccscd(t) level of theory in combination with an isodesmic reaction for error cancellation was chosen. Therefore all Br and I containing particles have been optimized with the ccscd(t)/aug-cc-pVTZ method.

7.2.1.3 Anchor Points

$\Delta_f H^\circ$ of $H_{4-n}CX_n$ and $H_{3-n}CX_n^+$ ($n = 1-3$):

For the calculations of $\Delta_f H^\circ$ of $H_{4-n}CX_{4-n}$ and $H_{3-n}CX_n^+$ ($n = 1-3$), $HCCl_3$, H_2CCl_2 , H_3CCl and HX ($X = F-I$) (Table 39) were taken as fix points, as their $\Delta_f H^\circ$ values are measured very well on experimental grounds. $\Delta_f H^\circ$ of the CF_3^+ cation has been established by the equation in

Scheme 9(a). As this reaction is not isodesmic, for $\Delta_f H^\circ$ the most accurate calculations possible have to be used, in this case the average values of G3 and ccscd(t)/CBS-Extrapolation (Table 38), which led to $\Delta_f H^\circ(\text{CF}_3^+) = 415.5 \text{ kJ/mol}$.

Table 39: $\Delta_f H^\circ$ of $\text{H}_{4-n}\text{CCl}_n$ ($n = 1-3$), HX ($X = \text{F-I}$) and CF_3^+ . All values are given in kJ/mol.

particle	$\Delta_f H^\circ$	method
HCCl_3	-103	exp. ^[261]
H_2CCl_2	-96	exp. ^[261]
H_3CCl	-84	exp. ^[261]
HF	-273	exp. ^[261]
HCl	-92	exp. ^[261]
HBr	-36	exp. ^[261]
HI	26	exp. ^[261]
CF_3^+	416	calc. (Table 38) ^(a)

^(a) [G3 + ccscd(t)/CBS-Extrapolation] / 2

$\Delta_f H^\circ$ of $\text{H}_{4-n}\text{BX}_n^-$ and $\text{H}_{3-n}\text{BX}_n$ ($n = 1-3$):

The $\Delta_f H^\circ$ values of $\text{H}_{4-n}\text{BX}_n^-$ ($n = 1-3$) could – in principle – be obtained analogously to those of the isoelectronic carbon compounds, but as there are no reliable experimental data available, which could serve as fix points, the values for $\text{H}_{4-n}\text{BCl}_n^-$ have to be established first by the set of isodesmic reactions shown in Scheme 10(a), using the experimental $\Delta_f H^\circ$ values of CH_4 , BH_4^- and $\text{H}_{4-n}\text{CCl}_{4-n}$ ($n = 1-3$) together with the $\Delta_f H^\circ$ at the G3 level. The values obtained by these reactions are listed in Table 40, together with that of BF_3 , which is used as reference point for the calculations of the neutral boron species.

Table 40: $\Delta_f H^\circ$ of $H_{4-n}BCl_n^-$ ($n = 1-3$), BH_4^- and BF_3 . All values are given in kJ/mol.

Particle	$\Delta_f H^\circ$	method
H_3BCl^-	-289	$H_3CCl + BH_4^- \rightarrow H_3BCl^- + CH_4$ (Scheme 10a)
$H_2BCl_2^-$	-490	$H_2CCl_2 + BH_4^- \rightarrow H_2BCl_2^- + CH_4$ (Scheme 10a)
$HBCl_3^-$	-676	$HCCl_3 + BH_4^- \rightarrow HBCl_3^- + CH_4$ (Scheme 10a)
BF_3	-1136	exp. ^[261]

With these values, $\Delta_f H^\circ$ of $H_{4-n}BX_n^-$ and $H_{3-n}B_n$ can then be calculated in an analogous way to those of the carbon compounds, like described in Scheme 10 (b) and (c).

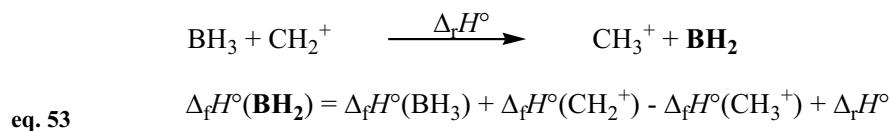
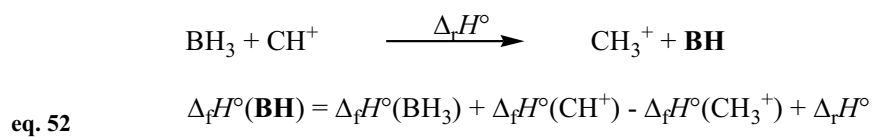
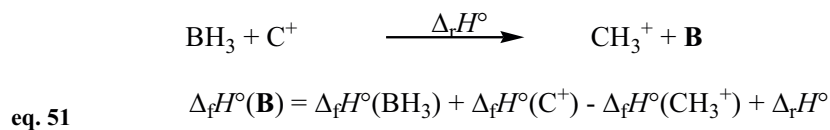
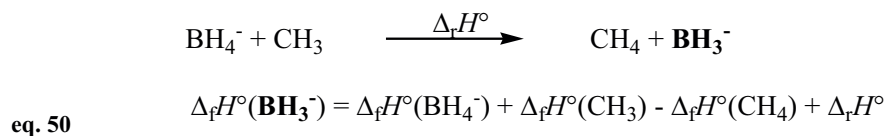
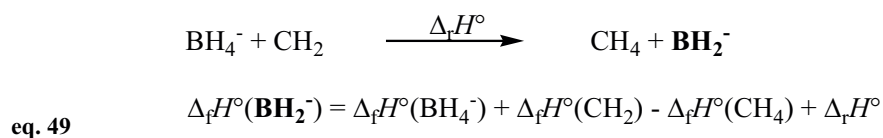
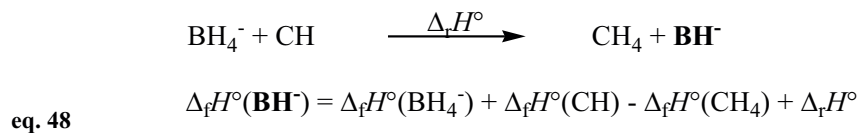
$\Delta_f H^\circ$ of small particles:

The heats of formation $\Delta_f H^\circ$ of small, neutral carbon-containing species like C, CH, CH₂, CH₃ as well as of the halogens have been determined experimentally in very high accuracy^[261] and therefore, these values can be used as anchor points for this study. Also their ionization energies are available^[276, 277], which gives an access to the $\Delta_f H^\circ$ of their cations C⁺, CH⁺, CH₂⁺ and CH₃⁺. These values are listed in Table 41.

Table 41: Experimental $\Delta_f H^\circ$ of CH_n, CH_n⁺, ($n = 0-3$), X and X⁺ (X = F-I) and calculated values for $\Delta_f H^\circ$ of BH_n⁻ ($n = 1-4$), BH_n ($n = 0-3$) (G3 method). All values are given in kJ/mol. Values used in this study are marked in bold.

particle	$\Delta_f H^\circ$			particle	$\Delta_f H^\circ$		
	G3	exp.	method		G3	exp.	method
C	-	717 ^[261]	direct	C ⁺	-	1803 ^[261, 277]	$\Delta_f H(C) + IE(C)$
CH (doublet)	-	549 ^[261]	direct	CH ⁺ (singlet)	-	1621 ^[261, 276]	$\Delta_f H(CH) + IE(CH)$
CH ₂ (triplet)	-	368 ^[261]	direct	CH ₂ ⁺	-	1372 ^[261, 277]	$\Delta_f H(CH_2) + IE(CH_2)$
CH ₃	-	146 ^[261]	direct	CH ₃ ⁺	-	1095 ^[261, 278]	$\Delta_f H(CH_3) + IE(CH_3)$
BH ₄ ⁻	-	-77 ^[279]	direct	B	579	560	direct
BH (singlet)	446	443 ^[261]	direct	BH ⁻ (doublet)	419	414 ^[261, 280]	$\Delta_f H(BH) + EA(BH)$
BH ₂	310	201 ^[261]	direct	BH ₂ ⁻ (singlet)	262	-	-
BH ₃	-	107 ^[261]	direct	BH ₃ ⁻	86	84 ^[281]	$\Delta_f H(BH_3) + EA(BH_3)$
F	-	79 ^[261]	direct	Br	-	112 ^[261]	direct
Cl	-	121 ^[261]	direct	I	-	107 ^[261]	direct

For the analogous boron compounds BH^- , BH_2^- , BH_3^- , B , BH and BH_2 , the experimental data are not very reliable, so that it seemed more accurate to calculate them using the following isodesmic equations at the G3 level and the experimental $\Delta_f H^\circ$ values of BH_4^- (-77 kJ/mol^[279]) and the carbon-containing species:



All values for $\Delta_f H^\circ$ of the small particles obtained from these reactions are also collected in Table 41.

7.2.1.4 $\Delta_f H^\circ$ of $H_{4-n}EX_n^{0/-}$ and $H_{3-n}EX_n^{+/0}$ (E = C, B; X = F-I)

As already described above in Scheme 9 and Scheme 10, the $\Delta_f H^\circ$ values of $H_{4-n}EX_n^{0/-}$ and $H_{3-n}EX_n^{+/0}$ (E = C, B; X = F-I) can be established through a set of isodesmic reactions. In the following tables (Table 42 to Table 45), the reaction enthalpies obtained by different methods are collected. As it can be seen, for the most part of the reactions the MP2/TZVPP values are in the same order of magnitude (max. deviation: 27 kJ/mol) than those from ccscd(t) or G3 calculations. However, the latter two methods are more accurate and will therefore be used in the discussion. G3 will be used as a reference for compounds containing F and Cl. For Br and I containing species, the G3 method cannot be used, and therefore, ccscd(t)/aug-cc-pVTZ values are used as reference values.

Table 42: Calculated enthalpies ($\Delta_r H^\circ$ in kJ/mol) according to Scheme 9(b). The best values are marked in bold.

	MP2/ TZVPP	ccsd(t) ^(a)	G3
$\text{H}_3\text{CCl} + \text{HX} \rightarrow \text{H}_3\text{CX} + \text{HCl}$			
F	30	20	26
Cl	0	0	0
Br	-11	-11	-
I	-26	-23	-
$\text{H}_2\text{CCl}_2 + 2 \text{HX} \rightarrow \text{H}_2\text{CX}_2 + 2 \text{HCl}$			
F	9	-8	4
Cl	0	0	0
Br	-17	-18	-
I	-46	-36	-
$\text{HCCl}_3 + 3 \text{HX} \rightarrow \text{HCX}_3 + 3 \text{HCl}$			
F	-47	-66	-51
Cl	0	0	0
Br	-22	-23	-
I	-65	-46	-

^(a) aug-cc-pVTZ for Br and I, 6-311+G(2df) for F and Cl.**Table 43:** Calculated enthalpies ($\Delta_r H^\circ$ in kJ/mol) according to Scheme 9(c). The best values are marked in bold.

	MP2/ TZVPP	ccsd(t) ^(a)	G3
$\text{H}_3\text{CX} + \text{CF}_3^+ \rightarrow \text{HCF}_3 + \text{H}_2\text{CX}^+$			
F	-21	-34	-28
Cl	-52	-34	-70
Br	-58	-83	-
I	-83	-108	-
$\text{H}_2\text{CX}_2 + \text{CF}_3^+ \rightarrow \text{HCF}_3 + \text{HCX}_2^+$			
F	-55	-59	-56
Cl	-112	-124	-127
Br	-123	-140	-
I	-159	-173	-
$\text{HCX}_3 + \text{CF}_3^+ \rightarrow \text{HCF}_3 + \text{CX}_3^+$			
F	0	0	0
Cl	-144	-150	-157
Br	-165	-175	-
I	-211	-217	-

^(a) aug-cc-pVTZ for Br and I, 6-311+G(2df) for F and Cl.

Table 44: Calculated enthalpies ($\Delta_r H^\circ$ in kJ/mol) according to Scheme 10(b). The best values are marked in bold.

	MP2/ TZVPP	ccsd(t) ^(a)	G3
$\text{H}_3\text{BCl}^- + \text{HX} \rightarrow \text{H}_3\text{BX}^- + \text{HCl}$			
F	23	20	24
Cl	0	0	0
Br	-17	-13	-
I	-36	-29	-
$\text{H}_2\text{BCl}_2^- + 2 \text{HX} \rightarrow \text{H}_2\text{BX}_2^- + 2 \text{HCl}$			
F	-9	-19	-10
Cl	0	0	0
Br	-17	-12	-
I	-36	-22	-
$\text{HBCl}_3^- + 3 \text{HX} \rightarrow \text{HBX}_3 + 3 \text{HCl}$			
F	-83	-102	-85
Cl	0	0	0
Br	-8	-3	-
I	-21	2	-

^(a) aug-cc-pVTZ for Br and I, 6-311+G(2df) for F and Cl.

Table 45: Calculated enthalpies ($\Delta_r H^\circ$ in kJ/mol) according to Scheme 10(c). The best values are marked in bold.

	MP2/ TZVPP	ccsd(t) ^(a)	G3
$\text{H}_3\text{BX}^- + \text{BF}_3 \rightarrow \text{HBF}_3^- + \text{H}_2\text{BX}$			
F	-28	-31	-32
Cl	43	42	40
Br	71	61	
I	100	91	
$\text{H}_2\text{BX}_2^- + \text{BF}_3 \rightarrow \text{HBF}_3^- + \text{HBX}_2$			
F	-42	-43	-43
Cl	69	71	69
Br	109	100	
I	144	137	
$\text{HBX}_3^- + \text{BF}_3 \rightarrow \text{HBF}_3^- + \text{BX}_3$			
F	0	0	0
Cl	98	102	100
Br	137	131	-
I	168	164	-

^(a) aug-cc-pVTZ for Br and I, 6-311+G(2df) for F and Cl.

7.2.2 Discussion

7.2.2.1 Heats of Formation $\Delta_f H^\circ$:

With the reaction enthalpies collected in Table 42 to Table 45 and the auxilliary data in Table 39 to Table 41 the enthalpies of formation $\Delta_f H^\circ$ of all $H_{4-n}EX_n^{0/-}$ and $H_{3-n}EX_n^{+/0}$ (E = C, B; X = F-I) were established according to Scheme 9 and Scheme 10; the “best values” are listed in Table 46, and the trends in the different series of species are graphically represented in Figure 58 and Figure 59. Only the values obtained with the most accurate method, i.e. G3 for F and Cl, and ccscd(t)/aug-cc-pVTZ for Br and I, are collected here.

Table 46: ΔE^0 of all $H_{4-n}EX_n^{0-}$ and $H_{3-n}EX_n^{+0}$ ($E = C, B; X = F-I$). All values are given in kJ/mol. Methods: G3 for F and Cl, ccsd(t)/aug-cc-pVTZ for Br and I. anchor = experimental data has been used as an anchor point for the calculations in this study.

X =	F			Cl			Br			I		
	calc.	exp.	calc.	exp.	calc.	exp.	calc.	exp.	calc.	exp.	calc.	exp.
H_3CX	-258	-234 ^[261]	anchor	-84 ^[261]	-39	-38 ^[282] , -36 ^[283] , -38 ^[284] , -38 ^[285] , -36 ^[286] , -34 ^[287]	12	14 ^[288] , 14 ^[283] , 14 ^[285] , 14 ^[289]				
H_2CX_2	-452	-451 ^[261]	anchor	-96 ^[261]	-2 (4 ^[273]) ^(a)	-36 ^[282] , 4 ^[263] , 10 ^[283] , 3 ^[284] , - 15 ^[285] , -11 ^[286] , 6 ^[290]	106 (108 ^[273]) ^(a)	118 ^[285] , 108 ^[284] , 120 ^[289] , 122 ^[291]				
H_2CX_3	-695	-697 ^[261]	anchor	-103 ^[261]	42 (52 ^[273]) ^(a)	55 ^[290] , 51 ^[263] , 60 ^[283] , 17 ^[285] , 24 ^[286]	207 (209 ^[273]) ^(a)	251 ^[289, 292] , 211 ^[285]				
H_3BX	-446	-	-289	-	-247	-	-200	-				
H_2BX_2	-860	-	-490	-	-390	-	-274	-				
HBX_3	-1302	-	-676	-	-512	-	-319	-				
H_2CX^+	824	838 ^[261, 293] , 827 ^[261, 293]	956	955 ^[261, 294] , 951 ^[261, 293]	1004	988 ^[261, 295] , 1037 ^[282, 296]	1030	1029 ^[285, 297] , 1029 ^[288, 297]				
$H_2CX_2^+$	602	559 ^[261]	888	884 ^[261]	984	976 ^[261, 263]	1059	1087 ^[298]				
CX_3^+	416	365 ^[261] , 449 ^[261] , 359 ^[261, 275]	850	862 ^[261] , 871 ^[261, 299] , 859 ^[300]	992	1031 ^[261, 301] , 995 ^[261, 302] , 999 ^[225]	1116	~1047 ^(b)				
H_2BX	-311	-	-83	-	-2	-	75	-				
HBX_2	-737	-734 ^[261]	-255	-248 ^[261]	-107	-105 ^[261]	46	-				
BX_3	anchor	-1136 ^[261]	-410	-403 ^[261]	-197	-204 ^[261]	29	71 ^[261]				

^(a) at the QC[SD(T)/6-311+G(3df,2p)] level, from Ref. 273. ^(b) J. M. L. Abboud, personal communication. The value of 531 kJ/mol given in Ref. 225 is wrong.

In 2005, Marshall *et al.* published a high-level computational study on the $\Delta_f H^\circ$ of bromine and iodine-containing methanes^[273], based on isodesmic reactions using QCISD(T)/6-311+G(3df,2p) energy values. The results of this study are also included in Table 46. Although different anchor points were chosen, the $\Delta_f H^\circ$ obtained by Marshall *et al.* are in very good agreement with the values obtained from the calculations (max. difference: 10 kJ/mol, which is within the error bars given in the reference 273) performed within this thesis, confirming the reliability of our data. Similarly the calculations in this study are also judged to have a maximum error bar of about ± 10 kJ/mol.

Comparing the calculated data with (less accurate) available experimental values for some systems, like HCX_3 ($\text{X} = \text{Br}, \text{I}$), H_2CBr_2 , CF_3^+ and BI_3 , the experimentally found $\Delta_f H^\circ$ differ considerably from the computed ones. In those cases, where several experimental values were found in the literature, they also vary considerably (up to 90 kJ/mol for CF_3^+) and therefore can not be considered to be reliable. For H_3CF and Cl_3^+ , the experimental values are in the same order of magnitude as the computed ones, but the difference is still too large to use them as a reliable reference. For the $\text{H}_{4-n}\text{BX}_n^-$, the H_2BX ($\text{X} = \text{Cl-I}$) and HBI_2 , there are no experimental data available to the best of our knowledge (SciFinder and NIST database search). Except for the carbenium ions, the iodomethanes and the iodoboranes, all particles have a negative heat of formation (see graphical representation in Figure 58 and Figure 59).

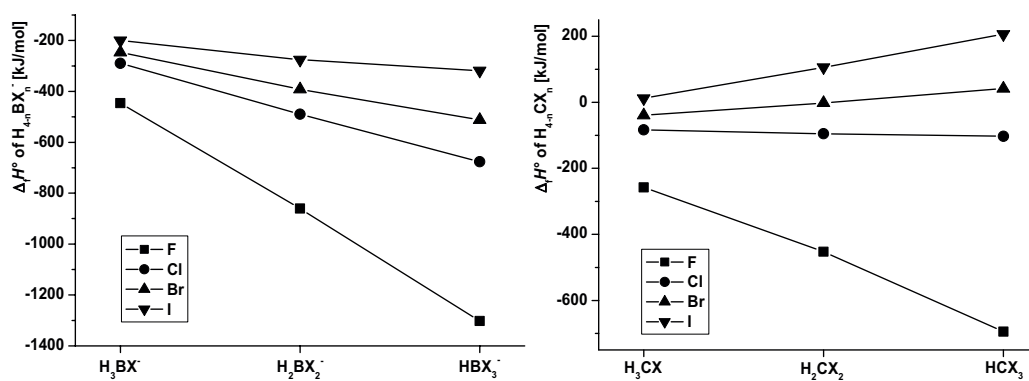


Figure 58: $\Delta_f H^\circ$ of $\text{H}_{4-n}\text{EX}_n^{-/0}$ ($n = 1-3$) in kJ/mol.

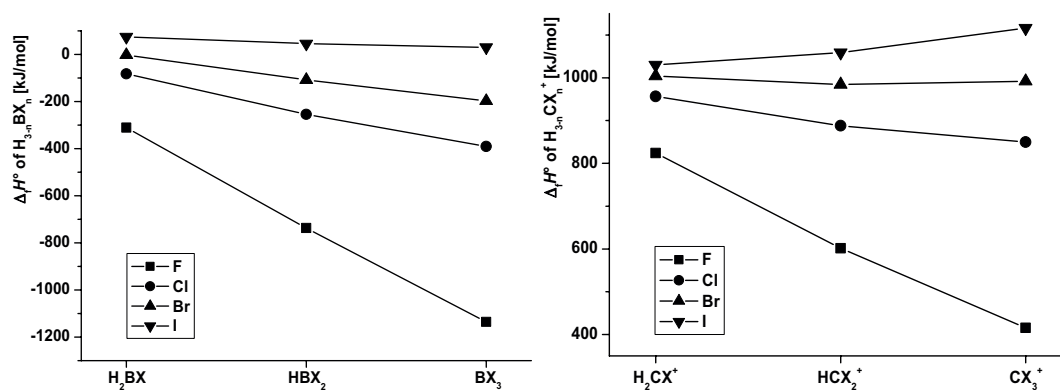


Figure 59: $\Delta_f H^\circ$ of $H_{3-n}EX_n^{+/-0}$ ($n = 1-3$) in kJ/mol.

In each of the series, the $\Delta_f H^\circ$ values increase from fluorine to iodine, and – except for the iodine-containing carbenium ions and the bromo- and iodomethanes – the $\Delta_f H^\circ$ is lower the more halogen atoms are present in the particle. The boron containing species have always a lower $\Delta_f H^\circ$ than the isoelectronic carbenium ions and methanes, and also the $H_{4-n}EX_n^{-/0}$ are lower in energy than the parent $H_{3-n}EX_n^{+/-0}$. This reflects the greater average B-X bond strengths (see *mBEs* below).

7.2.2.2 Mean E-X Bond Energies (E = B, C):

To obtain the *mBE* of the species, the values of the reaction enthalpies from eq. 44 to eq. 47 to have to be divided by the number of E-X bonds that are cleaved. The results, using the $\Delta_f H^\circ$ values listed in tables Table 41, and Table 46, are collected in Table 47 and Table 48.

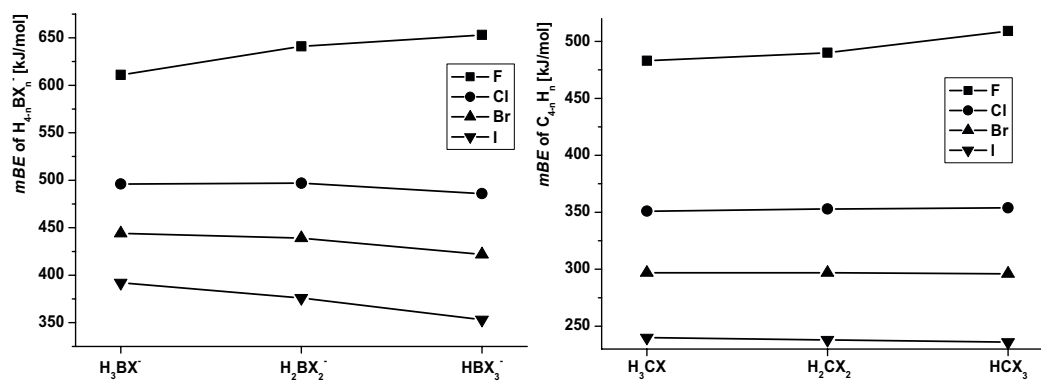
Table 47: *mBE* of $H_{4-n}CX_n$ and $H_{4-n}BX_n^-$ ($n=1-3$) in kJ/mol.

X =	H_3CX	H_2CX_2	$HCCX_3$	H_3BX^-	$H_2BX_2^-$	HBX_3^-
F	483	490	509	611	641	653
Cl	351	353	354	496	497	486
Br	297	297	296	444	439	422
I	240	238	236	392	376	353

Table 48: *mBE* of $\text{H}_{3-n}\text{CX}_n^+$ and $\text{H}_{3-n}\text{BX}_n$ ($n=1-3$) in kJ/mol

X =	H_2CX^+	HCX_2^+	CX_3^+	H_2BX	HBX_2	BX_3
F	627	589	542	700	671	651
Cl	536	488	439	514	471	444
Br	479	430	382	424	389	371
I	448	388	336	342	307	290

As it can be seen from Figure 60 and Figure 61, where the trends of the *mBE*s are represented graphically, in all species, the *mBE* decreases from fluorine to iodine, which is consistent with the electronegativities of the halogens. For all halomethyl cations and haloboranes, the *mBE*s are lowered, if a series contains more halogen atoms, while in the case of $\text{H}_{4-n}\text{EX}_n^{0/+}$, they remain nearly unchanged upon replacing H by X. The only two exceptions are the fluoromethanes and fluoroborates, where the *mBE* is increased if more fluorine atoms are present. Again, this is due to the high electronegativity of fluorine, which causes electrostatic interactions and therefore strengthens the E-F bond.

**Figure 60:** *mBE*s of $\text{H}_{4-n}\text{EX}_n^{0/+}$ ($n = 1-3$) in kJ/mol.

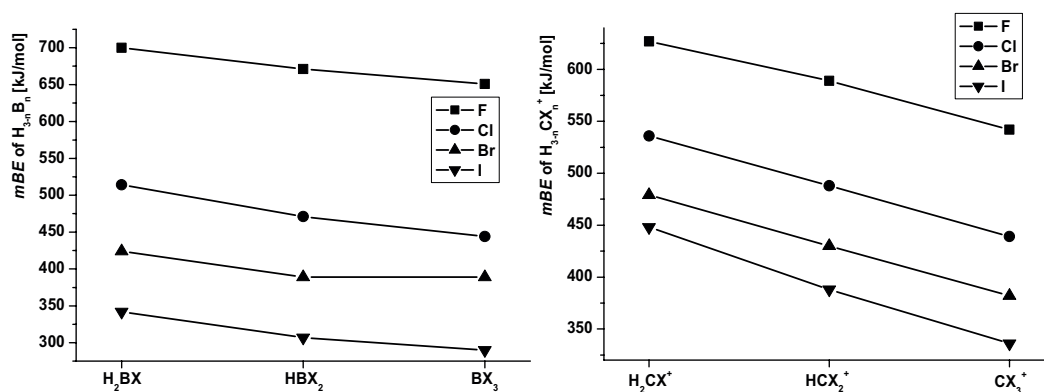


Figure 61: mBE s of $H_{3-n}EX_n^{0/+}$ ($n = 1-3$) in kJ/mol.

Especially for the haloborates, the values of the mBE s are very high. The highest mBE of the haloborates of 653 kJ/mol is found for HBX_3^- . However, by definition, eq. 44 to eq. 47 are the only way to determine mBE s for these compounds. The different bond strengths in the isoelectronic boron and carbon containing species and possible reasons for these differences will be discussed in the following section.

7.2.2.3 Relative E-X Bond Strengths in the Isoelectronic $H_{3-n}CX_n^+ / H_{3-n}BX_n$ and $H_{4-n}CX_n / H_{4-n}BX_n^-$ ($n = 1-3$) Pairs:

For the trihaloboranes and trihalocarbenium ions it is clear that the following π -MOs are formed and that the LUMO of all BX_3 as well as CX_3^+ particles corresponds to the π^* MO of a_2'' symmetry, cf. the top view of the MOs of π -symmetry in BX_3 and CX_3^+ in Figure 62:

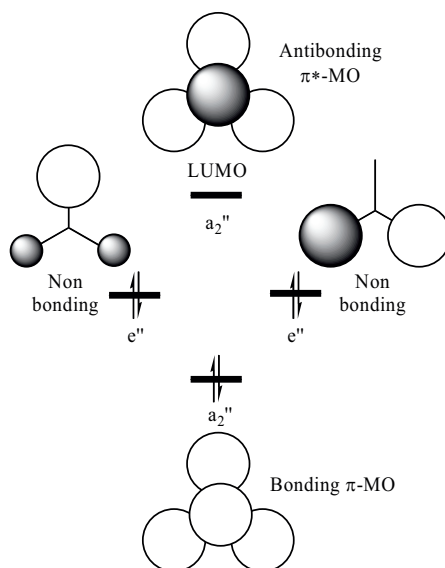


Figure 62: Top view (along the C_3 axis) of the π MOs of $EX_3^{0/+}$.

The bonding π -MO (a_2'') is occupied for all those particles. Similar MO considerations hold for the partly H-substituted particles $H_{3-n}EX_n^{0/+}$. However, no quantification of the amount of stabilization by π -bonding is possible only based on the presence of an occupied π -MO. Thus alternative quantitative approaches have to be adopted, like for example the comparison of the *mBEs* in the isoelectronic boron and carbon containing species.

In Figure 63, the different contributions, i.e. σ and π , to the E-X bonds in $EX_3^{0/+}$ and $HEX_3^{-/0}$ are sketched. For the other particles, analogous schemes can be drawn.

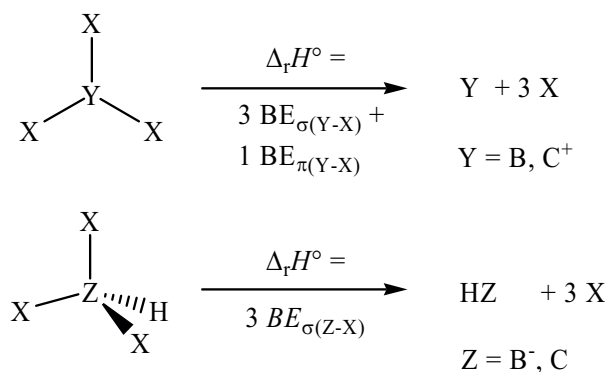
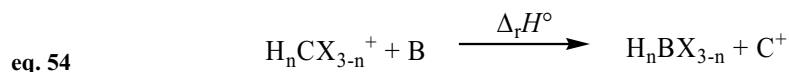


Figure 63: σ and π contributions to the E-X bonds in $EX_3^{0/+}$ and $HEX_3^{-/0}$.

Based on experimental observations as well as on quantum chemical calculations, it is postulated that in halocarbenium ions, the positive charge is delocalized over the entire cation and – especially for the heavier halogens – leads to a formation of strong π bonds (see chapters 7.1 and 7.3 as well as Refs. 47, 176, 222, and 303). However, until now, no quantitative information on the strengths of this π bonds is available. Here a comparison of the bond energies in $H_{3-n}CX_n^+$ with those of the isoelectronic $H_{3-n}BX_n$ is made based on their $\Delta_r H^\circ$. To find out if the E-X bond is stronger in the $H_{3-n}CX_n^+$ cations or in $H_{3-n}BX_n$, the C-B exchange reaction enthalpy of the following reaction has been calculated using the $\Delta_r H^\circ$ values:



In these reactions, all C-X bonds are cleaved, while the same number of B-X bonds is created. The reaction enthalpy $\Delta_r H^\circ$ (Table 49) directly corresponds to the difference of the E-X bond

energies. As a cross reference, the same has been done for the pairs $H_{4-n}CX_n$, $H_{4-n}BX_n^-$ ($n = 1-3$), where no π bonding is expected (eq. 55).

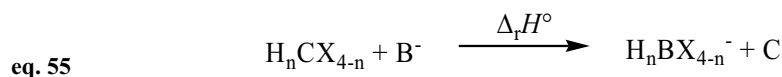


Table 49: $\Delta_r H^\circ$ values (in kJ/mol) for the reaction described in eq. 54 and eq. 55.

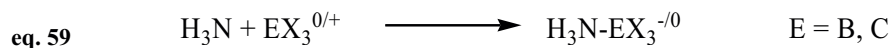
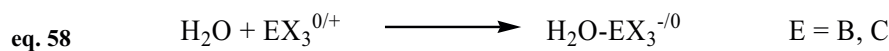
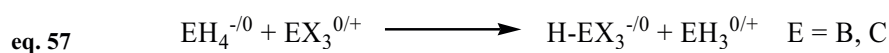
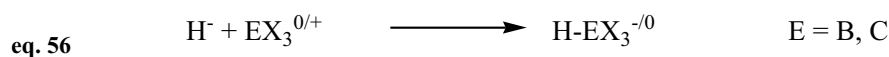
$\Delta_r H^\circ$ [kJ/mol]		$\Delta_r H^\circ$ [kJ/mol]	
$CF_3^+ + B \rightarrow BF_3 + C^+$	-327	$HCF_3 + B^- \rightarrow HBF_3^- + C$	-443
$CCl_3^+ + B \rightarrow BCl_3 + C^+$	-16	$HCCl_3 + B^- \rightarrow HBCl_3^- + C$	-408
$CBr_3^+ + B \rightarrow BBr_3 + C^+$	35	$HCBBr_3 + B^- \rightarrow HBBBr_3^- + C$	-388
$CI_3^+ + B \rightarrow BI_3 + C^+$	138	$HCI_3 + B^- \rightarrow HBI_3^- + C$	-360
$HCF_2^+ + B \rightarrow HBF_2 + C^+$	-114	$H_2CF_2 + B^- \rightarrow H_2BF_2^- + C$	-243
$HCCl_2^+ + B \rightarrow HBCl_2 + C^+$	82	$H_2CCl_2 + B^- \rightarrow H_2BCl_2^- + C$	-229
$HCBBr_2^+ + B \rightarrow HBBBr_2 + C^+$	132	$H_2CBBBr_2 + B^- \rightarrow H_2BBBr_2^- + C$	-224
$HCI_2^+ + B \rightarrow HBI_2 + C^+$	211	$H_2CI_2 + B^- \rightarrow H_2BI_2^- + C$	-259
$H_2CF^+ + B \rightarrow H_2BF + C^+$	90	$H_3CF + B^- \rightarrow H_3BF^- + C$	-23
$H_2CCl^+ + B \rightarrow H_2BCl + C^+$	185	$H_3CCl + B^- \rightarrow H_3BCl^- + C$	-41
$H_2CBr^+ + B \rightarrow H_2BBBr + C^+$	218	$H_3CBBBr + B^- \rightarrow H_3BBBr^- + C$	-43
$H_2CI^+ + B \rightarrow H_2BI + C^+$	269	$H_3CI + B^- \rightarrow H_3BI^- + C$	-47

In the case of the halocarbenium ions / haloboranes, the reaction enthalpies $\Delta_r H^\circ$ strongly increase from F to I, while for the halomethane / haloborate pairs, they remain nearly unchanged upon halogen variation. One notes the strongly increasing stability of the heavier halocarbenium ions. To our understanding, this can only be explained with stronger π bonding in the heavier halocarbenium ions with reference to the haloboranes. Thus, B-F bonds in all

$\text{H}_{3-n}\text{EF}_n^{+/0}$ particles ($\text{E} = \text{C}, \text{B}$) – that may exhibit π bonding – are always stronger than C-F bonds, but C-X bonds of $\text{H}_{3-n}\text{EX}_n^{+/0}$ ($\text{E} = \text{C}, \text{B}$; $\text{X} = \text{Cl-I}$) are always stronger than B-X bonds with the only exception of CCl_3^+ and BCl_3 which have almost identical *mBEs*. By contrast, the differences between the E-X bond strengths in the analogous saturated $\text{H}_{4-n}\text{EX}_n^{-/0}$ compounds with only σ bonding are less affected by exchanging C for B and always in favor of B-X bonds ($\text{X} = \text{F-I}$).

7.3 Water Adducts of BX_3 and CX_3^+ : Implications for Structure, Bonding and Reactivity

An effective method to gain a deeper insight in the different behaviour of the trihalocarbenium ions and the trihaloboranes is the investigation of these species with Lewis bases. One commonly used base for such studies is the naked fluoride ion F^- , leading to the *FIA* as a measure of the Lewis acidity of a given substance, but also hydride affinities (*HA*, eq. 56), methyl stabilization energies (*MSEs*), water complexation energies (*WCEs*, eq. 58) and NH_3 affinities (eq. 59) of CX_3^+ and BX_3 have been published^[222].



The calculated water complexation energies^[222] (*WCE*, eq. 58) of the CX_3^+ cations were in line with the Lewis acidities deduced from *FIA*, *HA*, *MSE* and NH_3 affinities: The formation of $\text{H}_2\text{O} \rightarrow \text{CX}_3^+$ got less favorable for the heavier halides and was even endothermic for $\text{X} = \text{I}$. By contrast, for BX_3 , similar values for each X were calculated^[222]. Thus the *WCEs* predicted BX_3 Lewis acidities contrasting the experimental findings^[304]. Moreover, it appeared unlikely

that the WCE of the Cl_3^+ cation is positive, which suggests that the obtained minimum structure with a normal calculated C-O bond length of 159.6 pm^[222] was not the global minimum of the $\text{H}_2\text{O} \rightarrow \text{Cl}_3^+$ potential energy surface (PES). To elucidate the $\text{H}_2\text{O} \rightarrow \text{EX}_3^{0/+1}$ global minima (E = B, C; X = H, F-I), several geometries of these water adducts have been recalculated at different levels of theory with larger DZ as well as TZ basis sets and drastically different minimum structures $\text{H}_2\text{O} \rightarrow \text{CX}_3^+$ (X = C-I) than those reported by Frenking *et al.*^[222] were obtained. Since structure and bonding of these water adducts turned out to be different for E = B and C, also additional calculations have been performed to analyze the influence of the positive charge in CX_3^+ in comparison to isoelectronic but neutral BX_3 . For this reason the discussion begins with a description of the structures of $\text{EX}_3^{0/+1}$, moves on to the $\text{H}_2\text{O} \rightarrow \text{EX}_3^{0/+1}$ water adducts and finishes with a series of related compounds such as $\text{X}_2\text{ENH}_2^{0/+1}$, $\text{B}_3\text{N}_3\text{H}_3\text{X}_3$ (borazine), Ph-X, $\text{X}_2\text{B-Do}^+$ (Do = NH_3 , H_2O , XH) and BX_2^+ (X = Cl, Br, I), in which the presence or absence of a positive charge leads to maximum changes of structure and bonding within the E-X bonds of the particles. Then the influence of a positive charge on structure, bonding and reactivity of these compounds is analyzed.

7.3.1 Structures of Free $\text{EX}_3^{0/+1}$

To analyze the influence of the coordination of water to the $\text{EX}_3^{0/+1}$ Lewis acids (E = B, C; X = H, F-I), the free and undisturbed $\text{EX}_3^{0/+1}$ particles were investigated first. In Table 50 experimental and calculated structural parameters for $\text{EX}_3^{0/+1}$ are collected.

Table 50: Calculated and experimental bond lengths of $\text{EX}_3^{0/+1}$ (MP2/TZVPP).

	$d_{\text{exp}}(\text{C-X})$ [pm]	$d_{\text{calc}}(\text{C-X})$ [pm]		$d_{\text{exp}}(\text{B-X})$ [pm]	$d_{\text{calc}}(\text{B-X})$ [pm]
CH_3^+	-	108.6	BH_3	-	118.7
CF_3^+	-	123.3	BF_3	130.7 ^[305]	131.6
CCl_3^+	162.1 ^[58]	164.4	BCl_3	174.2 ^[277]	173.9
CBr_3^+	180.7 ^[58]	180.8	BBr_3	189.5 ^[243]	189.9
CI_3^+	201.3(9) in 15	202.0	BI_3	212.5 ^[243]	211.4

The E-X distances obtained by MP2/TZVPP are in very good agreement with the experimental results (within 2.3 pm) suggesting that conclusions drawn from these calculations hold. From Table 50 is evident that the calculated and available experimental E-

X distances in charged CX_3^+ are by about 8-10 pm shorter than those in isoelectronic neutral BX_3 .

7.3.1.1 Structures of Isomers of the Water Adducts $H_2O \rightarrow EX_3^{0/+1}$

The structures of all isomers of the $H_2O \rightarrow EX_3^{0/+1}$ adducts were optimized at the MP2/TZVPP, BP86/TZVPP and B3-LYP/TZVPP levels; however, due to the better performance of MP2 to describe weak interactions, only the results based on the MP2/TZVPP calculations are discussed.

Minima on the $H_2O \rightarrow EX_3^{0/+1}$ PES:

For the $H_2O \rightarrow EX_3^{0/+1}$ ($E = B, C$; $X = H, F-I$) adducts, four different minimum geometries **I** to **IV** were found (see Figure 64), and some minimum geometries changed with the quantum chemical method. Only the C_s symmetric structures **I** and **II** in Figure 64 were reported in the previous calculation^[222]. They are considered as being "classical" with strong E-O bonds, while structures **III** (C_s) and **IV** (C_{2v}) are unexpected "non-classical" weakly bound water adducts^[vi]. Structures **III** and **IV** were obtained by using the geometries **I** and **II** as a starting point and replacing B by C^+ . Thus the energetic driving force to form the non-classical structures **III** and **IV** is considerable.

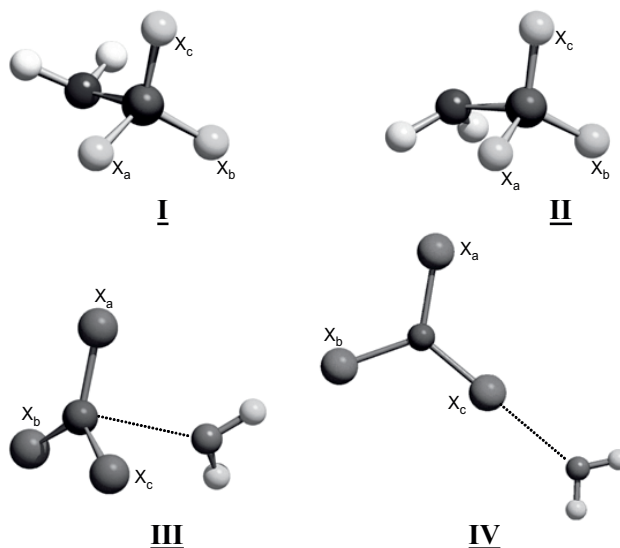


Figure 64: Minimum geometries of the water adducts $H_2O \rightarrow EX_3^{0/+1}$ ($E = B, C$; $X = H, F-I$): Covalent structures **I** and **II** vs. weakly bound structures **III** and **IV**. Symmetry: **I-III**: C_s , **IV**: C_{2v} .

Some water adducts have several minimum structures on the PES (cf. Table 51).

^[vi] Structure **III** may also be viewed as classical, but with a very long and weak C-O bond (272.5 pm).

Table 51: Local and global minima of the water adducts $\text{H}_2\text{O} \rightarrow \text{EX}_3^{0/+1}$ (E = B, C; X = H, F -I) and relative energies (in kJ/mol) of the different structures at the MP2/TZVPP level. Distances are given in pm. Abbreviations.: gm = global minimum; lm = local minimum; ts = transition state; spn = nth order saddle point.

Geometry ^(a)												
EX ₃ ^{0/+1} =	I		II		III		IV					
		<i>E</i> _{rel.}	<i>d</i> (E-O)		<i>E</i> _{rel.}	<i>d</i> (E-O)	<i>E</i> _{rel.}	<i>d</i> (E-O)	<i>E</i> _{rel.}	<i>d</i> (E-O)		
CH ₃ ⁺	gm	0	150.7	ts	+5.0	151.3	-	-	ts	+231.6	174.8	
CF ₃ ⁺	gm	0	155.0	ts	+2.7	155.4	-	-	sp3	+127.0	256.8	
CCl ₃ ⁺	-	-	-	-	-	-	gm	0	272.5	lm	+6.2	262.6
CBr ₃ ⁺	-	-	-	-	-	-	lm	+5.4	287.8	gm	0	266.4
Cl ₃ ⁺	-	-	-	-	-	-	lm	+14.6	303.9	gm	0	275.1
BH ₃	gm	0	170.9	ts	+2.6	172.7	-	-	sp3	+66.6	288.9	
BF ₃	ts	+0.2	178.8	gm	0	179.0	-	-	-	-	-	-
BCl ₃	gm ^(b)	0	166.1	lm ^(b)	+1.0	166.6	-	-	sp2	+31.0	312.4	
BBr ₃	gm ^(b)	0	163.8	lm ^(b)	+1.1	164.5	-	-	sp2	+33.7	319.7	
BI ₃	gm ^(b)	0	163.5	lm ^(b)	+2.6	164.4	-	-	ts	+28.7	326.5	

^(a) Geometries as shown in Figure 64. ^(b) For $\text{H}_2\text{O-BX}_3$ (X = Cl-I) structure **II** is the gm and structure **I** a lm at the BP86/TZVPP and B3-LYP/TZVPP levels. However, the energy differences between **I** and **II** are minimal.

At the MP2 level $\text{H}_2\text{O} \rightarrow \text{BF}_3$ prefers to adopt structure **II**, while **I** is a transition state albeit only 0.2 kJ/mol higher in energy. For the heavier $\text{H}_2\text{O} \rightarrow \text{BX}_3$ adducts, ($\text{X} = \text{Cl-I}$) the isomer **II** is a local minimum that is only 1.0 to 2.6 kJ/mol higher in energy than structure **I**, whereas the halogen bound isomers **IV** are transition states or saddle points with relative energies of $\approx +29$ kJ/mol. For the heavier $\text{H}_2\text{O} \cdots \text{CX}_3^+$ adducts, the energy differences between halogen and carbon bound structures are smaller. However, also the carbon bound heavier $\text{H}_2\text{O} \cdots \text{CX}_3^+$ adducts include very long $\text{C} \cdots \text{O}$ separations exceeding 250 pm and the halogen coordinated isomer of $\text{H}_2\text{O} \cdots \text{Cl}_3^+$ is about 15 kJ/mol more stable than structure **III**. Isomers with strong C-O bonds could not be found for the heavier CX_3^+ cations, even when starting the calculations with geometries **I** or **II**. This shows that the previous calculations^[222] gave the wrong minimum structures for the heavier $\text{H}_2\text{O} \rightarrow \text{CX}_3^+$ cations ($\text{X} = \text{Cl-I}$).

Calculations on other possible isomers of CH_2OX_3^+ ($\text{X} = \text{F-I}$) have also been performed. The most favorable isomer which can be seen as $\text{HX} \cdot \text{CX}_2\text{OH}^+$ (cf. Figure 65). Two different types of structures were found: For $\text{X} = \text{F}$, the halogen is weakly bond to the carbon atom, whereas for the heavier halogens the coordination occurs through H-bonding. These species are the global minima on the PES of the CH_2OX_3^+ system, but since they are no water adducts, their structural parameters are listed in the results section (Table 52) but are not discussed later.

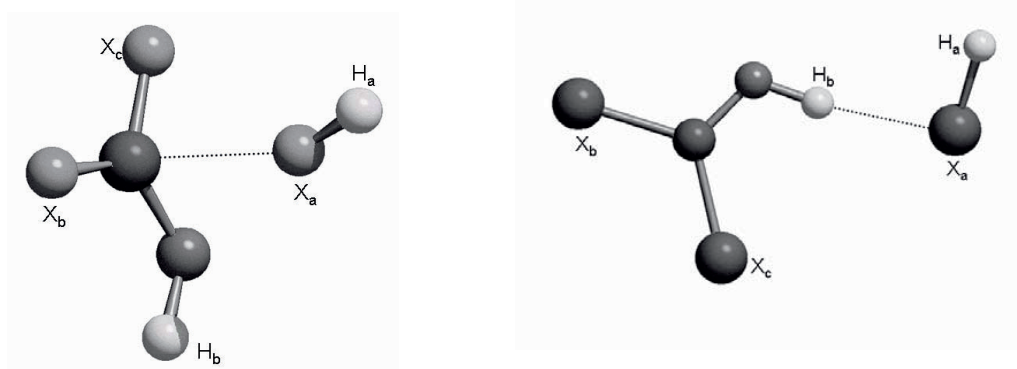


Figure 65: Calculated global minimum structures on the PES of CH_2OF_3^+ (left) and CH_2OX_3^+ ($\text{X} = \text{Cl-I}$; right) at the MP2/TZVPP level.

Table 52: Calculated structures of the global minima on the PES of CH_2OX_3^+ (X = F-I) at the MP2/TZVPP level.

X =	F	Cl	Br	I
$d(\text{C-X}_a)$ [pm]	242.6	373.1	391.5	412.7
$d(\text{C-X}_{b,c})$ [pm]	124.5 / 125.4	165.2 / 166.5	181.7 / 183.0	203.1 / 204.5
$d(\text{C-O})$ [pm]	124.9	126.1	126.4	127.1
$d(\text{X}_a\text{-H}_a)$ [pm]	92.6	128.2	142.0	161.0
$d(\text{X}_a\text{-H}_b)$ [pm]	299.6	194.5	210.2	228.5
$\Sigma(\text{X-C-X})$ and (X-C-O) angles	359.9°	360.0°	360.0°	360.0°
$E_{\text{rel.}}$ [kJ/mol]	-23.6	-75.4	-51.9	-4.9

Global Minimum Structures of the Water Adducts:

The global minimum structures of the water complexes of BX_3 as well as those of CH_3^+ and CF_3^+ are C_s symmetric with normal E-O bonds that range from 150.7 to 179.0 pm (Table 51). In contrast to the classical water adducts the global minimum structures of $\text{H}_2\text{O}\cdots\text{CX}_3^+$ (X = Cl-I) are built from trigonal planar π -bonded CX_3^+ cations and weakly interacting water molecules (266.4 to 275.1 pm, structures **III** and **IV**, Table 51). Similar weakly bound $\text{H}_2\text{O}\cdots\text{CX}_3^+$ structures (X = Cl-I) were also obtained by BP86 and B3LYP.

7.3.1.2 Structures of Related Compounds

From the preceding follows that π -interactions appear to be important for the heavier CX_3^+ cations (short C-X bonds, "non-classical" structures **III** and **IV**), but not for neutral isoelectronic BX_3 . Thus it became interesting to analyze the question in how far the positive charge in CX_3^+ may induce a stronger π -bonding if compared to neutral BX_3 . Therefore a series of related compounds was investigated, in which either (almost) no π -interaction in the E-X bond is possible (Ph-X, $\text{B}_3\text{N}_3\text{H}_3\text{X}_3$, H_2NBX_2) or in which a positive charge is introduced to the boron system (i.e. BX_2^+ and $\text{Do}\rightarrow\text{BX}_2^+$, Do = NH_3 , OH_2 , XH) or strong π -donors replace the X atom in $\text{EX}_3^{0/+1}$ ($\text{X}_2\text{E}(\text{NH}_2)^{0/+1}$ and $\text{XC}(\text{NH}_2)_2^+$)^[vii]. Figure 66 shows schematic drawings of the selected optimized particles.

^[vii] It is not suitable to include $\text{XB}(\text{NH}_2)_2$ into the discussion, since the (long) B-X bond in this molecule is affected by a predissociation to the borinium salt $[\text{H}_2\text{N-B-NH}_2]^+\text{X}^-$.

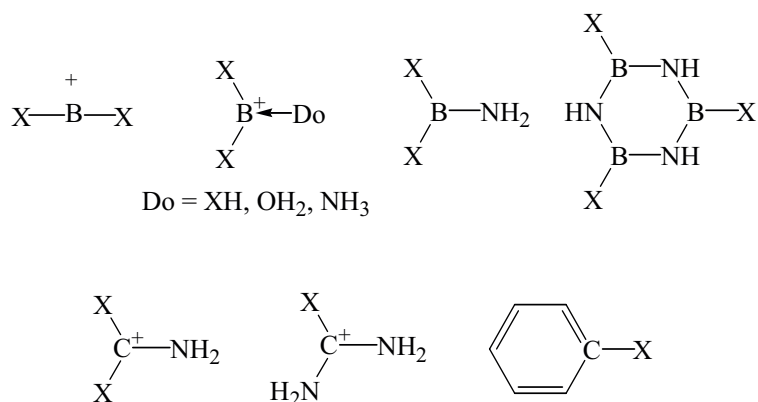


Figure 66: Schematic drawings of the additional particles optimized for X = Cl to I with MP2/TZVPP. Only formal charges with no physical meaning are shown.

The B-X and C-X bond lengths of the species as in Figure 66 are included in Table 55 (boron) and Table 56 (carbon) in the Discussion section below.

7.3.2 Discussion

Although the CX_3^+ cations and the BX_3 molecules are isoelectronic species with the same D_{3h} symmetric structures, their bond lengths and their chemical behavior differ considerably. In principle both, BX_3 and CX_3^+ , can be π -bonded by back donation of the lone pair orbitals of the X atoms to the empty p_z orbital of the C or B atoms (Figure 67).

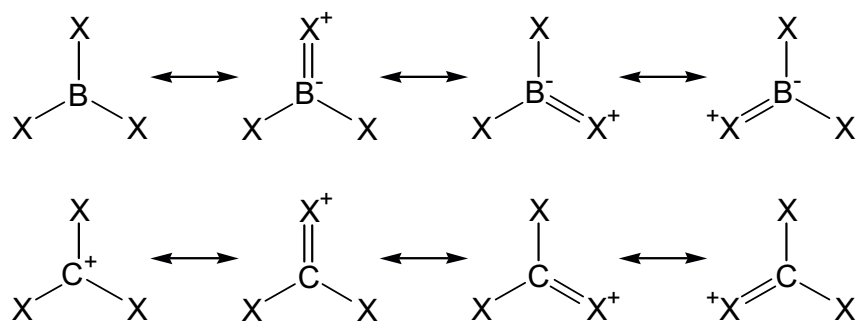


Figure 67: Possible mesomeric resonance structures for BX_3 und CX_3^+ .

However, the amount of π -bonding and its influence on structure and reactivity of $\text{EX}_3^{0/+1}$ is still under debate^[306]. One notes from Figure 67 that π -bonding leads to charge separation for BX_3 but to charge delocalization for CX_3^+ . Already this simple picture allows assuming that π -bonding is weaker in BX_3 than it is in CX_3^+ . In other words: C^+ is a better π -acceptor than B. This is in agreement with the findings in chapters 7.1 and 7.2 above. To shed light on the question if π -bonding is *structure determining* and thus important for the $\text{EX}_3^{0/+1}$ particles, first the water adducts will be discussed and then a short discussion of the related compounds as given in section 7.3.1.2 will be made.

7.3.2.1 H-Bonding as a Component of the Minimum Geometries of $\text{H}_2\text{O}-\text{BX}_3$

The aim of this section is to clarify why the *WCEs* of BX_3 appear *not* to follow the trend as expected from the known leveling of the Lewis acidities that increase in the order $\text{BF}_3 < \text{BCl}_3 < \text{BBr}_3 \approx \text{BI}_3$. The discussion starts with an analysis of the structures of the water adducts in Table 53 to understand the *WCEs* included in the same Table (MP2/TZVPP and reported^[222] values).

Table 53: Water Complexation Energies (*WCEs*) of $\text{H}_2\text{O} \rightarrow \text{BX}_3$ (values from Ref. 222 in parentheses); calculated bond lengths and the sum of the X-B-X bond angles of $\text{H}_2\text{O} \rightarrow \text{BX}_3$ at the MP2/TZVPP level.

$\text{BX}_3 =$	BF_3	BCl_3	BBr_3	BI_3
WCE [kJ/mol] ^(a)	40 (46)	35 (40)	41 (39)	39 (41)
$d(\text{B-O})$ [pm]	179.0	166.1	163.8	163.5
$d(\text{H-X}_{a,b})$ [pm]	263.2	281.6	291.7	307.3
$d(\text{H-X}_c)$ [pm]	308.0	282.8	293.6	309.8
$d(\text{B-X}_{a,b})$ [pm]	135.4	180.0	196.7	219.0
$d(\text{B-X}_c)$ [pm]	134.0	182.0	199.1	221.4
$d(\text{O-H})$ [pm]	96.4	97.0	97.1	97.3
Stretch. B-X [%] ^(b)	2.5	3.7	3.9	3.8
Shrink. O-H [%] ^(c)	0.6	1.1	1.3	1.4
$\Sigma(\text{X-B-X})$ angles [°]	350.14	345.27	344.31	344.14

^(a) all values are ΔU at 0 K. ^(b) compared to free BX_3 . ^(c) compared to free H_2O .

As may be seen from Table 53, the geometries of the $\text{H}_2\text{O} \rightarrow \text{BX}_3$ molecules are "normal" with the usual increase of the B-X bond lengths of 2.5 to 3.9 % if compared to free BX_3 . The relative increase of $d(\text{B-X})$ as well as the sum of the (X-B-X) angles follows that expected from the Lewis acidity arguments. Also the B-O bond in $\text{H}_2\text{O} \rightarrow \text{BF}_3$, containing the weakest Lewis acid, is the longest in the series of $\text{H}_2\text{O} \rightarrow \text{BX}_3$ (179 pm vs. 163-171 pm). Therefore all structural parameters in $\text{H}_2\text{O} \rightarrow \text{BX}_3$ are in agreement with the known leveling of the Lewis acidity of the BX_3 molecules. Why is it then that the *WCEs* of BX_3 do not show this trend and remain almost unchanged? An analysis of Table 53 and Figure 68 shows that some structures are affected by H-bonding, most noticeable $\text{H}_2\text{O} \rightarrow \text{BF}_3$, in which two hydrogen atoms interact with two separate fluorine atoms. The H-F distance in this molecule is 263.2 pm, which is 18.6 % shorter than the sum of the van der Waals radii of hydrogen and fluorine. Clearly this additional H-bonding makes the water adduct more stable than it would be according to the lower relative Lewis acidity of the BF_3 molecule.

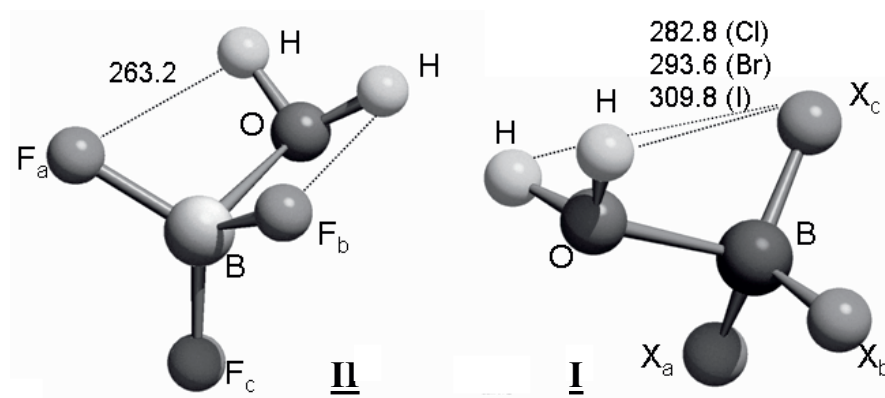


Figure 68: H-bonding in structure **I** ($\text{H}_2\text{O} \rightarrow \text{BF}_3$) and structure **II** ($\text{H}_2\text{O} \rightarrow \text{BX}_3$, $\text{X} = \text{Cl-I}$) at the MP2/TZVPP level.

This demonstrates that the higher calculated *WCE* of BF_3 of 40 kJ/mol is due to additional H-bonding and not due to the primarily investigated B-O bonding. To estimate the magnitude of H-bonding contributions in $\text{H}_2\text{O} \rightarrow \text{BF}_3$, also the energy of an isomer of $\text{H}_2\text{O} \rightarrow \text{BF}_3$ without any B-O interaction but with one or two H--F contacts (see Figure 69) has been calculated.

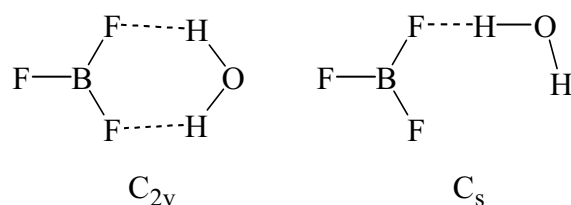


Figure 69: Geometries for the C_{2v} (left) and C_s (right) symmetric isomers of H_2O-BX_3 without B-O interactions.

However, none of these structures was a minimum on the PES of this molecule; still H-bonding stabilized both isomers by 5 (C_s) to 8 (C_{2v}) kJ/mol in comparison to the isolated monomers (MP2/TZVPP and BP86/SV(P)) while the H-F distance in the C_{2v} isomer was 254 pm and thus close to the situation in structure **II** (MP2: 263 pm). For all other $H_2O \rightarrow BX_3$ adducts an interaction as in Figure 69 only led to a minimal stabilization of at most 2 kJ/mol. Thus the *WCE* of BF_3 in Table 53 of 40 kJ/mol has to be diminished by about 8 kJ/mol as a result of the additional stabilization owing to the two (weak) H-bonds (to 32 kJ/mol). Then the revised *WCEs* of the BX_3 molecules are again in line with the experimentally known Lewis acidities that follow $BF_3 < BCl_3 < BBr_3 \approx BI_3$ or *WCEs* of $32 < 35 < 41 \approx 39$ kJ/mol.

7.3.2.2 π -Bonding as a Structure-Determining Component of the Minimum Geometries of $H_2O \cdots CX_3^+$

In the previous work, the water adducts of the heavier CX_3^+ cations were supposed to have the structures **I** and **II** with strong C-O bonds. This was due to the use of inflexible small basis sets: Our calculations with a 3-21G* basis also gave structures of these types. But already when the calculations were performed with the more flexible SV(P) or TZVPP basis sets, the weakly bound structures **III** and **IV** were obtained, even when the geometry optimizations were started from the “classical” structures **I** and **II**. Therefore the previously^[222] reported *WCEs* of the heavier CX_3^+ cations are wrong by a maximum of 67 kJ/mol for Cl_3^+ (Table 54, in parentheses).

Table 54: Water Complexation Energies (*WCEs*) of $\text{H}_2\text{O} \rightarrow \text{CX}_3^+$; calculated bond lengths and the sum of the X-C-X bond angles of $\text{H}_2\text{O} \rightarrow \text{CX}_3^+$ at the MP2/TZVPP level. $\text{X}_{\text{a,b,c}}$ are defined in Figure 64.

	$\text{CX}_3^+ =$	CH_3^+	CF_3^+	CCl_3^+	CBr_3^+	CI_3^+
<i>WCE</i> [kJ/mol] ^(a)		308 (299)	168 (183)	55 (46)	52 (21)	54 (-13)
<i>d</i> (C-O) [pm]		150.7	155.4	272.5	-	-
<i>d</i> (C- $\text{X}_{\text{a,b}}$) [pm]		108.1	128.9	164.4	181.4	202.6
<i>d</i> (C- X_{c}) [pm]		108.2	127.8	164.2	180.4	202.6
<i>d</i> (O-H) [pm]		97.4	97.9	96.1	96.1	96.1
Stretch. C-X [%] ^(b)		-0.4	4.1	-0.1	0.2	0.2
Shrink. O-H [%] ^(c)		2.0	2.1	0.3	0.3	0.3
$\Sigma(\text{X-C-X})$ angles [°]		338.56	341.74	359.94	360.00	360.00

^(a) all values are ΔU at 0 K. ^(b) compared to free CX_3^+ . ^(c) compared to free H_2O .

For $\text{H}_2\text{O} \rightarrow \text{CX}_3^+$ ($\text{X} = \text{H}, \text{F}$) the structure **I** may be viewed as protonated methanol or trifluoromethanol. Both are known from mass spectrometry^[307, 308], and the experimental *WCE* of CF_3^+ was found to be 153 ± 9 kJ/mol^[307] in good agreement with our value of 146 kJ/mol (both values: ΔH at 298 K^[viii]). Also the experimental and the calculated values of the proton affinity of trifluoromethanol match very well: at the MP2/TZVPP level, the proton affinity is 617 kJ/mol and the measured value is 632 ± 7 kJ/mol^[307] (both values: ΔH at 298 K^[viii]). However, the heavier $\text{H}_2\text{O} \rightarrow \text{CX}_3^+$ cations are unknown on experimental grounds providing additional evidence for the calculated minimum structures as *not* being protonated trihalomethanols, since those certainly would have been observed in the MS. In these $\text{H}_2\text{O} \cdots \text{CX}_3^+$ ($\text{X} = \text{Cl-I}$) complexes, the CX_3^+ unit is planar (sum of bond angles $\sim 360^\circ$) and - if compared to free CX_3^+ - the C-X distances in the heavier $\text{H}_2\text{O} \cdots \text{CX}_3^+$ cations remain unchanged within 0.6 pm (see Table 54).

This planar geometry and the short C-X distances in the heavier $\text{H}_2\text{O} \cdots \text{CX}_3^+$ are chemical proofs for a delocalized positive charge and for the formation of strong π -bonds. Therefore, the formation of halogen-bonded water adducts with nearly undisturbed CX_3^+ units is a result of efficient π -bonding. This indicates that for the heavier CX_3^+ cations the delocalized π -bond is more stable than the localized C-O σ -bond. Thus, in the heavier $\text{H}_2\text{O} \cdots \text{CX}_3^+$ cations the structure is *determined* by strong π -bonding.

^[viii] ZPE and thermal contributions to the enthalpy included on the basis of the MP2/TZVPP frequency calculation.

7.3.2.3 Positive Charge as an Efficient Driving Force for π -Bond Formation

Why do the minimum geometries of the isoelectronic $\text{H}_2\text{O} \rightarrow \text{EX}_3^{0/+1}$ ($\text{E} = \text{B}, \text{C}$; $\text{X} = \text{H}, \text{F}, \text{I}$) species differ so much? As shown in section 7.3.2.2, π -bonding plays an important role in CX_3^+ . What about BX_3 ? As shown in Figure 67 and chapter 7.1 above, mesomeric structures with partial double bonds can also be formulated for BX_3 . The formation of partial π -bonds causes a positive charge on the X atoms, if it is not overcompensated by σ -induction and, therefore, the difference in the electronegativities $\Delta\chi$ ($\text{E}-\text{X}$) is important. For the less electronegative halogens Br and I the transfer of the positive charge onto the halogens is easier and their ability to act as σ -acceptors is smaller. Thus, if π -bonding was important for BX_3 , at least for the heavier BX_3 molecules with $\text{X} = \text{Br}, \text{I}$ the formation of halogen-coordinated water adducts should be preferred. As shown above this is not the case and halogen coordinated water adducts are transition states or saddle points at high relative energy charge (Table 51). The formation of partial double bonds in BX_3 would lead to a separation of the he principle of electroneutrality. This suggests that the delocalization of the positive charge in CX_3^+ , which minimizes the overall charges, is the driving force for the formation of strong partial double bonds. Charge is absent in BX_3 and, therefore, π -interactions are weak. To support this theory, calculated as well as experimental E-X bond lengths in different neutral and charged E-X species in which

- X is replaced by a strong π -donor like $-\text{NH}_2$;
- the π -donating character of $-\text{NH}_2$ is removed by protonation to $-\text{NH}_3^+$;
- a positive charge is introduced to the B-X system;
- the C-X system bears no positive charge.

are compared.

The calculated and available experimental E-X bond lengths are included with Table 55 (boron) and Table 56 (carbon).

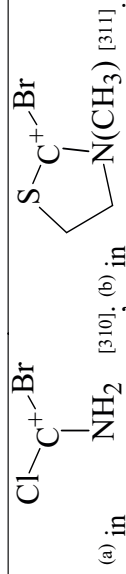
Table 55: Computed (MP2/TZVPP) and experimental^[277] (in parentheses) B-X distances of BX_2^+ , Do- BX_2^+ (Do = HX, H_2O , H_3N), BX_3 , trihalogenated borazines and halogenated aminoboranes $\text{X}_3\text{B}(\text{NH}_2)^{[\text{vii}]}$ (X = Cl-I). Distances are given in pm.

$d(\text{B-X}) =$	BX_2^+	HX-BX_2^+	$\text{H}_2\text{O-BX}_2^+$	$\text{H}_3\text{N-BX}_2^+$	BX_3	H_2NBX_2	$\text{B}_3\text{N}_3\text{H}_3\text{X}_3$
X = Cl	161.5 (-)	168.1 (-) ^(a)	169.3 (-)	170.0 (-)	173.9 (174.2)	176.2 (-)	176.8 (176.2) ^(b)
X = Br	176.5 (-)	184.1 (-) ^(a)	185.1 (-)	185.7 (-)	189.9 (189.5)	192.3 (-)	192.8 (-)
X = I	196.9 (-)	206.0 (-) ^(a)	206.4 (-)	205.9 (-)	211.4 (211.8)	213.7 (-)	210.9 (-)

^(a) The HX--B distances are 195.3 (Cl), 209.2 (Br) and 227.0 pm (I); ^(b) cf. average $d_{\text{exp.}}(\text{B-Cl})$ in $\text{B}_3\text{N}_3\text{Cl}_6 = 176.2$ pm^[309]

Table 56: Computed (MP2/TZVPP) and experimental^[277] (in parentheses) C-X distances of CX_3^+ , H_2NCX_2^+ , $(\text{H}_2\text{N})_2\text{CX}^+$ and Ph-X (X = Cl-I). Distances are given in pm.

$d(\text{C-X}) =$	CX_3^+	H_2NCX_2^+	$(\text{H}_2\text{N})_2\text{CX}^+$	Ph-X
X = Cl	164.4 (162.2 ^[272])	166.6 (169.0) ^(a)	168.5 (-)	173.5 (173.9)
X = Br	180.8 (180.7 ^[272])	183.0 (184.3) ^(a)	184.9 (184.9) ^(b)	189.2 (189.9)
X = I	202.0 (201.3 in 15)	204.5 (-)	206.4 (-)	209.3 (209.5)



Let us first turn to the situation of the B-X compounds in Table 55. Starting from neutral BX_3 the introduction of nitrogen lone pair orbitals as π -donors such as the exchange of X for $\text{NH}_2^{\text{[vii]}}$ or in the B_3N_3 borazine ring system leads to a slight elongation of the B-X bond lengths by a maximum of 2.9 pm. This is attributed to the diminished B-X π -bonding contribution, since the electron deficiency of the B atom is effectively reduced by formation of a strong dative $\text{B}=\text{N}$ double bond^[312, 313] or an aromatic 6π B_3N_3 ring. Thus it may be stated that the structural effect of the B-X π -bonding in free BX_3 leads at most to a bond shortening of 2.9 pm and is therefore weak. When the π -donating character of the $-\text{NH}_2$ group in $\text{X}_2\text{B}-\text{NH}_2$ is destroyed by protonation and formation of $\text{X}_2\text{B}\leftarrow\text{NH}_3^+$ the B-X bonds are shortened by 6.2 to 7.8 pm (Figure 70).

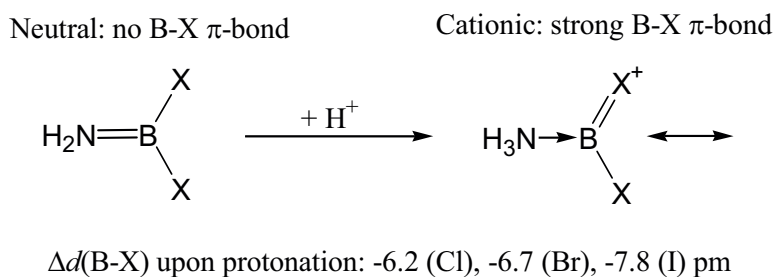


Figure 70: π -bond formation upon protonation of $\text{X}_2\text{B}-\text{NH}_2$ to $\text{X}_2\text{B}\leftarrow\text{NH}_3^+$.

Thus the introduction of a positive charge to the B-X system and the absence of other π -donors than X leads to a about three times stronger shortening of the B-X bonds as compared to the B-X bond lengthening in the BX_3 and $\text{X}_2\text{B}-\text{NH}_2$ couple (2.3 to 2.4 pm). This is attributed to the more efficient B-X π -bonding in $\text{X}_2\text{B}\leftarrow\text{NH}_3^+$, which is induced by the positive charge as a driving force. Replacing the stronger σ -donor NH_3 by weaker σ -donors such as OH_2 and XH leads to further albeit small B-X bond shortenings of at most 1.9 pm. This shows that with the weaker donors also more positive charge is left on the B atom (0th order, **VI**) which is then delocalized by π -bonding (**VII** and **VIII**) and that reduces the unfavorable localized charge formally residing on the boron atom (Figure 71).

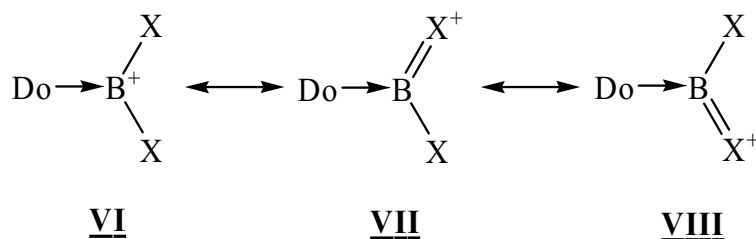


Figure 71: Positive charge delocalization as the driving force for efficient π -bond formation in $\text{Do} \rightarrow \text{BX}_2^+$.

Therefore the driving force for π -bond formation is higher for $\text{Do} \rightarrow \text{BX}_2^+$ with $\text{Do} = \text{OH}_2$ and XH and their B-X bonds are further shortened if compared to $\text{X}_2\text{B} \leftarrow \text{NH}_3^+$. As expected, the extreme is found for the isolated linear BX_2^+ cation (isoelectronic with CO_2) and for which a bond shortening of 12.5 to 14.5 pm in comparison to BX_3 was predicted. However, the coordination number in BX_2^+ is only 2 and the π -bond order in BX_2^+ (between 0.5 and 1) is higher than that possible at most for BX_3 (0.33 per B-X bond).

In the carbon system in Table 56 the situation is clear: starting from the neutral Ph-X , in which a sp^2 -carbon resides next to a single bonded halogen atom X with (almost) no π -interaction, the introduction of a positive charge in the $\text{X}_{3-x}\text{C}(\text{NH}_2)_x$ series leads to C-X bond shortening due to additional C-X π -bonding. The absolute shortening decreases from $x = 2$ (2.9 to 5.0 pm) to $x = 1$ (1.9 pm) and $x = 0$ (1.8 to 2.5 pm). In total, comparing Ph-X and CX_3^+ , the C-X shrinkage reaches 7.3 to 9.1 pm and thus is more pronounced than in the related $\text{X}_2\text{B-NH}_2/\text{X}_2\text{B} \leftarrow \text{NH}_3^+$ system (cf.: 6.2 to 7.8 pm).

Overall it may be stated that the effect of π -bonding is strong for CX_3^+ but weak for BX_3 . A positive charge leads to bond shortening due to π -bond formation that is more pronounced in the C-X system but is also important for the B-X system (about 85 % of that of a C-X bond if comparing the related cationic CX_3^+ and $\text{X}_2\text{B} \leftarrow \text{NH}_3^+$ couple). Therefore π -bonding is structure determining for cationic CX_3^+ but not for neutral BX_3 . For neutral BX_3 , haloborazines as well as Ph-X the positive charge as a driving force for π -bonding is absent and, therefore, the B-X bonds in neutral BX_3 ($\text{X} = \text{Cl-I}$) are by 9.1 to 9.5 pm longer than the respective C-X bonds in CX_3^+ . However, the E-X bond lengths of the related neutral couple Ph-X and trihaloborazine, which include (almost) no E-X π -bonding contribution, are comparable within 1.6 to 3.6 pm. This $\Delta(\text{E-X})$ is close to the intrinsic difference due to the different covalent single bond radii of B (82 pm) and C (77 pm). Therefore, the major reason

for the short C-X bonds in CX_3^+ are strong π -bonds, while the longer B-X bonds in BX_3 owe to the relative weakness of the structurally unimportant B-X π -bonds. Thus the positive charge is an efficient driving force for the formation of strong π -bonds.

This conclusion underlines earlier findings that positive charge delocalization *induces* non-classical thermodynamically stable np_π - np_π bonding ($n = 3-5$) in simple salts of heavier main group cations (i.e. E_4^{2+} , $E = S-Te$; $S_2I_4^{2+}$), while neutral isoelectronic species form alternative all σ -bonded classical structures. One of the extremes for this behavior is found for the $P_2I_4/S_2I_4^{2+}$ pair^[149, 150, 314]. In neutral P_2I_4 only σ -bonding is observed, upon isoelectronic replacement of P by S^+ the highly π -bonded $S_2I_4^{2+}$ with a S-S bond order (b.o.) of about 2.33 and an I-I b.o. of 1.33 is formed (Figure 72).

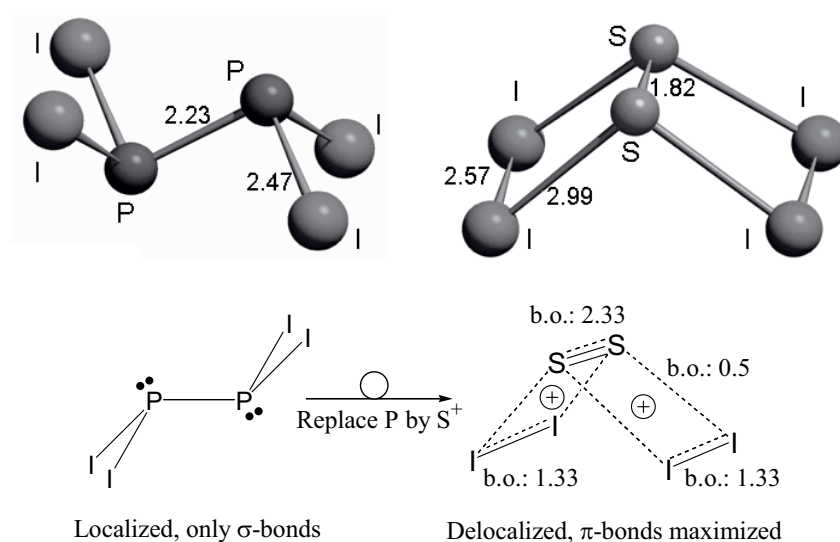


Figure 72: Structures and bond lengths of the isoelectronic species P_2I_4 (left)^[315] and $S_2I_4^{2+}$ (right, in $S_2I_4(SbF_6)_2$)^[149, 150, 314]. Distances given in Å.

7.4 Exploring the Chemistry of Free Cl_3^+ : Reactions with the Weak Lewis Bases PX_3 ($\text{X} = \text{Cl-I}$), AsI_3 and Et_2O

Is it possible to stabilize “non-classical” halogen-bound adducts of the Cl_3^+ cation? Since the quantum chemical calculations in section 7.3 predict such a structure, in which the Cl_3^+ cation acts as an I^+ donor, for the $\text{I}_2\text{C-I}\cdots\text{OH}_2^+$ complex, it was the logical consequence to search for an experimental proof for such an iodine-coordinated adduct. As Lewis bases, weak nucleophiles that mimic water (OEt_2) or other electronically deactivated weak nucleophiles (PX_3 , $\text{X} = \text{Cl-I}$; AsI_3) have been chosen.

7.4.1 Syntheses and NMR Characterization

Reaction with Et_2O :

According to quantum chemical calculations, the water adduct of the Cl_3^+ cation should have a “non-classical” structure in which the water molecule is coordinated via one iodine atom (Figure 65)^[257]. It is clear that the reaction of $[\text{Cl}_3]^+[\text{pftb}]^-$ with water can *not* be used because of hydrolysis; thus, we used diethyl ether as a substitute for H_2O to verify, if it is possible to stabilize such a “non-classical” iodine bound adduct. According to the quantum chemical calculations, the ether-coordination in CH_2Cl_2 is exergonic by 17.8 kJ/mol for the halogen-coordinated isomer and by 20.8 kJ/mol for the carbon coordinated one (MP2/TZVPP, eq. 60 and eq. 61 in Table 1). Since the free reaction energies of both isomers only differ by 3 kJ/mol, it seemed likely to find at least equilibrium between both structures in solution. However, the NMR spectra from an *in situ* NMR tube reaction recorded in CD_2Cl_2 only revealed ether cleavage instead of adduct formation: the observed signals were assigned to the cleaved products $\text{I}_3\text{C-OEt}$ ($\delta^{13}\text{C} = -160.0, 14.8, 67.2$), protonated ether $\text{H}(\text{OEt}_2)_2^+$ ($\delta^{13}\text{C} = 14.2, 69.0$; $\delta^1\text{H} = 1.34, 3.90, 16.50$ (br))^[316], C_2H_4 ($\delta^{13}\text{C} = 122.1$; $\delta^1\text{H} = 5.34$) as well as the $[\text{pftb}]^-$ anion ($\delta^{13}\text{C} = 121.7, \approx 79$; $\delta^{19}\text{F} = -75.7$; $\delta^{27}\text{Al} = 34.6$) The ether cleavage reaction probably follows eq. 62 in Table 57. Table 57 shows that ether cleavage is more exergonic than adduct formation. The ether cleavage reaction shows Cl_3^+ to behave as a strong Lewis acid. In this respect, there is some similarity of Cl_3^+ to the isoelectronic BI_3 molecule, which is known to be very effective in cleaving ethers at mild conditions^[317]. When the reaction was done in preparative scale, single crystals of $[\text{H}(\text{OEt}_2)_2]^+[\text{pftb}]^-$ were obtained (unit cell determination, same unit cell like in Ref. 316).

Table 57: Gibbs free energies at 298K ($\Delta_r G^\circ$ in kJ/mol) in the gas phase and in CH_2Cl_2 solution of hypothetical (eq. 60 and eq. 61) as well as observed reactions of Cl_3^+ with Et_2O (eq. 62; all MP2/TZVPP, COSMO solvation).

reaction	$\Delta_r H^\circ$ (gas)	$\Delta_r G^\circ$ (gas)	$\Delta_r G^\circ$ (CH_2Cl_2)
eq. 60 $\text{Cl}_3^+ + \text{Et}_2\text{O} \rightarrow \text{Et}_2\text{O} \cdots \text{I}-\text{Cl}_2^+$	-63.3	-60.0	-17.8
eq. 61 $\text{Cl}_3^+ + \text{Et}_2\text{O} \rightarrow \text{Et}_2\text{O} \cdots \text{Cl}_3^+$	-62.5	-60.8	-20.8
eq. 62 $\text{Cl}_3^+ + 3 \text{Et}_2\text{O} \rightarrow \text{I}_3\text{C}-\text{OEt} + \text{H}(\text{OEt}_2)_2^+ + \text{C}_2\text{H}_4$	-175.4	-142.2	-109.9

Reactions with PX_3 ($X = \text{Cl-I}$) and AsI_3 :

$[\text{Cl}_3]^+[\text{pftb}]^-$ was reacted with one equivalent of PX_3 ($X = \text{Cl-I}$) or AsI_3 in CH_2Cl_2 at low temperatures to give the adducts $[\text{I}_3\text{C}-\text{PCl}_3]^+[\text{pftb}]^-$ **19**, $[\text{I}_3\text{C}-\text{PBr}_3]^+[\text{pftb}]^-$ **20**, $[\text{I}_3\text{P}-\text{Cl}_3]^+[\text{pftb}]^-$ **21** and $[\text{I}_3\text{C}-\text{AsI}_3]^+[\text{pftb}]^-$ **22**, respectively. **19** to **21** formed in almost quantitative yield. However, **22** appears to be only stable in solution and never crystallized. In all cases, the anion remained intact during the reaction (^{19}F - and ^{27}Al -NMR; sealed NMR tubes). The singlet of Cl_3^+ ($\delta^{13}\text{C} = 96$ ppm) disappeared, and new peaks were detected in the ^{13}C NMR indicating the formation of the Cl_3^+ -adducts ($\delta^{13}\text{C} = -135.2$ (d, $^1J_{\text{C-P}} = 29$ Hz) **19**, $-120.0^{[\text{ix}]}$ **20**, -108.8 (d, $^1J_{\text{C-P}} = 42$ Hz) **21**, -118.3 (s) **22**). ^{31}P NMR spectra of the PX_3 adducts have been recorded ($\delta^{31}\text{P} = 75.8$ **19**, 38.9 **20**, -69.6 **21**) and indicate that for heavier halogens, the ^{31}P NMR signal is shifted towards higher field, a trend which is also found for the analogous $\text{I}_3\text{B}-\text{PX}_3$ molecules^[318] as well as the $\text{R}-\text{PI}_3^+$ and PX_4^+ cations (see Table 61 below for a discussion).

The comparison of the NMR data of **19** - **21** with related compounds in Table 61 suggests classical, C-coordinated structures of the adducts. Due to the similar ^{13}C spectra of $\text{I}_3\text{C}-\text{PX}_3^+$ and the AsI_3 adduct **22** it appears likely that it adopts a similar C-coordinated structure. This would be the first structurally characterized example of an iodine containing cationic or neutral As^{V} compound and a close relative to the yet unknown AsI_4^+ that recently withstood all attempts to preparation from AsI_3 , I_2 and $\text{Ag}^{+[\text{50}]}$. However, the As^{V} character appears to be intermediate (see discussion below).

If the reaction mixture of $[\text{Cl}_3]^+[\text{pftb}]^-$ and PI_3 in CH_2Cl_2 was left at room temperature for a few hours before crystallization, two different products were isolated in good yield:

^[ix] Despite many attempts the coupling constant could not be resolved, even at low temperatures.

$[\text{PI}_4]^+[\text{pftb}]^-$ and $[\text{I}_3\text{C-PI}_3]^+[\text{al-f-al}]^-$. This suggested I^+ donor reactivity of Cl_3^+ giving PI_4^+ ; the latter is well known^[48, 319] to decompose $[\text{pftb}]^-$ giving the observed $[\text{al-f-al}]^-$ anion.

For $[\text{I}_3\text{C-AsI}_3]^+[\text{pftb}]^-$ **22**, variable-temperature NMR measurements have been performed to study the dynamics of the $\text{I}_3\text{C-AsI}_3^+$ cation. From 193K up to 273 K, the ^{13}C NMR signal of the $\text{I}_3\text{C-AsI}_3^+$ cation is seen, but at 283K the signal disappears.

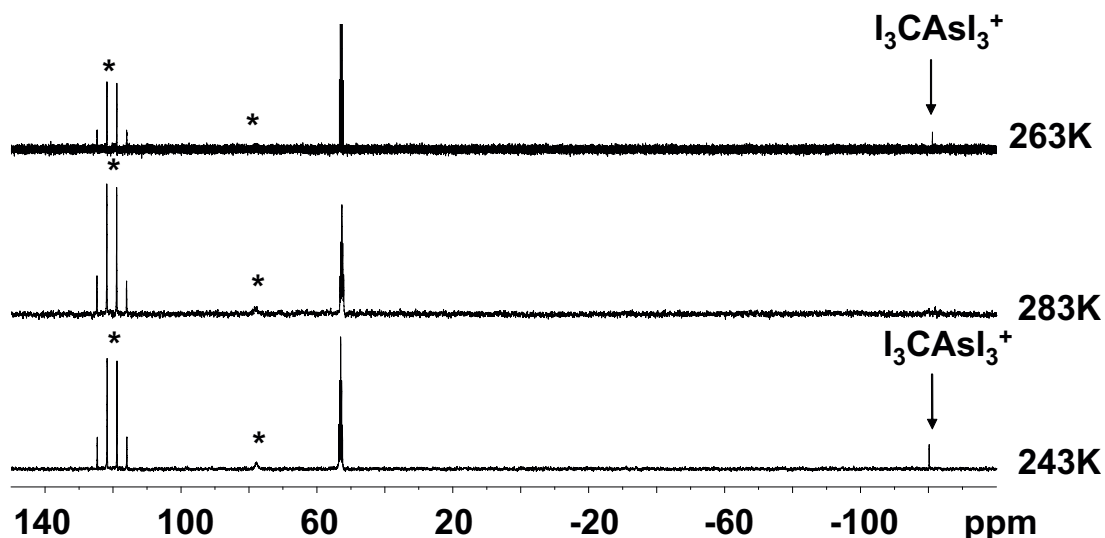


Figure 73: Variable temperature ^{13}C NMR spectra of $[\text{I}_3\text{CAsI}_3]^+[\text{pftb}]^-$ **22** in CD_2Cl_2 . The spectra have been recorded in the following order, to check if the process of adduct cleavage is reversible: 1.) 243K, 2.) 283K, 3.) 263K. Bands marked with * are assigned to the anion.

This process is reversible as long as the sample is not heated above r.t.. Heating to 318K, decomposes the $[\text{pftb}]^-$ anion to give the fluorine-bridged anion $[\text{((CF}_3)_3\text{CO)}_3\text{Al-F-Al(OC(CF}_3)_3)_3}]^-$ and $\text{C}_4\text{F}_8\text{O}$ ($\delta^{19}\text{F} = -69.3, -108.5$), which are typical decomposition products when the $[\text{pftb}]^-$ anion reacts with strong Lewis acids^[52].

7.4.2 Solid-State Structures

Of all $\text{I}_3\text{C-PX}_3^+$ salts, crystals suitable for X-ray diffraction could be obtained from highly concentrated solutions at low temperatures. Although the unit cell dimensions of all three salts with isostructural cations are related (seemingly tetragonal cells, with two axes at about 1400 pm and the third at 1900 (**19**), 2900 (**20**) or 3900 (**21**) pm), their true space groups and crystal symmetries are not. All three structures are affected by twinning and disordering, however, suitable models to describe the structures of the three compounds could be elaborated.

$[\text{I}_3\text{C-PCl}_3]^+[\text{pftb}]^-$ **19** crystallizes in the monoclinic space group $\text{P2}_1/\text{n}$ with $Z = 4$ (one cation and one anion in the asymmetric unit). A section of its solid-state structure is shown in Figure 74.

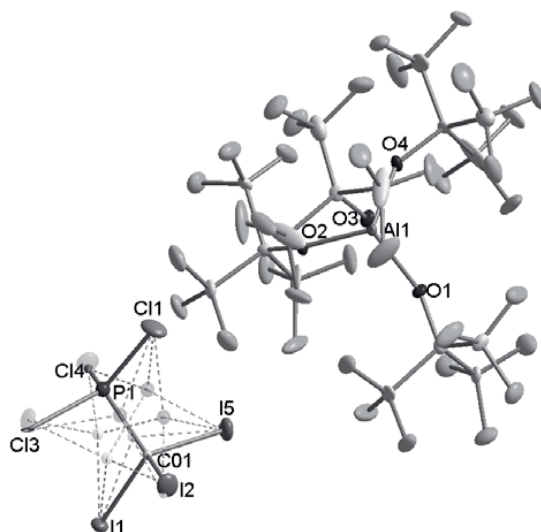


Figure 74: Section of the solid-state structure of $[\text{I}_3\text{C-PCl}_3]^+[\text{pftb}]^-$ **19** at 108K. Thermal displacement ellipsoids are drawn at the 25% probability level. C and P positions of the cations have been refined isotropically. Only one orientation of the cation is shown, the other orientations are drawn semi-transparent.

The PBr_3 adduct **20** crystallizes in the monoclinic space group $\text{P2}_1/\text{n}$ with $Z = 6$ (three half anions and three half cations are found in the asymmetric unit). A section of its solid-state structure is shown in Figure 75.

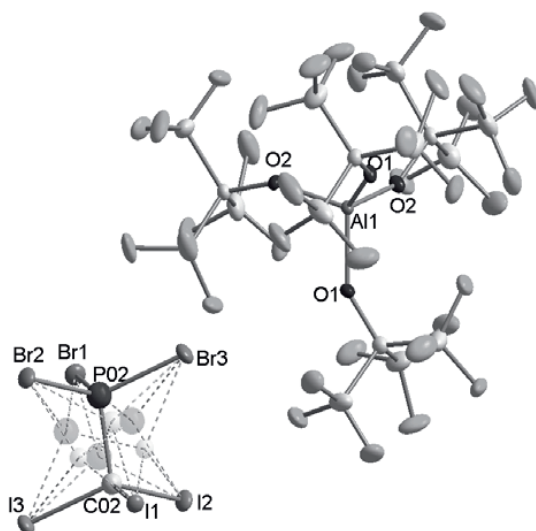


Figure 75: Section of the solid-state structure of $[\text{I}_3\text{C-PBr}_3]^+[\text{pftb}]^-$ **20** at 100K. Thermal displacement ellipsoids of the anion are drawn at the 25% probability level. C and P positions of the cations have been refined isotropically. Only one cation and one anion are shown, the other two have been omitted for clarity. Only one orientation of the cation is shown, the other orientations are drawn semi-transparent.

The largest unit cell is found for $[\text{I}_3\text{C-PI}_3]^+[\text{pftb}]^-$ **21**, which crystallizes in the monoclinic space group $\text{P}2_1/\text{c}$ with $Z = 8$ (two cations and two anions per asymmetric unit). A section of its solid-state structure is shown in Figure 76.

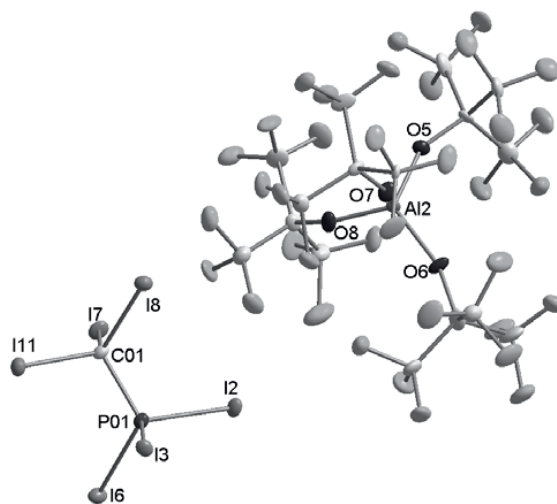


Figure 76: Section of the solid-state structure of $[\text{I}_3\text{C-PI}_3]^+[\text{pftb}]^-$ **21** at 100K. Thermal displacement ellipsoids of the anion are drawn at the 25% probability level. Only one cation and one anion are shown, the other two have been omitted for clarity.

In all three salts, the structural parameters of the anion are normal^[11]. In the case of **21**, no cation disorder is observed, while in **19** and **20**, the C and P positions are split into four different positions (cf. Figure 74 and Figure 75), which also causes a partial overlay of I positions with those of Cl resp. Br. This disorder is also the reason why the C and P positions in these salts could only be refined isotropically.

As the β angles of all three unit cells are very close to 90° , these structures can be described as pseudo-tetragonal. Due to this pseudo symmetry $\frac{1}{2}$ (for **19**), $\frac{2}{3}$ (for **20**) or $\frac{3}{4}$ (for **21**) of the data are weak, which leads to larger errors and therefore causes higher R1 values (4.28% for **19**, 6.97% for **20** and 8.85% for **21**). Especially in the case of **21**, the C and I positions only depend on the weak superstructure reflections, which implies a higher uncertainty of their position.

Even though point group symmetry of the three crystal structures is different, their packing is closely related: along the “special” axis (i.e. c for **19**, b for **20** and **21**), rows of cations and anions are stacked. In the cation stacks, the C and P direction are ordered. Along the other crystallographic axes, the packing can be described as a zigzag arrangement of cations and anions. As an example, the packing diagrams of **19** along the crystallographic axes is shown in Figure 77, those of **20** and **21** are shown in the appendix 12.5.

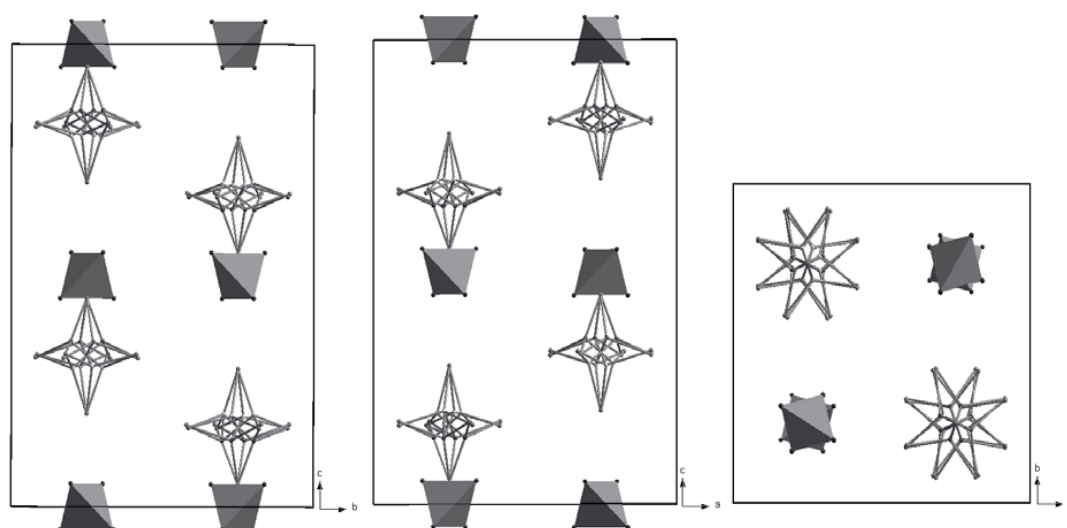


Figure 77: Packing diagram of $[\text{I}_3\text{C-PCl}_3]^+[\text{pftb}]^-$ **19** along the crystallographic axes. The AlO_4 -moieties of the anions are drawn as tetrahedra, the $\text{C}(\text{CF}_3)_3$ groups have been omitted for clarity.

In all three structures, ethane-analogue $\text{I}_3\text{C-PX}_3^+$ cations are found, which is in good agreement with the geometries deduced from NMR. Structural parameters of these cations are collected in Table 58 and compared to MP2 geometries.

Table 58: Comparison of the structural parameters of the I_3CPX_3^+ cation in **19**, **20** and **21** with the calculated values (MP2/TZVPP). Distances are given in pm, bond angles in $^\circ$.

	$\text{I}_3\text{CPCl}_3^+$ in 19	$\text{I}_3\text{CPCl}_3^+$ calc.	$\text{I}_3\text{CPBr}_3^+$ in 20	$\text{I}_3\text{CPBr}_3^+$ calc.	I_3CPI_3^+ in 21	I_3CPI_3^+ calc.
$d(\text{C-P})$ [pm]	173.2–189.7 av. 179.1	182.9	183.0–186.3 av. 185.2	184.1	184.9–185.1 av. 185.0	186.5
$d(\text{C-I})$ [pm]	206.8–221.2 av. 213.5	214.9	207.2–220.6 av. 216.0	214.9	214.7–218.6 av. 216.6	214.9
$d(\text{P-X})$ [pm]	201.8–221.8 av. 212.6	196.3	212.8–222.0 av. 217.7	213.9	236.3–239.5 av. 237.8	237.2

Despite the problems with the structure refinement (disorder, twinning), the agreement between the observed average structural parameters and the calculation is rather good. This is best seen for compound **21** which is not affected by disorder (only twinning). However, for the more detailed following discussions we only use the calculated MP2/TZVPP values. From Cl to I, $d(\text{C-P})$ and $d(\text{P-X})$ get longer, while $d(\text{C-I})$ remains constant. The elongation of the C-P bond from X = Cl to I is a bit unexpected, since this is opposite to the from Cl to I increasing Lewis basicities of PX_3 . Thus one would expect shorter P-C bonds for the heavier PX_3 adducts. However, steric hindrance is likely to level this out: In the $\text{I}_3\text{C-PI}_3^+$ cation, the large iodine atoms probably hinder the PI_3 moiety to further approach the carbon, as they already “touch” the iodine atoms of the ClI_3 moiety (cf. $d_{\text{av}}(\text{I-I}) = 397$ pm, sum of the van-der-Waals radii = 420 pm).

7.4.3 Vibrational Spectra of $[\text{X}_3\text{P-Cl}_3]^+[\text{pftb}]^-$ **19**, **20** and **21**

The compounds **19**, **20** and **21** have been investigated by vibrational spectroscopy. In contrast to the Raman spectra, which – even at very low laser intensities and low temperatures – only showed fluorescence and decomposed with higher Laser intensities, the signals of the cations were clearly identified in the IR spectra. In Table 59, the vibrational bands of the adducts are

listed, together with the values obtained by quantum chemical calculations at the MP2/TZVPP level^[x]. As an example, the experimental and simulated IR spectra of **19** are shown in Figure 78; those of **20** and **21** are given in the appendix 12.5.

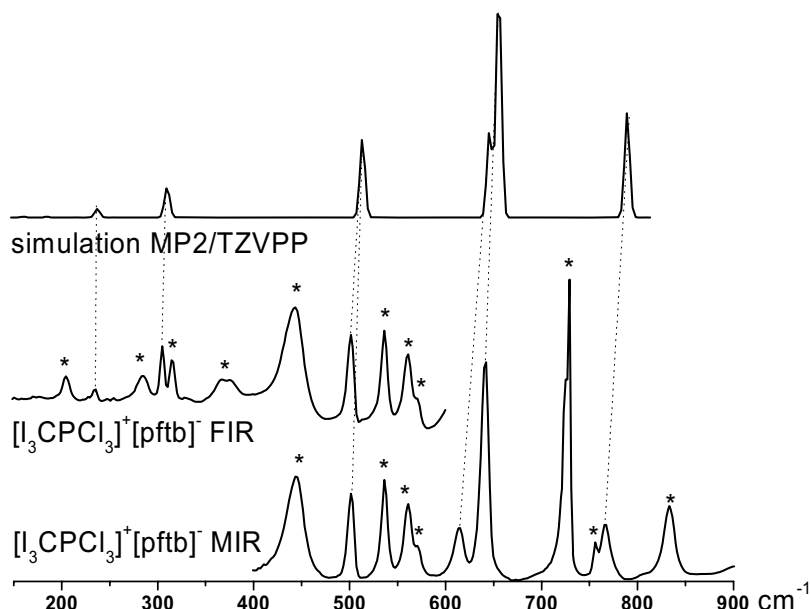


Figure 78: Comparison of the experimental and the simulated IR spectrum of $[\text{I}_3\text{CPCl}_3]^+[\text{pftb}]^-$ **19**. Simulation of the cation modes at the MP2/TZVPP level. Bands marked with * are assigned to the anion.

As seen from Table 59, the blueshifted modes of the PX_3 moieties are also found in the IR spectra of the adducts, while the bands of the Cl_3 part, which are observed in the free cation at 739 cm^{-1} (e' , strong) and 339 cm^{-1} (a_2'' , weak)^[320], are considerably redshifted due to the loss of π -bonding. The C-I stretching mode in all adducts is calculated to occur around 645 cm^{-1} , but as the intensity of this vibrational excitation is very low in the case of the PBr_3 and PI_3 adduct (below 1 km/mol), it is not observed. For the $\text{I}_3\text{C-PCl}_3^+$ cation, the calculated intensity of this vibration is somewhat higher (38 km/mol), and therefore, the IR spectrum of **19** is the only one where the band is observed (weak band at 614 cm^{-1}). The P-X vibration might be compared to two different systems: PX_3 (as pure $\text{P}^{(\text{III})}$ compounds) and PX_4^+ (as model for pure $\text{P}^{(\text{V})}$ character). One of the bands in each spectrum of the adduct is of comparable energy like that in the analogous PX_3 molecules ($\Delta\nu_{\text{max}} = 6\text{ cm}^{-1}$), but another band is found at higher energy (642 cm^{-1} in **19**, 509 cm^{-1} in **20** and 426 cm^{-1} in **21**). In **21**, this energy is even higher

^[x] This relatively expensive computational level has to be chosen, because using BP86/SV(P), the electronic situation in the adducts is not described properly and therefore, the vibrational frequencies are not calculated at the right energies.

than the one of the PX_4^+ cations: 653 cm^{-1} for PCl_4^{+} ^[321], 514 cm^{-1} for PBr_4^{+} ^[48] and 400 cm^{-1} for PI_4^{+} ^[48]. The main contribution to these bands are P-X vibrations, but as they are slightly coupled with C-I vibrations, their energy rises. In **19**, the C-I and P-Cl vibrations are of similar energy, and therefore, the energy remains the same. Nevertheless, this observation can be taken as a proof for partial $\text{P}^{(\text{V})}$ character of the $\text{I}_3\text{C-PX}_3^+$ adducts, which is in good agreement with other experimental and calculated data (see below).

The band with the highest energy is assigned to the $\nu(\text{C-P})$ mode. From **19** to **21**, this energy decreases (from 766 cm^{-1} to 717 cm^{-1}), representing the longer C-P distance (cf. Table 58).

Table 59: IR spectra of the $\text{I}_3\text{C-PX}_3^+$ cations ($\text{X} = \text{Cl-I}$) in **19**, **20** and **21** compared with the calculated vibrational spectra of the I_3CPX_3^+ cations at the MP2/TZVPP level. Exp. intensities: vw = very weak, w = weak, m = medium, calc. intensities in km/mol .

$\text{I}_3\text{CPCl}_3^+$ in 19 exp.	$\text{I}_3\text{CPCl}_3^+$ calc.	$\text{PCl}_3^{[322]}$ exp.	PCl_4^+ exp.	$\text{I}_3\text{CPBr}_3^+$ in 20 exp.	$\text{I}_3\text{CPBr}_3^+$ calc.	$\text{PBr}_3^{[322]}$ exp.	$\text{PBr}_4^{+[48]}$ exp.	I_3CPI_3^+ in 21 exp.	I_3CPI_3^+ calc.	$\text{PI}_3^{[323]}$ exp.	$\text{PI}_4^{+[48]}$ exp.	sym., assignment
81 (0.1)				71 (0.0)				61 (0.0)				$\text{e}, \delta_s(\text{P-X}) / \delta_s(\text{C-I})$
114 (0.0)				99 (0.0)				83 (0.0)				$\text{e}, \delta_a(\text{P-X}) / \delta_a(\text{C-I})$
127 (1.0)				101 (0.1)				84 (0.1)				$\text{a}_1, \delta_s(\text{P-X}) / \delta_s(\text{C-I})$
160 (0.3)				118 (e, 0.0)				103 (0.1)				$\text{e}, \delta_a(\text{P-X}) / \delta_a(\text{C-I})$
184 (0.4)				165 (1.7)				145 (1.1)				$\text{a}_1, \delta_a(\text{P-X}) / \delta_a(\text{C-I})$
234 (vw)	237 (3.1)	260		159 (e, 0.8)				132 (0.2)				$\text{e}, \delta_a(\text{P-X}) / \delta_a(\text{C-I})$
304 (w)	309 (22.0)			221 (a_1 , 1.8)				183				$\text{a}_1, \delta_s(\text{P-X})$
501 (w)	513 (56.3)	507		383 (w)	391 (22.0)	392		326 (vw)	340 (35.8)	303		$\text{a}_1, \delta_a(\text{P-X})$
										325		$\text{e}, \nu_s(\text{P-X})$
614 (w)	645 (31.7)			-	644 (0.8)			-	641 (0.5)			$\text{e}, \nu_a(\text{C-I})$
642 (m)	654 (84.2)		653	509 (m)	523 (89.4)		514	426 (w)	449 (69.1)		400	$\text{e}, \nu_a(\text{P-X})^{(a)}$
766 (w)	789 (750)			756 (vw)	742 (35.8)			717 (w)	694 (12.8)			$\text{a}_1, \nu(\text{P-C})$

^(a) includes small contributions of $\nu_a(\text{C-I})$, leading to a higher energy of this mode.

7.4.4 Bonding in $I_3C-PX_3^+$

Comparison of the Lewis acidity of CI_3^+ and BI_3

If compared to the isoelectronic BI_3 molecule, the CI_3^+ cation is a stronger Lewis acid in the gas phase, but in solution, both species have approximately the same acidity, as judged by their fluoride ion affinities (*FIAs*): $FIA(CI_3^+) = 809 / 299$ kJ/mol and $FIA(BI_3) = 444 / 275$ kJ/mol (gas phase / CH_2Cl_2)^[320]. But in contrast to the boron trihalides, the heavier CX_3^+ cations have two possible coordination sites: the carbon atom (which leads to classically bound adducts) or the halogen atoms (which has been shown by the calculated structures of the water adducts, cf. section 7.3). As it has been shown by NMR data and X-ray diffraction, even with the weak Lewis base PX_3 , the complexes have classical carbon coordinated structures. Similar ethane-like geometries have been observed for the isoelectronic I_3B-PX_3 molecules^{[318][xi]}. The calculated geometries are collected in Table 60.

Table 60: Comparison of the calculated geometries of $I_3E-PX_3^{0/+}$, PX_3 , CI_3^+ and BI_3 (E = B, C; X=Cl-I) at the MP2/TZVPP level. Distances are given in pm, bond angles in °.

	$d(E-P)$	$d(I-E)$	$d(X-P)$	$\angle(I-E-I)$	$\angle(X-P-X)$
$I_3C-PCl_3^+$	182.0	214.9	196.3	112.0	107.7
I_3B-PCl_3	195.4	220.1	199.8	114.7	104.3
$I_3C-PBr_3^+$	184.1	214.9	213.9	111.8	108.2
I_3B-PBr_3	197.3	220.0	217.5	114.7	104.8
$I_3C-PI_3^+$	186.5	214.9	237.2	111.3	108.9
I_3B-PI_3	199.2	219.8	240.6	114.5	105.8
PCl_3	-	-	205.1	-	100.2
PBr_3	-	-	222.5	-	101.0
PI_3	-	-	245.1	-	102.3
CI_3^+	-	202.0	-	120.0	-
BI_3	-	211.3	-	120.0	-

^[xi]Unfortunately, the calculations of I_3B-PX_3 in the literature have been carried out at the B3LYP level with relatively small basis sets. They had to be re-calculated using MP2/TZVPP in order to get reliable data for both systems. DFT methods are not suitable to describe these systems, what can be seen for example from the large difference of the calculated (213 pm) and the experimental (201 pm) B-P bond length in Br_3B-PBr_3 .

It can be seen from Table 60 that all intramolecular distances are longer in the I_3B-PX_3 molecules than those in the $I_3C-PX_3^+$ cations. This may be explained by the positive charge, which introduces Coulomb interactions into the system, when the Cl_3^+ cation binds to the lone pair of the phosphorus atom. This positive charge is missing in BI_3 and therefore, their adducts are weaker bound.

On the oxidation state of the phosphorus in $I_3C-PX_3^+$: $P^{(III)}$ or $P^{(V)}$?

An important question that arises when looking at the structures of the $I_3C-PX_3^+$ cations is the oxidation state of the phosphorus in these adducts, i.e. if these species are better described as $[I_3C \leftarrow P^{(III)}X_3]^+$ or as $[I_3C-P^{(V)}X_3]^+$. To find an answer to this question, one can use the ^{31}P NMR shifts of these complexes and compare them to other systems in which the oxidation state of the phosphorus is clear, e.g. $P^{(III)}X_3$ or $P^{(V)}X_4^+$. They are listed in Table 61.

Table 61: ^{31}P NMR shifts (in ppm) of $I_3CPX_3^+$ and comparison with those of $PX_4^{+[48, 81]}$, $PX_3^{[324]}$, $OPX_3^{[177, 325]}$, $R-PX_3^{+[326]}$ and $I_3B-PI_3^{[318]}$ ($X=Cl-I$). n.r. = not resolved.

X =	Cl	Br	I
$I_3C-PX_3^+$	+76 ($^1J_{C-P} = 29$ Hz)	+39 ($J = \text{n.r.}$)	-70 ($^1J_{C-P} = 42$ Hz)
PX_4^+	+73 – +96 ^[81] (b)	-66 – -80 ^[81] (b)	-494 ^[48] , -519 ^[81] (e), -517 ^[81] (f)
PX_3	+217 ^[324]	+226 ^[324]	+176 ^[324]
OPX_3	-2 ^[325]	-103 ^[325] -65 ^[177] (e)	-332 – -337 ^[177] (d)
$R-PX_3^+$	120 ($R = \text{Me}$) 129 ($R = \text{Et}$)	30.7 ($R = \text{Me}$)	-49 ^[326] ($R = \text{tBu}$) ^(b)
I_3B-PX_3	n.g. ^(a)	+105 ^[318]	-42 ^[318]

(a) n.g. = value is not given in the reference. (b) solid-state MAS NMR. (c) in $Br_3PO-Al(OC(CF_3)_3)_3$. (d) in $I_3PO-Al(OR)_2-(\mu-F)-Al(OR)_3$ with $R = C(CF_3)_3$. (e) in $[PI_4]^+[AsF_6]^-$, MAS NMR. (f) in $[PI_4]^+[SbF_6]^-$, MAS NMR.

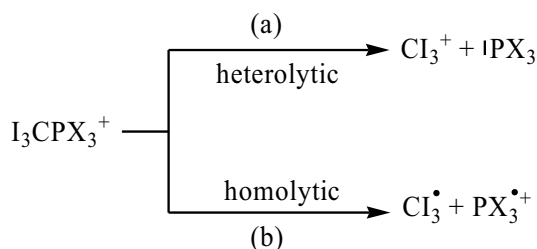
From Cl to I, the ^{31}P NMR shifts of all these compounds shift to higher field, a fact that can be explained by increasing relativistic contributions (“spin-orbit coupling”) for the heavier halogens (“inverse halogen dependence” *IHD* of the chemical shift of pentavalent $P^{(V)}$ -compounds due to a Fermi contact mechanism involving orbitals with s-character). The most drastic high-field shift is observed for the $P^{(V)}X_4^+$ cations and for $OP^{(V)}X_3$. By contrast $P^{(III)}X_3$, which utilizes only orbitals of 3p character for the P-X bonds, is not affected by the *IHD*:

$\Delta\delta(IHD)$ in PX_3 from Cl to I is only -50 ppm. Now we turn to the $I_3C-PX_3^+$ cations: If compared to the trihalides and the PX_4^+ cations, the ^{31}P chemical shifts are always $\delta(PX_3) > \delta(I_3C-PX_3^+) > \delta(PX_4^+)$ and $\Delta\delta(IHD) = -146$ ppm. This finding indicates that the p-character of the P-X bonds in the adducts is higher in the adducts than in PX_4^+ and correspondingly a weaker Fermi-contact-mechanism transmitting the relativistic influence of the halogens to the P nucleus is observed. Overall stronger s-p separation and more $P^{(III)}$ character follows for $I_3C-PX_3^+$. Roughly it might be said that the phosphorous atom has 50% of +III and 50 % of +V character *in solution*. As an even better comparison than PX_4^+ , one can use the OPX_3 series, because in these compounds, the number of the halogen atoms bound to the phosphorus atom is the same as in the adducts. But also in these $P^{(V)}$ compounds, the ^{31}P NMR shifts have a stronger influence by *IHD* ($\Delta\delta(IHD) = -335$ ppm) again suggesting roughly 50 % $P^{(V)}$ character.

As another point of evidence for the ambivalent character of the oxidation state of the phosphorus atom one can consider the P-X distances, however this time in the solid state: in all three adducts, the P-X bonds are considerably shorter than those in the uncomplexed PX_3 molecules (Table 60) and rather similar to those in the PX_4^+ cations (within 2 to 3 pm: 198 pm in $PCl_4^{+[327]}$, 211.1 pm in $PBr_4^{+[48]}$ and 237.0 pm in $PI_4^{+[48]}$). This would be in agreement with a rather high $P^{(V)}$ character *in the solid state*. This leads us to another approach to reveal the nature of the P-C bond:

Is the C-P bond in $I_3C-PX_3^+$ cations dative or covalent?

Haaland has developed a simple, but successful method to answer the question^[312] if a bond can be considered as dative or covalent. To classify the donor-acceptor bond in the $I_3C-PX_3^+$ cations (X = Cl-I) according to these categories we analyzed the energetics of homolytic and heterolytic cleavage of this bond (see Scheme 11). If the pathway (a) is favored, the bond can be considered to be dative; otherwise the two atoms are connected through a covalent bond.



Scheme 11: Heterolytic (a) vs. homolytic (b) cleavage of the C-P bond in $I_3CPX_3^+$ cations.

The reaction enthalpies for both bond cleavage pathways are collected in Table 62, together with the analogous reactions of $\text{I}_3\text{C-AsI}_3^+$ and $\text{I}_3\text{B-PX}_3$. It can be seen that for all adducts, the heterolytic dissociation reaction is more favorable and, therefore, the E-P (resp. C-As) bond in all adducts is considered dative. $\text{I}_3\text{C-PX}_3^+$ and $\text{I}_3\text{B-PX}_3$ dissociate giving systems that differ in their charge: Since the $\text{I}_3\text{C-PX}_3^+$ adducts are formed by the reaction between a cation and a neutral molecule, the attractive force is much higher and therefore, these adducts are stronger bound. The extremely high energies that are needed for the homolytic cleavage of the $\text{I}_3\text{B-PX}_3$ molecules is caused by the fact that during this process, a cation (PX_3^{++}) and an anion (BI_3^-) are formed, which is energetically disadvantageous and only in part compensated by solvation.

Table 62: Reaction enthalpies of the heterolytic and homolytic cleavage of the E-P bond in $\text{I}_3\text{E-PX}_3^{0/+}$ (E = B, C; X = Cl-I) and $\text{I}_3\text{C-AsI}_3^+$ according to Scheme 11. Calculations at the MP2/TZVPP level, all values are given in kJ/mol.

reaction	$\Delta_r H^\circ(\text{gas})$	$\Delta_r G^\circ(\text{gas})$	$\Delta_r G^\circ(\text{CH}_2\text{Cl}_2)$
eq. 63 (a) $\text{I}_3\text{C-PCl}_3^+ \rightarrow \text{Cl}_3^+ + \text{PCl}_3$	160.7	108.5	88.9
eq. 63 (b) $\text{I}_3\text{C-PCl}_3^+ \rightarrow \text{Cl}_3^\bullet + \text{PCl}_3^{++}$	402.9	342.2	285.2
eq. 64 (a) $\text{I}_3\text{C-PBr}_3^+ \rightarrow \text{Cl}_3^+ + \text{PBr}_3$	174.9	122.7	89.6
eq. 64 (b) $\text{I}_3\text{C-PBr}_3^+ \rightarrow \text{Cl}_3^\bullet + \text{PBr}_3^{++}$	380.6	319.8	275.6
eq. 65 (a) $\text{I}_3\text{C-PI}_3^+ \rightarrow \text{Cl}_3^+ + \text{PI}_3$	210.2	158.2	120.4
eq. 65 (b) $\text{I}_3\text{C-PI}_3^+ \rightarrow \text{Cl}_3^\bullet + \text{PI}_3^{++}$	354.0	293.1	261.8
eq. 66 (a) $\text{I}_3\text{C-AsI}_3^+ \rightarrow \text{Cl}_3^+ + \text{AsI}_3$	165.0	115.9	73.0
eq. 66 (b) $\text{I}_3\text{C-AsI}_3^+ \rightarrow \text{Cl}_3^\bullet + \text{AsI}_3^{++}$	332.1	273.6	239.2
eq. 67 (a) $\text{I}_3\text{B-PCl}_3^+ \rightarrow \text{BI}_3 + \text{PCl}_3$	72.9	23.1	32.4
eq. 67 (b) $\text{I}_3\text{B-PCl}_3^+ \rightarrow \text{BI}_3^\bullet + \text{PCl}_3^{++}$	899.1	840.4	476.0
eq. 68 (a) $\text{I}_3\text{B-PBr}_3^+ \rightarrow \text{BI}_3 + \text{PBr}_3$	78.2	28.6	29.5
eq. 68 (b) $\text{I}_3\text{B-PBr}_3^+ \rightarrow \text{BI}_3^\bullet + \text{PBr}_3^{++}$	867.9	809.3	453.8
eq. 69 (a) $\text{I}_3\text{B-PI}_3^+ \rightarrow \text{BI}_3 + \text{PI}_3$	97.8	48.4	49.6
eq. 69 (b) $\text{I}_3\text{B-PI}_3^+ \rightarrow \text{BI}_3^\bullet + \text{PI}_3^{++}$	825.6	767.0	429.3

For all $\text{I}_3\text{E-PX}_3^{0/+}$, the adduct stabilities both in the gas phase and in solution increase from Cl to I for the heterolytic path (Figure 79), which is in good agreement with the increasing Lewis basicity of the PX_3 molecules. The only exception is $\Delta_r G(\text{CH}_2\text{Cl}_2)$ of $\text{I}_3\text{B-PCl}_3$ and $\text{I}_3\text{B-PBr}_3$, which are almost equal.

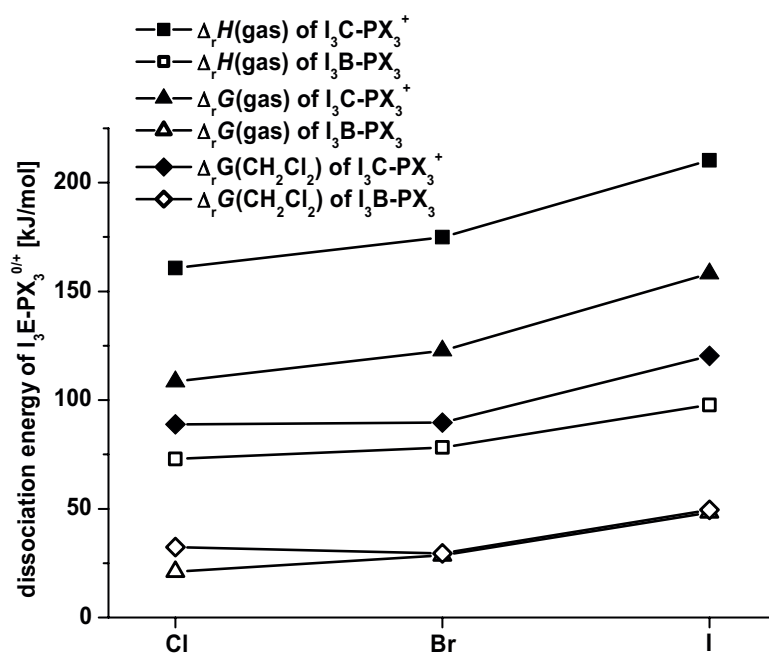


Figure 79: Heterolytic bond dissociation energies ($\Delta_r H$ (gas) $\Delta_r G$ (gas) and $\Delta_r G(\text{CH}_2\text{Cl}_2)$) of $\text{I}_3\text{E-PX}_3^{0/+}$ (E = B, C; X = Cl-I). All values are given in kJ/mol.

In $\text{I}_3\text{C-PI}_3^+$, the difference between the heterolytic and homolytic dissociation path is rather small if compared to the other adducts, indicating partial covalent contributions. This is also underlined by the ^{31}P NMR shifts (Table 61) as well as by the partial charges of the P and C atoms (Table 63) obtained by the paboon population analysis. In the case of the PCl_3 and PBr_3 adducts, the phosphorus atoms bear a full positive charge, while for the PI_3 adducts, the charge is diminished due to the lower electronegativity of the iodine atoms, which leads also to covalent contributions.

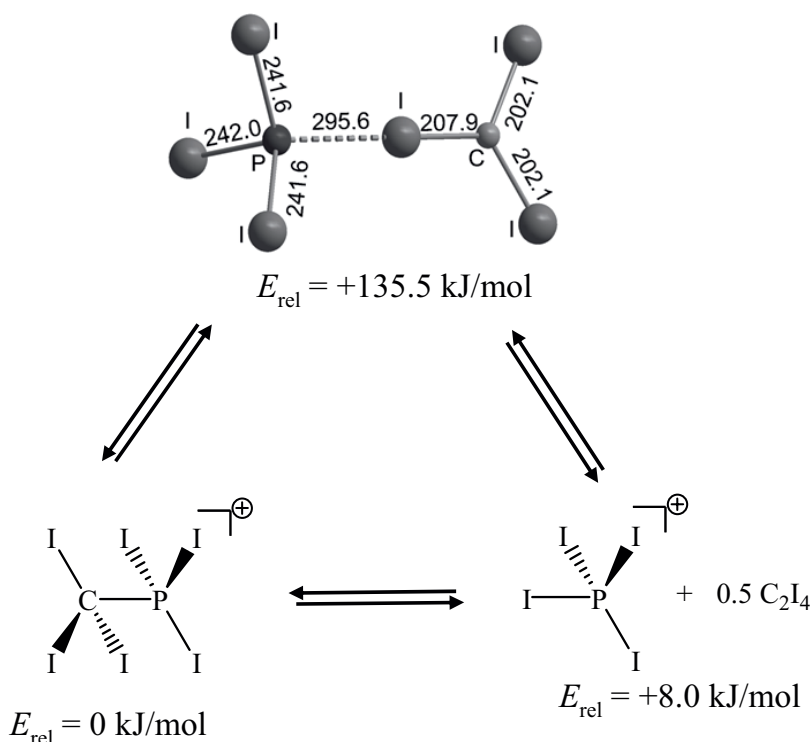
Table 63: Calculated partial charges q of in $I_3E-PX_3^{0/+}$, PX_3 and $EI_3^{0/+}$ ($E = B; C; X = Cl-I$), according to the paboon method (population analysis based on occupation numbers).

	$q(P)$	$q(E)$	$q(I)$	$q(X)$
$I_3C-PCl_3^+$	+1.194	-0.467	+0.166	-0.072
$I_3C-PBr_3^+$	+1.065	-0.467	+0.165	-0.031
$I_3C-PI_3^+$	+0.591	-0.454	+0.158	+0.130
$I_3C-AsI_3^+$	+0.627	-0.427	+0.161	+0.106
I_3B-PCl_3	+1.218	-0.753	-0.017	-0.137
I_3B-PBr_3	+1.073	-0.739	-0.013	-0.096
I_3B-PI_3	+0.614	-0.723	-0.011	+0.048
PCl_3	+0.633	-	-	-0.211
PBr_3	+0.514	-	-	-0.171
PI_3	+0.107	-	-	-0.036
Cl_3^+	-	-0.158	+0.386	-
BI_3	-	-0.393	+0.131	-

7.4.5 Further Reactivity of $I_3C-PI_3^+$: Evidence for a Non-Classical $I_2C-I\cdots PI_3^+$ Intermediate

When $[Cl_3]^+[pftb]^-$ is reacted with PI_3 in CH_2Cl_2 and left at ambient temperature for a few hours before cooling down for crystallization, two different compounds crystallize: $[I_3C-PI_3]^+[al-f-al]^-$ **23** and $[PI_4]^+[pftb]^-$ **24**. Both structures are hampered by disorder in the anion and/or cation part and are therefore mainly seen as structural proof for their formation. A section of the solid-state structure of **23** is shown in the appendix 12.5. For **24** it is interesting that not one of the two known modifications (cf. Ref. 48 and 319) is found, but a new one. The bond lengths are comparable in both modifications, but as the crystal structure obtained from **24** is not of a very good quality, it will not be discussed here.

The formation of the side product **23** can best be explained by a non-classical, iodine-coordinated $I_2Cl\cdots PI_3^+$ adduct, in which the Cl_3 moiety acts as an iodine donor towards the PI_3 (see Scheme 12). The PI_4^+ cation, which is formed in this reaction, is known to decompose the $[pftb]^-$ anion above $0^\circ C$ giving the fluorine-bridged $[al-f-al]^-$ anion^[177].



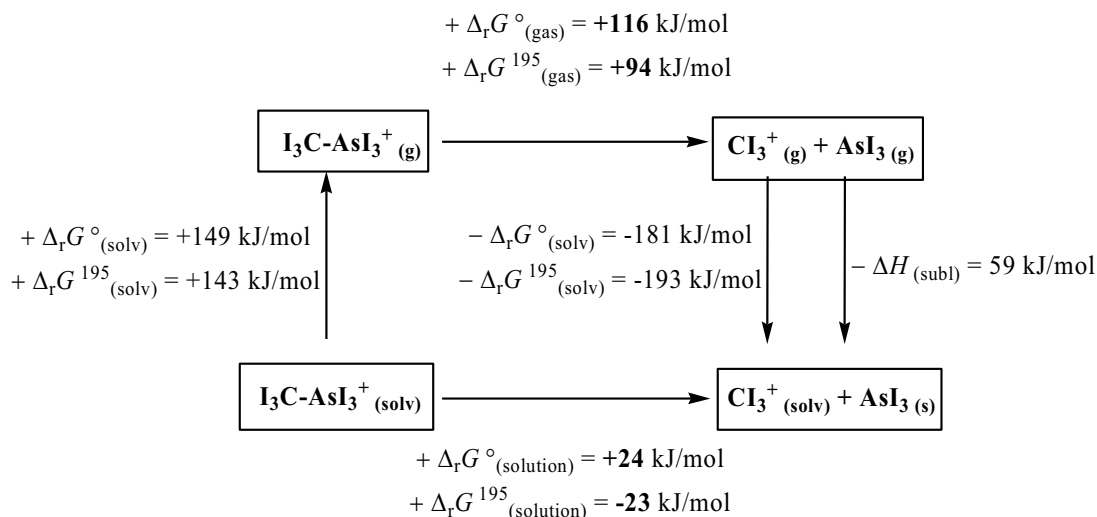
Scheme 12: Equilibria between the C and I coordinated adduct of Cl_3^+ and PI_3 with PI_4^+ and C_2I_4 as an explanation for PI_4^+ formation. Relative energies are given as $\Delta_r G^\circ$ values in CH_2Cl_2 .

Quantum chemical calculations show that these dismutation reactions are – for $\text{I}_3\text{C-P-Cl}_3^+$ and $\text{I}_3\text{C-P-Br}_3^+$ – exergonic in CH_2Cl_2 (Table 64), and only slightly endergonic in the case of the $\text{I}_3\text{C-P-I}_3^+$ cation. Therefore, it seems reasonable to find formation of **24**. However, the energetic difference between the classical carbon-bound and the non-classical iodine-bound isomer is 135.5 kJ/mol in CH_2Cl_2 , a barrier which has to be overtaken first before the PI_4^+ is formed. Due to this high energy difference it can be understood that formation of **24** is slow.

Table 64: Gibbs free energies ($\Delta_r G^\circ$ and $\Delta_r G^{195}$ in CH_2Cl_2) of the dismutation reactions of $\text{X}_3\text{P-Cl}_3^+$ ($\text{X} = \text{Cl-I}$) cations at the MP2/TZVPP level (in kJ/mol).

reaction	$\Delta_r G^\circ$ (CH_2Cl_2) [kJ/mol]	$\Delta_r G^{195}$ (CH_2Cl_2) [kJ/mol]
eq. 70 $\text{Cl}_3\text{P-Cl}_3^+ \rightarrow \text{PCl}_3\text{I}^+ + \frac{1}{2} \text{C}_2\text{I}_4$	-9.4	-13.9
eq. 71 $\text{Br}_3\text{P-Cl}_3^+ \rightarrow \text{PBr}_3\text{I}^+ + \frac{1}{2} \text{C}_2\text{I}_4$	-2.2	-6.4
eq. 72 $\text{I}_3\text{P-Cl}_3^+ \rightarrow \text{PI}_4^+ + \frac{1}{2} \text{C}_2\text{I}_4$	8.0	2.0

For **22**, all attempts to crystallize the product remained unsuccessful, and the only species crystallizing from this system was AsI₃. Its room-temperature structure has already been determined before^[328] and therefore, this structure is not discussed here.



Scheme 13: Born-Haber-cycle for the equilibrium between $\text{I}_3\text{C-AsI}_3^+$ and $\text{Cl}_3^+ + \text{AsI}_3$. The sublimation enthalpy $\Delta H_{(\text{subl})}$ of AsI_3 has been calculated to be 59.3 kJ/mol ^[329].

The crystallization of AsI_3 can be understood if calculating the dissociation enthalpies according to the Born-Haber cycle sketched in Scheme 13. If the reaction enthalpies are calculated at different temperatures (195.15 and 298.15 K) it can be seen, that in the gas phase the adduct is stable against dissociation. In solution, by contrast, the complex is more stable at higher temperatures and at lower temperatures a disproportionation with precipitation of AsI_3 appears to be more likely. However, the adduct could not be crystallized at room temperature because of beginning anion degradation.

7.5 Concluding Remarks

With the WCAs [pftb]⁺ and [al-f-al]⁺ it is possible to stabilize the Cl₃⁺ salts **15** and **16** in the condensed phase. Both, from experimental data (bond lengths, vibrational and electronic excitations) and theoretical considerations (trends of the Lewis acidities, MO energies), it becomes evident that the halocarbenium ions behave different from the isoelectronic BX₃ molecules. In the CX₃⁺ cations, partial C-X double bonds are formed, and the positive charge resides on the X atoms: The heavier the halogen is, the better the positive charge can be delocalized due to the higher σ and π donor ability of Br and I. In haloboranes, the positive charge is missing, and therefore, there is no driving force for π bond formation.

Attempts to prepare CHI₂⁺ and CH₂I⁺ salts from CHI₃ or CH₂I₂/Ag[pftb] mixtures remained unsuccessful; the reaction with CH₂I₂ lead to the formation of the adduct [Ag(CH₂I₂)₃]⁺[pftb]⁻ **17**, while for HCl₃, dismutation with formation of **15** as well as **17** was observed.

Within this thesis, highly accurate and reliable $\Delta_f H^\circ$ values for halomethanes, halomethyl cations and the isoelectronic boron compounds have been established based on a combination of exactly determined experimental data together with high-level quantum chemical calculations. These $\Delta_f H^\circ$ values and the derived mean bond enthalpies (*mBEs*) are very useful for comparing the bonding in the isoelectronic, but different compounds. The different behaviour of the halomethyl cations and the haloboranes has also been shown in a theoretical study of the water adducts of these species. Although the H₂O→EX₃^{0/+1} species are isoelectronic, their reactivity and bonding is totally different. The BX₃ molecules form “classical” adducts with strong B-O bonds that are stabilized by additional H-bonding (X = F). The latter is responsible for the similarity of the *WCEs* of all H₂O→BX₃ adducts. When the *WCEs* are corrected for H-bonding contributions, the *WCEs* follow the ordering as expected from the known Lewis acidities of the boron halides, i.e. *WCE*(BF₃) < *WCE*(BCl₃) < *WCE*(BBr₃) ≈ *WCE*(BI₃). The similarity of the E-X bond lengths in neutral Ph-X, halogenated aminoboranes or trihaloborazines and BX₃ - in contrast to the much shortened E-X bond lengths in CX₃⁺ and Do→BX₂⁺ - indicates that the influence of π -bonding on the structure of neutral BX₃ (X = Cl-I) is small and not structure determining. The formation of weak “non-classical” water complexes of CX₃⁺ (X = Cl-I) rather than covalent protonated trihalomethanols suggests that the delocalization of the positive charge to the less electronegative halogen atoms provides a sufficient driving force to form stable “non-

classical" π -bonded ions in preference over classical all σ -bonded species. Thus, in the heavier CX_3^+ cations the bond enthalpy (BE) of a localized C-O σ bond is lower than the BE of a delocalized C-X π bond.

In order to find an experimental proof for such an iodine-coordinated adduct, weak Lewis bases were reacted with the CI_3^+ cation. As Lewis bases, weak nucleophiles that mimic water (Et_2O) or other electronically deactivated weak nucleophiles (PX_3 , $X = Cl-I$; AsI_3) have been chosen. With Et_2O as a base, the cation behaves as a strong Lewis acid and cleaves the ether to give I_3C-OEt , C_2H_4 and $[H(Et_2O)_2]^+$. By contrast PX_3 and AsI_3 coordinate to the CI_3^+ cations and the adducts have classical, carbon-bound ethane-like structures, as proven by X-ray single-crystal diffraction, IR- and NMR spectroscopy. From variable temperature ^{13}C NMR studies, it followed for the $I_3C-AsI_3^+$ salt that the equilibrium between CI_3^+ and AsI_3 is reversible and temperature dependent in solution. The $I_3C-PI_3^+$ salt decomposes at room temperature giving PI_4^+ and C_2I_4 , likely through an iodine coordinated $I_2C-I\cdots PI_3^+$ intermediate. Thus CI_3^+ may also act as I^+ donor, like predicted from the theoretical study on the water adducts.

In Table 65, all experimentally known characteristics about the halomethylcations CX_3^+ and $CH_nX_{3-n}^+$ ($X = F-I$; $n = 1, 2$) are summarized, together with calculated values. From the values collected in Table 65 it can be seen that for the heavier $CH_nX_{3-n}^+$ cations, the C-X bond lengths shrink with decreasing halogen content (e.g. 204.0 pm in CI_3^+ , 200.0 pm in CHI_2^+ and 195.6 pm in CH_2I^+). This indicates higher partial double bond character for the cations with lower halogen content. By contrast, in the fluorine containing species, the C-F distance remains unchanged. This observation is in good agreement with little impact of π bonding to the C-F bond. Overall, the conclusions drawn from the CX_3^+ cations hold: the heavier the halogen is, the more π bonding and charge delocalization is favored. In CHX_2^+ and CH_2X^+ , the total positive charge of the cation has to be transferred to only 2 resp. 1 halogen atom, what gives a formal bond order of 1.5 for CHX_2^+ and even 2.0 for CH_2X^+ , resulting in considerably shorter C-X bonds. The stronger C-X bonds can also be observed in the IR spectra: for the heavier halogens, the C-X stretches shift to higher energy when more hydrogen atoms are present, while for the fluorine containing cations, the C-F frequency is even a bit lowered.

Table 65: Characteristics of CX_3^+ and $CH_nX_{3-n}^+$ ($X = F, I$; $n = 1, 2$). Values obtained from this work are marked in bold.

known	$d(E-X)$ [pm]		$\delta^{13}C$ [ppm]		ν (IR) [cm^{-1}]		λ_{max} [nm] ^(g)		$\Delta_f H^\circ$ [kJ/mol]	
	exp. ^(a)	calc. ^(b)	exp.	calc.	exp. ^(d)	calc. ^(f)	exp.	calc. ^(h)	exp.	establ. ⁽ⁱ⁾
CF_3^+	g	–	123.4	–	798, 1622, 1662 ^[259, 330]	573(11), 766(56), 1019(0), 1640(424)	–	115	365 ^[261]	416
CCl_3^+	g, sol, s	162.1 ^[58]	165.1	237.1 ^[58]	1037 ^[258]	304(0), 506(0), 527(0), 1011(254)	–	230	826 ^[261, 278]	850
CBr_3^+	g, sol, s	180.7 ^[58]	181.6	209.7 ^[58]	874 ^[268, 331]	177(0), 312(0), 423(3), 860(204)	–	151(sh), 220, 295	1004 ^[261, 263]	992
CI_3^+	g, sol, s	201.3 (in <u>15</u>) 200.6 (in <u>16</u>)	204.0	97.0	123.8	166(0), 209(0), 340(10), 715(174)	274, 307, 349	121, 148(sh), 202, 230, 308, 383	$\approx 1047^{(i)}$	1116

^(a) g = gas phase, sol = solution, s = solid state. ^(b) optimized at the ccscd(t)/aug-cc-pVTZ level. ^(c) $\delta^{13}C_{calc}$ [ppm] = 19.80 (CH_2^+), 21.08 (CH_3^+). ^(d) measured in the matrix, except CI_3^+ . ^(e) CD_2F^+ . ^(f) calculated at the (RI)BP86/SV(P) level. Values in parenthesis: IR intensities in $km\ mol^{-1}$. ^(g) only excitations from 100 – 800 nm have been considered. ^(h) TD-DFT at the (RI)BP86/SV(P) level. ⁽ⁱ⁾ values established through isodesmic reactions. ^(j) J. L.M. Abboud, personal communication. The value of 531 kJ mol^{-1} given in Ref. 225 is wrong.

Table 65 continued: Characteristics of CX_3^+ and $\text{CH}_n\text{X}_{3-n}^+$ (X = F-I; n = 1, 2). Values obtained from this work are marked in bold.

	known	$d(\text{E-X})$ [pm]		$\delta^{13}\text{C}$ [ppm]		ν (IR) [cm^{-1}]		λ_{max} [nm] ^(g)		$\Delta_f H^\circ$ [kJ/mol]	
	exp. ^(a)	exp.	calc. ^(b)	exp.	calc.	exp. ^(d)	calc. ^(f)	exp.	calc. ^(h)	exp.	establ. ⁽ⁱ⁾
CHF_2^+	g		123.3	–	–	1608 ^[260]	652(31), 1027(0), 1270(53), 1624(326), 3088(32)	–	118(sh), 178	599 ^[261]	602
CHCl_2^+	g		162.8	–	–	845, 860, 1044, 1291, 3033 ^{[258, 259,} 264-267]	350(2), 826(20), 851(19), 1044(253), 1282(36), 3074(37)	250 ^{[259](d)}	151(sh), 226	884 ^[261]	888
CHBr_2^+	g		178.5	–	–	897, 1229 ^{[260, 268,} 332]	213(0), 658(8), 778(34), 900(224), 1225(30), 3084(43)	–	145(sh), 190, 274	976 ^{[261,} 263]	984
CHI_2^+	g		200.0	–	229.8^(c)	–	43(0), 526(2), 686(45), 776(197), 1198(38), 3088(41)	–	130, 181, 262, 349	1087 ^{[261,} 298]	1059

^(a) g = gas phase, sol = solution, s = solid state. ^(b) optimized at the ccscd(t)/aug-cc-pVTZ level. ^(c) $\delta^1\text{H}_{\text{calc}}$ [ppm] = 19.80 (CHI_2^+), 21.08 (CH_2I^+). ^(d) measured in the matrix, except ClI_3^+ . ^(e) CD_2F^+ . ^(f) calculated at the (RI)BP86/SV(P) level. Values in parenthesis: IR intensities in km mol^{-1} . ^(g) only excitations from 100 – 800 nm have been considered. ^(h) TD-DFT at the (RI)BP86/SV(P) level. ⁽ⁱ⁾ values established through isodesmic reactions. ^(j) J. L.M. Abboud, personal communication. The value of 531 kJ/mol given in Ref. 225 is wrong.

Table 65 continued: Characteristics of CX_3^+ and $CH_nX_{3-n}^+$ (X = F-I; n = 1, 2). Values obtained from this work are marked in bold.

known		$d(E-X)$ [pm]		$\delta^{13}C$ [ppm]		ν (IR) [cm^{-1}]		λ_{max} [nm] ^(g)		$\Delta_f H^\circ$ [kJ/mol]	
exp. ^(a)		exp.	calc. ^(b)	exp.	calc.	exp. ^(d)	calc. ^(f)	exp.	calc. ^(h)	exp.	establ. ⁽ⁱ⁾
CH_2F^+	g	123.4	—	—	—	1530±30 ^{[267](c)}	1210(15), 1224(4), 1402(102), 1575(68), 2986(6), 3145(48)	—	—	838 ^[261]	824
CH_2Cl^+	g	159.7	—	—	—	1040±30 ^[266, 267]	1015(0), 1027(81), 1087(28), 1418(0), 3011(22), 3147(60)	—	172	955 ^[261]	956
CH_2Br^+	g	174.9	—	—	—	860±30 ^[266, 267]	854(62), 946(2), 1032(39), 1390(0), 3023(31), 3160(63)	—	199	988 ^[261, 263]	1004
CH_2I^+	g	195.6	—	287.1^(c)	—	—	726(42), 860(5), 962(47), 1359(0), 3034(39), 3173(59)	—	241	1029 ^[261, 270]	1030

^(a) g = gas phase, sol = solution, s = solid state. ^(b) optimized at the ccscd(t)/aug-cc-pVTZ level. ^(c) δ^1H_{calc} [ppm] = 19.80 (CH_2I^+), 21.08(CH_2F^+). ^(d) measured in the matrix, except Cl_3^+ . ^(e) CD_2F^+ . ^(f) calculated at the (RI)BP86/SV(P) level. Values in parenthesis: IR intensities in $km\ mol^{-1}$. ^(g) only excitations from 100 – 800 nm have been considered. ^(h) TD-DFT at the (RI)BP86/SV(P) level. ⁽ⁱ⁾ values established through isodesmic reactions. ^(j) J. L.M. Abboud, personal communication. The value of 531 kJ/mol given in Ref. 225 is wrong.

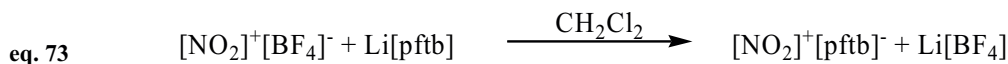
8 Synthesis, Characterization and Reactivity of $[\text{NO}_2]^+[\text{pftb}]^-$ **25**

The NO_2^+ cation plays an important role in many different fields of chemistry, e.g. it is the active species in nitration reactions of organic compounds. For these nitration reactions, the standard way is the use of nitrating acid, but many substances are not compatible with these hard reaction conditions. Therefore, NO_2^+ salts of WCAs are ideal, as they provide access to the nitrating species under mild conditions. Some NO_2^+ salts with nitratometallate counterions like $[\text{NO}_2]^+[\text{Ga}(\text{NO}_3)_4]^-$ are also used as attractive carbon- and hydrogen-free single-source precursors for the chemical vapor decomposition (CVD) of metal oxide films^[333]. Beside that, the NO_2^+ cation is a strong oxidizing agent (with an electron affinity of 9.60 eV^[334]) and the resulting species NO_2 is gaseous so it can very easily be removed after the reaction.

Some of its salts like $[\text{NO}_2]^+[\text{BF}_4]^-$ **26**, $[\text{NO}_2]^+[\text{ClO}_4]^-$ or $[\text{NO}_2]^+[\text{SbF}_6]^-$ are commercially available, but they are not or only hardly soluble in organic solvents. To overcome that problem and to make the NO_2^+ cation accessible in non-polar solvents like CH_2Cl_2 , the idea was to partner it with a large, weakly coordinating anion, which is robust enough not to react itself with the cation. The WCAs $[\text{pftb}]^-$, $[\text{f-alor}_3]^-$ ($[\text{f-alor}_3]^- = [\text{F-Al}(\text{OC}(\text{CF}_3)_3)_3]^-$)^[143] and $[\text{al-f-al}]^-$ ^[52] have been chosen as possible candidates for such salts.

8.1 Synthesis and NMR characterization

When reacting $[\text{NO}_2]^+[\text{BF}_4]^-$ **26** with $\text{Li}[\text{pftb}]$ in CH_2Cl_2 , the highly soluble $[\text{NO}_2]^+[\text{pftb}]^-$ **25** formed in one preparation by the following metathesis reaction (eq. 73):

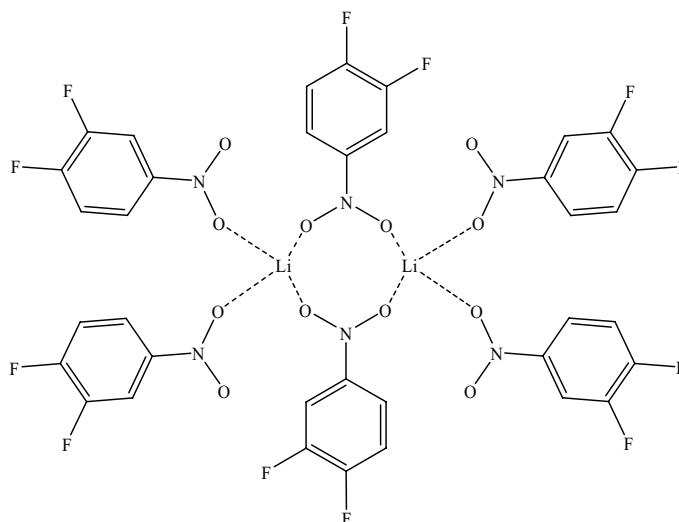


Many attempts to reproduce this result in CH_2Cl_2 as well as in SO_2 and 1,2-Difluorobenzene failed with various changing conditions (Table 66), even with $[\text{NO}_2]^+[\text{SbF}_6]^-$ as metathesis salt.

Table 66: Various attempts to synthesize $[\text{NO}_2]^+[\text{pftb}]^-$ **25**

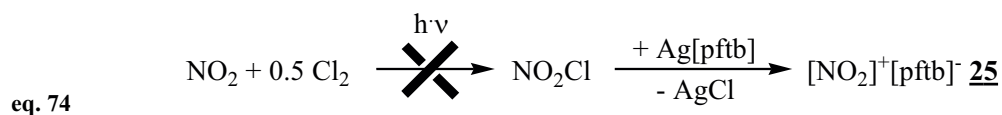
reactands	solvent(s)	treatment	observation
$\text{Li}[\text{pftb}] + [\text{NO}_2]^+[\text{BF}_4]^-$ 26	CH_2Cl_2	stirring at r.t., 2 days	no reaction
$\text{Li}[\text{pftb}] + [\text{NO}_2]^+[\text{BF}_4]^-$ 26	CH_2Cl_2	ultrasonic bath, 1 day	no reaction
$\text{Li}[\text{pftb}] + [\text{NO}_2]^+[\text{BF}_4]^-$ 26	SO_2	stirring at r.t.	no reaction
$\text{Li}[\text{pftb}] + [\text{NO}_2]^+[\text{SbF}_6]^-$	SO_2	stirring at r.t.	no reaction
$\text{Li}[\text{pftb}] + [\text{NO}_2]^+[\text{BF}_4]^-$ 26	1.) 1,2- $\text{C}_6\text{H}_4\text{F}_2$ 2.) CH_2Cl_2	stirring at r.t.	gas formation, nitration of 1,2- $\text{C}_6\text{H}_4\text{F}_2$

When the reaction of $\text{Li}[\text{pftb}]$ with $[\text{NO}_2]^+[\text{BF}_4]^-$ **26** is carried out in 1,2- $\text{C}_6\text{H}_4\text{F}_2$, the solvent is nitrated to give 3,4-Difluoronitrobenzene, which coordinates to the lithium cations, giving $[\text{Li}_2(3,4\text{-C}_6\text{H}_4\text{F}_2\text{NO}_2)_6]^{2+}[\text{pftb}]_2^-$ **27** (Figure 80).

**Figure 80:** Schematic drawing of the $[\text{Li}_2(3,4\text{-C}_6\text{H}_4\text{F}_2\text{NO}_2)_6]^{2+}$ dication in **27**.

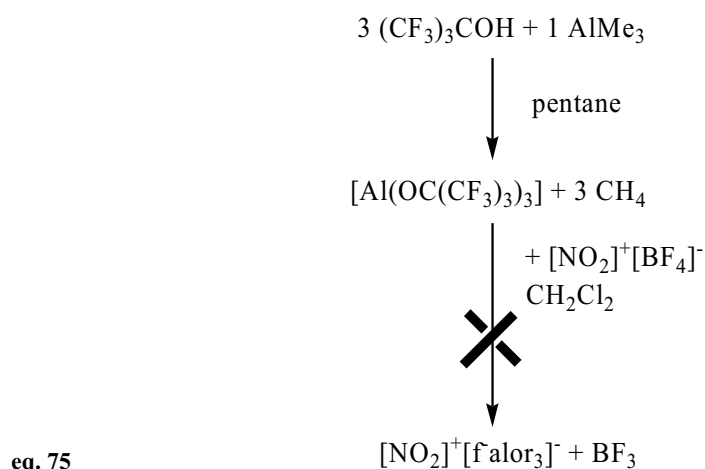
Unfortunately it is still not understood why **25** formed without any problems in the first preparation but never again in later attempts.

To overcome this and as an alternative route, the *in situ* formation of molecular NO₂Cl from NO₂/0.5 Cl₂ and subsequent reaction with Ag[pftb] was tried (eq. 74).

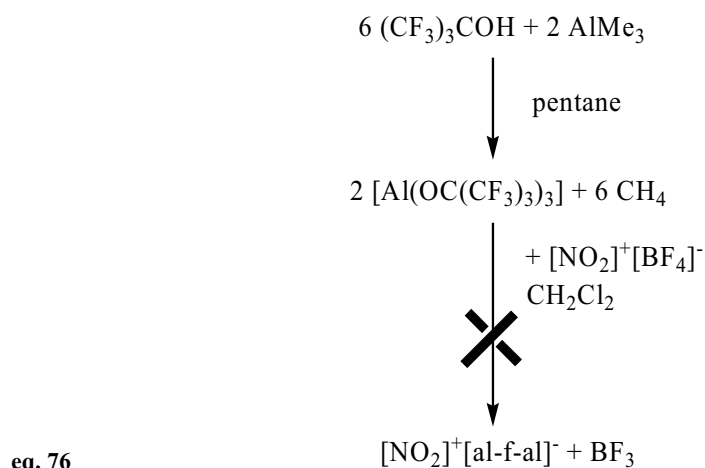


But since the irradiation of the NO₂ / Cl₂ mixture did not lead to any NO₂Cl formation (the pressure in the reaction vessel remained unchanged), this mixture was condensed onto the Ag[pftb] anyway, but without leading to the desired product (only minor AgCl precipitation).

As the WCA [f-alor₃][−] has some interesting properties – e.g. it is able to stabilize highly reactive cations like [SiMe₃]⁺ in an ion-like fashion^[335] – [NO₂]⁺[f-alor₃][−] would be an ideal precursor salt for such systems. But the reaction (eq. 75) did not give the intended product and only led to the re-crystallization of [NO₂]⁺[BF₄][−] 26.



In an analogous reaction, the synthesis of [NO₂]⁺[al-f-al][−] was planned (eq. 76).



The first step – the formation of $[\text{Al}(\text{OC}(\text{CF}_3)_3)_3]$ – was monitored via measuring the volume of methane which is produced. After all AlMe_3 had reacted, $[\text{NO}_2]^+[\text{BF}_4]^-$ **26** was added. The reaction mixture then turned orange-brown, and one of the crystals obtained from this reaction turned out to be the starting material $[\text{NO}_2]^+[\text{BF}_4]^-$ **26**.

A reason why both the reaction according to eq. 75 and eq. 76 did not give the desired NO_2^+ salts might be the known side reaction of the $[\text{Al}(\text{OC}(\text{CF}_3)_3)_3]$ intermediate^[336], which is not stable as such and tends to react with itself at temperatures above 0°C or in solvents like CH_2Cl_2 . In a second attempt, directly after the addition of $[\text{NO}_2]^+[\text{BF}_4]^-$ **26** 20 mL CH_2Cl_2 were condensed onto the mixture. Also here, re-crystallisation of $[\text{NO}_2]^+[\text{BF}_4]^-$ **26** was observed (X-ray unit cell determination). In the ^{19}F NMR which has been measured of the reaction mixture, no $[\text{al-f-al}]^-$ formation was observed (only one peak at -76 ppm, CF_3 groups). In the ^{14}N NMR, no signals at all were observed.

If the reaction is carried out using the room temperature stable fluorobenzene adduct of $\text{Al}(\text{OC}(\text{CF}_3)_3)$ and 1,2-difluorobenzene as a solvent, the reaction with $[\text{NO}_2]^+[\text{BF}_4]^-$ **26** only leads to nitration of the solvent. The 3,4-difluoronitrobenzene formed in this reaction is a stronger Lewis base than fluorobenzene or difluorobenzene and therefore forms the adduct 3,4- $\text{C}_6\text{H}_3\text{F}_2\text{NO}_2 \cdot \text{Al}(\text{OC}(\text{CF}_3)_3)_3$ **28**. This adduct remains stable, and the ligand can not be removed even in the vacuum ($1 \cdot 10^{-3}$ mbar).

8.2 Solid-State Structures

*Solid-State Structures of $[\text{NO}_2]^+[\text{pftb}]^-$ **25** and $[\text{NO}_2]^+[\text{BF}_4]^-$ **26***

25 crystallizes in the monoclinic space group Cc with $Z = 4$. A section of its solid-state structure is shown in Figure 81.

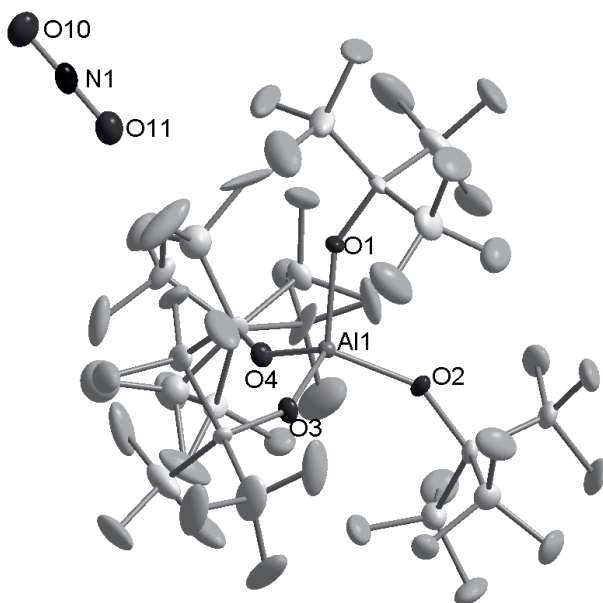


Figure 81: Section of the solid-state structure of $[\text{NO}_2]^+[\text{pftb}]^-$ **25** at 150 K. Thermal displacement ellipsoids are drawn at the 25% probability level. Selected bond lengths and angles: $d(\text{N1}-\text{O10}) = 110.2(8)$ pm, $d(\text{N1}-\text{O11}) = 110.5(8)$ pm, $\angle(\text{O10}-\text{N1}-\text{O11}) = 178.9(8)^\circ$.

The N-O bonds are rather short (110.2(8) and 110.5(8) pm) if compared to those in other NO_2^+ salts (cf. Table 67), which indicates very strong N=O double bonds. The bond angle in the cation deviates 1.1° from the ideal 180° angle, but this is most probably due to packing effects. The structural parameters of the anion are normal, but one of the $\text{C}(\text{CF}_3)_3$ groups is disordered (cf. Figure 81).

From the reaction described in eq. 75 large colorless crystals of $[\text{NO}_2]^+[\text{BF}_4]^-$ **26** were isolated. No structural information of this compound is available in the crystallographic databases, so its solid-state structure was determined. **26** crystallizes in the monoclinic space group $\text{P}2_1/\text{c}$ with $Z = 4$. A packing diagram of this compound is shown in Figure 82^[337].

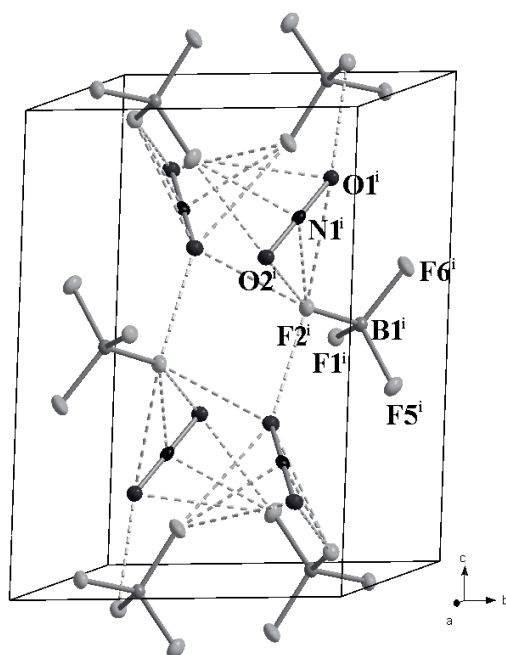


Figure 82: Packing diagram of $[\text{NO}_2]^+[\text{BF}_4]^-$ **26** at 100 K. Thermal displacement ellipsoids are drawn at the 25% probability level. Selected bond lengths and angles: $d(\text{N1-O1}) = 111.53(8)$ pm, $d(\text{N1-O2}) = 111.60(7)$ pm. $\angle(\text{O1-N1-O2}) = 179.89(8)^\circ$ ^[337].

In **26**, the N-O distances (111.53(8) and 111.60(7) pm) are longer than those in **25**, although the diffraction measurement was carried out at lower temperature (but in **25**, the standard deviations are higher due to the higher temperature, so the shortening can not be taken as absolute value). This observation is in line with the fact that the BF_4^- anion in **26** is more coordinating than the $[\text{pftb}]^-$ anion in **25** and the cation-anion contacts in **26** (dashed lines in Figure 82) are about 0.1 Å shorter than those in **25** (Figure 83). If the coordination is stronger, electron density is transferred to the π^* -LUMO of the NO_2^+ cation, which causes a reduction of the bond order. Therefore, the accurately determined bond lengths in NO_2^+ salts can be used as an indicator for the coordination ability of the counterion: The shorter the N-O distance is, the less the anion is coordinating. From the entries in Table 67 it can be seen that this distance is the shortest for the $[\text{pftb}]^-$ salt **25**. However, it may well be that this agreement is fortuitous, since temperatures of the structural determinations differ and the standard deviations of the compound are partly rather large.

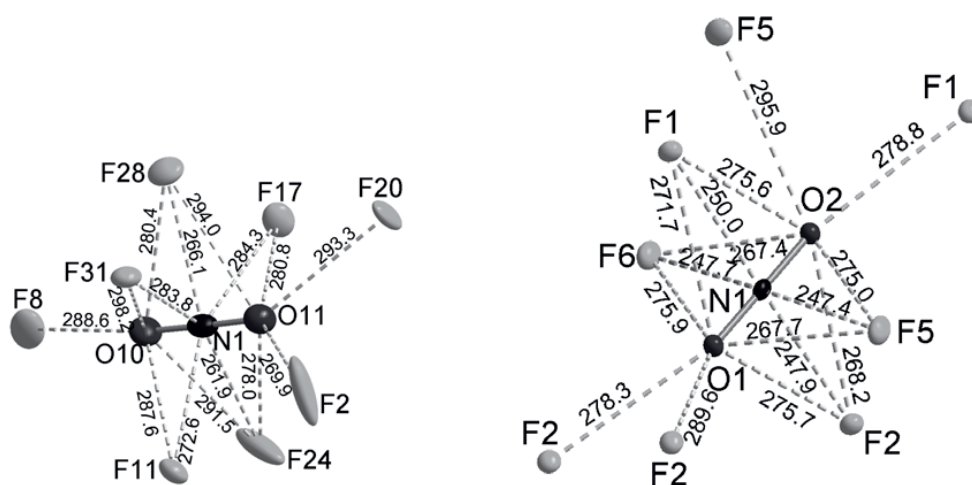


Figure 83: Cation-anion-interactions of $[\text{NO}_2][\text{pftb}]^-$ **25** (left) and $[\text{NO}_2]^+[\text{BF}_4]^-$ **26** (right) in the solid state.

Table 67: Comparison of $d(\text{N-O})$ [pm] and $\angle(\text{O-N-O})$ [$^\circ$] in different $[\text{NO}_2]^+$ salts with calculated values (ccsd(t) / aug-cc-pVTZ).

compound	T [K]	$d(\text{N-O})$ [pm]	$\angle(\text{O-N-O})$ [$^\circ$]
$[\text{NO}_2]^+$ calc.	-	112.5	180
$[\text{NO}_2]^+[\text{pftb}]^-$ 25	150	110.2(8) – 110.5(8) av. 110.4	178.9(8)
$[\text{NO}_2]^+[\text{BF}_4]^-$ 26 ^[337]	100	111.60(7) – 111.53(8) av. 111.57	179.89(7)
$[\text{NO}_2]^+[\text{Fe}(\text{NO}_3)_4]^-$ ^[338]	170	111.4(7) – 111.8(7) av. 111.6	n.a. ^(a)
$[\text{NO}_2]^+[\text{Zr}(\text{NO}_3)_5]^-$ ^[338]	180	107.9(6) – 113.1(6) av. 110.5	n.a. ^(a)
$[\text{NO}_2]^+[\text{Ga}(\text{NO}_3)_4]^-$ ^[333]	298	116.2(2)	180
$[\text{NO}_2]^+[\text{ClO}_4]^-$ ^[339]	298	110.4 (not very accurate)	175.2
$[\text{NO}_2]^+[\text{NO}_3]^-$ ^[339]	213	115.3(8) (not very accurate)	n.a. ^(a)
	213	115.4(10) ^[340]	180

^(a) n.a. = not available from the publication.

Solid-State Structure of 3,4- $\text{C}_6\text{H}_3\text{F}_2\text{NO}_2 \cdot \text{Al}(\text{OC}(\text{CF}_3)_3)_3$ **28**

3,4- $\text{C}_6\text{H}_3\text{F}_2\text{NO}_2 \cdot \text{Al}(\text{OC}(\text{CF}_3)_3)_3$ **28** crystallizes in the triclinic space group P-1 with $Z = 4$. A section of its solid-state structure is shown in Figure 84. Unfortunately, the crystals of **28** only

grow as very thin plates from CH₂Cl₂ even after recrystallization, and as they do not contain heavy elements – except only one Al atom – the quality of the data sets obtained from different attempts is rather poor. Therefore, one has to be very careful with the discussion of bond lengths.

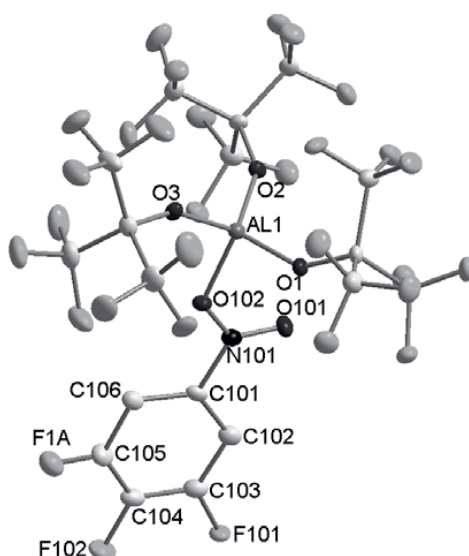


Figure 84: Section of the solid-state structure of 3,4-C₆F₂H₃NO₂·Al(OC(CF₃)₃)₃ **28** at 110K. Thermal displacement ellipsoids are drawn at the 25% probability level. Only one of the two molecules in the asymmetric unit is shown. H atoms are omitted. The 3,4-nitrodifluorobenzene moieties are disordered.

In Table 68, some bond lengths of **28** are compared to those of C₆H₅NO₂·AlCl₃^[341] and MeNO₂·AlCl₃^[341]. It is found that the values obtained for **28** are in the same order of magnitude than those for the compounds cited in the literature, but as already written before, the quality of the crystal structure of **28** is rather low so that the values can not be used for a detailed discussion.

Table 68: Comparison of the bond lengths (in pm) of C₆F₂H₃NO₂·Al(OC(CF₃)₃)₃ **28** with C₆H₅NO₂·AlCl₃^[341] and MeNO₂·AlCl₃^[341].

	28	C ₆ H ₅ NO ₂ ·AlCl ₃ ^[341]	MeNO ₂ ·AlCl ₃ ^[341] .
<i>d</i> (Al-O)	185.5 – 187.0 av. 186.3	185.6	186.7
<i>d</i> (N-O _{coord})	128.5	127.9	126.8
<i>d</i> (N-O _{free})	119.9.9 – 121.0 av. 120.0	119.8	117.0
<i>d</i> (N-C)	143.7 – 145.9 av. 144.7	142.9	147.0

8.3 The $[\text{NO}_2]^+$ Cation as an Oxidizing Agent: The Reaction of NO_2^+ with P_4

The NO_2^+ cation is a very strong oxidizing agent ($IE = 9.60 \text{ eV}^{[334]}$), which should be able to oxidize even white phosphorous ($IE = 9.34 \text{ eV}^{[342]}$) to give naked P_x^+ cations and NO_2 gas. These cations have already been studied in the gas phase by mass spectrometry and photo ionization^[343, 344] in combination with quantum chemical investigations^[344, 345], but despite many efforts, no P_x^+ cation has been stabilized in condensed phase. From the mass spectra it was noted that the intensities of uneven closed-shell P_x^+ ($x = 3, 5, 7, 9, \dots$) cations were much higher than those of open-shell even cations, a result that has also been confirmed by quantum mechanical calculations^[345]. From Figure 85 it can be seen that uneven open-shell P_x clusters are much easier to ionize than the even ones, which are closed-shell species, but except P_2^+ , all these cluster cations should be accessible by a redox reaction with the NO_2^+ cation in the gas phase.

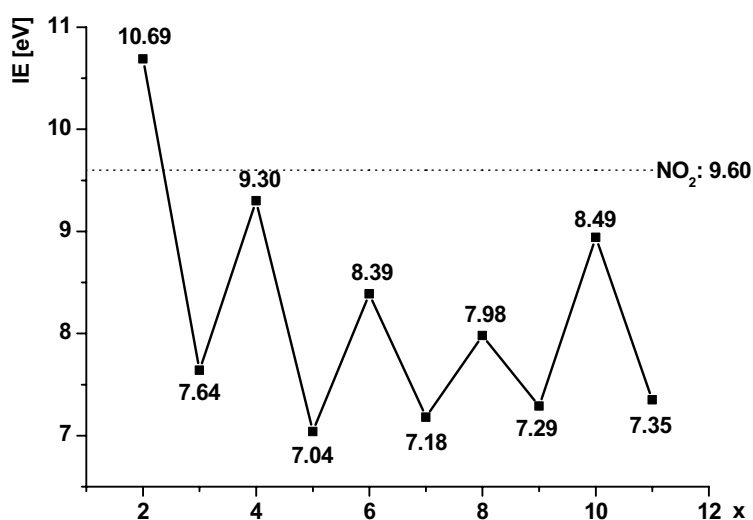


Figure 85: Calculated adiabatic ionization energies of P_x^+ cations ($x = 2-11$)^[345].

In Figure 86, the minimum geometries of some P_x^+ cations are shown. The P_9^+ cation has a similar structure than the $[\text{Ag}(\text{P}_4)_2]^+$ adduct which is formed upon reaction of $\text{Ag}[\text{pftb}]^-$ with P_4 ^[42].

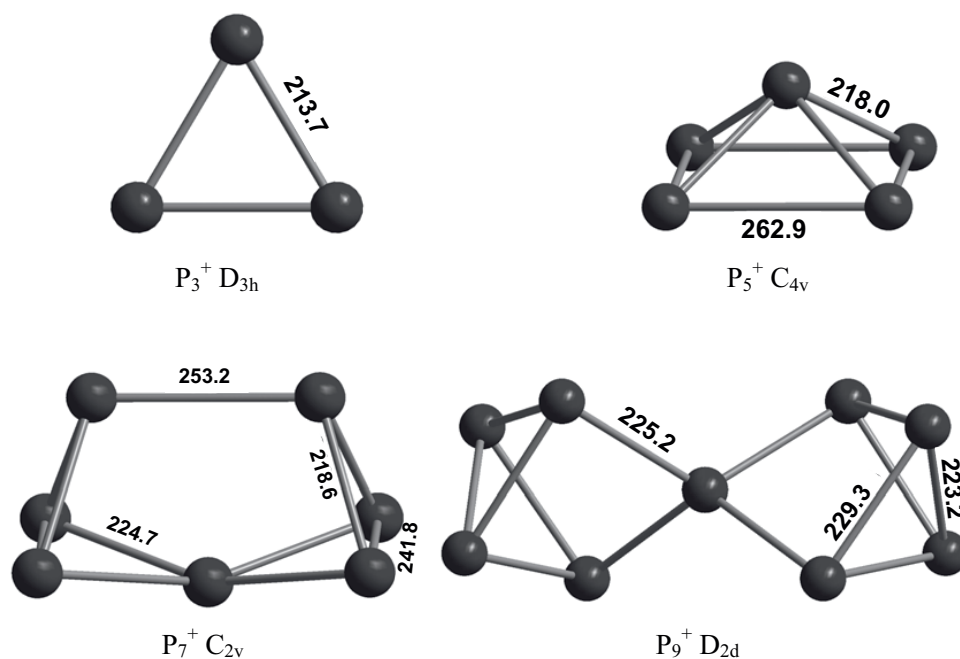


Figure 86: Minimum geometries and symmetry of some P_x^+ cations (BP86/SV(P)). Bond lengths are given in pm.

8.3.1 Preliminary Reactions of 25 with P_4 :

Some preliminary reactions of 25, which was prepared in the first successful reaction, were performed. Since it was not possible to reproduce the synthesis of 25, all of the following results need to be cross-checked when a successful preparation of 25 or a related soluble NO_2^+ salt is available.

In order to synthesize $[P_5]^+[pftb]^-$, which – according to their *IEs* – should be formed preferably, $[NO_2]^+[pftb]^-$ 25 was reacted in a sealed NMR tube in CD_2Cl_2 with 1.25 equivalents of P_4 . After the addition of CD_2Cl_2 , the reaction mixture first turns red, then bright yellow. From the ^{27}Al and ^{19}F NMR, which have been recorded at low temperature, it can be seen that the $[pftb]^-$ anion remains intact. In the ^{31}P NMR spectrum (Figure 87), apart from solid P_4 ($\delta = -457$, broad) two triplets at 355.4 and -231.0 ppm, both with $J_{PP} = 160$ Hz, are observed. This pattern does neither fit with that of the P_9^+ nor the P_5^+ cation. A comparison of the calculated properties of the P_5^+ cations and the reaction mixture is given in Table 69.

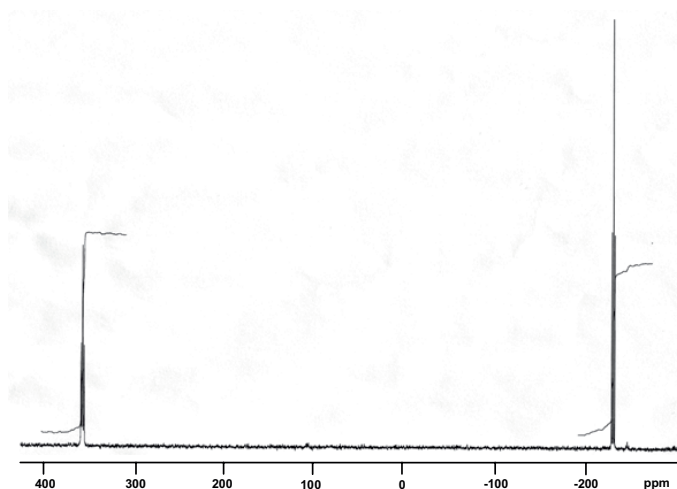


Figure 87: ^{31}P NMR spectrum of the *in situ* NMR tube reaction of $[\text{NO}_2]^+[\text{pftb}]^-$ **25** with 1.25 eq. P_4 . Spectrum recorded in CD_2Cl_2 at 243 K.

Table 69: Comparison of some properties of the reaction of $[\text{NO}_2]^+[\text{pftb}]^-$ **25** with P_4 with the calculated values for a P_5^+ cation (BP86/SV(P), TD-DFT) and the experimental values of P_5I_2^+ and P_5Br_2^+ salts.

	P_5^+ calc.	reaction mixture	$\text{P}_5\text{I}_2^{+[\text{49}]}$	$\text{P}_5\text{Br}_2^{+[\text{49}]}$
color	yellow	red, then yellow	yellow	colorless
^{31}P NMR	447.0(d)	355.5	168.2	161.4
		(t, J = 160 Hz)	(t, J = 153 Hz)	(t, J = 149 Hz)
	-373.9(quint.)	-231.0	-193.9	-235.9
		(t, J = 160 Hz)	(t, J = 153 Hz)	(t, J = 149 Hz)

The formation of the paramagnetic P_4^+ cation can also be excluded. One explanation for the observations made on this reaction is the formation of an adduct $[\text{P}_4\text{-NO}_2]^+$, as the ^{31}P NMR pattern is very similar to those of the P_5X_2^+ cations ($\text{X} = \text{Br}, \text{I}$)^[49]. In Figure 88, possible isomers of this cation and their relative energies are shown.

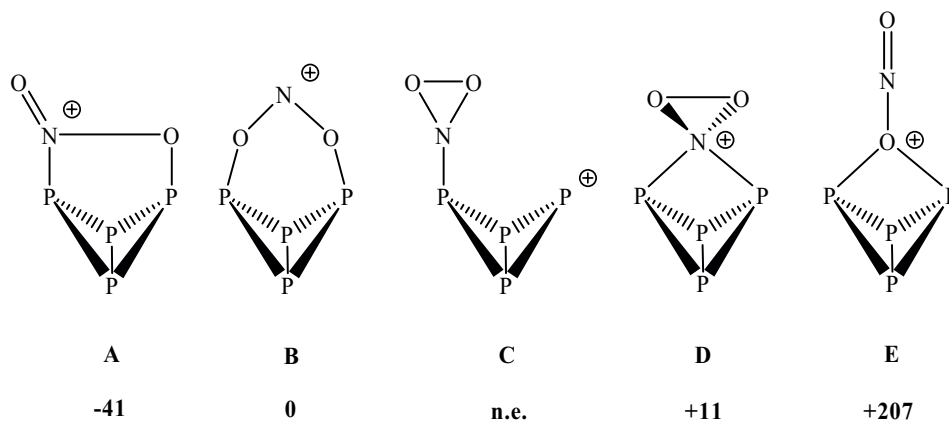


Figure 88: Possible isomers of the $[P_4-NO_2]^+$ cation **I** and their relative energies (BP86/SV(P)).

It can be seen that the PES of this species is very flat and one can not definitely decide from quantum mechanical calculations which isomer of **I** may be present in the reaction mixture. According to the ^{31}P NMR, only the isomers **IB** and **IE** are possible, but if the HOMO-LUMO interactions of NO_2^+ and P_4 are considered (Figure 89), only the isomer **IB** can be formed in a 1,3 cycloaddition. In this case, two different symmetries (C_s and C_{2v}) are possible.

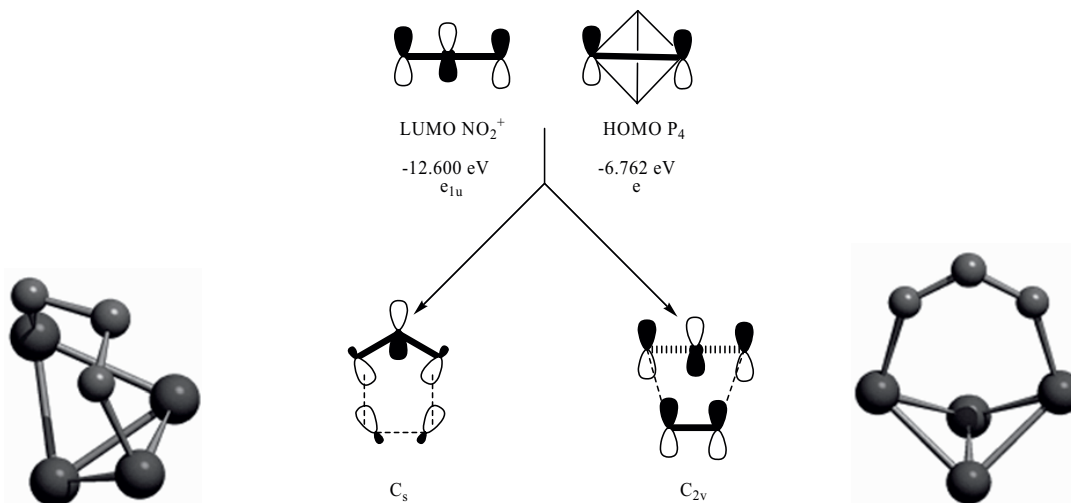


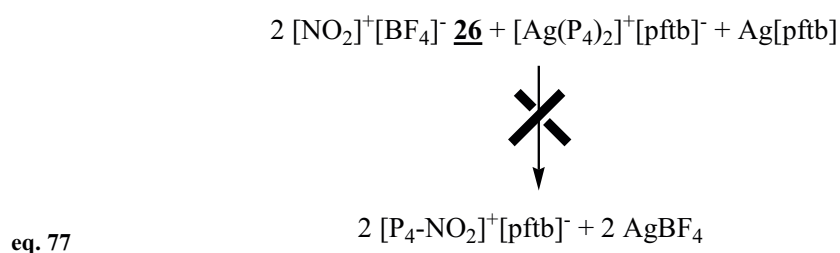
Figure 89: HOMO-LUMO interaction of NO_2^+ and P_4 . Two different geometries (C_s or C_{2v}) are possible.

8.3.2 Reaction of 26 with P₄:

Analogous reactions were performed with 26 as NO₂⁺ source, but due to its insolubility, no reaction at all was observed (³¹P NMR), even after the samples have been treated in an ultrasonic bath for one day.

8.3.3 Reaction of 26 with [Ag(P₄)₂]⁺[pftb]⁻:

In this experiment, [Ag(P₄)₂]⁺[pftb]⁻^[42] was chosen as a P₄ source. But when the educts were stirred together in CH₂Cl₂, no reaction according to eq. 77 was observed (³¹P NMR).



Therefore, NaCl was added to use the precipitation of AgCl as a driving force. But even after sonicating the reaction mixture for two days, no AgCl formation could be observed. Probably this is due to the fact that the [Ag(P₄)₂]⁺ adduct, which was still present in solution (³¹P NMR), is too stable and cannot be destroyed by addition of Cl⁻ ions. However, also the low solubility of NaCl may play a role.

9 Summary and Outlook

Within this thesis, several theoretical and experimental contributions to the chemistry of weakly coordinating anions were made.

Theoretical Investigation of the stability of WCAs:

18 of the most commonly used WCAs of the type $[M(L)_n]^-$ were examined based on the calculated fluoride ion and ligand affinities of their parent Lewis acids (*FIA* and *LA*), proton and copper decomposition reactions (*PD* and *CuD*), partial charges and frontier orbital energies. To obtain data that is more reliable, the assessed quantities were calculated through isodesmic reactions at the (RI)BP86/SV(P) level. If some parts of the calculations could not be done isodesmic, higher levels such as MP2/TZVPP, G2 and CBS-Q were selected to obtain reliable values for these reactions. Although the obtained results can certainly not be taken as absolute values, the trends and the relative ordering of the stabilities of all WCAs will undoubtedly be correct, since one methodology was chosen for the investigation in order to achieve maximum error cancellation. To include media effects, the decomposition reaction of these anions with SiMe_3^+ and Cp_2ZrMe^+ were also calculated in PhCl and 1,2- $\text{F}_2\text{C}_6\text{H}_4$ using the COSMO solvation model. This approach allows predicting the outcome of hitherto unknown reactions of a given cation with a set of very different anions such as fluorometallates or perfluoroorganoborates on thermodynamic grounds. Based on these data a rational decision to choose the “best” anion in a given cationic system is possible as well as Lewis acid reactions may be planned.

Depolymerization Energy and Fluoride Ion Affinity of Sb_nF_{5n} ($n = 1-4$):

During the work on the previous topic errors in the literature regarding the depolymerisation of Sb_nF_{5n} were realized. With a series of *ab initio* MP2 and DFT (BP86 and B3-LYP) computations with large basis sets up to cc-pVQZ quality it has been shown that the literature value of the standard enthalpy of depolymerization of $\frac{1}{4} \text{Sb}_4\text{F}_{20}(\text{g})$ to give $\text{SbF}_5(\text{g})$ (+18.5 kJ/mol, see Ref. 167) is by about 50 kJ/mol in error and that the correct value of $\Delta_r H^\circ_{\text{depoly.}}(\frac{1}{4} \text{Sb}_4\text{F}_{20}(\text{g}))$ is $+68 \pm 10$ kJ/mol. The standard enthalpies and standard Gibbs free energies $\Delta_r H^\circ_{\text{depoly.}}$, $\Delta_r H^\circ_{\text{interconv.}}$, $\Delta_r G^\circ_{\text{depoly.}}$ and $\Delta_r G^\circ_{\text{interconv.}}$ were assigned for Sb_nF_{5n} ($n = 2, 3, 4$) and the results were compared to available experimental gas phase data. Especially the MP2/TZVPP values, obtained in an indirect procedure that relies on isodesmic reactions or the highly accurate compound methods G2 and CBS-Q, are in excellent agreement with the

experiment and reproduce also the fine experimental details at temperatures of 423 and 498 K. Using these data and the calculated values for $[\text{Sb}_n\text{F}_{5n+1}]^-$ ($n = 1-4$), it was then possible to obtain values for the FIA as well as the $\Delta_f H^\circ$ of $\text{Sb}_n\text{F}_{5n}(\text{g})$ and $[\text{Sb}_n\text{F}_{5n+1}]^-(\text{g})$ (see Table 70).

Table 70: Calculated FIA (in kJ/mol) and $\Delta_f H^\circ$ of $n \text{ SbF}_5$, Sb_nF_{5n} and $[\text{Sb}_n\text{F}_{5n+1}]^-$.

	FIA (gaseous)	$FFIA^{(a)}$ (gaseous)	FIA (liquid)	$\Delta_f H^\circ$
SbF_5	514	512	434 \pm 18	-1301 \pm 15 ^[169, 346]
Sb_2F_{10}	559	521	-	-
Sb_3F_{15}	572	543	-	-
Sb_4F_{20}	580	561	434 \pm 18	-
2 SbF_5	667	585	506 \pm 18	-2708 \pm 21
3 SbF_5	767	651	528 \pm 18	-4098 \pm 26
4 SbF_5	855	697	534 \pm 18	-5476 \pm 30
SbF_6^-	-	-	-	-2064 \pm 18
$\text{Sb}_2\text{F}_{11}^-$	-	-	-	-3516 \pm 25
$\text{Sb}_3\text{F}_{16}^-$	-	-	-	-4919 \pm 31
$\text{Sb}_4\text{F}_{21}^-$	-	-	-	-6305 \pm 36

^(a) $FFIA$ = Free fluoride ion affinity, i.e. $\Delta_r G^\circ$.

Tetraalkylammonium Salts of Alkoxyaluminates:

In this project, the tetraalkylammonium salts of the weakly coordinating fluorinated alkoxyaluminates $[\text{pftb}]^-$, $[\text{hfip}]^-$ and $[\text{hftb}]^-$ have been investigated in order to obtain information on their undisturbed spectral and structural properties, as well as to study their electrochemical behavior (i.e. conductivities in non-polar solvents and redox stabilities). Several of the compounds qualify as Ionic Liquids with melting points as low as 40°C for $[\text{NBu}_4]^+[\text{hfip}]^-$. Simple and almost quantitative metathesis reactions yielding these materials in high purity were developed. These $[\text{NR}_4]^+$ salts serve as model compounds for undisturbed anions and their vibrational spectra – together with simulated spectra based on quantum chemical DFT calculations – were used for the clear assignment of the anion bands. Besides, the ion volumes of the anions ($V_{\text{ion}}([\text{pftb}]^-) = 0.736 \text{ nm}^3$, $V_{\text{ion}}([\text{hftb}]^-) = 0.658 \text{ nm}^3$, $V_{\text{ion}}([\text{hfip}]^-) = 0.577 \text{ nm}^3$) and their decomposition pathways in the mass spectrometer have been

established. The NBu_4^+ salts are highly soluble in non-polar solvents (up to 1.09 mol L^{-1} are possible for $[\text{NBu}_4]^+[\text{hftb}]^-$ in CH_2Cl_2 and 0.41 mol L^{-1} for $[\text{NBu}_4]^+[\text{hfip}]^-$ in CHCl_3) and their molar conductivities and electrochemical windows in these media are comparable or better to those of the analogous $[\text{B}(\text{C}_6\text{F}_5)_4]^-$ salts^[99], while they are simpler to prepare and in part also much cheaper (e.g. $[\text{hfip}]^-$). The most stable anion is the $[\text{pftb}]^-$ with an oxidation potential (vs. ferrocene) at 1.5 V (in CH_3CN) and a reduction potential at - 2.2 V (in CH_2Cl_2).

Weakly bound cationic $\text{Ag}(\text{P}_4\text{S}_3)$ complexes:

Already in 2002^[44], it has been shown that polymeric cationic $[\text{Ag}(\text{P}_4\text{S}_3)_n]^+$ complexes ($n = 1, 2$) are accessible, if partnered with a suitable weakly coordinating fluorinated alkoxyaluminate as counterion. Within this thesis, some important questions that remained unanswered in the first study, have been addressed: the influence of the anion on the structure of the $\text{Ag}(\text{P}_4\text{S}_3)$ complexes and the dynamic behaviour of these adducts.

Thus, in order to further investigate the counterion influence on the structure of the $\text{Ag}(\text{P}_4\text{S}_3)$ complexes, reactions with $\text{Ag}[\text{Al}(\text{OC}(\text{CH}_3)(\text{CF}_3)_2)_4]$ ($\text{Ag}[\text{hftb}]$) and $\text{Ag}[\{(\text{CF}_3)_3\text{CO}\}\text{Al-F-Al}(\text{OC}(\text{CF}_3)_3)_3]$ ($\text{Ag}[\text{al-f-al}]$) were performed. While $[\text{P}_4\text{S}_3\text{Ag}[\text{hftb}]]_\infty$ **13** is a molecular species, the adduct $[\text{Ag}_2(\text{P}_4\text{S}_3)_6]^{2+}[\text{al-f-al}]_2^-$ **14** is an isolated 2:1 salt. The experiments carried out in this study suggest that a maximum of three P_4S_3 cages may be bound on average to an Ag^+ ion. With the largest anion ($[\text{al-f-al}]^-$), isolated dimeric dicationic species are formed, whereas with all other smaller aluminates, polymeric species are obtained. Thermodynamic Born Haber cycle and DFT calculations as well as solution NMR and ESI mass spectrometry indicate that **14** exhibits an equilibrium between the dication $[\text{Ag}_2(\text{P}_4\text{S}_3)_6]^{2+}$ (in the solid state) and two $[\text{Ag}(\text{P}_4\text{S}_3)_3]^+$ monocations (in the gas phase and in solution).

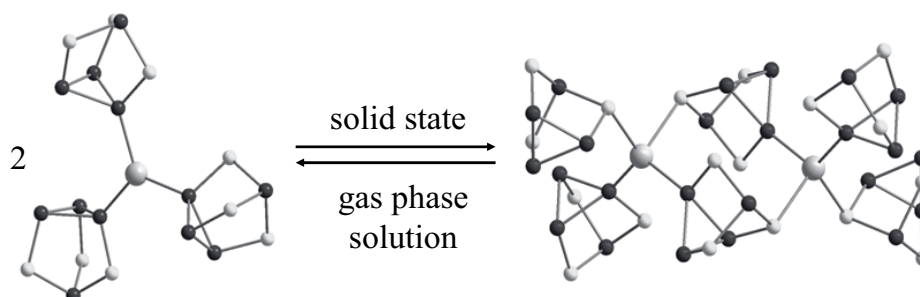


Figure 90: Likely equilibrium between 2 $[\text{Ag}(\text{P}_4\text{S}_3)_3]^+$ and $[\text{Ag}_2(\text{P}_4\text{S}_3)_6]^{2+}$ in **14**.

^{31}P -MAS-NMR revealed that all these adducts are highly dynamic species, even in the solid state and at low temperatures, although the X-ray diffraction measurements of the $\text{Ag}(\text{P}_4\text{S}_3)$ complexes investigated in this study suggest rigid structures. Since X-ray crystallography is an average method, this notion implies that the resting states for the dynamics observed by MAS-NMR are long lived. Those conformations, which are intermediates for the dynamic exchange, are very short lived and do not contribute as “disorder” to the intensity data of the crystal structure determination. This observation is also supported by DFT calculations of related model compounds, which show that the PES of $[\text{Ag}(\text{P}_4\text{S}_3)_n]^+$ ($n=1-3$) and $[\text{Ag}_2(\text{P}_4\text{S}_3)_2]^+$ is very flat. Two dimensional J-res experiments allowed to resolve the $^2J_{\text{PP}}$ coupling within the cages. Double quantum INADEQUATE experiments showed that the P atoms of the cages coordinated to the Ag^+ ions couple through the silver ions to the adjacent Ag-coordinated P atoms of the cage; however, coupling to $^{107/109}\text{Ag}$ was never observed likely due to the dynamics of the system even in the solid state at -70°C . Moreover the current MAS-NMR experiments showed that the symmetry of the published structures^[44] with the $[\text{Al}(\text{OR}^{\text{F}})_4]^-$ anions ($\text{R}^{\text{F}} = \text{C}(\text{H})(\text{CF}_3)_2$ and $\text{C}(\text{CF}_3)_3$) was lower than it appeared from the initial data collection and thus the structures were redetermined at lower temperature and with lower symmetry. The structures of α - and γ - P_4S_3 were also redetermined at low temperature and with unprecedented accuracy.

Chemistry of Halocarbenium Ions:

The Cl_3^+ salts **15** and **16** were prepared in the condensed phase. Both from experimental data and theoretical considerations can be seen that the halocarbenium ions behave different from the isoelectronic BX_3 molecules. In the CX_3^+ cations, partial C-X double bonds are formed, and the positive charge resides on the X atoms: The heavier the halogen is, the better the positive charge can be delocalized due to the higher σ and π donor ability of Br and I. In haloboranes, the positive charge is missing, and therefore, there is no driving force for π bond formation. Attempts to prepare CHI_2^+ and CH_2I^+ salts from CHI_3 or $\text{CH}_2\text{I}_2/\text{Ag}[\text{pftb}]$ mixtures remained unsuccessful; the reaction with CH_2I_2 lead to the formation of the adduct $[\text{Ag}(\text{CH}_2\text{I}_2)_3]^+[\text{pftb}]^-$ **17**, while for HCl_3 , dismutation with formation of **15** as well as **17** was observed.

Within this thesis, highly accurate and reliable $\Delta_f H^\circ$ values for halomethanes, halomethyl cations and the isoelectronic boron compounds have been established based on a combination of exactly determined experimental data together with high-level quantum chemical

calculations. These $\Delta_f H^\circ$ and the derived mean bond enthalpies (*mBEs*) are very useful for comparing the bonding in the isoelectronic, but different compounds. The different behaviour of the halomethyl cations and the haloboranes has also been shown in a theoretical study of the water adducts of these species. Although the $\text{H}_2\text{O} \rightarrow \text{EX}_3^{0/+1}$ species are isoelectronic, structures totally different (see Figure 91).

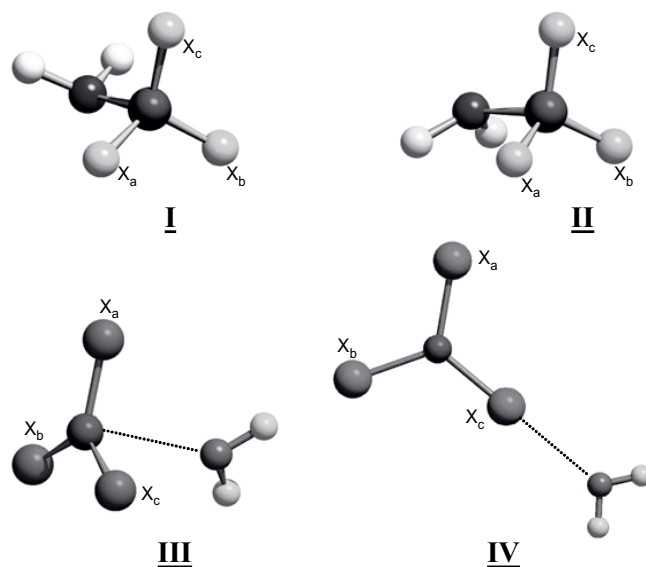


Figure 91: Minimum geometries of the water adducts $\text{H}_2\text{O} \rightarrow \text{EX}_3^{0/+1}$ ($\text{E} = \text{B}, \text{C}$; $\text{X} = \text{H}, \text{F} - \text{I}$): Covalent structures **I** and **II** vs. weakly bound structures **III** and **IV**. Symmetry: **I-III**: C_s , **IV**: C_{2v} .

The BX_3 molecules form “classical” adducts with strong covalent B-O bonds that are stabilized by additional H-bonding ($\text{X} = \text{F}$). The formation of weak “non-classical” water complexes of CX_3^+ ($\text{X} = \text{Cl-I}$) rather than covalent protonated trihalomethanols suggests that the delocalization of the positive charge to the less electronegative halogen atoms provides a sufficient driving force to form stable “non-classical” π -bonded ions in preference over classical all σ -bonded species. Thus, in the heavier CX_3^+ cations the bond enthalpy (*BE*) of a localized C-O σ bond is lower than the *BE* of a delocalized C-X π bond.

In order to find an experimental proof for such an iodine-coordinated adduct, different, weak nucleophiles that mimic water (OEt_2) or other electronically deactivated weak nucleophiles (PX_3 , $\text{X} = \text{Cl-I}$; AsI_3) have been chosen. With Et_2O as a base, the cation behaves as a strong Lewis acid and cleaves the ether to give $\text{I}_3\text{C-OEt}$, C_2H_4 and $[\text{H}(\text{Et}_2\text{O})_2]^+$. By contrast PX_3 and AsI_3 coordinate to the Cl_3^+ cations and the adducts have classical, carbon-bound ethane-like

structures. From variable temperature ^{13}C NMR it was seen that for the $\text{I}_3\text{C-AsI}_3^+$ salt **22** that the equilibrium between Cl_3^+ and AsI_3 is reversible and temperature dependent in solution. The $\text{I}_3\text{C-PI}_3^+$ salt decomposes at room temperature giving PI_4^+ and C_2I_4 , likely through an iodine coordinated $\text{I}_2\text{C-I}\cdots\text{PI}_3^+$ intermediate. Thus Cl_3^+ may also act as I^+ donor.

Synthesis and Reactivity of $[\text{NO}_2]^+[\text{pftb}]^-$ **25**:

The NO_2^+ salt of the $[\text{pftb}]^-$ anion **25** has been prepared from $\text{Li}[\text{pftb}]^-$ and $[\text{NO}_2]^+[\text{BF}_4]^-$ **26** by a metathesis reaction in CH_2Cl_2 . Unfortunately, the reaction was not reproducible, even under changing conditions (different solvents, different starting materials). Attempts to synthesize $[\text{NO}_2]^+[\text{f-alor3}]^-$ and $[\text{NO}_2]^+[\text{al-f-al}]^-$ remained also unsuccessful: If the reactions are carried out in pentane / CH_2Cl_2 , only $[\text{NO}_2]^+[\text{BF}_4]^-$ **26** could be recrystallized. If 1,2- $\text{C}_6\text{F}_2\text{H}_4$ has been used as solvent for this reaction, it was immediately nitrated by the NO_2^+ cation of **26**, giving the adduct $\text{C}_6\text{F}_2\text{H}_3\text{NO}_2\cdot\text{Al}(\text{OC}(\text{CF}_3)_3)_3$ **28**. Solvent nitration has also been observed in the reaction of **26** with $\text{Li}[\text{pftb}]^-$ in 1,2- $\text{C}_6\text{F}_2\text{H}_4$, in which the Li adduct $[\text{Li}_2(3,4\text{-C}_6\text{H}_4\text{F}_2\text{NO}_2)_6]^{2+}[\text{pftb}]_2^-$ **27** has been obtained.

However, with the successful batch of **25** a preliminary investigation of its chemistry was performed: Since the oxidation potential of the NO_2^+ cation is very high, $[\text{NO}_2]^+[\text{pftb}]^-$ **25** has been reacted with P_4 , in order to obtain naked phosphorous cations P_x^+ . But instead of oxidation, most probably the addition product $[\text{P}_4\text{-NO}_2]^+$ was formed, as it could be concluded from ^{31}P NMR spectra as well as from frontier orbital considerations and from quantum chemical calculations.



Figure 92: Two different possible geometries (C_s or C_{2v}) of the $[\text{P}_4\text{-NO}_2]^+$ cation.

10 Experimental Section

10.1 General Experimental Techniques

10.1.1 General Procedures and Starting Materials

Due to air- and moisture sensitivity of most materials all manipulations (if not mentioned otherwise) were undertaken using standard vacuum and Schlenk techniques as well as a glove box with an argon or nitrogen atmosphere (H_2O and $\text{O}_2 < 1$ ppm). All solvents were dried by conventional drying agents and distilled afterwards. The purification of some starting materials, which could not be used as purchased, is listed in Table 71.

Table 71: Purification of the starting materials.

starting material	method of purification
CH_2I_2	distillation
Cl_4	removing of all I_2 by sublimation in vacuum under the strict exclusion of light
LiAlH_4	extraction with Et_2O
P_4	sublimation, extraction with CS_2
PBr_3	distillation
PCl_3	distillation
P_4S_3	extraction with CS_2
$\text{R}^{\text{F}}\text{OH}$	distillation
SiCl_4	distillation

Since the syntheses of the Li and Ag salts were greatly improved with respect to the original publication^[11], it is described herein in detail.

Syntheses of $\text{Li}[\text{Al}(\text{OR}^{\text{F}})_4]$

$\text{Li}[\text{Al}(\text{OR}^{\text{F}})_4]^-$ ($\text{R}^{\text{F}} = \text{C}(\text{CH}_3)(\text{CF}_3)_2$, $\text{C}(\text{H})(\text{CF}_3)_2$, $\text{C}(\text{CF}_3)_3$) was formed by reaction of purified LiAlH_4 and the appropriate commercially available alcohols^[11, 12]. Due to the very low boiling points of the alcohols, especially the perfluorinated $\text{HOC}(\text{CF}_3)_3$ (b.p. = 45°C), a double reflux

condenser connected to a cryostat and set to a temperature of -20°C has been used. The solvent toluene, which was used as a solvent in the original publication^[11], always caused a discoloration of the product with some grayish precipitate (Al^0 ?) and made an additional purification by sublimation necessary. Therefore it was replaced by hexane or heptane (both work fine). While the occurrence of side reactions is significantly diminished in aliphatic solvents, it may happen that the LiAlH_4 does not completely react, especially in large scale reactions above 50 g. If residual Al-H bonds are in the mixture, they may easily be detected with Raman spectroscopy. To avoid this problem, which is caused by the poor solubility of the product even during reflux, the LiAlH_4 was finely ground prior to use^[347].

Synthesis of $\text{Ag}[\text{Al}(\text{OR}^F)_4]$

Syntheses of the according silver salts were performed by reaction of the lithium salts obtained by the procedure described above with AgF in CH_2Cl_2 .^[38] AgF has been purchased from Apollo Scientific, UK, exclusively; it should have a light orange / beige color and be stored with the exclusion of light. In a glove box, the Li^+ salt and 1.3 eq. AgF are weighed into one side of a special two bulbed Schlenk vessel with Young valves and frit plate (Figure 93)

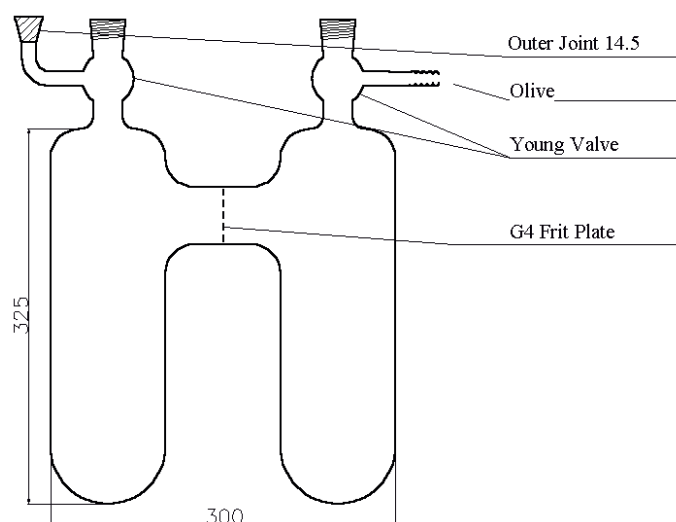


Figure 93: Two bulbed Schlenk vessel with Young valves and G4 frit plate. Measures are given in mm.

The reagents were suspended in CH_2Cl_2 (50 mL / 10 g Li^+ salt approx.); the vessel was evacuated until the solvent started to boil and left under the vapor pressure of the solvent. The mixture was left in an ultrasonic bath over night. The solutions turned slightly brownish with

only little of a dark brown (almost black) precipitate left. The darker the color of the solution, the more residual Al-H was presumably present. It appears that the dark color is due to colloidal Ag^0 . Prior to filtration the solution was stored in a -20 to -30°C freezer for at least 3 h to check whether unreacted Li^+ salt was still present (formation of a white microcrystalline precipitate). If not, the reaction was finished and the solution was filtered. Afterwards the Ag^+ salts were dried *in vacuo*, finely ground in a glove box, placed in a new flask and left directly hooked to a vacuum line until a constant weight was achieved. With this procedure one gets rid of the last traces of coordinated solvent and obtains solvent free naked $\text{Ag}^+[\text{Al}(\text{OR}^{\text{F}})_4]^-$ ^[347].

Synthesis of Ag[al-f-al]:

Ag[al-f-al] was prepared by reaction of Ag[pftb] with SiCl_4 in CH_2Cl_2 . Ag[pftb] was synthesized as described above, SiCl_4 has been freshly distilled prior to use. The silver salt was weighed into a flask as described in Figure 93 and dissolved in CH_2Cl_2 . SiCl_4 was added and the solution was stirred over night, whereby white AgCl precipitate was formed. After the insoluble AgCl was separated by filtration, all other side products were volatile and removed *in vacuo*. So pure Ag[al-f-al] remained as the sole soluble compound in the filtrate.^[52]

10.1.2 NMR Spectroscopy

NMR-spectra (in solution) were recorded on a Bruker AC 250 and on a Bruker AVANCE 400 spectrometer and referenced against the solvent (^1H , ^{13}C) or external aqueous AlCl_3 (^{27}Al) and 85% H_3PO_4 (^{31}P). Solid-state ^{31}P NMR spectra were recorded on a Bruker DRX 300 spectrometer equipped with 7.0 T widebore magnet, and utilizing 4-mm CPMAS probe head. Nicely powdered samples are packed under N_2 atmosphere into 4-mm outer diameter ZrO_2 rotors and the magic angle sample spinning was used at the rate of 14 kHz. Two-dimensional refocused INADEQUATE MAS spectra were recorded with rotor synchronization of the halves of the excitation and reconversion periods, the t_1 evolution period and the acquisition period. The J-resolved spectra were recorded with rotor-synchronization of the acquisition period and the halves of t_1 evolution period. Chemical shifts of ^{31}P are reported in ppm relative to an external 85% $\text{H}_3\text{PO}_4(\text{aq})$ standard. The absolute temperature was calibrated from the chemical shift difference of the proton resonances in liquid methanol that was spun up to 14 kHz in order to account for frictional heating of 14 K (room temperature 297 K + 14 K = 311 K)^[348].

10.1.3 Vibrational Spectroscopy

Raman spectra were recorded at r.t. on a Bruker IFS 66v and a Bruker RAM II FT-Raman spectrometer (using a liquid nitrogen cooled, highly sensitive Ge detector) in sealed NMR tubes or melting point capillaries (1064 nm radiation, 2 cm⁻¹ resolution). IR spectra were recorded on a Bruker VERTEX 70 and a Bruker IFS 66v spectrometer in Nujol mull between CsI or AgBr plates, or on a Nicolet Magna 760 spectrometer using a diamond Orbit ATR unit (extended ATR correction with refraction index 1.5 was used).

10.1.4 Melting Point Determination

Melting points were determined with a Setaram DSC 131 in 30 mL aluminium crucibles with an empty crucible of the same type as reference. The crucibles were filled and closed in a glovebox and then stored under Argon.

10.1.5 Mass Spectroscopy

ESI mass spectra were measured utilizing a Q-TOF ULTIMA mass spectrometer (MICROMASS, Manchester, UK) equipped with a Z-spray type ESI source. Phosphoric acid was used for the negative ion mass calibration range of 100-2000 m/z. Data were acquired and processed using MASSLYNX version 4.0. Electrospray conditions were as follows: capillary voltage, 3 kV; source temperature, 80°C; cone voltage, 35 V; and source block temperature, 150°C. The ESI nebulization and drying gases were nitrogen. The sample was introduced via a syringe pump operating at 10 mL/min.

10.1.6 X-Ray Diffraction and Crystal Structure Determination

Data collection for X-ray structure determinations were performed on a STOE IPDS II, a OXFORD DIFFRACTION SAPHIRE/KM4 CCD (kappa geometry) and a BRUKER APEX II diffractometer, all using graphite-monochromated Mo-K_α (0.71073 Å) radiation. Single crystals were mounted in perfluoroether oil on top of a glass fiber and then brought into the cold stream of a low temperature device so that the oil solidified. All calculations were performed on PC's using the SHELX97 software package. The structures were solved by the Patterson heavy atom method or direct methods and successive interpretation of the difference Fourier maps, followed by least-squares refinement. All non-hydrogen atoms were refined

anisotropically. The hydrogen atoms were included in the refinement in calculated positions by a riding model using fixed isotropic parameters.

10.1.7 Conductivity and Cyclovoltammetric Measurements

Conductivities have been measured using a Metrohm 712 Conductometer. Cyclovoltammetric measurements have been performed with an Autolab Ecochemie potentiostat in 1mL cells with 0.1M solutions. The working electrode (1mm²) was polished and dried before each use. As counter and reference electrodes, Pt resp. Ag electrodes were used.

10.2 Syntheses and Characterization of the Prepared Compounds

10.2.1 Syntheses and Characterization of the Compounds Addressed in Chapter 5

10.2.1.1 Synthesis of [NBu₄][pftb] **1**

In the glovebox 8.854 g (9.09 mmol) Li[pftb] and 2.930 g (9.09 mmol) [NBu₄]Br are weighted in two different beakers and then dissolved in a mixture of dest. H₂O and acetone. The two solutions are mixed and stirred for a few minutes at room temperature. The reaction mixture is kept over night at a warm place so that a part of the solvent is evaporated. The residue is filtered over a Buchner frit and washed first with water (until no more Br⁻ is present) and then two times with about 10 mL of hexane. The white, crystalline product is dried over night at 60°C.

Isolated yield: 10.461 g (95.1%).

IR (Diamond-ATR): $\tilde{\nu}$ = 288 (w), 315 (w), 367 (w), 382 (w), 444 (mw), 561 (w), 571 (w), 726(s), 830(w), 967(s), 1178(m), 1210(vs), 1232(s), 1274(m), 1295(m), 1349(w), 1474(vw), 2977(w) cm⁻¹.

Raman: $\tilde{\nu}$ = 100, 117, 174, 206, 232, 264, 291, 322, 369, 538, 561, 572, 744, 799, 831, 876, 908, 927, 975, 1008, 1036, 1065, 1111, 1131, 1174, 1237, 1276, 1321, 1354, 1395, 1460, 2757, 2886, 2947, 2979 cm⁻¹.

¹H NMR (400.0 MHz, CD₂Cl₂, 300K): δ = 1.00 (t, J = 7Hz, 3 H, CH₃), 1.60 (m, 2 H, CH₂), 1.57 (m, 2 H, CH₂), 3.03 (m, 3 H, N(CH₂)).

¹³C {¹H} NMR (100.6 MHz, CD₂Cl₂, 300K): δ = 13.9 (s), 20.2 (s), 24.5 (s), 49.8 (s), 79 (m), 122.0 (q, J = 293 Hz).

¹⁹F NMR (376.5 MHz, CD₂Cl₂ / CH₃CN, 300K): δ = -75.8.

²⁷Al NMR (104.3 MHz, CD₂Cl₂, 300K): δ = 31.9(s, $\omega_{1/2}$ = 9 Hz).

m.p. (DSC): 198°C.

elemental analysis found (calc.): 31.78 (31.55) % C, 3.00 (3.08) % H, 1.16 (1.10) % N.

10.2.1.2 Synthesis of [NEt₄][pftb] 2

In the glovebox 4.438 g (4.56 mmol) Li[pftb] and 0.967 g (4.60 mmol) [NEt₄]Br are weighted in two different beakers and then dissolved in a mixture of dest. H₂O and acetone. The two solutions are mixed and stirred for a few minutes at room temperature. The reaction mixture is kept over night at a warm place so that a part of the solvent is evaporated. The residue is filtered over a Buchner frit and washed first with water (until no more Br⁻ is present) and then two times with about 10 mL of hexane. The white, crystalline product is dried over night at 60°C.

Isolated yield: 4.347 g (86.9%).

IR (Diamond-ATR): $\tilde{\nu}$ = 285 (w), 316 (w), 367 (w), 377(w), 443 (mw), 537 (w), 561 (w), 726 (s), 756 (w), 781 (w), 832 (m), 968 (vs), 1161 (m), 1208 (vs), 1239 (m), 1271 (m), 1352 (w) 1398 (w), 1486 (vw), 2989 (vw) cm⁻¹.

Raman: $\tilde{\nu}$ = 100, 172, 206, 234, 289, 323, 368, 418, 538, 563, 572, 672, 747, 798, 834, 891, 904, 978, 1000, 1069, 1117, 1140, 1173, 1236, 1274, 1300, 1370, 1396, 1466, 1490, 2838, 2885, 2905, 2952, 2968, 3004 cm⁻¹.

¹H NMR (400.0 MHz, CD₂Cl₂ / CH₃CN, 300K): δ = 1.27 (tt, 3 H, CH₃), 3.20 (m, 2 H, N(CH₂)).

¹³C {¹H} NMR (63 MHz, acetone-d₆, 300 K): 7.5 (s), 52.9 (s), 122.0 (q, J = 293.5 Hz).

¹⁹F NMR (376.5 MHz, CD₂Cl₂ / CH₃CN, 300K): δ = -75.8 (s)

²⁷Al NMR (104.3 MHz, CD₂Cl₂ / CH₃CN, 300K): δ = 31.9 (s, $\omega^{1/2}$ = 12 Hz).

ESMS(-): m/z = 976.2 ([Al(OC(CF₃)₃)₄]⁻).

MS/MS: m/z = 967.1 ([Al(OC(CF₃)₃)₄]⁻), 751.1([F-Al(OC(CF₃)₃)₃]⁻).

m.p. (DSC): > 300°C.

elemental analysis found (calc.): 26.27 (25.96) % C, 1.84 (1.81) % H, 1.28 (1.20) % N.

10.2.1.3 Synthesis of [NMe₄][pftb] **3**

In the glovebox 4.677 g (4.80 mmol) Li[pftb] and 0.761 g (4.90 mmol) [NMe₄]Br are weighted in two different beakers and then dissolved in a mixture of dest. H₂O and acetone. The two solutions are mixed and stirred for a few minutes at room temperature. The reaction mixture is kept over night at a warm place so that a part of the solvent is evaporated. The residue is filtered over a Buchner frit and washed first with water (until no more Br⁻ is present) and then two times with about 10 mL of hexane. The white, crystalline product is dried over night at 60°C.

Isolated yield: 4.790 g (95.8%).

IR (Diamond-ATR): $\tilde{\nu}$ = 289 (w), 303 (w), 316 (w), 449 (mw), 529 (w), 565 (w), 571 (w), 725 (s), 756 (vw), 830 (w), 947 (m), 967 (s), 1164 (m), 1204 (vs), 1239 (m), 1272 (m), 1351 (w), 1487 (vw) cm⁻¹.

Raman: $\tilde{\nu}$ = 121, 172, 208, 235, 289, 322, 368, 453, 538, 562, 572, 748, 798, 832, 948, 977, 1096, 1136, 1166, 1240, 1273, 1307, 1353, 1455, 2757, 2828, 2905, 2934, 2966, 2990, 3046 cm⁻¹.

¹H NMR (400.0 MHz, CD₂Cl₂ / CD₃CN, 300K): δ = 3.03 (s).

¹³C{¹H} NMR (100.6 MHz, CD₂Cl₂ / CD₃CN, 300K): δ = 55.6 (s), 80 (m); 122.0 (q, J = 293 Hz).

¹⁹F NMR (376.5 MHz, CD₂Cl₂ / CD₃CN, 300K): δ = -75.7 (s).

²⁷Al NMR (104.3 MHz, CD₂Cl₂ / CD₃CN, 300K): δ = 35 (s, $\omega_{1/2}$ = 12 Hz).

m.p. (DSC): > 300°C.

elemental analysis found (calc.): 23.07 (23.48) % C, 1.66 (1.14) % H, 1.35 (1.27) % N.

10.2.1.4 Synthesis of [NBu₄][hfp] **4**

In the glovebox 3.744 g (5.33 mmol) Li[hfp] and 1.723 g (5.34 mmol) [NBu₄]Br are weighed together into a Schlenk vessel. 30 mL diethyl ether are added, the reaction mixture is stirred for 30 minutes at room temperature before the solvent is removed in vacuum. After the addition of 20 mL CH₂Cl₂ the mixture is filtered over a Al₂O₃ column. The solution is then concentrated until the product crystallizes at 2°C.

Isolated yield: 3.927 g (78.5 %).

IR (Diamond-ATR): $\tilde{\nu}$ = 328 (w), 377 (w), 445 (mw), 524 (mw), 536 (w), 567 (w), 597 (w), 684 (s), 726(w), 788 (m), 852 (s), 887 (m), 972 (w), 1096 (s) 1171 (vs), 1217 (s), 1287 (w), 1373(m), 1474(w), 2973 (vw) cm⁻¹.

Raman: $\tilde{\nu}$ = 198, 262, 296, 331, 367, 423, 525, 536, 568, 695, 726, 761, 858, 882, 908, 928, 992, 1034, 1058, 1110, 1132, 1153, 1178, 1216, 1291, 1322, 1380, 1453, 1462, 2713, 2754, 2884, 2925, 2978 cm⁻¹.

¹H NMR (400.0 MHz, CD₂Cl₂, 300K): δ = 1.02 (t, J = 7Hz, 3 H, CH₃), 1.42 (m, 2 H, CH₂), 1.59 (m, 2 H, CH₂), 3.07 (m, N(CH₂)), 4.51 (m, 1 H, CH).

¹³C{¹H} NMR (100.6 MHz, CD₂Cl₂, 300K): δ = 13.7 (s), 20.4 (s), 24.4 (s), 59.8 (s), 71.7 (sep), 123.8 (q, J = 285 Hz).

¹⁹F NMR (376.5 MHz, CD₂Cl₂, 300K): δ = -77.3 (d, J = 5.7 Hz).

²⁷Al NMR (104.3 MHz, CD₂Cl₂, 300K): δ = 57.8(s, $\omega^{1/2}$ = 73 Hz).

m.p. (DSC): 40°C (190°C: decomposition).

elemental analysis found (calc.): 38.68 (38.43) % C, 4.87 (5.07) % H, 1.41 (1.34) % N.

10.2.1.5 Synthesis of [NEt₄][hfip] **5**

In the glovebox 4.253 g (6.06 mmol) Li[hfip] and 1.281 g (6.09 mmol) [NEt₄]Br are weighed together into a Schlenk vessel. 30 mL diethyl ether are added, the reaction mixture is stirred for 1 hour at room temperature before the solvent is removed in vacuum. After the addition of 20 mL CH₂Cl₂ the mixture is filtered over a Al₂O₃ column. The solution is then concentrated until the product crystallizes at 2°C.

Isolated yield: 3.533 g (70.7 %).

IR (Diamond-ATR): $\tilde{\nu}$ = 315 (w), 330 (w), 367 (w), 382 (w), 444 (mw), 481 (w), 560 (w), 572 (w), 684(s), 726(w), 760 (w), 780(m), 793 (mw), 852(s), 888(m), 973(w), 1001(w), 1020(w), 1097(s), 1168(vs), 1206(s), 1261(w), 1288(w), 1376(w), 1487(w) cm⁻¹.

Raman: $\tilde{\nu}$ = 195, 299, 332, 357, 417, 492, 524, 536, 566, 673, 687, 696, 762, 784, 857, 892, 905, 1001, 1069, 1097, 1117, 1187, 1209, 1300, 1379, 1395, 1466, 1490, 1679, 1778, 2715, 2758, 2781, 2904, 2952, 2967, 3002 cm⁻¹.

¹H NMR (400.0 MHz, CD₂Cl₂, 300K): δ = 1.27 (tt, 3 H, CH₃), 3.12 (m, 2 H, N(CH₂)), 4.50 (m, 1 H, CH).

¹³C {¹H} NMR (100.6 MHz, CD₂Cl₂, 300K): δ = 7.7 (s), 53.3 (s), 72.0 (m), 123.2 (q, J = 285 Hz).

¹⁹F NMR (376.5 MHz, CD₂Cl₂, 300K): δ = -77.3 (s).

²⁷Al NMR (104.3 MHz, CD₂Cl₂, 300K): δ = 57.6 (s, $\omega_{1/2}$ = 90 Hz).

ESMS(-): m/z = 695.2 ([Al(OC(H)(CF₃)₂)₄]).

MS/MS: m/z = 695.2 ([Al(OC(H)(CF₃)₂)₄]), 547.2 ([FAl(OC(H)(CF₃)₂)₃]).

m.p. (DSC): 56°C.

elemental analysis found (calc.): 32.70 (32.45) % C, 3.66 (3.87) % H, 1.59 (1.47) % N.

10.2.1.6 Synthesis of [NMe₄][hfp] 6

In the glovebox 4.563 g (6.50 mmol) Li[hfp] and 1.028 g (6.67 mmol) [NMe₄]Br are weighed together into a Schlenk vessel. 30 mL diethyl ether are added, the reaction mixture is stirred over night at room temperature before the solvent is removed in vacuum. After the addition of 20 mL CH₂Cl₂ the mixture is filtered over a Al₂O₃ column. The solution is then concentrated until the product crystallizes at 2°C.

Isolated yield: 3.154 g (71.6 %).

IR (Diamond-ATR): $\tilde{\nu}$ = 444 (w), 522 (w), 537 (w), 570 (w), 685 (m), 777 (w), 858 (m), 891 (m), 1096 (m), 1107 (m), 1152 (s), 1178 (vs), 1217 (s), 1294 (ms), 1376 (m) cm⁻¹.

Raman: $\tilde{\nu}$ = 298 (m), 331 (m), 391 (mw), 525 (w), 571 (w), 698 (m), 730 (mw), 766 (m), 819 (m), 854 (m), 869 (mw), 933 (w), 1107 (w), 1190 (w), 1266 (w), 1298 (w), 1379 (m), 1456 (w), 2722 (w), 2739 (w), 2915 (s), 2953 (vs), 2993 (ms), 3017 (mw) cm⁻¹.

¹H NMR (400.0 MHz, CD₂Cl₂ / CD₃CN, 300K): δ = 3.03 (s, 3 H, N(CH₃), 4.50 (m, 1 H, CH).

¹³C{¹H} NMR (100.6 MHz, CD₂Cl₂ / CD₃CN, 300K): δ = 55.8 (s), 71.1 (sept), 126.1 (q, J = 285 Hz).

¹⁹F NMR (376.5 MHz, CD₂Cl₂ / CD₃CN, 300K): δ = -77.5 (s)

²⁷Al NMR (104.3 MHz, CD₂Cl₂ / CD₃CN, 300K): δ = 57.5 (s, $\omega/2$ = 95 Hz).

m.p. (DSC): 43 °C

10.2.1.7 Synthesis of [NBu₄][hftb] 7

In the glovebox 1.566 g (2.07 mmol) Li[hftb] and 0.652 g (2.02 mmol) [NBu₄]Br are weighed together into a Schlenk vessel. 15 mL diethyl ether are added, the reaction mixture is stirred for 30 minutes at room temperature before the solvent is removed in vacuum. After the addition of 15 mL CH₂Cl₂ the mixture is filtered over a Al₂O₃ column. The solution is then concentrated until the product crystallizes at 2°C.

Isolated yield: 1.702 g (85.1 %).

IR (Diamond-ATR): $\tilde{\nu}$ = 326 (w), 372 (w), 399 (w), 437 (w), 523 (mw), 566 (w), 622 (mw), 700 (s), 733 (w), 784(w), 862 (w), 882 (w), 995(m), 1026 (w), 1079(vs), 1113(s), 1180(vs), 1233(m), 1307(m), 1389(w), 1457 (w), 2794 (w), 2967(w) cm⁻¹.

Raman: $\tilde{\nu}$ = 194, 255, 295, 337, 367, 518, 536, 567, 622, 699, 735, 771, 810, 882, 913, 997, 1038, 1053, 1134, 1154, 1186, 1282, 1323, 1387, 1419, 1453, 1464, 2622, 2714, 2751, 2883, 2956, 3011 cm⁻¹.

¹H NMR (400.0 MHz, CD₂Cl₂, 300K): δ = 1.00 (t, J = 7Hz, 3 H, CH₃), 1.40 (m, 2 H, CH₂), 1.49 (s, 3 H, C(CH₃)), 1.57 (m, 2 H, CH₂), 3.04 (m, 3 H, N(CH₃)).

¹³C {¹H} NMR (100.6 MHz, CD₂Cl₂, 300K): δ = 13.7 (s), 18.1 (s), 20.1 (s), 24.4 (s), 59.6 (s), 75.9 (m), 125.3 (q, J = 289 Hz).

¹⁹F NMR (376.5 MHz, CD₂Cl₂, 300K): δ = -79.5 (s).

²⁷Al NMR (104.3 MHz, CD₂Cl₂, 300K): δ = 46.9 (s, $\omega_{1/2}$ = 9 Hz).

ESMS(-): m/z = 751.3 ([Al(OC(CH₃)(CF₃)₂)₄]⁻).

MS/MS: m/z = 751.2 ([Al(OC(CH₃)(CF₃)₂)₄]⁻), 667.2 (= [hftb]⁻ -1 CH₃, -1 CF₃), 589.3 ([FAl(OC(CH₃)(CF₃)₂)₃]⁻)

MS/MS: m/z = 751.2 ([Al(OC(CH₃)(CF₃)₂)₄]⁻), 667.2 (, 589.3 ([FAl(OC(CH₃)(CF₃)₂)₃]⁻).

m.p. (DSC): 106°C.

elemental analysis found (calc.): 29.10 (29.18) % C, 2.93 (2.92) % H, 1.70 (1.63) % N.

10.2.1.8 Synthesis of [NEt₄][hftb] **8**

In the glovebox 1.720 g (2.27 mmol) Li[hftb] and 0.481 g (2.29 mmol) [NEt₄]Br are weighed together into a Schlenk vessel. 15 mL diethyl ether are added, the reaction mixture is stirred for 1 hour at room temperature before the solvent is removed in vacuum. After the addition of 15 mL CH₂Cl₂ the mixture is filtered over a Al₂O₃ column. The solution is then concentrated until the product crystallizes at 2°C.

Isolated yield: 1.527 g (76.3 %).

IR (Diamond-ATR): $\tilde{\nu}$ = 370 (w), 522 (mw), 534 (w), 567 (w), 623 (w), 700(s), 733(w), 783(m), 801 (w), 994(m), 1078(vs), 1112(s), 1178(vs), 1235(m), 1308(m), 1386(w), 1487(w), 2960(w) cm⁻¹.

Raman: $\tilde{\nu}$ = 194, 294, 337, 369, 417, 517, 536, 568, 622, 672, 698, 735, 770, 867, 904, 998, 1069, 1117, 1174, 1242, 1278, 1300, 1396, 1464, 1490, 2703, 2756, 2779, 2904, 2958, 3007 cm⁻¹.

¹H NMR (400.0 MHz, CD₂Cl₂, 300K): δ = 1.31 (tt, 3 H, CH₃), 1.48 (s, 3 H, C(CH₃)), 3.14 (m, 2 H, N(CH₂)).

¹³C {¹H} NMR (100.6 MHz, CD₂Cl₂, 300K): δ = 7.9 (s), 18.3 (s), 53.4 (s), 77 (m), 125.0 (q, J = 291 Hz).

¹⁹F NMR (376.5 MHz, CD₂Cl₂, 300K): δ = -79.9 (s).

²⁷Al NMR (104.3 MHz, CD₂Cl₂, 300K): δ = 46.8 (s, $\omega_{1/2}$ = 7 Hz).

m.p. (DSC): 110°C.

elemental analysis found (calc.): 35.87 (35.19) % C, 4.30 (4.48) % H, 1.49 (1.40) % N.

10.2.1.9 Synthesis of [NMe₄][hftb] 2

In the glovebox 1.837 g (2.42 mmol) Li[hftb] and 0.390 g (2.53 mmol) [NMe₄]Br are weighed together into a Schlenk vessel. 15 mL diethyl ether are added, the reaction mixture is stirred overnight at room temperature and then for 5 hours under reflux before the solvent is removed in vacuum. After the addition of 15 mL CH₂Cl₂ the mixture is filtered over a Al₂O₃ column. The solution is then concentrated until the product crystallizes at 2°C.

Isolated yield: 1.702 g (85.1 %).

IR (Diamond-ATR): $\tilde{\nu}$ = 368 (w), 440 (w), 512 (w), 569 (w), 622 (m), 701(s), 774(w), 791(m), 864(m), 993(m), 1080(vs), 1115(s), 1183(vs), 1232(s), 1307(m), 1389(w), 1461(w), 2361(w), 2986 (vw) cm⁻¹.

Raman: $\tilde{\nu}$ = 196, 295, 337, 370, 388, 518, 536, 567, 622, 698, 742, 772, 866 (w), 931 (w), 944 (w), 1319 (w), 1378, 1456, 1465, 2282, 2904, 2958, 2994, 3021 cm⁻¹.

¹H NMR (400.0 MHz, CD₂Cl₂ / CD₃CN, 300K): δ = 1.42 (s, 3 H, C(CH₃)), 3.01 (m, 3 H, N(CH₃)).

¹³C{¹H} NMR (100.6 MHz, CD₂Cl₂ / CD₃CN, 275K): δ = 17.8 (s), 55.9 (s), 75.8 (m), 125.0 (q, J = 289.0 Hz).

¹⁹F NMR (376.5 MHz, CD₂Cl₂ / CD₃CN, 300K): δ = -79.8 (s).

²⁷Al NMR (104.3 MHz, CD₂Cl₂ / CD₃CN, 300K): δ = 50.2 (s, $\omega^{1/2}$ = 9 Hz).

m.p. (DSC): 94°C.

10.2.1.10 Synthesis of [NBu₄][al-f-al] **10**

Solid [Ag(CH₂Cl₂)] [al-f-al] (0.566 g, 0.34 mmol) and solid [NBu₄]Br (0.109 g, 0.34 mmol) were weighed into a two-bulb frit plate Schlenk vessel equipped with two J. Young valves. CH₂Cl₂ (15 mL) was added on this solid mixture and the resulting colorless solution above the white precipitate (AgBr) was stirred for a few minutes at r.t.. The suspension was filtered, the filtrate was highly concentrated and stored for a few days at -30°C for crystallization. Colourless crystalline plates of **10** were isolated in nearly quantitative yield.

IR (CsI pates, Nujol mull): $\tilde{\nu}$ = 285 (w), 315 (mw), 329 (w), 375 (w), 446 (ms), 536 (m), 562 (m), 571 (mw), 726 (s), 755 (m), 768 (ms), 821 (ms), 830 (ms), 882 (mw), 897 (mw), 968 (vs), 1035 (mw), 1061 (mw), 1113 (mw), 1163 (vs), 1213 (vs), 1242 (vs), 1276 (vs), 1300 (vs), 1350 (vs) cm⁻¹.

¹H NMR (250 MHz, CD₂Cl₂, 300K): δ = 0.98 (t, J = 7Hz, 3 H, CH₃), 1.37 (m, 2 H, CH₂), 1.55 (m, 2 H, CH₂), 3.04 (m, 3 H, N(CH₃)).

¹³C {¹H} NMR (63 MHz, CD₂Cl₂, 300K): δ = 13.3 (s), 19.8 (s), 24.0 (s), 59.3 (s), 121.0 (q, J = 292 Hz).

²⁷Al NMR (78 MHz, CD₂Cl₂, 300K): δ = 34.4 (s, $\omega^{1/2}$ = 2170 Hz).

10.2.2 Syntheses and Characterization of the Compounds Addressed in Chapter 6

(Ag(P₄S₃)₂)[pftb] **12** was synthesized as described in the literature.

10.2.2.1 Synthesis and Characterization of [(P₄S₃)Ag[hftb]] **13**

Solid Ag(CH₂Cl₂)[hftb] (0.301 g, 0.32 mmol) and solid P₄S₃ (0.070 g, 0.32 mmol) were weighed into a Schlenk vessel. CH₂Cl₂ (5 mL) was added at r.t. and the mixture was stirred for two hours after which a yellow solution over a smaller amount of dark brownish precipitate had formed. The suspension was filtered, the filtrate was highly concentrated and stored over night at r.t.. Large yellow, very air and moisture sensitive needles of [(P₄S₃)Ag[hftb]] formed.

Yield: 0.312g, 90.6%.

IR (AgBr plates, Nujol mull): $\tilde{\nu}$ = 298 (ms), 328 (mw), 338 (mw), 351 (w), 363 (w), 394 (ms), 438 (ms), 462 (w), 485 (mw), 495 (mw), 535 (ms), 573 (ms), 619 (ms), 628 (ms), 669 (w), 700 (s), 728 (vs), 770 (ms), 794 (s), 865 (s), 890 (w), 974 (s), 1016 (w), 1079 (m), 1089 (m), 1112 (ms), 1175 (ms), 1169 (ms), 1225 (ms), 1241 (m), 1262 (m), 1303 (ms) cm⁻¹.

Raman: $\tilde{\nu}$ = 117, 198, 223, 290, 299, 353, 365, 444, 470, 498, 536, 567, 697, 705, 773 cm⁻¹.

UV-Vis (Nujol mull): λ_{max} = 246, 340, 402 nm

¹H NMR (250 MHz, CD₂Cl₂, 300K): δ = 1.63 (s).

¹³C NMR (63 MHz, CD₂Cl₂, 300K): δ = 124.0 (q, J = 288,1 Hz), 76.3 (m), 18,0 (s).

¹⁹F NMR (235 MHz CD₂Cl₂, 300K): δ = -78.6 (s).

²⁷Al NMR (78 MHz, CD₂Cl₂, 300K): δ = 47.2 (s, broad, $\omega_{1/2}$ = 299 Hz).

³¹P NMR (101 MHz, CD₂Cl₂, 300K): δ = 66.2 (q, J = 61.8 Hz), -128.2 (d, J = 61.9 Hz).

10.2.2.2 Synthesis and Characterization of $[\text{Ag}_2(\text{P}_4\text{S}_3)_6]^{2+}[\text{al-f-al}]^-_2$ **14**

Solid $[\text{Ag}(\text{CH}_2\text{Cl}_2)_3][\text{al-f-al}]$ (0.491 g, 0.26 mmol) and solid P_4S_3 (0.266 g, 0.78 mmol) were weighed into a Schlenk vessel. CS_2 (2 mL) and CH_2Cl_2 (15 mL) were added at r.t. and the mixture was stirred over night after which a colorless solution over a smaller amount of dark brownish precipitate had formed. The suspension was filtered, the filtrate was highly concentrated and stored over night in a -25°C freezer. Large colorless, very air and moisture sensitive needles of $[\text{Ag}_2(\text{P}_4\text{S}_3)_6]^{2+}[\text{al-f-al}]^-_2$ formed.

Yield: 0.442g, 90.1%.

IR (CsI plates, Nujol mull): $\tilde{\nu} = 288$ (m), 318 (mw), 331 (w), 347 (w), 376 (ms), 409 (m), 430 (ms), 543 (ms), 491 (w), 536 (m), 569 (ms), 633 (s), 722 (s), 760 (mw), 810 (w), 863 (s), 953 (s), 974 (s) 1088 (mw, shoulder), 1152 (s), 1169 (s), 1217 (s), 1250 (s), 1303 (s) cm^{-1} .

Raman: $\tilde{\nu} = 193, 222, 246, 289, 325, 346, 415, 432, 447, 468, 493, 539, 571, 753, 816, 987$ cm^{-1} .

^{13}C NMR (63 MHz, CD_2Cl_2 , 300K): $\delta = 121.0$ (q, $J = 291$ Hz), 78.4 (m).

^{19}F NMR (376 MHz, CD_2Cl_2 , 300K): $\delta = -75.7$ (s, 54 F, CF_3), -184.8 (s, 1 F, Al-F).

^{27}Al NMR (104 MHz, CD_2Cl_2 , 300K): $\delta = 37.5$ (s, broad, $\omega_{1/2} = 3100$ Hz).

^{31}P NMR (101 MHz, CD_2Cl_2 , 300K): $\delta = -116.7$ (d, $J = 67.9$ Hz), 73.5 (q, $J = 67.9$ Hz).

10.2.3 Syntheses and Characterization of the Compounds Addressed in Chapter 7

10.2.3.1 Synthesis and Characterization of $[\text{Cl}_3]^+[\text{pftb}]^-$ **15**

Solid $[\text{Ag}(\text{CH}_2\text{Cl}_2)][\text{pftb}]$ (4.440 g, 3.83 mmol) and solid Cl_4 (1.990 g, 3.83 mmol) were weighed into a two-bulb frit plate Schlenk vessel equipped with two J. Young valves. CH_2Cl_2 (50 mL) was condensed on this solid mixture and the resulting dark red solution above the yellowish precipitate (AgI) was stirred over night at 0°C . The suspension was filtered; the filtrate was highly concentrated and stored for a few days at -80°C for crystallization.

Isolated yield (after crystallization): 4.385 g (84.2%).

IR (AgBr plates, Nujol mull): $\tilde{\nu} = 295$ (ms), 318 (m), 332 (mw), 337 (mw), 375 (ms), 453 (s), 537 (ms), 568 (ms), 640 (s), 724 (vs), 740 (s), 759 (w), 865 (ms), 973 (vs), broad signals between 1150 and 1250, 1261 (mw), 1302 (w), 1357 (m) cm^{-1} .

UV-Vis (quartz plates, Nujol mull): $\lambda_{\text{max}} = 276$ (60%), 308 (85%), 349 (100%) nm.

^{13}C NMR (101 MHz, CD_2Cl_2 , 300K): $\delta = 121.5$ (q, $J = 293$ Hz), 78.8 (m), 97.0(s).

^{27}Al NMR (104 MHz, CD_2Cl_2 , 300K): $\delta = 38.0$ (s, $\omega_{1/2} = 7$ Hz).

10.2.3.2 Synthesis and Characterization of $[\text{Cl}_3]^+[\text{al-f-al}]^-$ **16**

Solid $[\text{Ag}(\text{CH}_2\text{Cl}_2)_3][\text{al-f-al}]$ (2.836 g, 1.54 mmol) and solid Cl_4 (0.800 g, 1.54 mmol) were weighed into a two-bulb frit plate Schlenk vessel equipped with two J. Young valves. CH_2Cl_2 (50 mL) was condensed on this solid mixture and the resulting dark red solution above the yellowish precipitate (AgI) was stirred over night at -30°C . The suspension was filtered; the filtrate was highly concentrated and stored for a few days at -80°C for crystallization.

Isolated yield (after crystallization): 1.906 g (66.0%).

IR (AgBr plates, Nujol mull): $\tilde{\nu} = 295$ (ms), 318 (m), 332 (mw), 337 (mw), 375 (ms), 453 (s), 537 (ms), 568 (ms), 640 (s), 724 (vs), 740 (s), 759 (w), 865 (ms), 973 (vs), broad signals between 1150 and 1250, 1261 (mw), 1302 (w), 1357 (m) cm^{-1} .

UV-Vis (quartz plates, Nujol mull): $\lambda_{\text{max}} = 282$ (60%), 307 (85%), 340 (100%), 500 (I_2) nm.

^{13}C NMR (101 MHz, CD_2Cl_2 , 300K): $\delta = 121.0$ (q, $J = 291$ Hz), 78.8 (m), 97.0(s).

^{27}Al NMR (104 MHz, CD_2Cl_2 , 300K): $\delta = 33.0$ (s, $\omega_{1/2} = 2244$ Hz).

10.2.3.3 Synthesis and Characterization of $[\text{Ag}(\text{CH}_2\text{I}_2)_3]^+[\text{pftb}]^-$ **17**

Solid $[\text{Ag}(\text{CH}_2\text{Cl}_2)][\text{pftb}]$ (0.720 g, 0.62 mmol) was weighed into a two-bulb frit plate Schlenk vessel equipped with two J. Young valves. After the addition of 10 mL of CH_2Cl_2 and cooling to -78°C , liquid CH_2I_2 (150 μl , 1.86 mmol) was added by using a Hamilton syringe. The reaction mixture was kept at ambient temperature for a few hours before filtration. The filtrate was highly concentrated and stored for a few days at room temperature for crystallization. The product crystallizes in nearly quantitative yield.

IR (CsI plates, Nujol mull): $\tilde{\nu}$ = 287 (w), 315 (m), 369 (mw), 445 (s), 495 (w), 537 (mw), 561 (mw), 572 (mw), 726 (s), 755 (w), 833 (mw), 964 (s), 974 (ms), 1119 (mw), 1185 (m), 1224 (vs), 1244 (vs), 1273 (s), 1298 (ms), 1355 (m) cm^{-1} .

^1H NMR (250 MHz, CD_2Cl_2 , 300K): δ = 4.16 (s).

^{13}C NMR (63 MHz, CD_2Cl_2 , 300K): δ = 121.6 (q, J = 292.9 Hz), 78.9 (m), -55.8 (s).

10.2.3.4 Synthesis and Characterization of $[\text{Ag}(\text{CH}_2\text{Cl}_2)(\text{CH}_2\text{I}_2)]^+[\text{pftb}]^-$ **18**

Solid $[\text{Ag}(\text{CH}_2\text{Cl}_2)][\text{pftb}]$ (0.444 g, 0.383 mmol) was weighed into a Schlenk vessel. CH_2I_2 (31 μl , 0.383 mmol) was added using a Hamilton syringe. The reaction mixture was then stirred over night within the total exclusion of light. The beige solid was investigated by IR spectroscopy.

IR (CsI plates, Nujol mull): $\tilde{\nu}$ = 287 (w), 315 (m), 366 (w), 380 (w), 445 (m), 496 (w), 536 (m), 560 (m), 571 (m), 726 (s), 755 (mw), 831 (s), 967 (vs), 1120 (s), 1185 (s, shoulder), 1218 (vs), 1240 (s), 1273 (s), 1296 (ms), 1349 (m) cm^{-1} .

10.2.3.5 Reaction of CHI₃ with Ag[pftb]

Reaction in CH₂Cl₂:

Solid [Ag(CH₂Cl₂)]pftb (0.177g, 0.152 mmol) and solid CHI₃ (0.060 g, 0.152 mmol) were weighed into a two-bulb frit plate Schlenk vessel equipped with two J. Young valves. CH₂Cl₂ (10 mL) was condensed on this solid mixture and the resulting dark red solution above the yellowish precipitate (AgI) was stirred over night at -80°C. The suspension was filtered, and the solution was dried in vacuum.

IR (AgBr plates, Nujol mull): $\tilde{\nu}$ = 316 (m), 329 (w), 337 (w), 347 (w), 368 (m), 376 (m), 443 (m), 536 (m), 561 (m), 573 (m), 640 (w), 727 (s), 737 (m, shoulder), 755 (m), 833 (m), 864 (w), 973 (s), 1066 (w), 1108 (vs), 1170 (vs), 1219 (vs), 1244 (vs), 1275 (vs), 1301 (vs) cm⁻¹.

¹H NMR (250 MHz, CD₂Cl₂, 203K): δ = 3.90 (s), 4.12 (s), 5.03 (s).

¹³C NMR (63 MHz, CD₂Cl₂, 203K): δ = -140.3 (s), -52.4 (s), 78.7 (m), ca. 96 (s, very small), 121.5 (q, J = 292 Hz).

in-situ NMR tube reaction in CD₂Cl₂:

Solid Ag[pftb] (0.200g, 0.186 mmol) and solid CHI₃ (0.110 g, 0.279 mmol) were weighed into an NMR tube. CD₂Cl₂ (0.7 mL) was condensed on the mixture and immediately after warming to -80 °C, the NMR spectra were recorded.

¹H NMR (250 MHz, CD₂Cl₂, 203K): δ = 3.90 (s), 4.12 (s), 5.03 (s), 6.54 (s, very small).

¹³C NMR (63 MHz, CD₂Cl₂, 203K): δ = -140.3 (s), -52.4 (s), 78.7 (m), ca. 96 (s, very small), 121.5 (q, J = 292 Hz).

Solvent-free reaction:

Solid [Ag(CH₂Cl₂)]pftb (0.472g, 0.407 mmol) and solid CHI₃ (0.160 g, 0.407 mmol) were mixed together in a mortar. At the beginning, when only few CHI₃ was added, the mixture turns green, but after all CHI₃ is added, the color changes to red-brown.

10.2.3.6 Reaction of $[\text{Cl}_3]^+[\text{pftb}]^-$ with Et_2O

Preparative reaction:

Solid $[\text{Cl}_3]^+[\text{pftb}]^-$ (0.367 g, 0.27 mmol) was weighed into a two-bulb frit plate Schlenk vessel equipped with two J. Young valves. After the addition of 10 mL of CH_2Cl_2 and 4 mL of Et_2O , the brown-red solution was kept at -30°C . Few crystals of $[\text{H}(\text{Et}_2\text{O})_2]^+[\text{pftb}]^-$ were obtained from this reaction (X-ray diffraction).

in situ NMR-tube reaction:

Solid $[\text{Cl}_3]^+[\text{pftb}]^-$ (0.200 g, 0.15 mmol) was weighed into an NMR tube. After the addition of 0.7 mL of CD_2Cl_2 , 3 equivalents of Et_2O (0.33 g, 0.45 mmol) were condensed on the solution. The NMR tube was then flame-sealed and kept at -30°C .

^1H NMR (250 MHz, CD_2Cl_2 , 300K): δ = 1.34, 1.76, 3.20, 3.90, 5.43, 16.50.

^{13}C NMR (63 MHz, CD_2Cl_2 , 300K): δ = -160.0, 14.2, 14.8, 67.2, 69.0, 79, 121.7, 122.1 (q, $^1J_{\text{C-F}}$ = 293 Hz).

^{19}F NMR (235 MHz CD_2Cl_2 , 300K): δ = -75.7 (s).

^{27}Al NMR (78 MHz, CD_2Cl_2 , 300K): δ = 34.6 (s, $\omega_{1/2}$ = 4 Hz).

10.2.3.7 Synthesis and Characterization of $[\text{I}_3\text{C-PCl}_3]^+[\text{pftb}]^-$ **19**

Preparative reaction:

Solid $[\text{ClI}_3]^+[\text{pftb}]^-$ (0.640 g, 0.47 mmol) was weighed into a two-bulb frit plate Schlenk vessel equipped with two J. Young valves. After the addition of 10 mL of CH_2Cl_2 and cooling to -78°C , liquid PCl_3 (41 μL , 0.47 mmol) was added by using a Hamilton syringe. The resulting dark brownish solution was kept over night at -80°C . The solution was filtered, the filtrate was highly concentrated and stored for a few days at -30°C for crystallization. Orange-yellow plate-shaped crystals were obtained.

Yield: 0.618 g (87.7 %)

IR (Diamond-ATR): $\tilde{\nu}$ = 204, 235, 384, 305, 315, 367, 378, 440, 501, 536, 560, 571, 614, 642, 727, 833, 927, 1164, 1216, 1236, 1272, 1280, 1353 cm^{-1} .

^{13}C NMR (101 MHz, CD_2Cl_2 , 203K): δ = 120.5 ($^1J_{\text{C-F}}$ = 293 Hz), 78 (m), -135.2 ($^1J_{\text{C-P}}$ = 29 Hz)

^{19}F NMR (376 MHz CD_2Cl_2 , 297 K): δ = - 75.3 (s).

^{27}Al NMR (104 MHz, CD_2Cl_2 , 203 K): δ = 38.8 (s, $\omega_{1/2}$ = 25 Hz).

^{31}P NMR (101 MHz, CD_2Cl_2 , 203 K): δ = 218.3 (s).

in situ NMR-tube reaction:

Solid $[\text{ClI}_3]^+[\text{pftb}]^-$ (0.200 g, 0.15 mmol) was weighed into an NMR tube. After the addition of 0.7 mL of CD_2Cl_2 and cooling to -78°C , liquid PCl_3 (13 μL , 0.15 mmol) was added by using a Hamilton syringe. The NMR tube was flame-sealed and the resulting dark brownish solution was kept over night at -80°C before the NMR-spectra were recorded.

^{13}C NMR (101 MHz, CD_2Cl_2 , 203K): δ = 120.5 ($^1J_{\text{C-F}}$ = 293 Hz), 78 (m), -135.2 ($^1J_{\text{C-P}}$ = 29 Hz).

^{19}F NMR (376 MHz CD_2Cl_2 , 297 K): δ = -75.3 (s).

^{27}Al NMR (104 MHz, CD_2Cl_2 , 203 K): δ = 38.8 (s, $\omega_{1/2}$ = 25 Hz).

^{31}P NMR (101 MHz, CD_2Cl_2 , 203 K): δ = 218.3 (s).

10.2.3.8 Synthesis and Characterization of $[\text{I}_3\text{C-PBr}_3]^+[\text{pftb}]^-$ 20

Preparative reaction:

Solid $[\text{Cl}_3]^+[\text{pftb}]^-$ (0.553 g, 0.41 mmol) was weighed into a two-bulb frit plate Schlenk vessel equipped with two J. Young valves. After the addition of 10 mL of CH_2Cl_2 and cooling to -78°C , liquid PBr_3 (37 μL , 0.41 mmol) was added by using a Hamilton syringe. The resulting dark brownish solution was kept over night at -80°C . The solution was filtered, the filtrate was highly concentrated and stored for a few days at -40°C for crystallization. Amber plate-shaped crystals were obtained.

Yield: 0.512 g (84.1%)

IR (Diamond-ATR): $\tilde{\nu}$ = 205, 284, 316, 366, 383, 445, 509, 537, 561, 571, 727, 754, 834, 927, 1163, 1216, 1237, 1273, 1280, 1353 cm^{-1} .

^{13}C NMR (101 MHz, CD_2Cl_2 , 203 K): δ = 120.5 (q, $^1J_{\text{C-F}}$ = 292 Hz), 77.9 (m), -120.1 ($^1J_{\text{C-P}}$ not resolved).

^{19}F NMR (376 MHz CD_2Cl_2 , 297 K): δ = -75.3 (s).

^{27}Al NMR (104 MHz, CD_2Cl_2 , 203 K): δ = 38.8 (s, $\omega_{1/2}$ = 21 Hz).

^{31}P NMR (101 MHz, CD_2Cl_2 , 203 K): δ = 38.8 (s).

in situ NMR-tube reaction:

Solid $[\text{Cl}_3]^+[\text{pftb}]^-$ (0.200 g, 0.15 mmol) was weighed into an NMR tube. After the addition of 0.7 mL of CD_2Cl_2 and cooling to -78°C , liquid PBr_3 (14 μL , 0.15 mmol) was added by using a Hamilton syringe. The NMR tube was flame-sealed and the resulting dark brownish solution was kept over night at -80°C before the NMR-spectra were recorded.

^{13}C NMR (101 MHz, CD_2Cl_2 , 203 K): δ = 120.5 (q, $^1J_{\text{C-F}}$ = 292 Hz), 77.9 (m), -120.1 ($^1J_{\text{C-P}}$ not resolved).

^{19}F NMR (376 MHz CD_2Cl_2 , 297 K): δ = -75.3 (s).

^{27}Al NMR (104 MHz, CD_2Cl_2 , 203 K): δ = 38.8 (s, $\omega_{1/2}$ = 21 Hz).

^{31}P NMR (101 MHz, CD_2Cl_2 , 203 K): δ = 38.8 (s).

10.2.3.9 Synthesis and Characterization of $[\text{I}_3\text{C-PI}_3]^+[\text{pftb}]^-$ **21**

Preparative reaction:

Solid $[\text{ClI}_3]^+[\text{pftb}]^-$ (0.500 g, 0.37 mmol) and solid PI_3 (0.150 g, 0.37 mmol) were weighed into a two-bulb frit plate Schlenk vessel equipped with two J. Young valves. CH_2Cl_2 (15 mL) was condensed on this solid mixture and the resulting dark red-brown solution was kept over night at -80°C . The solution was filtered, the filtrate was highly concentrated and stored for a few days at -30°C for crystallization. The product crystallizes as yellow-orange blocks.

Yield: 0.457 g (83.0 %)

IR (Diamond ATR): $\tilde{\nu} = 424$ (m), 443 (m), 536 (m), 560 (m), 683(vw), 725 (s), 755(w), 831(m), 971 (s) 1156 (s), 1170 (vs), 1215 (vs), 1245 (vs), 1275 (vs), 1304 (vs) cm^{-1} .

^{13}C NMR (101 MHz, CD_2Cl_2 , 203K): $\delta = 120.6$ (q, $^1J_{\text{C-F}} = 292$ Hz), 78.0 (m), -109.1 (d, $^1J_{\text{C-P}} = 42$ Hz)).

^{19}F NMR (377 MHz CD_2Cl_2 , 203K): $\delta = -75.3$ (s).

^{27}Al NMR (104 MHz, CD_2Cl_2 , 203K): $\delta = 36.2$ (s, $\omega_{1/2} = 9$ Hz).

^{31}P NMR (101 MHz, CD_2Cl_2 , 103K): $\delta = -69.6$ (s).

in situ NMR-tube reaction:

Solid $[\text{ClI}_3]^+[\text{pftb}]^-$ (0.200 g, 0.15 mmol) and solid PI_3 (0.061 g, 0.15 mmol) were weighed into an NMR tube. After the addition of 0.7 mL of CD_2Cl_2 and cooling to -78°C , the NMR tube was flame-sealed and the resulting dark brownish-red solution was kept over night at -80°C before the NMR-spectra were recorded.

^{13}C NMR (101 MHz, CD_2Cl_2 , 203K): $\delta = 120.6$ (q, $^1J_{\text{C-F}} = 292$ Hz), 78.0 (m), -109.1 (d, $^1J_{\text{C-P}} = 42$ Hz)).

^{19}F NMR (377 MHz CD_2Cl_2 , 203K): $\delta = -75.3$ (s).

^{27}Al NMR (104 MHz, CD_2Cl_2 , 203K): $\delta = 36.2$ (s, $\omega_{1/2} = 9$ Hz).

^{31}P NMR (101 MHz, CD_2Cl_2 , 203K): $\delta = -69.6$ (s).

10.2.3.10 Synthesis and Characterization of $[\text{I}_3\text{C-PI}_3]^+[\text{al-f-al}]^-$ 23 and $[\text{PI}_4]^+[\text{pftb}]^-$ 24

Solid $[\text{ClI}_3]^+[\text{pftb}]^-$ (0.981 g, 0.72 mmol) and solid PI_3 (0.297 g, 0.72 mmol) were weighed into a two-bulb frit plate Schlenk vessel equipped with two J. Young valves. CH_2Cl_2 (20 mL) was condensed on this solid mixture and the resulting dark red-brown solution was kept over night at -25°C . The solution was then kept at room temperature for a few hours, filtered; the filtrate was highly concentrated and stored for a few days at -30°C for crystallization. Very few crystals of 23 and 24 have been obtained and were characterized by single-crystal X-ray diffraction.

10.2.3.11 Synthesis and Characterization of $[\text{I}_3\text{As-ClI}_3]^+[\text{pftb}]^-$ 23

Preparative reaction:

Solid $[\text{ClI}_3]^+[\text{pftb}]^-$ (0.607 g, 0.44 mmol) and solid AsI_3 (0.203 g, 0.44 mmol) were weighed into a two-bulb frit plate Schlenk vessel equipped with two J. Young valves. CH_2Cl_2 (15 mL) was condensed on this solid mixture and the resulting dark red-brown solution was kept over night at -30°C . The solution was filtered, the filtrate was highly concentrated and stored for a few days at -30°C for crystallization but only crystals of AsI_3 could be obtained.

^{13}C NMR (101 MHz, CD_2Cl_2 , 223K): $\delta = 120.2$ (q, $^1J_{\text{C-F}} = 293$ Hz), 77.7 (m), -119.2 (s).

^{19}F NMR (377 MHz CD_2Cl_2 , 193K): $\delta = -75.9$ (s).

^{27}Al NMR (104 MHz, CD_2Cl_2 , 223K): $\delta = 35.2$ (s, $\omega_{1/2} = 11$ Hz).

in situ NMR tube reaction:

Solid $[\text{ClI}_3]^+[\text{pftb}]^-$ (0.200 g, 0.15 mmol) and solid AsI_3 (0.067 g, 0.15 mmol) were weighed into an NMR tube. After the addition of 0.7 mL of CD_2Cl_2 and cooling to -78°C , the NMR tube was flame-sealed and the resulting dark brownish solution was kept over night at -80°C before the NMR-spectra were recorded.

^{13}C NMR (101 MHz, CD_2Cl_2 , 223K): $\delta = 120.2$ (q, $^1J_{\text{C-F}} = 293$ Hz), 77.7 (m), -119.2 (s).

^{19}F NMR (377 MHz CD_2Cl_2 , 193K): $\delta = -75.9$ (s).

^{27}Al NMR (104 MHz, CD_2Cl_2 , 223K): $\delta = 35.2$ (s, $\omega_{1/2} = 11$ Hz).

10.2.4 Syntheses and Characterization of the Compounds Addressed in Chapter 8

10.2.4.1 Synthesis of $[\text{NO}_2]^+[\text{pftb}]^-$ **25**

Solid $\text{Li}[\text{pftb}]$ (1.011 g, 1.04 mmol) and solid $[\text{NO}_2]^+[\text{BF}_4]^-$ **26** (0.138 g, 1.04 mmol) were weighed into a Schlenk vessel. CH_2Cl_2 (ca. 20 mL) was added by condensation and the reaction mixture was stirred at r.t. for 1 day. The suspension was filtered, the yellowish solution was highly concentrated and stored at -30°C . After a few days, very air and moisture sensitive colorless needles of **25** formed in good yield.

Raman: $\tilde{\nu} = 175$ (w), 212 (w), 243 (mw), 292 (mw), 327 (ms), 370 (m), 448 (w), 539 (m), 654 (m), 574 (m), 748 (s), 798 (s), 978 (w), 1120 (w), 1206 (w), 1249 (mw), 1275 (mw), 1314 (w), 1354 (w), 2343 (ms), 2759 (w), 2940 (w), 3005 (w) cm^{-1} .

^{13}C NMR (63 MHz, CD_2Cl_2 , 300K): $\delta = 121.5$ (q, $J = 292$ Hz), 79 (m).

^{19}F NMR (376 MHz, CD_2Cl_2 , 300K): $\delta = -75.4$ (s).

^{27}Al NMR (78 MHz, CD_2Cl_2 , 300K): $\delta = 34.2$ (s, $\omega_{1/2} = 34$ Hz).

10.2.4.2 Alternative attempt to synthesize $[\text{NO}_2]^+[\text{pftb}]^-$ **25** from $\text{Li}[\text{pftb}]$ and $[\text{NO}_2]^+[\text{BF}_4]^-$ **26** in 1,2- $\text{C}_6\text{F}_2\text{H}_4$

Solid $\text{Li}[\text{pftb}]$ (1.000 g, 1.03 mmol) and solid $[\text{NO}_2]^+[\text{BF}_4]^-$ **26** (0.136 g, 1.03 mmol) were weighed into a Schlenk vessel. $\text{C}_6\text{H}_4\text{F}_2$ (ca. 15 mL) was added by condensation and the reaction mixture was stirred at r.t. for a few hours. The color changed immediately to orange, and gas formation was observed. After all solvent was removed in vacuum, CH_2Cl_2 (20 mL) was added, and the yellowish reaction mixture was stirred at r.t. for 30 minutes. The suspension was then filtered, the yellowish solution was highly concentrated and stored at 2°C . After a few days, colorless block-shaped crystals of **27** formed.

Isolated yield: 0.177 g (8.9 %)

Raman: $\tilde{\nu} = 330$ (w), 368 (w), 437 (w), 539 (w), 561 (w), 572 (w), 590 (w), 645 (w), 747 (w), 785 (m), 799 (w), 826 (w), 948 (w), 1080 (m), 1218 (w), 1249 (w), 1292 (m), 1355 (s), 1379 (vs), 1438 (mw), 1497 (w), 1510 (w), 1535 (w), 1604 (ms), 2757 (w), 2909 (w), 2937 (w), 3104 (w) cm^{-1} .

10.2.4.3 Alternative attempt to synthesize $[\text{NO}_2]^+[\text{pftb}]^-$ **25** from Cl_2 , NO_2 and $\text{Ag}[\text{pftb}]$

Cl_2 (20 mbar, 0.234 mmol) and NO_2 (40 mbar, 0.468 mmol) were condensed into a vessel ($V = 0.291$ l) and irradiated at r.t. But since no reaction occurs (no change of pressure due to formation of NO_2Cl), this mixture was condensed onto a solution of $\text{Ag}[\text{pftb}]$ (0.487 mg, 0.468 mmol) and stirred for a few hours. But only little AgCl formed, even after further irradiation with UV light.

10.2.4.4 Attempt to synthesize $[\text{NO}_2]^+[\text{f-alor}_3]^-$

To a solution of 2.01 M AlMe_3 in heptane (1.40 mL, 2.82 mmol) and 20 mL of pentane, which was stirred at -5°C , $(\text{CF}_3)_3\text{COH}$ (1.30 mL, 9.33 mmol) was added drop-wise. After the quantitative formation of methane, $[\text{NO}_2]^+[\text{BF}_4]^-$ **26** (0.380 g, 2.84 mmol) were added. Then ca. 40 mL of CH_2Cl_2 were condensed onto the mixture and the reaction mixture was stirred over night at 0°C and then allowed to reach r.t.. Some colourless needle-shaped crystals of **26** formed from the orange-brown solution.

^1H NMR (400 MHz, CD_2Cl_2 , 300 K): $\delta = 0.93$ (m, n-pentane), 1.30 (m, n-heptane).

^{27}Al NMR (78 MHz, CD_2Cl_2 , 300 K): $\delta = 33.4$ (s, very weak).

^{13}C NMR (101 MHz, CD_2Cl_2 , 300 K): $\delta = 13.2$ (s), 21.6 (s), 33.5 (s), 52.5 (m).

^{19}F NMR (376 MHz, CD_2Cl_2 , 300 K): $\delta = -74.4$ (s).

10.2.4.5 Attempts to synthesize $[\text{NO}_2]^+[\text{al-f-al}]^-$

Reaction in pentane:

To a solution of 2.01 M AlMe_3 in heptane (1.40 mL, 2.82 mmol) and 20 mL of pentane, which was stirred at -5°C , $(\text{CF}_3)_3\text{COH}$ (1.30 mL, 9.33 mmol) were added drop-wise. After the quantitative formation of methane, $[\text{NO}_2]^+[\text{BF}_4]^-$ **26** (0.190 g, 1.42 mmol) were added. Then ca. 40 mL of CH_2Cl_2 were condensed onto the mixture and the reaction mixture was stirred over night at 0°C and then allowed to reach r.t.. Some colourless needle-shaped crystals of **26** form from the orange-brown solution.

^1H NMR (400 MHz, CD_2Cl_2 , 300 K): δ = 0.93 (m, n-pentane), 1.30 (m, n-heptane).

^{27}Al NMR (78 MHz, CD_2Cl_2 , 300 K): δ = 37.6 (m, broad).

^{13}C NMR (101 MHz, CD_2Cl_2 , 300 K): δ = 14.0 (s), 23.0 (s), 23.5 (s), 30.1 (s), 31.9 (s), 34.5 (s), 54.1 (s).

^{19}F NMR (376 MHz, CD_2Cl_2 , 300 K): δ = - 76.2 (s).

Reaction in 1,2- $\text{C}_6\text{F}_2\text{H}_4$:

In the glovebox, $[\text{NO}_2]^+[\text{BF}_4]^-$ **26** (0.133g, 1.00 mmol) was weighed into a Schlenk vessel. After the addition of 15 mL of 1,2- $\text{C}_6\text{F}_2\text{H}_4$ and cooling to 0°C , a 1.0 M solution of $\text{Al}(\text{OC}(\text{CF}_3)_3)_3$ in $\text{C}_6\text{H}_5\text{F}$ (2.0 mL, 2.0 mmol) was added. The reaction mixture was stirred at 0°C for 30 minutes and then another 30 minutes at r.t. before filtration. The brownish solution was concentrated and stored at 2°C . After 1 day, colorless plate-shaped crystals of 3,4- $\text{C}_6\text{H}_3\text{F}_2\text{NO}_2 \cdot \text{Al}(\text{OC}(\text{CF}_3)_3)_3$ **28** formed.

IR (Diamond ATR): $\tilde{\nu}$ = 203 (w), 221 (w), 289 (w), 310 (w), 334 (w), 377 (w), 404 (w), 448 (w), 497 (w), 536 (w), 575 (w), 657 (w), 727 (ms), 743 (w), 783 (w), 827 (w), 874 (w), 891 (w), 945 (w), 974 (s), 1077 (w), 1127 (w), 1162 (w), 1184 (m), 1222 (s), 1249 (vs), 1268 (vs), 1300 (ms), 1357 (mw), 1439 (w), 1417 (mw), 1557 (mw) 1603 (mw) cm^{-1} .

10.2.4.6 Reaction of $[\text{NO}_2]^+[\text{pftb}]^-$ **25** with 1.25 P_4

$[\text{NO}_2]^+[\text{pftb}]^-$ **25** (0.133 g, 0.131 mmol) and P_4 (0.036 g, 0.295 mmol) were weighed together in an NMR tube. 0.7 mL of CD_2Cl_2 were added and the sealed NMR tube was then stored at -80°C for a few days. The reaction mixture first turns red, and then bright yellow.

^{31}P NMR (101 MHz, CD_2Cl_2 , 243K): $\delta = 355.5$ (t, $J = 160$ Hz), -231.0 (t, $J = 160$ Hz), -457 (br, solid P_4).

^{19}F NMR (376 MHz, CD_2Cl_2 , 300K): $\delta = -75.1$ (s).

^{27}Al NMR (78 MHz, CD_2Cl_2 , 193K): $\delta = 37.2$ (s, $\omega_{1/2} = 28$ Hz).

10.2.4.7 Reaction of $[\text{NO}_2]^+[\text{pftb}]^-$ **25** with 2.25 P_4

$[\text{NO}_2]^+[\text{pftb}]^-$ **25** (0.519 g, 0.512 mmol) and P_4 (0.143 g, 0.115 mmol) were weighed together in a double-side Schlenk vessel. After the addition of 15 mL of CH_2Cl_2 , the reaction mixture was stirred at -50°C for 8 hours. The yellow solution was filtered, concentrated and kept at low temperatures, but no crystals could be obtained.

^{31}P NMR (101 MHz, CD_2Cl_2 , 243K): $\delta = 355.5$ (t, $J = 160$ Hz), -231.0 (t, $J = 160$ Hz), -457 (br, solid P_4), -518 (s, dissolved P_4).

^{19}F NMR (376 MHz, CD_2Cl_2 , 300K): $\delta = -75.2$ (s).

^{27}Al NMR (78 MHz, CD_2Cl_2 , 193K): $\delta = 37.2$ (s, $\omega_{1/2} = 28$ Hz).

10.2.4.8 Reaction of $[\text{NO}_2]^+[\text{BF}_4]^-$ **26** with $[\text{Ag}(\text{P}_4)_2][\text{pftb}]^-$ and $\text{Ag}[\text{pftb}]$

NO_2BF_4 (0.050 g, 0.376 mmol), $[\text{Ag}(\text{P}_4)_2]^+[\text{pftb}]^-$ (0.265 g, 0.188 mmol) and $\text{Ag}[\text{pftb}]$ (0.218 g, 0.188 mmol) were weighed together in a Schlenk vessel, and 20 mL CH_2Cl_2 were added by condensation. As after 6 days, no reaction was observed from the ^{31}P NMR, NaCl (0.038 g, 0.650 mmol) were added. But after 2 hours of ultrasonic treatment, still no reaction occurred.

^{31}P -NMR (162 MHz, CD_2Cl_2 , 300K): $\delta = -500.3$ (s, $[\text{Ag}(\text{P}_4)_2]^+$).

10.2.4.9 Attempt to synthesize $[\text{P}_4\text{-NO}_2]^+[\text{BF}_4]^-$

$[\text{NO}_2]^+[\text{BF}_4]^-$ **26** (0.053 g, 0.406 mmol) and P_4 (0.050 g, 0.404 mmol) were weighed together in an NMR tube. After the addition of CD_2Cl_2 , the sealed NMR tube was treated in an ultrasonic bath for one day. A yellowish suspension forms.

^{31}P -NMR (162 MHz, CD_2Cl_2 , 300K): $\delta = -522.4$ (s, P_4).

10.3 Quantum Chemical Calculations

Geometry Optimizations:

The model compounds have been investigated with density functional (BP86)^[349] as well as with *ab initio* (MP2^[350, 351] and ccsd(t)) calculations using the following basis sets: SV(P)^[352], TZVPP^[353, 354], aug-cc-pVTZ^[332, 355, 356] and aug-cc-pVQZ^[332, 356]. The latter two basis sets have been obtained from the EMSL Gaussian Basis set order form at <http://www.emsl.pnl.gov/forms/basisform.html>^[357]. For heavy elements, the core electrons were replaced by a quasi-relativistic electronic core potentials (ECPs) (Ag: 28 electrons^[358], I: 46 electrons^[359]). In some cases a complete basis set extrapolation according to the procedure described by Martin *et al.* was performed^[274]. All MP2 calculations have been performed using the frozen core optimization for the inner shells. Some small particles have also been calculated at the G3 level^[360]. The method and basis sets used for the different compounds are indicated in the main text. If not mentioned otherwise, the geometries of all calculated structures were optimized using the highest possible point group symmetry. The DFT and MP2 calculations have been performed with the program package TURBOMOLE^[361] (using the resolution of identity (RI) approximation^[350]), while for ccsd(t) computations, GAUSSIAN03^[362] was used.

Frequency Calculations, Thermal Corrections, Population Analyses and Solvation Energies:

Vibrational frequencies were calculated with AOFORCE^[363] at the (RI-)BP86/SV(P) level (if not specified otherwise). They were used to verify if the obtained geometry represents a true minimum on the potential energy surface (PES), as well as to determine the zero point vibrational energy (ZPE). Based on these frequency analyses, the thermal contributions to the enthalpy and Gibbs free energy have been calculated using the module FREEH implemented in TURBOMOLE. Calculations of solvation energies (solvent CH₂Cl₂ with $\epsilon_r(298\text{K}) = 8.93$ and $\epsilon_r(195\text{K}) = 14.95$) have been done with the COSMO^[364] module as (RI-)BP86/SV(P) single points using C₁ symmetry. For some species, a modified Roby-Davidson population analysis based on occupation numbers (paboon) has been performed.

NMR Shifts:

Non-relativistic NMR shifts have been performed with the MPSHIFT^[365] module included in TURBOMOLE as single point calculations on converged geometries using the all-electron SVPallS2^[352, 354] basis set for Ag and SV(P) for P and S.

To assess SO corrections to ¹³C and ¹H chemical shifts, additional DFT calculations were carried out at the MP2/TZVPP optimized structures with the ReSpect program package^[366]. Both initial nonrelativistic calculations and subsequent computations of SO corrections employed the BP86 functional^[349], gauge-including atomic orbitals (GIAOs)^[367], Huzinaga-Kutzelnigg-type IGLO-II basis sets^[368] for C, H, Cl and I (as well as Si for TMS), and a DZVP all-electron basis^[369] for Ag. Initial nonrelativistic shielding calculations at uncoupled DFT level^[370] were followed by calculation of SO corrections using the finite perturbation approach of Ref. 241 (by default, the finite perturbation Fermi-contact parameter λ was set to 10^{-3} a.u.), together with a full treatment of all one- and two-electron SO integrals of the Breit-Pauli SO Hamiltonian. Absolute shieldings at nonrelativistic level were converted to relative shifts using computed shieldings for SiMe₄ of 184.0 ppm and 32.02 ppm for ¹³C and ¹H shifts, respectively. SO-corrected shifts take into account also an SO correction of -0.4 ppm to the ¹³C shielding of SiMe₄ at the given level.

Electronic Excitation Energies:

Electronic excitations have been calculated by time-dependent DFT at the (RI-)BP86/SV(P) level, using the ESCF module included in TURBOMOLE^[371].

11 References

- [1] W. Beck, K. Sünkel, *Chem. Rev.* **1988**, *88*, 1405.
- [2] C. A. Reed, *Acc. Chem. Res.* **1998**, *31*, 133.
- [3] S. H. Strauss, *Chem. Rev.* **1993**, *93*, 927.
- [4] I. Krossing, I. Raabe, *Angew. Chem. Int. Ed.* **2004**, *43*, 2066.
- [5] E. Y.-X. Chen, T. J. Marks, *Chem. Rev.* **2000**, *100*, 1391.
- [6] A. J. Lupinetti, S. H. Strauss, *Chemtracts* **1998**, *11*, 565.
- [7] A. G. Massey, A. J. Park, *J. Organomet. Chem.* **1964**, *2*, 245.
- [8] D. M. Van Seggen, P. K. Hurlburt, O. P. Anderson, S. H. Strauss, *Inorg. Chem.* **1995**, *34*, 3453.
- [9] T. S. Cameron, I. Krossing, J. Passmore, *Inorg. Chem.* **2001**, *40*, 4488.
- [10] D. Stasko, C. A. Reed, *J. Am. Chem. Soc.* **2002**, *124*, 1148.
- [11] I. Krossing, *Chem. Eur. J.* **2001**, *7*, 490.
- [12] S. M. Ivanova, B. G. Nolan, Y. Kobayashi, S. M. Miller, O. P. Anderson, S. H. Strauss, *Chem. Eur. J.* **2001**, *7*, 503.
- [13] M. Bochmann, *Angew. Chem.* **1992**, *104*, 1206; K. Seppelt, *Angew. Chem.* **1993**, *105*, 1074.
- [14] K. Fujiki, S.-Y. Ikeda, H. Kobayashi, A. Mori, A. Nagira, J. Nie, T. Sonoda, Y. Yagupolskii, *Chem. Lett.* **2000**, 62.
- [15] J. H. Golden, P. F. Mutolo, E. B. Lobkovsky, F. J. DiSalvo, *Inorg. Chem.* **1994**, *33*, 5374.
- [16] J. van den Broeke, B.-J. Deelman, G. van Koten, *Tetrahedron Lett.* **2001**, *42*, 8085; K. Fujiki, J. Ichikawa, H. Kobayashi, A. Sonoda, T. Sonoda, *J. Fluorine Chem.* **2000**, *102*, 293.
- [17] F. A. R. Kaul, G. T. Puchta, H. Schneider, M. Grosche, D. Mihalios, W. A. Herrmann, *J. Organomet. Chem.* **2001**, *621*, 177.
- [18] L. Jia, X. Yang, A. Ishihara, T. J. Marks, *Organometallics* **1995**, *14*, 3135.
- [19] L. Jia, X. Yang, C. L. Stern, T. J. Marks, *Organometallics* **1997**, *16*, 842.
- [20] G. Rodriguez, P. Brant, *Organometallics* **2001**, *20*, 2417.
- [21] P. Biagini, G. Lugli, L. Abis, P. Andreussi, *Pentafluorophenyl derivatives of aluminum, gallium and indium and preparation from boron analog and metal alkyl*, (Enichem Elastomeri S.R.L., Italy). Application: EP, **1996**, p. 9 pp; M. Bochmann, M. J. Sarsfield, *Organometallics* **1998**, *17*, 5908.

- [22] S. J. Lancaster, D. A. Walker, M. Thornton-Pett, M. Bochmann, *Chem. Comm.* **1999**, 1533; R. E. Lapointe, *Catalyst activators comprising expanded anions for olefin polymerization*, (The Dow Chemical Company, USA). Application: WO, **1999**, p. 56 pp.
- [23] J. Zhou, S. J. Lancaster, D. A. Walker, S. Beck, M. Thornton-Pett, M. Bochmann, *J. Am. Chem. Soc.* **2001**, *123*, 223.
- [24] S. J. Lancaster, A. Rodriguez, A. Lara-Sanchez, M. D. Hannant, D. A. Walker, D. H. Hughes, M. Bochmann, *Organometallics* **2002**, *21*, 451.
- [25] E. Bernhardt, M. Finze, H. Willner, C. W. Lehmann, F. Aubke, *Angew. Chem. Int. Ed.* **2003**, *42*, 2077; D. J. Brauer, H. Buerger, Y. Chebude, G. Pawelke, *Inorg. Chem.* **1999**, *38*, 3972; M. Finze, E. Bernhardt, A. Terheiden, M. Berkei, H. Willner, D. Christen, H. Oberhammer, F. Aubke, *J. Am. Chem. Soc.* **2002**, *124*, 15385; G. Pawelke, H. Burger, *Coord. Chem. Rev.* **2001**, *215*, 243.
- [26] E. Bernhardt, G. Henkel, H. Willner, G. Pawelke, H. Burger, *Chem. Eur. J.* **2001**, *7*, 4696.
- [27] M. Schmidt, A. Kühner, K.-D. Franz, G.-V. Rösenthaller, G. Bissky, *Borate salts for the application in electrochemical cells*, (Merck Patent G.m.b.H., Germany). Application: DE, **2002**, p. 10 pp.
- [28] M. Schmidt, A. Kühner, H. Willner, E. Bernhardt, *Tetrakisfluoroalkylborate salts and their use as electrolyte salts*, (Merck Patent GmbH, Germany). Application: EP, **2002**, p. 20 pp.
- [29] S. Körbe, P. J. Schreiber, J. Michl, *Chem. Rev.* **2006**, *106*, 5208.
- [30] T. Jelinek, J. Plešek, S. Hermanek, B. Stibr, *Collect. Czech. Chem. Commun.* **1986**, *51*, 819.
- [31] M. Juhasz, S. Hoffmann, E. Stoyanov, K.-C. Kim, C. A. Reed, *Angew. Chem., Int. Ed. Engl.* **2004**, *43*, 5352.
- [32] E. S. Stoyanov, C. A. Reed, *J. Phys. Chem. A* **2006**, *110*, 12992.
- [33] K.-C. Kim, C. A. Reed, D. W. Elliott, L. J. Müller, F. Tham, L. Lin, J. B. Lambert, *Science* **2002**, *297*, 825.
- [34] C. A. Reed, K. C. Kim, R. D. Bolskar, L. J. Müller, *Science* **2000**, *289*, 101.
- [35] L. J. Mueller, D. W. Elliott, K.-C. Kim, C. A. Reed, P. D. W. Boyd, *J. Am. Chem. Soc.* **2002**, *124*, 9360.
- [36] K.-C. Kim, C. A. Reed, G. S. Long, A. Sen, *J. Am. Chem. Soc.* **2002**, *124*, 7662.
- [37] C. A. Reed, K.-C. Kim, E. S. Stoyanov, D. Stasko, F. S. Tham, L. J. Mueller, P. D. W. Boyd, *J. Am. Chem. Soc.* **2003**, *125*, 1796.

- [38] C. A. Reed, N. L. P. Fackler, K.-C. Kim, D. Stasko, D. R. Evans, P. D. W. Boyd, C. E. F. Rickard, *J. Am. Chem. Soc.* **1999**, *121*, 6314.
- [39] E. Molinos, G. Kociok-Koehn, A. S. Weller, *Chem. Commun.* **2005**, 3609.
- [40] M. V. Metz, Y. Sun, C. L. Stern, T. J. Marks, *Organometallics* **2002**, *21*, 3691; Y. Sun, M. V. Metz, C. L. Stern, T. J. Marks, *Organometallics* **2000**, *19*, 1625.
- [41] I. Krossing, A. Reisinger, *Eur. J. Inorg. Chem.* **2005**, 1979.
- [42] I. Krossing, *J. Am. Chem. Soc.* **2001**, *123*, 4603.
- [43] I. Krossing, L. Van Wüllen, *Chem. Eur. J.* **2002**, *8*, 700.
- [44] A. Adolf, M. Gonsior, I. Krossing, *J. Am. Chem. Soc.* **2002**, *124*, 7111.
- [45] T. S. Cameron, A. Decken, I. Dionne, M. Fang, I. Krossing, J. Passmore, *Chem. Eur. J.* **2002**, *8*, 3386.
- [46] I. Krossing, A. Reisinger, *Angew. Chem. Int. Ed.* **2003**, *42*, 5725.
- [47] I. Krossing, A. Bihlmeier, I. Raabe, N. Trapp, *Angew. Chem. Int. Ed.* **2003**, *42*, 1531.
- [48] M. Gonsior, I. Krossing, L. Müller, I. Raabe, M. Jansen, L. Van Wüllen, *Chem. Eur. J.* **2002**, *8*, 4475.
- [49] I. Krossing, I. Raabe, *Angew. Chem. Int. Ed.* **2001**, *40*, 4406.
- [50] M. Gonsior, I. Krossing, *Dalton Trans.* **2005**, 1203.
- [51] I. Krossing, *J. Chem. Soc., Dalton Trans.* **2002**, 500.
- [52] A. Bihlmeier, M. Gonsior, I. Raabe, N. Trapp, I. Krossing, *Chem. Eur. J.* **2004**, *10*, 5041.
- [53] D. M. Van Seggen, P. K. Hurlburt, M. D. Noirot, O. P. Anderson, S. H. Strauss, *Inorg. Chem.* **1992**, *31*, 1423.
- [54] H. P. A. Mercier, J. C. P. Sanders, G. J. Schrobilgen, *J. Am. Chem. Soc.* **1994**, *116*, 2921.
- [55] P. K. Hurlburt, J. J. Rack, J. S. Luck, S. F. Dec, J. D. Webb, O. P. Anderson, S. H. Strauss, *J. Am. Chem. Soc.* **1994**, *116*, 10003.
- [56] M. Gerken, P. Kolb, A. Wegner, H. P. Mercier, H. Borrmann, D. A. Dixon, G. J. Schrobilgen, *Inorg. Chem.* **2000**, *39*, 2813.
- [57] W. J. Casteel, Jr., P. Kolb, N. LeBlond, H. P. A. Mercier, G. J. Schrobilgen, *Inorg. Chem.* **1996**, *35*, 929.
- [58] H. P. A. Mercier, M. D. Moran, G. J. Schrobilgen, C. Steinberg, R. J. Suontamo, *J. Am. Chem. Soc.* **2004**, *126*, 5533.
- [59] S. Brownstein, *Can. J. Chem.* **1969**, *47*, 605; P. A. W. Dean, R. J. Gillespie, R. Hulme, *Chem. Commun.* **1969**, 990.
- [60] K. O. Christe, X. Zhang, R. Bau, J. Hegge, G. A. Olah, G. K. S. Prakash, J. A. Sheehy, *J. Am. Chem. Soc.* **2000**, *122*, 481.

- [61] R. Minkwitz, C. Hirsch, T. Berends, *Eur. J. Inorg. Chem.* **1999**, 2249; R. Minkwitz, F. Neikes, *Inorg. Chem.* **1999**, 38, 5960.
- [62] A. J. Edwards, G. R. Jones, R. J. C. Sills, *Chem. Commun.* **1968**, 1527.
- [63] T. Drews, K. Seppelt, *Angew. Chem. Int. Ed.* **1997**, 36, 273.
- [64] S. Seidel, K. Seppelt, *Science* **2000**, 290, 117.
- [65] T. Drews, S. Seidel, K. Seppelt, *Angew. Chem. Int. Ed.* **2002**, 41, 454.
- [66] Z. Zak, A. Ruzicka, *Z. f. Kristallogr.* **1998**, 213, 217.
- [67] R. Appel, G. Eisenhauer, *Chem. Ber.* **1962**, 95, 2468; B. Krumm, A. Vij, R. L. Kirchmeier, J. n. M. Shreeve, *Inorg. Chem.* **1998**, 37, 6295.
- [68] L. Turowsky, K. Seppelt, *Inorg. Chem.* **1988**, 27, 2135; G. Kloeter, H. Pritzkow, K. Seppelt, *Angew. Chem.* **1980**, 92, 954; Y. L. Yagupol'skii, T. I. Savina, *Zhurnal Organicheskoi Khimii* **1983**, 19, 79.
- [69] A. I. Bhatt, I. May, V. A. Volkovich, D. Collison, M. Helliwell, I. B. Polovov, R. G. Lewin, *Inorg. Chem.* **2005**, 44, 4934; F. Croce, A. D'Aprano, C. Nanjundiah, V. R. Koch, C. W. Walker, M. Salomon, *J. Electrochem. Soc.* **1996**, 143, 154.
- [70] Y. L. Yagupol'skii, T. I. Savina, I. I. Gerus, R. K. Orlova, *Zhurnal Organicheskoi Khimii* **1990**, 26, 2030; K. Takasu, N. Shindoh, H. Tokuyama, M. Ihara, *Tetrahedron* **2006**, 62, 11900; A. Sakakura, K. Suzuki, K. Nakano, K. Ishihara, *Org. Lett.* **2006**, 8, 2229; A. Dramska, M. Antoszczyszyn, E. Janus, *Przemysl Chemiczny* **2006**, 85, 47.
- [71] M. Kawamura, D.-M. Cui, S. Shimada, *Tetrahedron* **2006**, 62, 9201; A. K. Chakraborti, Shivani, *J. Org. Chem.* **2006**, 71, 5785.
- [72] K. Takasu, T. Ishii, K. Inanaga, M. Ihara, K. Kowalczyk, J. A. Ragan, *Organic Syntheses* **2006**, 83, 193; P. Goodrich, C. Hardacre, H. Mehdi, P. Nancarrow, D. W. Rooney, J. M. Thompson, *J. Ind. Eng. Chem.* **2006**, 45, 6640; G. Kaur, M. Kaushik, S. Trehan, *Tetrahedron Lett.* **1997**, 38, 2521.
- [73] S. Seki, Y. Kobayashi, H. Miyashiro, Y. Ohno, A. Usami, Y. Mita, N. Kihira, M. Watanabe, N. Terada, *J. Phys. Chem. B* **2006**, 110, 10228; R. Herr, H.-W. Praas, *Secondary lithium battery*, (Varta Batterie AG, Germany). Application: DE, **1994**, p. 5 pp; L. A. Dominey, T. J. Blakley, V. R. Koch, *Proceedings of the Intersociety Energy Conversion Engineering Conference* **1990**, 25th, 382; C. Michot, *Preparation of an electrolyte for lithium batteries*, Application: CA, **2004**, p. 6 pp.
- [74] Z. Fei, D. Kuang, D. Zhao, C. Klein, W. H. Ang, S. M. Zakeeruddin, M. Grätzel, P. J. Dyson, *Inorg. Chem.* **2006**, 45, 10407; T. Nishida, K. Hirano, M. Tomisaki, Y. Tashiro, H. Tsurumaru, A. Nabeshima, Y. Abe, H. Tokuda, A. Oka, *uaternary ammonium salt*,

electrolyte, electrolyte solution and electrochemical device, (Otsuka Chemical Co., Ltd., Japan; Stella Chemifa Corporation). Application: WO, **2006**, p. 97 pp.

[75] J.-Y. Cheng, Y.-H. Chu, *Tetrahedron Lett.* **2006**, 47, 1575.

[76] W. Li, Y. Oyama, M. Matsui, *Battery with molten salt electrolyte and high voltage positive active material*, (Toyota Technical Center USA, Inc., USA; Toyota Motor Company, Japan). Application: WO, **2006**, p. 23 pp.

[77] A. Babai, A.-V. Mudring, *Inorg. Chem.* **2006**, 45, 3249; C. Daguenet, P. J. Dyson, *Organometallics* **2006**, 25, 5811; H. Uchimura, M. Kikuta, *Preparation of superhigh purity ionic liquids*, (Dai-Ichi Kogyo Seiyaku Co., Ltd., Japan). Application: EP, **2006**, p. 14 pp.

[78] M. Lin, C. Liu, L. Zheng, *Wuli Huaxue Xuebao* **1995**, 11, 266.

[79] I. Kossing, A. Reisinger, *Angew. Chem. Int. Ed.* **2003**, 42, 5919.

[80] C. Aubauer, M. Kaupp, T. M. Klapötke, H. Nöth, H. Piotrowski, W. Schnick, J. Senker, M. Suter, *J. Chem. Soc., Dalton Trans.* **2001**, 1880; C. Aubauer, T. M. Klapötke, *Internet Journal of Vibrational Spectroscopy [online computer file]* **2001**, 5.

[81] M. Kaupp, C. Aubauer, G. Engelhardt, T. M. Klapötke, O. L. Malkina, *J. Chem. Phys.* **1999**, 110, 3897.

[82] P. Jutzi, A. Mix, B. Rummel, W. Schöllner, B. Neumann, H.-G. Stammer, *Science* **2004**, 305, 849.

[83] E. Niecke, *Doktorandenseminar Phosphorchemie* (Kaiserslautern, Germany) **2004**.

[84] W. E. Piers, T. Chivers, *Chem. Soc. Rev.* **1997**, 26, 345; W. E. Piers, G. J. Irvine, V. C. Williams, *Eur. J. Inorg. Chem.* **2000**, 2131; G. Erker, *Acc. Chem. Res.* **2001**, 34, 309; S. D. Ittel, L. K. Johnson, M. Brookhart, *Chem. Rev.* **2000**, 100, 1169.

[85] N. Bavarian, M. C. Baird, *Organometallics* **2005**, 24, 2889; M.-C. Chen, J. A. S. Roberts, A. M. Seyam, L. Li, C. Zuccaccia, N. G. Stahl, T. J. Marks, *Organometallics* **2006**, 25, 2833.

[86] R. E. LaPointe, G. R. Roof, K. A. Abboud, J. Klosin, *J. Am. Chem. Soc.* **2000**, 122, 9560.

[87] V. C. Williams, G. J. Irvine, W. E. Piers, Z. Li, S. Collins, W. Clegg, M. R. J. Elsegood, T. B. Marder, *Organometallics* **2000**, 19, 1619.

[88] R. Braun, J. Sauer, *Chem. Ber.* **1986**, 119, 1269; A. Flohr, H. Waldmann, *J. Prakt. Chem.* **1995**, 337, 609; P. A. Grieco, J. J. Nunes, M. D. Gaul, *J. Am. Chem. Soc.* **1990**, 112, 4595; A. Kumar, *Chem. Rev.* **2001**, 101, 1.

[89] S. Saito, *Lewis Acids in Organic Synthesis* **2000**, 1, 9.

[90] N. J. Patmore, C. Hague, J. H. Cotgreave, M. F. Mahon, C. G. Frost, A. S. Weller, *Chem. Eur. J.* **2002**, 8, 2088.

- [91] P. Wasserscheid, *Chem. i. u. Zeit* **2003**, 37, 52; P. Wasserscheid, W. Keim, *Angew. Chem. Int. Ed.* **2000**, 39, 3772; T. Welton, *Chem. Rev.* **1999**, 99, 2071.
- [92] A. Boesmann, G. Francio, E. Janssen, M. Solinas, W. Leitner, P. Wasserscheid, *Angew. Chem. Int. Ed.* **2001**, 40, 2697.
- [93] A.-V. Mudring, *in preparation*.
- [94] A. S. Larsen, J. D. Holbrey, F. S. Tham, C. A. Reed, *J. Am. Chem. Soc.* **2000**, 122, 7264.
- [95] I. Krossing, J. M. Slattery, C. Daguene, P. J. Dyson, A. Oleinikova, H. Weingaertner, *J. Am. Chem. Soc.* **2006**, 128, 13427.
- [96] C. Daguene, P. J. Dyson, I. Krossing, A. Oleinikova, J. Slattery, C. Wakai, H. Weingaertner, *J. Phys. Chem. B* **2006**, 110, 12682.
- [97] N. J. Stone, D. A. Sweigart, A. M. Bond, *Organometallics* **1986**, 5, 2553; C. G. Zoski, D. A. Sweigart, N. J. Stone, P. H. Rieger, E. Mocellin, T. F. Mann, D. R. Mann, D. K. Gosser, M. M. Doeff, A. M. Bond, *J. Am. Chem. Soc.* **1988**, 110, 2109.
- [98] P. G. Gassman, P. A. Deck, *Organometallics* **1994**, 13, 1934; P. G. Gassman, J. R. Sowa, Jr., M. G. Hill, K. R. Mann, *Organometallics* **1995**, 14, 4879; M. G. Hill, W. M. Lamanna, K. R. Mann, *Inorg. Chem.* **1991**, 30, 4687.
- [99] F. Barriere, W. E. Geiger, *J. Am. Chem. Soc.* **2006**, 128, 3980; A. Nafady, T. T. Chin, W. E. Geiger, *Organometallics* **2006**, 25, 1654.
- [100] <http://www.ionicliquids.de>
- [101] N. Ignat'ev, P. Sartori, *J. Fluorine Chem.* **2000**, 101, 203; F. Kita, H. Sakata, S. Sinomoto, A. Kawakami, H. Kamizori, T. Sonoda, H. Nagashima, J. Nie, N. V. Pavlenko, Y. L. Yagupolskii, *J. Power Sources* **2000**, 90, 27; L. M. Yagupolskii, Y. L. Yagupolskii, *J. Fluorine Chem.* **1995**, 72, 225; F. Kita, H. Sakata, A. Kawakami, H. Kamizori, T. Sonoda, H. Nagashima, N. V. Pavlenko, Y. L. Yagupolskii, *J. Power Sources* **2001**, 97-98, 581.
- [102] W. Xu, C. A. Angell, *Electrochem. Solid-State Lett.* **2000**, 3, 366.
- [103] H. Suzuki, H. Naganawa, S. Tachimori, *Phys. Chem. Chem. Phys.* **2003**, 5, 726.
- [104] H. Naganawa, H. Suzuki, J. Noro, T. Kimura, *Chem. Commun.* **2005**, 2963.
- [105] T. J. Barbarich, S. T. Handy, S. M. Miller, O. P. Anderson, P. A. Grieco, S. H. Strauss, *Organometallics* **1996**, 15, 3776.
- [106] T. J. Barbarich, S. M. Miller, O. P. Anderson, S. H. Strauss, *J. Mol. Catal. A: Chem.* **1998**, 128, 289.
- [107] S. H. Strauss, B. G. Nolan, B. P. Fauber, *Weakly coordinating anions containing polyfluoroalkoxide ligands*, (Colorado State University Research Foundation, USA). Application: WO, **2000**, p. 32 pp.

- [108] M. Gonsior, I. Krossing, N. Mitzel, *Z. Anorg. Allg. Chem.* **2002**, 628, 1821.
- [109] I. Krossing, H. Brands, R. Feuerhake, S. Koenig, *J. Fluorine Chem.* **2001**, 112, 83.
- [110] A. Reisinger, *Chemistry with Weakly Coordinating Anions - Strong Brønsted Acids and Group 11 Metal Complexes*, PhD thesis, Albert-Ludwigs-Universität, Freiburg i. Br., **2006**.
- [111] J. J. Rockwell, G. M. Kloster, W. J. DuBay, P. A. Grieco, D. F. Shriver, S. H. Strauss, *Inorg. Chim. Acta* **1997**, 263, 195.
- [112] F. A. R. Kaul, G. T. Puchta, H. Schneider, M. Grosche, D. Mihalios, W. A. Herrmann, *J. Organomet. Chem.* **2001**, 621, 184.
- [113] K. Moock, K. Seppelt, *Z. Anorg. Allg. Chem.* **1988**, 561, 132.
- [114] H. Nishida, N. Takada, M. Yoshimura, T. Sonoda, H. Kobayashi, *Bull. Chem. Soc. Jap.* **1984**, 57, 2600.
- [115] R. Taube, S. Wache, *J. Organomet. Chem.* **1992**, 428, 431.
- [116] A. D. Hennis, J. D. Polley, G. S. Long, A. Sen, D. Yandulov, J. Lipian, G. M. Benedikt, L. F. Rhodes, J. Huffman, *Organometallics* **2001**, 20, 2802; N. A. Yakelis, R. G. Bergman, *Organometallics* **2005**, 24, 3579.
- [117] M. Brookhart, B. Grant, A. F. Volpe, Jr., *Organometallics* **1992**, 11, 3920; D. J. Tempel, L. K. Johnson, R. L. Huff, P. S. White, M. Brookhart, *J. Am. Chem. Soc.* **2000**, 122, 6686.
- [118] K. Fujiki, M. Kashiwagi, H. Miyamoto, A. Sonoda, *J. Fluorine Chem.* **1992**, 57, 307.
- [119] M. Parvez, W. E. Piers, I. Ghesner, *Acta Cryst. E* **2005**, E61, m1801.
- [120] J. C. W. Chien, W. M. Tsai, M. D. Rausch, *J. Am. Chem. Soc.* **1991**, 113, 8570; J. A. Ewen, M. J. Elder, *Preparation of metallocene catalysts for polymerization of olefins*, (Fina Technology, Inc., USA). Application: EP, **1991**, p. 9 pp.
- [121] P. Jutzi, C. Müller, A. Stammli, H.-G. Stammli, *Organometallics* **2000**, 19, 1442.
- [122] G. G. Hlatky, D. J. Upton, H. W. Turner, *Supported ionic metallocene catalysts for olefin polymerization*, (Exxon Chemical Patents, Inc., USA). Application: WO, **1991**, p. 40 pp; H. W. Turner, in *Soluble catalysts for polymerization of olefins*, (Exxon Chemical Patents, Inc., USA). Application: EP, **1988**, p. 22 pp.
- [123] K. Ren, J. H. Malpert, H. Li, H. Gu, D. C. Neckers, *Macromolecules* **2002**, 35, 1632.
- [124] D. Vagedes, G. Erker, R. Fröhlich, *J. Organomet. Chem.* **2002**, 641, 148.
- [125] V. C. Williams, W. E. Piers, W. Clegg, M. R. J. Elsegood, S. Collins, T. B. Marder, *J. Am. Chem. Soc.* **1999**, 121, 3244.
- [126] L. D. Henderson, W. E. Piers, G. J. Irvine, R. McDonald, *Organometallics* **2002**, 21, 340.

- [127] D. J. Liston, Y. J. Lee, W. R. Scheidt, C. A. Reed, *J. Am. Chem. Soc.* **1989**, *111*, 6643; K. Shelly, C. A. Reed, Y. J. Lee, W. R. Scheidt, *J. Am. Chem. Soc.* **1986**, *108*, 3117; Z. Xie, B.-M. Wu, T. C. W. Mak, J. Manning, C. A. Reed, *J. Chem. Soc., Dalton Trans.* **1997**, *7*, 1213.
- [128] Z. Xie, T. Jelinek, R. Bau, C. A. Reed, *J. Am. Chem. Soc.* **1994**, *116*, 1907.
- [129] Z. Xie, J. Manning, R. W. Reed, R. Mathur, P. D. W. Boyd, A. Benesi, C. A. Reed, *J. Am. Chem. Soc.* **1996**, *118*, 2922.
- [130] D. Stasko, S. P. Hoffmann, K.-C. Kim, N. L. P. Fackler, A. S. Larsen, T. Drovetskaya, F. S. Tham, C. A. Reed, C. E. F. Rickard, P. D. W. Boyd, E. S. Stoyanov, *J. Am. Chem. Soc.* **2002**, *124*, 13869.
- [131] B. T. King, B. C. Noll, J. Michl, *Collect. Czech. Chem. Commun.* **1999**, *64*, 1001; J. Michl, B. T. King, Z. Janousek, *Synthesis and one-electron oxidation of weakly nucleophilic borate and carborate anions*, (Board of Regents of the University of Colorado, USA). Application: US, **1998**, pp. 13 pp; J. Michl, B. King, Z. Janousek, *Weakly nucleophilic anions*, (University of Colorado, USA). Application: WO, **1996**, p. 42 pp; S. Moss, B. T. King, A. de Meijere, S. I. Kozhushkov, P. E. Eaton, J. Michl, *Org. Lett.* **2001**, *3*, 2375.
- [132] C.-W. Tsang, Q. Yang, E. T.-P. Sze, T. C. W. Mak, D. T. W. Chan, Z. Xie, *Inorg. Chem.* **2000**, *39*, 3582.
- [133] Z. Xie, C.-W. Tsang, E. T.-P. Sze, Q. Yang, D. T. W. Chan, T. C. W. Mak, *Inorg. Chem.* **1998**, *37*, 6444.
- [134] Z. Xie, C.-W. Tsang, F. Xue, T. C. W. Mak, *J. Organomet. Chem.* **1999**, *577*, 197.
- [135] B. T. King, B. C. Noll, A. J. McKinley, J. Michl, *J. Am. Chem. Soc.* **1996**, *118*, 10902.
- [136] B. T. King, J. Michl, *J. Am. Chem. Soc.* **2000**, *122*, 10255.
- [137] C.-W. Tsang, Q.-C. Yang, T. C. W. Mak, Z.-W. Xie, *Chin. J. Chem.* **2002**, *20*, 1241.
- [138] S. V. Ivanov, J. J. Rockwell, O. G. Polyakov, C. M. Gaudinski, O. P. Anderson, K. A. Solntsev, S. H. Strauss, *J. Am. Chem. Soc.* **1998**, *120*, 4224; S. H. Strauss, *Special Publication - Royal Society of Chemistry* **2000**, *253*, 44.
- [139] S. H. Strauss, S. V. Ivanov, *Preparation of fluoroborate salts and their use as catalysts*, (Colorado State University Research Foundation, USA). Application: US, **2002**, pp. 15 pp; S. H. Strauss, S. V. Ivanov, *Weakly coordinating fluoroborate anion salts of reactive cations, methods of preparation and uses as catalyst components*, (Colorado State University Research Foundation, USA). Application: WO, **2002**, p. 38 pp; S. H. Strauss, S. Ivanov, A. J. Lupinetti, *Polyhalogenated monoheteroborane anion compositions*, (Colorado State University Research Foundation, USA). Application: WO, **1998**, p. 50 pp; S. H. Strauss, S. V.

Ivanov, *Fluorinated amino polyhedral borate compounds*, (Colorado State University Research Foundation, USA). Application: US, **2002**, p. 20 pp.

[140] A. Kapustinskii, *Z. Phys. Chem.* **1933**, B22, 257.

[141] H. D. B. Jenkins, H. K. Roobottom, J. Passmore, L. Glasser, *Inorganic Chemistry* **1999**, 38, 3609.

[142] D. R. Lide in *Handbook of Chemistry and Physics: 77th Edition*, Vol. CRC Press, **1996**; in *Nist Database*, <http://www.nist.gov/chemistry>, Vol. National Institute of Science and Technology; S. G. Lias, J. E. Bartmess, J. F. Liebman, J. L. Holmes, R. D. Levin, W. G. Mallard, *J. Phys. Chem. Ref. Data, Supplemental* **1988**, 17, 861 pp; D. D. Wagman, W. H. Evans, V. B. Parker, R. H. Schumm, I. Halow, S. M. Bailey, K. L. Churney, R. L. Nuttall, *J. Phys. Chem. Ref. Data* **1982**, 11, Suppl. No. 2, 392 pp.

[143] I. Krossing, M. Gonsior, L. Müller, *Method for the production of salts of weakly fluorinated alcoholato complex anions of main group elements*, (Universität Karlsruhe (TH), Germany). Application: WO, **2005**, p. 27 pp.

[144] L. Müller, D. Himmel, I. Krossing, *in preparation*;

[145] H. J. Frohn, S. Jakobs, G. Henkel, *Angew. Chem.* **1989**, 101, 1534.

[146] E. S. Stoyanov, K.-C. Kim, C. A. Reed, *J. Am. Chem. Soc.* **2006**, 128, 8500.

[147] T. E. Mallouk, G. L. Rosenthal, G. Müller, R. Brusasco, N. Bartlett, *Inorg. Chem.* **1984**, 23, 3167.

[148] K. O. Christe, D. A. Dixon, D. McLemore, W. W. Wilson, J. A. Sheehy, J. A. Boatz, *J. Fluorine Chem.* **2000**, 101, 151.

[149] S. Brownridge, I. Krossing, J. Passmore, H. D. B. Jenkins, H. K. Roobottom, *Coord. Chem. Rev.* **2000**, 197, 397.

[150] T. S. Cameron, R. J. Deeth, I. Dionne, H. Du, H. D. Jenkins, I. Krossing, J. Passmore, H. K. Roobottom, *Inorg. Chem.* **2000**, 39, 5614.

[151] M. Finze, E. Bernhardt, M. Zähres, H. Willner, *Inorg. Chem.* **2004**, 43, 490.

[152] I.-C. Hwang, K. Seppelt, *Angew. Chem. Int. Ed.* **2001**, 40, 3690.

[153] Standard enthalpies of formation were taken from the website <http://webbook.nist.gov/chemistry/>, National Institute of Standards and Technology.

[154] L. A. Curtiss, K. Raghavachari, G. W. Trucks, J. A. Pople, *J. Chem. Phys.* **1991**, 94, 7221; J. W. Ochterski, G. A. Petersson, J. A. Montgomery, Jr., *J. Chem. Phys.* **1996**, 104, 2598; G. A. Petersson, T. G. Tensfeldt, J. A. Montgomery, Jr., *J. Chem. Phys.* **1991**, 94, 6091.

[155] I. A. Koppel, P. Burk, I. Koppel, I. Leito, T. Sonoda, M. Mishima, *J. Am. Chem. Soc.* **2000**, 122, 5114.

- [156] J. B. Lambert, L. Kania, S. Zhang, *Chem. Rev.* **1995**, 95, 1191.
- [157] M. Finze, E. Bernhardt, M. Zaehres, H. Willner, *Inorg. Chem.* **2004**, 43, 490.
- [158] W. V. Konze, B. L. Scott, G. J. Kubas, *Chem. Comm.* **1999**, 1807.
- [159] D. A. Walker, T. J. Woodman, D. L. Hughes, M. Bochmann, *Organometallics* **2001**, 20, 3772.
- [160] M.-C. Chen, J. A. S. Roberts, T. J. Marks, *Organometallics* **2004**, 23, 932.
- [161] K. O. Christe, B. Hoge, J. A. Boatz, G. K. S. Prakash, G. A. Olah, J. A. Sheehy, *Inorg. Chem.* **1999**, 38, 3132.
- [162] E. Bernhardt, H. Willner, F. Aubke, *Angew. Chem. Int. Ed.* **1999**, 38, 823.
- [163] A. Vij, W. W. Wilson, V. Vij, F. S. Tham, J. A. Sheehy, K. O. Christe, *J. Am. Chem. Soc.* **2001**, 123, 6308; O. Christe Karl, H. D. B. Jenkins, *J. Am. Chem. Soc.* **2003**, 125, 9457; P. Benkic, H. D. B. Jenkins, M. Ponikvar, Z. Mazej, *Eur. J. Inorg. Chem.* **2006**, 1084.
- [164] A. J. Edwards, P. Taylor, *Chem. Commun.* **1971**, 1376.
- [165] J. Brunvoll, A. A. Ishchenko, I. N. Myakshin, G. V. Romanov, V. P. Spiridonov, T. G. Strand, V. F. Sukhoverkhov, *Acta Chim. Scand. A* **1980**, A34, 733.
- [166] J. Fawcett, A. J. Hewitt, J. H. Holloway, M. A. Stephen, *J. Chem. Soc., Dalton Trans.* **1976**, 2422.
- [167] J. Fawcett, J. H. Holloway, R. D. Peacock, D. K. Russell, *J. Fluorine Chem.* **1982**, 20, 9.
- [168] R. D. W. Kemmitt, D. W. A. Sharp, *Fluorides of the main group elements*, **1965**, p. 142; R. C. Shaw, W. Stroog, *Ind. Chem. Eng.* **1961**, 1624.
- [169] H. D. B. Jenkins, H. K. Roobottom, J. Passmore, *Inorg. Chem.* **2003**, 42, 2886.
- [170] Z. Fei, D. Kuang, D. Zhao, C. Klein, W. H. Ang, S. M. Zakeeruddin, M. Graetzel, P. J. Dyson, *Inorg. Chem.* **2006**, 45, 10407.
- [171] L. Pospisil, B. T. King, J. Michl, *Electrochim. Acta* **1998**, 44, 103.
- [172] I. Krossing, I. Raabe, *Chem. Eur. J.* **2004**, 10, 5017.
- [173] B. G. Nolan, S. Tsujioka, S. H. Strauss, *Fluorinated Materials for Energy Conversion* **2005**, 195.
- [174] H. Tokuda, S.-i. Tabata, S. Seki, M. Watanabe, *Kobunshi Ronbunshu* **2006**, 63, 1; H. Tokuda, M. Watanabe, *Electrochim. Acta* **2003**, 48, 2085; M. Watanabe, S. Tsujioka, *Room-temperature molten compounds having ate complexes and showing high ionic conductivity at room temperature for battery electrolytes*, (Yokohama TLO Company, Ltd., Japan; Central Glass Co., Ltd.). Application: JP, **2004**, p. 12 pp.

- [175] S. Tsujioka, B. G. Nolan, H. Takase, B. P. Fauber, S. H. Strauss, *Journal of the Electrochemical Society* **2004**, *151*, A1418.
- [176] I. Raabe, S. Müller, N. Trapp, M. Kaupp, I. Krossing, *Chem. Eur. J.*, submitted.
- [177] M. Gonsior, L. Müller, I. Krossing, *Chem. Eur. J.* **2006**, *12*, 5815.
- [178] M. Gonsior, I. Krossing, E. Matern, *Chem. Eur. J.* **2006**, *12*, 1703.
- [179] M. Gonsior, I. Krossing, E. Matern, *Chem. Eur. J.* **2006**, *12*, 1986.
- [180] I. Raabe, S. Antonijevic, I. Krossing, *Chem. Eur. J.*, submitted.
- [181] M. Gonsior, S. Antonijevic, I. Krossing, *Chem. Eur. J.* **2006**, *12*, 1997.
- [182] A. Reisinger, F. Breher, D. V. Deubel, I. Krossing, *Chem. Eur. J.*, submitted.
- [183] H. K. Roobottom, H. D. B. Jenkins, J. Passmore, L. Glasser, *J. Chem. Ed.* **1999**, *76*, 1570.
- [184] A. Reisinger, W. Scherer, I. Krossing, *Chem. Eur. J.*, submitted.
- [185] L. Glasser, H. D. B. Jenkins, *Chem. Soc. Rev.* **2005**, *34*, 866.
- [186] A. Carpy, M. Goursolle, J. M. Leger, E. Nivaud, *C. R. Acad. Sci., Ser. C* **1977**, 285, 311.
- [187] T. M. Miller, B. Berderson, *Adv. At. Mol. Phys* **1997**, *13*.
- [188] M. Di Vaira, M. Peruzzini, P. Stoppioni, *Inorg. Chem.* **1983**, *22*, 2196.
- [189] M. Scheer, L. J. Gregoriades, A. V. Virovets, W. Kunz, R. Neueder, I. Krossing, *Angew. Chem. Int. Ed.* **2006**, *45*, 5689.
- [190] A. W. Cordes, R. D. Joyner, R. D. Shores, E. D. Dill, *Inorg. Chem.* **1974**, *13*, 132.
- [191] C. Aubauer, E. Irran, T. M. Klapötke, W. Schnick, A. Schulz, J. Senker, *Inorg. Chem.* **2001**, *40*, 4956.
- [192] E. Kuwabara, R. Bau, *Acta Cryst. C* **1994**, *C50*, 1409.
- [193] M. Di Vaira, P. Stoppioni, *Coord. Chem. Rev.* **1992**, *120*, 259; L. Y. Goh, W. Chen, R. C. S. Wong, *Angew. Chem.* **1993**, *105*, 1838; O. J. Scherer, *Chem. i. u. Zeit* **2000**, *34*, 374; J. Wachter, *Angew. Chem. Int. Ed.* **1998**, *37*, 751.
- [194] L. Y. Goh, W. Chen, R. C. S. Wong, K. Karaghiosoff, *Organometallics* **1995**, *14*, 3886.
- [195] G. Brunklaus, J. C. C. Chan, H. Eckert, S. Reiser, T. Nilges, A. Pfitzner, *Phys. Chem. Chem. Phys.* **2003**, *5*, 3768.
- [196] K. Seppelt, *Z. Anorg. Allg. Chem.* **2003**, 629, 2427.
- [197] A. Reisinger, F. Breher, D. V. Deubel, I. Krossing, *in preparation* **2006**.
- [198] A. Reisinger, W. Scherer, I. Krossing, *in preparation* **2006**.
- [199] E. Guidoboni, I. de Rios, A. Ienco, L. Marvelli, C. Mealli, A. Romerosa, R. Rossi, M. Peruzzini, *Inorg. Chem.* **2002**, *41*, 659.

- [200] I. de los Rios, F. Mani, M. Peruzzini, P. Stoppioni, *J. Organomet. Chem.* **2004**, 689, 164; M. Di Vaira, I. de los Rios, F. Mani, M. Peruzzini, P. Stoppioni, *Eur. J. Inorg. Chem.* **2004**, 293.
- [201] E. R. Andrew, A. Bradbury, R. G. Eades, *Nature* **1958**, 182, 1659.
- [202] W. P. Aue, J. Karhan, R. R. Ernst, *J. Chem. Phys.* **1976**, 64, 4226.
- [203] A. Bax, R. Freeman, T. A. Frenkiel, *J. Am. Chem. Soc.* **1981**, 103, 2102.
- [204] T. A. Early, B. K. John, L. F. Johnson, *J. Magn. Reson.* **1987**, 75, 134; C. A. Fyfe, Y. Feng, H. Gies, H. Grondey, G. T. Kokotailo, *J. Am. Chem. Soc.* **1990**, 112, 3264; R. Benn, H. Grondey, C. Brevard, A. Pagelot, *Chem. Commun.* **1988**, 102; A. Lesage, C. Auger, S. Caldarelli, L. Emsley, *J. Am. Chem. Soc.* **1997**, 119, 7867.
- [205] A. Lesage, M. Bardet, L. Emsley, *J. Am. Chem. Soc.* **1999**, 121, 10987.
- [206] F. Fayon, D. Massiot, H. Levitt Malcolm, J. Titman Jeremy, H. Gregory Duncan, L. Duma, L. Emsley, S. P. Brown, *J. Chem. Phys.* **2005**, 122, 194313.
- [207] S. P. Brown, M. Perez-Torralba, D. Sanz, R. M. Claramunt, L. Emsley, *Chem. Commun.* **2002**, 1852.
- [208] T. Chattopadhyay, E. Gmelin, H. G. Von Schnering, *J. Phys. Chem. Solids* **1982**, 43, 925.
- [209] T. K. Chattopadhyay, W. May, H. G. Von Schnering, G. S. Pawley, *Z. f. Kristallogr.* **1983**, 165, 47.
- [210] H. L. Clever, E. F. Westrum, Jr., A. W. Cordes, *J. Phys. Chem.* **1965**, 69, 1214.
- [211] M. Gardner, *J. Chem. Soc., Dalton Trans.* **1973**, 691.
- [212] H. Gerding, J. W. Maarsen, P. C. Nobel, *Recueil des Travaux Chimiques des Pays-Bas et de la Belgique* **1957**, 76, 757; J. O. Jensen, D. Zeroka, A. Banerjee, *Theochem* **2000**, 505, 31.
- [213] M. G. Gibby, A. Pines, W. K. Rhim, J. S. Waugh, *J. Chem. Phys.* **1972**, 56, 991.
- [214] E. R. Andrew, W. S. Hinshaw, M. G. Hutchins, A. Jasinski, *Chem. Phys. Lett.* **1974**, 27, 96.
- [215] E. R. Andrew, W. S. Hinshaw, A. Jasinski, *Chem. Phys. Lett.* **1974**, 24, 399.
- [216] R. K. Harris, P. J. Wilkes, P. T. Wood, J. D. Woollins, *J. Chem. Soc., Dalton Trans.* **1989**, 809.
- [217] M. M. Maricq, J. S. Waugh, *J. Chem. Phys.* **1979**, 70, 3300; A. Schmidt, S. Vega, *J. Chem. Phys.* **1987**, 87, 6895.
- [218] Y.-C. Leung, J. Waser, *Acta Cryst.* **1957**, 10, 574; S. van Houten, A. Vos, G. A. Wiegers, *Recueil des Travaux Chimiques des Pays-Bas et de la Belgique* **1955**, 74, 1167.

- [219] G. A. Olah, *Interscience Monographs on Organic Chemistry: Friedel-Crafts Chemistry*, **1973**, p. 581 pp; G. K. S. Prakash, P. v. R. Schleyer in *Stable Carbocation Chemistry*, Vol. **1997**, p. 587 pp.
- [220] G. A. Olah, *Angew. Chem.* **1973**, 85, 183.
- [221] H. Basch, T. Hoz, S. Hoz, *J. Phys. Chem. A* **1999**, 103, 6458; C. H. Reynolds, *Chem. Commun.* **1991**, 975; J. W. Hudgens, R. D. Johnson, III, B. P. Tsai, S. A. Kafafi, *J. Am. Chem. Soc.* **1990**, 112, 5763; G. A. Olah, G. Rasul, L. Heiliger, G. K. S. Prakash, *J. Am. Chem. Soc.* **1996**, 118, 3580; G. A. Olah, G. Rasul, A. K. Yudin, A. Burrichter, G. K. S. Prakash, A. L. Chistyakov, I. V. Stankevich, I. S. Akhrem, N. P. Gambaryan, M. E. Vol'pin, *J. Am. Chem. Soc.* **1996**, 118, 1446; H. Vancik, K. Percac, D. E. Sunko, *J. Am. Chem. Soc.* **1990**, 112, 7418.
- [222] G. Frenking, S. Fau, C. M. Marchand, H. Grützmacher, *J. Am. Chem. Soc.* **1997**, 119, 6648.
- [223] H. Grützmacher, C. M. Marchand, *Coord. Chem. Rev.* **1997**, 163, 287.
- [224] G. A. Olah, A. Burrichter, T. Mathew, Y. D. Vankar, G. Rasul, G. K. S. Prakash, *Angew. Chem. Int. Ed.* **1997**, 36, 1875; G. K. S. Prakash, J. W. Bausch, G. A. Olah, *J. Am. Chem. Soc.* **1991**, 113, 3203; T. S. Sorensen, *Angew. Chem. Int. Ed.* **1998**, 37, 603.
- [225] J. L. M. Abboud, O. Castano, M. Herreros, J. Elguero, N. Jagerovic, R. Notario, K. Sak, *Int. J. Mass Spectrom. Ion Processes* **1998**, 175, 35.
- [226] R. H. Martin, F. W. Lampe, R. W. Taft, *J. Am. Chem. Soc.* **1966**, 88, 1353.
- [227] R. Minkwitz, S. Reinemann, O. Blecher, H. Hartl, I. Brüdgam, *Inorg. Chem.* **1999**, 38, 844.
- [228] M. Gonsior, I. Krossing, *Chem. Eur. J.* **2004**, 10, 5730.
- [229] R. Minkwitz, S. Schneider, *Angew. Chem. Int. Ed.* **1999**, 38, 714.
- [230] D. Ohlmann, C. M. Marchand, H. Grützmacher, G. S. Chen, D. Farmer, R. Glaser, A. Currao, R. Nesper, H. Pritzkow, *Angew. Chem. Int. Ed.* **1996**, 35, 300.
- [231] T. Laube, E. Bannwart, S. Hollenstein, *J. Am. Chem. Soc.* **1993**, 115, 1731.
- [232] S. Hollenstein, T. Laube, *J. Am. Chem. Soc.* **1993**, 115, 7240.
- [233] C. Douvris, E. S. Stoyanov, F. S. Tham, C. A. Reed, *Chemical Communications* **2007**, 1145.
- [234] G. A. Olah, L. Heiliger, G. K. S. Prakash, *J. Am. Chem. Soc.* **1989**, 111, 8020.
- [235] M. Kaupp, O. L. Malkina, V. G. Malkin, *Chem. Phys. Lett.* **1997**, 265, 55.
- [236] M. Kaupp in *Relativistic Effects on NMR Chemical Shifts*, (Ed. P. Schwerdtfeger), Elsevier, Amsterdam, **2004**.

- [237] M. Kaupp, O. L. Malkina, V. G. Malkin, P. Pyykkö, *Chem. Eur. J.* **1998**, *4*, 118.
- [238] M. Garcia-Viloca, R. Gelabert, A. Gonzalez-Lafont, M. Moreno, J. M. Lluch, *J. Phys. Chem. A* **1997**, *101*, 8727.
- [239] P. J. Craig, M. I. Needham, N. Ostah, G. H. Stojak, M. Symons, P. Teesdale-Spittle, *J. Chem. Soc. Dalton Trans.* **1996**, 153.
- [240] M. Kaupp, O. L. Malkina, *J. Chem. Phys.* **1998**, *108*, 3648.
- [241] V. G. Malkin, O. L. Malkina, D. R. Salahub, *Chem. Phys. Lett.* **1996**, *261*, 335; O. L. Malkina, B. Schimmelpfennig, M. Kaupp, B. A. Hess, P. Chandra, U. Wahlgren, V. G. Malkin, *Chem. Phys. Lett.* **1998**, *296*, 93; J. Vaara, O. L. Malkina, H. Stoll, V. G. Malkin, M. Kaupp, *J. Chem. Phys.* **2001**, *114*, 61.
- [242] C. Finbak, O. Hassel, *Z. Phys. Chem.* **1937**, *B36*, 301.
- [243] G. Santiso Quiñones, I. Krossing, *in preparation*.
- [244] R. Scholl, W. Steinkopf, *Chem. Ber.* **1906**, *39*, 393.
- [245] J. Powell, M. Horvath, A. Lough, *Chem. Commun.* **1993**, 733.
- [246] J. Powell, M. J. Horvath, A. Lough, *J. Chem. Soc., Dalton Trans.* **1996**, 1669.
- [247] J. Powell, M. J. Horvath, A. Lough, A. Phillips, J. Brunet, *J. Chem. Soc., Dalton Trans.* **1998**, 637.
- [248] I. Raabe, S. Antonijevic, I. Krossing, *Chem. Eur. J.*, *in press*.
- [249] Z. Kisiel, L. Pszczolkowski, W. Caminati, P. G. Favero, *J. Chem. Phys.* **1996**, *105*, 1778; Z. Kisiel, L. Pszczolkowski, L. B. Favero, W. Caminati, *J. Mol. Spectrosc.* **1998**, *189*, 283.
- [250] Gmelin, *Handbuch der Anorganischen Chemie, Teil 19*, Springer Verlag, Berlin, Heidelberg, New York, **1978**, p. 211.
- [251] H. J. Maria, J. R. McDonald, S. P. McGlynn, *J. Am. Chem. Soc.* **1973**, *95*, 1050.
- [252] A. A. Planckaert, P. Sauvageau, C. Sandorfy, *Chem. Phys. Lett.* **1973**, *20*, 170.
- [253] G. Santiso Quiñones, I. Krossing, *in preparation*.
- [254] A. Finch, P. J. Gardner, I. J. Hyams, *Faraday Trans.* **1965**, *61*, 649; T. Wentink, Jr., V. H. Tiensuu, *J. Chem. Phys.* **1958**, *28*, 826.
- [255] F. Bessac, G. Frenking, *Inorg. Chem.* **2003**, *42*, 7990.
- [256] I. Fleming, *Frontier Orbitals and Organic Chemical Reactions*, Wiley, London, **1976**, p. 258 pp; K. Fukui, *Acc. Chem. Res.* **1971**, *4*, 57; K. Fukui, *Reactivity and Structure Concepts in Organic Chemistry, Vol. 2: Theory of Orientation and Stereoselection*, **1975**, p. 134 pp.
- [257] I. Krossing, I. Raabe, *J. Am. Chem. Soc.* **2004**, *126*, 7571.

- [258] M. E. Jacox, D. E. Milligan, *J. Chem. Phys.* **1971**, *54*, 3935.
- [259] M. E. Jacox, *Chem. Phys.* **1976**, *12*, 51.
- [260] L. Andrews, F. T. Prochaska, *J. Chem. Phys.* **1979**, *70*, 4714.
- [261] M. W. Chase, Jr., *J. Phys. Chem. Ref. Data* **1998**, *27*, i.
- [262] S. G. Lias, "Ionization Energy Evaluation" in *NIST Chemistry WebBook, NIST Standard Reference Database Number 69* (<http://webbook.nist.gov>), National Institute of Standards and Technology, Gaithersburg MD, 20899, **2005**, p.
- [263] S. J. Paddison, E. Tschuikow-Roux, *J. Phys. Chem. A* **1998**, *102*, 6191.
- [264] B. J. Kelsal, L. Andrews, *J. Mol. Spectr.* **1983**, *97*, 362.
- [265] T. D. Fridgen, X. K. Zhang, J. M. Parnis, R. E. March, *J. Phys. Chem. A* **2000**, *104*, 3487.
- [266] L. Andrews, J. M. Dyke, N. Jonathan, N. Keddar, A. Morris, *J. Chem. Phys.* **1983**, *79*, 4650.
- [267] L. Andrews, J. M. Dyke, N. Jonathan, N. Keddar, A. Morris, A. Ridgha, *J. Phys. Chem.* **1984**, *88*, 2364.
- [268] L. Andrews, C. A. Wight, F. T. Prochaska, S. A. McDonald, B. S. Ault, *J. Mol. Spectrosc.* **1978**, *101*, 9.
- [269] B. P. Tsai, A. S. Werner, T. Baer, *J. Chem. Phys.* **1975**, *63*, 4384; A. S. Carson, P. G. Laye, J. B. Pedley, A. M. Welsby, *J. Chem. Thermodyn.* **1993**, *25*, 261.
- [270] S. A. Kudchadker, A. P. Kudchadker, *J. Phys. Chem. Ref. Data* **1976**, *5*, 529.
- [271] I. Raabe, D. Himmel, I. Krossing, *J. Phys. Chem. A*, submitted.
- [272] H. P. A. Mercier, M. D. Moran, G. J. Schrobilgen, R. J. Suontamo, *J. Fluorine Chem.* **2004**, *125*, 1563.
- [273] P. Marshall, G. N. Srinivas, M. Schwartz, *J. Phys. Chem. A* **2005**, *109*, 6371.
- [274] D. Feller, K. A. Peterson, *J. Chem. Phys.* **1998**, *108*, 154; J. M. L. Martin, *Chem. Phys. Lett.* **1996**, *259*, 669; J. M. L. Martin, T. J. Lee, *Chem. Phys. Lett.* **1996**, *258*, 136.
- [275] E. R. Fischer, P. B. Armentrout, *Int. J. Mass Spectrom. Ion Processes* **1990**, *101*, 1.
- [276] K. P. Huber, G. Herzberg, *Molecular Spectra and Molecular Structure, 4: Constants of Diatomic Molecules*, **1979**, p. 716 pp.
- [277] D. R. Lide, Editor, *Handbook of Chemistry and Physics: 77th Edition*, **1996**, p. 2512 pp.
- [278] S. G. Lias, *Ionization Energy Evaluation in: NIST Chemistry WebBook, NIST Standard Reference Database*, National Institute of Standards and Technology, Gaithersburg MD, 20899, **2005**, p.
- [279] D. B. Workman, R. R. Squires, *Inorg. Chem.* **1988**, *27*, 1846.

- [280] C. J. Reid, *Int. J. Mass Spectrom. Ion Processes* **1993**, 127, 147.
- [281] C. T. Wickham-Jones, S. Moran, G. B. Ellison, *J. Chem. Phys.* **1989**, 90, 795.
- [282] P. Fowell, J. R. Lacher, J. D. Park, *Trans. Faraday Soc.* **1965**, 61, 1324.
- [283] L. V. Gurvich, I. V. Veyts, C. B. Alcock, *Thermodynamic Properties of Individual Substances*, Hemisphere, New York, **1992**.
- [284] A. F. Lago, J. P. Kercher, A. Bödi, B. Sztáray, B. Miller, D. Wurzelman, T. Baer, *J. Phys. Chem. A* **2005**, 109, 1802.
- [285] S. A. Kudchadker, A. P. Kudchadker, *J. Phys. Chem. Ref. Data* **1976**, 5, 529.
- [286] J. Bickerton, M. E. M. Da Piedade, G. Pilcher, *J. Chem. Thermodyn.* **1984**, 16, 661.
- [287] K. C. Ferguson, E. N. Okafo, E. Whittle, *J. Chem. Soc., Faraday Trans. 1* **1973**, 69, 295.
- [288] J. D. Cox, G. Pilcher, *Thermochemistry of Organic and Organometallic Compounds*, Academic Press, New York, **1970**, p. 636.
- [289] A. S. Carson, P. G. Laye, J. B. Pedley, A. M. Welsby, *J. Chem. Thermodyn.* **1993**, 25, 261.
- [290] T. S. Papina, V. P. Kolesov, Y. G. Golovanova, *Russ. J. Phys. Chem. (Engl. Transl.)* **1982**, 56, 1666.
- [291] S. Furuyama, D. M. Golden, S. W. Benson, *J. Phys. Chem.* **1968**, 72, 4713.
- [292] I. Nitta, S. Seki, *J. Chem. Soc. Jpn.* **1943**, 64, 475.
- [293] F. P. Lossing, *Bull. Soc. Chim. Belg.* **1972**, 81, 125.
- [294] A. G. Harrison, T. W. Shannon, *Can. J. Chem.* **1962**, 40, 1730.
- [295] B. P. Tsai, T. Bär, A. S. Werner, S. F. Lin, *Journal of Physical Chemistry* **1975**, 79, 570.
- [296] O. Kaposi, M. Riedel, K. Vass-Balthazar, G. R. Sanchez, L. Lelik, *Acta Chim. Acad. Sci. Hung.* **1976**, 89, 221.
- [297] J. L. Holmes, F. P. Lossing, R. A. McFarlane, *Int. J. Mass Spectrom. Ion Phys.* **1988**, 86, 209.
- [298] B. P. Tsai, T. Baer, A. S. Werner, S. F. Lin, *J. Phys. Chem.* **1975**, 79, 570.
- [299] J. B. Farmer, I. H. S. Henderson, F. P. Lossing, D. G. H. Marsden, : *J. Chem. Phys.* **1956**, 24, 348.
- [300] J. W. Hudgens, R. D. Johnson, S. Timonen, J. A. Seetula, D. Gutman, *J. Phys. Chem.* **1991**, 95.
- [301] R. I. Reed, W. Snedden, *J. Chem. Soc., Farady Trans.* **1958**, 54, 301.
- [302] Y. J. Kime, D. C. Driscoll, P. A. Dowben, *J. Chem. Soc., Farady Trans.* **1987**, 83, 403.

- [303] I. Krossing, I. Raabe, *J. Am. Chem. Soc.* **2004**, *126*, 7571.
- [304] R. R. Holmes, *J. Inorg. Nucl. Chem.* **1960**, *12*, 266; H. C. Brown, R. R. Holmes, *J. Am. Chem. Soc.* **1956**, *78*, 2173.
- [305] E. A. Robinson, S. A. Johnson, T.-H. Tang, R. J. Gillespie, *Inorg. Chem.* **199**, *36*, 3022; S. Yamamoto, R. Kuwabara, N. Takami, K. Kuchitsu, *J. Mol. Spectrosc.* **1986**, *115*, 333.
- [306] D. R. Armstrong, P. G. Perkins, *J. Chem. Soc. A* **1967**, 1218; M. F. Lappert, M. R. Litzow, J. B. Pedley, P. N. K. Riley, A. Tweedale, *J. Chem. Soc. A* **1968**, 3105; Y. A. Buslaev, E. A. Kravchenko, L. Kolditz, *Coord. Chem. Rev.* **1987**, *82*, 3; V. Branchadell, A. Oliva, *Theochem* **1991**, *82*, 75.
- [307] L. J. Chyall, R. R. Squires, *J. Phys. Chem.* **1996**, *100*, 16435.
- [308] J. E. Szulejko, T. B. McMahon, *J. Am. Chem. Soc.* **1993**, *115*, 7839.
- [309] U. Müller, *Acta Cryst.* **1997**, B27.
- [310] R. Minkwitz, W. Meckstroth, H. Preut, *Zeitschrift für Naturforschung B* **1993**, *48*, 19.
- [311] F. A. Devillanova, P. Deplano, F. Isaia, V. Lippolis, M. L. Mercuri, S. Piludu, G. Verani, F. Demartin, *Polyhedron* **1998**, *17*, 305.
- [312] A. Haaland, *Angew. Chem.* **1989**, *101*, 1017.
- [313] M. F. Lappert, A. R. Sanger, R. C. Srivastava, P. P. Power, *Metal and Metalloid Amides: Synthesis, Structure, and Physical and Chemical Properties*, **1980**, p. 847 pp.
- [314] M. P. Murchie, J. P. Johnson, J. Passmore, G. W. Sutherland, M. Tajik, T. K. Whidden, P. S. White, F. Grein, *Inorg. Chem.* **1992**, *31*, 273; I. Krossing, J. Passmore, *Inorg. Chem.* **1999**, *38*, 5203.
- [315] Z. Zak, M. Cernik, *Acta Cryst. C* **1996**, C52, 290.
- [316] I. Krossing, A. Reisinger, *Eur. J. Inorg. Chem.*
- [317] T. P. Povlock, *Tetrahedron Lett.* **1967**, 4131.
- [318] C. Aubauer, G. Engelhardt, T. M. Klapötke, H. Nöth, A. Schulz, M. Warchhold, *Eur. J. Inorg. Chem.* **2000**, 2245.
- [319] M. Gonsior, L. Müller, I. Krossing, *Chem. Eur. J.* **2006**, *12*, 5815.
- [320] S. Müller, N. Trapp, I. Raabe, I. Krossing, M. Kaupp, *Chem. Eur. J.*, submitted.
- [321] A. Müller, A. Fadini, *Z. Anorg. Allg. Chem.* **1967**, *349*, 164.
- [322] P. J. Davis, R. A. Oetjen, *J. Mol. Spectrosc.* **1958**, *2*, 253.
- [323] T. Shimanouchi, *J. Phys. Chem. Ref. Data* **1972**, *6*, 993.
- [324] B. W. Tattershall, N. L. Kendall, *Polyhedron* **1994**, *13*, 1517.
- [325] N. Müller, P. C. Lauterbur, J. Goldenson, *J. Am. Chem. Soc.* **1956**, *78*, 3557.

- [326] W.-W. du Mont, V. Stenzel, J. Jeske, P. G. Jones, A. Sebal, S. Pohl, W. Saak, M. Bätcher, *Inorg. Chem.* **1994**, 33, 1502.
- [327] D. Clark, H. M. Powell, A. F. Wells, *Journal of the Chemical Society* **1942**, 642.
- [328] A. S. Kanishcheva, Y. N. Mikhailov, A. P. Chernov, *Izvestiya Akademii Nauk SSSR, Neorganicheskie Materialy* **1980**, 16, 1885; R. Enjalbert, J. Galy, *Acta Cryst. B* **1980**, B36, 914; J. Trotter, *Z. f. Kristallogr.* **1965**, 121, 81.
- [329] M. Gonsior, I. Krossing, *Dalton Trans.* **2005**, 2022.
- [330] D. Forney, M. E. Jacox, K. K. Irikura, *J. Chem. Phys.* **1994**, 101, 8290; L. Andrews in *Chemistry and Physics of Matrix-Isolated Species*, Vol. Eds.: L. Andrews and M. Moskovits), Elsevier, Amsterdam, **1989**; F. T. Prochaska, L. Andrews, *J. Am. Chem. Soc.* **1978**, 100, 2102; T. M. Halasinski, J. T. Godbout, J. Allison, G. E. Leroi, *J. Phys. Chem.* **1994**, 98, 3930.
- [331] L. Andrews, J. M. Grzybowski, R. O. Allen, *J. Phys. Chem.* **1975**, 79, 904; F. T. Prochaska, L. Andrews, *J. Chem. Phys.* **1977**, 67, 1091.
- [332] R. A. Kendall, T. H. Dunning, Jr., R. J. Harrison, *J. Chem. Phys.* **1992**, 96, 6796.
- [333] D. G. Colombo, V. G. Young, Jr., W. L. Gladfelter, *Inorg. Chem.* **2000**, 39, 4621.
- [334] D. E. Clemmer, P. B. Armentrout, *J. Chem. Phys.* **1992**, 97, 2451.
- [335] D. Himmel, L. Müller, I. Krossing, *in preparation*.
- [336] L. Müller, I. Krossing, *in preparation*.
- [337] I. Krossing, I. Raabe, E. Birtalan, *Acta Cryst.* **2007**, E63, i43.
- [338] G. Tikhomirov, I. Morozov, K. Znamenkov, E. Kemnitz, S. Troyanov, *Z. Anorg. Allg. Chem.* **2002**, 628, 872.
- [339] M. R. Truter, D. W. J. Cruickshank, G. A. Jeffrey, *Acta Cryst.* **1960**, 13, 855.
- [340] E. Grison, K. Eriks, J. L. de Vries, *Acta Cryst.* **1950**, 3, 290.
- [341] M. Lanfranchi, M. A. Pellinghelli, G. Predieri, F. Bigi, R. Maggi, G. Sartori, *J. Chem. Soc., Dalton Trans.* **1993**, 1463.
- [342] J. Drowart, J. Smets, J. C. Reynaert, P. Coppens, *Advan. Mass Spectrom.* **1978**, 7A, 647.
- [343] A. V. Bulgakov, O. F. Bobrenok, V. I. Kosyakov, *Chem. Phys. Lett.* **2000**, 320, 19; M. D. Chen, R. B. Huang, L. S. Zheng, C. T. Au, *Main Group Met. Chem.* **1999**, 22, 479; R. Huang, H. Li, Z. Lin, S. Yang, *J. Phys. Chem.* **1995**, 99, 1418; R. Huang, H. Li, Z. Lin, S. Yang, *Surface Review and Letters* **1996**, 3, 167.
- [344] M. D. Chen, J. T. Li, R. B. Huang, L. S. Zheng, C. T. Au, *Chem. Phys. Lett.* **1999**, 305, 439.
- [345] R. O. Jones, G. Seifert, *J. Chem. Phys.* **1992**, 96, 7564.
- [346] K. O. Christe, H. D. B. Jenkins, *J. Am. Chem. Soc.* **2003**, 125, 9457.

- [347] I. Krossing, A. Reisinger, *Coord. Chem. Rev.* **2006**, *250*, 2721.
- [348] A. L. Van Geet, *Analyt. Chem.* **1970**, *42*, 679.
- [349] A. D. Becke, *Phys. Rev. A* **1988**, *38*, 3098; J. P. Perdew, K. Burke, Y. Wang, *Phys. Rev. B* **1996**, *54*, 16533.
- [350] F. Weigend, M. Häser, *Theor. Chem. Acc.* **1997**, *97*, 331.
- [351] F. Weigend, M. Häser, H. Patzelt, R. Ahlrichs, *Chem. Phys. Lett.* **1998**, *294*, 143; C. Möller, M. S. Plesset, *Phys. Rev.* **1934**, *46*, 618.
- [352] A. Schäfer, H. Horn, R. Ahlrichs, *J. Chem. Phys.* **1992**, *97*, 2571.
- [353] K. Eichkorn, F. Weigend, O. Treutler, R. Ahlrichs, *Theor. Chem. Acc.* **1997**, *97*, 119.
- [354] A. Schäfer, C. Huber, R. Ahlrichs, *J. Chem. Phys.* **1994**, *100*, 5829.
- [355] T. H. Dunning, Jr., *J. Chem. Phys.* **1989**, *90*, 1007; A. K. Wilson, D. E. Woon, K. A. Peterson, T. H. Dunning, Jr., *J. Chem. Phys.* **1999**, *110*, 7667.
- [356] D. E. Woon, T. H. Dunning, Jr., *J. Chem. Phys.* **1993**, *98*, 1358.
- [357] EMSL Gaussian Basis Set Order Form: <http://www.emsl.pnl.gov/forms/basisform.html>.
- [358] M. Dolg, H. Stoll, H. Preuss, R. M. Pitzer, *J. Phys. Chem.* **1993**, *97*, 5852.
- [359] D. Andrae, U. Häussermann, M. Dolg, H. Stoll, H. Preuss, *Theor. Chim. Acta* **1990**, *77*, 123.
- [360] L. A. Curtiss, K. Raghavachari, P. C. Redfern, V. Rassolov, J. A. Pople, *J. Chem. Phys.* **1998**, *109*, 7764; L. A. Curtiss, P. C. Redfern, K. Raghavachari, V. Rassolov, J. A. Pople, *J. Chem. Phys.* **1999**, *110*, 4703.
- [361] R. Ahlrichs, M. Bär, M. Häser, H. Horn, C. Kölmel, *Chem. Phys. Lett.* **1989**, *162*, 165.
- [362] M. J. T. Frisch, G. W.; Schlegel, H. B.; Scuseria, G. E.; Robb, M. A.; Cheeseman, J. R.; Montgomery, Jr., J. A.; Vreven, T.; Kudin, K. N.; Burant, J. C.; Millam, J. M.; Iyengar, S. S.; Tomasi, J.; Barone, V.; Mennucci, B.; Cossi, M.; Scalmani, G.; Rega, N.; Petersson, G. A.; Nakatsuji, H.; Hada, M.; Ehara, M.; Toyota, K.; Fukuda, R.; Hasegawa, J.; Ishida, M.; Nakajima, T.; Honda, Y.; Kitao, O.; Nakai, H.; Klene, M.; Li, X.; Knox, J. E.; Hratchian, H. P.; Cross, J. B.; Bakken, V.; Adamo, C.; Jaramillo, J.; Gomperts, R.; Stratmann, R. E.; Yazyev, O.; Austin, A. J.; Cammi, R.; Pomelli, C.; Ochterski, J. W.; Ayala, P. Y.; Morokuma, K.; Voth, G. A.; Salvador, P.; Dannenberg, J. J.; Zakrzewski, V. G.; Dapprich, S.; Daniels, A. D.; Strain, M. C.; Farkas, O.; Malick, D. K.; Rabuck, A. D.; Raghavachari, K.; Foresman, J. B.; Ortiz, J. V.; Cui, Q.; Baboul, A. G.; Clifford, S.; Cioslowski, J.; Stefanov, B. B.; Liu, G.; Liashenko, A.; Piskorz, P.; Komaromi, I.; Martin, R. L.; Fox, D. J.; Keith, T.; Al-Laham, M. A.; Peng, C. Y.; Nanayakkara, A.; Challacombe, M.; Gill, P. M. W.; Johnson, B.; Chen, W.;

Wong, M. W.; Gonzalez, C.; Pople, J. A., *Gaussian 03, Revision C02*, Gaussian, Inc., Wallingford CT, **2004**, p.

[363] P. Deglmann, F. Furche, R. Ahlrichs, *Chem. Phys. Lett.* **2002**, 362, 511.

[364] A. Klamt, G. Schüürmann, *J. Chem. Soc., Perkin Trans.* **1993**, 799.

[365] M. Häser, R. Ahlrichs, H. P. Baron, P. Weis, H. Horn, *Theor. Chim. Acta* **1992**, 83, 455; T. Ziegler, G. Schreckenbach, *J. Phys. Chem.* **1995**, 99, 606.

[366] V. G. Malkin, O. L. Malkina, R. Reviakine, A. V. Arbuznikov, M. Kaupp, B. Schimmelpfennig, I. Malkin, M. Repiský, S. Komorovský, P. Hrobarik, E. Malkin, T. Helgaker, K. Ruud in *ReSpect program, version 2.1*, **2005**.

[367] K. Wolinski, J. F. Hinton, P. Pulay, *J. Am. Chem. Soc.* **1990**, 112, 8251.

[368] W. Kutzelnigg, U. Fleischer, M. Schindler, *NMR Basic Principles and Progresses*, Springer Verlag, Berlin / Heidelberg, **1991**.

[369] N. Godbout, D. R. Salahub, J. Andzelm, E. Wimmer, *Can. J. Chem.* **1992**, 70.

[370] V. G. Malkin, O. L. Malkina, M. E. Casida, D. R. Salahub, *J. Am. Chem. Soc.* **1994**, 116, 5898.

[371] R. Bauernschmitt, R. Ahlrichs, *Chem. Phys. Lett.* **1996**, 256, 454; R. Bauernschmitt, R. Ahlrichs, *J. Chem. Phys.* **1996**, 104, 9047; R. Bauernschmitt, M. Häser, O. Treutler, R. Ahlrichs, *Chem. Phys. Lett.* **1997**, 264, 573; C. Ochsenfeld, J. Gauss, R. Ahlrichs, *J. Chem. Phys.* **1995**, 103, 7401; H. Weiss, R. Ahlrichs, M. Häser, *J. Chem. Phys.* **1993**, 99, 1262.

[372] H. D. B. Jenkins, I. Krossing, J. Passmore, I. Raabe, *J. Fluorine Chem.* **2004**, 125, 1585.

12 Appendix

12.1 List of Named Compounds

Synthesized compounds are numbered with Arabic numerals, while calculated model compounds are numbered with Roman numerals.

Table 72: List of numbers assigned to compounds discussed in this thesis

number	compound	number	compound
<u>1</u>	$[\text{NBu}_4]^+[\text{pftb}]^-$	<u>15</u>	$[\text{Cl}_3]^+[\text{pftb}]^-$
<u>2</u>	$[\text{NEt}_4]^+[\text{pftb}]^-$	<u>16</u>	$[\text{Cl}_3]^+[\text{al-f-al}]^-$
<u>3</u>	$[\text{NMe}_4]^+[\text{pfip}]^-$	<u>17</u>	$[\text{Ag}(\text{CH}_2\text{I}_2)_3]^+[\text{pftb}]^-$
<u>4</u>	$[\text{NBu}_4]^+[\text{hfip}]^-$	<u>18</u>	$[\text{Ag}(\text{CH}_2\text{Cl}_2)(\text{CH}_2\text{I}_2)]^+[\text{pftb}]^-$
<u>5</u>	$[\text{NEt}_4]^+[\text{hfip}]^-$	<u>19</u>	$[\text{I}_3\text{C-PCl}_3]^+[\text{pftb}]^-$
<u>6</u>	$[\text{NMe}_4]^+[\text{hfip}]^-$	<u>20</u>	$[\text{I}_3\text{C-PBr}_3]^+[\text{pftb}]^-$
<u>7</u>	$[\text{NBu}_4]^+[\text{hftb}]^-$	<u>21</u>	$[\text{I}_3\text{C-PI}_3]^+[\text{pftb}]^-$
<u>8</u>	$[\text{NEt}_4]^+[\text{hftb}]^-$	<u>22</u>	$[\text{I}_3\text{C-AsI}_3]^+[\text{pftb}]^-$
<u>9</u>	$[\text{NMe}_4]^+[\text{hftb}]^-$	<u>23</u>	$[\text{I}_3\text{C-PI}_3]^+[\text{al-f-al}]^-$
<u>10</u>	$[\text{NBu}_4]^+[\text{al-f-al}]^-$	<u>24</u>	$[\text{PI}_4]^+[\text{pftb}]^-$
<u>11</u>	$[(\text{P}_4\text{S}_3)\text{Ag}[\text{hfip}]]$	<u>25</u>	$[\text{NO}_2]^+[\text{pftb}]^-$
<u>12</u>	$[\text{Ag}(\text{P}_4\text{S}_3)_2][\text{pftb}]$	<u>26</u>	$[\text{NO}_2]^+[\text{BF}_4]^-$
<u>13</u>	$[(\text{P}_4\text{S}_3)\text{Ag}[\text{hftb}]]$	<u>27</u>	$[\text{Li}_2(3,4\text{-C}_6\text{H}_3\text{F}_2\text{NO}_2)_6]^{2+}[\text{pftb}]^-_2$
<u>14</u>	$[\text{Ag}_2(\text{P}_4\text{S}_3)_6]^{2+}[\text{al-f-al}]^-_2$	<u>28</u>	$3,4\text{-C}_6\text{H}_3\text{F}_2\text{NO}_2 \cdot \text{Al}(\text{OC}(\text{CF}_3)_3)_3$

12.2 Appendix to Chapter 3

Total Energies and Structural Parameters of Selected WCAs and their Parent Lewis Acids

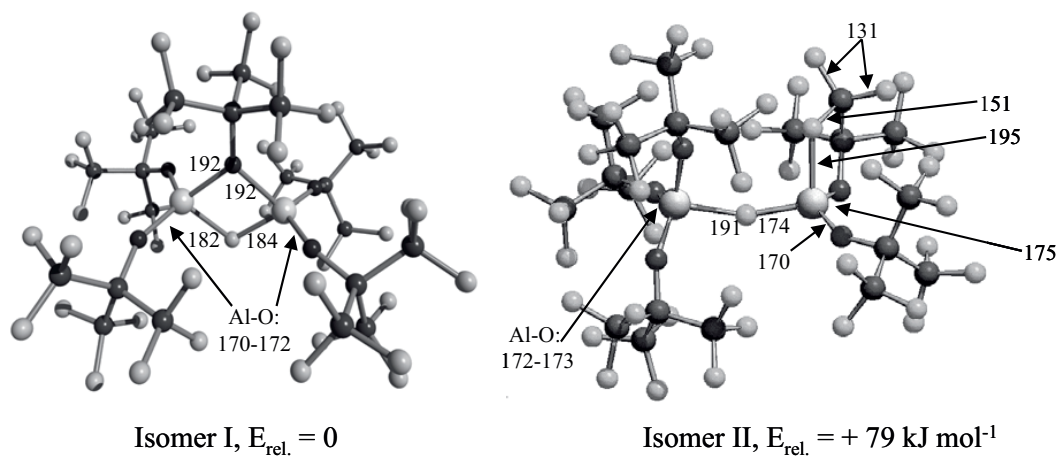


Figure 94: Calculated structures of the two isomers of $\text{Al}_2(\text{OR})_5\text{F}$ (with $\text{R} = \text{C}(\text{CF}_3)_3$) at the (RI)BP86/SV(P) level. Isomer II was obtained by simply deleting one OR ligand of the structure of the $[(\text{RO})_3\text{Al-F-Al}(\text{OR})_3]^-$ anion and optimizing the resulting neutral while isomer I was preoptimized with molecular mechanics and subsequently fully optimized by DFT. Isomer I may be viewed as the thermodynamic product of OR^- abstraction from $[(\text{RO})_3\text{Al-F-Al}(\text{OR})_3]^-$ and isomer II as the kinetic (vertical) product. Bond distances are given in pm.

Table 73: Total energies (BP86/SV(P)) and selected structural parameters of BF_3 , BF_4^- , MF_5 , MF_6^- (M = P, As, Sb), Sb_2F_{10} , $\text{Sb}_2\text{F}_{11}^-$, Sb_3F_{15} , $\text{Sb}_3\text{F}_{16}^-$, Sb_4F_{20} and $\text{Sb}_4\text{F}_{21}^{-[372]}$.

species	total energy [H]	$d(\text{M-F}_{\text{terminal}})$ [pm]	Exp.: $d(\text{M-F}_{\text{terminal}})$ [pm]	$d(\text{M-F}_{\text{bridge}})$ [pm]	Exp.: $d(\text{M-F}_{\text{bridge}})$ [pm]
BF_3	-324.31769	132	130	-	-
BF_4^-	-424.20099	142	137	-	-
PF_5	-840.24920	ax.: 161 eq.: 159	ax.: 158 eq.: 153	-	-
PF_6^-	-940.15393	165	158	-	-
AsF_5	-2734.77740	ax.: 174 eq.: 172	ax.: 171 eq.: 166	-	-
AsF_6^-	-2834.69432	177	168	-	-
SbF_5	-504.34073	ax.: 191 eq.: 193	-	-	-
SbF_6^-	-604.28148	196	188	-	-
Sb_2F_{10}	-1008.72990	191-192	-	214 (2x)	-
$\text{Sb}_2\text{F}_{11}^-$	-1108.68393	193-194	av.: 185	212	av.: 202
Sb_3F_{15}	-1513.10046	191	181	211-212 (3x)	204-205
$\text{Sb}_3\text{F}_{16}^-$ (trans)	-1613.06689	192-193	181-184	218 (2x, outer)	197
				206 (2x, center)	210
Sb_4F_{20}	-2017.47178	191	182	211-212 (4x)	av.: 203
$\text{Sb}_4\text{F}_{21}^-$ (trans)	-2117.43906	192-193	184-185	221 (2x, outer)	210
				203 (2x, middle)	198
				211 (2x, center)	201

12.3 Appendix to Chapter 5

*Solid-State Structure of $[\text{NEt}_4]^+[\text{pftb}]^-$ **2***

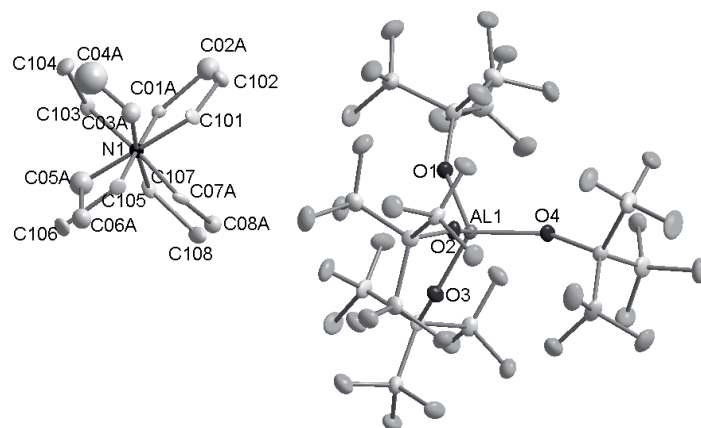


Figure 95: Section of the solid-state structure of $[\text{NEt}_4]^+[\text{pftb}]^-$ **2** at 100K. Thermal ellipsoids are drawn at the 25% probability level. In the asymmetric unit, there is one entire disordered cation and one entire anion. H atoms at the ethyl groups have been omitted for clarity. Selected distances and bond angles: $d(\text{Al1}-\text{O1}) = 172.3(4)$ pm, $d(\text{Al1}-\text{O2}) = 172.8(4)$ pm, $d(\text{Al1}-\text{O3}) = 174.2(4)$ pm, $d(\text{Al1}-\text{O4}) = 174.2(4)$ pm, $\angle(\text{O4}-\text{Al1}-\text{O1}) = 107.6(2)^\circ$, $\angle(\text{O4}-\text{Al1}-\text{O3}) = 113.7(2)^\circ$, $\angle(\text{O1}-\text{Al1}-\text{O3}) = 108.1(2)^\circ$, $\angle(\text{O4}-\text{Al1}-\text{O2}) = 107.7(2)^\circ$, $\angle(\text{O1}-\text{Al1}-\text{O2}) = 112.7(2)^\circ$, $\angle(\text{O3}-\text{Al1}-\text{O2}) = 107.2(2)^\circ$.

*Solid-State Structure of $[\text{NBu}_4]^+[\text{al-f-al}]^-$ **10***

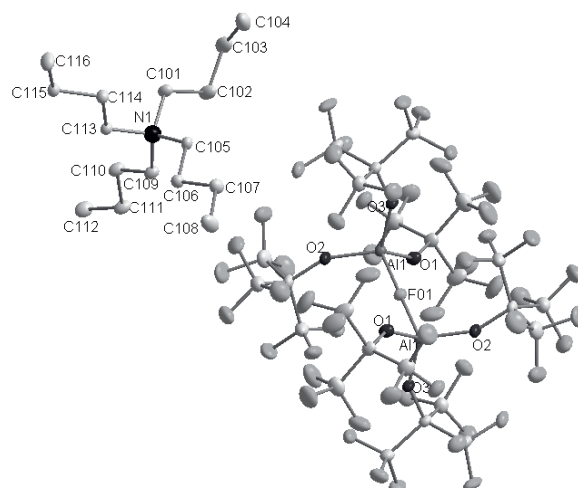


Figure 96: Section of the solid-state structure of $[\text{NBu}_4]^+[\text{al-f-al}]^-$ **10** at 150K. Thermal ellipsoids are drawn at the 25% probability level. Only one of the two anions and cations is shown. Selected distances and bond angles: $d(\text{Al1}-\text{O1}) = 169.9(2)$ pm, $d(\text{Al1}-\text{O2}) = 169.4(2)$ pm, $d(\text{Al1}-\text{O3}) = 170.0(2)$ pm, $d(\text{Al1}-\text{F01}) = 176.98(9)$ pm, $\angle(\text{F01}-\text{Al1}-\text{O1}) = 99.99(8)^\circ$, $\angle(\text{F01}-\text{Al1}-\text{O3}) = 106.03(8)^\circ$, $\angle(\text{O1}-\text{Al1}-\text{O3}) = 112.74(11)^\circ$, $\angle(\text{F01}-\text{Al1}-\text{O2}) = 108.11(8)^\circ$, $\angle(\text{O1}-\text{Al1}-\text{O2}) = 116.76(11)^\circ$, $\angle(\text{O3}-\text{Al1}-\text{O2}) = 111.85(10)^\circ$.

Cation-Anion Contacts in $[\text{NEt}_4]^+[\text{pftb}]^- \mathbf{2}$:

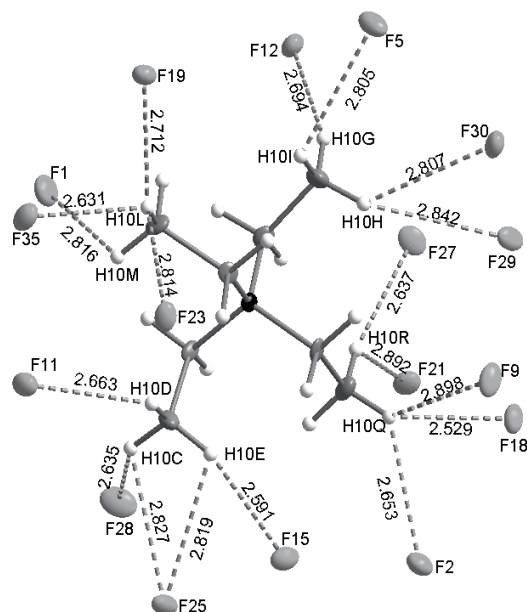


Figure 97: Cation-anion contacts in $[\text{NEt}_4]^+[\text{pftb}]^- \mathbf{2}$ at 100K.

Examples of the Kohlrausch Fits of the Limiting Molar Conductivities of the $[\text{NBu}_4]^+$ Salts:

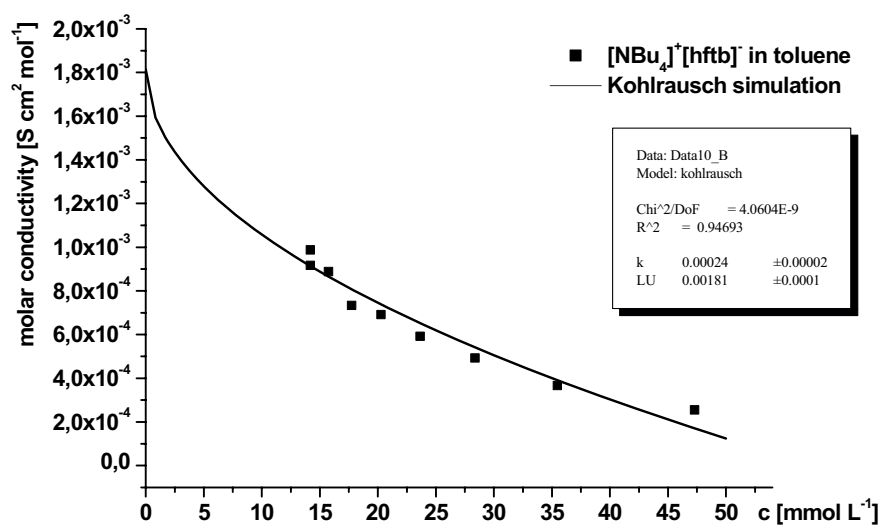


Figure 98: Kohlrausch fit for the molar conductivity of $[\text{NBu}_4]^+[\text{hftb}]^- \mathbf{7}$ in toluene at 25°C.

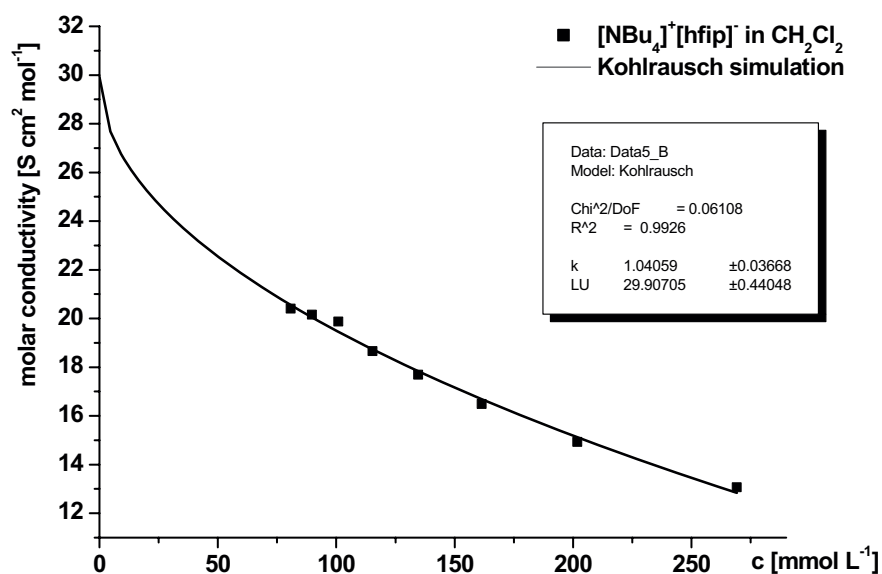


Figure 99: Kohlrausch fit for the molar conductivity of $[\text{NBu}_4]^+[\text{hfip}]^-$ **4** in CH_2Cl_2 at 25°C.

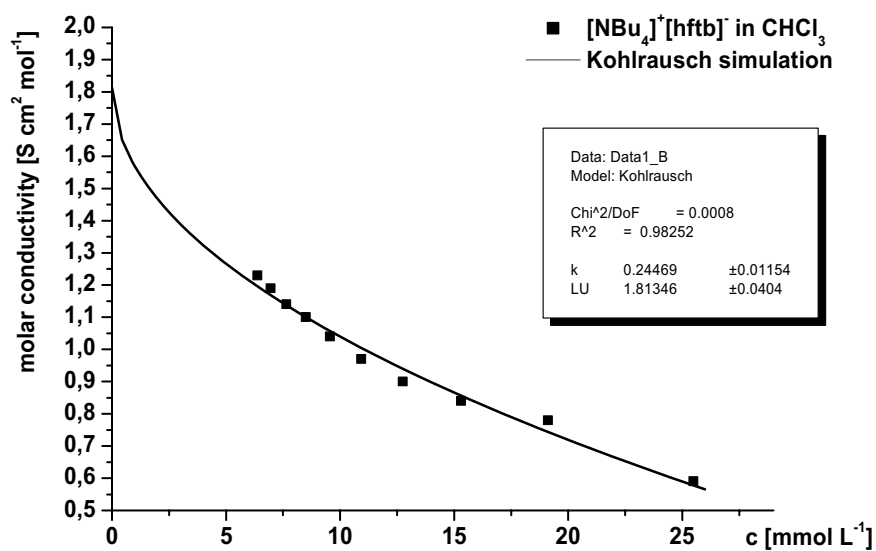


Figure 100: Kohlrausch fit for the molar conductivity of $[\text{NBu}_4]^+[\text{hftb}]^-$ **7** in CHCl_3 at 25°C.

12.4 Appendix to Chapter 6

Solid-State Structures of P_4S_3 :

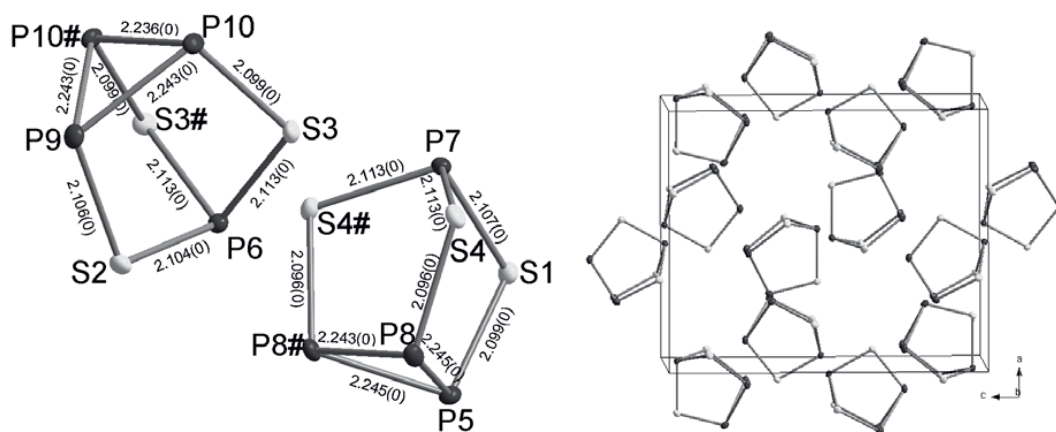


Figure 101: Solid state structure of α - P_4S_3 at 140K: bond lengths in Å (left) and packing diagram (right).

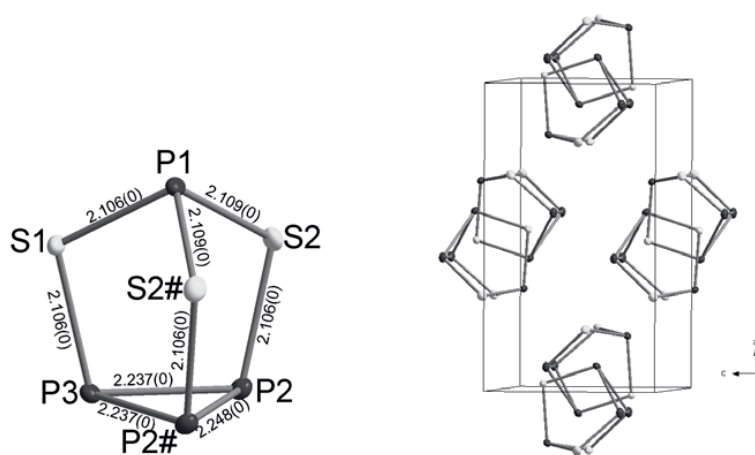


Figure 102: Solid state structure of γ - P_4S_3 at 140K: bond lengths in Å (left) and packing diagram (right).

*Cation-Anion Interactions in **12**:*

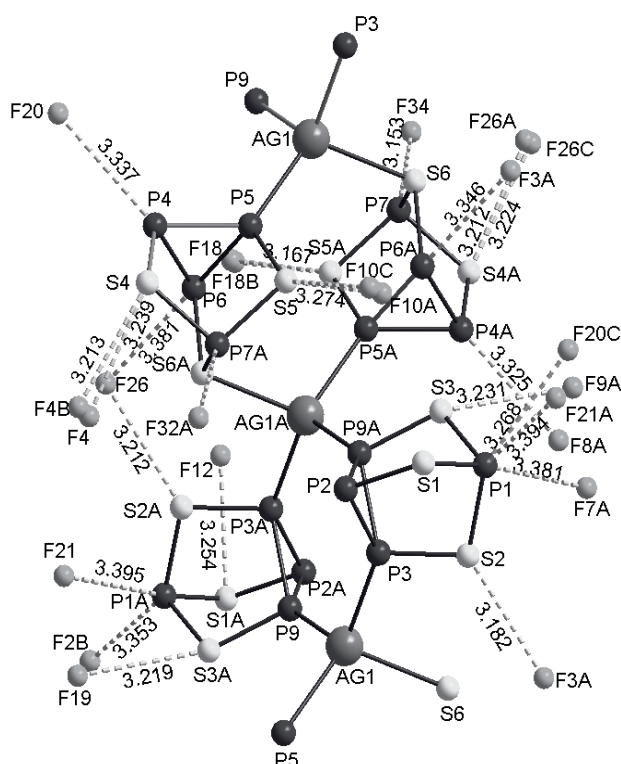


Figure 103: Fluorine contacts in **12** below the Van-der-Waals limits of 340(P+F) and 330 (S+F) pm.

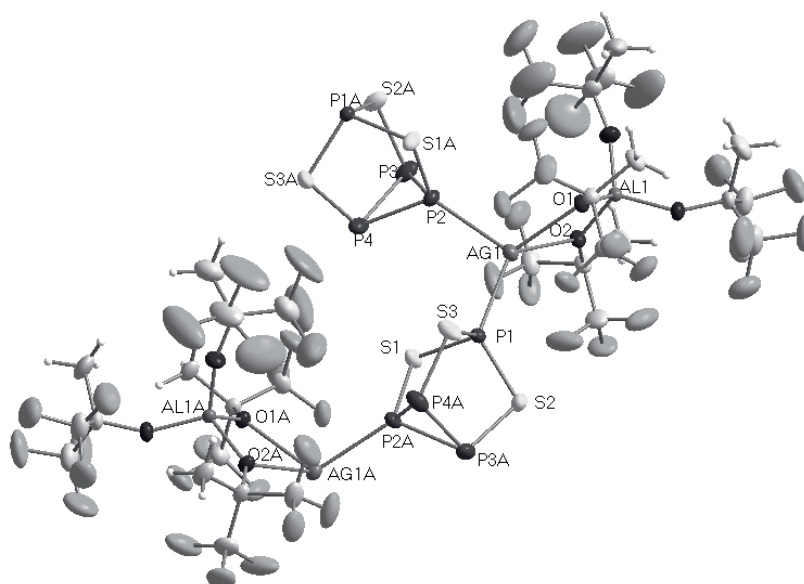


Figure 104: Asymmetric unit of the solid state structure of $[(P_4S_3)Ag[hftb]]$ **7** at 283 K, thermal displacement ellipsoids showing 25 % probability.

12.5 Appendix to Chapter 7

*Solid-State Structure of $[I_3C-PI_3]^+[al-f-al]^-$ **23**:*

23 crystallizes in the monoclinic space group C2/m with $Z = 2$. In this compound, the thermal displacement ellipsoids of the anion are very big, indication motion of the CF_3 groups. The iodine positions of the $I_3CPI_3^+$ cation are well defined (small ellipsoids), but the position of phosphorus and carbon are disordered. Therefore, all E-I bond lengths are nearly the same (224.02 and 224.29 pm), which is in between the C-I and the P-I bond lengths of the $I_3CPI_3^+$ cation in **21** (Table 58).

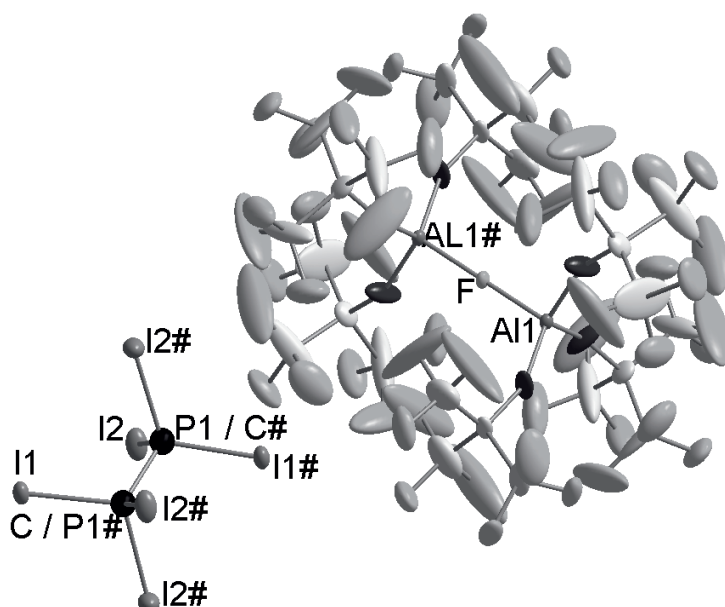


Figure 105: Section of the solid-state structure of $[I_3C-PI_3]^+[al-f-al]^-$ **23** at 150K.

Reaction Enthalpies of the Anion Decomposition Pathways:

Table 74: Reaction enthalpies ($\Delta G^\circ(\text{gas}) / (\Delta G^\circ(\text{CH}_2\text{Cl}_2))$) of the decomposition pathways (a) and (b) from Scheme 8 (BP86/SV(P)). All values are given in kJ/mol. Values are standardized per mole of the cation. Positive values indicate that the anion is thermodynamically stable against decomposition.

	(a)	(a1)	(b)	(b1)
CF_3^+	-319 / -132	-588 / -199	-313 / 128	-317 / 38
CCl_3^+	-214 / -56	-348 / -47	-217 / 60	-124 / 173
CBr_3^+	-195 / -46	-309 / -27	-199 / -52	-88 / 191
Cl_3^+	-176 / -34	-272 / -3	-184 / -43	-58 / 208
HCF_2^+	-302 / -113	-523 / -162	-293 / -106	-276 / 81
HCCl_2^+	-240 / -74	-400 / -84	-236 / -72	-162 / 149
HCBBr_2^+	-227 / -69	-374 / -74	-223 / -68	-137 / 158
HCl_2^+	-212 / -60	-343 / -56	-210 / -62	-110 / 171
H_2CF^+	-320 / -130	-559 / -196	-300 / -112	-290 / 69
H_2CCl^+	-289 / -113	-497 / -161	-268 / -95	-227 / 103
H_2CBr^+	-281 / -111	-482 / -157	-261 / -93	-212 / 107
H_2Cl^+	-272 / -107	-463 / -149	-251 / -89	-193 / 115

Reaction enthalpies of the homolytic E-X bond cleavage of $H_{4-n}EX_n^{-/0}$ and $H_{3-n}EX_n^{0/+}$ ($E=\text{B}, \text{C}$; $X=\text{F-I}$):

Table 75: Reaction enthalpies (in kJ/mol) of the homolytic C-X cleavage in halomethanes.

reaction	F	Cl	Br	I
$\text{H}_3\text{CX} \rightarrow \text{X} + \text{CH}_3$	493	351	297	240
$\text{H}_2\text{CX}_2 \rightarrow 2 \text{X} + \text{CH}_2$	980	707	594	476
$\text{HCX}_3 \rightarrow 3 \text{X} + \text{CH}$	1527	1061	888	708

Table 76: Reaction enthalpies (in kJ/mol) of the homolytic B-X cleavage in haloboranes.

reaction	F	Cl	Br	I
$\text{H}_3\text{BX}^- \rightarrow \text{X} + \text{BH}_3^-$	611	496	444	392
$\text{H}_2\text{BX}_2^- \rightarrow 2 \text{X} + \text{BH}_2^-$	1281	994	877	751
$\text{HBX}_3^- \rightarrow 3 \text{X} + \text{BH}^-$	1959	1459	1266	1058

Table 77: Reaction enthalpies (in kJ/mol) of the homolytic C-X cleavage in halomethyl cations.

reaction	F	Cl	Br	I
$\text{H}_2\text{CX}^+ \rightarrow \text{X} + \text{CH}_2^+$	627	536	479	448
$\text{HCX}_2^+ \rightarrow 2 \text{X} + \text{CH}^+$	1178	975	860	776
$\text{CX}_3^+ \rightarrow 3 \text{X} + \text{C}^+$	1626	1317	1147	1008

Table 78: Reaction enthalpies (in kJ/mol) of the homolytic B-X cleavage in haloboranes.

reaction	F	Cl	Br	I
$\text{H}_2\text{BX} \rightarrow \text{X} + \text{BH}_2$	699	514	424	342
$\text{HBX}_2 \rightarrow 2 \text{X} + \text{BH}$	1341	943	778	614
$\text{BX}_3 \rightarrow 3 \text{X} + \text{B}$	1952	1333	1112	869

Relative Energies of the Isomers \underline{V} of the Water Adducts:

Table 79: Relative energies and E-O distances of $\text{H}_2\text{O}-\text{EX}_3^{0/+1}$ (structure type \underline{V}) at the MP2/TZVPP level.

$\text{EX}_3^{0/+1}$		$E_{\text{rel.}}[\text{kJ/mol}]$	$d(\text{E-O})[\text{pm}]$
CH_3^+	ts	+10.2	149.5
CF_3^+	ts	+8.2	153.6
CCl_3^+	lm	+0.2	272.6
CBr_3^+	lm	+5.4	287.6
Cl_3^+	lm	+14.6	303.9
BH_3	ts	+14.0	170.8
BF_3	ts	+9.0	200.5
BCl_3	ts	+14.6	164.1
BBr_3	ts	+14.7	161.3
BI_3	ts	+15.4	160.5

Packing Diagrams of $[I_3C-PBr_3]^+[pftb]^-$ 20 and $[I_3C-PI_3]^+[pftb]^-$ 21:

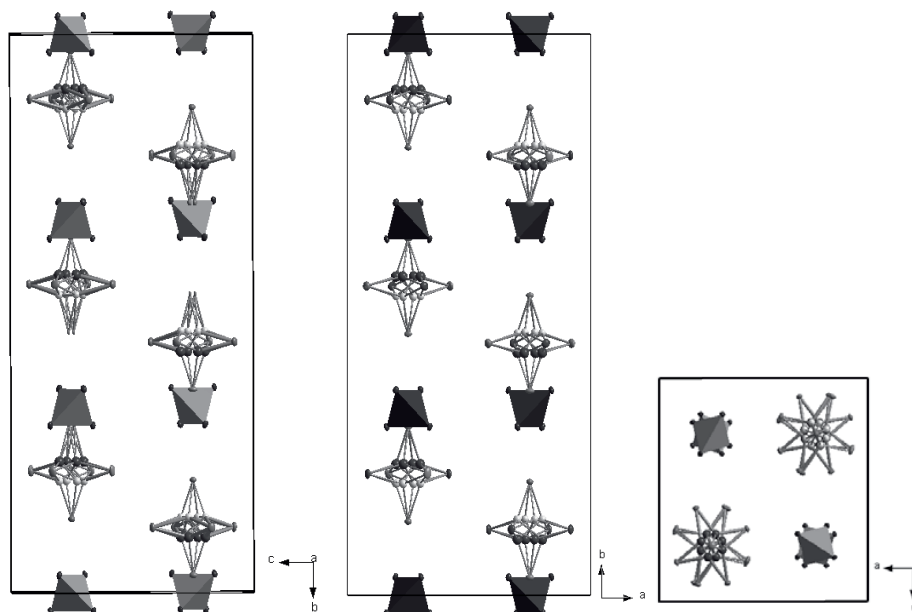


Figure 106: Packing diagram of $[I_3C-PBr_3]^+[pftb]^-$ 20 along the crystallographic axes. The AlO_4^- moieties of the anions are drawn as tetrahedra, the $C(CF_3)_3$ groups have been omitted for clarity.

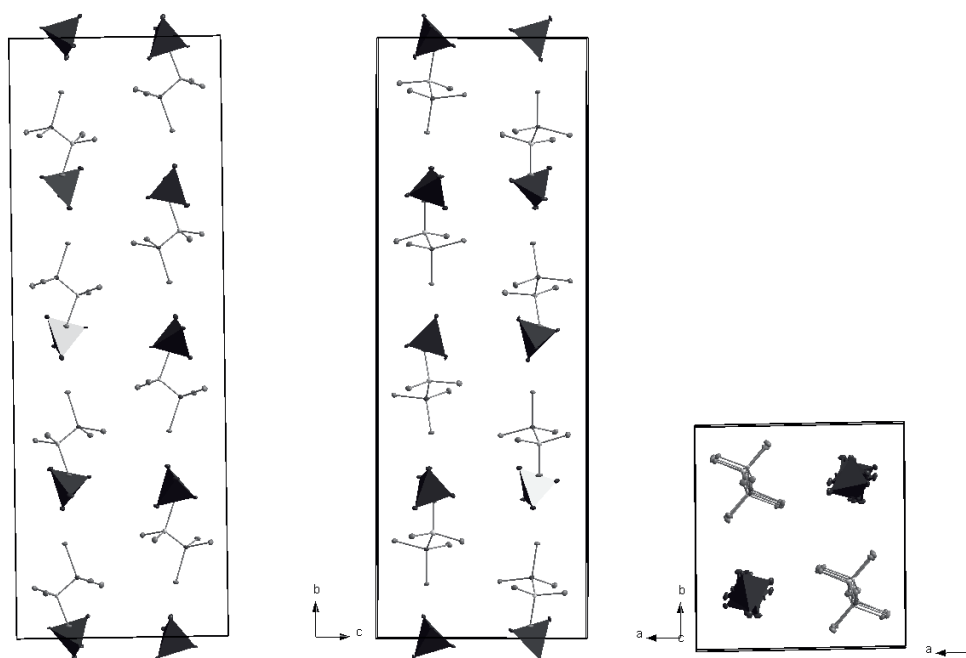


Figure 107: Packing diagram of $[I_3C-PI_3]^+[pftb]^-$ 21 along the crystallographic axes. The AlO_4^- moieties of the anions are drawn as tetrahedra, the $C(CF_3)_3$ groups have been omitted for clarity.

Experimental and Simulated IR Spectra of $[I_3C-PX_3]^+[pftb]^-$ ($X = Br$ 20, I 21):

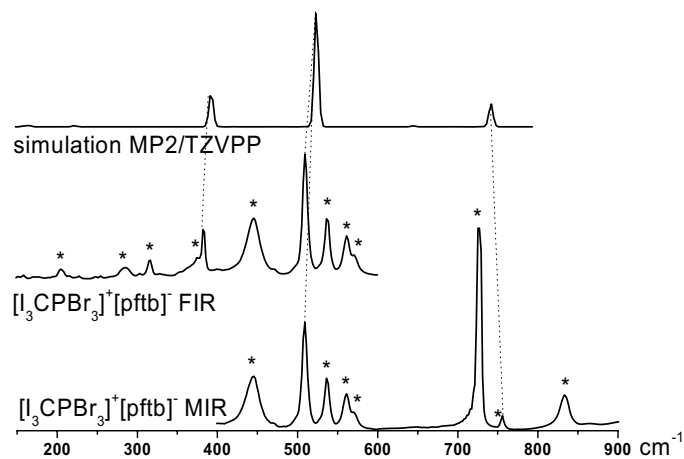


Figure 108: Comparison of the experimental and the simulated IR spectrum of $[I_3CPBr_3]^+[pftb]^-$ 20. Simulation at the MP2/TZVPP level. Bands marked with * can be assigned to the anion.

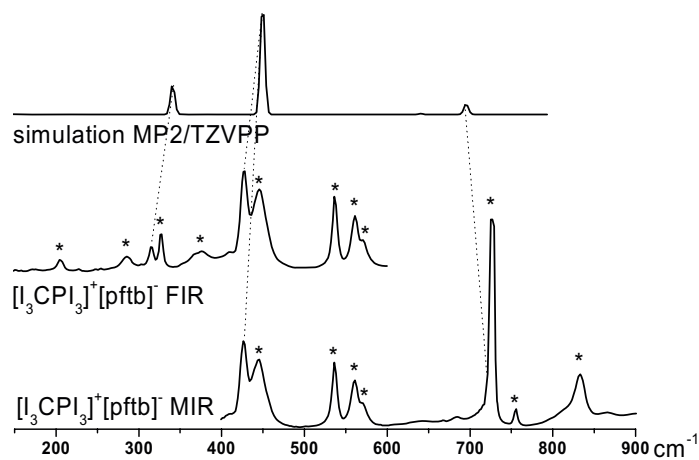


Figure 109: Comparison of the experimental and the simulated IR spectrum of $[I_3CPI_3]^+[pftb]^-$ 21. Simulation at the MP2/TZVPP level. Bands marked with * can be assigned to the anion.

12.6 Crystal Structure Tables

Table 80: Crystallographic details of compounds **2**, **5** and **6**.

	2	5	5	6
database number	-	-	-	-
crystal size [mm]	0.2 x 0.2 x 0.2	0.3 x 0.3 x 0.1	0.2 x 0.3 x 0.2	0.2 x 0.2 x 0.3
crystal system	monoclinic	monoclinic	monoclinic	monoclinic
space group	P2 ₁ /c	P2 ₁ /c	P2 ₁ /c	P2 ₁ /c
<i>a</i> [pm]	1393.6(3)	926.00(19)	925.27(19)	1061.3(2)
<i>b</i> [pm]	1889.7(4)	1900.2(4)	1899.9(4)	1381.1(3)
<i>c</i> [pm]	1420.8(3)	1851.3(4)	1854.6(4)	1898.8(4)
α [°]	90	90	90	90
β [°]	91.43(3)	99.28(3)	99.17(3)	91.42(3)
γ [°]	90	90	90	90
<i>V</i> [nm ³]	3.7405(13)	3.2149(11)	3.2186(11)	2.7822(10)
<i>Z</i>	4	4	4	4
ρ_{calc} [Mg m ⁻³]	1.949	1.705	1.703	1.837
μ [mm ⁻¹]	0.270	0.231	0.231	0.260
abs. correction	none	none	none	none
F (000)	2160	1648	1648	1520
index range	-16 ≤ <i>h</i> ≤ 16 -22 ≤ <i>k</i> ≤ 22 -16 ≤ <i>l</i> ≤ 16	-10 ≤ <i>h</i> ≤ 10 -22 ≤ <i>k</i> ≤ 22 -21 ≤ <i>l</i> ≤ 21	-11 ≤ <i>h</i> ≤ 8 -23 ≤ <i>k</i> ≤ 23 -22 ≤ <i>l</i> ≤ 18	-13 ≤ <i>h</i> ≤ 13 -17 ≤ <i>k</i> ≤ 17 -24 ≤ <i>l</i> ≤ 24
Max 2 θ	49.42	49.42	51.92	54.60
<i>T</i> [K]	100(2)	100(2)	140(2)	100(2)
diffractometer type	BRUKER APEX II	BRUKER APEX II	KUMA CCD	BRUKER APEX II
unique reflns. [<i>I</i> > 2 σ (<i>I</i>)]	6241	5085	5968	6274
Data / restraints / parameters	6241 / 42 / 672	5085 / 0 / 491	5968 / 0 / 527	6274 / 0 / 416
GOOF	1.660	1.049	1.024	1.036
final R1 [<i>I</i> > 2 σ (<i>I</i>)]	0.1128	0.0731	0.0563	0.0378
final <i>w</i> R2	0.3314	0.1345	0.1419	0.0934
largest residual peak [e Å ⁻³]	0.877	0.446	0.372	0.821
largest residual hole [e Å ⁻³]	-0.845	-0.376	-0.424	-0.385

Table 80 continued: Crystallographic details of compounds **7**, **9**, **10** and **12**.

	7	9	10	12
database number	-	-	-	CCDC 625079
crystal size [mm]	0.3 x 0.3 x 0.4	0.2 x 0.2 x 0.1	0.2 x 0.5 x 0.5	0.3 x 0.3 x 0.4
crystal system	monoclinic	tetragonal	triclinic	monoclinic
space group	P2 ₁ /c	I-4	P-1	P2 ₁
<i>a</i> [pm]	1758.0(4)	1291.70(18)	1282.2(3)	16.360(3)
<i>b</i> [pm]	1410.2(3)	1291.70(18)	1923.0(4)	10.954(2)
<i>c</i> [pm]	1958.1(4)	9.3184(19)	2487.1(5)	26.516(5)
α [°]	90	90	88.35(3)	90
β [°]	115.41(3)	90	86.72(3)	94.66(3)
γ [°]	90	90	98.21(3)	90
<i>V</i> [nm ³]	4.3848(15)	1.5548(4)	6.21(1)	4736.1(16)
<i>Z</i>	4	2	4	2
ρ_{calc} [Mg m ⁻³]	1.505	1.763	1.873	2.232
μ [mm ⁻¹]	0.184	0.239	0.261	1.242
abs. correction	none	none	none	numerical
F (000)	2032	824	3408	3064
index range	-20 ≤ <i>h</i> ≤ 20	-17 ≤ <i>h</i> ≤ 17	-15 ≤ <i>h</i> ≤ 15	<i>h</i> : -13 to 20
	-16 ≤ <i>k</i> ≤ 13	-17 ≤ <i>k</i> ≤ 17	-23 ≤ <i>k</i> ≤ 23	<i>k</i> : -13 to 12
	-21 ≤ <i>l</i> ≤ 23	-12 ≤ <i>l</i> ≤ 12	-30 ≤ <i>l</i> ≤ 30	<i>l</i> : -32 to 31
Max 2 θ	49.42	57.80	52.04	51.96
<i>T</i> [K]	100(2)	100(2)	150(2)	150
diffractometer type	BRUKER APEX II	BRUKER APEX II	STOE IPDS II	STOE IPDS II
unique reflns. [<i>I</i> > 2 σ (<i>I</i>)]	7225	2054	23694	13100
Data / restraints / parameters	7225 / 0 / 560	2054 / 0 / 137	23694 / 149 / 2216	13100 / 235 / 1788
GOOF	1.064	1.040	1.051	1.042
final R1 [<i>I</i> > 2 σ (<i>I</i>)]	0.0428	0.0244	0.0753	0.0299
final <i>w</i> R2	0.0849	0.0608	0.1999	0.0775
largest residual peak [e Å ⁻³]	0.542	0.215	1.500	0.559
largest residual hole [e Å ⁻³]	-0.323	-0.144	-1.377	-0.474

Table 80 continued: Crystallographic details of compound **13**, γ -P₄S₃ and α -P₄S₃.

	13	13	γ -P ₄ S ₃	α -P ₄ S ₃
database number	CCDC 625080	CCDC 625081	CSD 417155	CSD 417154
crystal size [mm]	0.4 x 0.4 x 0.4	0.3 x 0.3 x 0.2	0.2 x 0.2 x 0.2	0.2 x 0.2 x 0.2
crystal system	triclinic	triclinic	orthorhombic	orthorhombic
space group	P1	P1	Pnma	Pnma
<i>a</i> [pm]	10.547(2)	10.656(2)	10.8734(10)	10.4738(7)
<i>b</i> [pm]	11.443(2)	11.596(2)	9.7634(9)	9.5861(7)
<i>c</i> [pm]	14.459(3)	14.477(3)	6.4321(6)	13.6715(10)
α [°]	89.94(3)	89.96(3)	90	90
β [°]	83.50(3)	83.40(3)	90	90
γ [°]	89.90(3)	89.90(3)	90	90
<i>V</i> [nm ³]	1733.7(6)	1777.1(6)	682.84(11)	1372.66(17)
<i>Z</i>	2	2	4	8
ρ_{calc} [Mg m ⁻³]	2.067	2.017	2.141	2.130
μ [mm ⁻¹]	1.128	1.101	1.896	1.886
abs. correction	empirical	empirical	empirical	empirical
F (000)	1048	1048	432	864
index range	<i>h</i> : -13 to 13 <i>k</i> : -14 to 14 <i>l</i> : -18 to 18	<i>h</i> : -16 to 16 <i>k</i> : -14 to 18 <i>l</i> : -21 to 21	<i>h</i> : -14 to 14 <i>k</i> : -11 to 10 <i>l</i> : -8 to 8	<i>h</i> : -13 to 13 <i>k</i> : -12 to 13 <i>l</i> : -18 to 18
Max 2 θ	54.00	69.22	58.32	58.38
<i>T</i> [K]	100	283	140	140
diffractometer type	BRUKER APEX II	BRUKER APEX II	Oxford KM4 / CCD	Oxford KM4 / CCD
unique reflns. [<i>I</i> > 2 σ (<i>I</i>)]	15640	17701	854	1800
Data / restraints / parameters	15640 / 3 / 957	17701 / 3 / 957	854 / 0 / 37	1800 / 0 / 73
GOOF	1.147	1.018	0.946	1.071
final R1 [<i>I</i> > 2 σ (<i>I</i>)]	0.0165	0.0570	0.0173	0.0278
final <i>w</i> R2	0.0441	0.165	0.0439	0.0682
largest residual peak [e Å ⁻³]	0.448	1.676	0.252	0.556
largest residual hole [e Å ⁻³]	-0.342	-0.786	-0.291	-0.322

Table 80 continued: Crystallographic details of compounds **14**, **15**, **16** and **17**.

	14	15	16	17
database number	CCDC 625082	CCDC 193387	CCDC 646518	CCDC 646517
crystal size [mm]	0.5 x 0.08 x 0.08	0.25 x 0.08 x 0.08	0.35 x 0.35 x 0.1	0.7 x 0.4 x 0.2
crystal system	monoclinic	orthorhombic	monoclinic	monoclinic
space group	P2 ₁	Pna2 ₁	P2 ₁ /c	P2 ₁ /c
<i>a</i> [pm]	1751.8(4)	1969.8(4)	2083.6(4)	1039.7(2)
<i>b</i> [pm]	1254.8(3)	955.40(19)	1780.2(4)	1472.7(3)
<i>c</i> [pm]	3004.6(6)	1843.5(4)	1387.4(3)	2894.6(6)
α [°]	90	90	90	90
β [°]	91.26(3)	90	108.12(3)	97.13(3) ^o
γ [°]	90	90	90	90
<i>V</i> [nm ³]	6.603(2)	3.4694(12)	4.8909(17)	4.3978(15)
<i>Z</i>	2	4	4	4
ρ_{calc} [Mg m ⁻³]	2.625	2.603	2.548	2.837
μ [mm ⁻¹]	1.104	2.951	2.205	4.873
abs. correction	numerical	numerical	numerical	numerical
<i>F</i> (000)	4336	2520	3512	3416
index range	<i>h</i> : -21 to 21	-23 ≤ <i>h</i> ≤ 19	0 ≤ <i>h</i> ≤ 24	-11 ≤ <i>h</i> ≤ 11
	<i>k</i> : -15 to 10	-11 ≤ <i>k</i> ≤ 10	-20 ≤ <i>k</i> ≤ 0	-16 ≤ <i>k</i> ≤ 16
	<i>l</i> : -35 to 36	-21 ≤ <i>l</i> ≤ 21	-16 ≤ <i>l</i> ≤ 15	-32 ≤ <i>l</i> ≤ 32
Max 2 θ	52.06	49.96	49.00	47.92
<i>T</i> [K]	130	150(2)	150(2)	140(2)
diffractometer type	STOE IPDS II	STOE IPDS II	STOE IPDS II	STOE IPDS II
unique reflns. [<i>I</i> > 2 σ (<i>I</i>)]	11686	6006	7857	6459
Data / restraints / parameters	11686 / 0 / 982	6006 / 103 / 607	7857 / 0 / 824	6459 / 0 / 605
GOOF	0.973	0.987	0.938	1.053
final R1 [<i>I</i> > 2 σ (<i>I</i>)]	0.0542	0.0671	0.0548	0.0720
final <i>w</i> R2	0.1345	0.1550	0.1367	0.1883
largest residual peak [e Å ⁻³]	0.855	1.91	1.434	1.617
largest residual hole [e Å ⁻³]	-0.673	-1.69	-1.114	-2.174

Table 80 continued: Crystallographic details of compounds **19**, **20**, **21** and **23**.

	19	20	21	23
database number	-	-	-	-
crystal size [mm]	0.2 x 0.1 0.1	0.2 x 0.1 x 0.1	0.2 x 0.1 x 0.1	0.2 x 0.3 x 0.4
crystal system	monoclinic	monoclinic	monoclinic	monoclinic
space group	P2 ₁ /c	P2 ₁ /n	P2 ₁ /n	C2/m
<i>a</i> [pm]	1383.2(3)	1392.0(3)	1446.6(3)	1324.3(3)
<i>b</i> [pm]	1383.3(3)	3003.5(6)	3894.4(8)	1632.5(3)
<i>c</i> [pm]	1988.6(4)	1392.4(3)	1462.3(3)	1313.9(3)
α [°]	90	90	90	90
β [°]	90.01	90.00(3)	90.53(3)	94.75(3)
γ [°]	90	90	90	90
<i>V</i> [nm ³]	3.8049(13)	5.821(2)	8.238(3)	2.8309(10)
<i>Z</i>	4	6	8	2
ρ_{calc} [Mg m ⁻³]	2.614	2.791	2.857	2.402
μ [mm ⁻¹]	2.948	5.773	4.778	3.556
abs. correction	multiscan	multiscan	multiscan	numeric
F (000)	2784	4500	6432	1864
index range	-20 ≤ <i>h</i> ≤ 20	-19 ≤ <i>h</i> ≤ 19	-15 ≤ <i>h</i> ≤ 15	-16 ≤ <i>h</i> ≤ 16
	-20 ≤ <i>k</i> ≤ 20	-41 ≤ <i>k</i> ≤ 42	-42 ≤ <i>k</i> ≤ 42	-20 ≤ <i>k</i> ≤ 20
	-29 ≤ <i>l</i> ≤ 29	-19 ≤ <i>l</i> ≤ 19	-15 ≤ <i>l</i> ≤ 16	-16 ≤ <i>l</i> ≤ 16
Max 2 θ	64.52	61.18	45.98	52.00
<i>T</i> [K]	108(2)	100(2)	100(2)	150(2)
diffractometer type	BRUKER	BRUKER	BRUKER	STOE IPDS II
	APEX II	APEX II	APEX II	
unique reflns. [<i>I</i> > 2 σ (<i>I</i>)]	13942	17862	11204	2876
Data / restraints / parameters	13942 / 0 / 637	17862 / 0 / 967	11204 / 60 / 1172	2876 / 43 / 247
GOOF	1.009	1.023	1.082	1.043
final R1 [<i>I</i> > 2 σ (<i>I</i>)]	0.0428	0.0697	0.0885	0.00682
final wR2	0.1026	0.1841	0.2176	0.1871
largest residual peak [e Å ⁻³]	2.404	2.366	3.336	1.544
largest residual hole [e Å ⁻³]	-0.796	-3.305	-3.180	-1.552

Table 80 continued: Crystallographic details of compounds **24**, **25**, **26** and **28**.

	24	25	26	28
database number	-	-	-	-
crystal size [mm]	0.3 x 0.2 x 0.2	0.1 x 0.5 x 0.2	0.2 x 0.2 x 0.4	0.3 x 0.3 x 0.1
crystal system	monoclinic	monoclinic	monoclinic	triclinic
space group	P2 ₁ /n	Cc	P2 ₁ /c	P-1
<i>a</i> [pm]	1378.9(3)	1942.7(4)	655.67(13)	1058.4(2)
<i>b</i> [pm]	1947.1(4)	951.38(19)	682.43(14)	1308.8(3)
<i>c</i> [pm]	1400.0(3)	1893.0(4)	912.44(18)	2270.4(5)
α [°]	90	90	90	101.06(3)
β [°]	90.09(3)	120.05(3)	104.40(3)	96.99(3)
γ [°]	90	90	90	113.35(3)
<i>V</i> [nm ³]	3.7589(13)	3.0286(11)	3.9544(14)	2.7649(10)
<i>Z</i>	4	4	4	4
ρ_{calc} [Mg m ⁻³]	2.661	2.222	0.558	2.141
μ [mm ⁻¹]	3.589	0.328	0.075	0.306
abs. correction	numerical	none	none	multiscan
F (000)	2768	1952	64	1728
index range	-16 ≤ <i>h</i> ≤ 16	-23 ≤ <i>h</i> ≤ 21	-8 ≤ <i>h</i> ≤ 8	-12 ≤ <i>h</i> ≤ 13
	-23 ≤ <i>k</i> ≤ 23	-11 ≤ <i>k</i> ≤ 11	-8 ≤ <i>k</i> ≤ 8	-16 ≤ <i>k</i> ≤ 16
	-17 ≤ <i>l</i> ≤ 17	-20 ≤ <i>l</i> ≤ 23	-11 ≤ <i>l</i> ≤ 11	-29 ≤ <i>l</i> ≤ 27
Max 2 θ	52.04	51.94	52.00	55.96
<i>T</i> [K]	150(2)	150(2)	100(2)	100(2)
diffractometer type	STOE IPDS II	STOE IPDS II	STOE IPDS II	RIGAKU SPIDER
unique reflns. [<i>I</i> > 2 σ (<i>I</i>)]	7303	4752	768	11235
Data / restraints / parameters	7303 / 300 / 767	4752 / 89 / 582	768 / 0 / 73	11235 / 30 / 1021
GOOF	1.127	1.054	1.156	1.050
final R1 [<i>I</i> > 2 σ (<i>I</i>)]	0.1037	0.0684	0.0185	0.1268
final <i>w</i> R2	0.2005	0.1673	0.0597	0.3051
largest residual peak [e Å ⁻³]	1.607	0.676	0.130	1.703
largest residual hole [e Å ⁻³]	-1.855	-0.433	-0.123	-1.122

12.7 Publications and Conference Contributions

Publications in journals:

- Raabe, Ines; Himmel, Daniel; Krossing, Ingo: “A computational study of the enthalpies of formation $\Delta_f H^\circ$ and mean bond enthalpies (*mBEs*) of $H_{4-n}EX_n^{0/-}$ and $H_{3-n}EX_n^{+/0}$ (E = C, B; X = F-I)”, *Journal of Physical Chemistry A*, submitted.
- Raabe, Ines; Röhr, Caroline; Krossing, Ingo. “Exploring the chemistry of free Cl_3^+ : reactions with the weak Lewis bases PX_3 (X = Cl-I), AsI_3 and Et_2O ”, *Journal of the Chemical Society, Dalton Transactions*, in preparation.
- Raabe, Ines; Wagner, Katrin; Gutsche, Kristin; Steinfeld, Gunther, Krossing, Ingo. “Tetraalkylammonium salts of weakly coordinating aluminates: Materials for electrochemical applications and useful compounds for anion investigation”, *Journal of the Chemical Society, Dalton Transactions*, in preparation.
- Krossing, Ingo, Raabe, Ines. $[NBu_4]^+[(OC(CF_3)_3)_3Al-F-Al(OC(CF_3)_3)_3]^-$, *Acta Crystallographica E*, submitted.
- Krossing, Ingo; Raabe, Ines; Wagner, Katrin. “ $[(Li(OC(CF_3)_3)_2 \cdot 5 H_2O)]^+$ ”, *Acta Crystallographica C*, in preparation.
- Raabe, Ines; Müller, Sonja; Trapp, Nils; Kaupp, Martin; Krossing, Ingo. “Stable Cl_3^+ salts and attempts to prepare CHI_2^+ and CH_2I^+ ”, *Chemistry – A European Journal*, submitted.
- Raabe, Ines; Antonijevic, Saša; Krossing, Ingo. “Weakly bound cationic $Ag(P_4S_3)$ complexes – dynamics and counterion-dependence of their structures”, *Chemistry – A European Journal*, in press.
- Krossing, Ingo; Raabe, Ines; Birtalan, Esther. “Nitronium tetrafluoroborate”, *Acta Crystallographica* 2007, E63, i43 – i44.

- Jenkins, H. Donald Brooke; Krossing, Ingo; Passmore, Jack; Raabe, Ines. “A computational study of Sb_nF_{5n} ($n = 1-4$). Implications for the fluoride ion affinity of n SbF_5 ”, *Journal of Fluorine Chemistry* 2004, 125, 1585 – 1592.
- Bihlmeier, Angela; Gonsior, Marcin; Raabe, Ines; Trapp, Nils; Krossing, Ingo. “From weakly coordinating to non-coordinating anions? A simple preparation of the silver salt of the least coordinating anion and its application to determine the ground state structure of the $\text{Ag}(\eta^2\text{-P}_4)_2^+$ cation”, *Chemistry–A European Journal* 2004, 10(20) 5041 – 5051.
- Krossing, Ingo; Raabe, Ines. “Relative stabilities of weakly coordinating anions: A computational study”, *Chemistry–A European Journal* 2004, 10(20), 5017 – 5030.
- Krossing, Ingo; Raabe, Ines. “Water Adducts of BX_3 and CX_3^+ : Implications for structure, bonding and reactivity”, *Journal of the American Chemical Society* 2004, 126(24), 7571 – 7577.
- Krossing, Ingo; Raabe, Ines. “Noncoordination anions - Fact or fiction? A survey of likely candidates”, *Angewandte Chemie, International Edition* 2004, 43(16), 2066 – 2090.
- Krossing, Ingo; Bihlmeier, Angela; Raabe, Ines; Trapp, Nils. “Structure and characterization of $\text{Cl}_3^+[\text{Al}\{\text{OC}(\text{CF}_3)_3\}_4]^-$; Lewis acidities of CX_3^+ and BX_3 ”, *Angewandte Chemie, International Edition* 2003, 42(13), 1531 – 1534.
- Gonsior, Marcin; Krossing, Ingo; Müller, Lutz; Raabe, Ines; Jansen, Martin; van Wüllen, Leo. „ PX_4^+ , P_2X_5^+ and P_5X_2^+ ($\text{X} = \text{Br}, \text{I}$) salts of the superweak $\text{Al}(\text{OR})_4^-$ anion [$\text{R} = \text{C}(\text{CF}_3)_3$]”, *Chemistry – A European Journal* 2002, 8, 4475 – 4492.
- Krossing, Ingo; Raabe, Ines. “ P_5X_2^+ ($\text{X} = \text{Br}, \text{I}$), a phosphorus-rich binary P-X cation with a C_{2v} -symmetric P_5 cage”, *Angewandte Chemie, International Edition* 2001, 40(23), 4406 – 4409.

Conference contributions:

- “Lithium- und Tetraalkylammonium-Salze schwach koordinierender Anionen: Mögliche Materialien für den Einsatz in der Elektrochemie“, lecture, Kolloquium des Freiburger Materialforschungszentrums, Rust, 10 / 2006.
- “Weakly coordinated cationic $\text{Ag}(\text{P}_4\text{S}_3)$ complexes – similar counterions, different structures”, poster contribution, SCS Fall Meeting, Lausanne, 10 / 2005.
- “Weakly coordinated cationic $\text{Ag}(\text{P}_4\text{S}_3)$ complexes – similar counterions, different structures”, poster contribution, GDCh-Jahrestagung Chemie, Düsseldorf, 09 / 2005.
- “Weakly coordinated cationic $\text{Ag}(\text{P}_4\text{S}_3)$ complexes – similar counterions, different structures”, lecture, Doktorandenseminar Phosphorchemie, Bonn, 03 / 2005.
- “Auf dem Weg zu kationischen Phosphorverbindungen“ lecture, Doktorandenseminar Phosphorchemie, Kaiserslautern, 03/2004.
- “[Cl_3][$\text{AlOC}(\text{CF}_3)_3$]₄] – Ein stabiles Salz des Cl_3^+ -Kations” poster contribution, GDCh-Jahrestagung Chemie, München, 10 / 2003.

12.8 Curriculum Vitae

Name	Ines Raabe
Date of birth	8. July 1977
Nationality	german

Education

since 02/2003	PhD work in chemistry in the group of Prof. Dr. Ingo Krossing (University of Karlsruhe, EPF Lausanne, University of Freiburg i.Br.)
01/2003	Diploma in chemistry, University of Karlsruhe (“very good”)
10/1999	“Vorexamen” (undergraduate exam) in food chemistry at the University of Karlsruhe (“good”)
09/1988 – 06/1997	„Abitur“, Gymnasium Neureut in Karlsruhe (“very good”)

Professional Experiences

since 03/2006	Scientific coworker at the Institute of Inorganic and Analytical Chemistry, University of Freiburg i. Br. Assistant in the students’ lab (analytical chemistry) Supervision of an apprentice
10/2004 – 02/2006	Scientific coworker at the Institut des Sciences et Ingénierie Chimiques, EPF Lausanne Assistant in the students’ lab (analytical chemistry, organometallic chemistry)
02/2003 – 09/2004	Scientific coworker at the Institute of Inorganic and Analytical Chemistry, University of Karlsruhe Assistant in the students’ lab (analytical chemistry, advanced inorganic chemistry) Supervision of an apprentice
02/2001 / 09/2001	“Wissenschaftliche Hilfskraft” (part-time lab assistant) at the Institute of Inorganic and Analytical Chemistry, University of Karlsruhe

Languages

German	Native speaker
French	Fluent (written and oral) 9 years at school, 1 ½ year-long stay in Lausanne (participation at language courses up to C1 level), conversational and written French throughout PhD work
English	Fluent (written and oral) 6 years at school, conversational and written English throughout PhD work, writing of scientific publications
Latin	“Kleines Latinum” (3 years at school)